Public reporting burden for this collection of information is estimated to average 1 hour per response, including the time for reviewing instructions, searching existing data sources, gathering and maintaining the data needed, and completing and reviewing the collection of information. Send comments regarding this burden estimate or any other aspect of this collection of information, including suggestions for reducing this burden to Washington Headquarters Services, Directorate for Information Operations and Reports, 1215 Jefferson Davis Highway, Suite 1204, Arlington, VA 22202-4302, and to the Office of Management and Budget, Paperwork Reduction Project (0704-0188), Washington, DC 20503.

1. AGENCY USE ONLY (Leave blank)	2. REPORT DATE	3. REPORT TYPE AND DATES COVERED
	1 December 1998	Conference Proceedings

4. TITLE AND SUBTITLE

XXIII International Conference on Phenomena in Ionized Gases, VOL 4

5. FUNDING NUMBERS

F6170897W0048

6. AUTHOR(S)

Conference Committee

7. PERFORMING ORGANIZATION NAME(S) AND ADDRESS(ES)

Universite Paul Sabatier
118 Route de Narbonne
Toulouse Cedex 31062
France

8. PERFORMING ORGANIZATION REPORT NUMBER

N/A

9. SPONSORING/MONITORING AGENCY NAME(S) AND ADDRESS(ES)

EOARD
PSC 802 BOX 14
FPO 09499-0200

10. SPONSORING/MONITORING AGENCY REPORT NUMBER

CSP 97-1013

11. SUPPLEMENTARY NOTES

One book of Invited Papers and five volumes of Proceedings and Contributed Papers

12a. DISTRIBUTION/AVAILABILITY STATEMENT

Approved for public release; distribution is unlimited.

12b. DISTRIBUTION CODE

A

13. ABSTRACT (Maximum 200 words)

The Final Proceedings for XXIII International Conference on Phenomena in Ionized Gases, 17 July 1997 - 22 July 1997

kinetic, thermodynamics, and transport phenomena; elementary processes; low pressure glows; coronas, sparks, surface discharges, and high pressure glows; arcs; high frequency discharges; ionospheric magnetospheric, and astrophysical plasmas; plasma diagnostic methods; plasma surface effects; plasma processing; plasma flows; non ideal plasmas; waves and instabilities; non-linear phenomena; particle and laser beam interactions with plasmas; plasma sources of radiation; modeling; plasma for environmental issues; plasma thrusters; surface treatment; high pressure, non-thermal plasmas.

14. SUBJECT TERMS

EOARD, Space Environment, Pulsed Power, Astrodynamics, Coatings, Fluids & Lubrication, Electromagnetics, High Power Generation, Lasers

15. NUMBER OF PAGES

Too Many to Count

16. PRICE CODE

N/A

17. SECURITY CLASSIFICATION OF REPORT	18. SECURITY CLASSIFICATION OF THIS PAGE	19. SECURITY CLASSIFICATION OF ABSTRACT	20. LIMITATION OF ABSTRACT
UNCLASSIFIED	UNCLASSIFIED	UNCLASSIFIED	UL

F61708-97-W0048
CSP 97-1013

XXIII International Conference on Phenomena in Ionized Gases

Editors: M.C. Bordage and A. Gleizes

19981216 005

Proceedings

Contributed Papers

Vol. IV

Monday, July 21

Organizers :

Centre de Physique des Plasmas et leurs Applications de Toulouse (CPAT)
Laboratoire de Génie Electrique de Toulouse (LGET)
From the Université Paul Sabatier, Toulouse France.

International Scientific Committee

R. d'Agostino	Italy
J. Allen	Great Britain
A. Bouchoule (Chairman)	France
E. Desoppere	Belgium
H. Kikuchi	Japan
E.E. Kunhardt	USA
J. Mentel	Germany
B. Milic	Yugoslavia
D. Morrow	Australia
A.H. Oien	Norway
A.A. Rukhadze	Russia
M. Sicha	Czech. Republic

Local Organizing Committee

J.P. Bœuf	M.C. Bordage (Sec.)
H. Brunet (co-Chair.)	J.P. Couderc
B. Despax	M. Dziadowiec
A. Gleizes	B. Held
F. Massines	L.C. Pitchford (co-Chair.)
Y. Segui	S. Vacquie
M. Yousfi	G. Zissis

Sponsors

Association pour le Développement de la Physique Atomique (ADPA)
International Union of Pure and Applied Physics (IUPAP)
Centre National de la Recherche Scientifique (CNRS)
Université Paul Sabatier (UPS) of Toulouse
Direction de la Recherche et Technologie (DRET)
Commissariat à l'Energie Atomique (CEA), Cycle de Combustible
Electricité de France through :
Club Arc Electrique, Club Chimie des Hautes Températures and Novelect
Conseil Régional de la Région Midi-Pyrénées
Conseil Général du Département de la Haute-Garonne
Mairie de Toulouse
CRT Plasma-Laser
Union Radio Scientifique Internationale (URSI)
US Department of Energy, US BMDO
US Air Force through the EOARD

The Local Organizing Committee wishes to express appreciation to the following corporations for their support :

AGA S.A.	Thomson Tubes Electroniques
Motorola Semiconducteurs S.A.	Schneider Electric
Osram-Sylvania Inc.	Philips Lighting (for the Penning Award)

FOREWORD

This volume is the fourth of five volumes which contain contributed papers that were accepted by the Local Organizing Committee of the XXIII ICPIG for presentation in poster sessions. These papers are to be listed in the INSPEC data base.

The contributions were submitted in camera-ready form by the authors. Therefore, the responsibility for the contents and the form of the papers rests entirely with the authors.

The first four volumes have been arranged by topics, the sequence of which corresponds to that of the respective poster sessions. The fifth volume is comprised of 'late' papers, those for which the authors registered after the deadline for printing of their papers.

The texts of the invited talks are to be published shortly after the conference in a special issue of Journal de Physique.

The editors would like to acknowledge the contributions of Mrs L. Fourmeaux, Mr J.M. Barachet and Mr J.P. Chaucheprat in the preparation of these volumes. The computer file of contributed papers and authors was prepared by C. de Peco, and her careful execution of this task is gratefully acknowledged.

April 1997 The Editors

For additional copies of this publication, please contact :
M.C. Bordage, CPAT, Université Paul Sabatier, 118 Route de Narbonne, 31062 Toulouse cedex 4 France

Printed in France, in the Université Paul Sabatier of Toulouse , 1997

Topic number	SCHEDULE FOR POSTERS
VOLUME 1	THURSDAY, JULY 17
MORNING	
1	Kinetics, thermodynamics and transport phenomena (Part A)
2	Elementary processes (Part A)
6	High frequency discharges (Part A)
13	Waves and instabilities, including shock waves (Part A)
AFTERNOON	
1	Kinetics, thermodynamics and transport phenomena (Part B)
2	Elementary processes (Part B)
6	High frequency discharges (Part B)
12	Non-ideal plasmas. Clusters and dusty plasmas
13	Waves and instabilities, including shock waves (Part B)
18	Plasmas for environmental issues
VOLUME 2	FRIDAY, JULY 18
MORNING	
3	Low pressure glows (Part A)
5	Arcs (Part A)
17	Numerical modeling (Part A)
AFTERNOON	
3	Low pressure glows (Part B)
5	Arcs (Part B)
11	Generation and dynamics of plasma flows
14	Non-linear phenomena and self-organization processes
17	Numerical modeling (Part B)
VOLUME 3	SATURDAY, JULY 19
7	Ionospheric, magnetospheric, and astrophysical plasmas
16	Plasma sources of radiation
19a	Highly ionized, low pressure plasmas
19b	High pressure, non-thermal plasmas
VOLUME 4	MONDAY, JULY 21
MORNING	
4	Coronas, sparks, surface discharges and high pressure glows (Part A)
8	Plasma diagnostic methods (Part A)
10	Physical aspects of plasma chemistry, plasma processing of surface and thin film technology (Part A)
AFTERNOON	
4	Coronas, sparks, surface discharges and high pressure glows (Part B)
8	Plasma diagnostic methods (Part B)
9	Plasma wall interactions, electrode and surface effects
10	Physical aspects of plasma chemistry, plasma processing of surface and thin film technology (Part B)
15	Particle and laser beam interaction with plasmas
VOLUME 5	LATE PAPERS

CONTENTS

Topic 4 :
Coronas, sparks, surface discharges and high pressure glows.

THE EFFECT OF RELATIVISTIC RUNAWAY ELECTRON AVALANCHES ON X-RAY MODULATION INSIDE THUNDERSTORM — IV-2
Babich L.P., Kutsyk I.M., Kudryavtsev A.Yu.

THE DD-ANALOGY BREAKDOWN CONCEPT — IV-4
Djakov A.F., Bobrov Yu.K.

THE IMPULSE ARC DD-ANALOGY — IV-6
Djakov A.F., Bobrov Yu.K., Bobrova L.N.

POSITIVE-STREAMER PHENOMENA IN POSITIVE AND NEGATIVE POINT-PLANE GAPS IN HYDROGEN — IV-8
Kudelcik J., Surda V., Zahoranova A., Cernak M.

TEMPERATURE MEASUREMENTS BY A SPECTROSCOPIC METHOD IN HIGH-DENSITY NITROGEN POSITIVE CORONA DISCHARGES — IV-10
Nur M., Denat A., Bonifaci N.

NON-THERMAL ELECTRON MOBILITY IN HIGH DENSITY GASEOUS NITROGEN AND ARGON IN DIVERGENT ELECTRIC FIELD — IV-12
Nur M., Bonifaci N., Denat A.

EXCITATION OF N_2 ($C^3\Pi_u$) STATE IN PULSED POSITIVE CORONA DISCHARGE — IV-14
Simek M., Babicky V., Clupek M., De Benedictis S., Dilecce G., Sunka P.

STUDY OF THE LOCAL DISCHARGE PROPAGATION DIRECTION ON TWO ELECTROLYTE WATER CHANNELS (PART I) — IV-16
Boudjella A., Hadi H., Flazi S., Yumoto M., Sakai T., Hosokawa T.

ON THE RATE OF GAS HEATING BY SMALL-SCALE NEGATIVE DC CORONA DISCHARGES — IV-18
Jones J.E.

GAS TEMPERATURE ESTIMATIONS FOR SMALL-SCALE NEGATIVE DC CORONA DISCHARGES IN AIR — IV-20
Jones J.E.

A DEGENERATE PROBLEM IN THE VARIATIONAL APPROACH TO CHARGE DRIFT — IV-22
Jones J.E.

PHYSICS OF SUPER UNDERCRITICAL STREAMER DISCHARGE IN UHF ELECTROMAGNETIC WAVE — IV-24
Khodataev K.V.

DEVELOPMENT OF A LOW OZONE GENERATION CORONA CHARGER AND APPLICATION FOR NH_3 REDUCTION IN WASTE GAS — IV-26
Kogoma M., Inomata T., Okazaki S.

MEMORY EFFECTS IN THE ELECTRICAL BREAKDOWN OF A LOW PRESSURE GAS IV-28
Kudrle V., Le Duc E., Fitaire M.

POSITIVE STREAMER IN STRONG FIELD IN AIR: THE MECHANISM OF EXPANSION AND ACCELERATION IV-30
Kulikovsky A.A.

UV LIGHT CONTROLLED REPETITION RATE OF TRICHEL PULSES IV-32
Paris P., Laan M., Tiirik A.

ABOUT THE POSITIVE CORONA DISCHARGE FORMS IN O_2-N_2 MIXTURES IV-34
Kudu K., Lagstad I.H., Sigmond R.S.

DECAY RATE OF EXCITED XE-ATOMS IN SINGLE FILAMENT OF A DIELECTRIC BARRIER DISCHARGE IV-36
Lange H., Wendt R.

THEORY OF SECONDARY STREAMER GENERATION IN POSITIVE CORONA IV-38
Morrow R.

TRANSITION TIMES FROM GLOW TO ARC AND FROM ARC TO GROW ON INTER-GLOW-ARC FLIP-FLOP TRANSITION IV-40
Nogaki M., Suginuma Y.

VOLT-AMPERE CHARACTERISTICS OF PULSED HOLLOW CATHODE - HOLLOW ANODE DISCHARGES IV-42
Glisic S., Zivkovic J.V., Strinic A.I., Petrovic Z.Lj.

INVESTIGATION OF THE ROLE OF NITROGEN IMPURITIES ON THE BEHAVIOUR OF AN ATMOSPHERIC-PRESSURE GLOW DISCHARGE IN HELIUM IV-44
Rabehi A., Segur P., Massines F., Ben Gadri R., Bordage M.C.

SPATIOTEMPORAL EVOLUTION OF GAS TEMPERATURE IN A CORONA DISCHARGE IV-46
De Souza A.R., Touzeau M., Marode E., Deschamps N.

BREAKDOWN DEVELOPMENT AT HIGH OVERVOLTAGE : ELECTRIC FIELD, ELECTRONIC LEVELS EXCITATION AND ELECTRON DENSITY IV-48
Anikin N.B., Pancheshnyi S.V., Starikovskaia S.M., Starikovskii A.Yu.

SPATIAL HOMOGENEITY OF PLASMA CREATED BY FAST IONIZATION WAVE IN THE BIG DISCHARGE VOLUME IV-50
Starikovskaia S.M., Starikovskii A.Yu., Zatsepin D.V.

PLANE VUV OPTICAL SOURCE ON THE BASE OF MULTI-CHANNEL SLIDING DISCHARGE IV-52
Tcheremiskine V.I., Sentis M.L., Delaporte Ph.C., Mikheev L.D., Zuev V.S.

CORRELATION BETWEEN CORONA SPECTRAL INTENSITIES AND DISCHARGE GEOMETRY IV-54
Toedter O., Muller H.J., Koch A.W.

TEMPORARY CORROSION RESISTANCE USING CORONA-ASSISTED COATING IV-56
Toedter O., Koch A.W.

HIGH-VOLTAGE IONIZATION WAVE CONDITIONS AFFECTION ON THE IGNITION DELAY TIME IN H_2-AIR MIXTURES AT HIGH TEMPERATURES IV-58
Kof L.M., Starikovskaia S.M., Starikovskii A.Yu.

Topic 8 :
Plasma diagnostic methods.

NEGATIVE ION DIAGNOSTICS IN A NON-MAXWELLIAN PLASMA CONTAINING NEGATIVE IONS IV-60
Amemiya H.

VALIDITY OF ELECTRICAL PROBE MEASUREMENTS IN RF PLASMA CHECKED BY OPTICAL SPECTROSCOPY DIAGNOSTIC IV-62
Hallil A., Amemiya H., Shimizu K.

ATOMIC GROUND-STATE DENSITY OF MERCURY IN NON LOCAL-THERMODYNAMIC-EQUILIBRIUM CONDITIONS IV-64
Elloumi H., Aubes M.

3D-MODELING OF N ATOM TITRATION BY NO IN AR-N_2 POST-DISCHARGES IV-66
Belmonte T., Czerwiec T., Ricard A., Michel H.

SPECTROSCOPIC MEASUREMENTS IN PLASMAS WITH SILICA ABLATED WALLS IV-68
Bezborodko P., Fauconneau J.

TALIF AND OES MEASUREMENTS FOR TESTING THE VALIDITY OF ACTINOMETRY APPLIED TO H-ATOM DENSITY ESTIMATION UNDER DIAMOND DEPOSITION CONDITIONS IV-70
Gicquel A., Chenevier M., Hassouni K., Booth J.P.

DETERMINATION OF PLASMA PARAMETERS FROM ION BRANCH OF PROBE CHARACTERISTIC IV-72
Abdullin I.Sh., Bragin V.E., Bykanov A.N.

METHOD OF INVESTIGATION OF A CONDUCTING COLUMN BY MEANS OF A MAGNETIC DIAGNOSIS IV-74
Gary F., Velleaud G., Laurent A., Mercier M., Cajal D., Maftoul J.

ON VALIDATION OF MAGNETIC PROBE MEASUREMENTS IN INDUCTIVE PLASMAS IV-76
Piejak R., Godyak V., Alexandrovich B.

SPECTROSCOPIC TEMPERATURES MEASUREMENTS IN AN AR-CO_2-N_2 PLASMA IV-78
Faure G., Coitout H.

LIF MEASUREMENT OF N_2 ($A^3\Sigma_u^+$,v=4) POPULATION DENSITY IN A PULSED RF DISCHARGE IV-80
De Benedictis S., Dilecce G., Simek M.

STARK PROFILES OF HYDROGEN SPECTRAL LINES IN ELECTRIC FIELDS OF PLASMA TURBULENCE IV-82
Gavrilenko V.P.

THE ANALYTIC MODEL FOR ION-DYNAMIC EFFECTS IN STARK-BROADENING THEORY OF HYDROGENIC EMITTERS IV-84
Golosnoy I.O.

MEASUREMENT OF PARTICLE DENSITIES IN AR-HG DISCHARGE PLASMA USED FOR LIQUID CRYSTAL DISPLAY BACKLIGHTING IV-86
Goto M., Ohtani K., Arai T.

MEASUREMENTS OF CF, CF_2 AND CF_3 RADICALS IN A DC CF_4 ETCHING PLASMA IV-88
Arai T., Goto M., Fujioka H., Horikoshi K., Mashino S.

MEASUREMENTS OF DIFFUSION COEFFICIENT OF CF RADICAL IN CF_4/H_2 DISCHARGE PLASMA IV-90
Mashino S., Horikoshi K., Fujioka H., Goto M., Arai T.

TIME RESOLVED TEMPERATURE MEASUREMENTS IN H_2 HIGH DENSITY PULSED DISCHARGE IV-92
Rousseau A., Teboul E., Gousset G., Leprince P.

FRANCK-CONDON FACTORS CALCULATION FOR THE $A^3\Sigma^+_u \rightarrow C^3\Pi_u$ AND $A^3\Sigma^+_u \rightarrow B^2\Sigma^+_u$ TRANSITIONS OF N_2 IV-94
Champain H., Djermoune D., Hartmann G.

THE ROLE OF THE METASTABLE STATE $A^3\Sigma^+_u$ IN THE EXCITATION MECHANISM OF MOLECULAR NITROGEN. APPLICATION TO THE SPONTANEOUS EXTINCTION OF THE LOW CURRENT ARC IV-96
Tioursi M., Haug R., Hartmann G.

SPECTRAL DIAGNOSTICS OF GLID-ARC UP TO 1.1 MPA IV-98
Janca J., Tesar C.

DETECTION OF DESORBED HYDROCARBONS BY CN CHEMILUMINISCENCE IN N_2 FLOWING AFTERGLOW AT LOW TEMPERATURES IV-100
Krcma F., Janca J.

ELECTRON ENERGY DISTRIBUTION FUNCTIONS SPATIALLY RESOLVED IN THE EXPANSION OF A MICROWAVE DISCHARGE CONTAINING AR-CH_4 GAS MIXTURE IV-102
Cinelli M.J., Jauberteau J.L., Jauberteau I., Aubreton J., Catherinot A., Lasgorceix P.

PLASMA PARAMETER MEASUREMENT FROM THE PROBE TEMPERATURE IV-104
Kando M., Kinoh Y., Etoh A.

INFLUENCE OF THE RETARDING POTENTIAL OF A COLLECTOR AND PARAMETERS OF A PLASMA FLOW ON THE DEPOSITION OF ACCELERATED ISOTOPE ION COMPONENT FOR ICR-SEPARATION METHOD IV-106
Karchevsky A.I., Potanin E.P.

DETERMINATION OF TEMPERATURE PROFILES AND PARTICLE NUMBER DENSITIES IN HIGH PRESSURE MERCURY AND MERCURY IODIDE PLASMAS IV-108
Kindel E., Schimke C., Schopp H., Kettlitz M.

RADIATIVE SPECTRUM OF HYDROGEN IN THE NONEQUILIBRIUM GAS-DISCHARGE PLASMAS AND ITS APPLICATION FOR GAS TEMPERATURE DETERMINATION IV-110
Chebotarev A.V., Kossyi I.A., Otorbaev D.K., Silakov V.P.

A DIAGNOSTICS LASER APPARATUS FOR INVESTIGATION OF PLASMA IN A WIDE RANGE OF ELECTRON DENSITIES IV-112
Bashutin O.A., Vovchenko E.D., Kurnaev V.A., Savjolov A.S., Lee Z.H.

ELECTRON DENSITY AND ELECTRON DISTRIBUTION FUNCTION MEASUREMENTS IN COPPER VAPOUR LASER IV-114
Gigant L., Lemaire P., Maury J.

TRANSITION PROBABILITIES OF NI LINES FROM LASER INDUCED BREAKDOWN SPECTROSCOPY IV-116
Matheron P., Deha I., Redon R., Richou J.

APPLICATION OF A DIGITAL CAMERA TO IMAGING SPECTROSCOPY OF TPD-S PLASMA IV-118
Mimura M., Uneyama T., Hamada T., Ishida A., Sato K.

MEASUREMENT OF ELECTRON DENSITY IN DIELECTRIC BARRIER DISCHARGES IV-120
Gerova E., Muller S.

DETERMINATION OF THE SPATIAL DISTRIBUTION OF THE ELECTRON DENSITY IN AN ARGON ARC BY DIGITAL SPECKLE-PATTERN-INTERFEROMETRY IV-122
Hipp M., Fliesser W., Neger T., Jager H.

A NONLINEAR FIZEAU INTERFEROMETER FOR REAL-TIME DETERMINATION OF SPATIAL DISTRIBUTIONS OF ELECTRON DENSITIES IN A MINI-ARC PLASMA IV-124
Flieser J., Morozov A., Neger T., Jager H.

SPATIALLY-RESOLVED DETERMINATION OF THE ELECTRON DENSITY IN A HIGH PRESSURE MERCURY LAMP USING TWO-WAVELENGTHS SPECKLE-INTERFEROMETRY IV-126
Fliesser W., Hipp M., Neger T., Jager H.

OPTICAL DIAGNOSTICS OF PLASMA PRODUCED IN LASER BEAM WELDING PROCESS IV-128
Pavlik J., Novak S., Hrach R., Kuba P., Kosecek A.M., Fodrek P., Kolenic F.

CHARACTERIZATION OF A MULTI-COMPONENT PLASMA IN AN IONOSPHERIC PLASMA SIMULATION CHAMBER IV-130
Roussel J., Viel V., Bernard J.F.

MEASUREMENT OF LINE INTENSITY RATIOS FROM LOW-PRESSURE, WEAKLY-IONIZED HELIUM PLASMAS IV-132
Sasada T., Matsuoka M., Kawaguchi M.

AN ELECTRON ENERGY ANALYSER IN MAGNETIZED PLASMAS IV-134
Antoni V., Bagatin M., Desideri D., Martines E., Serianni G., Vallone F., Yagi Y.

VIBRATIONAL AND TRANSLATIONAL TEMPERATURE MEASUREMENTS IN NITROGEN AND AIR GLOW DISCHARGE BY 2λ-CARS SPECTROSCOPY METHOD IV-136
Gordeev O.A., Vereshchagin K.A., Smirnov V.V., Shakhatov V.A.

PROBE DIAGNOSTICS OF STRONGLY IONIZED NOBLE GAS PLASMA AT ATMOSPHERIC PRESSURE IV-138
Baksht F.G., Mitrofanov N.K., Rybakov A.B., Shkol'nik S.M.

PRIMARY ELECTRONS INFLUENCE TO THE PLASMA PARAMETERS IN MULTIPOLAR MAGNETIC-CONFINED DEVICE IV-140
Stamate E., Inagaki K., Ohe K.

EVOLUTION OF THE VIBRATIONAL ENERGY CARRIED BY $N_2(X^1\Sigma^+_g)$ FROM A MICROWAVE DISCHARGE IV-142
Supiot P., Blois D., Barj M., Chapput A., Dessaux O., Goudmand P.

DENSITY MEASUREMENT OF OH FREE RADICAL IN A MAGNETIZED SHEET PLASMA CROSSED WITH VERTICAL GAS-FLOW IV-144
Tonegawa A., Kobayashi Y., Kawamura K., Takayama K.

ON THE HYDROGEN BALMER H_α LINE SHAPES IN AN ABNORMAL GLOW DISCHARGE OPERATING IN HELIUM-HYDROGEN MIXTURE IV-146
Videnovic I.R., Kuraica M.M., Konjevic N.

LANGMUIR PROBE MEASUREMENTS IN THE AFTERGLOW OF RF-DISCHARGES IV-148
Remscheid A., Rudakowski S., Wiesemann K.

OPTICAL ABSORPTION TECHNIQUES USED IN DIAGNOSTICS OF A ROTATING ARC IN AN ELECTRICAL CIRCUIT-BREAKER IV-150
Fleurier C., Hong D., Ciobanu S.S., Fievet C.

COMPARISON OF ELECTRON ENERGY DISTRIBUTIONS DETERMINED BY SPECTROSCOPIC AND ELECTROSTATIC PROBE METHODS IV-151
McFarland J., Mahony C.M.O., Toader E.I., Graham W.G.

Topic 9 :
Plasma wall interactions, electrode and surface effects.

EXPERIMENTAL INVESTIGATION OF THE INTERACTION OF A C-SIC WALL WITH A LOW PRESSURE CO_2-N_2 PLASMA JET IV-152
Boubert P., Robin L., Vervisch P.

BOUNDARY WALL EFFECTS ON NEUTRAL DYNAMICS IN MICROCAVITIES IN AIR IV-154
Eichwald O., Jugroot M., Yousfi M., Bayle P.

DISTRIBUTIONS OF PLASMA PARAMETERS IN A SPUTTER DISCHARGE IV-156
Funato Y., Kiyooka C., Akaishi K., Kubota Y., Mushiaki M.

NEAR-ELECTRODE LAYERS ORIGINATING AT MAGNETIZED PLASMA ACCELERATION IV-158
Garanin S.F.

SURFACE AND VOLUME KINETICS OF $O(^3P)$ ATOMS IN A LOW PRESSURE O_2-N_2 MICROWAVE DISCHARGE IV-160
Zvonicek V., Guerra V., Loureiro J., Talsky A., Touzeau M.

COLLECTOR FLOATING POTENTIALS IN A TWO-ELECTRON TEMPERATURE PLASMA IV-162
Cercek M., Rovtar J., Gyergyek T., Stanojevic M.

INTERACTION OF CATHODE MICROTIPS AND DENSE PLASMAS IV-164
Schmoll R., Hartmann W.

RELATION BETWEEN CRATER DIMENSIONS AND VOLTAGE FLUCTUATIONS IN LOW CURRENT COLD CATHODE ELECTRIC ARCS IV-166
Tioursi M., Haug R.

BREAKDOWN PHENOMENA BETWEEN A HYDROGEN PLASMA BEAM AND THE DISK AS A WALL IV-168
Hosokawa T., Fukuda M., Kaneda T.

MOMENTUM ACCOMMODATION AT LOW ENERGY IONS-SOLID SURFACE INTERACTION IV-170
Kolosov V. Yu., Sukhomlinov V.S.

BACKSCATTERING BY A SOLID SURFACE OF ITS OWN IONS IN THE CASE OF THEIR NORMAL INCIDENCE IV-172
Kolosov V. Yu., Sukhomlinov V.S.

FORMATION OF SUPERSONIC ATOM FLUX IN THE CATHODE REGION OF VACUUM ARC IV-174
Korolev Yu.D., Kozyrev A.V.

THE BENEFITS OF USING A STEERED ARC IN THE CONTINUOUS MODE OVER GRAPHITE CATHODES IV-176
Kandah M., Meunier J.L.

TEMPERATURE DEPENDENCE OF THE SURFACE RECOMBINATION COEFFICIENT OF NITROGEN ATOMS ON COPPER OXIDE IV-178
Markovic V.Lj., Pejovic M.M., Petrovic Z.Lj.

INFLUENCE OF A POLYMER SAMPLE ON WIRE-TO-PLANE CORONA DISCHARGE REGIMES IV-180
Gresser L., Peyrous R., Spyrou N., Held B.

INTENSIVE STATIONARY ELECTRIC DISCHARGES WITH THE ELECTRODE HOMOGENEOUSLY EVAPORATED IN VACUUM (ISEDEHEV) IV-182
Saenko V.A.

SECONDARY ELECTRON EMISSION DUE TO HYDROGEN ION AND NEUTRAL BOMBARDMENT IV-184
Simko T., Bretagne J., Gousset G.

MAGNETIC PRESHEATH IN FRONT OF AN OBLIQUE END-PLATE IN A MAGNETIZED SHEET PLASMA IV-186
Tonegawa A., Ono M., Shibamoto M., Sakamoto S., Kawamura K., Takayama K.

INVESTIGATION OF THE $1S_J$ DENSITIES IN THE VICINITY OF THE ELECTRODES OF A NEON GLOW DISCHARGE IV-188
Dinklage A., Deutsch H., Scheibner H., Wilke C.

Topic 10 :
Physical aspects of plasma chemistry, plasma processing of surface and thin film technology.

EFFECTS OF H_2 DILUTION ON SURFACE LOSS PROBABILITY OF CH_3 ON A C:H IN CH_4+H_2 RF DISCHARGES IV-190
Videlot H., Shiratani M., Jolly J., Perrin J.

DOPPLER BROADENING OF ATOMIC LINES IN A LOW PRESSURE RADIO FREQUENCY DISCHARGE OF AR-TETRAMETHYLSILANE IV-192
Badie J.M., Andrieux M., Ducarroir M., Bisch C.

THE EFFECT OF HYDROGEN ADMIXTURES ON THE NITRIDING OF AISI-316 STAINLESS STEEL IV-194
Baldwin M., Kumar S., Fewell M., Haydon S., Collins G., Short K., Tendys J.

IONS AND NEUTRALS IN THE AR-TETRAETHOXYSILANE (TEOS) RF DISCHARGE IV-196
Basner R., Foest R., Schmidt M., Hempel F., Becker K.

B ATOMS REACTION WITH OXYGEN IN AR-BCL_3-(O_2) FLOWING MICROWAVE DISCHARGES IV-198
Czerwiec T., Pierson J.F., Belmonte T., Michel H., Ricard A.

NITROGEN ACTIVE SPECIES IN A MICROWAVE FLOWING POST-DISCHARGE REACTOR IV-200
Bockel S., Ablitzer D., Michel H., Ricard A.

CFX RADICAL SURFACE PRODUCTION AND LOSS MECHANISMS IN FLUOROCARBON RIE PLASMAS IV-202
Booth J.P., Cunge G., Chabert P., Neuilly F., Schwarzenbach W., Derouard J., Sadeghi N.

NANOCHRYSTALLINE THIN FILMS ELABORATION USINGAR-SIH_4 LOW PRESSURE PULSED RF DISCHARGES IV-204
Boufendi L., Hadjadj A., Huet S., Roca i Cabarrocas P.

SUPER-PURE PLASMA CHEMISTRY IN NON-EQUILIBRIUM PLASMA PROCESSES IV-206
Chumak G.M.

PHYSICO-CHEMICAL AND ELECTRICAL PROPERTIES OF PECVD A-SIN_XH_Y FILMS IV-208
Dupont G., Despax B.

OPTICAL DIAGNOSTICS OFR.F. ARGON AND XENON MAGNETRON DISCHARGES IV-210
Dony M.F., Debal F., Wautelet M., Dauchot J.P., Hecq M., Bretagne J., Ricard A.

REACTIONS OF SMALL HYDROCARBON IONS CH_3^+, $C_2H_3^+$ AND $C_2H_5^+$ WITH SILANE IV-212
Bano G., Glosik J., Luca A., Lindinger W.

POSITIVE AND NEGATIVE CHLORINE ION KINETICS IN INDUCTIVELY-COUPLED CHLORINE AND BORON TRICHLORIDE CONTAINING PLASMAS IV-214
Hebner G.A., Fleddermann C.B.

THEORETICAL AND EXPERIMENTAL STUDY OF SIH RADICAL DENSITY AND THIN FILM GROWTH RATE IN PECVD H_2/SIH_4 RADIO FREQUENCY DISCHARGES IV-216
Leroy O., Dorval N., Hertl M., Jolly J., Pealat M.

SPECTROSCOPIC STUDY OF METHANE CONVERSION IN THE FLOWING AFTERGLOW OF A DINITROGEN MICROWAVE PLASMA IV-218
Diamy A.M., Hrachova V., Legrand J.C., Hrach R.

CARBURATION OF STEEL PERFORMED IN AN AR-CH_4 MICROWAVE EXPANDED PLASMA. CORRELATIONS WITH PLASMA CHARACTERISTICS IV-220
Cinelli M.J., Jauberteau J.L., Jauberteau I., Aubreton J., Catherinot A., Cahoreau M.

HIGH POWER RADIO FREQUENCY - AND MICROWAVE - DISCHARGES ; COMPARISON UNDER A PLASMACHEMICAL TREATMENT OF HYDROGEN SULFIDE IV-222
Bagautdinov A., Eremenko Yu., Jivotov V.K., Kalachov I., Konstantinov E., Kosbagarov A., Musinov S., Overchuk K., Rusanov V., Zoller V.

THE PLASMA CATALYSIS EFFECTS AT THE METHANE DISSOCIATION INTO HYDROGEN AND CARBON IV-224
Babaritskiy A., Baranov I.E., Dyomkin S.A., Etievant C., Jivotov V.K., Potapkin B.V., Rusanov V.D., Ryazantsev E.I.

THE ATMOSPHERIC PRESSURE TORCH DISCHARGE PLASMA-CHEMICAL REACTOR IV-226
Kapicka V., Sicha M., Klima M., Novak M., Tous M., Slavicek P., Brablec A., Jastrabik L., Soukup L., Behnke J., Tichy M.

THE RF PLASMA-CHEMICAL REACTOR WITH THE SYSTEM OF MULTI-HOLLOW-CATHODES FOR THE SURFACE AND COATING TECHNOLOGIES IV-228
Hubicka Z., Sicha M., Novak M., Soukup L., Jastrabik L., Kapoun K., Sery M., Kapicka V.

MONOATOMIC ION RICH PLASMAS FOR ION IMPLANTATION BY PLASMA IMMERSION: ION PRODUCTION MECHANISMS IN DISTRIBUTED ECR DISCHARGES IV-230
Le Cœur F., Arnal Y., Burke R., Pelletier J.

NITROGEN DISSOCIATION IN A N_2-H_2 GLOW DISCHARGE IV-232
Amorim J., Lino J., Thomaz J., Loureiro J., Pinheiro M.J., Baravian G., Sultan G.

ON FORECASTING MATERIALS PROPERTIES OBTAINED UNDER ION BOMBARDMENT CONDITIONS IV-234
Katkalo A.A., Lyapin A.I.

CARBONITRIDE HYDROGENATED DEPOSITION USING VARIOUS PRECURSORS IV-236
Ion L., Marty-Dessus D., Held B., Trinquecoste M., Delhaes P.

REACTIVE SPECIES IN SiH_4-NH_3 RF DISCHARGE IV-238
Ion L., Marty-Dessus D., Held B.

PLASMACHEMICAL REACTOR FOR PRECISION ETCHING OF ELEMENTS WITH SUBMICRON SIZE IV-240
Pavlenko V.N., Panchenko V.G., Ustalov V.V., Fedorovich O.A.

SURFACE MODIFICATIONS OF HE-O_2 CORONA TREATED POLY(ETHYLENE TEREPHTALATE) (PET) IV-242
Placinta G., Verdes D., Popa G.

USE OF DYNAMIC ACTINOMETRY FOR THE DIAGNOSTICS OF A MICROWAVE H_2-CH_4-N_2 PLASMA FOR DIAMOND DEPOSITION IV-244
Chatei H., Bougdira J., Remy M., Alnot P.

SPACE RESOLVED EXCITATION MECHANISM AND ARGON ION TRANSPORT IN A HIGH DENSITY ICP REACTOR IV-246
Sadeghi N., Van de Grift M., Hbid T., Kroesen G.M.W., De Hoog F.J.

THE VACUUM ARC DISCHARGE IN ANODE MATERIAL VAPOUR IV-248
Borisenko A.G., Pavlenko V.N., Panchenko V.G., Saenko V.A.

DC NEGATIVE CORONA DISCHARGE IN AIR + CCl_2F_2 MIXTURES IV-250
Cicman P., Pavlik M., Rahel J., Matejcik S., Mark T.D., Skalny J.D.

CATALYST SYNTHESIS BY PLASMA ASSISTED DEPOSITION IV-252
Thomann A.L., Charles C., Brault P., Laure C., Andreazza-Vignolles C., Andreazza P.

OPTICAL EMISSION SPECTROSCOPY ON AR/N_2 AND AR/N_2/C_2H_2 EXPANDING THERMAL PLASMAS IV-254
De Graaf A., Van de Sanden M.C.M., Schram D.C., Aldea E., Dinescu G.

MONTE CARLO SIMULATION OF THIN FILM DEPOSITION FROM LOW DENSITY JET EXCITED BY AN ELECTRON BEAM IV-256
Vasenkov A.V., Sharafutdinov R.G., Skrynnikov A.V.

EMISSION SPECTROSCOPY IN A DEPOSITION ZONE OF THE MAGNETRON SYSTEM FOR THE PREPARATION OF CARBON NITRIDE FILMS IV-258
Vlcek J., Rusnak K., Hajek V.

INFLUENCE OF DISCHARGE AND SUBSTRATE PARAMETERS ON PECVD OF TEOS/ARGON MIXTURES IV-260
Zajickova L., Bursikova V., Janca J.

Topic 15 :
Particle and laser beam interaction with plasmas.

MOLECULAR ADMIXTURES ROLE IN THE KINETICS AND RADIATION OF HELIUM BEAM PLASMA IV-262
Amirov A.H., Korshunov O.V., Chinnov V.F., Lomakin B.N., Sunarchin A.A., Tichonov M.G.

C_2 EMISSION OF LASER PRODUCED CARBON PLASMA IN AN AMBIENT GAS IV-264
Abdelli S., Kerdja T., Si-Bachir M., Malek S.

COHERENT STRUCTURE EMITTED BY AN ELECTRON BEAM IN A BEAM-PLASMA SYSTEM IV-266
Mori I., Morimoto T., Kawakami R., Tominaga K.

ELECTRON DENSITY OF HIGH PRESSURE ARGON PLASMA PRODUCED BY EXCIMER LASER IV-268
Tsuda N., Yamada J.

REFLECTED AND RESONANCE TRANSITION RADIATION FROM MICRO BEAM PLASMA IV-270
Skvortsov V.A., Vogel N.I.

OPTIMIZATION OF MULTICHARGED ION EMISSION FROM PLASMA PRODUCED BY SHORT PULSE, SHORT WAVELENGTH LASERS IV-272
Wolowski J., Parys P., Woryna E., Krasa J., Laska L., Masek K., Rohlena K.

Topic 4

Corona, sparks, surface discharges and high pressure glows.

The effect of relativistic runaway electron avalanches on x-ray modulation inside thunderstorm.

L. P. Babich*, I. M. Kutsyk*, A.Yu. Kudryavtsev**
*Russian Federal Nuclear Center-VNIIEF
**Department #4 of Moscow Physics Engineering Institute.
Sarov, 607190, Region of Nizgnii Novgorod, Russia.
Phone: 7-831-30-15041.E-mail: babich@expd.vniief.ru.

1. Introduction

McCarthy and Parks have reported results of flight measurements of x-rays carried out inside a space domain of a thunderstorm electric field [1]. They have detected up to 1000 fold enhancement of x-ray flux over the background value when their plane entered thunderstorm cloud. The measurements were arranged so as to eliminate any possible effect of electromagnetic disturbance caused by thunderstorm electromagnetic activity, on a detector used. Production of the enhanced flux terminated coincident with a lightning discharge. To treat the origin of this phenomenon the authors have attracted an idea that large-scale thunderstorm electric field increased the range of high-energy electrons of the megaelectronvolt domain and thus increased the production of bremsstruhlung [2]. These electrons are permanently generated by cosmic ray showers and by the decay of airborne radionuclids. Lightning discharges terminated the acceleration of electrons due to thundercloud voltage collapse. McCarthy and Parks have carried out calculations results of which occurred *8* times lower the observed enhancement. Some additional reasons attracted by the authors to reduce the discrepancy, were not successful. In the present communication an attempt is undertaken to resolve the divergence. The adequate calculations were based on the hypothesis of relativistic runaway electron avalanching process in a rather weak (in comparison with the conventional laboratory self-breakdown value) thunderstorm electric field. The hypothesis was proposed and substantiated by Gurevich, Roussel-Dupre, Milikh, and Tunnel [3, 4]. The intensity of the electric force eE to be over the relativistic minimum of electron energy losses per unit path L_{min} was proposed as a criterion sufficient for the relativistic avalanche to develop. The minimum is in the vicinity of electron energy $\varepsilon \approx 1$ MeV. A dimension of a space domain where the above criterion is to be met, should be very much longer than the characteristic length necessary for relativistic electron number increase due to ionizing collisions of runaway electrons with air molecules. The last demand is analogous to the conventional avalanche of low energy electrons. Exactly the enhancement of the penetrating radiation inside thunderclouds observed by McCarthy and Parks, was an experimental basis of this promising hypothesis able to push forward the physics of electric phenomena related to thunderstorm activity.

2. Model

The simplest model of thundercloud electric field was used in our calculations. The negative charge $q = 30$ *coulombs* of the lower part of the cloud was supposed to be homogeneously distributed within a sphere with a radius *1 km* at the height *5 km*. The enhancement of x-rays relative to the background was factorized as $K = K_1 \times K_2$. Here $K_1 = L_1/\lambda_1$ is the enhancement coefficient due to the increase of high-energy electron range considered by McCarthy and Parks, whereas by means of $K_2 = exp(L_2/\lambda_e)$ the avalanching of these electrons was taken into account, with λ_e being a distance necessary for e - fold relativistic avalanche enhancement. The range of high-energy electrons in the atmosphere without electric field is designated as λ_1, and L_1 is a dimension of the space domain adjacent to the sphere with the field intensity $E > L_{min}/e$, where $L_{min} \cong 1$ *keV/cm* is the relativistic minimum of electron energy losses per unit path at the height *5 km* [2, 3]. Under the conditions chosen (pressure *0.5 atm* and electron energy $\varepsilon = 1 - 2$ *MeV*), we estimated values $L_1 \cong 650$ *m* and $\lambda_1 \cong 10$ *m* to obtain $K_1 \cong 65$. To characterize the intensity of the external electric field an "overvoltage" $\delta = eE/L_{min}$ over the minimum $L_{min} \approx 1$ *keV/cm* is convenient to be introduced [4]. The avalanching was supposed to take place within the space domain with the dimension $L_2 \cong 350$ *m* along the field vector, where" $\delta \in [1.5, 3]$. At larger distances from the sphere the avalanching rate is too low due to small values of the "overvoltage" δ realized there. To simplify calculations a homogeneous electric field with an average $\langle\delta\rangle = 2$ was adopted throughout the avalanching space domain L_2.

3. Calculations and Results

For the purpose of the present study it was impossible to use directly the results on the avalanche characteristics calculated by Roussel - Dupre et. al. [4], because the large-angle scattering of electrons was discounted. We incorporated the elastic scattering in a

Monte - Carlo code to investigate its effect on the production of secondary runaway electrons. Only elastic collisions of electrons were followed up stochastically. Rutherford elastic scattering cross section with Molier shielding parameter [5] was adopted. Along the path between neighbor elastic collisions electrons were assumed to move under the joint action of accelerating electric $-eE$ force and decelerating friction force $-F(\varepsilon)\times p/p$, where the elementary electric charge $e > 0$, p is the electron momentum and $F(\varepsilon)=L(\varepsilon)$ was calculated from Bethe formula [6] available as well at [4]. By means of the friction force total average energy losses of electrons due to inelastic interactions with atomic particles of a background gas were taken into account. The runaway energy threshold $\varepsilon_{min} \cong 600\ keV$ calculated for the 'overvoltage" $\delta = 2$, appeared to be a few times above the value obtained by Roussel - Dupre et. al. [4]. We used $600\ keV$ as a lower limit to integrate Moller differential ionization cross section σ_{dif} [7] used also by Roussel - Dupre et. al. [4], and to calculate the total ionization cross section σ_i for the production of secondary runaway electrons

$$\sigma_i(\varepsilon_0, \varepsilon_{min}) = \int_{\varepsilon_{min}}^{\varepsilon_0/2} \sigma_{dif}(\varepsilon, \varepsilon_0) d\varepsilon.$$

It allowed to evaluate the avalanching length $\lambda_e = 1/N\sigma_i \cong 120\ m$, the enhancement coefficient due to the avalanching of relativistic electrons $K_2 \cong 20$, and the total enhancement coefficient $K = K_1 \times K_2 \cong 1300$. The last value is in a reasonable agreement with observations reported by McCarthy and Parks [1].

4. Conclusion

In spite of our calculations are approximate, they are very illuminative in regards to indicate that development of relativistic runaway electron avalanches is to be taken into account to treat correctly the observed x-ray modulation within the space domain of thundercloud electric fields. It is possible to improve the accuracy of simulations provided that an information on the absolute field intensity distribution would be available from observations of McCarthy and Parks [1]. Both L_2 and λ_e depend very much on the intensity and spatial extension of a specific thunderstorm electric field so that the accuracy of the available information on the field strongly affects the results of calculations. The agreement between the results of present calculations and of the observations carried out by McCarthy and Parks, strongly supports the hypothesis of Roussel-Dupre, Gurevich, Tunnel, and Milikh on the possibility of relativistic runaway electron avalanches to develop within the space domain of relatively weak large-scale thunderstorm electric fields [3, 4].

5. References

[1] M.P. McCarthy, G.K. Parks: Geophys. Res. Lett., **12** (1985) 393.
[2] M.P. McCarthy, G.K. Parks: J. Geophys. Res., **97**, No D5 (1992) 5857.
[3] A.V. Gurevich, G.M. Milikh, R.A. Roussel-Dupre: Phys. Lett. A., **165** (1992) 463.
[4] R.A. Roussel-Dupre, A.V. Gurevich, T. Tunnel, G.M. Milikh: Phys. Rev. E., **49**, No 3 (1994) 2257.
[5] G. Molier: Zh. Naturforsch. **3a**, №2, (1948) 48.
[6] H.A. Bethe: Ann. Phys., **5**, (1930) 325.
[7] C. Moller: Ann. Physik, **14** (1932) 531.

The DD-analogy breakdown concept

A.F. Djakov, Yu.K. Bobrov*,
Russian Joint-Stock Company of Energy and Electrification "EES ROSSII", 7 Kitaigorodsky proezd, Moscow, 103074, RUSSIA
*High Voltage Research Center of All-Russia Electrotechnical Institute, Istra-2, Moscow Region, 143500, RUSSIA

1. Introduction

The numerous studies of breakdown stages in air and other dense gases stressed by the direct, power frequency and impulse high tensions have resulted in data related to the dielectric-conductance transition intricate events and a lot of the alternative breakdown models were developed /1-3/. The identification of the discharge nucleation and propagation mechanisms for avalanche-streamer, streamer-leader, return and final (impulse arc) stages was the main objective of the investigations. However, it may be stated not only significant achievements of those investigations by inductive method commonly used but the necessity of the further deductive approach. The physical concept of definite generality to realize the electrical breakdown phenomena can be formulated in accordance with the similarity to detonation and deflagration of combustible gases (DD-analogy) /2,8,10-12/. Such a concept had been applied to the HF and optical discharges /4/. For the first time the idea was promoted by E.P.Velikhov and A.M.Dykhne as to the impulse arc channel expansion in rarefied noble gas /5/. The electrical breakdown as a problem of reactive systems theory in scope of DD-analogy concept is considered here.

2. General properties of ionization waves

The numerical modeling results of ionizing waves being related to the initial streamer and final impulse arc breakdown stages reveal the most attributive feature of thin boundary ionization zones, fig.1,2. The experimental data on the discharge radiation front structures and the calculations reasonably coincide to each other /6,7/.
The identical Arrenius form of ionization and combustion rate functions is sufficient for the statement above. The sharp exponential dependence on the temperature or electric field leads to the interruption of the ionization process even with a small lowering these parameters. That is why the reaction zone and products (deflagrated gas or discharge plasma) temperatures are practically equal to each other, the propagation mechanism directly determining by the heat energy conductance in similarity to combustion process.

3. Comparison of reaction properties

The general properties and peculiarities of the exothermic chemical and breakdown plasma reactions being tabulated in confrontation allow to evaluate the adequacy of DD-analogy concept.

Comparison of reactive fronts in propagation

Combustible gas deflagration and detonation	Breakdown plasma propagation
*Reaction rate function**	
$F(T) \sim \exp(-A/RT)$	$F(T_e, p) \sim \exp(-I/kT_e); \sim \exp(-I/kT_p)$ $\sim \exp[-I/(E/\sigma_e n)]$
Propagation regime	
Mechanism	
Thermal conductance (diffusion) - deflagration; heating by shock wave front - detonation; spontaneous deflagration in divergent temperature fields	Thermal conductance (electronic, radiative, reactive); heating by heat wave front; ionization in non-uniform electric fields
Peculiarities	
Narrow reaction zone Threshold character of exotermic reaction with chemical energy released Effect of particle and particle energy losses on regime limits Flame front piston effect	Narrow reaction zone Threshold character of ionization reaction, Joule energy dissipation proceeding Effect of electron and electron energy losses on breakdown characteristics Leader and impulse arc plasma piston effect

Discrepancies	
Constant caloricity of active chemical medium	Time and space Joule energy function as a caloricity of external electric field
No heating in products of combustion	Residual current Joule heating follows breakdown plasma formation and propagation
Reaction front causes gas parameter perturbations	

* T- temperature, A- activation energy, R- universal gas constant, E- electric field for avalanche-streamer formation, T_e- free electron temperature, T_p- radiative heat wave temperature; I - ionization potential, σ_e- electron-molecule collision cross-section, n- gas number density

Because of the caloricity of external electric field at ionization front position is to be known for the solving of hydrodynamic problem, the total problem involves the electrodynamic problems for the multimedia plasma-gas and plasma-plasma propagations and interactions with electric field in self-consistent formulation.

4. Conclusion

In comparison with combustion processes the breakdown plasma propagation is similar to deflagration and detonation as to the reaction front structures and the general heat wave mechanism of energy transfer and plasma propagation. The remarkable difference is appeared to consist of the heat transfer function directly depending on the local and temporal magnitudes of electric field entering the breakdown plasma. Therefore, the breakdown plasma propagation problem should be related to the mechanics of the reactive systems traditionally developed for the combustion processes only.

The work has been carried out according to the project "Fundamental theory of electrical discharges in energetics" of Russian Joint Stock Company "EES ROSSII".

5. References.

[1] Physical concept and basic statements of fundamental theory of electric discharges: Scientific report.- Headed by A.F.Djakov.- RJSC "EES Rossii".- Moscow.- 1995 (In Russian, unpublished)
[2] Yu.K. Bobrov "The self-consistent models of the breakdown plasma regimes of propagation in gases", D. Sc. Theses, Istra, 1991, 361 p. (in Russian)
[3] J.M. Meek, J.D. Craggs, ed. "Electrical Breakdown of Gases", J.Wiley and Sons, N.Y.-Toronto, 1978
[4] Yu.P. Raizer: Usp. Fiz. Nauk, **108** (1972) 429 (in Russian)
[5] E.P. Velikhov, A.M. Dykhne: 7-th Int. Conf. on Phenomena in Ionized Gases, Beograd (1965) 47
[6] N. Ikuta, A. Kondo: 4-th Int. Conf. on Gas Discharges, Swansea (1976) 227
[7] I.K. Fedchenko, Yu.K. Bobrov: Electrichestvo, **5** (1971) 53 (in Russian)
[8] Yu.K. Bobrov: Zh. Techn. Fiz., **44** (1974) 2340 (in Russian)
[9] Yu.K. Bobrov, V.V. Vikhrev, I.P. Fedotov:, Fizika plasmy, **14** (1988) 1222 (in Russian)
[10] Yu.K. Bobrov: Zh. Techn. Fiz., **50** (1980) 1621 (in Russian)
[11] Yu.K. Bobrov, M.G. Schats: Techn. Electrodinamica, **3** (1981) 67 (in Russian)
[12] Yu.K. Bobrov: 7-th Int. Symp. on High Voltage Engineering, Dresden (1991) 59

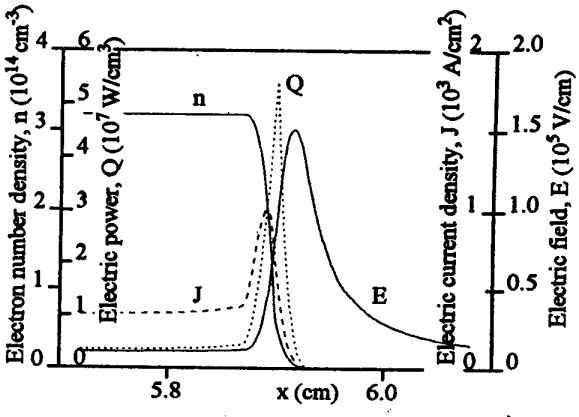

Fig.1. Streamer plasma characteristics in air (results of quasi-two-dimensional modeling).

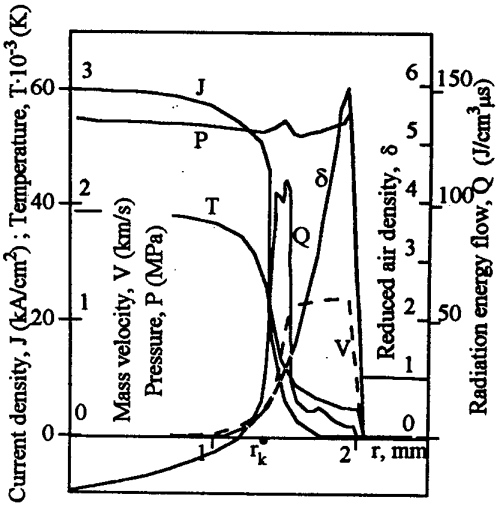

Fig. 2. Radial impulse arc characteristics in air.

The Impulse Arc DD-analogy

A.F. Djakov, Yu.K. Bobrov*, L.N. Bobrova*
Russian Joint-Stock Company of Energy and Electrification "EES ROSSII", 7 Kitaigorodsky proezd, Moscow, 103074, RUSSIA
*High Voltage Research Center of All-Russia Electrotechnical Institute, Istra-2, Moscow Region, 143500, RUSSIA

1. Introduction

The analogy of the discharge plasma propagation and chemical detonation and deflagration reactions in combustible gases (DD-analogy) is to be accepted as the general deductive idea in electric breakdown theory /1-8/.

2. Parameters of impulse arc plasma

By the methods of stark broadening and relative intensities of spectral lines the space-temporal physical characteristics were obtained for heavy impulse arc in air, fig.1. The plasma boundary 3-4 corresponds to the steep temperature front, the channel expanding by radiative heat wave mechanism /3-6/. In contrast to weak time temperature dependence the electron number density follows strictly the discharge current variations, the data receiving by means of stark broadening parameters of spectral lines *NII* 442,7, 453,0 nm and H_β 486,1 nm /2/. In accordance with well-known streak-camera resolutions the shock wave front 1-2 leads plasma channel boundary, fig.2-a. In plasma 4 the conditions of local thermal equilibrium are achieved, so it is possible to come to light for the pressure p and relative air density δ having the temperature and electron number density data simultaneously received. Adiabatic-shell area 2-3 of shock wave is the region of thermodynamic equilibrium as well, nevertheless the electron number density in profile 2-3, fig.1, exceeds significantly the equilibrium magnitudes due to photoionization by channel radiation. Noticeable pressure step is appeared to exist within plasma boundary, the pressure decreasing from adiabatic relatively cool area 3 to hot plasma 4 $(p_4 / p_3)\langle 1$. Due to great excess of the plasma pressure over the external air pressure $(p_4 / p_1)\rangle\rangle 1$ and low gas density $(n_4 / n_3, n_1)\langle\langle 1$ the boundary 3-4 creates the gas velocity head in adiabatic area 3-2 and front 1-2 of shock wave. Pressure step Δp_{3-4} causes the neutral gas flow into the plasma, the temperature and ionization extent decreasing and, on the contrary, electron number density increasing. Therefore, the experimental data show that plasma boundary is similar to the semi-transparent piston likely to the property of flame front propagating in combustible gas /9/.

According to the heat wave model the radiation energy flux is absorbed by the cool gas in adjacent narrow layer, the gas heating up to the ionization temperature and then Joule energy of the discharge current dissipating to reach the plasma channel conditions /3/. Then energy balance equation is reduced to the quasi-stationary condition

$$\nabla(\kappa \nabla T) = Q, \qquad (1)$$

where κ- radiative thermal conductivity, Q- Joule power dissipation. The solution of equation (1) leads to the known formula for the velocity of flame front /9/ and allows to obtain relations in quasi-stationary approximation for the impulse arc channel radius, expansion velocity, pres-sure, density, temperature and active resistance /10/. The self-modeling results give the space-temporal relations for the impulse arc gasdynamic parameters as well /4,5/. For the practical calculations (normal density $\rho_1 = 1{,}29 \cdot 10^{-3}$ g/cm^3) it may be applied:

$$r_3 = 9 \cdot 10^{-2} k_1^{-1/6} i^{1/3} t^{1/2} = 9 \cdot 10^{-2} k_1^{1/3} i^{5/6} i'^{1/2},$$

$$T_4 = 2.62 \cdot 10^4 k_1^{-1/3} i^{-1/6} i'^{1/2},$$

$$p_4 = 0.2\, i^{-0.32} i'^{0.56} \quad (k_1 = 1),$$

$$R_4 = 0.35\, l i^{-0.7} t^{-0.9} \quad (k_1 = 1),$$

where $i = At^k$ - kA, l - arc length, cm, t - μs, r_3 - cm, T_4 - K, p_4 - MPa, R_4 - active resistance, Ω. The same method leads to formulae for the impulse arc in water /11/. In difference with the channel radius formula by Braginsky /12/ the expression above are applicable for any power parameter k_1 in discharge current approximation.

3. Impulse arc detonation and deflagration stages

It is known the impulse arc is accompanied by the shock wave (front 1-2) propagating in a gas medium 1, Joule energy dissipating within the boundary plasma-gas layer 3-4 in the wave tail of adiabatic-shell area 2-3, fig.2-a. Hugoniot adiabats $H_{d-d}(Q' \rangle Q'' \rangle Q''')$ and the transitions from gas initial state 1 to the plasma final conditions 4',4'',4''' are shown in the diagram, fig.2-b. There are two types of transitions. The first

corresponding to initial arc stage $0 \le t \le t_{dt}$ presents the direct transitions $1-4'$, $1-4''$, the last in Jouguet point J. It may be observed the "overpressed detonation" according to the transition $1-4'$ of cool gas particles (p_1, V_1) through the heat wave front with heating and compression $(p_{4'}, V_{4'})$, the normal Jouguet point J regime approaching the moment t_{dt}. Later on $(t \ge t_{dt})$ the transitions $1-2-3-4'''$ occur by the shock wave front compression (2) according to shock Hugoniot adiabat H_{sh}, expansion in adiabatic-shell area $(2-3)$ and rarefaction in plasma channel $(3-4''')$ like a deflagration transition. The diagram demonstrates the impulse arc gasdynanic regimes in sequence of detonation and deflagration stages secondary to energy input decrease as a function of time (dashed line $4'-4''(J)-4'''$). It is possible to make the definite predictions in qualitative analysis and interpretation of breakdown impulse arc properties by theoretical and experimental methods received.

4. Conclusions

The impulse arc channel is an appropriate illustration of gasdynamic similarity to the regimes of detonation and deflagration of combustible gases previously successfully studied. The DD-analogy approach enables to make clear and simple solutions to the complicated problem of electrical breakdown of gases.

5. References.

[1] E.P. Velikhov, A.M. Dykhne: Atomic energy Rev., **142** (1976) 325

[2] I.K. Fedchenko, Yu.K. Bobrov: Elektrichestvo, **5** (1971) 53 (in Russian)

[3] Yu.K. Bobrov : Zh. Techn. Fiz., **44** (1974) 2340 (in Russian)

[4] Yu.K. Bobrov, M.G. Schats: Techn. Electrodinamica, **3** (1981) 67 (in Russian)

[5] Yu.K. Bobrov: Zh. Techn. Fiz., **50** (1980) 1621 (in Russian)

[6] Yu.B. Bobrov, V.V. Vikhrev, I.P. Fedotov: Fiz. plasmy, **14** (1988) 1222 (in Russian)

[7] Yu.P.Raizer: Usp. Fiz. Nauk, **108** (1972) 429 (in Russian)

[8] Yu.K. Bobrov: 7-th Int. Symp. on High Voltage Engineering, Dresden (1991) 59

[9] Ya.B. Zeldovich: Zh. Fiz. Khim., **12** (1938) 100 (in Russian)

[10] Yu.B. Bobrov, V.V. Vikhrev, I.P. Fedotov: Techn. Electrodinamica, **3** (1988) 3 (in Russian)

[11] Yu.K. Bobrov, A.A. Matveev, I.P. Fedotov: Techn. Elektrodinamika, **5** (1990) 41 (in Russian)

[12] S.I. Braginsky: Zh. Experim. Techn. Fiz., **34** (1958) 1548 (in Russian)

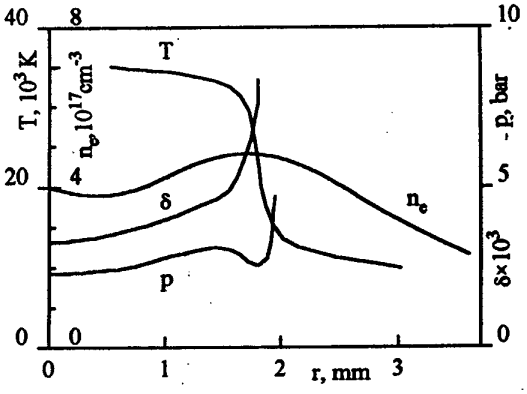

Fig.1. The radial profiles of impulse arc parameters: T - temperature, n_e - electron number density, p - pressure, $\delta=\rho/\rho_1$ - reduced air density (ρ_1=1.29 10^3 g/cm^3). The air gap length - 50 cm, current crest value - 25 kA, time to crest - 19 μs, registration time - 4 μs [2].

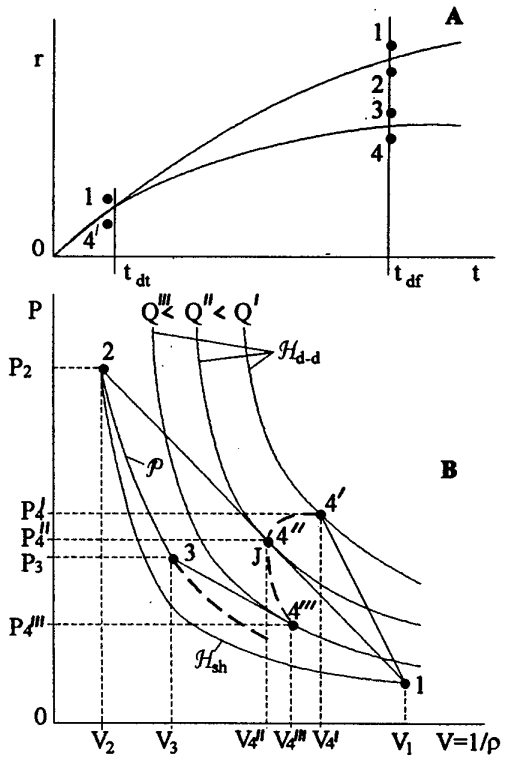

Fig. 2. A - The cylindrical shock wave (1-2) and impulse arc channel (3- 4) fronts radial expansions;
B - Hugoniot adiabates of plasma states ($\mathcal{H}_{d-d}$), shock wave ($\mathcal{H}_{sh}$) and transsitions from the normal state 1 to the plasma states : 1- 4', 1- 4" (J) ("detonation"), 1-2-3--4"' ("deflagration "), $\mathcal{P}$ - pressure, V - specific volume.

Positive-streamer phenomena in positive and negative point-plane gaps in hydrogen

J. Kúdelčík, V. Šurda, A. Zahoranová and M.Černák
Faculty of Math. and Physics, Comenius University, Mlynská dolina F2, 842 15 Bratislava, Slovakia

1 Introduction

Negative corona discharge burning in regime of Trichel pulses find widespread applications in applied electrostatics. Apparently, from an application point of view, it is particularly important that Trichel pulse formation be well understood theoretically. Moreover, as speculated in [1,2], studies of this particular discharge phenomenon are particularly useful in helping to obtain a fuller understanding of the development of cathode region of high-pressure electrical discharges.

Our previous results [3-7] show persuasively that the major issue in an understanding of the negative corona pulse formation is whether the pulse current rise is associated with the Townsend ionisation mechanism, or whether it can be attributed to a streamer ionisation mechanism. It has been hypothesised that the characteristic Trichel pulse current shape is generated at the arrival of a positive-streamer-like ionising wave at the cathode [3-7]. If it is true, than it is realistic to assume that the Trichel pulse has much common with the current signal induced in a cathode probe hit by the primary positive streamer in a positive point-plane geometry.

The objectives of this paper is to present an experimental study on the negative corona current pulses and positive corona prebreakdown streamers in hydrogen. These results are an extension of our previous work [2-8] and augment experimental basis for a general model for the formation of an active cathode region at higher gas pressures.

2. Experimental results and discussion

Discharges were generated in point-plane gaps with the electrode spacing S. The point electrodes had radii of curvature r_0= 0.5 mm and 0.05 mm for negative and positive coronas, respectively. In the case of negative corona pulses special emphasis was given on determining the role played by cathode photoemission. To this end, copper iodide, which has an exceptionally high photoelectric yield, was used as an alternative cathode surface material to copper. Current waveforms were measured at the cathodes by procedure described in details in [7,9] . The positive corona planar cathode had a 2-diam copper central probe. The measurements were limited by the 100 MHz bandwidth of Iwatsu TS-8123 oscilloscope used.

Figure 1 shows current signal induced in the small cathode probe hit by the primary positive streamer in the positive corona gap. This current signal resembles close that simulated for the streamer arrival at the cathode in N_2 [8], and its interpretation is clear: The initial current spike denoted by "A" is due to the displacement current induced in the probe at the streamer approach. The following current hump ("B") is due to conductive current of incoming positive ions and corresponds to the establishment of an abnormal-glow-discharge-type cathode region.

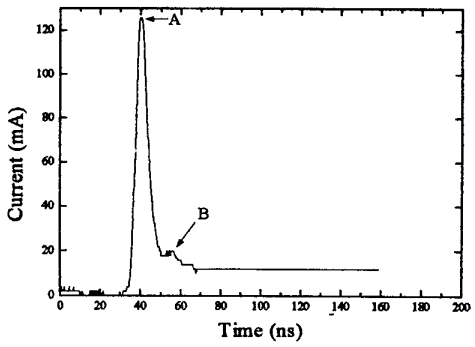

Fig.1 Current signal corresponding to the prebreakdown positive streamer measured in the positive corona gap (S = 5 mm) at 26.7 kPa and 2.8 kV

Note, that the streamer trace in H_2 is very random and experimental scatter in the waveforms like that in Fig.1 is large. This is indicative of low cathode electron photoemission during the streamer propagation.

A waveform of the first negative corona Trichel pulse is shown in Fig.2. A current hump (denoted by "Y") on the pulse trailing part, following the pulse peak ("X") in some X ns, can be seen. Based on the streamer hypothesis for the Trichel pulse formation the pulse shape in Fig.2 can be explain as follows: The initial current rise is due to formation of a positive-streamer like ionising wave and the pulse peak "X", similarly as the peak "A" in Fig.1,

corresponds to a displacement current. The current hump "Y" is due to conductive current of incoming positive ions.

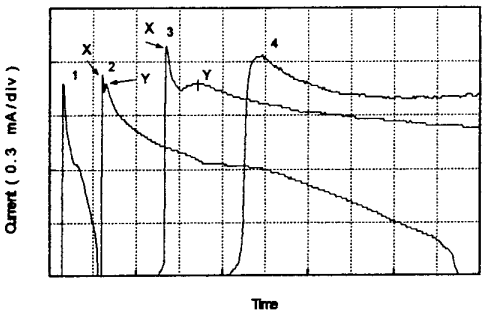

Fig.2 Oscillographs of a complex negative corona pulse measured at a pressure of 13.3 kPa and gap voltage of 3.62 kV. Time scales: (1) 50μs/div, (2) 5 μs/div (3) 500 ns/div, (4) 50 ns/div

It is noteworthy that at similar conditions, i.e., relatively low pressure and blunt cathode in many gases, as for example N_2 and air [1], N_2+SF_6 [3], O_2[10], CO [5], and CO_2[6], a current step on the pulse leading edge due to cathode photoemission was observed. Such step, however, was absent in hydrogen, which in agreement with the above mentioned random motion of the streamer in the positive corona gap, indicate low cathode secondary photoemission there.

An attempt was made to observe the step on the leading edge of negative corona pulse in H_2 using copper iodine coated cathode surface, which has an exceptionally high photoelectric yield. This gave the surprising result shown in Fig.3 that no negative corona pulse was observed, but the current grew exponentially to the breakdown.

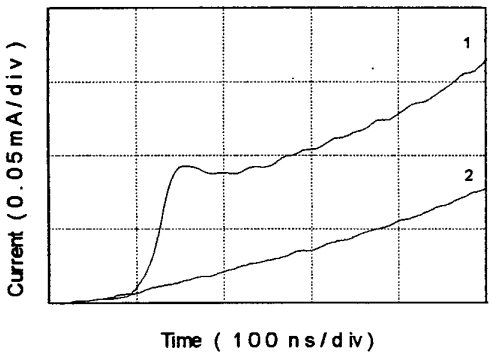

Fig.3 Comparison of the current growth waveforms measured at 3.3 kPa and 1.25 kV using: (1) Copper cathode and (2) CuI-coated cathode

Such discharge behaviour reminds that observed by Korge in pure N_2 and can be explained as follows: The common shape of the current waveform (1) corresponding to a typical negative corona current pulse and is due to the discharge development according to the streamer mechanisms. The current peak is generated at the arrival of the streamer to the cathode. The enhanced cathode photoemission obstructed the streamer formation and resulted in monotonous current growth that, apparently, is due to the discharge development according to the Townsend mechanism. This is in line with the statistical theory of the transition between the streamer and mechanisms [10]

3. Conclusions

i) The results provide further support for the positive-streamer-based model for the negative corona current pulses published in [2-7].
ii) The close similarity between the measured current waveforms induced in a cathode probe at the streamer arrival in H_2 and those simulated for N_2 in [10], indicates that the model is applicable for a wide range of gases.

Acknowledgements

The work was supported by the Slovak Scientific Grant Agency Grant No. 95-5195-136.

4. References

[1] Korge H.,Laan M.: *XVI. ICPIG*, 1983, pp.168-9
[2] Černák M.: *Book of Invited Papers of 22nd ICPIG*, Hoboken, New Jersey 1995, pp.136-46.
[3] Černák M. and Hosokawa T.:*IEEE Trans.* EI-**24** (1989)699.
[4] Černák M., Hosokawa T., and Inoshima M.:*Appl. Phys. Letters* **57**(1990)339.
[5] Černák M. and Hosokawa T.: *Phys. Rev.* **A 43**(1991)1107.
[6] Černák M. and Hosokawa T.:*Austral. J. Phys.* **45**(1992)193.
[7] Černák M., Hosokawa T.,and Odrobina I.: *J. Phys.D: Appl. Phys.* **26**(1993)607
[8] Odrobina I. and Černák M.:*J.Appl. Phys.* **78**(1995)3635-42.
[9] Černák M., Hosokawa T., and Inoshima M.: *Jpn. J. Appl. Phys.* **29**(1990)1165.
[10] Morrow R.: *Phys. Rev.* **A 32** (1985) 3821.
[11] Korge H.: PhD.-Thesis, Tarty 1992, Estonia
[12] Hodges R. V., Varney R.N. and Riley J.F: *Phys. Rev.* **A 31** (1985) 2610

Temperature measurements by a spectroscopic method in high-density nitrogen positive corona discharges

M. Nur, A. Denat and N. Bonifaci
Laboratoire d'Electrostatique et de Matériaux Diélectriques, C.N.R.S - Joseph Fourier University
BP 166, 38042 Grenoble Cedex 9, France

Introduction

Spectroscopic study of corona discharges is one way to analyze the physics of these type of discharges. In particular, measuring the discharge temperatures gives access to information concerning the chemical reactivity of the medium [1]. The different temperatures: electronic T_e, rotational T_r and vibrational T_v can be evaluated from the spectral analysis of the light emitted by the discharge [2,3,4]. Measurements of T_e, T_r and T_v in nitrogen at atmospheric pressure (or lower) have already been published [3,4,5]. Rotational and vibrational temperatures for negative glow discharges in very high density nitrogen (up to 2.4×10^{21} cm^{-3}) have been previously reported [6,7]. The aim of the present work is to determine the temperatures of positive corona discharges occurring in nitrogen at 295 K as a function of density (in the range 7.4×10^{19}-7.3×10^{20} cm^{-3}) and voltage by using the method described in [6,7].

Experimental methods

The experimental arrangement has been described elsewhere [8] and so, will only be briefly pointed out here. The spectroscopic instrumentation is composed of Spectrosil B lenses focusing the light discharge onto the entrance slit (25 µm) of a HRS Jobin-Yvon spectrograph. The slit can be used to select any part of the light area localized at, say, X µm from the tip. The spectrograph of 600 mm focal length is equipped with a grating of 1200 g/mm and it is coupled to a photodiode array detector. This detector, connected to an EG&G optical multichannel analyzer, has a 200-850 nm spectral range. In order to reduce the dark current, the detector was cooled to a temperature of -40°C. The nitrogen gas (N60 from Alphagaz) was further purified by passage over oxygen and moisture traps [9]. We used in this work a point-plane distance d equal to 9 mm and a point radius of 5-10 µm.

Results and discussion

In all the studied density range, the spectra of positive corona discharges in very pure nitrogen consist of the second positive system ($2s^+$, $C^3\Pi_u$--$B^3\Pi_g$), the first negative system ($1s^-$, $B^2\Sigma_u^+$--$X^2\Sigma_g^+$) and, with a weaker intensity, the first positive system ($1s^+$, $B^3\Pi_g$-$A^3\Sigma^+_g$) of N_2.

Assuming that the population of the molecules in the upper electronic state follow a Boltzmann distribution, T_r and T_v can be evaluated from a comparison of experimental and simulated spectra of vibrational bands of a given transition (e.g. $\Delta\upsilon$=-2 of $2s^+$), taking into account the measured instrumental function. The temperatures are determined by minimizing the surface delimited between experimental and simulated spectra [6,7]. Here, T_r and T_v are given for the excited $C^3\Pi_u$ state.

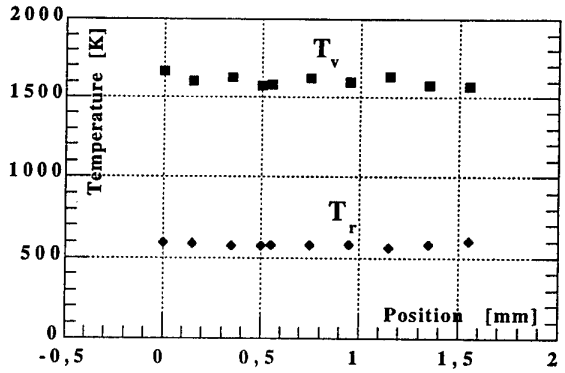

Fig. 1. T_r and T_v as a function of the position X. The tip is at X=0. N = 3.6×10^{20} cm^{-3} and I = 6 µA.

An example of the variations of T_r and T_v with the distance X from the point, for a positive corona discharge at a constant value of the current, is given in fig. 1. Whatever the density, the values of T_r and T_v are independent of the position along the discharge region.
We have also determined T_r and T_v as a function of the nitrogen density, for a discharge mean current of 4 µA and, at a X value where the emitted light is maximum (fig. 2).

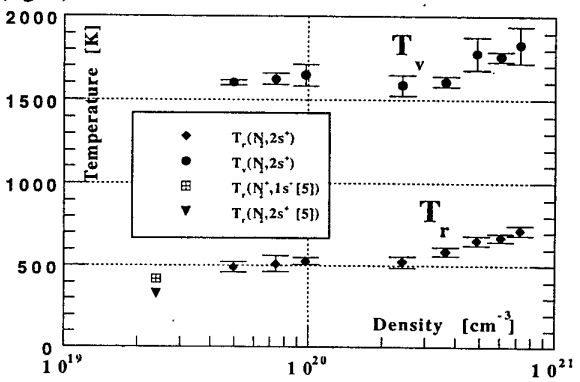

Fig. 2. Density dependence of T_r and T_v.

As shown in fig. 2, a reasonable agreement is observed between our results for T_r and the values of T_r obtained by Hartmann [5] for a régime of positive streamers in air at atmospheric pressure. Moreover, T_v and T_r both increase slightly with density. Fig.3 shows T_r and T_v as a function of the discharge current for a given density. These temperatures also increase slowly with the

current, e.g. for $N=2.4x10^{20}$ cm^{-3} and I=1 and 7 μA, T_V=1400 and 1500 K and T_r=400 and 500 K respectively (Fig.3). This behaviour can be explained by the increasing of the electron density with the current, which produces greater rotational and vibrational excitations of the molecules [7].

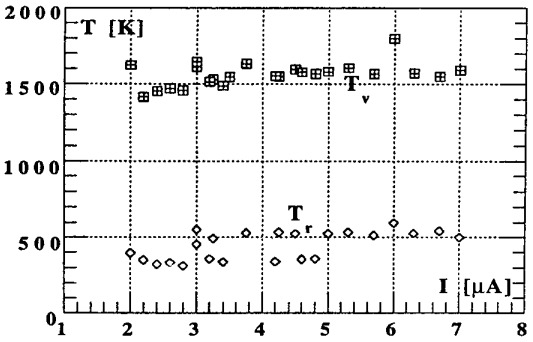

Fig.3. T_r and T_V against discharge current.

The first negative system of N_2^+ is detected from low density ($7.4x10^{19}$ cm^{-3}) until high density (up to $2.4x10^{20}$ cm^{-3}) of nitrogen. The relative intensities of the $N_2(2s^+)$ and $N_2^+(1s^-)$ bands, can be used to evaluate the electron mean energy (or electronic temperature) in the discharge [4]. To do this we have measured the ratio of two very close bands: the $I_{(0,0)}$ band of the $1s^-$ transition on $I_{(2,5)}$ band of the $2s^+$ transition.

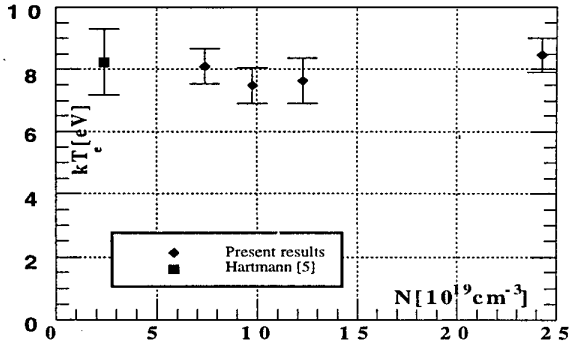

Fig. 4: The electronic temperature as a function of density.

If we suppose a direct excitation of the second positive and the first negative systems and that the electron energy distribution is maxwellian , the mean electronic energy <ε> or "electronic temperature" kTe can be computed [4]. The deactivation rates are taken from [10] and [4].

Fig. 4 shows plots of kT_e versus the gas density. This temperature is practically independent of density (in the range of our experiments). Our values of kT_e are also in good agreement with Hartmann's values [5].

The typical dependence of kTe on the discharge current taken at a nitrogen density of $1.2x10^{20}$ cm^{-3} is given in Fig. 5. We can remark here, kTe tends to be constant with discharge current in our experiment condition (from2 to 10 μA). Whatever the density, this tendency has been observed.

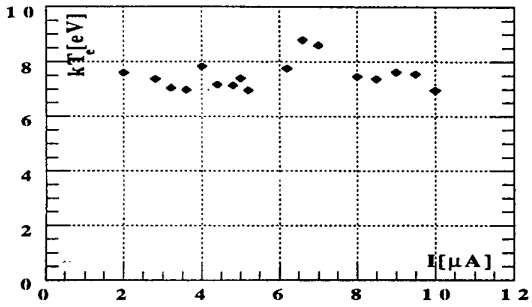

Fig. 5. Electronic temperature as a function of discharge current. N = $1.2x10^{20}$ cm^{-3}.

In all our experiments, the electronic temperature is much greater than the vibrational and rotational temperatures, the vibrational temperature being greater than the rotational one. This indicates that the positive corona discharge, even at the highest pressure, is a non-equilibrium plasma.

Conclusion

In nitrogen, the determination of temperatures, deduced from a comparison of experimental and simulated spectra, can be made from low density to very high density. For positive corona discharges, on the contrary of negative ones, the evaluation of the electronic temperature can be obtained from the analysis of the second positive and the first negative systems of nitrogen.

Acknowledgements
M.Nur acknowledges the financial assistance of the SUDR Project of Indonesia, which is organized by SFERE.

References

[1] B.R.Gordiets, C. M. Ferriera, V.L. Guerra, J.M.A.H. Loureiro, J.Nahorny, D.Pagnon, M.Touzeou and M. Vialle, IEEE Trans.on Plasma Science, Vol. 23, No4, pp. 750-767

[2] A. Chelouauh, E. Marode, G. Hartmann and S. Achat, J.Phys.D:Appl.Phys.27 pp.940-945, 1994.

[3] G. Herzberg (London: D Van Nostarnd, 1950

[4] I. Gallimberti, J.K. Hepworth and R.C. Klewe, J.Phys.D:Appl. Phys., Vol. 7, pp 880-898, 1974. The Mitchell data are in this paper on Table 3.

[5] G. Hartmann, Thèse d'Etat, Université Paris Sud d'Orsay, 1977

[6] M.Nur, J.L. Hernandez-Avila, N. Bonifaci, A. Denat, Proc. ICPIG XXII , Hoboken, New Jersey USA, pp 135-136, 1995

[7] M.Nur, J.L. Hernandez-Avila, N. Bonifaci, A. Denat and A.A.Belevtsev Proc. ICDL XII , Roma, Italy, pp 238-242, 1996

[8] J.L. Hernandez-Avila, N. Bonifaci, A. Denat, IEEE Transactions on Dielec. Elect. Insul. Vol 1, pp 412-418, 1994

[9] M.Nur, N. Bonifaci and A. Denat, this conference.

[10] J. M. Calo and R. C. Axtmann, J. Chem. Phys. Vol 54, No 3, pp 1332-1341, 1971.

Non-Thermal Electron Mobility in High Density Gaseous Nitrogen and Argon in Divergent Electric Field

M. Nur, N. Bonifaci and A. Denat
C.N.R.S-Laboratoire d'Electrostatique et de Matériaux Diélectriques-Joseph Fourier University
BP 166 38042 Grenoble Cedex 9, France

Introduction

The effect of gas density on electron and ion transport in nitrogen and argon have been reported by a number of authors [1-6]. Most of these studies were made in plane parallel geometry by using a time of flight method (called here direct method). For example, Bartels [1] studied electron drift velocity in argon for E/N values down to 2×10^{-21} Vcm^2, where electrons are in thermal equilibrium with the gas. Borghesani et al [2] did measurements on high density argon gas. Allen and Prew [4] measured electron drift velocity at room temperature in a range of E/N where electrons are not thermalized (around 10^{-17} Vcm^2).
Conduction phenomena (charge transport, charge creation, prebreakdown and breakdown processes) depend on gas density as well as on fluid nature and purity and, electrode configuration. In point-plane geometry, in some conditions it is possible to evaluate ion mobility from current-voltage characteristics [7,8]. However, as far as we know, no results concerning electronic charge carriers have been published when using this method.
In this paper, we present some results of non-thermal electron mobility measurements, deduced from I(V) characteristics of negative corona (this is an indirect determination of mobility), in argon and nitrogen gases over a wide range of density ($3\times10^{19}<N<3\times10^{21}$ cm^{-3}) at room temperature. The results which depend greatly on gas purification are discussed and compared to those obtained by other authors by a direct method.

Experimental techniques

The starting materials were nitrogen and argon gases (N60 from Alphagaz). The purification line consisted of a series of traps. First, an Oxisorb cartridge operating at room temperature eliminates oxygen and water. Then, a trap filled with a mixture of molecular sieves (3A to 10A) and charcoal, activated under vacuum typically at 350°C for 3 days, is cooled to -110°C (using a mixture of LN_2 + acetone) to increase its adsorption capacity for CO_2, CO, C_nH_m and water. The gas was then transferred into a stainless-steel coaxial cell which was previously pumped to about 10^{-5} Pa using a turbomolecular pump before filling. This cell could withstand pressures up to 10 MPa. After initial cleaning and assembly, vacuum leak tests were carried out assuming that there are no leaks larger than 10^{-8} Pa m^3s^{-1} which is the highest sensitivity of our helium leak tester. Then, the experimental test cell and the pipes have been cleaned to a high degree of purity by making the same gas circulating several times through them and the purification line before measurements (about 20 times).

Point electrodes, made by electrolytic etching of a tungsten wire, were used opposite a stainless steel plane electrode. Tip radii of the points were in the range 5-15 μm while the point-plane distance d was 8-12 mm.

Results and discussion

In all our experiments with well purified gases (= 20 passages through the purification line), a localized and stable negative corona regime occurs above a threshold voltage V_S. For $V=V_S$, the current increases abruptly - from a non detectable value, i.e. $<10^{-14}$ A, to some 100 μA - and it appears to be continuous and space charge limited according to the saturation current limit established by Sigmond [7] : $I_S=2\mu\varepsilon_0V^2/d$ (1).
Here μ is the mobility, ε_0 the permitivity and V the voltage. The spatial and spectral analysis of the emitted light has shown that the maximum length of the corona region is about 1 mm. In these conditions, the unipolar transport region is close to d and the apparent mobility of the charge carriers can be deduced from current-voltage curves.

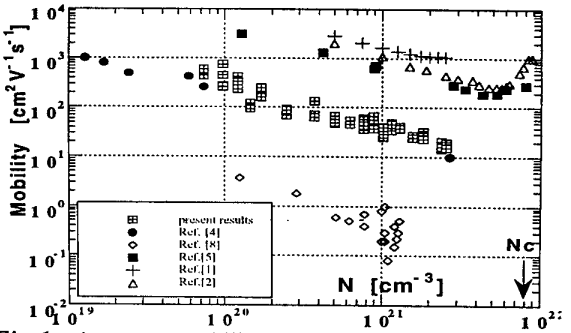

Fig.1: Apparent mobility versus density for purified (present results) and non-purified [8] argon. Data for thermal electrons [1,2,6] and for non-thermal electrons [4].

For similar conditions (same point radius and gap distance), the value of the space charge limited current (SCLC) decreases with the residence time of the gas in the test cell (this corresponds to degradation of its purity level) when V_S is independent of it. After several days inside the cell or for a non-purified gas, the SCLC becomes composed of pulses and its mean value follows the Townsend approximation: $I_S=C\mu\varepsilon_0V(V-V_O)/d$ (2) where C is a constant for a given point radius [7].
The density-normalized electric field strength, E/N, is an important parameter for transport phenomena. For point-plane geometry in the SCLC regime, the mean electric field in the transport zone can be estimated to be of the order of V/d [9] and consequently $E/N\cong V/dN$. However, V can only be varied between the threshold voltage V_S and the breakdown voltage V_b and as V_S and

V_b are function of density, the available range of V/dN values is limited and roughly independent of N.

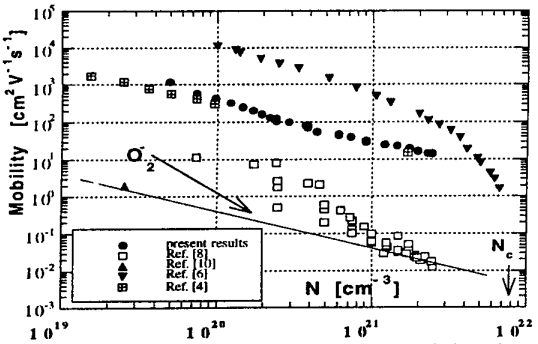

Fig.2: Idem to fig. 1 for purified (present results) and non-purified [8] nitrogen. Mobilities of O_2^- from [11]

For our better purified gases, apparent mobilities deduced from I(V) curves (by using equ. 1) are shown in figure 1 for argon and figure 2 for nitrogen. The experimental data of thermal and non-thermal electron mobilities measured by a direct method by other authors [1-6] are also marked on the corresponding figures. Our mobilities which correspond to V/dN values comprised in the range $0.5x10^{-17}$-$3x10^{-17}$ Vcm^2, are in good agreement with experimental data of [4] for non thermal electron mobilities in the same range of E/N.
This indicates that, for a negative glow corona in well-purified non-electronegative gas, charge carriers are hot electrons and that their apparent mobility can really be evaluated from I(V) characteristics.

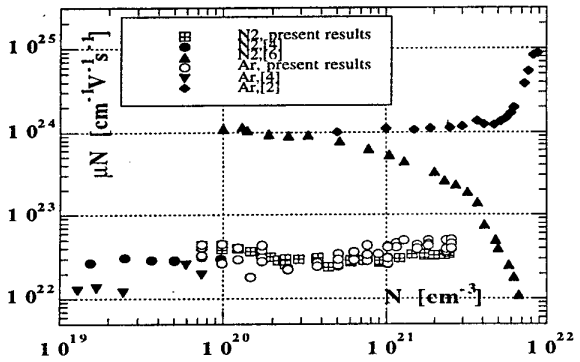

Fig. 3. Experimental density-normalized thermal and non-thermal electrons mobilities μN as a function of nitrogen and argon density.

After a residence time of several days of the gas in the test cell or without purification of the gas circuit [8], charge carriers mobility deduced from I(V) curves (by using equ. 1 or 2) decreases with time up to reach, after a long time, a mobility close to that of O_2^- ions (see fig. 1 and 2). The time needed to get ionic mobility decreases when the gas density increases. This is consistent with a three body attachment process of electron on oxygen impurity represented by the equation: $X+O_2+e \rightarrow X+O_2^-$
In this case, the attachment efficiency increases with gas density as a result of an electron lifetime decreasing as N^{-2}. Here X is Ar or N_2.

In fig. (3) we show the density-normalized non-thermal electron mobilities ($\mu^E N$) with density N. ($\mu^E N$) tends to be constant with density. This tendency is very interesting if we compare with the zero field density-normalized mobility ($\mu_0 N$) . Ar and N_2 are typical example of two kinds of behavior in gases: N_2 show a negative effect i.e. ($\mu_0 N$) decreases with increasing density. On the other hand, Ar show a positive density effect i.e. ($\mu_0 N$) increases with increasing density. A number of multiple scattering theories has been developed to account for the experimental observations [12]. However these theories were developed in the limit of small electric field (E≅0). None of them is able to account for all of the observed phenomena, in particular the observed field dependence of the mobility at a given density.

Conclusion

We have shown that when using well purified gases, one could obtain, with point-plane geometry, reliable indirect measurements of mobility as a function of density and electric field. The large influence of the degree of impurities has been stressed out, the mobility values decreasing from that corresponding to non-thermal electrons to that of ions. Single scattering theory seems to be followed over a large range of density; however it would be of great interest to study carrefully the behavior near the critical point where as a contrary multiple scattering phenomena become important for thermal electron.

Acknowledgements
The authors would like to thank L.Saragossi for his excellent technical help. M.N acknowledges the financial assistance of the SUDR Project of Indonesia which is organized by SFERE.

References

[1] A. Bartels, Physics Letters, **44A** (1973) 403
[2] A. F. Borghesani, M. Santini and P. Lamp, Phys. Rev. A, **46** (1992) 7902
[3] S. S. Huang and G. R. Freeman, Phys. Rev. A, **24** (1981) 714
[4] N. L. Allen and B. A. Prew, J. Phys. B: Atom. Molec. Phys., **3** (1970) 1113
[5] N. Gee, M. A. Floriano, T. Wada, S. S. Huang and G.R. Freeman, J. Appl. Phys. **57** (1985) 1097
[6] T. Wada and G.R. Freeman, Phys. Rev. A, **24** (1981) 1066
[7] R.S.Sigmond, J. Electrostatics, **18** (1986) 249
[8] J. L. Hernandez-Avila, N. Bonifaci and A. Denat, IEEE Trans. on Dielec. Elect. Insul., **1** (1994) 412
[9] P. Atten, Rev. Gen. d'Elec., **83** (1974) 143
[10] P. Langevin , Ann. Chim. et Phy. 8 (1905) 245
[11] E.W. McDaniel, Collision phenomena in ionized gases", pp.409, Ed. John Wiley&Sons, New York, London, 1964.
[12] T.F. O'Malley, J. Phys. B: At. Mol. Opt. Phys. **25** (1992) 163

Excitation of $N_2(C^3\Pi_u)$ State in Pulsed Positive Corona Discharge

Milan Šimek, Václav Babický, Martin Clupek,
Santolo DeBenedictis#, Giorgio Dilecce#, Pavel Šunka

Institute of Plasma Physics, Academy of Sciences of the Czech Rep.
Za Slovankou 3, P.O. Box 17, 18200 Prague 8 , Czech Republic
#Centro di Studio per la Chimica dei Plasmi C.N.R., Dipartimento
di Chimica, Universita di Bari, Via Orabona 4 , 701 26 Bari, Italy

1. Introduction

Pulsed corona discharge is considered as a promising generator of non-equilibrium plasma at atmospheric pressure for environmental applications. For predicting the removal efficiency for different pollutants (NO_x, SO_x, hydrocarbons ...) the determination of plasma (streamer) parameters is important and interesting subject for experimental as well as numerical studies. A powerful diagnostic tool to this purpose is time-resolved multichannel emission spectroscopy. Using this technique we have analyzed N_2-2.positive system ($C^3\Pi_u \rightarrow B^3\Pi_g$) emission produced in pulsed positive corona discharge in pure nitrogen.

2. Experimental set-up

Details of the corona discharge experiment can be found in [1]. Corona is generated in coaxial geometry with Ag coated Cu central wire anode (Φ=0.75 mm) and grounded stainless steel cylinder (Φ = 56 mm). Pulsed HV power supply with maximum ratings 100 kV/1kA/ 7 ns risetime/ ~100ns fall time delivers up to 2 J/pulse with up to 10Hz repetition rate at atmospheric pressure into the discharge volume ~ 1500 cm^3.

Emission coming out of the discharge region is observed along the symmetry axis through quartz window and collecting optics by ISA Jobin Yvon HR320 monochromator equipped with Princeton Instruments,inc. intensified (proximity focused MCP image intensifier gated through FG-100 Gate Pulse Generator) multichannel array detector IRY512/G/B . Spectra acquisition is performed through ISA J.Y. Spectralink controller and SpectraMax software.

Time resolution down to 25 nanoseconds with the jitter ± 5 ns has been obtained by synchronizing Spectralink data acquisition system and FG-100 pulser with the HV circuitry for the corona discharge. Position of the gate for microchannel plate intensifier has been controlled observing FG-100 pulse monitor output simultaneously with corona current and voltage on high speed digitizing HP54542A oscilloscope.

Corona discharge was operated under single shot regime or with 1 Hz repetition frequency. Constant flow (4000 sccm) of nitrogen (99.999) was maintained through the reactor at atmospheric pressure

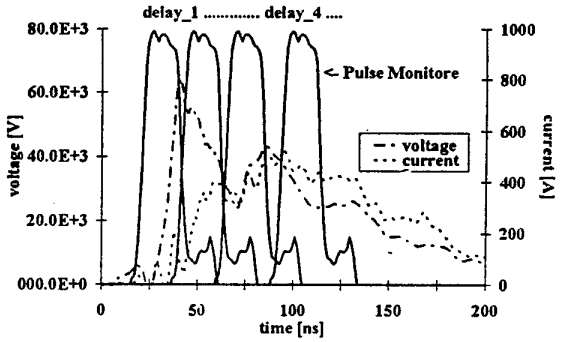

Fig.1 Corona current,voltage and FG100 pulse monitor

(in order to reduce the leak of air the discharge pressure was kept ~30 Torr over the ambient pressure). For each position of the FG-100 gate with respect to corona pulse single PDA acquisitions were stored in the case of single shot spectra or 100 pulses were averaged in the case of 1 Hz repetition frequency. The Δv = -1,-2 sequences of N_2-2.positive system ($C^3\Pi_u \rightarrow B^3\Pi_g$) were stored and treated as described in [2].

3. Results and discussion

We have taken two data sets. In the first set FG-100 gate (25 ns) was moved inside corona pulse (Fig.1) to monitor possible intensity changes in emission during active corona current pulse with present electric field. In the second set emission during and just after corona current pulse (with gate of 200 ns or 2.5 μs respectively) was averaged.

Generally all acquired 2.positive system spectra show very cold $C^3\Pi_u$-state vibrational distribution both during HV pulse and afterglow. Results for v=0,1,2 levels are summarized in Tab.1 and Tab.2. Under the discharge conditions (Tab.2) we observe decrease of v=1 level population with respect to v=0 with slight increase at the end of the pulse. This may reflect the evolution of EEDF during discharge. Comparison of distributions averaged over all HV pulse and in the afterglow (Tab.1) shows increasing relative population of v=1 level in the afterglow. This may indicate relative change in importance of different processes producing

C-state under discharge and post-discharge conditions. Because of short length of HV pulse the $C^3\Pi_u$-state distribution during discharge period is influenced by limited number of processes : transfer of energy of free electrons towards nitrogen (i),(iii), radiative and collisional quenching of $C^3\Pi_u$-state (iv)-(vi). Important can be the influence of energy redistribution within nitrogen ground state vibrational manifold (ii) which can significantly lower the excitation threshold for direct excitation (iii). In the afterglow, energetic electrons as a source of N_2 internal excitation (i),(iii) quickly relax, consequently most of internal energy redistribution goes through heavy particle collisions (ii),(v),(vi) and, in addition, pooling reactions may become dominant source for $C^3\Pi_u$-state excitation (vii).

$$N_2(v) + e \rightarrow N_2(v^*>v) + e \quad \text{(i)}$$

$$N_2(v) + N_2(w) \rightarrow N_2(v') + N_2(w') \quad \text{(ii)}$$

$$N_2(v) + e \rightarrow N_2(C^3\Pi_u,v') + e \quad \text{(iii)}$$

$$N_2(C^3\Pi_u,v) \rightarrow N_2(B^3\Pi_u,v') + h\nu \ (2.PG) \quad \text{(iv)}$$

$$N_2(C^3\Pi_u,v) + M \rightarrow N_2 + M \quad \text{(v)}$$

$$N_2(C^3\Pi_u,v) + N_2 \rightarrow N_2(C^3\Pi_u,v') + N_2,\ v'<v \quad \text{(vi)}$$

$$N_2(A^3\Sigma_u,v) + N_2(A^3\Sigma_u,w) \rightarrow N_2(C^3\Pi_u,v) + N_2(v) \quad \text{(vii)}$$

We have analyzed observed $C^3\Pi_u$ - state vibrational distribution using kinetic model [3], assuming both Maxwellian (T_e=1-10eV) and Druyvestein ($\langle\varepsilon\rangle$=2-3 eV) EEDF as well as both Boltzmann (T_v=500-3000 K) and modified Treanor (θ^*_1=2000-2500 K, T_g=300 K, with a plateau extending up to $v_D \leq$10-15 and deactivated tail at T_D=1000 K up to v≤25) vibrational distribution for N_2 ground state . Some examples of such model distributions together with experimental results from Tab.1 are on Fig.2. It seems that observed vibrational distributions cannot be well explained on the base of excitation/relaxation model using overall quenching coefficients for the $C^3\Pi_u$ - state vibrational levels and within the range of other model parameters (even using quite low EEDF parameters). Actually there are at least two points in $C^3\Pi_u$ state excitation model requiring further improvement.

(1) Considering that overall quenching rate of C-state at atmospheric pressure by N_2 (~ $4\cdot10^8$ s^{-1} [4]) is about one order higher than radiative one (~$3\cdot10^7$ s^{-1}[5]) , more information on vibrationally dependent rate coefficients for electronic quenching (v) as well as for vibrational quenching (vi) is necessary.

(2) Set of excitation rate coefficients for process (iii) was calculated using Franck-Condon scaled Cartwright cross section approximation [6]. However strong non-Franck-Condon excitation of vibrational levels in the near-threshold region has been recently observed (the ratios of v'=1,2 cross section to that of v'=0 are close to FCF ratios only close electron energy ~14 eV) [7].

More complex analysis including study of $N_2(B^3\Pi_u)$ and $NO(A^2\Pi)$ state excitation is in progress.

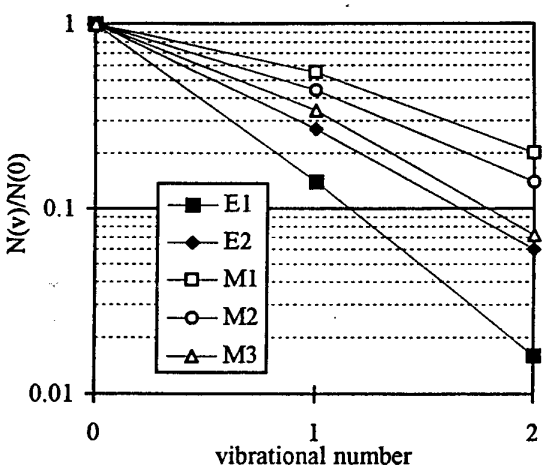

Fig.2 : $N_2(C^3\Pi_u,v)$-state distributions. Experimental results : E1) HV pulse, E2) afterglow ; model results : M1) MaxwEEDF T_e=8 eV and BoltzVDF T_v=1000 K, M2) MaxwEEDF T_e=1 eV and BoltzVDF T_v=1000 K, M3) Druyvesteyn EEDF $\langle\varepsilon\rangle$=2.5 eV, Treanor VDF θ^*_1=2500 K, T_g=300 K, v_D=10,T_D=1000 K, v≤25.

4. Acknowledgements

This work was supported by Grant Agency of the Czech Republic under contract No.202/96/0746, S.DeBenedictis and G.Dilecce undertook this work within the frame of Joint Project C.N.R.- AV CR.

5. References

[1] P. Šunka et al., HAKONE V. , Milovy (1996), 305
[2] M.Šimek et al., ESCAMPIG 13, Poprad (1996), 257
[3] S.DeBenedictis, G.Dilecce , Chem.Phys. 192, (1995), 149
[4] Yu.S.Akishev et al., Plas.Phys.Rep. 20, (1994), 525
[5] F.R.Gilmour et al., J.Phys.Chem.Ref.Data 21, (1992), 1005
[6] L.Loureiro et al., J.Phys.D 23, (1990), 1371
[7] M.Zubek , J.Phys.B 27, (1994), 573

Tab.1 Averaged $N_2(C^3\Pi_u,v)$ - state distribution over HV pulse and in afterglow.

v	HV pulse	afterglow
0	1	1
1	0.14	0.27
2	0.016	0.06

Tab.2 : Evolution of $N_2(C^3\Pi_u,v)$ - state vibrational distribution inside HV pulse.

v	delay 1	delay 2	delay 3	delay 4	delay 5
0	1	1	1	1	1
1	0.16	0.113	0.094	0.091	0.114
2	0.08	0.025	0.015	0.016	-

Study of the local discharge propagation direction on two electrolyte water channels (part I)

A.Boudjella[1], H.Hadi[2], S.Flazi[2], M.Yumoto[3], T.Sakai[3] and T.Hosokawa[4]
(1) Centre Universitaire de Mostaganem, Algeria
(2) Universite des Sciences et de la Technologie d'Oran, Algeria
(3) Mussashi Institute of Technology, Tamazutsumi, Setagaya-ku, Tokyo 158, Japan
(4)Hosei University, Department of Electronic & Electrical Engineering, Koganei, Tokyo, Japan.

Abstract

the study of the local discharge propagation direction on the solution surface of high voltage laboratory insulator of two electrolyte water channels is presented. The experimental results show that the local discharge propagation direction is influenced by the magnitude of the channel current when the gradient of potential in the electrolyte are approximately the same. On the other hand, under different gradient, the discharge moves on the direction of the channel where high gradient is expected.

1 Introduction

Because of the difficulty to carried out experiment on real polluted insulator, laboratory insulator has been proposed. The well known experimental apparatus is Obenaus model with one direction of the discharge propagation[1]. The characteristics and mechanism of the discharge development have been reported[2][3][4].

Hampton predicted that the local discharge started to elongate when the gradient of potential in the pollution is high than that of the column of the discharge [2].

Wilkins explained the discharge propagation by the increase of the discharge current[3].

At present, only quantitative explanations have been reported, but were not verified. Under Obenaus condition, it is difficult to distinct between Hampton and Wilkin's assumptions.

In the present investigation, to clarify the mechanism of the flashover phenomena, experiments were carried out on laboratory insulator of two electrolyte water channels giving to the local discharge two directions of propagation under controlled of gradient of potential, channel current and channel length.

2 Electrical description

An example of the cell used to carried out experiments is shown in figure 1. The point electrode was placed at the intersection of the channel 1 and 2 at few mm above the aqueous solution of NaCl to simulate the surface of wet polluted insulator. The channel length L_1 and L_2 are defined as the axial distance from the point to the ground electrode. r_1 or r_2 and I_1 or I_2 represented the resistance of the electrolyte by unit of length and the current in the channel 1 and 2 respectively.

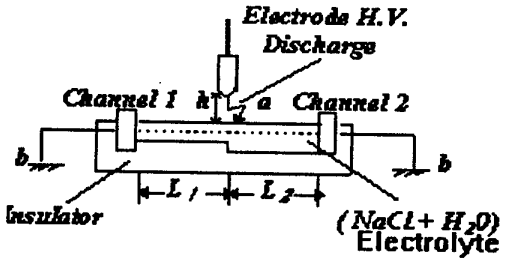

Figure 1

3 Static characteristic

The gradient of potential of the channel 1 and 2 are estimated at the local discharge length h.

$E_1=Uab/L_1 = r_1.I_1$ (1), $E_2=Uab/L_2 = r_2.I_2$ (2)

Table 1: Experimental results

	h(cm)	Voltage(KV)	Discharge direction
L1 = 10 cm R1 = 25 KΩ L2 = 10 cm R2 = 50 KΩ E1 = E2 R1 < R2	0.5	U = 12 U = 13.2 U = 14 U = 16	Channel 1
L1 = 15 cm R1 = 37.5 KΩ L2 = 5 cm R2 = 25 KΩ E1 < E2 R1 > R2	0.3	U = 7 U = 8 U = 10	Channel 2
L1 = 14.2 cm R1 = 35.5 KΩ L2 = 10 cm R2 = 50 KΩ E1 < E2 R1 < R2	0.3	U = 12 U = 13.2	Channel 2

3 Experimental results

In the following experiment, the gradient of potential and the channel current are compared under the condition of the local discharge length h.

When the gradient of potential of the channel 1 (E_1)

in the electrolyte in front of the local discharge tip is approximately equal to E_2 of the channel 2, the discharge moves on the direction of the channel 1.

In the case of high gradient of potential $E_2>E_1$ and the resistance of electrolyte in the channel 2 (R_2) is high than that of the channel 1 (R_1), the local discharge propagates on the solution surface of the channel 2.

When E_2 is kept high than that of E_1 and $R_1=37.5k\Omega>R_2=50k\Omega$, the discharge moves on the direction of the channel 2.

To know about the influence of the channel length on the local discharge propagation, resistance ohmic R_Ω is added to channel 2.

The experimental results in the table 2 shows that the local discharge can elongate towards the channel of high gradient of potential or high magnitude of current of long or short channel length.

Table2: Experimental results

R2T=R2 + R Ω	h(cm)	Voltage (KV)	Discharge direction
L1 = 10 cm, R1 = 50 KΩ L2 = 5 cm, R2 = 25 KΩ R2 = 30 KΩ,R2T = 55 KΩ E1 > E2, L1>L2,R1<R2T r1=r2=5KΩ/cm	0.5	13.5	Channel 1
L1 = 10 cm, R1 = 26.8 KΩ L2 = 6 cm, R2 = 16 KΩ R2 = 5 KΩ,R2T = 21 KΩ E1 < E2, L1>L2,R1>R2T r1=r2=2.68 KΩ/cm	0.5	10	Channel 2
L1 = 10 cm, R1 = 26.8 KΩ L2 = 6.3 cm, R2 = 16.88 KΩ R2 = 10 KΩ,R2T = 26.8 KΩ E1 = E2, L1>L2,R1<R2T r1=r2=2.68 KΩ/cm	0.5	11	Channel 1 or 2
L1 = 12 cm, R1 = 64 KΩ L2 = 4 cm, R2 = 18 KΩ R2 = 5 KΩ,R2T = 23 KΩ E1 < E2, L1>L2,R1>R2T r1=r2= 4.5 KΩ/cm	0.5	10	Channel2

4 Discussion

When $E_1=E_2$, the evolution of the discharge on the channel of low electrolyte resistance, the authors suggested that the discharge direction is affected by the magnitude of the channel current.

In ours results, maybe Hampton's condition is expected in both channels because $E_1=E_2$. But experimentally, the flashover is observed only in the channel of high magnitude of current. Under different gradient of potential, the local discharge moves on the channel of high gradient independently of the channel current.

If it was supposed that the local discharge moves onthe channel 1 or 2, the increase of the discharge current is expected in both conditions. So, the discharge development can not explained only by Wilkin's condition[3].

The local discharge appears to propagate by ionizing of a small space air in the front of the local discharge tip[3]. In ours results, the discharge development on the channel of high gradient of potential could be explained by an important ionization due to the high electric field near the local discharge tip. Under this condition, the current flowing from the discharge tip through the solution surface has no effect on the discharge direction.

The photoemission intensity from the local discharge tip has an important role in the propagation of the local discharge on the surface solution and is considered to be influenced by the current flowing into the solution through the local discharge tip[5].

When the gradient of potential $E_1=E_2$, the same ionization by the electric field in front of the local discharge tip is expected in both channels. Under this condition, may be the channel current giving high iniatory of electron by the phoemission which affected the discharge direction.

The propagation of the local discharge on the channel of high gradient of potential with low channel current, the authors suggested that the ionization process by the electric field is more effective to drive the local discharge towards the flashover compared to that of the photoemission.

5 Conclusion

The influence of the gradient of potential, current in the channel and channel length on the local discharge propagation direction towards the flashover has been investigated experimentally:

1) When the gradient of potential in the pollution of both channels are approximatelly the same, the flashover is observed on the channel of high current.

2) When the gradient of potential are different, the discharge choices the direction of the channel of high gradient independently of the channel current or the channel length.

From these results, it was deduced that the gradient of potential in the pollution in front of the local discharge tip plays an important role for the discharge propagation compared to that of the channel current.

References

[1]F. Obenaus
Die Vberschlags pannug Verschmutzter Isolatoren ETZ,Vol.56 pp.369-370,(1935).

[2]B. H. Hampton
Proc. IEE, Vol.11, No5, pp985-990(1964)

[3]R.Wilkins and A.A.J.Al Baghdadi
Proc.IEE, Vol.118,pp.1886-1892,(1971).

[4]D.C.Jolly, T.C.Cheng and D.M.Otten
Conference paper C74-068-3, IEEE PES Winter Power Meeting, (1974).

[5]H.Matsuo, T.Fujishima and T.Yamashita
IEEE Trans.on Dielectrics & Electrical Insulation, Vol.3, No3, pp444-449, (1996).

ON THE RATE OF GAS HEATING BY SMALL-SCALE NEGATIVE DC CORONA DISCHARGES

J.E. JONES

School of Mathematics, University of Wales, Cardiff, 23 Senghennydd Road, Cardiff CF2 4YH, Wales

Background

In a recent paper [1] the characteristics of the transition from a pulsed to a pulseless regime mid-way in the current range for a point-plane negative discharge were discussed where the gap separations d were in the range 4 - 20 mm. Although the transition is smooth rather than abrupt, it is nevertheless quite distinct and can be clearly identified in the plots of the central peak of the planar current j_0 against the overall current I. It has also been shown to be associated with the disappearance of the central current-dimple [2] in the planar current profiles, so that Warburg's law is exactly obeyed, and with the planar current disc attaining its asymptotic diameter. Briefly, it was shown from the measurements that transition occurs when I has a critical value $I_c(d)$ given by

$$I_c(d) = Cd \text{ where } C \cong 15\,\mu\text{A/mm} \quad (1)$$

and when j_0 has the critical value j_c given by

$$j_c(d) = D/d \text{ where } D \cong 7{\cdot}5\,\mu\text{A/mm} \quad (2)$$

which can be confirmed theoretically. Above the transition, the central planar current j_0 obeys the exponential law

$$j_0 = \overline{j_0(d)}\,\exp\left(\alpha(d)\,I\right) \quad (3)$$

where

$$\overline{j_0} \propto 1/d \text{ and } \alpha \propto 1/d^{2.5} \quad (4)$$

so that the current on the central axis of the discharge rapidly increases with the total current I or voltage V. These are the relevant findings as far as the present paper is concerned. However, many other qualitative and quantitative properties of the transition and of the region that lies beyond it were presented in the original paper [1].

The reason put forward for both the transition and the behaviour of the pulseless regime leading to breakdown is the axial gas heating in the central channel. It was suggested [1] that this is associated with a critical energy deposition by the ionic currents in the region beneath the coronating point. This suggestion is in line with the observations of Kurimoto and Farish [3] and with the breakdown theory for positive coronae proposed by Marode [4]. The present paper gives an initial survey of the theory of this heating and quantifies the rate of temperature increase for these small-scale negative discharges in air.

Gas Heating by Ionic Currents

Current distributions **j** do work at a rate per unit volume given by

$$\mathbf{E}\cdot\mathbf{j} = \mu\rho\,\mathbf{E}^2 \quad (5)$$

where **E** is the electric field, μ is the ionic mobility and ρ is the charge density. This is the rate at which the electrostatic energy is transferred to the thermal free-energy of the gas [5], so that the rate of increase of energy per molecule is $\mu\rho\,\mathbf{E}^2/n$ where n is the number density of neutral molecules (much larger than the number density of ions). As gas temperature can be defined by the classical form

$$\frac{2}{3}\frac{1}{R}\overline{\frac{1}{2}mq^2} \quad (6)$$

where $\overline{\frac{1}{2}mq^2}$ is the mean kinetic energy per molecule and $R = 1{\cdot}379 \times 10^{-23}$ kg m^2/s^2 K is Boltzmann's constant, the local rate of increase of the gas temperature is given by

$$\frac{2}{3}\frac{1}{Rn}\,\mu\rho\,\mathbf{E}^2. \quad (7)$$

The above form (7) is true for the drift region and the glow, the reasoning for the glow region being as follows: if a charge-carrier (ion or electron) is being created at a rate r_k, $k = 1\ldots$ at any point, then for each type of carrier, the electrostatic field is supplying energy at a rate $r_k\phi$ where ϕ is the local electrostatic potential. However, summing over the carriers shows the total of this energy supply $\sum r_k\phi$ to be zero as ϕ is independent of k and $\sum r_k = 0$ (charge cannot be created or destroyed but only separated).

Temperature Increase in the Pulsed Regime

As part of a comprehensive study [6, 7], finite-element techniques have been used to solve the field equations with a gap separation d of 10mm and an overall current I of 100 μA in a negative DC discharge. Transition at this gap separation takes place at about 150 μA [1] so that the solution is typical of the pulsed regime. As the temperatures in the central channel are the largest in the interelectrode gap, the numerical solution for **E** and **j** has been used to give the rate of heating on the axis as a function of the upward distance

z from the plane. Note that the neutral molecule density $n \cong 2{\cdot}5 \times 10^{25}$ for air. Results are given in the figure. As can be seen, rates of temperature increase for the lower half of the gap are circa 500 K/s; in the upper half temperature rates increase steeply so that in the vicinity of the tip near the edge of the glow, (not shown) they are of the order 10^4 K/s.

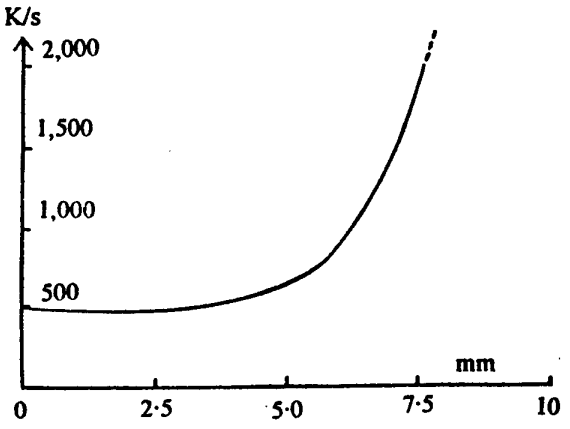

Axial rates of heating plotted against distance z for d = 10mm

Temperature Increases in the Pulseless Regime

In the absence of accurate numerical results for pulseless coronae, reasonable estimates of field values in the gap have to be used in this preliminary study. Only on the plane are measured values of the current distribution known [1], and even here accurate values are obscured by measurement difficulties [8]. There are good reasons for thinking that true values are higher than the "measured" values which are spatial averages. Taking a gap separation d of 10 mm, the shown tabular estimates of the temperature rates of increase have been obtained from known theoretical relationships. For example, there is Warburg's general form [9] giving the current-voltage-separation relationship; and also asymptotic charge-drift methods [10] which show that the average planar values of the charge density, current and power transfer are $\varepsilon_0 V/d^2$, $\varepsilon_0 \mu V^2/d^3$ and $\varepsilon_0 \mu V^3/d^4$ respectively (here ε_0 is permittivity). The range of quoted values run from transition upwards (breakdown was not risked in the experiments in order to protect the apparatus).

	Plane centre	Drift average	Glow tip on axis
E (kV/mm = 10^6 V/m)	0·6 − 0·8 +	1·2 − 1·7 +	2·5
J (μA / mm^2 = A / m^2)	0·7 − 2·0 +	0·27 − 0·55 +	3·5 − 10 +
temperature rate (K/s)	850 − 3,200 +	650 − 1,900 +	17,500 − 50,000 +

Conclusions

Given the previously mentioned likely increase of true current values over measured values because of the averaging effect of current probes, it seem that the temperature rates of increase (heating effects) in the pulseless regime are considerably larger than those for pulsed corona. Moreover, the volume where this heating effect is significant (the central channel) is strongly localized in the region near the central axis. These findings support the suggestion of a critical energy. Readers should note the the quoted values are only notional rates of heating as there are cooling mechanisms (conduction, convection, the electric wind) present to counteract the heating so that stable constant temperature situations exist. Nevertheless, the quoted values seem to be in line with the suggested 500 K excess temperature values of the initial study [1].

Acknowledgements

This work has been supported by the British Council in Paris and also by the Royal Society.

References

1. A. Goldman, M. Goldman and J.E. Jones, Proc. X Int. Conf. Gas Discharges, Swansea (1992) 270, ISBN 0 9519465.

2. M.Davies, A. Goldman, M. Goldman and J.E. Jones, Proc. XVIII ICPIG, Swansea (1987) 656 ISBN 0 9511848 0 6.

3. A. Kurimoto and O. Farish, IEE Proc. (1980) 127A (no 2) 89.

4. E. Marode, F. Bastien and M. Bakker, J. Appl. Phys. 50 (1979) 140.

5. J.E. Jones, J. Phys. D: Appl. Phys. 23 (1990) 164.

6. M. Davies, A. Goldman, M. Goldman and J.E. Jones, Proc. 5th ISH Braunschweig 32-04 (1987).

7. J.E. Jones and M. Davies, J. Phys. D: Appl. Phys. 25 (1992) 1749.

8. J.E. Jones, to be published in Prox. XI Int. Conf. Gas Discharges Greifswald (1997).

9. E. Warburg, Wied. Ann 67 (1899) 68.

10. J.E. Jones, J. Electrostatics 27 (1992) 283.

GAS TEMPERATURE ESTIMATIONS FOR SMALL-SCALE NEGATIVE DC CORONA DISCHARGES IN AIR

J. E. JONES

School of Mathematics, University of Wales, Cardiff, 23 Senghennydd Road, Cardiff CF2 4YH, Wales

Introduction

The voltage range for small scale point-plane negative DC corona in air can be divided into two regimes [1]. At lower voltages V the discharge is pulsed and displays the characteristics of an increasing planar current radius and a central dimple-like suppression of the Warburgian current [2]. There follows a smooth transition whose mathematical description can be found in another paper in these proceedings [3]. At higher voltages the discharge is pulseless with a fixed planar current radius and an axial current augmentation that behaves exponentially with the total current I. The coefficients of this exponential law are dependent on the gap separation d [1,3], and breakdown is approached as the voltage/current is further increased.

In the original paper [1], the reason put forward for the transition and the formation of the axial current channel was the gas temperature increase associated with a critical energy deposition by the ionic currents. This corresponds to the suggestions of other researchers [4,5]. As pressure $p = nRT$ (usual notation) will not vary greatly across the gap, an increased axial temperature T implies a reduced gas molecule number density n in the central region. Values of E/n on the Paschen characteristic are increased so preparing the gap for breakdown. In the inaugural paper [1], a 500K estimate of this temperature was given for the pulseless regime that was based on the work of Yamada et al. [6]. Here, a theory based on the balance between ionic heating and conduction leads to alternative temperature predications based on the field equations.

The Temperature Distribution

In a sister paper in these proceedings [3] it is shown that the local rate of gas heating by ionic currents in both the drift and glow regions is

$$\frac{2}{3}\frac{1}{Rn}Ej = \frac{2}{3}\frac{1}{Rn}\mu\rho E^2 \qquad (1)$$

where R is Boltzmann's constant, j is spatial current magnitude, E is field strength, μ is mobility and ρ is space charge density. Estimates for the size of the axial heating in K/s for both the pulsed and the pulseless regime are given in the paper. This is a notional rate of heating, however, as conduction, convection, the electric wind etc. counterbalance the heating so that a stable situation exists. In this paper, only the conduction of the gas in the axial direction is taken into account. Perhaps this is an over-simplification leading to exaggerated values, but it seems a reasonable way forward at this stage in the development of a theory.

The local rate of temperature increase by conduction is

$$\frac{k}{\overline{m}nC_v}\frac{\mathrm{d}^2T}{\mathrm{d}z^2} \qquad (2)$$

where k is the conduction coefficient, $\overline{m}$ the mean molecular mass, C_v the specific heat at constant volume and z is the axial coordinate measured upwards from the plane. This is an ordinary Fourier expression as the radial Laplacian terms have been omitted. As this rate of increase is given by the transfer of energy from the electrostatic field (1), it follows that

$$\frac{\mathrm{d}^2T}{\mathrm{d}z^2} = \frac{2}{3}\frac{\mu\overline{m}C_v}{kR}\rho E^2 \equiv \gamma\rho E^2 \qquad (3)$$

defining the coefficient γ. Using a classical approach [6] it can be shown that γ is temperature invariant.

Charge Drift Field Estimations

Charge continuity when viewed from a Lagrangian point of view [7] results in the charge drift equation

$$\frac{\mathrm{d}\rho}{\mathrm{d}t} = -\frac{\mu}{\varepsilon}\rho^2 \qquad (4)$$

which is easily integrated to give

$$\frac{1}{\rho} - \frac{1}{\rho_0} = \frac{\varepsilon}{\mu t} \qquad (5)$$

where t is the time of flight, ρ_0 is the initial density and ε is permittivity. As stated in the original paper [1], there are arguments that can be put forward to justify the assumption of a uniform electric field in the gap. At a central position at a distance z above the plane, the time of flight from the point would therefore be

$$t = \frac{(d-z)\,d}{\mu V} \qquad (6)$$

so that an upper bound (asymptote) for ρ is

$$\rho = \frac{\varepsilon V}{(d-z)d} \geq \overline{\rho} \equiv \frac{\varepsilon V}{d^2} \text{ if } 0 \leq z \leq d. \quad (7)$$

Using the above in equation (3) gives

$$\frac{d^2T}{dz^2} = \frac{\gamma\varepsilon V^3}{(d-z)d^3} \equiv \frac{\Gamma d}{d-z} \quad (8)$$

using ρ and defining Γ, and

$$\frac{d^2T}{dz^2} = \frac{\gamma\varepsilon V^3}{d^4} \equiv \Gamma \quad (9)$$

using the simpler form $\overline{\rho}$.

Integration of the forms (8) and (9) is straightforward and results in

$$T - T_0 = \Gamma d\left[(d-z)\ln\left(\frac{d-z}{d}\right) + z\right] \quad (10)$$

and

$$T - T_0 = \frac{\Gamma}{2}z^2 \quad (11)$$

respectively, where T_0 is the ambient temperature. Here the boundary conditions $T = T_0$ at $z = 0$ and $\frac{dT}{dz} = 0$ at $z = 0$ are used which are reasonable. Hence the temperature adjacent to the tip at $z = d$ is given by

$$T - T_0 = \Gamma d^2 \text{ or } \frac{\Gamma d^2}{2} \quad (12)$$

depending on whether form (10) or (11) is used. Further consideration of the charge drift theory [7] shows that these are bounds of the linearized conduction equation (3).

Numerical Results and Discussion

The standard values

$\mu = 1{\cdot}8\times10^{-4}$ V/ms, $\overline{m} = 6\times10^{-26}$ kg,

$\varepsilon = 8{\cdot}85\times10^{-12}$ C²/Nm², $R = 1{\cdot}4\times10^{-23}$ kg m²/s²K

$k/C_v = 3{\cdot}3\times10^{-5}$ kg/ms (viscous coefficient) (13)

were used with the published values [1]. In the experiments, gap separations d were in the range 4-18 mm, and transitional total current values were deduced to be given by

$$I_C = Cd \quad (14)$$

where C = 15 μA/mm, if I_C is measured in μA and d in mm. Hence, by Warburg's general form in which Id varies as V^2, it follows that

$$\frac{V}{d} \cong 1{\cdot}34\,\text{kV/mm} \quad (15)$$

at transition. The range of V above transition was restricted in order not to risk equipment damage at breakdown, but voltage values increase by at least 50% above transition. The $(V/d)^3$ term in Γ therefore increases by at least a factor of 3.

As can be seen from equations (3), (8) and (9), the temperature excess varies as $(V/d)^3 d$, so that taking d = 10 mm as a reference value, the bounds given by equation (12) for $T - T_0$ at transition are

$$690\text{ K} \leq T - T_0 \leq 1380\text{ K}. \quad (16)$$

If, for example, bounds for d = 4 mm are required then they will be 40% of the above. As radial conduction, convection etc. have been ignored, it is the lower of the bounds that is likely to be of the order of the magnitude of the true temperatures; and this corresponds to the 500 K prediction of the original paper [1]. When breakdown is approached, using the previously explained factor of ~ 3 it seems that temperature excesses for d = 10 mm could be as much as

$$2{,}000\text{ K} \leq T - T_0 \leq 5{,}000\text{ K}. \quad (17)$$

However, other physical effects of the sorts already mentioned are likely to substantially attenuate these temperatures. Nevertheless, the linearized theory of gas conduction implies gas temperature excesses of at least several hundred degrees, possibly a few thousand, in the central current channel for the pulseless regime.

Acknowledgements

This work has been supported by the British Council in Paris and also by the Royal Society. It forms part of a collaboration with A. and M. Goldman of CNRS/ESE near Gif sur Yvette.

References

1. A. Goldman, M. Goldman and J.E. Jones, Proc. X Int. Conf. Gas Discharges, Swansea (1992) 270, ISBN 0 9519465.

2. M.Davies, A. Goldman, M. Goldman and J.E. Jones, Proc. XVIII ICPIG, Swansea (1987) 656, ISBN 0 9511848 0 6.

3. J. E. Jones, Proc.XXIII ICPIG, Toulouse (1997).

4. A. Kurimoto and O. Farish, IEE Proc. 127A2 (1980) 89.

5. E. Marode, F. Bastien and M. Bakker, J. Appl. Phys. 50 (1979) 140.

6. J.E. Jones, to be published.

7. J.E. Jones, J. Phys. D: Appl. Phys. 23 (1990) 164.

A DEGENERATE PROBLEM IN THE VARIATIONAL APPROACH TO CHARGE DRIFT

J. E. JONES

School of Mathematics, University of Wales, Cardiff, 23 Senghennydd Road, Cardiff, CF2 4YH, Wales

Introduction

The calculus of variations gives rise to perhaps the most powerful techniques for solving problems in mathematical physics. But as with most methods there are strengths and weaknesses. For example, there are occasions when integral functionals are physically meaninglesss even though their extremals are based on physical principles. There are also difficulties if the integral is an exact differential as the Euler-Lagrange equation is identically zero; and not all of the governing equations of phenomena can be associated with the variation of an integral. Nevertheless, the success of variational techniques in the field problems of electrostatics is well-known.

In the theory of corona discharges the two main equations to be solved are Poisson's equation and the charge continuity equation. As an alternative to the latter, charge drift methods can be used [2-6], and variational principles for the two field equations have been established. In this new formulation [2, 4, 5] the simultaneous nested minimization of two integrals is the equivalent of solving the field equations. In the Poissonian integral, the electric potential ϕ is assumed known and an extremal is sort for the variable charge distribution σ; whereas in the charge drift integral the charge distribution ρ is taken as known and the potential function ψ is allowed to vary. The dual approach with the roles of the two distributions interchanged in the integrals was not given, as an integral functional for the charge drift equation with a known potential ϕ and unknown distribution σ could not be found. The inability to formulate this problem is the subject of this paper and the consequent implications for the theory of charge drift are also considered.

Poissonian and Charge Drift Variations

It is well known that the minimum of the integral

$$\int_D \left[\frac{1}{2}\,\varepsilon(\nabla\psi)^2 - \rho\psi\right] \mathrm{d}D \qquad (1)$$

is achieved when $\psi = \phi$ where ϕ is given by

$$\nabla^2\phi = -\rho/\varepsilon. \qquad (2)$$

This has a physical meaning as the integral (1) over all space D is a Hamilton-like principle involving a field energy minimization where the charge distribution is ρ and the potential is ψ. The dual of this variation is the extremizing of the integral

$$\int_D \left[\frac{1}{2}\sigma^2 - \varepsilon\nabla\phi.\nabla\sigma\right] \mathrm{d}D \qquad (3)$$

where the extremal ρ of the functions σ satisfies Poisson's equation (2). It is significant that this integral does not have a physical meaning.

The previously published charge drift formulation [2, 4, 5] now comes from the time rate of change of the energy integral (1) when power is consumed by ion-molecule collisions characterized by a mobility coefficient μ. This gives

$$\int_D \left[\mu\rho(\nabla\psi)^2 + 2\psi\frac{\partial\rho}{\partial t}\right] \mathrm{d}D \qquad (4)$$

whose minimal satisfies the drift equation [2-6]

$$\frac{\mathrm{d}\rho}{\mathrm{d}t} = -\frac{\mu}{\varepsilon}\rho^2 \left(= \mu\rho\nabla^2\phi\right) \qquad (5)$$

where the total time derivative is taken when travelling with the ions. The previously mentioned simultaneous minimization of the integrals (3) and (4) is therefore equivalent to solving the continuity and Poisson's equations. The dual approach utilizing (1) and the time rate of change of (3) is therefore an important consideration as it would be the basis of an alternative finite element method to that given by the above.

Degeneracy

It is easy to demonstrate that an integral in terms of a known ϕ and unknown σ which has an extremal ρ given by equation (5) cannot be found. The algebraic possibilities for the integrand are soon exhausted (exact differentials appear); and the non-existence can be shown more formally as follows. If the integrand $F(t, \rho, \rho')$ satisfies the Euler-Lagrange equation (5), in the simple time-dependent case when moving with the ions, the extremal $\rho(t)$ is given by

$$\frac{\mathrm{d}F_{\rho'}}{\mathrm{d}t} - F_\rho \equiv \frac{\mathrm{d}}{\mathrm{d}t}\left(\frac{1}{\rho} - \frac{\mu t}{\varepsilon}\right) = 0. \qquad (6)$$

Expanding the first term in the usual way, as there is

no term in ρ'' in the second expression involving ρ, it follows that F is at most linear in ρ' so that it has the form

$$F = \rho' f(\rho, t) + g(\rho, t) . \qquad (7)$$

Substituting this back into equation (6) gives a contradiction as the tems in ρ' cancel in the left-hand expression so that it cannot equal the second expression which involves ρ'. An integrand F satisfying equation (6) therefore does not exist.

As the charge drift integral (4) has been shown to be the time rate of change of the Poissonian integral (1), it is interesting to find the extremal of the time rate of change of the dual charge drift integral (3). Using the divergence theorem and the boundary conditions on ϕ at infinity (σ can be piecewise continuous), then the time rate of change of (3) can be written

$$\left(\frac{\partial}{\partial t} - \mu \nabla\phi . \nabla\right) \int_D \left[\frac{1}{2}\sigma^2 + \varepsilon\sigma\nabla^2\phi\right] \mathrm{d}D \qquad (8)$$

which can be expanded in the usual way. Hence, allowing time to be part of the domain D (this does not alter the extremal of (3)), the Euler-Lagrange equation reads

$$\mu\rho\nabla^2\phi + \mu\varepsilon\left(\nabla^2\phi\right)^2 = 0 \qquad (9)$$

so that either Laplace's equation or Poisson's equation (2) is recovered rather than the required charge drift relation (5), and nothing has been gained by this approach.

In the above analysis, time is regarded as an independent variable. If, alternatively, only the spatial variables are considered, the Euler-Lagrange equation becomes

$$\frac{\partial\rho}{\partial t} + \mu\rho\nabla^2\phi + \varepsilon\nabla^2\frac{\partial\phi}{\partial t} + \mu\varepsilon\left(\nabla^2\phi\right)^2 = 0 \qquad (10)$$

which is also degenerate and identically zero as in any field calculation Poisson's equation must always be satisfied. In conclusion, whatever manipulations have been tried, the term involving the time derivative of the charge distribution in the drift equation is problematical as it either always directly cancels in the Euler-Lagrange equation or it is balanced by a time derivative of ϕ which similarly cancels when Poisson's equation is used.

Implications of Degeneracy

The strength of variational techniques make them an obvious choice of method when solving problems in field theory. In the theory of charge drift [2, 4, 5], the author found that these methods were not effective when dealing with temporal changes in space charges, and other approaches had to be used. Two major results in particular seemed to defy variational methods. The first of these is that a cloud of ions with mobility μ inexorably expands at a linear rate given by

$$D = D_0 + \frac{\mu Q}{\varepsilon} t \qquad (11)$$

where D represents the volume of the cloud of total charge Q. The second is the asymptotic shape theorem [2, 4, 5], which for ions of a single mobility implies that any distribution of space charge approaches a spherical shape before it disperses by the mutual repulsion of the ions. The reason for this lack of success (not reported in the publications) can now be seen from the findings of the previous section.

The only variational formulation of the charge drift equation (5) is the minimizing of the integral (4) in which both ρ and its time derivative are known functions. This effectively removes the physical charge movements from the mathematical formulation: the time derivative of ρ is a given function that appears in the integrand so that the allowed variations in ψ do not describe the ionic flow in any way. This variational principle is therefore useless in describing any temporal changes in the charge distribution. The lack of a dual principle in which ϕ is known and σ is allowed to vary with time is therefore crucial to the effectiveness of the whole approach. There is no foothold for the calculus of variations in charge drift problems unless the time rate of change of the charge distribution at any position is found by some other means. Only under these circumstances can variational methods be used by the simultaneous minimizing of integrals (3) and (4).

Acknowledgement

This work has been supported by the Royal Society.

References

1. P. Hammond, Energy Methods in Electromagnetism (1981), Oxford: Clarendon.

2. J. E. Jones, J.Phys.D: Appl.Phys. 23 (1990), 164.

3. J. E. Jones, M. Davies, A. Goldman and M. Goldman, J. Phys. D: Appl. Phys 23 (1990), 542.

4. J. E. Jones, J. Electrostatics, 27 (1992), 283.

5. J. E. Jones, *Essays on the Formal Aspects of Electromagnetic Theory* (1993), 228, World Scientific. ISBN 981-02-0854-5.

6. J. E. Jones, J.Phys.D. Appl.Phys. 27 (1994), 1835.

Physics of super undercritical streamer discharge in UHF electromagnetic wave

K.V.Khodataev
Moscow Radiotechnical Institute, Russian Ac. of Sci.
Warshavskoe shosse 132, Moscow 113519, Russia
Fax: 7(095) 314-1053. e-mail: khodataev@glas.apc.org

1. Introduction

The streamer discharge in UHF electromagnetic fields is one of the finest and the most misunderstood nature phenomena. It arises in dense gas in a beam of electromagnetic wave radiation. In a dense gas an electrodeless UHF discharge have a complicated filamentary structure. The discharge is shaped as a net of very thin luminous filaments with bright fragments, which length approximatelly equals half wave length of radiation The discharge consists of thin filaments selforganized into electrodynamic resonant vibrators and loops, rising one from another and propagating away from initiating point. The observations show that filament fragments of discharge net do not exist simultaniously but are arising one from another The 5-10 cm wave length radiation and 0.3-1 atm air pressure are good conditions for observation of the discharge [1,2,3,]. After creation the arised discharge can be supported by radiation with electric field amplitude much less than critical value E_{cr}. It was found experimentally that the electrodeless discharge can continiously exist even if undercritical parameter E/Ecr equals 1/50 and less [4]. It is possible by due to streamer effect. The electric field on the ends of thin filament is much more than unperturbed field.

There are many experimental studies of the UHF streamer discharges, but a satisfactory theory of this phenomenon is absent today. It is caused by very hard mathematical difficulties from one side and absence of clearness in physical mechanisms driving the process, from other side. The mathematical model for discription of a discharge fragment of the undercritical UHF discharge and numerical investigations of its spatio-temporary evolution are presented in the paper.

2.Theoretical model

It is clear that mathematical model of the streamer discharge in UHF electromagnetic wave must take in to account the 3D geometry, fully electromagnetic field discription selfconsistent with discharge , plasma chemistry and gas dynamics. So as investigation of filament net is very complicated the single filament fragment of the net is chosen as modelling object.

It is found the method of calculation of the electromagnetic fields at thin filament with radius-length ratio up to minus several orders of value and with arbitrary conductivity distribution along filament by means of the integral Pocklington type [5,6] equation for electric field amplitude E on the filament axis z:

$$E(z) = E_{ext} + i\cdot\int_{-\infty}^{\infty} E(z')\cdot W(z',z)\cdot k\cdot dz',$$

where

$$W(z',z) = \frac{2\pi\sigma(z')}{\varpi}\cdot\Psi(\sigma(z'))\cdot G'(z',z),$$

$$G'(z',z) = \frac{G(R)}{R^2}\times\left[(1-i\cdot kR)\cdot\left(2-3\frac{a^2}{R^2}\right)+(ka)^2\right],$$

$$G(R) = \exp(i\cdot kR)/R,$$

$$R(z',z) = \sqrt{a^2+(z'-z)^2},$$

$$\Psi(\sigma) = \int_0^a J_0\left[-\sqrt{1+i\cdot 4\pi\sigma/\varpi}\cdot k^2 r dr\right],$$

$k=\varpi/c$- wave number, a- the filament radius, σ- conductivity, ϖ- field frequency, E_{ext}- external wave field. The integral equation have solved numerically together with hydrodynamic equations in frame of isobaric approximation, which take into account the next physical-chemical processes: 1)ionization in electric field by electron impact and in heated gas, 2)electron dissotiative and 3-body attachment, 3)recombination, 4)electron diffusion, ambipolarity field and electron drift in UHF electric field [7], 5)gas heating [8], 6)radiative losses.

$$\frac{d\sigma_n}{dt} = \left[K_i(E,N) - K_a(E,N) - R_{rec}(E,N)\cdot\sigma_n\right]\sigma_n N +$$

$$+\frac{1}{N}\cdot\nabla\cdot\left(D(E,N,\sigma)\cdot\nabla(\sigma_n N)\right),$$

$$\frac{dN}{dt} = -N\cdot[\sigma\cdot\Theta(\sigma)\cdot E^2 - Irad(N)],$$

$$\sigma = \sigma_n + \sigma_{Saha}$$

where

K_i, K_a- impact ionization and attachment velocity rates, $R_{rec} = \alpha\cdot mK_{tr}/e^2$ (α- recombinatin coefficient), σ_n - nonequelibrium conductivity, σ_{Saha} - equilibrium conductivity, D - effective diffusion coefficient, I_{rad} - radiation losses, θ takes into accout a skin effect.

3.The simulation result

It is shown that only correct accounting of all the mentioned factors and their dependenses on electron

and gas temperature gives possibility to simulate the evolution of the streamer discharge in UHF electromagnetic field, which is less than critical one. It must be noted especially the key role of free electron diffusion and oscillatory drift on the streamer ends [7] and gas heating. Fig.1 and 2 demonstrate the behavior of the undercritical streamer discharge. One can see on Fig.1 that initial hot plasmoid with small length and conductivity is rising slowly until its length reach the resonant value. At that moment (t = 13 mks) the streamer ends velocity is maximum and equals ~$2 \cdot 10^5$cm/s. After the resonance the streamer growth is stoped.

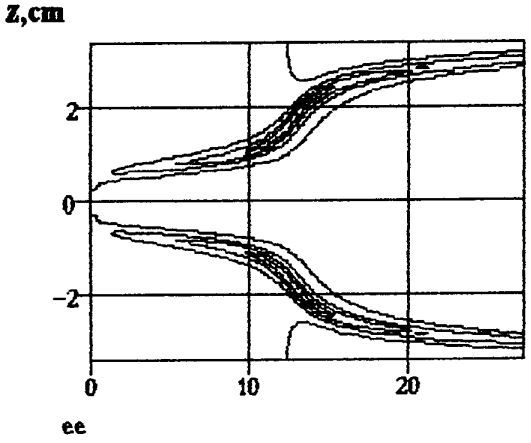

Fig1. Contour plot of electric field amplitude on the filament axis E(z,t). E_{ext}=0.25·E_{cr}, λ=8.5cm.

Fig.2 shows that streamer effect takes place indeed. The field increases on the ends of filament so as difference between ionization and attachment frequencies is positive inside the streamer.

The conductivity in medium part of the filament at resonance moment is enough for the skin layer to be less than filament radius. It is the necessary condition for high enough quality of a resonant vibrator. But conductivity on the streamer head is relatively small, it is less than $\omega/4\pi$.

The calculated discharge filament velocity and length are similar to that observed.

After resonance achivement the filament does not grow but heating continues. The temperature grows up to 2÷3 eV along whole filament. The temperature rises slowly when the wave field is undercritical, so isobaric approximation is applicable.

4.Discussion

The real phenomena is much more complicated than the model. The question about streamer radius remains to be open. In frame of usual plasma hydrodynamics one can suggest that the streamer head radius is defined by necessary field growth at the streamer head but it can not be less than ionization avalanche front depth [7]. In a real discharge there are many filaments. Their currents influence one another. The filament placed nearer to the wave radiation source has advantage and shields the filaments situated farther from the source. The shielding effect limits the life time of a filament after arising of the next one.

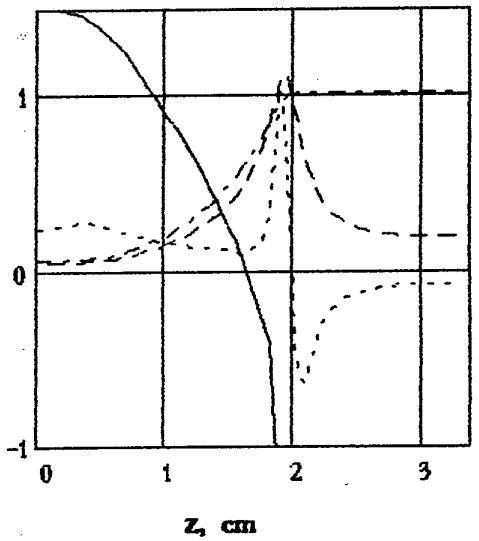

Fig. 2. The distributions along filament axis in resonance moment t=13 mks.
log(4πσ/ω)-solid, $(\nu_i-\nu_a)/\nu_{ar}$-dot, E-dash, N/N_0-dadot line.

The developed UHF streamer model will be used for more detail study of streamer behavior at any conditions.

I bring my thanks to Dr. L.P.Grachov and Dr. I.I.Esakov for useful discussions.

5.References

[1] L.P.Grachov, I.I.Esakov, G.I.Mishin, K.V.Khodataev. Jurnal Technicheskoy Physiki (Russian), т.66, 7 (1996) 32

[2]L.P.Grachov, I.I.Esakov, G.I.Mishin, K.V.Khodataev. Jurnal Technicheskoy Physiki (Russian), т.65, 5 (1995) 21

[3]L.P.Grachov, I.I.Esakov, G.I.Mishin, K.V.Khodataev. Jurnal Technicheskoy Physiki (Russian), т.65, 11 (1995) 86

L.P.Grachov, I.I.Esakov, G.I.Mishin, K.V.Khodataev. Jurnal Technicheskoy Physiki (Russian), т.65, 7 (1995) 60

[5] .Pocklington H.C., Camb. Phil. Soc. Proc., 9 (1897) 324.

[6] Richmond J.H., Proc. IEEE, 53 (1965) 796

[7]K.V.Khodataev, B.R.Gorelik. Physika plasmy (Russian), т.23, 3, (1997) 1

[8]K.V.Khodataev. Himicheskaia physika (Russian), т.12, 3 (1993) 303

Development of a Low Ozone Generation Corona Charger and Application for NH_3 Reduction in Waste Gas

M.Kogoma , T.Inomata , S.Okazaki

Faculty of Science and Technology

Sophia University ,

Kioicho 7-1,Chiyoda-ku, Tokyo 102 , JAPAN

Introduction

A charge - up process on photo semiconductor surfaces for laser printer and eletro-photography is generally used for negative corona discharge , but the negative corona charger encounters more ozone formation than that obtained during application of a positive corona. However, the sensitivity of the photo-semiconductor is not sufficient for the positive corona , so one must use the negative corona. To solve these problems , recently we reported the development of new type corona charger which has strongly restrained the ozone production by using of catalyst coated heating wire electrode [1] .

In general, because of the criteria of environment about the waste gas control through a discharge system, we need to reduce the concentration of residual ozone in the exhausted gas to the ambiance. For example, the waste gas exhausted from a biodegradation system of home perishable dust contain important concentrations of ammonia gas that is main reason of its smell. So, we tried to much ozone production or bi-producted NOx by applying the new type corona charger.

In the corona discharge, ozone is produced in the region of the center wire electrode; this phenomenon has been well studied. The oxygen atom formation reaction (1) produces the ozone in the next reaction (2) .

$$O_2 + e \rightarrow 2O + e \quad (1)$$
$$O + O_2 + M \rightarrow O_3 + M \quad (2)$$

The main reaction of ozone formation(2)has a negative activation energy, so the amount of ozone shall be decreased with ascending temperature of center wire electrode.

If the surface of the wire electrode is covered with ozone dissociating catalyst, also, the catalystic reaction occurs on the center electrode. So, it is expected that the ammonia dissociation reaction will be prior to the ozone formation reaction in the discharge zone.

Experimental

A corona discharge tube has a fine wire electrode (50micrometer radius) of tungsten in the center of stainless tube of 2.2cm diameter. In fig.1, a circuit for applying continuous voltage, for heating of the fine wire and for measurement of wire temperature is shown.

Heating of the wire is done by direct current. Wire temperature was measured from the change of wire resistance , which was analyzed in a bridge circuit . The bridge circuit and heating circuit was separated by a blocking condenser.

Sample gases are air and NH_3 mixed(100ppm) air. Ozone concentration was measured by the KI titration method. the flow rate of air was $600cm^3min^{-1}$. NH_3 concentration measurement was done by the detection tube(Gas-Tech Corporation). Tungsten corona wire length was 225mm; inner diameter of tube electrode was 22mm.

Results and Discussion.

Fig.2 shows the ozone yield as a function of discharge current of negative corona. This means the amounts of ozone formation are directly proportional to the discharge current. It is clear that the ozone yields are decreased with increasing of the wire temperature and coating of catalyst on the wire surfaces.

Fig. 3 shows the ozone yield as a function of discharge current of positive is like as in the negative corona ,ozone concentration level is much larger than in positive corona. The different efficiency between the polarites is may be attributed to the difference of cross section areas of discharge zone. In the case of positive corona, the electrons formed at the edge of discharge zone, which is close to the center positive electrode are swarming to the electrode and change quickly. On the contrary, in negative corona, all of electrons are going to outer electrode which is far from the discharge zone. Then, the reaction(1) is faster than that in positive corona.

Fig.4 shows reduction rate of NH_3 as a function of discharge current. On the reduction efficiency, a negative corona has a value about twice as high as that of positive corona. But, in the ozone formation rate , a negative corona has a value about ten times faster than that of in positive corona. So, the ratio of ozone formation to reduction rate of NH_3 is much better in positive corona. Thus we need low concentration of ozone in waste gases.

Fig.5 shows NOx yield vs. discharge current . In the case of positive corona, NOx concentration is rapidly increase with increasing of current. On the other hand, in the negative corona , we have no NOx formation. So, There is some antagonistic advantage between ozone formation and NOx reduction rate.

In conclusion, catalyst coated heating wire corona discharge system is able to reduce NH_3 from waste air .

[1]Okazaki, M.Kogoma, T.Inomata, Proceedings of HAKONE V, p.283(1996) Milovy,Czch Republic

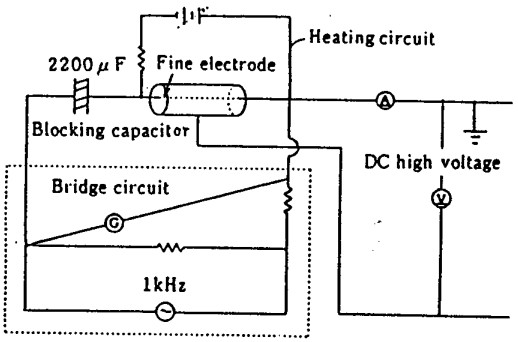

Fig.1 Schematic of corona discharge apparatus

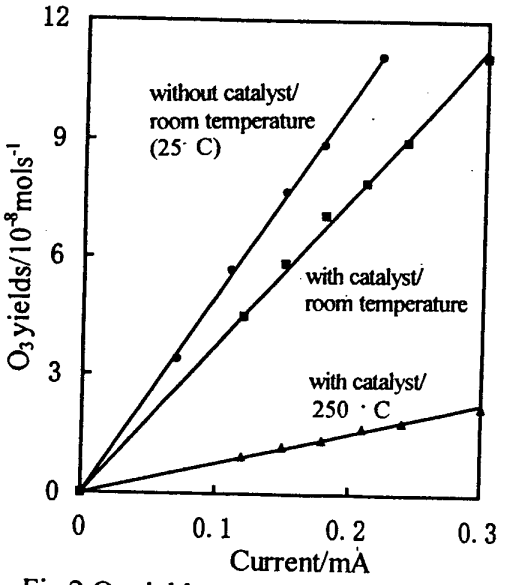

Fig.2 O_3 yields vs. discharge current (negative corona)

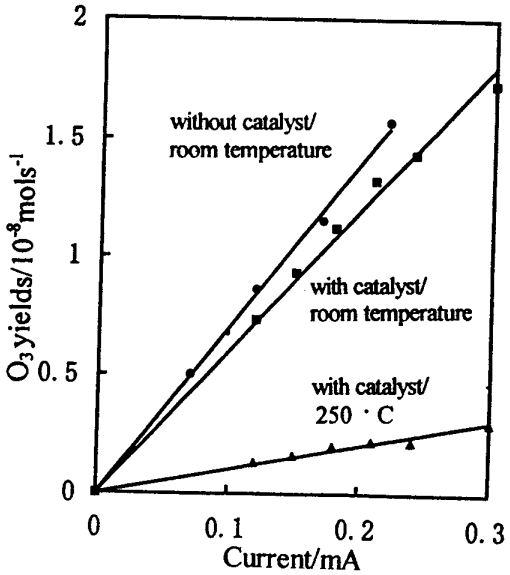

Fig.3 O_3 yields vs. discharge current (positive corona)

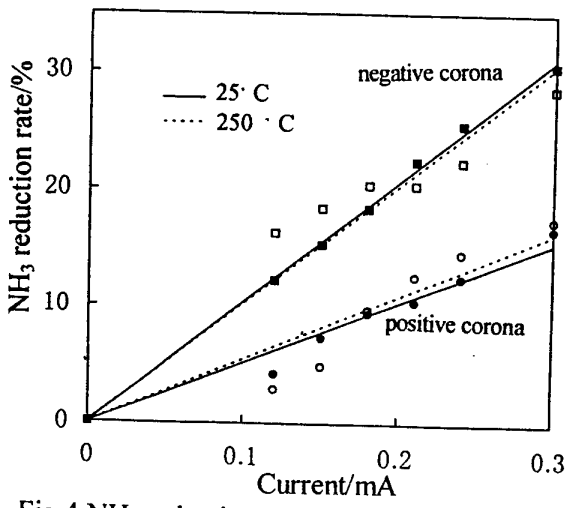

Fig.4 NH_3 reduction rate vs.discharge current

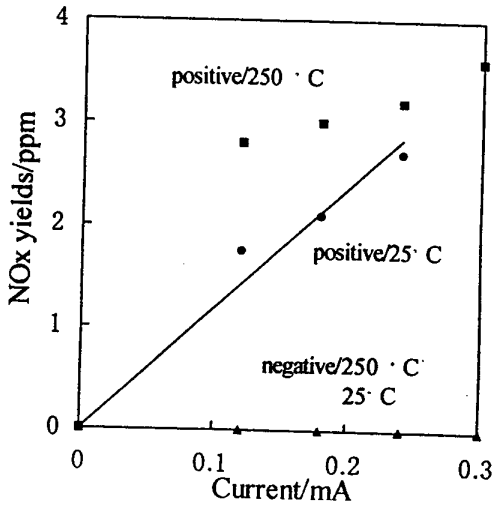

Fig.5 NOx yields vs.current

Memory effects in the electrical breakdown of a low pressure gas

V. Kudrle†, E. Le Duc and M. Fitaire

Laboratoire de Physique des Gaz et des Plasmas, Bât. 210
Université Paris–Sud, 91405 Orsay Cedex, France
† on leave from Department of Physical Electronics, Faculty of Science
Masaryk University, Kotlářská 2, 611 37 Brno, Czech Republic

Introduction

The delay between the application of a DC high voltage on an electrode gap and the electrical breakdown of a gas may generally be divided into two principal components: statistical delay time and formative time lag. The former is the time necessary for appearance of the first electron, which, accelerated by the electric field, will give rise to successful series of electronic avalanches. The latter is the time interval, which is needed to develop a selfsustained discharge from that initial electron.

Due to the stochastic nature of the appearance of the first electron, discharge delay time is also random. Theory [1,2] predicts an exponential probability density function for breakdown delays if formative time lag is neglected. In this work, direct observation of both, statistical and formative time lags is presented.

A discharge may change the probability of the next breakdown, as shown in [3] for argon and stainless steel electrodes. Comparable results are here presented for helium gas and aluminium electrodes, thus suggesting that this phenomenon is common to breakdown experiments.

Experimental

All measurements are done using a pyrex discharge tube (inner diameter 2 cm) with two circular (1.4 cm diameter) aluminium electrodes (interelectrode distance 2 cm). The working gas (helium) flows through the discharge tube at 30 sccm/min (controlled using a mass flowcontroller). The temperature and pressure of the gas are 300 K and 4 torr, respectively.

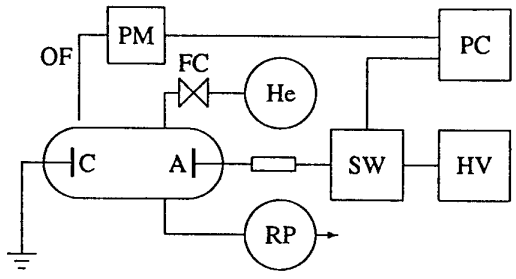

Figure 1: Experimental setup: FC flowcontroller, RP rotary pump, HV high voltage supply, SW switch, PC computer, OF optic fiber, PM photomultiplier.

The cathode is grounded and the anode is driven by a high voltage supply (U=600 V) through a load resistance and a fast (computer controlled) solid state high voltage switch. Onset of the discharge is detected using an optic fiber and a photomultiplier.

The time interval T between the rising edge of the voltage on the anode and the electrical breakdown of the gas is measured with a precision of 1 μs. The discharge is switched off after a predefined time T_d. To obtain statistically significant data, the measurements are repeated ($N \approx 10^2$ to 10^3) with fixed period T_{rep}.

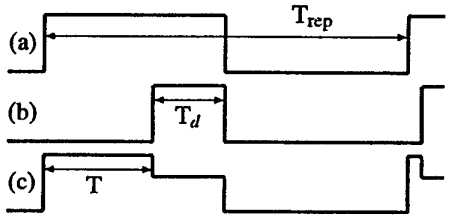

Figure 2: Schematic drawing of signals: a) switch command b) discharge current c) voltage on anode.

Results

The breakdown delay time T is measured for several repetition rates (T_{rep}=10 to 50 s) and different discharge durations (T_d=50 to 1200 μs). For long discharge durations ($T_d \approx$ 1 ms), probability density function of breakdown delay times T has a shape as shown in Fig.3. The resulting curve is interpreted as a combination of two effects: a slow exponential fall due to the statistical delay time T_s and a rapid growth near the value of the formative time lag T_f. The values are found to be $T_s \approx 22.5$ μs and $T_f \approx$ 87 μs.

For short discharge durations, apparently different results are obtained, as shown in Fig.4. The rising part of the probability density function is totally hidden by the decreasing exponential, which extends to much higher discharge delay times. By fitting the exponential, one finds $T_s \approx 28312$ μs.

This type of curve is comparable with previous results for argon and much longer repetition rates, as may be found in [4].

In Fig.5, average discharge delay T versus discharge duration T_d is plotted for three repetition rates T_{rep}. For longer T_{rep} between measurements, average discharge delay T is more sensitive to variations of T_d. For short T_d it tends to be linear in loglogplot, i.e. $T \propto T_d^{-3.33}$.

Conclusions

Two factors have an influence on statistical delay time of the breakdown: (i) initial electronic current near the cathode and (ii) probability that the discharge will evolve from one initial electron. The k^{th} discharge may change both the number of charged particles remaining in the tube and the state of the cathode surface for measurement $k+1$. The lifetimes (i) of charged particles in volume due to recombination and/or diffusion and (ii) of excited states in gas, are much shorter than repetition rates of our experiment (up to 50 s). One thus can conclude that a discharge modifies the "state" of the surface of the cathode and consequently, the probability of the next breakdown.

Acknowledgment

One of the authors (V.K.) is supported by the Scholarship of the French Government.

References

[1] R.A.Wijsman: Phys.Rev. **75** (1949) 833
[2] S.Laubé: Ph.D. thesis, Université Paris XI (1992)
[3] M.Agache *et al*: contribution to conference *Elementary Processes and Chemical reactions in Low Temperature Plasma*, Stará Lesná, Slovakia (1994)
[4] M.Agache: Ph.D. thesis, Université Paris XI (1995)

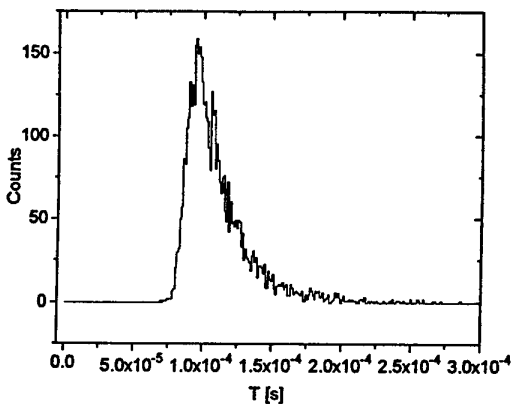

Figure 3: Probability density function of T for T_{rep}=10 s and T_d=800 μs.

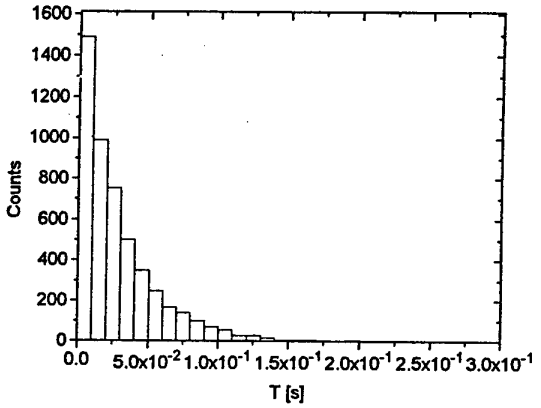

Figure 4: Probability density function of T for T_{rep}=10 s and T_d=50 μs.

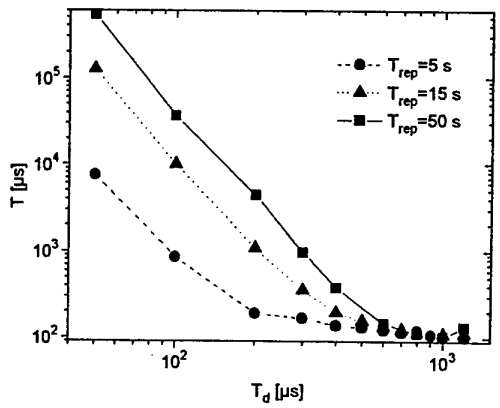

Figure 5: Dependency of average discharge delay T on T_d for various T_{rep}

Positive streamer in strong field in air: the mechanism of expansion and acceleration

A.A.Kulikovsky

Moscow State University, Research Computing Center (NIVC)
Moscow 119899, Russia
e-mail: akul@oberon.phys.msu.su

Two–dimensional numerical simulation have shown recently that positive streamer in strong uniform external field quickly accelerates and exhibit expansion in radial direction [1,2]. Both effects were detected in nitrogen with small admixture of O_2 [1] and in air [2].

The simulations [1,2] were made for STP conditions and for uniform Laplacian field 50 kV/cm. The results display that in 1–cm gap streamer reaches velocity of the order 4×10^8 cm/s, which is far above the drift velocity of electrons in the peak field at the tip of the streamer. Rapid (exponential in time) acceleration is accompanied by the exponential expansion of streamer head in radial direction. In this report the physical mechanism which is responsible for both effects is described.

To clarify the physics of these effects 2D simulations of cylindrically symmetric streamer in air in 1–cm gap under applied voltages V_0 40, 50 and 60 kV have been performed. Streamer dynamics was described within the scope of diffusion–drift model (see details in [2]).

Streamer was initiated by a small initial plasma spot at the anode. Air pressure was 760 Torr, temperature 300 K. Fig.1 shows electron density contour lines for each voltage when streamer length was about 0.7–0.8 cm. It is seen that expansion occurs faster in a higher Laplacian field.

A comparison of the rates of the processes have shown that photoionization is essential only at the early stage of streamer formation. Streamer behaves as a flash lamp: it produces photoelectrons in the gap at the early stage of its formation, and then these electrons are multiplied in ionizing collisions.

The analysis of structure of streamer head shows that streamer advancement occurs in accordance with the mechanism offered by Loeb [3]: a new segment of streamer is created due to avalanche ionization in a thin space charge layer. In this ionization domain (ID) ionization dominates other processes and exponential growth of plasma density occurs until time of maxwellian relaxation becomes comparable with the ionization time. Then newborn plasma "pushes out" electric field towards the direction of propagation and the process continues.

Analysis of simulation results shows that ID is a region where electron density $n_0 \simeq 10^{12}$ cm^{-3} is converted to the density in the streamer channel $n_s \simeq 10^{14}$ cm^{-3} during a fixed time interval (numerical values are related to the air under STP). Thus it is reasonable to assume that the current position of the contour line $n_0(r,z)$ ahead of streamer coincides with the outer border of the ID.

The main idea of the proposed mechanism is that position of n_0 contour is defined by exponential growth of primary photoelectrons in the gap and the shape of the streamer head coincides with the current position of the contour line $n_0(r,z)$. Consider temporal evolution of axial profile of primary photoelectrons $n_{ph}(z)$. In strong field this profile exhibit exponential growth in the undisturbed field. The point n_0 moves towards the cathode, and the velocity of this point *is* streamer velocity.

Evidently, this velocity depends on the shape of the curve $n_{ph}(z)$ ($z = 0$ is placed at the cathode). Let $n_{ph}(z)$ decreases towards the cathode as a power of distance from the anode

$$n_{ph}(z) = n_0 \left(\frac{d-z}{\sigma_z}\right)^{-m} ; \quad z < d-\epsilon$$

where σ_z being characteristic scale of the curve, d is the distance between electrodes. Then, as time progresses, this profile exhibit exponential growth in undisturbed field

$$n_{ph}(z,t) = n_0 \left(\frac{d-z}{\sigma_z}\right)^{-m} \exp\left(\frac{t}{\tau_0}\right)$$

where τ_0 being time of ionization in Laplacian field $E_0 = V_0/d$. Axial position $z(n_0)$ is derived from

$$n_0 = n_0 \left(\frac{d-z}{\sigma_z}\right)^{-m} \exp\left(\frac{t}{\tau_0}\right)$$

and hence the velocity of this point is

$$v_s = \frac{\partial(d-z)}{\partial t} = \frac{\sigma_z}{m\tau_0} \exp\left(\frac{t}{m\tau_0}\right) \qquad (1)$$

that is exponentially increases with time. Note that characteristic time of velocity growth is m times more than the time of ionization τ_0. The motion of the point $z(n_0)$ is illustrated in Fig.2.

The velocity (1) does not depend on n_e. This means that all values of n_e move towards the cathode with the same velocity. Hence, to verify this mechanism, motion of relatively low level of n_e which is not affected by the space charge field should be 'measured' in numerical simulation.

Fig.3 shows the velocity of the point $n_e = 10^8$ cm^{-3} and the streamer velocity (i.e., the velocity of the peak field) for the three voltages. It is seen, that the mechanism described explaines exponential growth of velocity. We note that in all cases streamer moves faster than do the point $z(10^8)$. Evidently, this additional acceleration is related to the space charge field of the streamer head, which provides additional growth of electron density ahead of the tip.

Due to ionization growth the contour $n_0 = 10^{12}$ cm^{-3} is expanded in radial direction and the profile of streamer head follows this expansion. This mechanism also clarify the formation of positive streamers in nonuniform fields. Around stressed electrode there is a zone, where field is high and streamer formation occurs in accordance with the mechanism of exponential growth. When crossing this region streamer accelerates and expands. Then in the low field streamer moves with the constant radius, which was established in the high field region.

[1] A.A.Kulikovsky: J.Phys.D:Appl.Phys. **28** (1995) 2483
[2] A.A.Kulikovsky: J.Phys.D:Appl.Phys. **30** (1997) (To be published).
[3] L.B.Loeb: Science **148** (1965) 1417

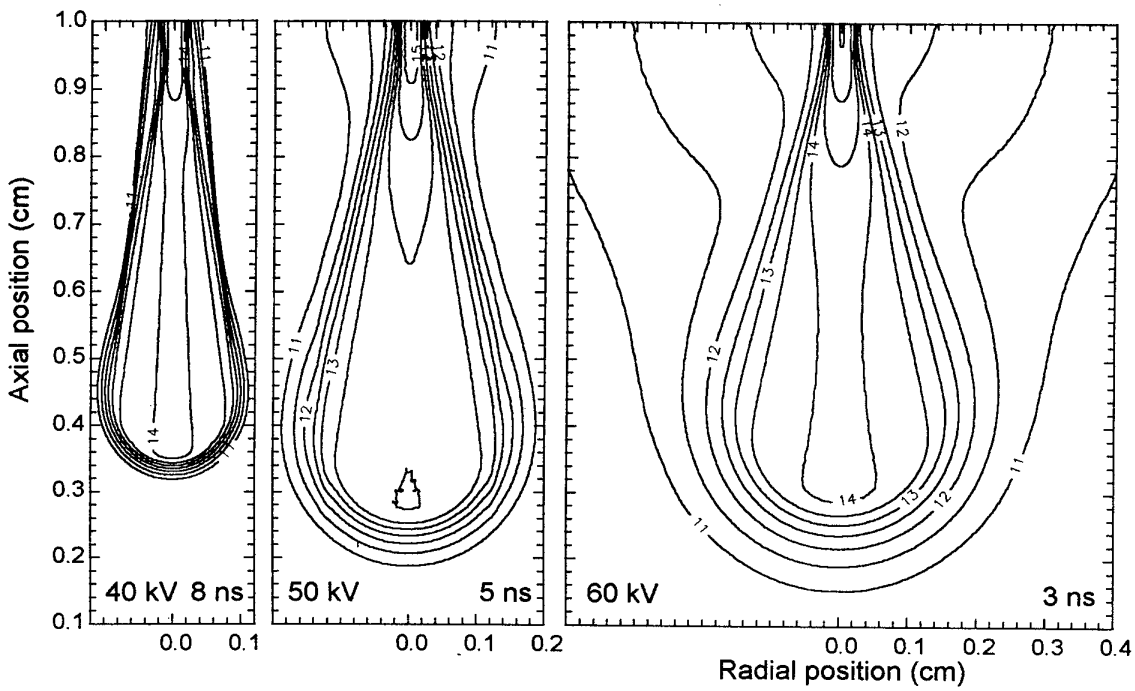

Figure 1: Positive streamer in air in 1-cm gap for three applied voltages: 40, 50 and 60 kV. Shown are electron density contour lines 10^{11} cm^{-3}, $10^{11.5}$, 10^{12} and so on. In all cases the outermost level is 10^{11} cm^{-3}.

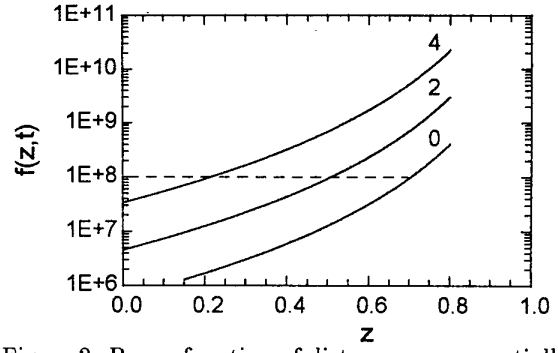

Figure 2: Power function of distance z exponentially increases with time. The position of a given function value moves towards the cathode and accelerates. $f(z,t) = 10^{11}((1.1 - z)/0.1)^{-5}\exp(t)$. Time moments t are shown above each curve.

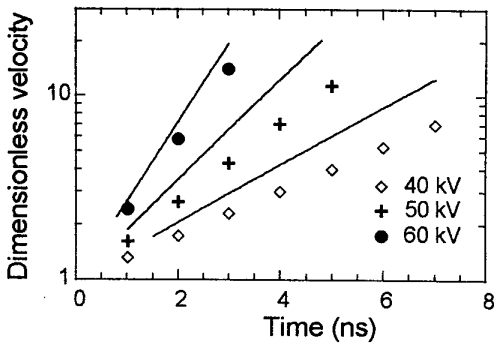

Figure 3: Comparison of streamer velocity obtained from the sumulation (solid lines) with the velocity of motion of the level $n_e = 10^8$ cm^{-3} towards the cathode (points).

UV light controlled repetition rate of Trichel pulses

P.Paris , M. Laan, A. Tiirik
The University of Tartu,
Tähe 4, EE2400 Tartu, Estonia

1. Introduction

In our recent studies [1,2] on negative corona in an air flow, Trichel pulses were triggered by the radiation of a deuterium lamp of quasicontinuous spectrum (215 - 400 nm) and of low intensity (input power < 20 W). The experiments were carried out in a 4 cm point-plane gap. In these experiments the repetition rate (RR) of Trichel pulses was at every voltage adequately related to the intensity of UV light: the increase of intensity causes the increase of RR. The corresponding dependence is sublinear: while the intensity increases the slope of the dependence diminishes gradually. A problem arises: does the further increase of intensity lead to the saturation of the dependence, i.e. does RR become independent on the intensity of UV?
At this paper the results of the experiments with a quasimonochromatic light source of considerably higher intensity are presented.

2. Experimental

The pulse mode of DC negative corona (Trichel pulses) is studied in a dust-free air flow. The rate of the air flow is ≈4 m/s. The pressure, relative humidity and temperature are recorded. It is possible to change temperature in the limits of 20^0-35^0C. Experiments in an air flow allow to diminish the influence of any possible accumulation process in the gas medium to the characteristics of discharge. The discharge chamber is an aluminum cylinder of inner diameter of 8 cm. The axis of the point-plane discharge gap coincides with that of the cylinder. The gap spacing is 1 cm, the point electrode is a hemispherically capped Pt wire of diameter of 1 mm. The plane electrode is a brass disk of diameter of 5 cm, the central part of anode is brass grid of small mesh size. The plane electrode is stressed. The stabilized power supply allows the voltage to be varied with the smallest step of 10 V. The gap is illuminated in two different ways: (i) the light collected by a quartz lens is directed along the gap axis through the anode aperture and focused at the point surface; (ii) the beam is directed perpendicularly to the gap axis, it is possible to focus it at any point of the gap. In all cases (if not mentioned otherwise) (i) is used. The light source is an excimer lamp (λ = 308 nm) excited by a HF (27 MHz) discharge. The maximum intensity of the focused beam is 200 $\mu W/cm^2$. With the calibrated grids and diaphragms it is possible to change the light intensity nearly by three orders of magnitude. It is possible to record simultaneously the mean current of discharge and the RR of Trichel pulses. Every point of the RR presented in the figures is a mean value of at least ten measurements.

3. Results

When the Trichel pulses are noninitiated (i.e. UV radiation is missing during of the recording of the RR), the onset depends on the prehistory of the discharge gap. If the point electrode is not influenced neither by UV radiation nor by discharge for a long time (20 hours), the corona pulses start at 9.9 kV. In the case of the temperature and the pressure of the gas being the same but the point being previously radiated by UV during half an hour, the onset of noninitiated pulses lowers to 9.7 kV. Near the onset the RR of noninitiated pulses is low: it changes from 0.2 pps at 9.7 kV to 60 pps at 9.9 kV. For comparison: for pulses initiated by the UV of maximum intensity the RR is 6600 and 15000 pps, respectively. The RR of Trichel pulses as a function of the UV intensity for the different voltages U and for the temperature 20.3^0C is presented in Fig.1. There are no qualitative differences between the curves presented and those recorded for 4-cm gap and described in Introduction, but the values of RR differ considerably: the RR of Trichel pulses initiated by the faint source was always less than 3000 pps. At the constant voltage RR varies in narrow limits. Even at low values of RR which correspond to the very weak intensities of initiating radiation, Trichel pulses have a regular character: the error bars in Fig.2 present the standard deviation of 15 recordings. Such a stability of noninitiated Trichel pulses is never observed at so low values of RR.

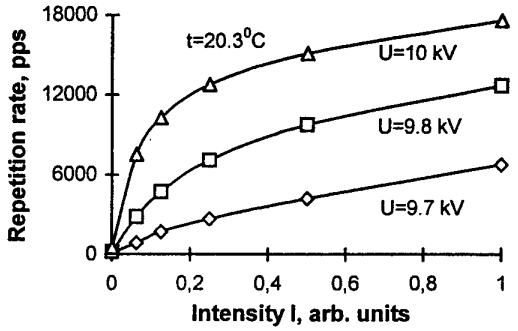

Figure 1. The repetition rate of Trichel pulses as a function of UV intensity

In the case of other parameters being fixed, the small changes of temperature lead to large changes of RR. For more detailed study of the phenomena the dependence of RR on temperature is recorded while keeping the production UT (T - abs. temperature) constant. As the pressure is constant, the reduced field $E/N \propto UT$ and the constancy of UT means the constancy of E/N as well. Consequently, if RR was determined only by ionization

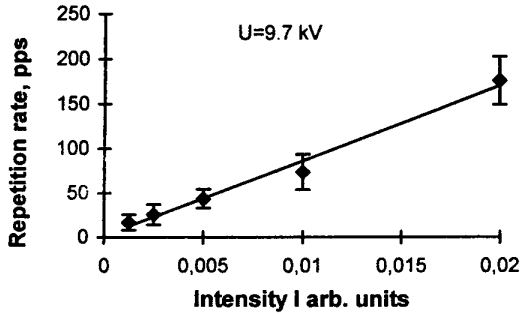

Figure 2. The repetition rate as a function of UV intensity for lower intensities

processes in the gas medium, RR would be independent on temperature. The curves, presented in Fig. 3 are corresponding to different values of E/N, at E/N = const RR is changing - to higher voltages (as UT = const) higher values of RR correspond. So RR is dependent rather on the field E than on the reduced field E/N.

If the gap is radiated by an IR radiation (λ = 1 - 3 μm), RR is almost the same as in the case of noninitiated pulses. But the simultaneous action of UV and IR radiations causes the changes of the RR. The temporal changes are presented in Fig. 4. As the experiments take place in an air flow the observed comparatively slow changes of RR must be caused by the cathode processes. The interaction of UV radiation with the gas medium does not change the RR: if the radiation is directed perpendicularly to the gap axis and it does not hit the point, no remarkable changes of RR are observed.

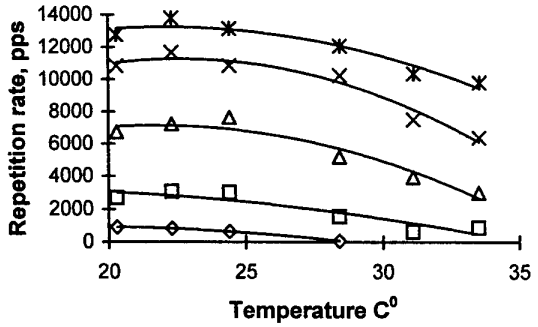

Figure 3. The repetition rate of corona pulses as the function of temperature, for every curve E/N=const

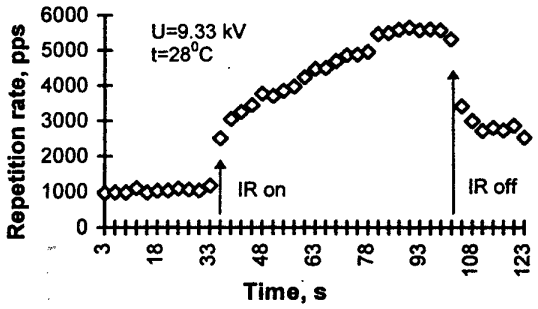

Figure 4. The temporal changes of the repetition rate caused by IR radiation

4. Discussion

Experiments carried out at a certain voltage confirm that RR is controlled by UV radiation in a wide range of intensities. On the other side: it is stated that the RR is determined by the space-charge field of negative ions. At first glance there is no contradiction between the present experiment and the statement: under the influence of UV electrons may be detached and so the radiation changes the RR. But there is a contradiction: the changes of RR take place only when the radiation hits the point electrode. i. e. the interaction of UV radiation with the gas medium does not change the RR. So, at a certain voltage the emission of the point controls RR. The latter assumption is supported by curves in Fig.3: if the processes in the gas were dominating then the curves would be as straight lines parallel to x-axis.

It is hard to explain the emission by a simple photoeffect mechanism as there is a strong dependence on temperature. Besides, the influence of IR radiation to RR is most likely also the effect of temperature: the step-like switch-on of IR (Fig. 4) causes the slow increase of RR. The experiments are carried out in an air flow. For this reason the IR radiation is not able to warm up the gas and the observed temporal increase of the RR can be explained only by the increase of point temperature.

So it may be concluded that RR at a certain voltage is determined by the cathode emissivity and UV-induced emission depends strongly on temperature.

A more detailed discussion and links with other similar experiments are presented in [2].

5. References

[1] Laan M, Repän V, Aarik J, Sammelselg V, To be published in J Phys D: Appl Phys 1997

[2] Laan M, *Triggering of negative corona*, Invited papers of this conference

[3] Korge H, Laan M, Paris P. *On the formation of negative corona* J Phys D: Appl Phys 26 (1993) 231-236

About the positive corona discharge forms in O_2-N_2 mixtures

K.Kudu[1], I.H.Lågstad[2] , R.S.Sigmond[2]
1 University of Tartu, Tartu, Estonia, 2 Norwegian University of Science and Technology, Trondheim, Norway

1. Introduction

It is well known that under open-air conditions *negative* point-to-plane corona discharges start as Trichel pulses, which at high currents turn into a pulseless glow. This corona form occurs in all O_2-N_2 mixtures at atmospheric pressure and even well below. The current-voltage ranges where these corona forms exist vary with the gas pressure and composition [1]. Negative coronas will not be treated here.

In the case of *positive* potential at the point electrode, the corona in air starts at the corona threshold voltage with burst pulses, which probably are just trains of avalanches coupled through gas photoionization. At a little higher applied voltage pre-onset streamers occur together with these pulses. With increasing voltage the rate of pre-onset streamers increases, and then decreases to zero at the onset of steady burst pulse corona or glow. At still higher overvoltages streamers again appear, concurrent with a background of steady positive glow. Now they are called pre-breakdown streamers. They are more powerful than pre-onset streamers, and their length and number per unit time increase with the voltage. If some of them reach the plane electrode, a spark breakdown may follow. This is the general sequence of discharge phenomena in the case of positive corona in atmospheric air [1].

This positive corona sequence in air can be modified by changing the geometry of the discharge gap, the ionization level, air humidity, or the content of electro-negative impurities. For instance, if one in dry air has a point electrode, like a wire with a hemispherical tip, and an external ionization source like UV radiation of sufficient intensity, then the pre-onset streamers (and even pre-breakdown streamers) may not occur at all. The burst pulses then grow with increasing voltage straight into a steady burst pulse corona. At higher over-voltages, already the first pre-breakdown streamer may launch the spark breakdown.

In other cases, with rod points with a sharp conical end, the burst pulses are too weak to occur and to prevent the streamers to develop. The corona starts in this case with streamers, and their length and number per unit time increase with the voltage till they bridge the discharge gap. Finally one of the streamers may initiate the breakdown, i.e., develop into a spark and then, an arc.

For short gaps the pre-onset streamers themselves can bridge the gap and launch the breakdown (breakdown type I). If one somehow escapes this and manages to move into the voltage region of the steady burst pulse corona in a short gap, then the breakdown could be reached either by decreasing the voltage (breakdown type I) or by increasing it (breakdown type II) [1].

One comment is needed in connection with the term "steady burst pulse corona". As Beattie [2] has shown, this is often not a steady corona, but may exhibit high frequency oscillations in its luminosity and current. These oscillations may be very regular, or modulated and fluctuating. Thus the designation "steady burst pulse corona" may be a better name than the synonymously used "pulseless glow", "steady glow" or "Hermstein's glow".

2. Experimental

We have studied the positive point-plane corona in O_2-N_2 mixtures over wide ranges of composition and pressures. The stainless steel "point-electrode" had a 1 mm diameter shaft ending in a 1.5 mm diameter sphere. The plane electrode was a stainless steel plate with a 5 mm diameter circular probe in its centre. The gap length was 6.05 mm. The mean currents, I_1 to the probe and I_2 to the surrounding plate, were measured with two light spot galvanometers. The gap voltage was measured directly using a digital multimeter (Fluke 77) with a Fluke 1000 MΩ voltage probe. The current oscillogrammes have been recorded with a Tektronix digital oscilloscope TDS 540.

The discharge gap was mounted in a metal vacuum chamber. The gases we used were O_2 and N_2 of technical purity. The discharge chamber was pumped to about 10^{-3} Pa and filled with the desired content of O_2. N_2 was then added to get a mixture at near atmospheric pressure. Then a positive DC voltage was applied to the point electrode and increased. The onset voltages of the different discharge phenomena were registered together with their mean currents and the current wave forms. Then the pressure was lowered without changing the gas, and the procedure repeated until reaching about 1 kPa. The content of O_2 in the O_2-N_2 mixtures was varied from zero to 100 %.

3. Results

Our measurements show that in all O_2-N_2 mixtures with more than 1% O_2 usually the same discharge forms occur as in air at atmospheric pressure. For mixtures

with less than 1% O_2 a new discharge form is added to the menagerie: A real pulseless, spiked glow, without any oscillations in luminosity or current. The light of this corona mode is concentrated in a conical column protruding from the point electrode surface like a spike. At higher currents even two or three spikes may be seen. A pulseless glow has also been seen by Korge et al [3], but that was in extremely pure nitrogen. In that case the discharge occured like a luminous channel bridging the whole gap of 4 cm length. Most probably the nature of both these phenomena is the same.

The "living places" of different positive point discharge forms are best visualized by pressure-voltage diagrams. Such diagrams were made for all the O_2-N_2 mixtures we studied, but here only the one for 0.3% O_2+N_2 is shown in figure 1. More will be presented at the conference.

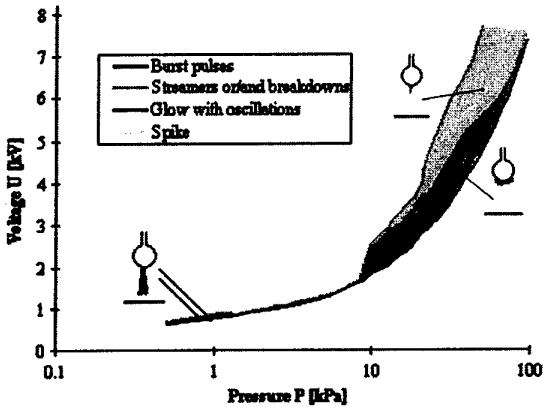

Figure 1. Pressure-voltage diagram of 0.3% O_2+N_2

The lower the content of O_2 in the O_2-N_2 mixture, the larger the area occupied by the pulseless glow in the pressure-voltage plane. In pure nitrogen we did not find any steady burst pulse corona with oscillations at all. If the O_2 content exceeds about 1%, the pulseless glow do not exist anymore.

4. Discussion and concluding remarks

Only one pressure-voltage diagram from our present extensive survey of point-to-plane corona forms in O_2-N_2 mixtures could be shown in this short paper. Nevertheless, the figure illustrate all the main corona types seen in the survey, of course including the hitherto unreported steady spike.

The mapping of discharge types presented in this work is a necessary part of our long lasting search for the true mechanisms behind the oscillations of the positive glow corona.

Why are most positive point-to-plane coronas unstable, and what types of instabilities are operating? Three types seem to be relevant for the surveyed coronas:

- Quantization fluctuations: One electron entering the corona ionization region will form an avalanche of average size given by the gas, field and geometry. This will be the smallest discrete unit of charge transport through the region. Secondary ionization processes may increase this minimum charge package, and the stochasticity of the processes tends to give them an exponential (Furry) size distribution. Thus, at low currents all discharges will consist of pulses of fluctuating size and intervals.
- Longitudinal instabilities: A stochastic current change will change the corona space charge distribution in such a way that the current change is amplified. This positive feedback will lead to damped and undamped oscillations following any current disturbance. This is the mechanism of the initial stage of Trichel pulse formation in negative coronas.
- Transversal instabilities: Here, a stochastic current density increase in some part of the discharge cross section will increase the efficiency of the ionization processes in just that part, and lead to further current density increase and discharge contraction. The sudden contraction of a spread-out positive glow corona into a streamer is one example, and the final rise of a Trichel pulse is another.

All combinations of the above instability mechanisms are possible.

At present one understands the quantization fluctuations, and has a fair knowledge about what causes the positive streamers. In contrast, the causes of the longitudinal positive glow (or Hermstein glow) oscillations are still unknown to us. For instance, we still cannot predict whether the addition of a trace gas of known properties to a non-oscillating positive corona in argon or pure nitrogen will induce oscillations or not. We expect, however, that further experiments and computer simulations will produce some answers in time for the conference.

5. References

[1] L.B.Loeb, Electrical coronas, University of California Press, 1965

[2] J.Beattie, The positive glow corona discharge, Ph.D thesis at the University of Waterloo, Canada, april 1975

[3] H.Korge et al, The discharge in pure nitrogen at atmospheric pressure in point-to-plane discharge gap, Third International Symposium on High Voltage Engineering, Milan 28.-31. August 1979

Decay rate of excited Xe-atoms in single filament of a dielectric barrier discharge

H. Lange and R. Wendt
Institute of Low Temperature-Plasma Physics Greifswald
R.-Blum-Str.8-10, 17489 Greifswald, Germany, lange@public.inp-uni-greifswald.de

Introduction

Dielectric barrier discharges (DBD) in rare gases and rare gas/halogen mixtures have been investigated for several years because of their application as UV- or VUV-radiation source in many technological processes. These discharges exist between glass covered electrodes at a broad pressure range and are often described by the presence of large statistically distributed micro discharges (filaments)[1-3]. Excited atoms in the lowest metastable and resonance state of the rare gas play an important role in the generation process of excimers. They are the starting point for many reactions including neutral rare gas atoms or other excited species for producing the narrow band incoherent excimer radiation. This paper reports experimental results about the temporal density variation of excited species of $Xe(^3P_2)$ metastable state and the $Xe(^3P_1)$ resonance state in a single filament of a DBD in Xenon.

Experimental arrangement

The method used for the density determination was essentially the one used by classic absorption experiments and the principle arrangement is shown in Fig. 1. The discharge tube for the generation of a single filament was a special stainless steel chamber with two glass covered electrodes (discharge gap 1.5 mm) and a gas handling system. One of the electrodes is movable for the variation of the electrode distance. The gas filling pressure was varied from 20 torr to 600 Torr. We generate the DBD in the chamber by means of sinusoidal power amplifier and a transformator at a frequency of 16 KHz. Typical voltages are 2-3 kV (peak to peak) and discharge currents of some mA. Perpendicular to the discharge axis the chamber has two glass windows at the brewster angle for determining the density of excited atoms by means of the absorption method. The continous radiation of a diode laser is focused on the discharge gap with a resolution of 200 µm. The diode laser with a spectral width of less than hundred MHz operates at the central wavelenght of the optical transition, whose lower level should be investigated. The transmitted beam through the discharge gap was measured with a fast photodiode and detected by a digital oscilloscope (2G samples/s). If a DBD occurs (typical half width of the current pulse is about 10 ns) in a half wave of the sinusoidal sustaining voltage, the laser radiation is partly absorbed by Xe atoms excited to the metastable level (823.16 nm) or by atoms excited to the lowest resonance level (828.01 nm).

Results and discussion

The development of a DBD in a half wave of the applied sustaining voltage can be described by a Townsend phase, the space charge wave, the streamer phase and the afterglow or recombination phase [4]. In this paper we report about measurements of the absorption especially in the afterglow or recombination phase.
An example of the temporal behaviour of the density of the $Xe(^3P_2)$ atoms is shown in Fig. 2 in a semilogarithmic plot. The measured temporal variation of the density can be fitted by a single exponential decay and can be characterized with a decay rate, which was obtained from the slope of the semi-log plots of the densities against time. Fig. 3 and Fig. 4 show the decay rates of both measured excited atom densities. The pressure range studied was from 20 to 600 Torr. In Fig. 3 the values of the decay rates of the density of Xe resonance atoms are compared with the rates for the quenching of the atoms at the metastable state and at resonance state according to the reactions [5]:

$$Xe(^3P_2) + 2Xe(^1S_0) \rightarrow Xe_2(1u(^3P_2)) \text{ high } \nu + Xe(^1S_0) \quad (1)$$

$$Xe(^3P_1) + 2Xe(^1S_0) \rightarrow Xe_2(O^+_u) + Xe(^1S_0) \quad (2)$$

The solid lines in Fig. 3 and Fig. 4 represent the decay rates (in Hz) of Berejny [5], equal to

$$1/\tau\ (ns^{-1}) = 0.649*10^{-7}p^2 \quad (3)$$

for the metastable state and equal to

$$1/\tau\ (ns^{-1}) = 0.25*10^{-3} + 0.127*10^{-6}p^2 \quad (4)$$

for the resonance state.
This comparision suggests, that the decay of the atom densities in the afterglow phase of a filamentary DBD can partly be characterized by three-body collisions in a small pressure range and the agreement is moderately good.
At higher pressures we cannot measure this pronounced exponential decay of the atom density versus time (Fig. 5), especially for the excited metastable atoms. Our hypothesis is, that the decay of the density in the afterglow phase of the DBD is governed by an additional repopulation of the metastable state. The source of this repopulation is quenching of the $Xe(^3P_1)$ state [5].
Fig. 6 shows the temporal variation of the near infrared emission(Xe $6p_j \rightarrow 6s_i$, Paschen notation) and the time behaviour of the atom density excited to the meatstable state. The near infrared emission decays very fast and at the same time the density of excited atoms at the metastable state grows. This is an indication of the cascade transition which determines the density increase of metastable atoms.

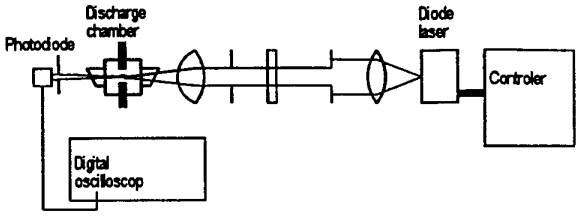

Fig. 1.Schematic of the experimental set up.

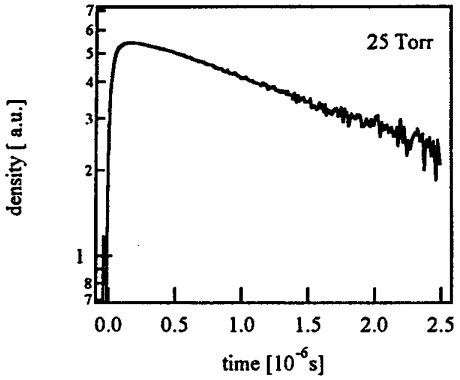

Fig. 2. Temporal variation of the density of the $Xe(^3P_2)$.

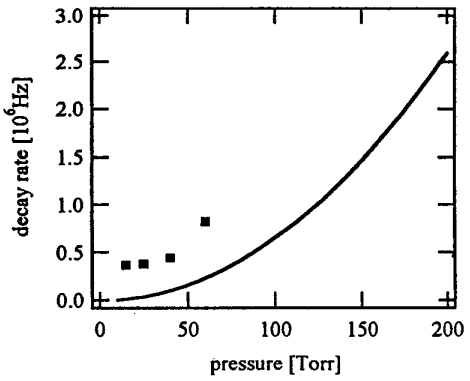

Fig. 3. Decay rates of the density of the $Xe(^3P_2)$ atoms in dependence of the gas pressure. The solid line represents data by Berejny et. al. [5].

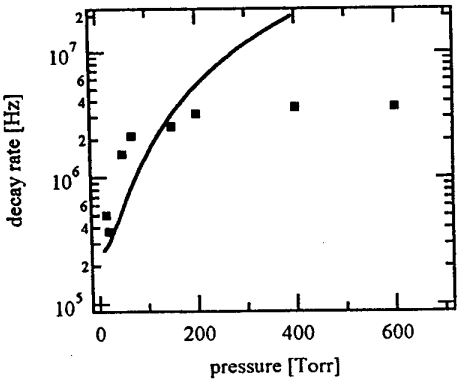

Fig. 4. Temporal variation of $Xe(^3P_1)$ atoms against the pressure of xenon.The line represents values obtained for quenching of the atoms by a three-body collisions [5].

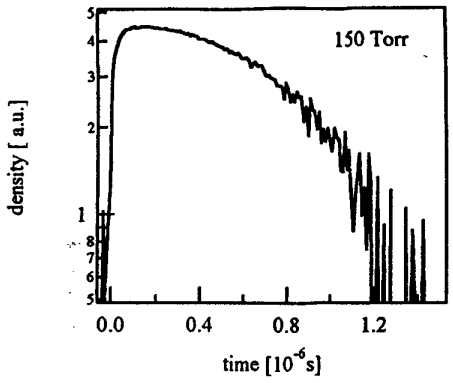

Fig. 5. Density of the $Xe(^3P_2)$ atoms versus time in a filamentary discharge at 150 Torr.

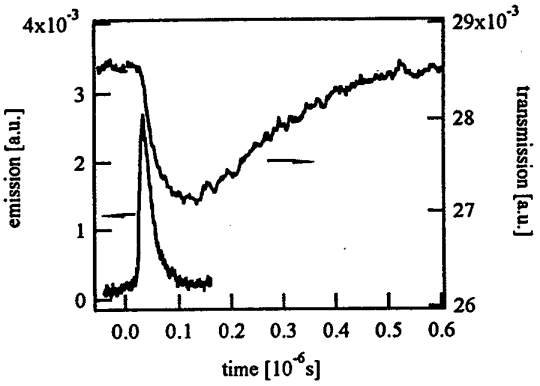

Fig. 6. Time behaviour of the near infrared emission of a single filament of a DBD at 100 Torr xenon and the transmission of the laser radiation (823 nm).

References

[1] B. Gellert, U. Kogelschatz: Appl. Phys. B 52 (1991) 1
[2] H. Müller, M. Neiger, V Schorpp, K.Stockwald: 5.Int. Symp.on Light Sources, York, England, (1989) 171
[3] S. Müller, R. J. Zahn, H. Lange, E. Kindel: Proc.XXI. ICPIG, Bochum, 1993, Bd.1, 341
[4] S.Müller, R.J. Zahn: 7.Int. Symp.on Light Sources, Kyoto, Japan,171
[5] P. Berejny, P. Millet, M. Saissac, Y. Salamero: J. Phys. B: At. Mol. Opt. Phys. 26 (1994) 3339

Theory of Secondary Streamer Generation in Positive Corona

R. MORROW

CSIRO Division of Telecommunications and Industrial Physics,
Sydney, Australia.

INTRODUCTION: The first observations of streamer propagation were made in the 1930s; streamer propagation was described as the rapid movement of a luminous front from a point anode, across an air gap towards a plane cathode, not necessarily causing an arc. Since then, observations of the properties of such streamers have revealed secondary and tertiary streamer fronts moving across the gap from anode to cathode [1]. Often, the current measured for such gaps is in the form of many pulses, or 'bursts' of current. Previous theoretical results for the propagation of a primary streamer, most of the way across a positive point–plane gap [2,3], showed that: (1) as the residual positive charge in the streamer channel moves away from the anode, the electric field begins to recover; (2) ionisation activity can restart.

The type of discharge that occurs due to the renewed ionisation activity is shown here to depend on the availability of seed electrons as the electric field recovers; if few seed electrons are available, then the electric field near the anode becomes high before a discharge occurs, leading to the formation of secondary and tertiary streamers, and consequently a series of burst current pulses.

THEORY: Theoretical calculations presented are for the development of secondary streamers (after the passage of a primary streamer) from the positive point of a point–plane gap, in air at atmospheric pressure. The point is a hyperboloid with a $\sim$ 1 mm radius of curvature at the tip, and a gap of 5 cm, with an applied voltage of 20 kV. The streamers are constrained to move along a 100 μm channel, allowing one–dimensional electron and ion dynamics to be used, while the electric field is computed in two dimensions, with azimuthal symmetry, by solving Poisson's equation in cylindrical coordinates. The electron, positive ion, and negative ion continuity equations, including ionisation, attachment, recombination, and photoionisation are solved simultaneously with Poisson's equation to give distributions of electron and ion densities, and the electric field [2,3]. (Note that in the figures the anode is at X = 0 cm, and the cathode at X = 5 cm. Also, the calculation is started at t = 0 s with a few seed electrons.)

RESULTS: In Fig. 1, by plotting the axial electric field at the times indicated, the propagation of the primary streamer at the start of the discharge is shown. When the streamer has stopped propagating the net charge in the gap is positive [3]; as this charge moves away from the anode, the electric field starts to recover at the anode, as shown in Fig. 2. The circuit current due to the primary streamer is shown in Fig. 3.

After $\sim$ 10 μs the electric field at the anode recovers sufficiently for any free electron to initiate a self–sustained discharge at the anode. (In the calculations, the very small, but finite, electron number densities left in the gap provide seed electrons, but some time is taken for them to multiply to significant numbers, simulating the effect of scarce seed electrons.) A discharge starts at the anode, and a secondary streamer propagates out into the gap, as shown in Figs. 4 and 5. Because of the pre–existing space–charge in the gap the secondary streamer propagation (Fig. 4) is different from that of the primary streamer (Fig. 1); for example, the secondary streamer amplitude remains relatively constant. In Fig. 5 the anode electric field, just before the secondary streamer is initiated, is shown as a "dotted" curve.

The circuit current due to the secondary streamer (Fig. 6) is an order of magnitude smaller than that due to the primary streamer (Fig. 3).

CONCLUSIONS: The formation of secondary streamers in positive point–plane gaps is shown to be due to the recovery of the electric field at the anode when the remnant positive space–charge moves away from the anode. If seed electrons are scarce, the field becomes large enough for any free electron to trigger a secondary streamer. Tertiary streamer formation also occurs.

REFERENCES:

[1] G. G. Hudson and L. B. Loeb, *Phys. Rev.*, **123**, p 29-43, 1961.

[2] R. Morrow and J. J. Lowke *Aust. J. Phys.*, **48**, p 453-460, 1995.

[3] R. Morrow and J. J. Lowke *J. Phys. D*, **30**, p 614-627, 1997.

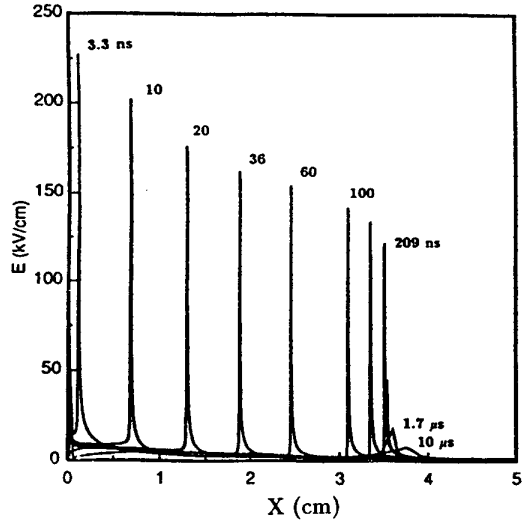

Fig. 1 Primary streamer electric field.

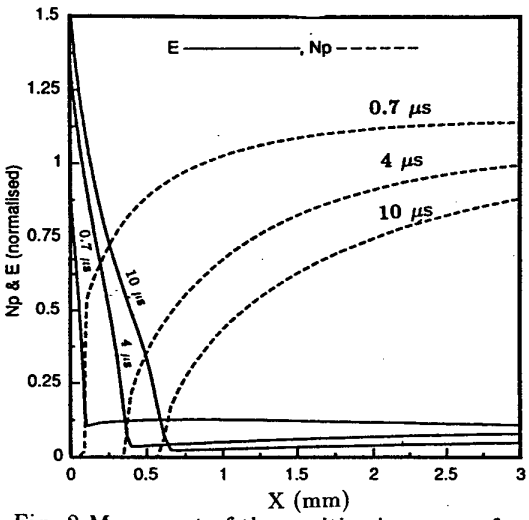

Fig. 2 Movement of the positive ions away from the anode, and recovery of the electric field near the anode.

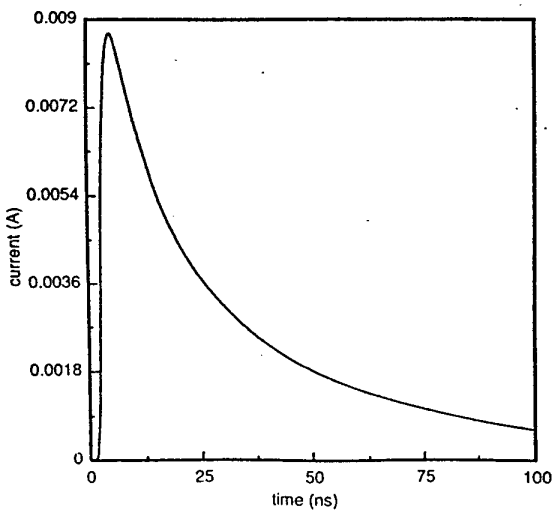

Fig. 3 Primary streamer current.

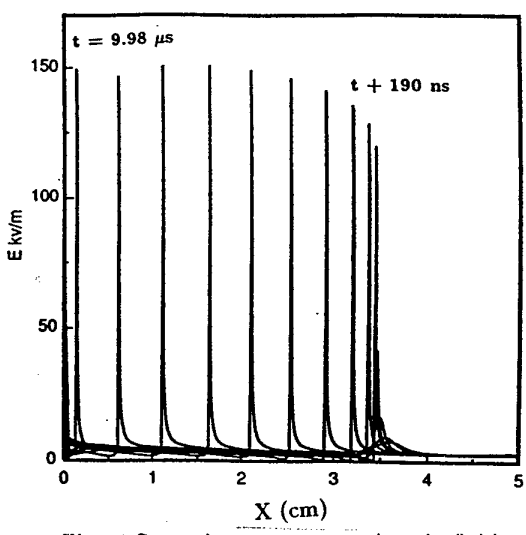

Fig. 4 Secondary streamer electric field.

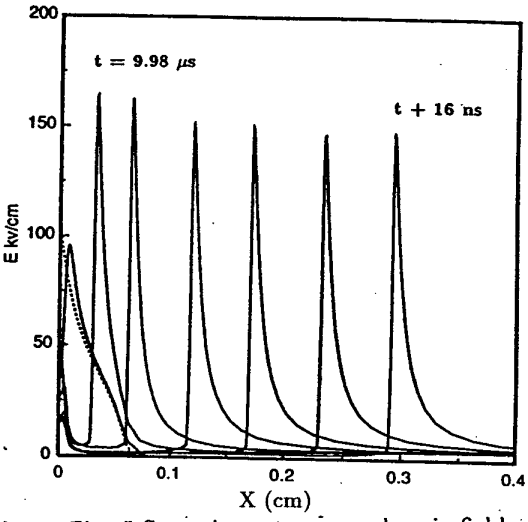

Fig. 5 Secondary streamer electric field near the anode.

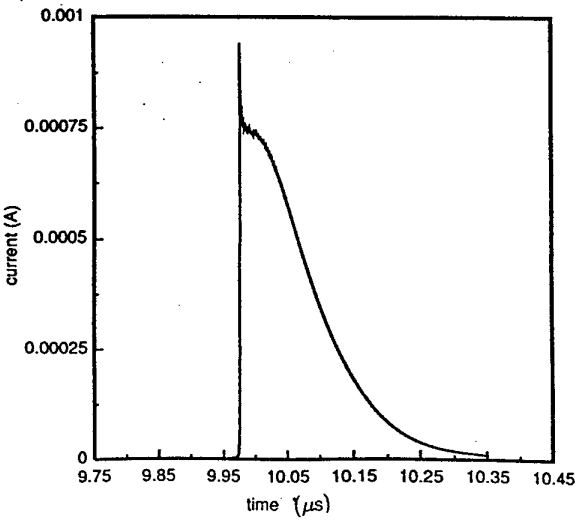

Fig. 6 Secondary streamer current.

Transition Times from Glow to Arc and from Arc to Grow on Inter-Glow-Arc Flip-Flop Transition

Masayoshi Nogaki Yositaka Suginuma

Dept. of Electrical Engineering and Electronics, Faculty of Engineering, Seikei University

3-3-1, Kichijyoji-Kitamati, Musashino-shi, Tokyo, 180, JAPAN

1.Introduction

Transitions of discharge voltage from glow to arc (G-A) and from arc to glow (A-G) in air (1 atm.), N_2(93kPa) and He+O_2 (93 kPa, O_2 20%) were investigated by many data of discharge voltage waveforms. Both Transitions of G-A and A-G have that first fast transition part is period of about 1 μs and slowly transition part followed fast it.

2.Experiment

Condition and Procedure

gases : air 1atm., N_2 93kPa, He + O_2 (93kPa,O_2 20%)
anode and cathode : Ag, 4mm ϕ, cathode :water cooling,
gap length : 6.0mm, series resistor R :15 k Ω,
average discharge current I : several 10~300mA.

The discharge waveforms of both Transitions of G-A and A-G were measured from the point of small current to the point of large current in order.

The measured discharge voltage was led to the input terminal of the oscilloscope though the voltage divider and the delay cable. Both terminals of delay cable are matched by 1800 Ω resistor as the characteristic impedance of delay cable. The trigger signal of the oscilloscope was a voltage of near point after starting point of transition voltage of G-A and A-G.
The oscilloscope is Tektronix 7844 (max. freq. 400Mhz).

3.Result and Discussion

The model of voltage waveforms for transition of G-A and A-G is shown in Fig.1. The explanation and the definitions of each parts in the transition waveform is written below the Fig.1 . The transition of G-A is the section between the starting point P_1 and the final point P_3 and one of A-G is the section between P_4 and P_6 .
First there is fast transition(P_1-P_2) then on near point P_2 it changes to slowly transition(P_2-P_3). In the same way on the transition for A-G(P_4-P_6) there is first fast transition(P_4-P_5) then on near point P_5 it changes to slowly transition(P_5-P_6).

On G-A we defined the rate ξ_{ga1} of voltage(V_{ga1}) per time(t_{ga1}) for first fast transition part.

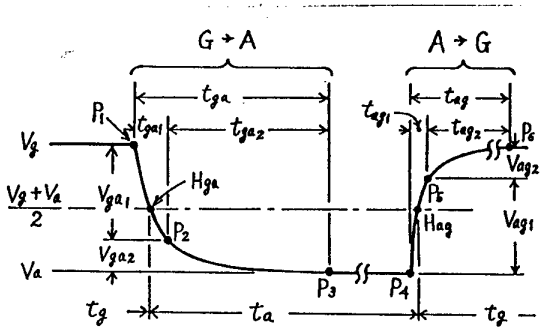

Fig.1 Model of discharge voltage waveform from glow to arc (G-A)and from arc to glow (A-G) on FFTGA.
V_g,V_a: discharge voltage level of glow and arc respectively, V_{ga1},V_{ag1}:voltage of first fast transition part of G-A and A-G respectively, V_{ga2},V_{ag2}:voltage of second slowly transition part of G-A and A-G respectively, t_{ga1},t_{ag1}: period of first fast transition part of G-A and A-G respectively, t_{ga2},t_{ag2} : voltage of second slowly transition part of G-A and A-G respectively, P_1, P_4 : starting point of G-A and A-G respectively, P_3, P_6 : ended point of G-A and A-G respectively, P_2, P_5 : switching point of change from fast to slow of G-A and A-G respectively.

And the rate ξ_{ga2} of voltage(V_{ga2}) per time(t_{ga2}) is also defined for later slowly transition. On A-G in the same way, their rates ξ_{ag1} and ξ_{ag2} were defined for first fast transition and second slowly it. Thus their equations follow: $\xi_{ga1} = V_{ga1} / t_{ga1}$, $\xi_{ga2} = V_{ga2} / t_{aa2}$,
$\xi_{ag1} = V_{ag1} / t_{ag1}$, $\xi_{ga2} = V_{ag2} / t_{ag2}$.

On G-A and A-G, the characteristics of the time T_{ga1} and t_{agi} -I are shown in Fig.2. Both times of t_{ga1} and t_{ag1} are 1.0 ~ 1.7 μs when the current is low (I=70 mA). When the current is middle (I=150 mA), t_{ga1} and t_{ag1} are 0.2 ~ 0.5 μs. And when the currents are large (I = 260 mA), t_{ga1} and t_{ag1} are 0.2 ~ 0.5 μs. In all gases of Air, N_2 and He+O_2, t_{ga1} and t_{ag1} decrease with the increase of discharge current.

On G-A a second slow transition part is continuously, after the first fast transition ended. The

second transition time is further longer than the first transition. There is a moment that a A-G transition happens on the way before second slowly transition gets to the final point P_3. On that occasion, the discharge voltage does not reach to Va, it is Va'. On that case, V_{ga2} and t_{ga2} do not reach the final value but they are V_{ga2}' and t_{ga2}' (these values on the way), because the arc is yet in complete. And V_{ga2}' and t_{ga2}' have various values. We define ζ_{ga2}' = V_{ga2}'/t_{ga2}' for a set of V_{ga2}' and t_{ga2}' like the ζ_{ga2} was defined before. Then the characteristic of ζ_{ga2}' - t_{ga2}' is shown in Fig.3. The maximum value of t_{ga2}' is the final point P_3 of transition to arc, and the maximum t_{ga2}' is final value of the t_{ga2} in Fig.3. The minimum ζ_{ga2}' become to ζ_{ga2}, and V_{ga2} is calculated by the equation $V_{ga2} = \zeta_{ga2} \times t_{ga2}$ too. On the result, the t_{ga2} is 200 ~ 400 μs, and the ζ_{ga2} is 0.3 ~ 0.6 V/μs. Therefore, V_{ga2} was 60 ~240 V .

On A-G a second slow transition part also make for final point P_6 past a point P_5 after the first fast transition. There are that many start points P_1 of G-A happen before the slowly second process get yet up the point P_6. In these cases, they define final point P_6' for the start point of G-A(P_1). Therefore V_{ag2}', t_{ag2}' and ζ_{ag2}' are obtained for P_5 and P_6' so that the unfinished transition A-G (O_5-P_6') happened. A characteristic of ζ_{ag2}' vs. t_{ag2}' is shown in Fig. 4. It was determined t_{ag2} for the maximum value of t_{ga2}'. And the ζ_{ag2} equal to ζ_{ag2}' of the t_{ag2}. On Fig.4 t_{ag2} are about 200 μs and ζ_{ag2} is obtained about 0.1 ~0.3 V/ μs . Thus V_{ag2} are 20 ~ 60 V.

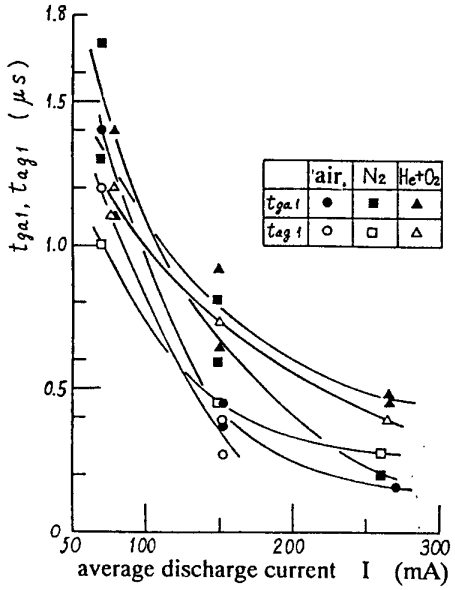

Fig.2 period of time on first fast transition parts t_{ga1}, t_{ag1} I characteristics for G-A and A-G

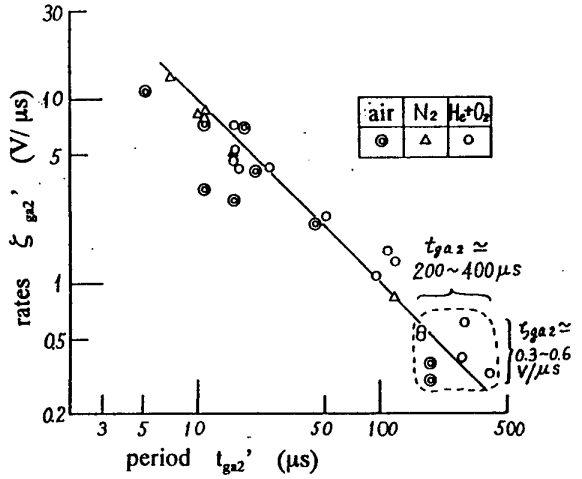

Fig.3 rates of transition voltage per its transition times ζ_{ga2}' vs. its times t_{ga2}' on slowly transition parts of G-A

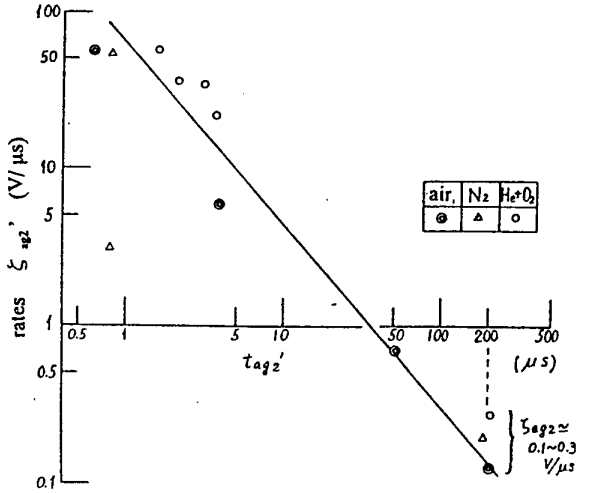

Fig.4 rates of transition voltage per times ζ_{ag2}' vs. its times t_{ag2} ' on slowly transition part of A-G

4.Conclusion

On the measurement of discharge voltage, both transition of G-A and A-G have the transition of first fast part and second slowly part in high pressre gases of about 1atm.. On both transition , the period of first fast part is about 1 μs and the period of second slowly part are 200~ 400 μs.

Volt-ampere characteristics of pulsed hollow cathode- hollow anode discharges

Srboljub Glišić, Jelena V. Živković, Aleksandra I. Strinić and Zoran Lj. Petrović

Institute of Physics, University of Belgrade, POB 57, 11001 Belgrade, Yugoslavia

1. Introduction

Hollow cathode, hollow anode discharges operating to the left of Paschen minimum are often known as pseudo spark discharges [1]. These discharges have complex behavior that is often beyond explanation and further experimental and theoretical work is required. In this paper we present experimental results for voltage - current characteristics of the pulses in hydrogen, nitrogen and argon which were obtained by application of a di/dt probe with a very wide bandwidth thus providing us with an opportunity to make a higher resolution recordings of the voltages and currents than the data yet available in the literature.

2. Experimental setup

The pseudo spark device used here has a standard cathode - anode geometry. The hole diameters in both electrodes was 8.4 mm and the thickness of the walls was 7 mm. The gap between the two electrodes is very small 2-6 mm allowing operation well below the Paschen minimum at high breakdown voltages. Discharge pulses are initiated by an overvoltage. A 14.8 nF capacitor was used to discharge through an overdamped circuit. Standard high frequency high voltage probe was used to record the voltage transients. A special di/dt probe was put close to the flat (strip) connection on the grounded side of a quick RLC discharge circuit. The bandwidth of the probe and the overall detection system exceeds 100 MHz. The discharge chamber was evacuated by a diffusion pump to some very low pressure and a gas flow at a constant pressures between 50 and 20 Pa was maintained by a leak valve.

3. Results

Discharges could be operated in a single shot and in repetition regime. Paschen curves were recorded for all gases and showed different modes of operation corresponding to different available voltage. A narrow region with hystheresis (it occurs at 29 Pa and is only 0.5 Pa wide) was observed with the transition to the high voltage- superdense glow mode.

During the hollow cathode phase the plasma acts as a virtual anode [1] giving large current density beams of electrons [2] which are accelerated in the high interelectrode fields. In the superdense glow phase extraordinary emission of electrons from the cathode surface occurs. This is the result of an intense ion - cathode surface interaction. Most studies were concerned with the occurrence of superdense glow as a function of capacitance that discharges through the system and material of the electrodes. If the system cannot sustain the high emissivity of the cathode surface, current quenching occurs [3,4].

Our technique allows us to give a reliable current and di/dt waveforms required to describe both the beam

and the superdense glow development as well as the current quenching process.

Three distinct modes are observed in voltage and current pulses. At highest pressures current pulse is smooth with relatively low peak values. At somewhat lower pressures, pulsed voltage and di/dt and consequently i(t) waveforms show development of the hollow cathode discharge and beams of electrons followed by numerous oscillations. A pronounced quenching occurs at the end of di/dt pulse. The peak current, however, is only a factor of 2 higher than that in the higher pressure mode. A further small decrease of pressure of the order of 5 Pa leads to a dramatic increase in breakdown voltage of a factor of more than 2 and almost a factor of 10 in current. The waveforms for this mode are shown in Figure 1. The increase of the current in this case is rapid following a small peak due to e^- beam, with only very few oscillations associated with the onset and the end of the current pulse. The discharge shows all the characteristics of superdense glow which occur in pseudo spark switches. The maximum current growth is of the order of 10^{10} A/s even with a low capacitance used in our experiment and is an order of magnitude larger than in the moderate pressure range. The current quenches when potential drops below 1.5 kV which appears to be the threshold to sustain the superdense glow in our system. The transition between the two modes is very well defined on the Paschen curve.

4. Conclusion

In this paper we have shown the voltage and current pulses in low pressure hollow anode, hollow cathode pulsed discharges that correspond to the pseudo spark switch geometries. Oscillations associated with the development of the superdense glow stage of pseudo spark discharges are observed as well as current quenching. Quenching occurs due to a failure to develop the superdense glow or due to the failure to supply the discharge with sufficient charge from the capacitor to maintain the required voltage which in the case of hydrogen and the geometry of our apparatus appears to be 1.5 kV.

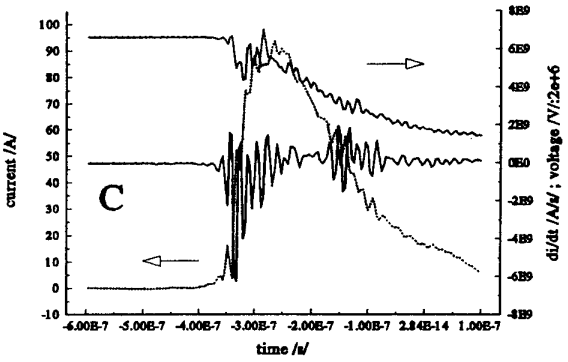

Figure 1 Lower solid curve - di/dt; upper solid curve- voltage; dashed curve- current.

References

[1] M.A. Gundersen and G. Schaefer, 'Physics and Application of Pseudosparks', (Plenum, New York, 1989)

[2] M.Favre, H. Chuaqui, E.S. Wyndham and P.Choi, IEEE Proc. Plasma Sci. **PS-20** (1992) 53.

[3] W.Hartman and M.A. Gundersen, Phys. Rev. Lett. **60** (1988) 2371.

[4] W.Hartman, G.F. Kirkman and M.A. Gundersen, Appl. Phys. Lett. **58** (1991) 574.

Investigation of the role of nitrogen impurities on the behaviour of an atmospheric-pressure glow discharge in helium

by
A. Rabehi*, P. Ségur*, F. Massines°, R. Ben Gadri° and M.C. Bordage*
*Centre de Physique des Plasmas et de leurs Applications de Toulouse
°Laboratoire de Génie Electrique de Toulouse
Université Paul Sabatier, 118 route de Narbonne
31062 Toulouse Cedex, FRANCE

I. Introduction

Even though the existence of an atmospheric-pressure glow discharge controlled by a dielectric barrier has been demonstrated for a long time [1] in helium, the fundamental mechanisms controlling this type of discharge have not been, till now, clearly understood. Recent experiments suggest that residual impurities such as nitrogen and oxygen play a very important role in the existence of a stable and periodic discharge. As helium has metastable states with an energy threshold of the order of 20 eV, it can easily transfer a large part of the energy stored in these states to ionise molecular impurities. This is the well known Penning effect which, obviously, cannot occur in pure gases. At atmospheric pressure, helium excimers are formed in the discharge. These excimers, through dissociation, are able to produce photons with an energy of the order of 15 eV. No photoionisation processes can occur in pure helium but, clearly, nitrogen or oxygen molecules can be ionised by these photons. It is therefore likely that an increase of the percentage of impurities in helium will also increase the importance of the ionisation process. However, as in most usual experimental situations the percentage of helium impurities is lower than, say 500 PPM, in this work, we will ignore the photoionisation process and we will only consider the role of the Penning effect. Furthermore, for simplification, we will only consider the influence of nitrogen impurities.

II - Description of the physical model :

To carry out this study, we use a numerical model based on the solution of the continuity equations for electrons and ions coupled to the Poisson equation. The accumulation of charge on the dielectric as the discharge propagates is carefully taken into account. Furthermore as the discharge is followed over times of the order of several microseconds, the motion of neutral excited species must be considered through the solution of diffusion equations. These equations are solved simultaneously with the equations for charged particles. The model is one-dimensional and gives the time variation of the total current, of the gas voltage and of the memory voltage (see [2]). Space and time variation of most physical quantities (electron, ion and neutral densities, electric field , etc) can also be obtained.

Emission of secondary electrons at the cathode is assumed to be due to the impact of various ionic species. In this work, three different ionic species are considered i.e. atomic helium ions, He^+, molecular ions, He_2^+ and N_2^+. A simplified kinetic scheme is used for helium in which only the first metastable state $He(2^3S)$ is taken into account. According to the reactions given in table I, this metastable state is created by direct electron-atome excitation (2), after recombination between an ion He_2^+ and an electron (10). Population of the 2^3S state by cascade effects not being considered in this work, it is likely that our calculations underestimate the rate of production of this metastable state. Destruction of this state occurs through two-body (14-15) and three-body (5) interactions. Three types of recombination processes have been considered for every ionic helium species including two-body (6) and three-body (7-8) recombination. Three-body recombination plays an important role in our case since the gas is at atmospheric pressure.

All the reactions taken into account, together with the corresponding reaction rates, are given in table I.

The drift velocity of the electrons, the diffusion coefficients and excitation and ionisation frequencies were calculated using a numerical solution of the Boltzmann equation.

	Reaction rate
Direct processes	
1- $He + e \longrightarrow He^+ + e + e$	
2- $He + e \longrightarrow He(2^3S) + e$	
Three-body interactions	
3- $He^+ + 2He \longrightarrow He_2^+ + He$	$6.3\ 10^{-32}\ cm^6s^{-1}$
4- $He_2^+ + e + He \longrightarrow He_2^* + He$	$5\ 10^{-27}\ cm^6s^{-1}$
5- $He(2^3S) + 2\ He \longrightarrow He_2^* + He$	$2.5\ 10^{-34}\ cm^6s^{-1}$
Recombinations	
6- $He^+ + e \longrightarrow He + h\nu$	$2\ 10^{-12}\ cm^3s^{-1}$
7- $He^+ + 2e \longrightarrow He + e$	$7.1\ 10^{-20}\ cm^6s^{-1}$
8- $He^+ + e + He \longrightarrow He^* + He$	$1\ 10^{-27}\ cm^6s^{-1}$
9- $He_2^+ + e \longrightarrow He_2^* + h\nu$	$5\ 10^{-10}\ cm^3s^{-1}$
10- $He_2^+ + e \longrightarrow He(2^3S) + He$	$5\ 10^{-9}\ cm^3s^{-1}$
11- $He_2^+ + 2e \longrightarrow 2He + e$	$2\ 10^{-20}\ cm^6s^{-1}$
12- $N_2^+ + e \longrightarrow N + N$	$4.8\ 10^{-4}\ cm^3s^{-1}$
13- $N_2^+ + 2e \longrightarrow N_2 + e$	$1.4\ 10^{-26}\ cm^6s^{-1}$
Two-body interactions	
14- $He(2^3S) + e \longrightarrow He + e$	$2.9\ 10^{-9}\ cm^3s^{-1}$
15- $He(2^3S) + He(2^3S) \longrightarrow e + He^+ + He$	$2.9\ 10^{-9}\ cm^3s^{-1}$
Penning ionisation	
16- $He(2^3S) + N_2 \longrightarrow N_2^+ + He + e$	$8\ 10^{-11}\ cm^3s^{-1}$

Table I : Various reactions and reaction rates used in this work

Drift velocity and diffusion coefficients for ions were obtained from [3]. The secondary emission coefficient was assumed equal to 0.02 for helium ions and to 0.01 for nitrogen ions.

III - Results :

The calculations were made in standard experimental conditions [2] i.e for an applied voltage of amplitude 1200 volts, a frequency of 10 kHz, a gap distance of 0.5 cm. The thickness of the dielectric on the electrodes was 0.06 cm The radius of the electrodes was 2 cm. Different percentages of nitrogen in helium were investigated ranging from 5 PPM to 500 PPM.

Figure 1 shows, for two cycles, the variation of the various electrical parameters (i.e. the discharge current, the applied voltage, the gas voltage and the memory voltage) for 500 PPM of nitrogen in helium. A stable periodic state was clearly reached in which the various electrical parameters were reproduced every half cycle. Furthermore, a very special shape for the discharge current was observed in which a fast varying part corresponding to the main discharge current is followed by a slowly decreasing tail. This particular shape can be compared to the experimental results of Massines et al. [2]. However, in the present case, the width of the current pulse is longer and its amplitude lower. This difference is likely to be due to our simplified physical scheme in which, as no cascade effects are taken into account, production of metastable states is underestimated. The results can also be compared to the calculations of Ben Gadri et al. [4]. These calculations were made in pure helium. However, to obtain a stable discharge, an overestimated high recombination coefficient was used. In these conditions, the width of the current pulse was very narrow and no slow

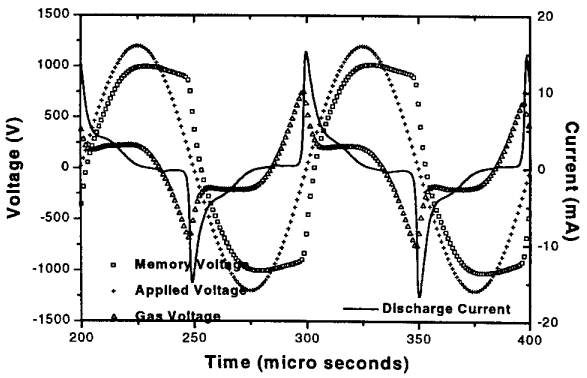

Figure 1 : Applied voltage, gas voltage, memory voltage and discharge current for 500 PPM of nitrogen in helium (over two cycles of the applied voltage)

decreasing tail was observed. Clearly the particular shape obtained in our present calculations comes from the influence of the Penning effect (16) in the creation of new electrons following the interaction of helium

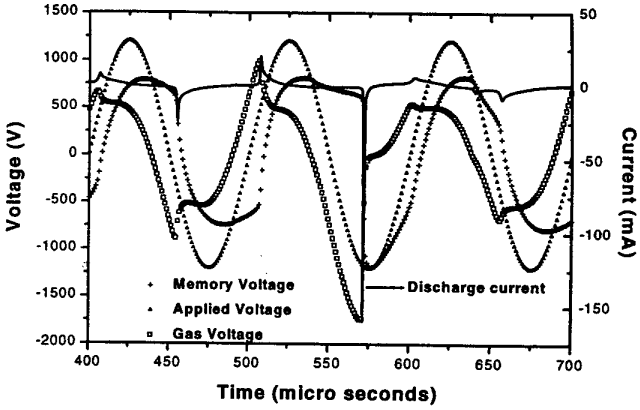

Figure 2 : Applied voltage, gas voltage, memory voltage and discharge current for 10 PPM of nitrogen in helium (over three cycles of the applied voltage)

metastable state with a nitrogen molecule.

As we decrease the percentage of nitrogen in helium, the discharge becomes increasingly unstable. For nitrogen concentration lower than 500 PPM and higher than 10 PPM, the discharge is reproduced every two cycles. For 10 PPM the discharge is neither stable nor periodic. Figure 2 shows the results obtained in this case. Current pulses of different sizes occur corresponding to very different gas voltages.

This strong difference between successive pulses comes from the fact that, for low nitrogen concentrations, the production of electrons by Penning effect being very small, the loss of electrons by recombination becomes higher than the production rate. Consequently, after a certain number of small amplitude pulses, the number of electrons between two pulses is so small that the gas voltage must be strongly increased to obtain a new pulse. This is for example the case of the fourth current pulse in figure 2. For a concentration of 5 PPM no more current pulses can be observed.

From these results, it is then clear that a sufficient amount of impurity must be present in an atmospheric pressure glow discharge in order to maintain a sufficient number of electrons between two current pulses to have breakdown starting at low gas voltage. It follows that no atmospheric pressure glow discharge can then be obtained in completely pure helium.

IV - References :

[1] S. Kanazawa, M. Kogoma, T. Moriwaki and S. Okazaki, J. Phys. D: Appl. Phys. 21, 836-840 (1988)

[2] F. Massines, R. Ben Gadri, Ph. Descomps, A. Rabehi, P. Ségur, C. Mayoux, XXII ICPIG, Hoboken, Invited papers, 306-315 (1995)

[3] H. W. Ellis, R. Y. Pai and E. W. McDaniel, At. Dat. and Nucl. Dat. Tables, 17, 177-210 (1976) ; L. A. Viehland ; E. A. Mason, At. Dat. and Nucl. Dat. Tables, 60, 37-95 (1995)

[4] R. Ben Gadri, A. Rabehi, F. Massines and P. Ségur, ESCAMPIG, 228-229 (1994)

SPATIOTEMPORAL EVOLUTION OF GAS TEMPERATURE IN A CORONA DISCHARGE

A.R. de Souza*, M.Touzeau, E. Marode and N. Deschamps
LPGP-Université Paris Sud-91405 Orsay/France
* LABMAT/EMC/ UFSC-88041-900 Florianopolis/SC/Brazil

1.Introduction

Corona discharges in air is a well known mean for applications such as ozone generation [1,2,3] air pollution control [4,5].

One fondamental problem in order to understand the physical and chemical properties of theses discharges is the evolution of the gas temperature during the development of the streamer and it's filamentary high pressure positive column (or secondary streamer). In particular this knowledge is necessary to model the ozone production in this type of discharge. The importance of this question has already been pointed out Spyrou et *al* [6,7].

In this paper we present the evolution of the rotational temperature in a positive point to plane discharge with a time resolution of 5ns and a space resolution of 100μm by a spectroscopic technique. Rotational temperatures T_r are derived from the (0,0) band of the second positive nitrogen group $N_2(C^3\Pi_u - B^3\Pi_g)$ at 337 nm.

2.Experimental

The experiments are performed in a cell containing synthetic air. After each experiment, the gas is changed in the cell.

The anode of the discharge is a Rhodium point with a radius of curvature of 50 μm and a copper plane having a diameter of 10 mm and a gap length of 12 mm. The discharge filament is focused perpendicularly to the slit of a HR640 Jobin Yvon monochromator with a magnification of 1. From the positive point self repetitive streamer discharges are launched with periode in the range of 60 to 120 μs. The signal is analysed with a fast photomultiplier on a 2 channel digital analyser (Tektronics) triggered by the discharge current pulses.

By means of oscilloscopic averaging, the intensity spectrum between 335 and 337.4 nm is recorded with a step of 0.05 nm and a spectral resolution of 0.1 nm. With various sets of data, we are able to build the spectral emission of the 337 nm band during the development of the discharge. The temperature is then deduced by fitting this spectrum with a calculated synthetic spectrum based on the same apparatus function [8,9]. An example is given in fig.1.

3. Results

When observing, with a slit, a specific position of the discharge axis, the intensity of the 337 nm band exhibits two peaks corresponding to the streamer passage followed by the emission of the filamentary positive column (figure 2, plain). The time resolved rotational temperatures show rapid changes in time (figure 2, black points). It is taken 9 mm from the negative plane at 10.8 kV with a repetition rate of 70 μs and an energy per pulse of 14 μJ. Tr is of the order of 380 K for the streamer while, after a pronounced dip, the temperature increases again until reaching values of the order of 400 K. It is remarkable that the temperature dip goes to 315 K in a time as small as 20 ns.

The maxima of these two peaks are ploted as a function of positions from the cathode on figure 3. Streamer maxima are in white circles, while squares are maxima of the filamentary column. It is seen that the intensity of the streamer is maximum near the plane while the intensity of the filamentary positive column is maximum at a complementary region, near the point. This behavior has already be explained in [10]. From the emitted light, integrated in time, the mean value of the rotational temperature is found to be constant all along the gap, increasing slightly near the positive point electrode. This temperature increases from 320 to 450 K when the voltage increases from 8.5 to 11 kV.

In contrast with the result presented heren, the difference of values of Tr between the streamer and filamentary column are very different in [6,7] for a gap slightly larger (15mm). In addition the mean Tr values along the discharge axis are changing in [6,7] while it is roughly constant

here. The time resoution of Tr is here larger, since it is possible to compare the streamer and column Tr's for the same discharge.

4. Discussion and Conclusion

A critical analysis should now be developped before stating that the rotational temperature is equal to the gas temperature. Certainly, Tr is not far from T. However, the measured Tr changes so rapidly in time that the interpretation can not be straightforward. Cooling down, through simple thermal cooling, is not possible, since the associated time constant lies in the range of 50 microseconds. A possible explanation could be that the very fast decrease of the gas temperature, just after the streamer passage, is due to a strong streamer channel expansion, which induces some adiabatic channel cooling [11]. This is under investigation.

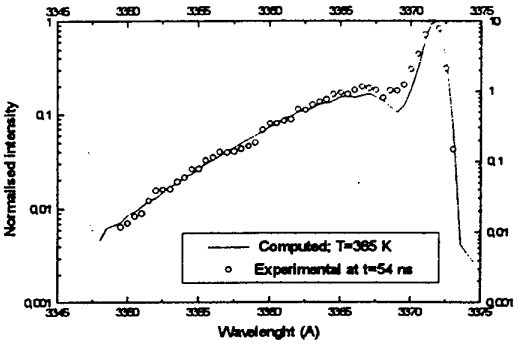

Figure 1: An exemple of measured and calculated discharge spectrum of the (0,0) band of the second positive nitrogen groupe.

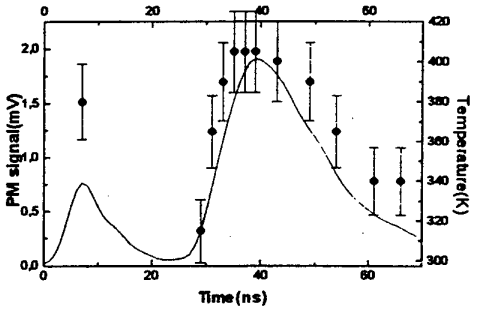

Figure 2: Time resolved rotational temperature (black dots), and total emitted light (plain).

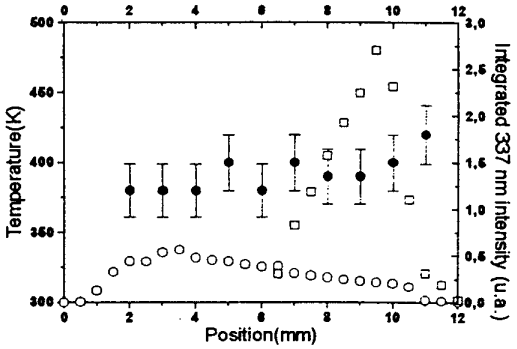

Figure 3: Spatial evolution of the rotational temperature as a function of position from the cathode plane (black dots). Streamer light maxima (open circle) and column light maxima (open square). V = 12.3 kV; P=0.2 watt.

REFERENCES

1. Lecuiller M, Goldman M,1988, J Phys D:Appl.Phys.,21, 51-56

2. Amirov R. H. Asinovsky E I Samoilov I. S. Shepeli A. V., 1991, Proc. XX ICPIG, Barga, Italy, p.279- 28

3. Gordeenya E.A. Kostinsky A.J. Terekchin V.E. Trapeznikov A.F. 1991, Barga, Italy, Proc. XX ICPIG, pp. 923-924

4.Gallimberti I., PURE Appl.Chem.60,663-674,1988

5. Marode E., GoldmanA., Goldman M. NATO ASI Series, vol 34, serie G, Ecological Sciences, Ed:B.Penetrante, S.E.Schultheis, Springer Verlag (1993)

6.Spyrou N., Peyrous R., Gibert A. 4th Int. Symp. on High Voltage Eng., Athens, Greece, Sept. 1983

7. Spyrou N., Held B., Peyrous R., Manassis Ch., Pignolet P. J. Phys. D: Appl. Phys. 25 (1992) 211-216

8. L.Hochard, personnal communication.

9. Chelouah A., Marode E., Hartmann G., Achat S., J. Phys. D Appl. Phys. 27, no. 5, p. 940-945, (1994)

10. Marode E., 1981, in "Electrical Breakdown and Discharges in gases, E.Kunhardt, L.H.Luessen, ed. NATO Series ASI, Serie B volume 89b p. 119-166 (1981), Plasmas"

11. Marode E.,Bastien F.,Bakker M., 1979, J.Appl.Phys 12 p. 249-263

Breakdown Development at High Overvoltage: Electric Field, Electronic Levels Excitation and Electron Density

N.B.Anikin, S.V.Pancheshnyi, S.M.Starikovskaia, A.Yu.Starikovskii

Moscow Institute of Physics and Technology, Dolgoprudny, 141700, Russia

1. Introduction

Pulsed discharge at high overvoltage develops in the streamer form or it the form of fast ionization wave (FIW) [1]. In spite of common features of plasma created the main distinctions between these types of breakdown are spatial homogeneity and high reproducibility of the FIW unlike the streamer. It seems to be useful to understand basic features of breakdown development at high overvoltages by the example of FIW. In this work electric field in FIW front and electron concentration behind the front are restored from the experimental data. Electronic levels population dynamics analysis is performed on the basis of reduced electric field values.

2. Experimental setup and restoration procedure

Negative polarity voltage pulses with U=15.5 kV peak pulse amplitude, 40 Hz repetitive frequency, 25 ns duration and 3 ns rise time were used to initialize the FIW. Glass discharge tube of 60 cm length and 1,75 cm inner diameter with the plate electrodes at the ends was surrounded by coaxial metallic screen 6 cm in diameter.

Modification of electrical signal along the tube was monitored with the aid of capacitance detector at intervals of every 3 mm along the tube axis. Space sensitivity function of capacitive gauge was determined from the special experiment. Irradiation from discharge was detected using time resolved emission spectroscopy technique. Experiments have been performed in air for the pressure range 1–16 Tor. Pressure range was taken to be optimal for the FIW propagation at the high voltage pulse parameters mentioned before.

The main idea of the restoration procedure was based on the suggestion of axial symmetry of breakdown [2]. In the symmetric charge system signal on capacitance detector $V(x_d)$ placed in the point x_d is defined by charge per unit of length q:

$$V(x_d) = \int_{-\infty}^{+\infty} q(x) f_d(x - x_d)\, dx \qquad (1)$$

Here f_d is spatial sensitivity function of the detector, x – coordinate along the discharge tube. Charge distribution in the system may be founded through the reverse task solving. Then average in the discharge tube cross-section longitudinal electric field will be expressed as

$$E(x_d, t) = \int_{-l}^{l} \frac{q(x,t)}{(x_d - x)^2} \mathrm{sign}(x_d - x)\, dx, \qquad (2)$$

where double halfwidth of f_d was taken as an integration limits: $l \sim 2\Delta_f$. Singularity at $x = x_d$ was eliminated through analitycal expansion of function under the integral.

Electrons concentration behind the FIW front at the point x_0 may be restored in the drift approximation on the basis of longitudinal charge and electric field data:

$$n_e(x_0, t) = \frac{1}{\mu_e e E(x_0, t)} \int_{x_0}^{\infty} \frac{dq(x,t)}{dt}\, dx. \qquad (3)$$

Here μ_e – electron mobility, e – charge of electron.

3. Results

It was founded that electric field profile *vs* time is asymmetric. It rises up to peak value during 3-4 ns and drops during ~2 ns, after that smooth diminution up to zero or, alternatively, secondary maxima observed depending upon pressure.

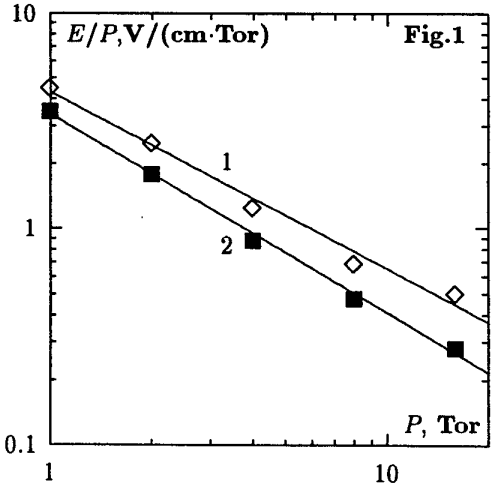

Peak values of reduced electric field in the cross section 20 cm spaced from the high voltage electrode

for the different pressures represented on the Fig.1, curve (1), may be approximated by power dependence: $E/P = 4.3P^{-0.82}$kV/ (cm · Tor). On curve (2) of the same picture E/P maximum value restored without detector sensitivity function consideration (at the $f_d = \delta(x - x_d)$) is represented. E/P peak value is diminishes strongly with the pressure growth. It must influence sharply on the energy distribution direction in the discharge. Really, at the P=16 Tor maximum reduced field reaches 4.5 kV/(cm · Tor) and, so, exceeds critical value for the "runaway" electrons. On the contrary, at the P=16 Tor peak E/P value reduces to 0.5 kV/ (cm · Tor) and corresponds to effective ionization and electronic levels excitation.

It is of interest to compare time dynamics of electronic levels population with the electric field strength data. We controlled shapes of ionic transition $N_2{}^+$, $B^2\Sigma_u^+ \rightarrow X^2\Sigma_g^+$ and N_2, $C^3\Pi_u \rightarrow B^3\Pi_g$ transition countours temporary evolution in the FIW at different pressures. Figure 2 shows the time τ while radiation intensity growths from 0.1 of its maximal value up to the maximum. Curve (1) corresponds to the second positive system of nitrogen (λ = 337.1 nm), and curve (2) corresponds to the first negative system (λ = 391.4 nm).

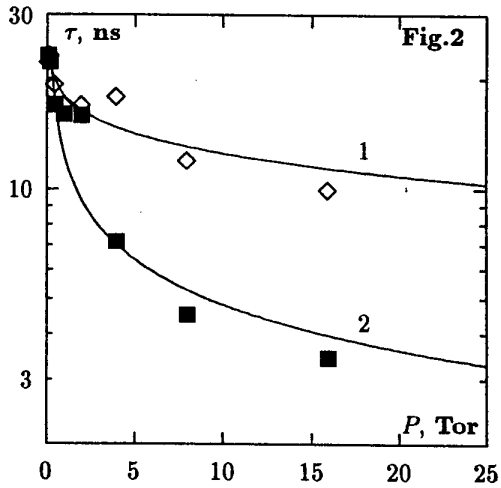

At low pressures levels with different excitation energy (ϵ_{1^-} = 18.75 eV for 1^- and ϵ_{2^+} = 11.03 eV for the 2^+ system) are populated during practically the same time. It means the absence of selectivity of energy distribution between these two channels. With the pressure growth rise time of radiation becomes much more smaller for the 1^- system than for the 2^+.

From the electric field and electronic levels population dynamics it may be deduced that at low pressures, where maximum E/N exceeds significantly critical value for run-away electrons arising, electron energy distribution function (EEDF) in the nonelastic processes energy region remains practically the constant. It leads to the loss of selectivity in the energy distribution processes.

Pressure increase from 0.3 to 4 Tor tends to the reduced electric field diminution from 10 to 1.5 kV/ (cm·Tor). As this take place, "runaway" criterion is true only in the narrow zone of FIW front where electric fields are maximum. The fall of the EEDF in the nonelastic thresholds region becomes significant and leads to the strong dependence of electronic level population velocity *vs* its energy threshold. $N_2^+(B^2\Sigma_u^+)$ – level is populated with characteristic time ~ 3 *ns*. It coincides with the halfwidth of electric field pulse in the FIW front. To the contrary, $N_2(C^3\Pi_u)$ – level population takes place all the time until pulse back front come in the cross- section, that is population extends over the approximately weak fields behind the FIW front.

Ionization degree behind FIW front represented in the form $\alpha = n_e/N$, where N is neutral gas density is shown on the Fig.3.

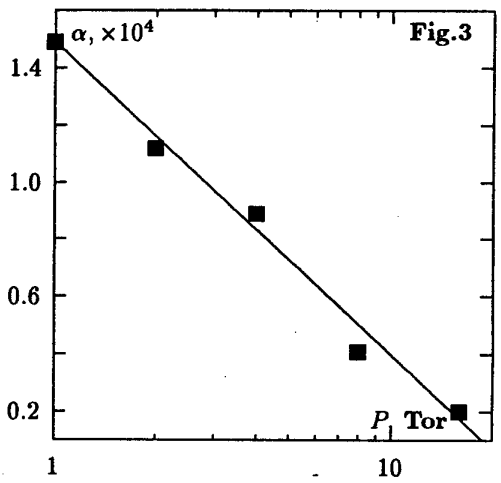

Ionization degree diminishes with pressure, while electron concentration reaches its maximum value $1.2 \cdot 10^{13}$ cm^{-3} at the pressure, correponding to the maximum of FIW front velocity.

4. Conclusions

Thus, correlation between electric field and electronic levels population velocity in the FIW front has been demonstrated on the basis of experimental investigation. Electron concentration behind the front of ionization wave has been determined. This work was supported in part by grants *96-03-32746* and *96-02-18297* from Russian Basic Research Foundation.

5. References

[1]. L.M.Vasilyak, S.V.Kostyuchenko, N.N.Kudryavtsev et al.: Physics – Uspekhi. 163 N3 (1994) 263
[2]. S.V.Kostyuchenko, N.N.Kudryavtsev, S.M.Starikovskaia et al.: Chem.Phys.Repts. 13 N10 (1995) 1670.

Spatial Homogeneity of Plasma Created by Fast Ionization Wave in the Big Discharge Volume.

S.M.Starikovskaia, A.Yu.Starikovskii, D.V.Zatsepin

Moscow Institute of Physics and Technology, Dolgoprudny, 141700, Russia

1. Introduction

Different types of discharges are nowadays widely used for technical applications: plasma etching, material deposition and so on. One of the main problems remains spatially uniform discharge production in the big volume of the gas.

It is known that at the great overvoltage on the discharge chamber electrodes breakdown develops in the form of fast ionization wave (FIW). Due to high velocity and non-local character of propagation FIW allows to obtain relatively uniform nonequilibrium plasma in the big volume of gas at the time moments $\simeq 10^{-8}$ s. The most characteristic features of FIW breakdown for the pulse altitude $U = 15 \div 30$ kV and few nanoseconds rise time are the follows: FIW front velocities $v = 10^8 - 10^{10}$ cm/s, electrons density behind the FIW front $n_e \sim 10^{11} \div 10^{12}$ cm^{-3}, pressures $P = 0.1 \div 50$ Tor, reduced electric field values $E/N = 10^{-16} \div 10^{-14}$ V·cm^2. Obtained plasma may be interesting both for technical applications and elementary processes studying.

The principal question in the FIW investigation is the role of discharge chamber walls in the FIW development and propagation [1]. Up to now FIW propagation studied in the long discharge tubes or in the high- ionized channel of laser spark, where cold gas around the channel play the role of the discharge sell walls. At the big diameter of discharge tube it is possible to choose experimental conditions so that discharge will be uniform in the cross- section of the discharge chamber. In [2] it was shown for the 5 cm diameter discharge sell. The only work is known [3] where FIW was studied in the conical glass shell 28 cm in diameter and 50 cm in height by the electronic- optical camera with nanosecond temporary resolution.

The aim of this work – more detail analysis of spatial homogeneity of discharge propagated in the form of fast ionization wave in the big volume discharge chamber.

2. Experimental setup and restoration procedure

Experimental setup is presented on Fig.1. Discharge in the form of FIW was organized in the cupola glass chamber 40 l in volume. High voltage stainless electrode 20 mm in diameter was surrounded by section of glass tube 35 mm inner diameter. Low voltage grounded electrode 200 mm in diameter was placed at 350 mm from the high voltage electrode. Diameter of the lower plate of the discharge chamber was 370 mm. Discharge volume may be pumped to the pressure $P \sim 10^{-3}$ Tor.

High voltage electrode was connected with pulsed voltage generator (PVG) by coaxial cable with 50 Ohm wave resistance 10 m in length. Cable screen was coupled to the grounded electrode by a copper bar.

Discharge volume was pumped to the pressure 10^{-3} Tor by oil pump end then filled by air or nitrogen through the special hole in the grounded electrode. Pressure was registered by pressure gauges PMT-2 and 6MDx4S.

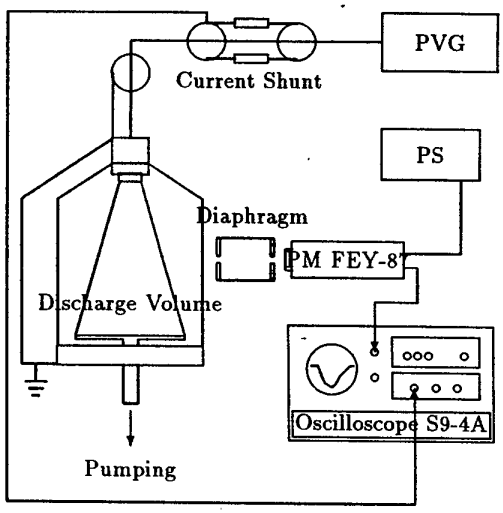

Fig.1: Experimental setup.

High voltage negative polarity pulses with 15.5 peak pulse amplitude, 25 ns duration and 3 ns rise time from the pulsed voltage generator were applied to the electrodes with repetitive frequency 40 Hz. Voltage pulse parameters were controlled by calibrated low-inductive current shunt included in the coaxial cable connected PVG with a discharge chamber. Cable screen was connected with the grounded electrode by copper strip.

The velocity of FIW front propagation in direction from high to low-voltage electrode was measured through the luminescence front propagation control. Emission from the discharge volume was registered by photomultiplier FEY-87 (300 – 600 nm spectral

region) moved along the axis of the discharge volume.

3. Results

At the pressures $10^{-2} - 10$ Tor in air it was observed either discharge conically filled space between electrodes or barrel form discharge. At 2-5 Tors visually spatial violet shining was observed. With the diminishing of pressure shine region near the discharge sell axis arose.

Dependencies of emission intensity upon the time for the different distances are represented on Fig.2. Measurements were made at 20 mm intervals in vertical direction. Maximum of intensity is reached after a $10 \div 15$ ns after high voltage is applied to the electrodes of discharge chamber. Sharp diminishing of the emission intensity was observed as distance from the high voltage electrode increased.

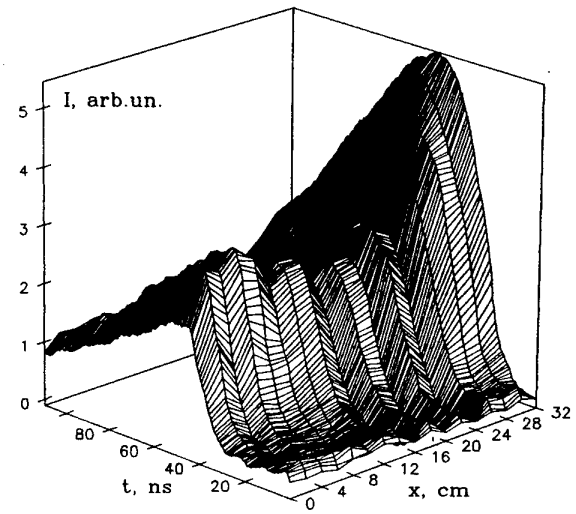

Fig.2: $N_2(C^3\Pi_u) \rightarrow N_2(B^3\Pi_g)$ system emission intensity during discharge development along the discharge axis.

FIW front propagation was determined from the $H-t$ diagrams of the optical emission on the base 0–18 cm from the high voltage electrode at the pressure 2 Tor and 0–32 cm at the lower pressures. At the $P =$ 2 Tor delay of the FIW velocity was observed. In all the cases FIW amplitude attenuation was detected at the motion from high voltage to grounded electrode.

Dynamics of emission in the cross section of discharge chamber have been obtained at distances 12.5 and 25 cm from the low voltage electrode. In the both cross sections emission dependency has strong maxima upon the time and radius. Increasing of the emission with time (40 ns from the moment of FIW reach the cross-section) corresponds to the registration system aperture fulfillment and emission intensity increasing in the every point of discharge volume due to finite curvature and duration of FIW front. Decay of the emission explained by the finite time of electronic levels excitation in FIW and radiative–quenching depopulation of these levels (Fig.3).

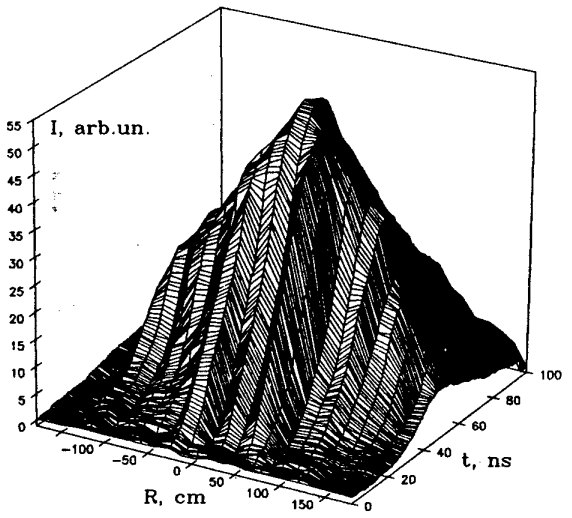

Fig.3: $N_2(C^3\Pi_u) \rightarrow N_2(B^3\Pi_g)$ system emission intensity during discharge development in the cross-section 12.5 cm from low-voltage electrode.

Maximum of emission intensity dependence upon radius is related to the diminishing of the FIW intensity with the distance from the axis and simultaneous diminishing of the optical length of gas gap. Real emission intensity distribution $I(R,t)$ in the cross-section may be restored through the reverse task solving. It was obtained that intensity of the emission drops very smoothly: intensity from the regions near the walls was only 15-20% less than from the center of discharge volume: $(I(R_0,t)/I(0,t) \simeq 0.8)$ in the both cross-section studied.

4. Conclusions

Thus, opportunity is demonstrated to realize free boundary fast ionization wave in the big volume of the gas. Obtained plasma is characterized by high spatial homogeneity.

This work is particularly supported by Russian Foundation of Fundamental Researches (Grants N *96-03-32746* and *96-02-18297*)

5. References

[1]. I.V.Filiouguine, S.V.Kostiouchenko, N.N.Koudriavtsev, L.M.Vasilyak: Physics - Uspekhi 37 (1994) 247.

[2]. I.V.Filyigin, S.V.Kostyuchenko, N.N.Kudryavtsev, S.M.Starikovskaya, A.V.Tret'yakov: Chem. Phys. Reports 13 (1995) 1670

[3]. R.Kh.Amirov, E.I.Asinovskii, I.S.Samoilov: Teplofizika Vysokikh Temperatur 29 N 5 (1991) 833

Plane VUV optical source on the base of multi-channel sliding discharge.

V.I.Tcheremiskine, M. L.Sentis, Ph.C. Delaporte

Institut de Recherche sur les Phénomènes Hors Equilibre, UMR 6594 CNRS, Aix-Marseille I and II Universities, Campus de Luminy, case 918, 13288 Marseille Cedex 09, France

L.D.Mikheev and V.S.Zuev

P.N.Lebedev Physical Institute, Quantum Radiophysics Department, Photochemical Processes Laboratory, Leninskiy prospekt 53, 117924 Moscow, Russia.

1. Introduction

High-current open discharge is one of the most powerful laboratory sources of radiation in the VUV spectral region. Its application to optical pumping of photolytically excited laser mediums allows to obtain high output and specific laser energetic characteristics [1-3]. A variety of initiation techniques, such as electrically exploding wires [1,2], formed-ferrite surface discharge [4] and dielectric-barrier discharge [3,5,6] are applied for spatial and temporal stabilization of open discharges. The last-mentioned method is commonly used for preionization, as plasma electrode [7], or for direct excitation in gas lasers. Its main advantages are the possibility of pulse periodic operation and achievement of large area discharge plasma sheet formation. However, due to the relatively low electric current density in the plasma sheet, this type of discharge has a low brightness temperature in VUV being transparent in this spectral region [5].
The main goal of our work was to develop a large area VUV radiating plasma source on the base of multi-channel sliding discharge along the surface of dielectric material. This approach allows to increase the electric current density in the discharge channels (relatively to the plasma sheet) which results in plasma electronic and optical densities rise that leads to the increase of discharge brightness temperature in VUV. The spatial expansion of plasma channels during the excitation pulse will lead to obtaining sufficiently large radiating area if the channels are formed closely to each other. It should be noted that an optimum of plasma channels arrangement density exists for fixed experimental conditions which is set by dependence of discharge energetic parameters on the number of the channels.

2. Experimental setup

Schematic of the device is introduced on Fig. 1. A scheme with three electrodes is chosen in order to obtain simultaneous breakdown of seven parallel 15 cm length 8 mm spaced discharge channels. High voltage and ground electrodes are fixed on the opposite sides of the Teflon substrate and are connected with the energy storage capacitor (C_o = 0.22μF) by current return metal rods which are located at 1,5 mm under the dielectric surface. Separated intermediate trigger electrodes are charged up to the one third of the initial voltage of the storage capacitor (Vo) and driven by an abrupt high voltage negative polarity trigger pulse.

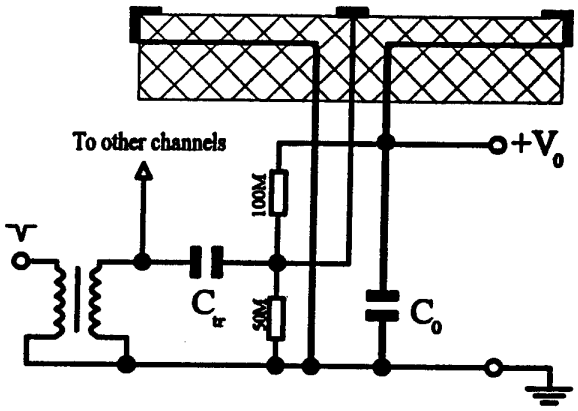

Fig. 1 : Schematic of the experimental setup.

Voltage and current wave forms were monitored with a high-voltage probe (Tektronix model P 6015) and a Rogowsky coil, respectively. Time and spatial plasma evolution was registred by a fast gated intensified CCD camera.

3. Results and discussion

Fig. 2 represents the time evolution of the current and voltage of a discharge in 1 atm of a gas mixture Ar:N2=10:1. The process of gap breakdown is characterized by three stages that were observed with the CCD camera. During the first stage (0-200ns) the trigger pulse initiates barrier discharge along the substrate surface which results in the right gap breakdown. Trigger capacitors (C_{tr} = 0.14nF) are charged up to almost Vo tension. Then the left gap breakdown occurs allowing trigger capacitors to discharge to the ground electrode (200-300ns). During the third stage the discharge of storage capacitor along the formed plasma channels takes place which exhibits good impedance matching with the load and uniform radiation of the plasma channels (Fig.3).

We found out that the uniformity of the plasma channels is mainly controlled by the trigger pulse characteristics and that the increase of charging voltage Vo leads to a significant current pulse shortening. We observed that uniformity of the channels was only dependent on the two initial stages. This discharge behaviour allows to easily scale the main circuit energetic characteristics and to reach plasma brightness temperature values in the VUV spectral region up to ~30 kK [1-3].

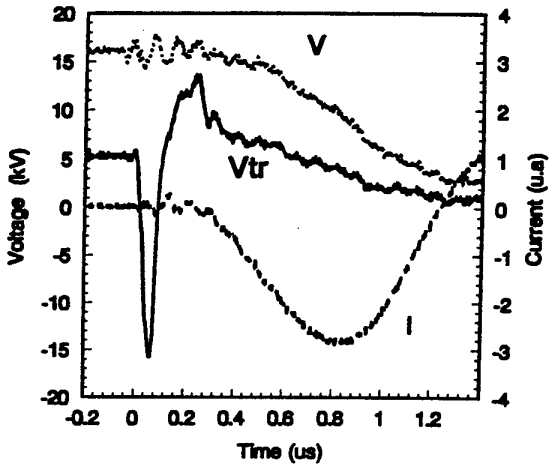

Fig. 2 : Trigger voltage (V_{tr}), main voltage (V) and current (I) of a discharge with seven channels in 1 bar of Ar:N_2 - 10:1 and a charging voltage V_0 = 17 KV.

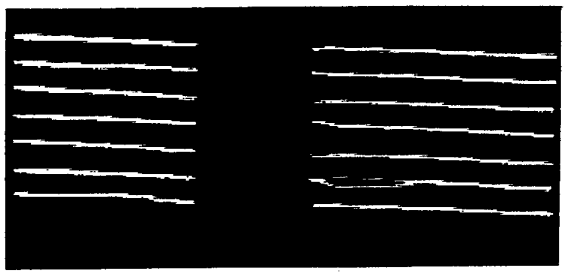

Fig. 3a : Integrated CCD camera photograph of seven plasma channels working simultaneously in 1 bar of Ar:N_2 - 10:1 and a charging voltage of 17 kV (scale 1cm ≡ 2cm).

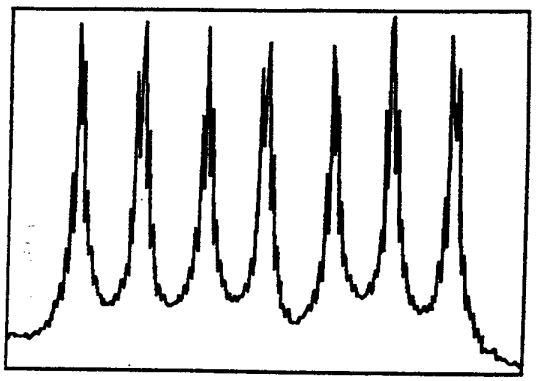

Fig. 3b : Transverse section of the spatial light intensity distribution emitted by the plasma channels of the surface discharge device.

4. Conclusion

In the present work we have proposed a multi-channel surface discharge scheme without any high power switch to trig the main energy reservoir. CCD camera studies have shown that many parallel plasma channels can be simultaneously initiated with a high uniformity of the plasma radiation. The scalability of the proposed scheme energetic parameters makes it possible obtaining high brightness temperature values in VUV spectral region.
The report will present a more detailed study on the performed VUV radiation plasma source and its electrical and optical characteristics.

This work was supported by the DRET (Direction des Recherches et des Etudes Techniques) of the french Defense Agency.

References

1. B.L. Borovich, V.S. Zuev, V.A. Katulin, L.D. Mikheev, F.A.Nikolaev, O.Yu.Nosach, V.B.Rozanov, High Current Radiating Discharges and Gas Lasers with Optical Pumping, VINITI, Moscow, 1978.
2. V.S. Zuev and L.D. Mikheev, Photochemical Lasers, Harwood Academic Publishers, Chur etc., 1991.
3. V.S. Zuev, G.N. Kashnikov and S.B .Mamaev, Sov. J. Quantum Electron. **22**, 973-976, 1992.
4. V.I. Tcheremiskine, M.L. Sentis, Ph.C. Delaporte, V.S. Zuev and L.D. Mikheev, J. Appl. Phys. **80**, 2094-2096, 1996.
5. R.E. Beverly III, J. Appl. Phys. **60**, 104-124, 1986.
6. B.Eliasson and U.Kogelschatz, Appl. Phys. B **46**, 299-303, 1988.
7. S.I.Andreev, I.M.Belousova, P.N.Dashuk, D.Yu.Zaroslov, E.A.Zobov, N.V.Karlov et al., JETP Lett. **21**, 194-195, 1975.

Correlation between Corona Spectral Intensities and Discharge Geometry

Toedter, O. , Müller, H.J. and Koch, A.W.
Laboratory for Measurement Technology (LMT), University of the Saarland,
P.O. Box 15 11 50, D-66 041 Saarbrücken, Germany, lmt@ee.uni-sb.de

1. Introduction

Corona discharges are of increasing importance for applications like flue gas treatment, deNO_x reactions or cleaning of motor exhaust fumes. Besides other common geometries like point-plane or wire-wire con-figurations the wire-cylinder geometry is very popular. A good relation of discharge volume to active volume and the possibility to implement optical diagnostics lead to a variety of investigations [1].

Optical emission spectroscopy is a powerful tool to study corona discharges [2,3]. The intensity of the emitted light is nearly proportional to the intensity of the discharge power which is dissipated by electron impact.

2. Basic Considerations

The mechanical parameters of a wire-cylinder configuration depend mainly on the tension of the wire. Fixed at its both ends the wire represents a mechanical resonance system with the resonance frequency being a function of the wire tension. In order to control the tension we implement a spring with variable elongation. The deformation of the spring corresponds to Hook's law:

$$\sigma = \frac{D}{A} \cdot \Delta s$$

with Δs being the elongation of the spring, A the sectional area and D the elastic constant. When corona starts the intensity depends on the diameter of the wire, its distance to the cylinder and the applied voltage. During DC-voltage all parameters remain constant. Using AC voltage with frequencies near the mechanical resonance frequency of the wire in the tube the corona intensity oscillates with the supply frequency and drives the wire mechanically. Therefore the distribution of streamers in the discharge is reduced due to the wire being mechanically displaced by the discharge. The mean value of the emitted light intensity decreases subsequently corresponding to the decrease of the discharge intensity.

3. Experimental Set-Up

The investigation of the frequency dependence of the corona intensity consists of three parts:

1. The AC power supply in the range of the expected resonance frequencies.
2. The wire-cylinder configuration is adjustable by a variable tension.
3. The optical emission is monitored on line.

The power supply used in these experiments provides 20kV at currents of up to 5mA and frequencies up to 1kHz. The signal form and the frequency are adjusted by a microcontroller (s. figure2).

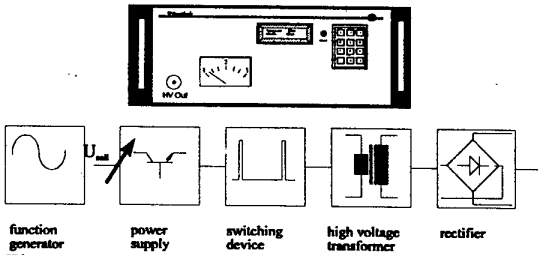

Figure 2: AC high voltage power supply

The discharge reactor bases on two tubes connected via a M38x2 thread. Turning one part against the

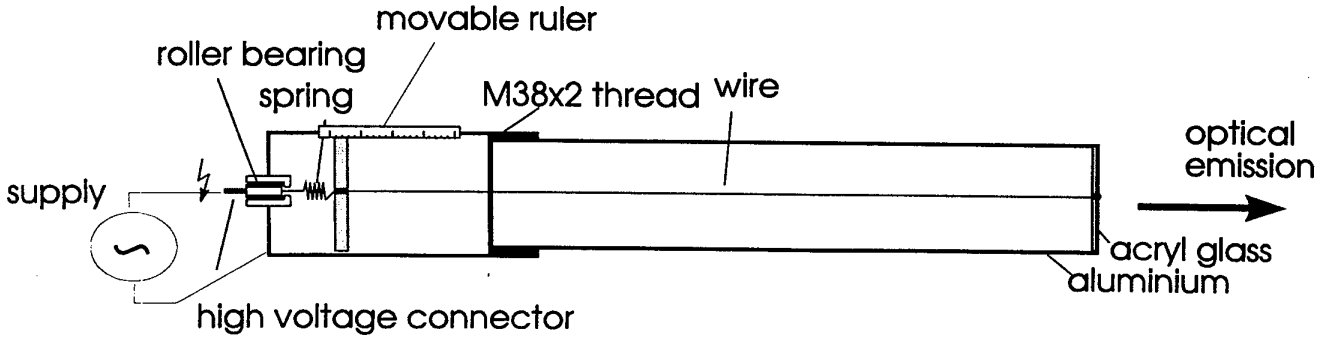

Figure 1: Experimental wire-tube arrangement

other the total length of the reactor can be adjusted. Botton and top plates are made of acryl glass and teflon, respectively. Thus the experiments are not disturbed by torsion problems.

The detection unit consists of an UV-C-sensitive tube (UV-TRON, Hamamatsu) and the counting electronics (s. figure 3). For a predeterminated time of one minute the unit counts all incoming UV-C-photons with a sensitivity of 1000 counts per 10^{-12}W/cm^2. The spectral response ranges from 180nm to 230nm.

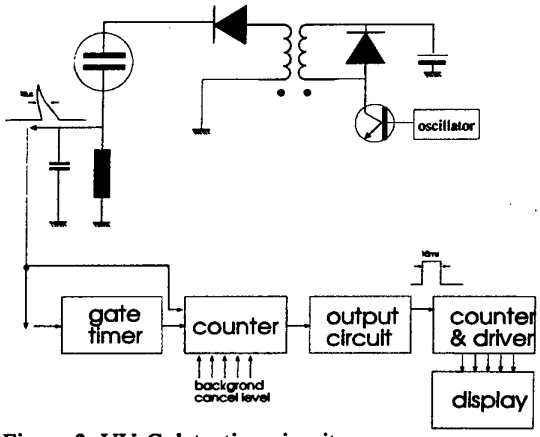

Figure 3: UV-C detection circuit

4. Results

Figure 4 shows the dependence of the emitted light as a function of the supply voltage and frequency.

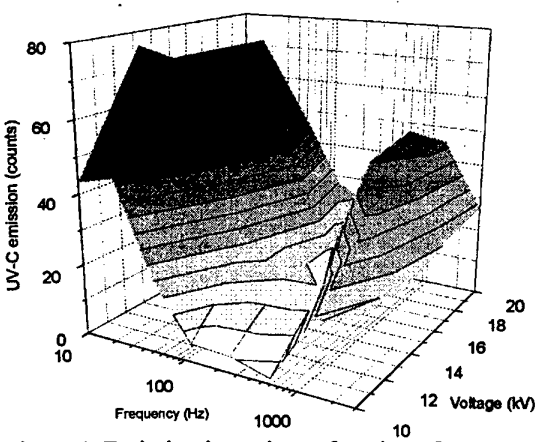

Figure 4: Emission intensity as function of supply voltage and frequency

In this experiment the resonance frequency of the reactor was adjusted to about 300 Hz at the following discharge parameters: diameter of the wire: 0.4mm and diameter of the tube: 30mm. The intensity increases gradually from 10kV to 14kV. Over the whole voltage range from 10kV to 20kV an objective minimum at about 300Hz can be observed.

5. Conclusion

The experiments show an intensity dependence of the corona discharge on discharge geometry and mechanical parameters. When using geometrical configurations like wire-cylinder configurations for applications like pollution control the user has to take into consideration the relation of electrical (supply voltage, frequency) to mechanical (tension, geometry) parameters. We can conclude that the supplied electrical power is subject to mechanical absorption at experimental conditions where the supplied frequency corresponds to the mechanical resonance.

5. References

[1] Creyghton, Y.L.M. *Pulsed Positive Corona Discharges,* Dissertation, TU Eindhoven, 1977

[2] Koch, A.W. *In-situ-Charakterisierung von plasmaunterstützen Beschichtungsprozessen,* VDI-Fortschrittsberichte, Reihe 8 Nr. 357, ISBN 3-18-145708-6, 1993

[3] Spyrou, N., Manassis, C. *Spectroscopic study of a positive streamer in a point-to-plane discharge in air: evaluation of the electrical field distribution,* J. Phys. D: Appl. Phys 22, 1989, p. 120-128

Temporary Corrosion Resistance using Corona-assisted Coating

Toedter, O. and Koch, A.W.
Laboratory for Measurement Technology (LMT), University of the Saarland,
P.O. Box 15 11 50, D-66 041 Saarbrücken, Germany, lmt@ee.uni-sb.de

1. Introduction

Up to now, temporary corrosion resistance for cold rolled steel is realized by coating the surface with oil at the end of the production line. Removement of this oil is very expensive and causes a lot of environmental problems. On the other hand, the process of cold rolling is responsible for displacement errors e.g. for gaseous enclosures which appear as sharp defects on the surface (s. figure 1). These surface areas are corrosion sensitive. Organic coating is a commonly employed corrosion resistance technique [1]. Polymer films exhibit the advantage of high water resistance. Corona-assisted coating using organic gases offers the possibility to coat steel in an easy and cost-effective manner under atmospheric pressure [2].

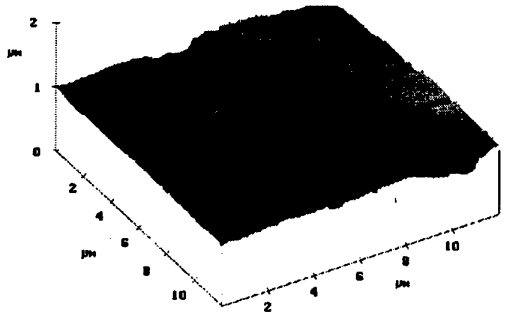

Figure 1: Defects in cold rolled steel

2. Basic Mechanisms

The use of a point-plane-configuration in a butane (C_4H_{10}) atmosphere results in a thin polymer-like film deposited on the substrate. A computer simulation of a positive corona discharge shows electrons which are accelerated up to 20keV. They crack the butane chain when they hit it. The gaseous molecules and the fragments of the collisions are ionized or excited by further electron impacts [3]. The fragments of the butane are radicals (e.g. C_2H_2 or C_3H_7) and ionized particles. The ions are accelerated by the electric field towards the substrate. When they reach the steel surface they firstly hit an oxygen atom of the oxidation layer of the steel surface. Through a chemical reaction the ions should build up polymer-like structures in combination with the surface oxygen atoms. The radicals generated by the corona are accelerated in axial direction by the electric wind and in tangential direction by the drifting ions. When they also reach the surface, they enhance the polymerization reaction.

The inhomogenities of the surface proves to be a singularity of geometry which forces the local field to peak. Thus ions near these shrink holes are deposited essentially at the edges of these holes. Therefore corona-based coating can be regarded as a very effective corrosion protection.

3. Experimental Set-up and Procedure

In order to test the efficiency of corona coating and the influences of different electrode geometries of different gas mixtures and of different supply voltages a special corona reactor has been designed. It is connected to a gas reservoir of butane and argon. Using a valve the reactor can be filled with air or evacuated to 50mbar. At first the reactor is flushed with argon, pumped a second time an then filled with butane or a combination of butane and argon. The reactor walls are made of polyacryl and allow the scientist to observe the discharge. Using a silicon glass lens the discharge is imaged onto the entrance slit of a monochromator. The spectrally resolved intensity is monitored by a multi-channel-plate intensified CCD camera attached at the position of the exit slit [4].

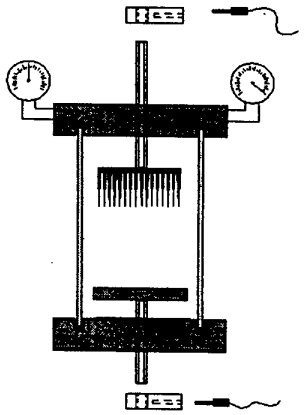

Figure 2: Schematic of the corona reactor

The electrode mount is designed for several kinds of electrode configurations. Besides a DC source we built up a 20kV (5mA, 1kHz) AC source and a pulse-width modulation-controlled pulse source (34kV, 84 mJ). Both sources are provided with a microcontroller, a user interface and a RS485 serial

connection. In combination with the stepping motor of the monochromator and the programmable camera the experimental set-up is automated. All components of the set-up are prepared for the use in an integrated production process with on-line control. The process control is based on the optical emission spectroscopy (for setup see [4]).

4. Results

The first effect which is observed during the coating process are soot spots on the surface in the centre of each discharge streamer. The rest of the coating is invisible.

One of the specific features of the polymer coating is the high water rejection function being tested by saturating the probe with steam. As shown in figure 3, an area of diffuse reflection is visible. These areas correspond to the coating.

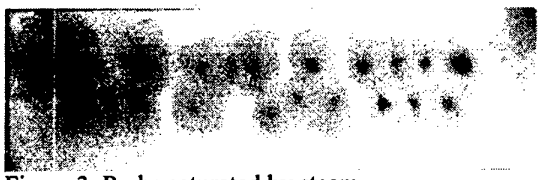

Figure 3: Probe saturated by steam

In order to examine the coating ex-situ several scanning electron microscope images were taken. Figure 4 shows a soot particle on a coated probe. The SEM images do not exhibit the coating directly. The only way to recognize the effect is to observe the contrast of two images of uncoated and a coated rolled steel. The sharp edges of the shrink holes are smoothed by the discharge process.

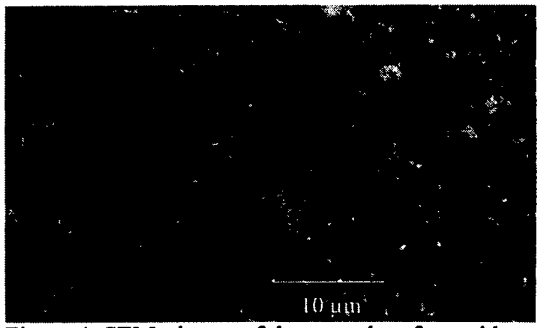

Figure 4: SEM-picture of the coated surface with carbon particles in the foreground

The surface of cold rolled steel is usually too rough (the height of the coating being thin as compared to the R_q value) for a correct thickness measurement. Therefore a silicon wafer has been coated and examined by a scanning probe device. The polymer film does not allow the use of optical scanning probes and before using a diamond needle probe the coating will have to be hardened by a second corona discharge under air. Figure 5 shows a height plot with a maximum deposition of 2 µm.

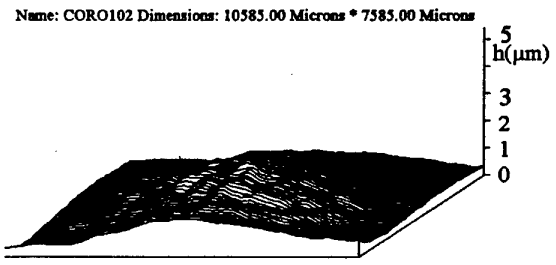

Figure 5: Height plot of a coated silicon surface

Finally the coatings have been tested for corrosion resistance. Thus a four-days-test with sprinkled salt water is performed using a probe being partially coated. The untreated area corrodes shortly after the test. The coated area is resistant but finally the corrosion process surrounds the coated area and begins to start at the coated part of the probe, too (see figure 6).

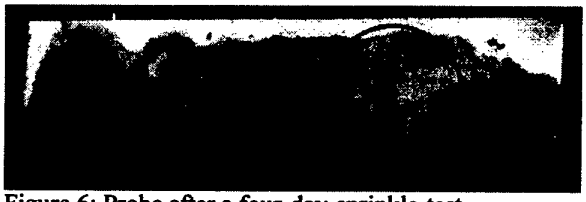

Figure 6: Probe after a four-day-sprinkle-test

5. Conclusion

In conclusion we can state that corona-assisted coating is an efficient way to realize a temporary corrosion resistance, e.g. for the protection of steel for transport purposes.

6. References

[1] Peters, U. *Korrosionsschutz durch organische Beschichtung,* Hanser Verlag 1994

[2] Salge, J., *Plasma-Assisted Deposition at Atmospheric Pressure,* Journal de Physique IV, 1995

[3] Koch, A.W., *Plama Deposition: Processes and Diagnostics,* in: Plasma Technology - Fundamentals and Applications, eds M.Capitelli and C. Gorse, Plenum Press, New York, ISBN 0-306-44207-8, 1992

[4] Toedter, O. Koch, A.W. *Correlation between Corona Spectral Intensities and Discharge Geometry*, Intern. Conf. on Phen. Ionized Gases ICPIG XXIII, Toulouse 1997, submitted to this conference

High-Voltage Ionization Wave Conditions Affection on the Ignition Delay Time in H_2-Air Mixtures at High Temperatures

L.M.Kof, S.M.Starikovskaia, A.Yu.Starikovskii

Moscow Institute of Physics and Technology, Dolgoprudny, 141700, Russia

1. Introduction

The problem of ultra fast and spatially homogeneous ignition of combustible mixtures is very topical for internal combustion engines elaboration. The aim of present work was an experimental study and numerical analysis of the high-voltage pulse nanosecond discharge adaptation for spatially homogeneous ignition of H_2-O_2 mixtures.

2. Experimental setup

Experimental setup, which provide separated and controlled excitation of internal and translational degrees of freedom consists of the shock tube – shock wave generator, connected with the 30 cm-length coaxial discharge dielectric section. Shock tube was made from stainless steel and has a square section 25 × 25 mm with the low-pressure channel length 1.6 m. High-voltage nanosecond breakdown ionization waves in discharge section is generated by pulse Marks generator. The voltage increasing rate at the high-voltage electrode was about 0.5 MV/ns. Total energy, emitting in the discharge during 25 ns, was in the range of 5 – 50 J.

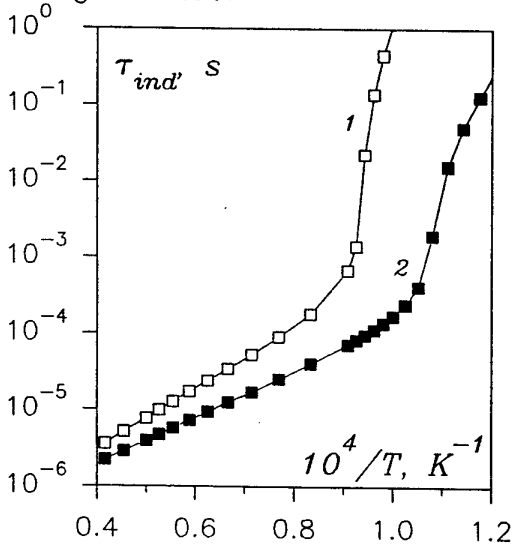

Shock wave causes the gas translational degrees of freedom heating. Variation of the reduction electric field E/N in the discharge defines direction of the energy contribution. When value of E/N is small ($\sim 10^{-17}-10^{-15}$ V·cm^2) the main part of the energy transmits to the vibrational degrees of freedom and particularly to the rotations. When E/N is more high, then effective gas ionization and excitation of electronic levels of the molecules by electrons begins.

3. Numerical model

Numerical model, used in the present work for ignition description in the H_2-O_2-N_2 system, was based on the kinetics scheme [1]. This model was completed by the set of reactions, which describe free radicals appearing due to the ionization wave development. It was assumed that fast ionization wave can be described as a momentary source of the H, O and N atoms. Atom concentrations estimation at the discharge break-off time ($\tau \simeq 25$ ns) was made on the basis of data [2-4]. Ionization wave influence ($U \simeq 250$ kV) on the mixture H_2:O_2:$N_2 = 5 : 19 : 76$ induction time τ_{ind} at $p_0 \simeq 1$ atm were shown on the figure.

Calculations shown additional increasing of the discrepancy between different ignition regimes with the translational temperature decreasing ($\tau^1_{ind}/\tau^2_{ind} \simeq$ 10 and 1000 at $T = 1100$ and 1000 K, respectively).

4. Conclusions

We demonstrate a high efficiency of the high voltage ionization wave for spatially-uniform excitation of the chemically-reacting systems. Data for ignition time delays was found for oxygen-hydrogen mixtures and numerical analysis of chemical kinetics was performed under shock wave and high voltage ionization wave simultaneous affection on the gas. This work was supported in part by grants *96-03-32746* and *96-02-18297* from Russian Basic Research Foundation.

5. References

[1]. A.Yu.Starikovskii: Khimicheskaya Fizika 13 N 1 (1994) 151

[2]. S.M.Starikovskaya: Fizika Plazmy 21 N6 (1995) 541

[3]. S.M.Starikovskaia, A.Yu.Starikovskii: Int. Symp. "Gas Discharges and Their Applications". Tokyo. 1995. V.2. P.345.

[4]. R.Kh.Amirov, E.I.Asinovskii, V.V.Markovets: High Temperature Teplophysics 22 N 5 (1984) 1002.

Topic 8

Plasma diagnostic methods.

Negative Ion Diagnostics in a Non-Maxwellian Plasma Containing Negative Ions

H. Amemiya

The Institute of Physical and Chemical Research (RIKEN)
Hirosawa, Wako, Saitama-Pref. 351-01, Japan

1. Introduction

Negative ion diagnostics was made by a probe in e.g. H^- sources [1]. The main principle was in the use of the current ratio (CR) between electron and ionic parts of the probe characteristics. However, when the negative ion density ratio is not large, the method is difficult to evaluate the parameter. Another reason is that, if the electron temperature T_e is much higher than the negative ion temperature T_n, the Bohm criterion was kept almost at $\kappa T_e/2$. A method of using the second derivative of the probe current was thereafter applied [2]. In strongly electronegative gases, like iodine, where the Bohm criterion decreases toward $\kappa T_n/2$, the both methods were found to be reasonable [3]. The change of the criterion was then fully analyzed [4] and recently using this the CR method has been refined for the case of relatively large negative ion density ratio [5]. However, all these methods are valid only for the case where the electron energy distribution f(E) is Maxwellian. In many cases of plasmas containing negative ions, f(E) is non-Maxwellian. In view of these facts, the purpose of the present paper is to consider the diagnostics in non-Maxwellian cases.

2. Formulation

We follow Allen's method [6] of using the dispersion relation which is given by

$$\omega_{pe}^2\int_{-\infty}^{\infty}\frac{f_e(v)dv}{(\omega - kv)^2}+\omega_{pn}^2\int_{-\infty}^{\infty}\frac{f_n(v)dv}{(\omega - kv)^2}+\omega_p^2\int_{-\infty}^{\infty}\frac{f_i(v)dv}{(\omega - kv)^2} = 1, \qquad (1)$$

where ω: angular frequency, k:wave number, f_e, f_n, f_i: velocity distributions for electrons, negative ions and positive ions, respectively, $\omega_{pe}=N_e e^2/\varepsilon_o m$, $\omega_{pn}=N_n e^2/\varepsilon_o M_n$, $\omega_p=N_p e^2/\varepsilon_o M$, N_e, N_n, N_p: densities of electrons, negative ions and positive ions, m,M_n,M: mass of each species. The integration is performed along the Landau's contour. A steady state $\omega=0$ is assumed. The charge neutrality holds at the sheath edge

$$N_e + N_n = N_p . \qquad (2)$$

Multiplying $(k\lambda_D)^2$ on both sides of eq.(1), we obtain

$$\frac{(1-\alpha)}{m}\int_{-\infty}^{\infty}\frac{f_e(v)dv}{v^2} + \frac{\alpha}{M_n}\int_{-\infty}^{\infty}\frac{f_n(v)dv}{v^2} + \frac{1}{M}\int_{-\infty}^{\infty}\frac{f_i(v)dv}{v^2} = (k\lambda_D)^2/(m\langle v_e^2\rangle/2), \qquad (3)$$

where the Debye length is defined as $\lambda_D\equiv\omega_{pe}\langle v_e\rangle$, $\langle v_e\rangle$: average electron velocity and $\alpha\equiv N_n/N_p$. In the limit of $k\lambda_D\to 0$, and assuming $f_n(v)$ is Maxwellian with a negative ion temperature T_n, we have

$$\frac{1}{M}\langle v_i^2\rangle = -\frac{(1-\alpha)}{m}\int_{-\infty}^{\infty}\frac{f_e(v)dv}{v^2} + \frac{\alpha}{\kappa T_n}, \qquad (4)$$

where an asymptotic formula in the dispersion relation [7] was used for the negative ion term.

3. Sheath criterion and the positive ion current

Assume that $f_e(v)$ can be measured by probes directly or by using the Druyvesteyn method [8] in the form of kinetic energy distribution F(E); $E=mv^2/2$. The integral of the second term of RHS of eq.(4) is partially integrated and by way of the relation $\partial f_e(v)/\partial v=-(m/2)F(E)$, eq.(4) leads to

$$\frac{1}{M}\langle v_i^2\rangle = \frac{(1-\alpha)}{2}\int_0^{\infty}F(E)E^{-1}dE + \frac{\alpha}{\kappa T_n}. \qquad (5)$$

In order for positive ions to have this kinetic energy at the sheath edge, the sheath edge potential Vs can be expressed as

$$eV_s = \left[(1-\alpha)\int_0^{\infty}F(E)E^{-1}dE + \frac{2\alpha}{\kappa T_n}\right]^{-1}. \qquad (6)$$

The positive ion density at the sheath edge N_p is balanced by the electron density there N_e which is given by almost reflected components for a deeply negative electrode potential as

$$\delta_e\equiv\frac{N_e}{N_{eo}} = 2\int_{v_s}^{\infty}\frac{vf(v)dv}{\sqrt{v^2-2eV/m}} = \int_{eV_s}^{\infty}\sqrt{1-\frac{eV_s}{E}}F(E)dE, \qquad (7)$$

where V_s is the sheath edge potential. The negative ion density N_n is given by

$$\delta_n\equiv N_n/N_{no}=\exp(-eV_s/\kappa T_n). \qquad (8)$$

N_{eo} and N_{no} are electron and negative ion densities in the unperturbed plasma with the density N_o. Therefore,

$$N_{eo} + N_{no} = N_o. \qquad (9)$$

Putting $\alpha_o\equiv N_{no}/N_o$, we obtain from eq.(7)-eq.(9)

$$\alpha = \frac{\alpha_o \delta_n}{\delta_e(1 - \alpha_o)+\alpha_o \delta_n}. \quad (10)$$

The positive ion current is given by

$$L_+ = eSN_p(2eV_s/M)^{1/2};\ S: \text{probe area}, \quad (11)$$

where eq.(2), eq.(6)-eq.(8) should be used.

4. Electron and Negative Ion Currents

The electron current and negative ion current are

$$I_e = \frac{eSN_{eo}}{4}\int_{eV_p}^{\infty}(1-\frac{eV_p}{E})\sqrt{\frac{2E}{m}}\,F(E)dE, \quad (12a)$$

$$I_n = eSN_{no}\sqrt{\frac{\kappa T_n}{2\pi M_n}}\,e^{-\gamma\eta};\ \eta=\frac{eV_p}{\kappa T_e},\ \gamma=\frac{T_e}{T_n}. \quad (12b)$$

The saturated current I_S at V_p=0 (space potential) is

$$I_s = \frac{eSN_o}{4}\left\{(1 - \alpha_o)\langle v_e\rangle + \alpha_o\sqrt{\frac{\kappa T_n}{2\pi M_n}}\right\}, \quad (13)$$

where $\langle v_e\rangle$ is the mean electron velocity.

5. Experimental study

Experiments have been performed in a radio frequency (RF) discharge in oxygen [10]. The second derivative has been measured by the AC method [11], modified such that by the crystal control the superimposed frequencies included a prime number 17 distinct from 113 contained in 13.56MHz to avoid coupling of overtones with RF. Moreover, symmetric electrodes suppressed fluctuation.

Figure 1 shows the probe current I_p, and the derivative I_p" where peaks 1,2 denote electrons and negative ions.

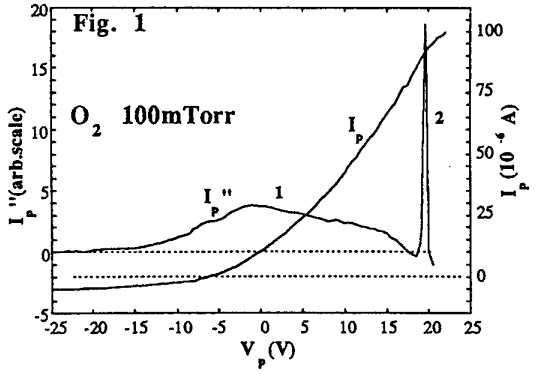

In the first method, $N_{no}/N_{eo}(=\alpha_o/(1-\alpha_o))$ is directly obtained from the ratio of peak areas in I_p"-curve as

$$\frac{N_{no}}{N_{eo}} = \sqrt{\frac{\pi M_n}{m}}\,\frac{T_n^{3/2}}{2}I_n''(0)\Big/\int_0^{\infty} I_e''(V_p)V_p^{1/2}dV_p, \quad (14)$$

where V_p is the probe voltage measured from the space potential to a negative bias. We obtain $T_n \cong 0.25$eV. We obtain α_o=0.55 for O^- and 0.62 for O_2^- by eq.(14).

Figure 2 shows the electron energy distribution F(E) compapred with Maxwellan and Druyvesteyn.

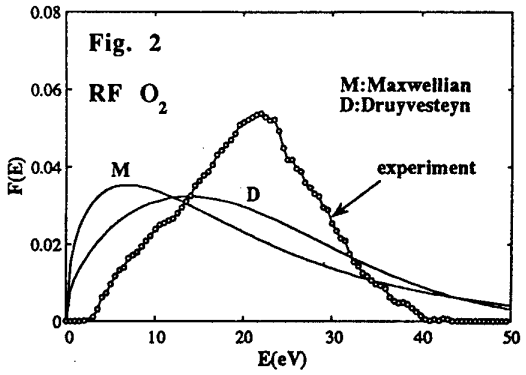

In the second method, the current ratio $R=(I_s+I_n)/I_+$ which is a function of F(E) and α_o is utilized. However, contrary to the method of using I_p", eq.(6), (8)-(10) should be iteratively used to solve α_o. For the data of Fig. 1, we obtain R=20, and α_o exceeds 0.9. The discrepancy from the first method suggests that the probe perturbs the plasma and erroneously reduces I_s. It is necessary to know the value of R for the case without negative ionsto to determine α_o in a calibrated way [3]. The neglect of a finite $k\lambda_D$ effect in the sheath model would restrict the applicability to a relatively dense plasma. Furthermore, in the case of RF discharges, the effect of a finite ω should be included for a more accurate description of the sheath criterion [11].

6. Conclusion

The method of using the second derivative is useful for negative ion diagnostics when T_n is so low that the negative ion peak 2 in I_p" is separable from that of electrons. In the opposite case, which happens e.g. in DC hollow cathode discharges in electronegative gases [12], the CR method becomes inevitable but should be used by calibrating R with that of electropositive gases.

References

[1] M.Bacal and H.J.Doucet: IEEE Trans. Plasma Sci. **PS-1** (1973) 91.
[2] H.Amemiya and Y.Sakamoto: Japan.J.Appl.Phys. **26** (1987) 1170.
[3] H.Amemiya: J.Phys.Soc.Japan **57** (1988) 887.
[4] N.S.J.Braithwaite and J.E.Allen: J.Phys.D **21** (1988) 1733.
[5] A.G.Nikitin, F.El.Balghiti and M.Bacal: Plasma Source Sci.Technol. **5** (1996) 37.
[6] J.E. Allen: J.Phys.D **9** (1976) 2331.
[7] B.D.Fried and S.D.Conte: *The Plasma Dispersion Function* , Acad. Press (1961).
[8] M.J.Druyvesteyn: Z.Physik **64** (1930) 781.
[9] H.Amemiya and N.Yasuda: J.Phys.Soc.Japan **66** (1997) No.3.
[10] K.Wiesemann: Ann.Phys. **219** (1969) 462.
[11] J.E.Allen and M.A.Skorik: J.Plasma Phys. **50** (1993) 243.
[12] H.Amemiya and K.Ogawa: J.Phys.D **30** (1997) in press.

Validity of electrical probe measurements in RF plasma checked by optical spectroscopy diagnostic

Abdelbasset Hallil, Hiroshi Amemiya and Kazuo Shimizu

The Institute of Physical and Chemical Research ,
Hirosawa 2-1, Wako-Shi, Saitama, 351-01, Japan

1. Introduction

The kinetics of the generation of reactive species in plasma is controlled by the electron energy distribution function (EEDF). Only Langmuir probe diagnostic method leads concisely to such quantity after calculation of the second derivative f(E) of the probe characteristic. Although, the widely used cylindrical probe permits a reliable determination of f(E) only for energies less than 9 kTe [1], due to the important contribution of the ion current second derivative in f(E) at high energies. To determine f(E) more precisely at high energies, spherical or planar probes are suitable, because they are insensitive to the ion part in the second derivative. Notice that in spherical probe the ion current varies linearly with the voltage while in the planar one it is constant. This obviously leads to zero second derivative of the ion current and therefore to more reliable determination of f(E) at high energies.

Moreover, still doubts exist in the high energy tail of f(E) due to the contribution of noise. Therefore, it seems necessary to check the validity of the second derivative by means of other simple and reliable discharge diagnostic methods like optical emission spectroscopy.

Here, for a particular spectral line in RF argon discharge at different powers and pressures, we report comparisons between optical emission intensities measured by spectrophotometer and those calculated by integration of the probe measured electron energy distribution function multiplied by the excitation cross section of the considered spectral line.

2. Experimental method and apparatus

The RF plasma reactor used for the study has been described in detail elsewhere [2]. Briefly, it consists of a 6-in.-diameter Pyrex glass vessel containing two parallel plates of 8 cm diameter separated by a distance of 2.5 cm. The power was supplied to the electrodes by a 13.56 MHz RF oscillator through a matching element of the bridge type. The plasma was confined in a multicusp magnetic field MC of SmCo magnets constructed in a drum-type configuration. After evacuating the vessel by a diffusion pump below 10^{-5} Torr, argon gas was introduced through a mass-flow controller in the range of 10 to 220 mTorr. A stainless steel plane probe with a diameter of 3 mm was placed at the discharge center between the two electrodes. To avoid distortion of current-voltage probe characteristics [3], due to the fall of the RF plasma voltage and its harmonics in the probe-sheath impedance, an original filter, using coaxial cables with distributed constants, was designed [4]. Data of the probe characteristics were acquired and processed by a personal computer. The electron energy distribution function and the electron density were determined from the numerical second derivative [5] of the probe current-voltage characteristic .

The optical emission of the plasma was gathered to the photomultiplier through a 2 mm diameter optical fiber, which is set behind the quartz viewing port, in the same horizontal level as the probe.

3. Results and discussion

When the electron plasma density is low as in our case ($n_e \sim 10^8$-10^{10} cm^{-3}) [6], the plasma can be described by a corona equilibrium model [7]. In this model, the excited states are formed by direct impact on ground state species of argon and the de-excitation is postulated to appear radiatively:

Excitation: $Ar + e \longrightarrow Ar_i^* + e$

De-excitation: $Ar_i^* \longrightarrow Ar_j^* + \omega_{ij}$

ω_{ij} is the photon energy arising from the transition i——> j of the excited argon atom Ar_i^*. Taking into account the equilibrium between the rate of excitation and de-excitation in the steady state, the intensity I_{ij} of a particular spectral line at frequency ν_{ij} can be given by:

$$I_{ij} = N n_e \int_0^\infty \frac{1}{4} \left(\frac{2E}{m}\right)^{\frac{1}{2}} F(E)\, \sigma_{ij}(E)\, dE$$

where N is the concentration of the ground state species of argon, $\sigma_{ij}(E)$ is the excitation cross section for the emission of a photon of frequency ν_{ij}. F(E) is the electron energy distribution function and m is the electron mass.

The spectral line chosen for the study corresponds to the atomic argon transition $3p^54p \longrightarrow 3p^54s$ at a wavelength 750.3 nm and its excitation cross section is well known [8]. This line is intense and can be measured easily for variable plasma conditions. Although, the population of the upper level $3p^54p$ is mainly due to the electron excitation of argon atoms from the ground state. Contributions to this population from de-excitation of other levels are negligible at low pressures.

Figure 1 shows the measured electron energy probability function (EEPF or f(E)) for variable pressures at a fixed power 4 watts. The shape is bi-Maxwellian and the processes leading to such behavior are well described elsewhere [1].

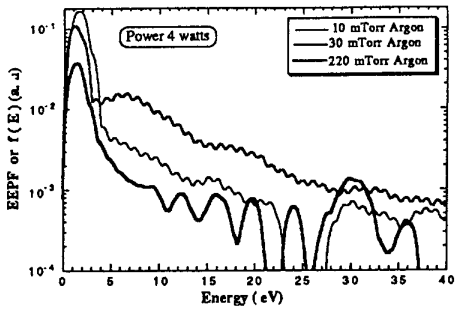

Fig.1 EEPFs in argon at variable pressures

The calculated emission intensity from these EEPFs is shown in fig.2. Notice that the increase of the intensity observed at 30 and 40 mTorr is predictable from the observation of the EEPF which contains bigger amount of high energy electrons at these pressures. Thus, this leads to more excitation of ground state argon atoms and to more de-excitation.

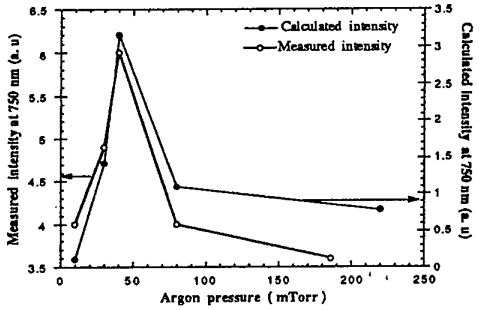

Fig.2 Calculated and measured emission intensities at variable pressures

For all pressures, the calculated and measured optical intensities show good qualitative agreement. This asserts the validity of our measured electron energy probability functions at high energies and makes the choice of the planar probe more convenient. The slight disagreement observed at high pressure (220 mTorr) should be due to the appearance of other de-excitation mechanisms of the argon excited atoms such as collisions with ground state argon atoms, making the calculations by the corona model non valid.

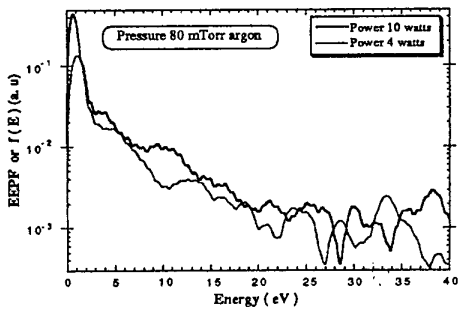

Fig.3 EEPFs at variable powers

The measured EEPFs at variable powers for a fixed pressure 80 mTorr are shown in fig.3, while the calculated and measured emission intensities are represented in fig.4.

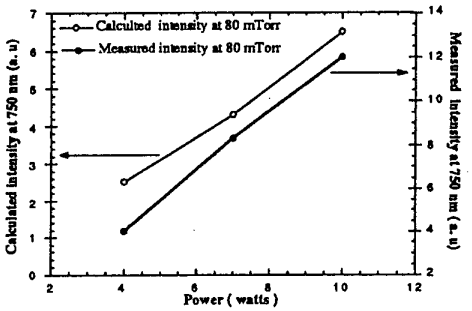

Fig.4 Calculated and measured emission intensities at variable powers

Here also good qualitative agreement is found between the two intensities. This confirms the validity of planar probe measurements at high energies and their insensitivity to the second derivative of the ion current. For the variable pressures and powers considered, the argon excitation cross section is higher in the energy range between 15 and 30 eV. This helps to reduce errors in emission intensity calculations due to the limitation of f(E) until 40 eV.

Finally, the validity of probe measurements checked by optical measurements will allow a reliable application of our measured electron energy distribution functions in the simulation of chemical processes in argon RF discharges.

Acknowledgments

One of us (A. Hallil) acknowledges the Japan International Science and Technology Exchange Center for the financial support to carry out this work under STA fellowship program.

References

[1] V.A. Godyak, R.B. Piejak and B.M. Alexandrovich: Plasma Sources Sci. Technol. 1, 36 (1992)

[2] H. Amemiya, N. Yasuda and M. Endou: Plasma. Chem. and Plasma Process. 14, 209 (1994)

[3] J.D. Swift and M.J.R. Schwar, Electrical Probes for Plasma Diagnostics, Illife Books, London, 1970

[4]K. Shimizu, A. Hallil, and H. Amemiya: Rev. Sci. Instrum, 1997 (to be published)

[5] A. Savitzky and M.J.E. Golay: Anal. Chem. 36, 1627 (1964)

[6]A. Hallil, H. Amemiya and K. Shimizu: Proceedings of ICRP-3/SPP-14, Nara-Japan, 1997

[7] Huddlestone R.H. and Leonard S.L. 1965, Plasma Diagnostic Techniques, (New York: Academic)

[8] P.Laborie, J.M. Rocard and J.A. Rees. 1968, Electronic Cross-Sections and Macroscopic Coefficients, (Paris: Dunod)

Atomic ground-state density of mercury in nonlocal-thermodynamic-equilibrium conditions

H. Elloumi and M. Aubès

Centre de Physique des Plasmas et de Leurs Applications de Toulouse

Université Paul Sabatier, ESA 5002
118, Route de Narbonne, 31062 Toulouse cedex, France

1. Introduction

There are various methods of spectroscopic characterization of a high pressure mercury discharge [1] if the plasma is in local thermodynamic equilibrium (LTE). These methods are based mainly on the measurement of the total intensity of optically thin spectral lines.

Number density of excited atoms can be determined by emission spectroscopy. However, the ground state density which represents the major part of the atomic density, can only be deduced from such measurement if LTE is assumed.

Nevertheless, recent measurements in mercury arcs suggest the existence of departures from the thermal equilibrium in the axis and in the periphery of such an arc [2].

In this present study we describe a procedure for determining the local ground-state density in a high pressure mercury discharge. This method is based on the properties of the strongly self-reversed resonance line λ=253.7 nm. This method can be applied to a large range of pressure (0.2 to 5 bar), and does not require any knowledge of the thermodynamic state of the system. Indeed, we established a relation between the position of the wavelength at the maximum intensity of the red wing resonance line and the atomic ground-state density regardless all other parameters of the plasma.

2. Experimental set-up

The measurement of the apparent line profile is carried on by a monochromator (THR1500) with a dispersion less than 1.3 Å/mm working in double pass configuration. The alignment of the optical system is performed with a He-Ne laser beam. The detection system is a photomultiplier tube having a good ultra-violet response and fitted with a time resolving electronic device allowing temporal measurements.

We worked on a set of cylindrical lamps of same internal diameter (18.2 mm) and inter-electrode distance (72 mm). The main filling and electrical characteristics of the studied discharges are given in table 1.

Time resolved intensity measurements are made midway between the electrodes. Acquisition and storage of experimental data are carried out by an automated system controlled by a personal computer.

A detailed description of the experimental set up is given by Sewraj et al [3].

Discharge	filling mHg (mg)	Uarc (Volts)	Iarc (A)	Power (W)
D1	4	48	3.2	150
D2	8	52	3.2	164
D3	16	74	3.2	288
D4	70	151	3.2	400

Table 1. Characteristics of the studied discharges.

3. Ground state density

3.1 Line profile

The local profile of the self reversed resonance line (λ=253.7 nm, 6^3P_1-6^1S_0) has been studied by many authors [5,6...]. In a recent communication [4] we also studied the shape of the apparent line profile of this line. So, we showed that :

(i) the blue wing of the resonance line can be described by a Lorentzian profile with a constant half width.

(ii) the red wing can be represented in Van der Waals interaction by the quasi-static approximation with $\Delta\lambda_0$ ($\Delta\lambda_0$=Cw n_{Hg}^2) as characteristic width.

According to Stormberg [5] the total line profile can be approximated by the convolution of the Lorentzian and the quasi-static profile

3.2 procedure

Bartels [7] has shown that, for the self-reversed resonance line, the maximum occurs for optical thickness τ_0 very close to 2. It may be written, at the wavelength of the maximum intensity of the red wing :

$$\tau(\lambda_R) = \int_{-x_0}^{x_0} K(\lambda_R, x)\,dx = 2 \qquad (1)$$

where $K(\lambda_R,x)$ is the local absorption coefficient at the wavelength λ_R which is proportional to the ground-state density.

At the wavelength of the reversal maximum of the red wing we can write that $|\lambda_R-\lambda_0|>>\Delta\lambda_0$. Thus the expression of the local profile at λ_R can be written :

$$P(\Delta\lambda) = \frac{\sqrt{C_w}}{2(\lambda_R-\lambda_0)^{3/2}} n_{Hg} \qquad (2)$$

Combining equations 1 and 2, one can obtain :

$$\alpha(\lambda_R - \lambda_0)^{3/2} = \int_{-x_0}^{x_0} n_{Hg}{}^2(x)dx \qquad (3)$$

where α is a constant characterizing the resonance line equal to 1.428 10^{61} $m^{-13/2}$.

It follows from equation 3 that the mercury density depends only on the λ_R position. So, we have measured the apparent line profile at different radial position from the arc axis (figure 1) and established the ground state densities using Abel inversion.

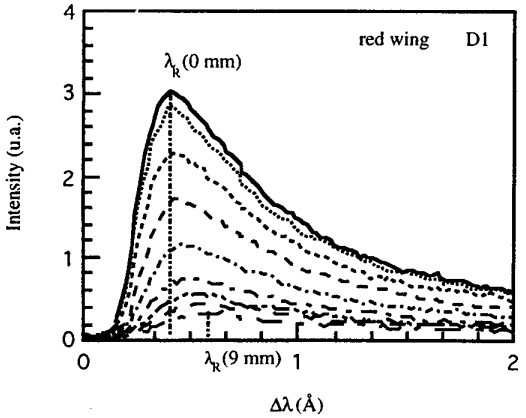

Figure 1. Apparent line profile of the 253.7 nm resonance line (red wing) at different radial positions.

4. Results and conclusion

We first check the applicability of this method under LTE conditions by investigating the D4 discharge. Because of its high pressure this discharge is assumed to be close to LTE. The results are shown in figure 2 together with the values obtained by assuming LTE.

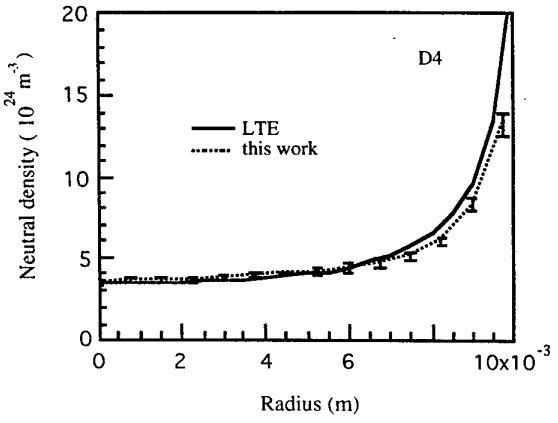

Figure 2. Measured ground-state density, (____) : calculated under LTE assumptions ; (....) : calculated using the reversal maximum of the red wing.

Furthermore, as far as the discharges referenced in table 1 are concerned, we have determined the radial distribution of ground-state density by applying the method described in section 3. Here we give the result corresponding to the D1 discharge (figure 3). (D4).

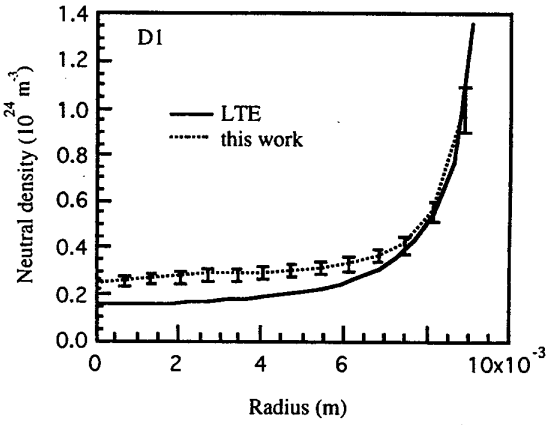

Figure 3. Measured ground-state density, (____) : calculated under LTE assumptions ; (....) : calculated using the reversal maximum of the red wing. (D1).

As it can be seen in figures 2 and 3, a good agreement is found for the more loaded discharge but discrepancies appears for the low loaded discharge.

⇒ Three main advantages are to be retained :

i) this method does not require the LTE assumption;

ii) no additional information is needed such as pressure and temperature;

iii) only relative values of the apparent line profiles are needed.

Acknowledgments

Authors are indebted to Pr J. J. Damelincourt for numerous discussions on this subject. We also thank Dr N. Sewraj for his help in the realization of this work.

References

[1] J J Damelincourt, D Karabourniotis, L Scoarnec and P Herbet, J. Phys. D: Appl. Phys., **11**, (1978) 1029.
[2] D Karabourniotis and S Couris, Optic. Comm. **67**, (1988) 214.
[3] N Sewraj and H Elloumi, XIth Int. Conf. GD (1995)
[4] H Elloumi, M Aubès, J J Damelincourt and L Dassieu, XIIIth ESCAMPIG (1996)
[5] H P Stormberg and R. Schafer, J. Appl. Phys. **54**, (1983) 4338.
[6] P Laporte and H Damany, J. Quant. Spectrosc. Radiat. Transfert. **22**, (1979) 447.
[7] H Zwicker, Plasma Diagnostics, edited by W Lochte Holtegreven (North Holland,Amsterdam, 1968)

3D-MODELING OF N ATOM TITRATION BY NO IN Ar-N_2 POST-DISCHARGES

T. Belmonte, T. Czerwiec, A. Ricard and H. Michel

Laboratoire de Science et Génie des Surfaces (URA CNRS 1402), Ecole des Mines de Nancy, Institut National Polytechnique de Lorraine, Parc de Saurupt, 54042 Nancy cedex, France.

1. Introduction

Containing nitrogen flowing post-discharge are studied for surface treatments like steel nitriding [1]. The thickness and the composition of γ' and ε iron nitride layers are strongly dependent on the atomic nitrogen content in the gas phase [2]. The determination of atomic nitrogen density can be achieved by NO titration in N_2, Ar-N_2 and Ar-N_2-H_2 post-discharges [3]. With this method, the accuracy of the measurements is strongly dependent on the way NO diluted in argon is introduced in the zone where the titration occurs. Indeed, the formation of atomic oxygen from NO and its reaction with either N or NO to produce respectively NO(B) and NO_2* is rather slow. Therefore, the mixture conditions determine a minimum distance over which the diagnostic is available. Otherwise, measurement of the nitrogen atom density is perturbed. The aim of the present work is to describe, by a 3D-modeling, the influence of the mixture conditions on the determination of N atom density. For this reason, no care was taken to mix the gas so that the worse mixture conditions are studied to validate the modeling.

2. Experimental apparatus

NO titration method is fully described elsewhere [3]. It is done here in a quartz cylinder of 28 mm ID. The plasma is created by a surfaguide wave launcher with a power equal to 130W. Ar-5%N_2post-discharge enters this cylinder in a quartz tube of 5 mm ID at 70 cm from the plasma outlet whereas the 1.4%NO-Ar mixture is introduced via a manifold of 0.5 mm ID. With a total plasma flow rate of 1050 sccm, at 1500 Pa, assuming all the temperatures equal to 300 K, the extinction is obtained at $Q_{(NO\text{-}Ar)}$=85 sccm, what leads to [N]=4.1 10^{14} cm^{-3}, i.e. a total mass fraction of 4.16 10^{-4}.

3. Modeling

The model used in this study is obtained by solving the conservation equations of continuity, momentum and energy. Equations are solved considering a stationary state. Pressure in the system is assumed large enough to consider the gas phase as satisfying the conservation equations in a continuum medium (the knudsen number is 2 10^{-3}). The set of partial differential equations which expresses the conservation of component i, momentum and energy is closed by the ideal gas law :

(1) $\nabla.(\rho\omega_i\vec{v} - D_i\rho\vec{\nabla}\omega_i) = S_{\omega i}$

(2) $\nabla.\rho\vec{v}\vec{v} - \nabla.\vec{\vec{\tau}} = -\vec{\nabla}P + \rho\vec{g}$

(3) $\nabla.(\rho C_p T\vec{v} - k\vec{\nabla}T) = S_T$

ρ is the fluid density; $\vec{v}$ the velocity; ω_i the mass fraction and $S_{\omega i}$ is the consumption source of the reactive species (the reaction rates) as specified further. The species balance (1) can be solved to yield the mass fraction fields. The dilution assumption in argon, for each reactive species, allows the use of a simple form of Fick's law. D_i is then considered as the binary diffusion coefficient in argon. $\vec{\vec{\tau}}$ is the stress tensor. $\rho\vec{g}$, T, P, Cp and k are respectively the gravitation force, fluid temperature, pressure, specific heat at constant pressure and thermal conductivity. S_T are heat sources. The flow is laminar (Reynolds number is 20). The kinetic model used herein is based on that described by [3] and completed by reactions neglected by these authors. The set of reactions and the kinetic rates used are described in table 1.

Table 1 : Reactions considered for the modeling at 300 K (units are s^{-1} or mol^{-1} m^3 s^{-1}or mol^{-2} m^6 s^{-1})

Volume reactions		
$N+NO \rightarrow N_2+O$	$k_1=2.23\ 10^7$	[3]
$N+O+M \rightarrow NO+M$	$k_{2(M=Ar)}=2.75\ 10^3$	[7]
	$k_{2(M=Ar)}=3.62\ 10^3$	[7]
$N+O+M \rightarrow NO(B)+M$	$k_{3(M=Ar)}=8.99\ 10^1$	[3]
	$k_{3(M=N2)}=1.12\ 10^2$	[3]
$N+N+M \rightarrow N_2+M$	$k_{4(M=Ar)}=3.7\ 10^3$	[4]
$NO+O+M \rightarrow NO_2+M$	$k_{5(M=Ar)}=1.1910^4$	[5]
	$k_{5(M=N2)}=1.1910^4$	
$NO+O+M \rightarrow NO_2$*$+M$	$k_{6(M=N2)}=1.34\ 10^4$	[3]
	$k_{6(M=N2)}=2.10\ 10^4$	[3]
$NO(B) \rightarrow NO+h\nu$	$k_7=5\ 10^5\ s^{-1}$	[6]
$NO(B)+M \rightarrow NO+M$	$k_{8(M=Ar)}=2.11\ 10^5$	
	$k_{8(M=N2)}=2.11\ 10^5$	[7]
$NO_2+O \rightarrow O_2+NO$	$k_9=5.72\ 10^6$	[5]
NO_2*$\rightarrow NO_2+h\nu$	$k_{10}=2.5\ 10^4\ s^{-1}$	[3]
NO_2*$+M \rightarrow NO_2+M+h\nu$	$k_{11(M=Ar)}=2.35\ 10^7$	[3]
	$k_{11(M=N2)}=3.61\ 10^7$	[3]
$N_2(B) \rightarrow N_2(A)+h\nu$	$k_{12}=10^5$	[2]
$O+O+M \rightarrow O_2+M$	$k_{13(M=Ar)}=3.78\ 10^2$	[7]
Surface reactions		
$N \rightarrow 1/2\ N_2$ on quartz	$\gamma_1=10^{-4}$	[8]
$O \rightarrow 1/2\ O_2$ on quartz	$\gamma_2=1.4\ 10^{-4}$	[9]

The (Oz) velocity component v_Z is assumed to be zero on the walls parallel to (Oz). The mesh is 20x35x50 cells for φ, r, z in cylindrical coordinates. Incorporating the axisymmetry assumption, the computational domain is reduced to a half of the reactor. The implicit Phoenics code is used for this calculation. Radial dimension is multiplied by a scale factor of 5 for the presentation of results.

The inlet mass fractions of N, $N_2(B)$, N_2, NO are respectively taken equal to 4.16 10^{-4}, 1 10^{-3} ω_N [10], 3.38 10^{-2}, 1.06 10^{-2} (before mixture). The choice of this latter value corresponds to the extinction conditions.

Thermal conductivity, heat capacity and viscosity of mixtures are estimated by considering pure argon properties, assuming a very diluted medium. Binary diffusion coefficients in argon are given in table 2.

Table 2 : Binary diffusion coefficients in argon

$D_{N/Ar}=1.12\ 10^{-4}\ T^{1.88}\ /\ P$	[11]
$D_{N2/Ar}=1.71\ 10^{-4}\ T^{1.75}\ /\ P$	[12]
$D_{O/Ar}=5.85\ 10^{-4}\ T^{1.75}\ /\ P$	[13]
$D_{O2/Ar}=1.71\ 10^{-4}\ T^{1.75}\ /\ P$	[14]
$D_{NO/Ar}=1.00\ 10^{-4}\ T^{1.75}\ /\ P$	[15]
$D_{NO(B)/Ar}=1.00\ 10^{-4}\ T^{1.75}\ /\ P$	Equal to $D_{NO/Ar}$
$D_{NO2/Ar}=6.24\ 10^{-6}\ T^{1.75}\ /\ P$	†
$D_{NO2*/Ar}=6.24\ 10^{-6}\ T^{1.75}\ /\ P$	Equal to $D_{NO2/Ar}$

† Calculated from critical values available in [14].

4. Results and discussion

The calculations were performed at the extinction point, and compared with experimental results obtained by photographs and reproduced as a drawing on Fig. 1. The correlation between the modeling and the experimental results is then carried out qualitatively. The lengths for the mixture of both gases are very close to those calculated. In each case (Fig. 1 and 2) a mixture length of 0.15 m is found. All the species mass fraction fields are provided by the model.

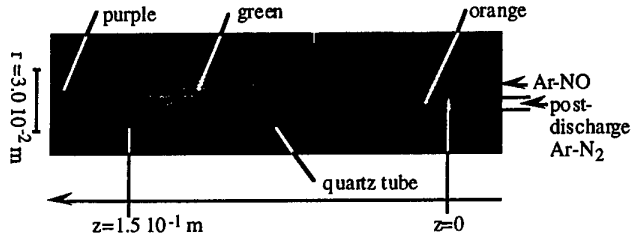

Fig. 1 : Drawing from a scanned photograph of N titration by NO. Conditions are given within the text.

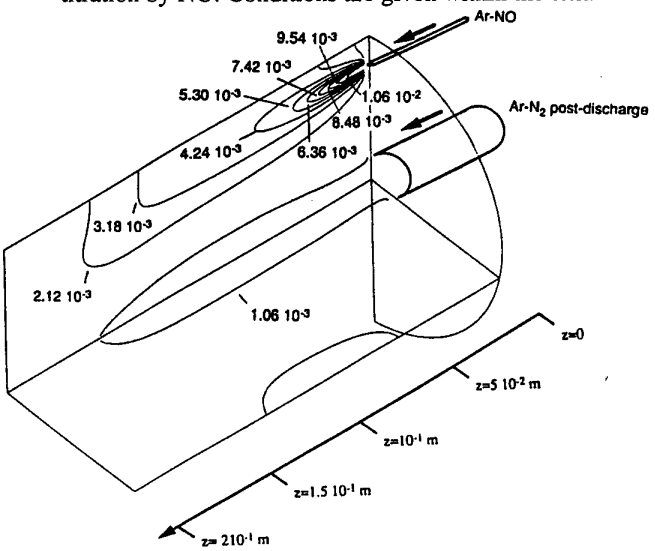

Fig. 2 : NO_2* mass fractions calculated by the model.

The yellow-orange emission of the 1^+ system is very well explained by the model. In the N stream, the mass fraction of N atoms evolves from $4.16\ 10^{-4}$ to $8.32\ 10^{-5}$ over 0.12 m. The dark zone between the two streams is also given by the calculations.

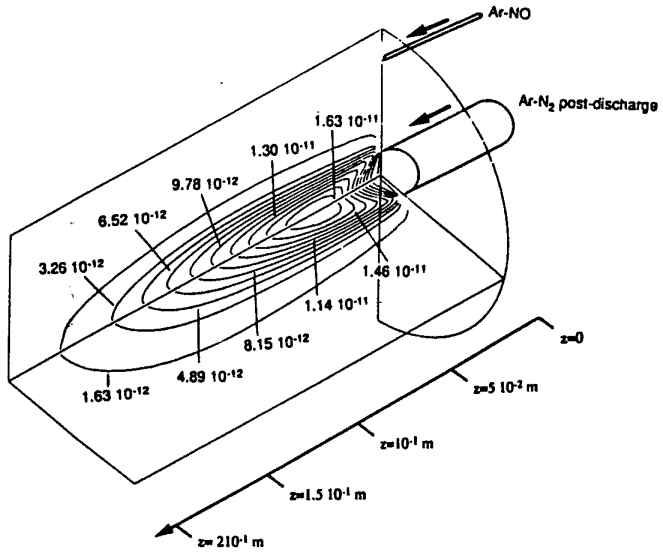

Fig. 3 : NO(B) mass fractions calculated by the model.

Fig. 3 shows that the mass fraction of NO(B) is very weak when compared to NO_2* and that is why the N stream turns from the orange to the green. The very pale purple NO(B) emission stands at the end of the mixture zone and is due to the fact that the experiment was carried out at a NO flow rate of 85 sccm which is very slightly greater than the extinction point. NO(B) is still present when NO_2* is completely consumed. The model permits predictions on the mixture length required to do accurate titration but also will help to conceive mixture devices.

References

[1] A. Ricard, J. Oseguera-Pena, L. Falk, H. Michel, M. Gantois, IEEE Trans. Plasma Sc. 18 (1990) 940
[2] H. Malvos, H. Michel, A. Ricard, J. Phys. D: Appl. Phys. 27 (1994) 1328
[3] T. Czerwiec, J. Gavillet, T. Belmonte, H. Michel and A. Ricard, J. Phys. III France 6 (1996) 1205
[4] T. Yamashita, J. Chem. Phys. 70-9 (1973) 4248
[5] R.A. Young, G. Black, T.G. Slanger, J. Chem. Phys. 49-11 (1968) 4758
[6] B. Gordiets, A. Ricard, Plasma Sources Sci. Technol. 2 (1993) 158
[7] Chem. kin. Data base for combustion chemistry, J. Phys. Chem. Ref. Data 15-3 (1986)
[8] Y.C. Kim, M. Boudart, Langmuir 7 (1991) 2999
[9] M. Brake, J. Hinkle, J. Asmussen, M. Hawley, R. Kerber, Plasma Chem. Plasma Proc. 3-1 (1983) 63
[10] C. Gorse, M. Capitelli, J. Appl. Phys. 62-10 (1987) 4072
[11] G.N. Hays, C.J. Tracy, H.J. Oskam, J. Chem. Phys. 60-5 (1965) 2027
[12] H. Malvos, INPL Ph.D (1993) Nancy, France.
[13] J.E. Morgan, H.I. Schiff, Can. J. Chem. 42 (1964) 2300
[14] Handbook of Chemistry and Physics, Ed. by CRC Press Inc., 75th edition (1994)
[15] A. Boushehri, J. Bzowski, J. Kestin, E.A. Mason, J. Phys. Chem. Ref. Data 3-16 (1987) 445

Spectroscopic measurements in plasmas with silica ablated walls.

P.Bezborodko, J.Fauconneau.
Laboratoire.Arc.Electique et.Plasmas.Thermiques,
URA 828 CNRS, Université Blaise Pascal, Clermont Ferrand, France.

1.Introduction

The aim of this work is to obtain some experimental values of temperature and electronic density in arcs with ablated wall in silica. Arcs are due to the vaporisation of silver (or copper) fuse elements in silica sand. The main application of this type of study is in the manufacturing of fuses. At the present time, the electrical characteristics of a fuse are essentially determined by its geometry, for instance : the width and the thickness of the element, the section of the striction, the number of strictions, the granulometric composition of the sand. Modelling estimations concerning the prearcing period are well established as they generaly take into account the different ways of heat transfer [1]. On the other hand, phenomena connected with arcs are not well known. Empirical methods are often used to study this part of the phenomenon [2]. Some calculations also can be attempted, but one needs to know the values of the temperature and the conductivity of the arc plasma [3]. So, the question which takes precedence over all others is to know the temperature and electronic density in the arc plasma, which determine then the electrical properties of fuses.
Spectroscopic methods have been previously reported [4] [5], which use metallic lines or use Si lines. Unfortunately in the latter case, filters were used instead of spectrometer recording. We will see that this may induce some errors in temperature estimations.

2.Experimental set up

Fuse elements have an effective length of 36 mm, are 0.105 mm thick, 5 mm wide, 99.99% pure silver (or copper). They have a single row of notches (0.5 mm in diameter) punched in the center of the strip.
To permit spectroscopic measurements, we have used special fuses which are like a half-fuse with a glass wall [6]. On the one side, a 4 mm wide glass wall is put on the fuse element. On the other side, the fuse is filled with silica grains with a mean diameter of 0.4 mm. To obtain arcs in it, a capacitor bank is used, which can release an energy of 2100 J. The test fuse is associated with a 1.5 meter focal length spectroscope with two gratings (600, 2400 grooves/mm). The detector is a Charge Coupled Device array (512x512 pixels). The CCD detector is used in streak mode operation (also called kinetic mode). The light is focused on a limited area of the array (10 or 15 rows high), succesive spectra are acquired and then shifted down to the rest of the array providing a storage area for data. An electronic control gear enables us to visualise the exact timing of spectra acquisitions (as short as 0.1 ms each) associated with the behavior of the current.

3. Experimental results

3.1 Metallic lines measurements

Previous experiments have been carried out with a shorter focal length spectroscope (500 mm), and an exposure time longer (30 ms) than the phenomena. We have seen that only Cu lines at 511 and 515 nm were suitable for our measurements. Morever, it is well known [7] that these lines are not often self-absorbed. The spectra obtained with our existing spectroscope show a high level of continuous ligth which can overshadow lines, and this, particularly during the flow of current (Fig.1). It is interesting to note that this result shows up the weakness of temperature measurements obtained by the way of filters rather than spectroscopic viewing. Nevertheless it is possible to calculate temperatures where metallic lines emerge from the continuous lumen. The ratio of relative lumen intensity of 515.32 and 510.55 nm (respectively Em-En=6.19-3.79 eV, Em-En=3.82-1.39 eV), of Cu is used to calculate plasma temperature. It is seen on Fig.2 that temperatures around 12000K are obtained after the flow of current. We have to note that this method gives us temperature values for the outer layer of the plasma, due to the phenomenon of ionic migration as AgI or CuI particules have a lower ionisation potential than SiI particules. Morever, these lines cannot measure higher temperatures because of their characteristics of emissivity against temperature. To obtain inner layer temperature values we tried to use Si lines.

3.2 Si lines measurements

Numerous viewings of spectral areas where previous authors had observed Si lines have been done. The lines observed in our plasma are reported in Tab.1. To carry out calculations about these lines it is necessary to verify that they are not self-absorbed. Self absorbtion may be due to the reabsorbtion of the cold outer layer of the same element which has a lower electronic density [8]. We verified on SiII multiplets (2) and (4) the ratio between line strenght due to L-S coupling [9]. The results are given on Tab.1. It shows that there is no self-absorbtion for these lines. Subsequent measurements will have to be done with a suitable spectroscope, which will enable us to obtain a temperature estimation of the inner layer of the plasma. We have also studied the profile shape of the SiII lines obtained (fig.3). The lines have a Lorentz profile, which permits us to verify that broadening is due to the Stark

effect. An extrapolation of results obtained by Lesage et al. [10] with a different kind of plasma gives us a value for n_e between 2.5 and 4.10^{17} cm^{-3}.

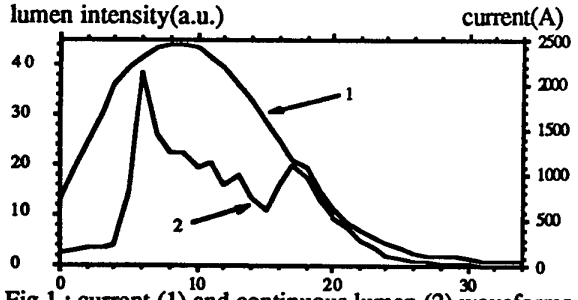

Fig.1 : current (1) and continuous lumen (2) waveforms against time (1 track=0.2ms).

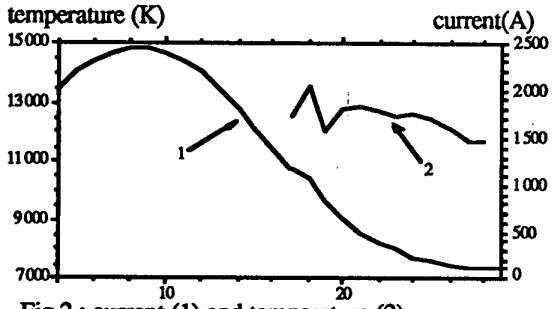

Fig.2 : current (1) and temperature (2) waveforms against time (1 track=0.2ms).

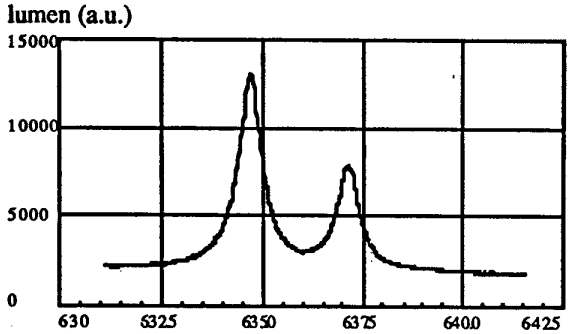

Fig.3: SiII multiplet profile shape at 635.51nm.

Si state	wavelength (nm)	highlevel (eV)	line strength S (u.at)	ratio
II	637.14	10.06	17.7	
II	634.71	10.07	35.3	2 (th)
II (2)	635.51		53	1.9 (exp)
II	597.89	12.14	17	1.9 (th)
II	595.76	12.14	8.7	
II (4)	597.21		26	1.7 (exp)
I	390.55	5.08	1.28	

Tab.1: tabulated characteristics of lines detected in our plasma.

4.Conclusion

The recording of the evolution of spedctra against time has enabled us to see that during the maximum flow of current the light emitted was mainly given by continuous lumen. Any measurements based on luminous intensity of lines should take this into account.

At the present time, it seems that electronic densities between 2.5 and 4.10^{17} cm^{-3} and temperatures higher than 12000K, can be reached in plasma fuses. In such conditions, the attenuation caused by the liquid layer of silica surrounding the plasma [11] of the ligth emitted should be taken into account.

5.References

[1] J.G. Leach, A. Wright : "Analysis of high-rupturing-capacity fuselink prearcing phenomena by a finite difference method", Proc. IEE., vol 125, n°9, sept. 1973, pp 323-327.

[2] K.K. Namitokov, Z.M. Frenkel : "Influence of the constructional features of the fusible element on arc processes in fuses", Elektroteknika, vol. 55, n°9, 1984, pp 59-61.

[3] Z. Frenckel : "The calculation of the parameter of the plasma of the arc in a fuse", Proc. of the fourth ICEFA. Nottingham, UK, 1991, pp 235-240.

[4] L.A.V. Cheim, A.F. Howe : "Spectroscopic observation of high breaking capacity fuse arcs ", IEE Proc.-Sci. Meas. Technol., vol 141, n°2, March 1994, pp 123-128.

[5] T.Chikata, Y. Ueda, Y. Murai, T. Miyamoto : "Spectroscopic observations of arcs in current limiting fuse through sand", Proc. ICEFA Liverpool, UK, 1976, pp 114-132.

[6] P. Bezborodko, J.Fauconneau, R.Pellet : "Experimental set up for spectroscopic measurements of plasma arcs in fuses", Proc. of the fifth ICEFA Ilmenau, Germany, pp 259-264.

[7] S. Vacquié : "L'arc électrique et ses applications", Club EDF Arc Electrique, Ed. CNRS, Tome I, 1984, pp 255-334.

[8] N. Konjevic, W.L. Wiese : "Experimental Stark widths and shifts for non-hydrogenic spectral lines of ionized atoms", J.Phys. Chem. Ref. Data, Vol 5, n°2, 1976, pp 259-308.

[9] W.L. Wiese, M.W. Smith, B.M. Miles : "Atomic transition probalities", NSRDS-NBS (US) 22, vol II, oct.1969.

[10] A. Lesage, B.A. Rathore, I.S. Lakicevic, J. Puric : "Stark widths and shifts at singly ionized silicon spectral lines". Physical Review A, vol 28, n°4, oct. 1983, pp 2264-2268.

[11] G.J. Lindford : "Time-resolved Xenon flash-lamp opacity measurements". Applied Optics, vol 33, n°36, dec.1994, pp 8333-8345.

TALIF and OES measurements for testing the validity of actinometry applied to H-atom density estimation under Diamond Deposition conditions

A. Gicquel[a], M. Chenevier[b], K. Hassouni[a], J. P. Booth[b],

a-Laboratoire d'Ingéniérie des Matériaux et des Hautes Pressions
CNRS-UPR 1311- Université Paris-Nord
Avenue J. B. Clément 93430, Villetaneuse France
b- Laboratoire de spectrométrie Physique
CNRS-URA 008, Université Joseph Fourier de Grenoble
B. P. 87, 38402, Saint Martin d'Hères, Cedex, FRANCE

Abstract
A study concerning the validity of the actinometry method applied to H-atom density measurements is carried out. A theoretical approach and measurements involving Two Photon Allowed Transition (TALIF) and Optical Emission Spectroscopy (OES) are used.

1- Introduction

In low pressure diamond deposition reactors operating in H_2 + CH_4 mixtures, the role of the H atoms is now largely accepted. Measurements of H-atom concentration in volume and at the plasma / surface interface may provide a better control of the diamond deposition reactors. Although laser diagnostics allowing these measurements are available today, their use in industrial environments is unrealistic. On the opposite, OES is well adapted for industrial reactors.
OES can be a very powerful technique for accessing indirectly to ground electronic state species densities and temperatures and then for better understanding the processes occuring in a plasma. However, measurements made by OES have to be used with many cares. OES only provides measurements on species in electronic excited states which participate only in a minor proportion to the plasma or plasma/surface chemistry and which are at concentration level of less than 10^{-4} with respect to species in the electronic ground state. Extracting informations concerning the plasma processes by measuring relative concentrations and temperatures from OES implies first to establish relationships between species in electronic excited states (analyzed by OES) and those in the electronic ground state (the key species for the studied process which can be analyzed by laser diagnostics). Concerning species densities measurements, Coburn and Chen [1] have introduced in the early 80's years the actinometry technique which offers the possibility in reaching relative densities of a ground state species from emission intensities measurements. Actinometry requires the introduction of a gas as an impurity in the feed gas, which constitutes the actinometer. The actinometer compensates changes in the electron density or energy, and then plays a normalisation role for the species emission intensity. If actinometry is valid, then the emission intensities ratio (species over actinometer) is proportional to the relative density of the species in its electronic ground state. The conditions of validity of this technique are restrictive, and have to be carefully analyzed before any use.
We report here a study which aims at drawing the domain of validity of actinometry applied to H-atom density measurements in plasma diamond deposition reactors. Firstly, a theoretical approach is carried out in order to determine some boundary (frontier) conditions for which the validity of actinometry might be critical. Secondly, since this approach only provides an estimation of the frontier, a comparison between axial and radial distributions of relative ground state H-atom densities obtained respectively by TALIF and OES allows us to demonstrate that actinometry is valid for these conditions. Thirdly, calculations, using a 1 D H_2 plasma model, allow us to extend the domain of diamond deposition conditions for which actinometry can be used.

2- Technical description

**Reactor:* The reactor consists in a silica bell jar low pressure chamber, fed with a mixture of 0 - 5 % CH_4 diluted in hydrogen. The plasma is activated by a 2.45 GHz microwave generator. The pressure and power ranges are respectively 800 Pa to 140000 Pa, and 400 to 3000 W. The averaged power density is then varying from 5 W cm^{-3} to 40 W cm^{-3}. The substrate temperature is fixed independently from the plasma parameters at 900 °C. Argon, the actinometer, was introduced at 1 % in the plasma.

* ***OES*** : A Jobin Yvon THR 1000 mounted with a 1800 groves per mm grating, blazed at 450 nm and equiped with a photomultiplier (Hamamatsu R 3896) and a red region intensified OMA III (EGG-Princeton Instrument -1460) was used to measure emission

intensities of H_α (λ= 656.5 nm), and of $2p_1$ --> $1s_2$ argon transition (λ =750.3 nm). The light emitted from the plasma was collected by a optical collimator and transported via a one millimeter in diameter optical fiber to the entrance slit of the monochromator. A spatial resolution of approximately 2 mm is reached. The optical system was mounted on a computer controlled moving table, allowing axial and radial measurements. Abel inversion was used for accessing to radial distributions.

* ***TALIF*** : Two photons allowed transition laser induced fluorescence (TALIF) [2] measurements were conducted in the reactor equiped with two U.V. grade silica windows allowing transmission of 205 nm light. The whole reactor was accurately translated vertically and horizontally with respect to the laser beam in order to obtain axial and radial profiles. Under the experimental conditions, the observed two-photon line profile is Doppler broadening dominated.

3- Results

1- A theoretical approach[3] allowed us to show that for an electron temperature (Te) of 11000 K and a H-atom mole fraction of 4 %, the validity of actinometry is well established. On the opposite, for an electron temperature of 20000 K and a H-atom mole fraction of 4 %, the dissociative excitation mechanism is strongly competing with the direct excitation mechanism for producing H atoms in the n=3 excited state. These latter plasma parameters are reached for conditions where the pressure is 2500 Pa and the power 600 W, the corresponding power density is then 9 W cm^{-3}.

2- As the calculations allowing the estimate of these boundary conditions are only approximated, the second step was to establish experimentally whether or not actinometry is valid under these critical conditions. At 9 W cm^{-3}, a comparison was made between spatial distributions (axial and radial) of H-atom mole fractions provided by OES and those provided by TALIF. The H-atom mole fraction was deduced from OES taking into account for the quenching effects due to collisions of the excited species (H(n=3)) and Ar(2p1)) by molecular and atomic hydrogen in their ground electronic states [3,4,5]. Also, owing to the small H-atom mole fraction (4 %), the variations of Ar-atom mole fraction was neglected. As shown by calculations [6], electron temperature is distributed spatially, leading to spatial variations in the excitation rate constants ratio of Ar atoms and H atoms (k^e_{Ar}/ k^e_H), which should be considered. However, up to date, we were not able to determine with enough accuracy the spatial distributions of Te. As a consequence, the effect of the spatial variation of k^e_{Ar}/ k^e_H could not be still included.

Nevertheless, the comparison of axial and radial distributions of H-atom relative mole fraction obtained by TALIF and OES showed a very good agreement except in the plasma region where Te is varying strongly (at the plasma edges). We can conclude that, at 9 W cm^{-3}, H atoms are directly excited from ground state. This is in agreement with the fact that, under these conditions, H atoms in the n=3 excited state and in ground state were seen to be in thermal equilibrium[2]. Actinometry can then be used at 9 W cm^{-3}.

3- When increasing the power density, calculations [6] showed that Te decreases while the H-atom mole fraction (x_H) increases (owing to thermal effects). As a consequence of our theoretical approach (section 3), the direct excitation of H(n=3) is favoured at higher density. As a conclusion, actinometry can be applied to measurements of H-atom mole fraction under diamond deposition conditions at power densities higher than 9 W cm^{-3}. These conditions are largely used for deposition of diamond. However, an accurate estimation of H-atom density requires the knowledge of the quenching cross sections. However, very little is known concerning cross sections involving collisions with H atoms in ground state. As their contributions increase with the dissociation yield, accurate estimation of H-atom density at high power density will be difficult. When adding methane in the feed gas at up to 5 %, Te and x_H are seen to remain within the same magnitude, and then actinometry is still valid.

Acknowledgement

This work was financially supported by DRET and EC (BRITE EURAM II). Y. Breton is thanked for his contribution in OES measurements.

References

[1] J. W Coburn, M. Chen, J. Appl. Phys. 51 (6) (1980) 3134-36

[2] A. Gicquel, M. Chennevier, Y. Breton, M. Petiau, J. P. Booth, K. Hassouni, Journal de Physique III, Vol 6 (1996) pp 1167-1180

[3] A. Gicquel, M. Chenevier, Kh. Hassouni, Y. Breton, A. Tserepi, in preparation

[4] J. Bittner, K. Kohse-Höinghaus, U. Meier, Th. Just. Chem. Phys. Letters, Vol. 143 n° 6 (1988).

[5] B. L. Prepperneau, K. Pearce, A. Tserepi, E. Wurzberg and T. A. Miller, Chemical Physics (1995);

[6] K. Hassouni, S. Farhat, C. D. Scott, A. Gicquel, Journal de Phys. III, vol 6 (1996) 1229-1243

DETERMINATION OF PLASMA PARAMETERS FROM ION BRANCH OF PROBE CHARACTERISTIC

I.Sh. Abdullin, V.E. Bragin*, A.N. Bykanov*

State Scientific Industry Cooperation «Medinstrument», Tinchurin street 31, Kazan, 420022, Tatarstan

* Moscow Inst. of Physics and Technology, Institutsky per. 9, Dolgoprudny, Moscow reg., 141700, Russia
E-mail: root@mpd.mipt.ru

It is difficult to carry out correct measurements of Langmuir probe Current-Voltage (CV) characteristics over all range of voltage bias in some cases. In relatively dense plasma (for pressure about some torr) this is complicated by significant heating caused by intensive current if probe potential is in the region of electron current. The characteristics can be distorted because of RF current rectification by nonlinear nearprobe sheath in RF discharge. So it is difficult sometimes to measure the plasma potential V_s with respect to base electrode and electron temperature T_e (or electron energy distribution function, EEDF) by traditional methods. Nevertheless the ion current and floating potential can be measured more correctly. The errors of measurements can be estimated [1]. Besides the disturbances introduced by the probe into plasma are very small in the ion current region. The present paper suggests an algorithm for determination the main plasma parameters only from ion-current part of probe characteristic including also floating potential.

One of the most important assumption of main known theories of ion current collection by Langmuir probe is Maxwellian distribution function for electrons. The electron temperature is used in Bohm theory [2] for estimation of ion velocity on the boundary of charged sheath. The later theories (Laframboise [3] and Allen–Boyd–Reynolds (ABR) [4]) are based on solution of Poisson equation. It is assumed in these theories that electron concentration is described by Boltzmann distribution with electron temperature and potential corresponding to electric field of the probe. The Debye length λ_D for nonequilibrium plasma is used for normalization of probe radius R_p and other geometrical parameters. The concept of Debye length is also based on Maxwellian EEDF and existence of electron temperature. If EEDF is not Maxvellian, one cannot use the conception of electron temperature and the mentioned theories of ion current collection become noncorrect. The application of any equivalent of temperature (such as average electron energy) for the cases of non-Maxwellian EEDF demands additional consideration.

The plasma potential V_s can be measured as the point of zero value of probe current second derivative. Electron temperature is defined from the slope of CV characteristic plotted in semi-logarithm axis according to traditional algorithm of probe characteristic analysis. Sometimes the linear part is not very pronounced or there are two or three linear parts on the graph. So the concept "temperature" is not quite correct. Nevertheless the values measured in such way are substituted into normalizing expressions for determination electron concentration n_e from ion part of characteristic on the base of different theories. In the case of ABR theory the single point (for probe potential $V_p = V_s - 15T_e$) is used for evaluating n_e. The results of ABR theory are expressed usually via normalized current for this potential (so called Sonin plot [5]).

The Orbit Motion Limited (OML) theory [6] allows to obtain more useful information from ion current analysis. This theory have no any suggestion about EEDF and gives the next relation for ion current:

$$I_i \approx A_p n_e e \left(\frac{-2e(V_p - V_s)}{\pi^2 M_i} \right)^{1/2} \qquad (1)$$

where A_p is the square of metal part of cylindrical probe contacting with plasma, V_p — probe potential with respect to base electrode, M_i — ion mass. So the graph of ion current plotted in axes $I_p^2 - V_p$ (for high negative potential we can write $I_i \approx I_p$) will represent the straight line for some voltage range. The slope of this line allows to determine n_e and the intersection with voltage axis corresponds to V_s. The electron temperature is defined as usually.

But the OML theory is valid only for rare plasmas. There is limitation on potential distribution within probe sheath and it is assumed that the sheath radius is infinite. For many important cases it is not realized and more adequate theories are to be used.

The ABR theory is considered to be reliable for wide range of plasma parameters. But it does not allow to apply such simple analysis of Current-Voltage dependence as for OML theory because appropriate functions are not so simple. Nevertheless the approximation formula [7] describing ABR

theory for wide range of parameters with good accuracy permits to execute some statistical processing of experimental data. The single assumption of this attempt corresponds to assumption of ABR theory, that is Maxwellian EEDF. If it is not so the statistical analysis will not be correct together with ABR theory.

The essence of analysis is the next. It is chosen sufficient number of experimental points (usually not less than 40-50). These points are to be quite negative with respect to plasma potential for electron component of probe current was negligible. Or it should be taken into account. Then one should chose a set of parameters T_e, n_e and V_s and calculate the discrepancy δ of experimental points and theoretical ABR points for these parameters. The discrepancy is defined as:

$$\delta = \sum_i \left[\frac{I_i^{experim} - I^{theor}(V_i^{experim})}{I_i^{experim}} \right]^2 \qquad (2)$$

The parameters T_e, n_e and V_s are varied for discrepancy minimization. The task is unstable in such form for small perturbations of current and voltage because the curve is described by three dimensional parameters. For degeneration removal some relation between parameters should be established. The most natural relation is the expression for floating potential. It was estimated on the base of ABR theory for ion current and traditional for Maxwellian EEDF exponential dependence of electron current on probe potential. Floating potential depends upon ion mass. Figure 1 represents dimensionless floating potential for two gases of different masses. The usual normalization of parameters is used:

$$\eta_p = \frac{eV_p}{kT_e}; \qquad \xi_p = \frac{R_p}{\lambda_D}, \qquad (3)$$

The approximation of floating potential dependence on probe radius for Ar is the next:

$$|\eta_{fl}| \approx 3.67 + 0.51\gamma - 0.031\gamma^2 - \qquad (4)$$

$$- 0.0041\gamma^3 + 0.0002\gamma^4, \text{ where } \gamma = \ln(\xi_p).$$

The accuracy of this formula is better than 0.5% over all interval of radius variation.

The obtained set of parameters T_e, n_e and V_s thus describes the theoretical curve which is best adjusted to experimental one. In the next step it is possible to use another number of experimental points (for example, increasing previous by unity) or to shift the window of selection and to get another set of parameters. And so on. The most probable values and the trusting intervals can be obtained by averaging.

The testing calculations have shown good agreement of parameters determined by such algorithm with initial values used for modelling probe

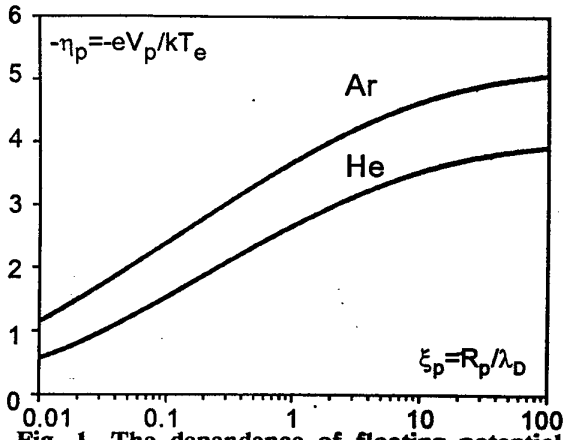

Fig. 1. The dependence of floating potential on probe radius for two gases on the base of ABR –theory

characteristics. An arbitrary noise of 1% amplitude was added to characteristics. The typical error interval was about 2-5%. It can be reduced by narrowing the parameters variation intervals. It is necessary to pay attention for the coincidence of obtained dimensionless parameters to ranges of formulas applicability. The number of points on characteristic should be not less than 100.

The described attempt can be used as independent method for plasma parameters determination if some problems during electron branch measurements occur. And also it can be used to enlarge traditional algorithms of probe characteristics processing and to test the validity of ABR assumptions (in particular, Maxwellian EEDF) in real experiments.

References

[1] I.Sh. Abdullin, V.E. Bragin, A.N. Bykanov: Contributed Papers of ICPIG-XXII **2** (1995) Hoboken, USA 193

[2] D. Bohm: The Characteristics of Electrical Discharges in Magnetic Fields; ed. A. Guthrie, R.K. Wakerling, (1949) New York, Magrow Hill

[3] J.G. Laframboise: Rarefied Gas Dynamics, ed. J.H. De Leenw, **11** №4, (1966) Academic Press, New York, pp 22-42

[4] J.E. Allen, R.L.F. Boyd, P. Reynolds: Proc. Phys. Fluids. B, **2** (1959) 112

[5] J.E. Allen: Plasma Sources Science and Technology **4** (1995) 234

[6] I. Langmuir, H. Mott-Smith: Gen. Elec. Rev., **27** (1924) 449

[7] I.Sh. Abdullin, V.E. Bragin, A.N. Bykanov: Approximation formula for ABR theory of ion current to cylindrical probe (report for ICPIG-XXIII proceedings)

Method of investigation of a conducting column by means of a magnetic diagnosis

F. Gary, G. Velleaud, A. Laurent, M. Mercier, D. Cajal
Université Blaise Pascal de Clermont-Ferrand. Laboratoire d'Electrotechnique de Montluçon.
Av. A. Briand 03107 MONTLUÇON. FRANCE
J. Maftoul,
Groupe Schneider, Centre de Recherches de Grenoble, 38050 GRENOBLE. FRANCE.

1.Introduction [1]

Under certain breaking conditions, in an automatic circuit-breaker, the electric arc first appears in the shape of a diffuse conducting column. It will consequently be noticed that the characteristics of the arc suddenly alter in accordance with the current I. It transforms itself into a concentrated discharge. Then the arc diffuses again. We must therefore change as quickly as possible from the concentrated to the diffuse arc stage in order to obtain high performances.

In this article, we are going to present methods which will allow the determination of the condition of the arc whether concentrated or diffuse. In this study the column material will be a conductor made of solid copper.

2.Experimental device

A copper conductor of predetermined shape is placed between two contacts, and we have to interpret the azimuthal inductions sensed by Hall effect probes positioned around these contacts (figure 1).

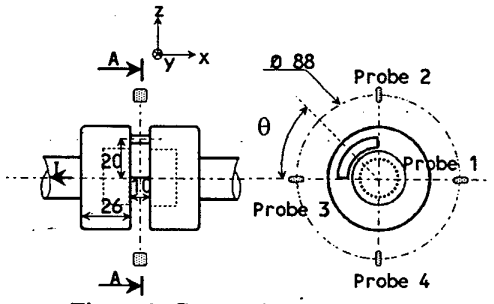

Figure 1. Geometric configuration

The short-circuit current is generated by an L.C. station which is able to deliver currents that can reach 8000 A in 5 ms. Hall effect probes have a sensitiveness of the order of 10 V/T. For reasons of technological imperatives these probes are positioned on a circle, 88 mm in diametre around the contact axis.

3.Characterization of a "bridge" of current

3.1 Size of the "bridge"

Portions of a hollow copper cylinder, 5 mm thick, with a 20 mm curvature radius and aperture angles of 90° and 180° will materialize a "bridge" in the case of a rotating arc. They are 10 mm wide (the distance between the contacts). Once they are welded to the contacts, one can measure the current and the induction by rotating the whole in a discrete manner from 0° to 350° by 10° steps. The average position of the "bridge" will be determined by angle θ with respect to probe 3, taken as a reference. (figure 1).The signals obtained from a specified probe are shown in figure 2. In order not to depend on the variations in current from one test to the next, the induction measured is reduced to the current unit. It will be observed that the wider the aperture angle, the wider and more damped the signal.

When computing the ratio $\frac{\left(\Delta B/I\right)_{max}}{\Delta\theta}$ from these signals in which Δθ is the signal width equal to 50 % of the maximum variation of (B/I), one obtains :

for 90° : 13.10^{-6} mT/A(°)

for 180° : $3{,}2.10^{-6}$ mT/A(°)

The ratio obtained with a cylinder of solid copper, 5 mm in diametre (concentrated arc) is : 30.10^{-6} mT / A(°).

In all cases, $(\Delta B/I)_{max}$ is obtained when the axis corresponding to the average position of the copper "bridge" used faces the reference probe.

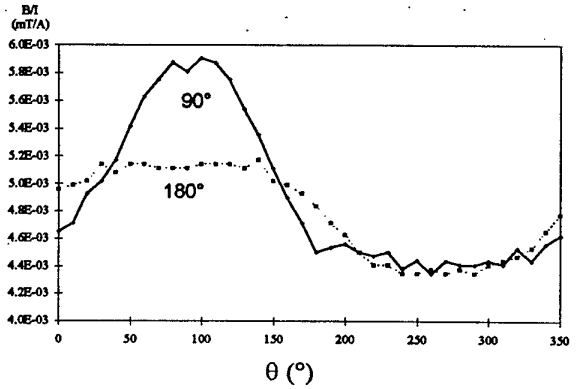

Figure 2 : Induction generated by a "bridge"

We can therefore conclude that the lower the ratio is, the more the "bridge" of current spreads out.

We have noticed that the ratio of the maximum induction over the induction corresponding to the angular value of the size of the copper portion

measured on the curves in figure 2, is 1/3. So, the size of the "bridge" can be obtained by measuring the width of the signal taken at 70 % of the maximal amplitude of the variation. We thus come back to the "bridges" at 90° and 180°.

3.2 Position of the "bridge" on the contacts

The position of the copper cylinder portion in one of the four sectors determined by two probes can be found by adding the two signals delivered by these probes.

4. Characterization of a cylinder of current

4.1 Size

The above method cannot apply in the case of a current flowing throughout the whole cylinder. Indeed the signals obtained with different sizes of cylinder (5 mm, 25 mm) centred 12.5 mm away from the axis of the contacts are quite close. This is the reason why two induction-sensitive probes have been used along x (figure 3).

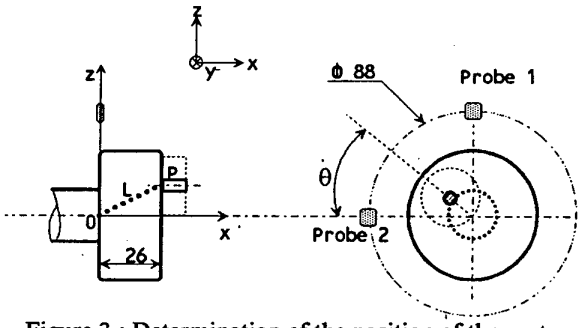

Figure 3 : Determination of the position of the roots

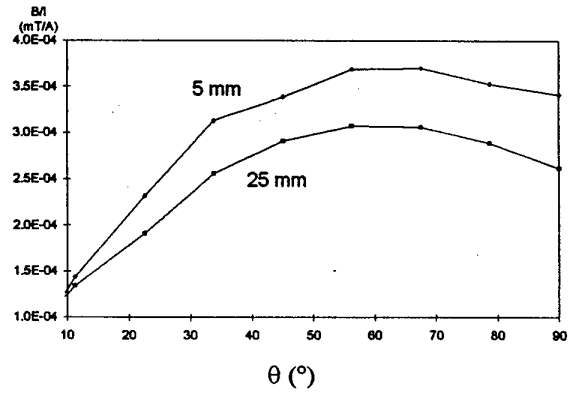

Figure 4 : Induction versus diametre

Along this direction, only the contribution of the threads of current L, situated in the contacts is taken into account. It has been seen that for a single position and a single current the induction generated in the case of a 5 mm diametre cylinder is higher than with a 25 mm one (figure 4). As a consequence the evolution of the diametre can be deduced from the computation of the ratio of these inductions.

4.2. Determination of the position of a cylinder [2]

The position P(xp, yp, zp) of the end of the average line of current representing the cylinder can be determined through data given by two consecutive probes 90° apart. (figure 3).). In order to do so, the length L and the direction cosines k1, k2 and k3 of the current segment inside the contact, will have to be computed. These values will be determined by solving the following system of equations :

$$Bx1 = \frac{10^{-7} \cdot I \cdot k2}{zs1 \cdot \left(1 - k3^2\right)} \cdot \left(\frac{L - k3 \cdot zs1}{\sqrt{L^2 + zs1^2 - 2 \cdot L \cdot k3 \cdot zs1}} + k3 \right)$$

$$Bx2 = \frac{-10^{-7} \cdot I \cdot k3}{ys2 \cdot \left(1 - k2^2\right)} \cdot \left(\frac{L - k2 \cdot ys2}{\sqrt{L^2 + ys2^2 - 2 \cdot L \cdot k2 \cdot ys2}} + k2 \right)$$

$$1 = k1^2 + k2^2 + k3^2$$

$$e = k1 \cdot L$$

where Bx1 and Bx2 are the inductions along the axis Ox measured by each of the two Hall effect probes, I being the current and k1·L the thickness of the contacts. With this method one can determine the position of the centre of the copper cylinder.

5. Conclusion

The results obtained for a "bridge" of current allow us to consider applying it to the case of the rotating arc. The cylinder model needs to be improved to apply to the case of an electric arc.

6. References

[1] Y. Pelenc : « Le point sur les grandes techniques de coupure »
L'arc électrique et ses applications, Editions du C.N.R.S, Tome 2 (1985) p 54 - 60.

[2]M. Mercier,D. Cajal,A. Laurent,G. Velleaud,F. Gary « Evolution of a low-voltage electric arc »
J. Phys. D: Appl. Phys. **29** (1996) 95-98.

ON VALIDATION OF MAGNETIC PROBE MEASUREMENTS IN INDUCTIVE PLASMAS

R. Piejak, V. Godyak and B. Alexandrovich
OSRAM SYLVANIA INC.
71 Cherry Hill Drive, Beverly, MA 01915

The spatial distribution of the time varying magnetic field (dB/dt or B-dot) has been measured in a cylindrical discharge in which the plasma is maintained by a time varying electromagnetic field induced by a planar induction coil located just outside the discharge chamber. Based on B-dot measurements, the magnitude and relative phase of the electric field and the current density in the discharge were determined through Maxwell's equations. Traditionally, such measurements have been made with a B-dot probe enclosed by an cylindrical dielectric envelope to keep the plasma from interacting with the probe. The primary objective of this work is to compare B-dot measurements made using a "traditional" (hereupon referred to as an enclosed probe) B-dot probe with those made using a B-dot probe which is directly immersed in the plasma with no dielectric enclosure (hereupon referred to as an immersed probe). To check the accuracy of the electric field determined from the two B-dot probes, a third probe consisting of a large wire loop is used to independently measure the electric field directly.

Experiment Apparatus and Methods

Experiments were carried out in a cylindrical metal discharge chamber having an inner diameter of 19.8 cm and a height of 10.5 cm with a Pyrex glass bottom plate. A planar (pancake) induction coil, designed to produce a discharge with a high degree of azimuthally symmetry, was located just below the glass plate. An electrostatic shield and an air gap between the glass and the induction coil practically eliminated capacitive coupling between the coil and the plasma. Measurements were made at 6.78 MHz at gas pressures ranging between 1 and 100 mTorr of argon. Discharge power was determined by measuring the power transmitted into the discharge and subtracting matcher and coil losses. All mention of power from hereon refers to power dissipated in the plasma.

The immersed B-dot probe consisted of three bare wire loops, each constructed of 0.15 mm diameter molybdenum and having an OD of 4 mm. The loops were oriented such that one loop measured the radial component of the magnetic field B_r, while the other two loops formed a figure "8" and were positioned to determine dB_z/dr. The enclosed probe measurements were made with two probes with B_r and dB_z/dr components measured separately but inside the same cylindrical tube. All B-dot probe measurements were made at 4 cm (radially) from the axis of the discharge. The large loop probe was made of 0.75 mm diameter nickel wire with an 80 mm OD and located to make measurements at the same radial position as the B-dot probes.

To determine the azimuthal electric field, E_θ, using B-dot probes, the magnitude and phase of $dB_r(z)/dt$ were measured at 0.25 cm intervals along the z-axis between the top plate and the glass (bottom) plate. E_θ was determined from Faraday's Law: **rot E** = $-d\mathbf{B}/dt$ by integrating $dB_r(z)/dt$ along an axial (z) path: $E_\theta = -10^{-8} j\omega \int B_r(z)\, dz$. From the voltage V measured on the large loop probe, E_θ is: $E_\theta = V/2\pi b = -10^{-8} j\omega b^{-1} \int r B_z(r) dr$, where b = 4 cm. The discharge current density was determined from Ampere's law: **rot B** = $\mu_0 \mathbf{J}$ (ignoring displacement current). Thus , the azimuthal current is: $J_\theta = \mu_0^{-1}[dB_r/dz - dB_z/dr]$ where μ_0 is the vacuum permeability.

Before making measurements, both B-dot probes were calibrated at a fixed position near the coil with E_θ measured with the large loop probe. Based on this, as expected, E_θ in vacuum was found to be identical at all z positions for all three probes. The dB_z/dr component from both B-dot probes was calibrated in vacuum by equating **rot B** to zero at one point. Based on this both probes show $J_\theta = 0$ for all z in vacuum ($dB_r/dz = dB_z/dr \neq 0$. All measurements of the magnitude and relative phase of B-dot were made with a vector voltmeter. The phase in all data in this work is taken with respect to E_θ measured in vacuum.

Results and Discussion

The magnitude and the phase of the rf azimuthal electric field and current density distributions (inferred from B-dot probes and loop probe data) is shown in Figs. 1 and 2, respectively. As shown in Fig. 1, the agreement in both relative phase and magnitude between the immersed B-dot probe and the large loop probe is excellent. Although not shown here, excellent agreement

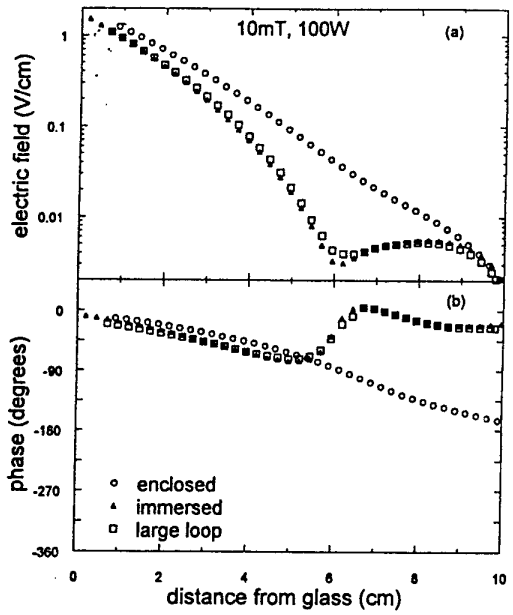

Figure 1

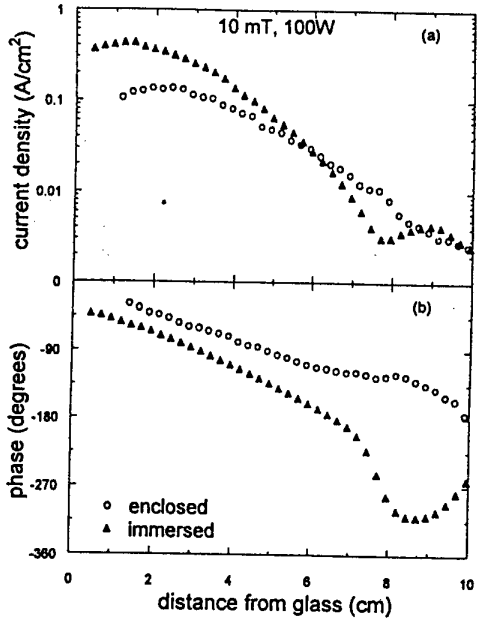

Figure 2

has been observed over a wide range of gas pressure (1 mT - 100mT) and discharge power (up to 200W). Based on this, we can safely say that the electric field determined from the immersed probe appears to be correct. Clearly, however, there is considerable disagreement between the enclosed probe and the immersed probe. The enclosed probe fails to determine the minimum in the electric field that occurs near 6 cm; at this point it predicts an electric field about an order of magnitude larger than actually exists. The agreement in the relative phase between the B-dot probes is equally poor. The immersed probe determines a relative phase shift which makes a transition from lagging to leading while the enclosed probe determines a phase shift lag that simply increases with distance from the coil.

Comparison of the magnitude and relative phase of the plasma current density measured with the immersed and the enclosed probes show essential disagreement. Near the coil, in the skin layer, the current densities from the two probes differ by about four times. The slopes of $|J_\theta(z)|$ are considerably different and the curves cross at about 6 cm from the glass. The immersed probe data suggests a second current layer far from the coil that is oppositely directed to the current in the skin layer (near the coil) while the enclosed probe fails to show this.

Conclusions

Although they agree perfectly in vacuum, E_θ determined with the immersed and the enclosed probe have significant disagreement in a discharge. For E_θ, comparison of the B-dot probes with the large loop shows the error of the enclosed probe. It is believed that these errors arise from perturbation of the plasma current path and density due to the physical presence of the probe enclosure. Apparently perturbations of $B_r(z)$ due to the immersed probe are negligible. Showing validity of the B-dot probes in determining J_θ is not as straight forward as for E_θ since no independent check could be made with the discharge present. However, a case can be made for the validity of the immersed probe since in vacuum it predicts J=0 for all z and, as shown, perturbation of B_r is negligible. Thus, for validity of the immersed probe one need only assume that the perturbation of dB_z/dr is also negligible (as appears likely). Clearly, J_θ determined from the enclosed B-dot probe is in error: First, because J_θ is dependent upon the derivative of B_r whose integral (from E_θ determination) is shown to be in error, and second because no current flows at the precise point within the glass tube where J_θ is being determined. A non-zero J_θ probably due to the loss of azimuthal symmetry introduced by the probe enclosure.

Measurements of the electric field and current density based on enclosed B-dot probes are troubling because the results are quite believable and thus they can be misleading. Based on the evidence given here, previous results based on these probes should be viewed with reservation. Using B-dot probes to determine E-field and current density should be reviewed carefully before relying on such methods.

Spectroscopic temperatures measurements in an Ar-CO_2-N_2 plasma

G. Faure and H. Coitout
Laboratoire Arc Electrique et Plasmas Thermiques U.R.A. 828 CNRS
Université Blaise Pascal
24 avenue des Landais, 63177 Aubière cedex France.

Introduction

Most plasmas present a disequilibrium between the electronic temperature and the temperatures of heavy particles. This disequilibrium is one of the fundamental parameters in the calculations of plasma composition.[1]
Rotational and vibrational temperatures are measured in a gas discharge by optical emission spectroscopy. The discharge is produced in a N_2 -CO_2 mixture with inert gas Ar.
The Boltzmann plot is not applicable in a lot of spectra (the Swan system of C_2 ($\Delta v=0$) nor in the violet system of CN ($\Delta v=0$)) due to the overlapping of the rotational lines. Consequently we used the calculated spectra to determine these parameters.
The measurement of rotational and vibration temperatures is based on the comparison of one experiment ro-vibrational spectrum with the spectra calculated for different temperatures.

Experiment

The wall stabilised arc is produced in a modified Maecker chamber which is made of hollow copper cupels cooled with water. Bakelite cupels provide electric isolation between copper cupels, and tangential injection to the arc column of CO_2-N_2 mixture. The anode and the cathode are in tungsten and are protected with argon. The current discharge is 30 A. The proportion of gas is 75.1 % Ar, 10.2 % CO_2 and 14.7 % N_2. With this mixture, the tension is equal to 49 V. The light emitted is observed perpendicularly to the arc column and is analysed with a high resolution monochromator (THR 1500 Jobin Yvon, focal length 1.5 m, grating 2400 grooves per mm) which is coupled to an optical multichannel analyser (O.M.A. 4000 EGG, matrix of 512×512 pixels). To reduce the dark current the detector was cooled to a temperature of −70 °C. The detector is efficient for wavelengths ranging from 320 nm to 800 nm. Figure 1 presents a spectrum of the violet system of CN with an entrance slit equal to 80 µm. We also observe C_2 (Swan system) and N_2^+ (first negative system) spectra.

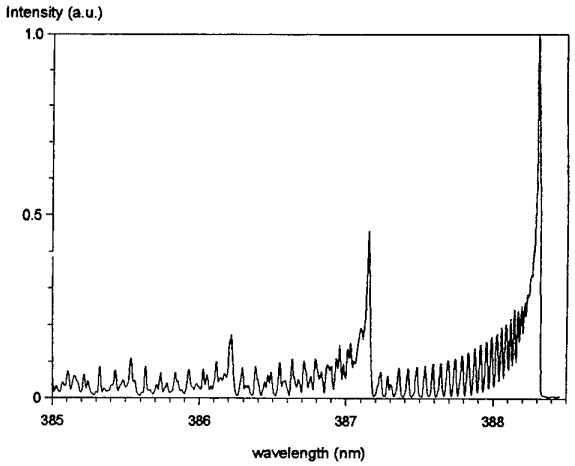

Figure 1 : Violet system of CN ($B^2\Sigma^+ \rightarrow X^2\Sigma^+$) ($\Delta v=0$) in the extremity of the arc. I=30A, V=49V, entrance slit=80µm.

Determination of temperatures

To determine the rotational and vibrational temperatures we calculated the spectra for different values of these parameters. First we calculated wavelength of each rotational line [2], its intensity which is proportional, among others, to the Holn-London factors [3], band strengths [4], the density of particules in the upper electronic level, the rotational temperature and the vibrational temperature. We supposed the excitation of the upper electronic level caused by electron impact. We applied a Gaussian profile (the full width at half maximum FWHM is determined experimentally) for each line and after the spectrum has convoluated. We repeated this for each band and added them to obtain the final spectrum for a given temperature of rotation and for a given vibrational temperature. Figures 2, 3, 4 and 5 present the spectra calculated for different temperatures of rotation and vibration.

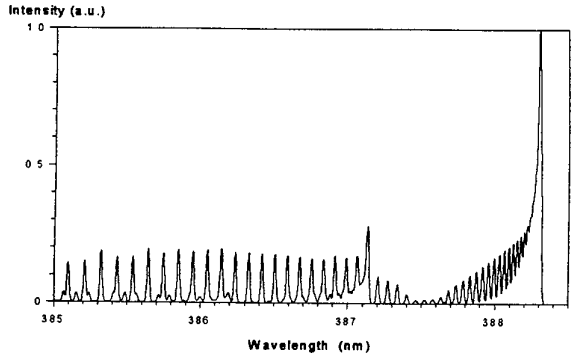

Figure 2 : Violet system of CN ($\Delta v=0$) ; T_{ROT} = 2000 K T_{VIB} = 2000 K ; FWHM = 0.018 nm.

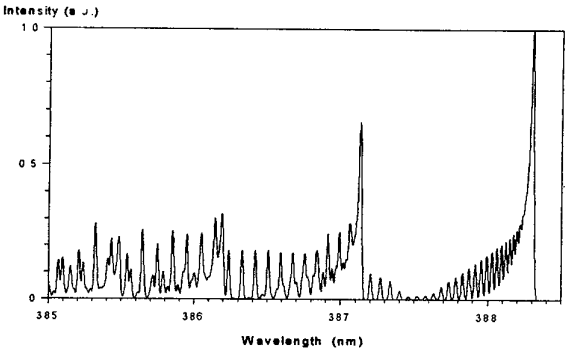

Figure 3 : Violet system of CN ($\Delta v=0$) ; T_{ROT} = 2000 K T_{VIB} = 8000 K; FWHM = 0.018 nm.

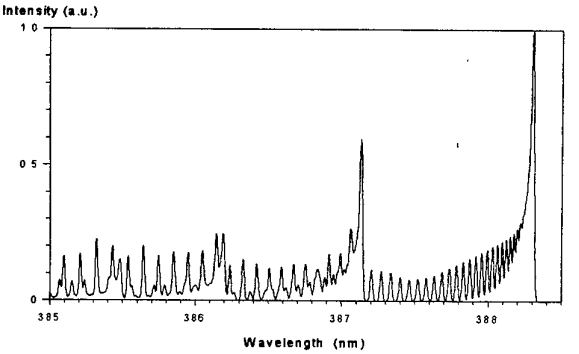

Figure 4 : Violet system of CN ($\Delta v=0$) ; T_{ROT} = 5000 K T_{VIB}= 5000 K; FWHM = 0.018 nm.

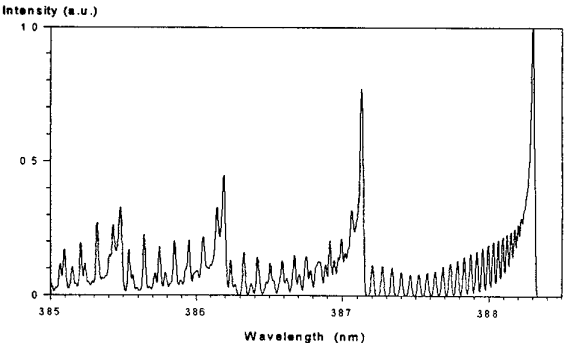

Figure 5 : Violet system of CN ($\Delta v=0$) ; T_{ROT} = 5000 K T_{VIB} = 10000 K; FWHM = 0.018 nm.

First we determine the rotational temperature with band (0-0), before band (1-1) overlaps band (0-0). We chose a few characteristic peaks which were not perturbed and we calculated the sum of the square of the difference between the intensity calculated and the intensity of experimental spectrum. This sum is a function of the rotational temperature and when this sum is minimum we obtain the rotational temperature. Once the rotational temperature is obtained we can estimate the vibrational temperature. We compared the spectra calculated with the result of the rotational temperature and the experimental spectra. The result of vibrational temperature is obtained when the superposition is the better.

Results

This method to determine the rotational and vibrational temperatures is applied on the violet system of CN. At the end of the arc we find that T_{ROT} = 5600 K from the spectrum of CN in Figure 1. The rotational temperature is almost constant for the whole of the plasma radius. As far as the vibrational temperature is concerned, we can estimate that $T_{VIB} \approx T_{ROT}$.

References

[1] P. Andre, IEEE Transactions of plasma science, **23**, 3 (1995) 453.
[2] Huber, K.P., Herzberg, G., Molecular spectra and molecular structure T4, Constants of diatomic molecules, Van Nostrand Reinhold, New York, 1979
[3] Kovacs, Rotational structure in the spectra of diatomic molecules. Adam Hilger LTD - London 1969.
[4] L.L. Danylewych, R.W. Nicholls, Proc. R. Soc. Lond. A. 360, (1978), 557-573

LIF MEASUREMENT OF $N_2(A^3\Sigma_u^+, v = 4)$ POPULATION DENSITY IN A PULSED RF DISCHARGE

S. De Benedictis, G. Dilecce and M. Simek#

Centro di studio per la Chimica dei Plasmi - CNR
c/o Dipartimento di Chimica Università di Bari, via Orabona, 4 - 70126 Bari - Italy
Institute of Plasma Physics, ASCR Za Slovankou 3, 18200 Prague 8, Czech Republic

1. Introduction

Time resolved plasma diagnostics (induced emission spectroscopy, laser spectroscopy, Langmuir probe), now at disposal in many laboratories, favour a renewed interest in the study of microscopic kinetics in pulsed discharges [1]. The kinetics of excited species as well as of radicals and non emitting species can be directly monitored in the time domain. In N_2 pulsed discharge particular attention has been devoted to $N_2(A^3\Sigma_u^+)$ metastable kinetics because of its key role in the coupling of neighbouring electronic states B, W. In this context one step is the measurement of population density of each vibrational level of $N_2(A^3\Sigma_u^+)$. Various approaches have been employed to this purpose like N_2(FPS) absorption (actually by diode laser), N_2(V.K.) emission, and Laser Induced Fluorescence (LIF). We have recently used LIF methods for measuring relative vibrational distribution of $N_2(A^3\Sigma_u^+, v)$ [2]. In this work we have employed LIF technique for measuring the population density of v=4 level by an appropriate single excitation - detection LIF experiment [3] in order to extend this data for inferring the absolute density of N_2(A,v) states.

2. Experimental

The discharge is a typical parallel plates, capacitively coupled configuration, with 10 cm id. electrodes spaced by 5.5 cm. The 27 MHz rf excitation is fully modulated by a 100 Hz square pulse.

The laser beam, produced by Nd-YAG, pumped dye laser with Rhodamine 610, is sent into the plasma chamber at the middle of the gap. The laser firing is synchronised to the discharge pulse under computer control. The laser induced fluorescence volume is focused (1:1 optics) and rotated by 90° by a Dove prism to match the entrance slit of a 1 m fl monochromator. The fluorescence light is revealed by a fast side-on photomultiplier, and measured by both photon counter and boxcar. The phototube is gated to avoid the saturation due to the high discharge background light. In order to further minimise the contribution of the FPS background radiation, the measurement has been carried out at 200 μs in the post discharge where the background emission is greatly reduced with respect to LIF signal.

Single line excitation-detection LIF experiment has been carried out on the transition:

$$(A^3\Sigma_u^+, v = 4, J) + h\nu_L \rightarrow (B^3\Pi_g, v'=8, J')$$

$$(B^3\Pi_g, v'=8, J') \rightarrow (A^3\Sigma_u^+ v''=5, J'') + h\nu_B$$

of First Positive System as discussed in [4]. In particular, we have excited one almost isolated rotational line of P_{12} branch that, although weaker than P_{11} branch (generally used in our previous experiments [1,2, 3]), has very little overlap with other branches and a larger rotational spacing. This is particular important for density measurement experiment because the contemporary excitation of several lines makes difficult the quantitative analysis of the results. The energy of laser beam has been reduced to about 2 mJ by inserting neutral filters in the laser path. This allows to operate measurements under almost linear excitation regime [4] as well as to minimise the excitation of lines by the 0.2 cm^{-1} laser line wings

3. Results

3.1 Spectroscopy

In fig. 1 it is shown an excitation spectra obtained at 0.1 Torr N_2 discharge by scanning the laser in the region 596.5-597.0 nm of P_{12} branch of (8,4) band with detection toned to the Q_{11}(J=8) line of (8,5) band at λ_B = 645.96 nm with a spectral window of 0.08 nm. The detection gate is 1 μs. The strong excitation line at 596.786 nm corresponds to $P_{12}(9)$ line exciting $^3\Pi_{0e}$, J=8 level that directly fluoresces through $Q_{11}(8)$. The weak lines at 596.84 nm correspond to $Q_{13}(8)$ and the line at 596.87 nm has not been assigned. However, the *e-f* propensity rule can be overcome by collisions then increasing the number of possible emissions. This can be seen on the fluorescence spectrum shown in Fig. 2, obtained tuning the laser on $P_{12}(9)$ line and scanning the monochromator in the range 645.5 - 648.1 nm. In this case it is observed that together with $Q_{11}(8)$ line, also additional lines of minor intensity. In

particular $P_{11}(9)$ comes out by *e-f* collisional rearrangement.

3.2 Absolute density measurement

Since the predominant excitation and emission is on $P_{12}(9)$ and $Q_{11}(8)$ lines we have chosen this two lines for the $N_2(A,4)$ absolute population measurement $Q_{11}(8)$ has been detected with a spectral window 0.08 nm. The measurement of the LIF intensity integrated in a τ = 100 ns gate has been made both by photon counter and by boxcar. The result has then been converted in number of photons per second incident to the photocathode by the known radiant sensitivity (or quantum efficiency) of the photomultiplier. The two instruments give the same result indicating the correctness of the photon counting method. This LIF intensity is then used to calculate the density of the metastable roto-vibrational state, N_{AvJ}, through the following relations:

$$I_{LIF}^{v'J',vJ} = N_{Bv'J'} F A_{vJ}^{v'J'} \int_0^{\tau} Q_{v'J'}(t)dt$$

$$N_{AvJ} = \frac{N_{Bv'J'}}{K_P^{vJ,v'J'}} \qquad F = V_s T_r \Omega / 4\pi$$

where:

V_s is the sampled volume, determined by the slit width and the photocatode dimensions; T_r is the optical transmission of the whole path of the fluorescence through windows, lenses, Dove prism and monochromator; $\Omega/4\pi$ is the sampled solid angle fraction; $A_{vJ}^{v'J'}$ is the Einstein coefficient of the transition; $Q_{v'J'}(t)$ is the quenching function of the laser excited roto-vibrational B state. This function has been measured by time-resolved photon counting; $K_P^{vJ,v'J'}$ is the fraction of A molecules pumped by the laser to the B state. This number depends on the saturation of the transition that, in our case of spatially non-homogeneous laser beam, cannot be calculated a priori. We therefore adopt the following semi – empirical procedure:

- We measure the saturation characteristics of the transition varying the laser intensity by neutral filters.
- Then we use a rate equation model analogous to an atomic case [5] (since we are in a line-to-line case) in which the laser pumping rate, and its spatial distribution, is a parameter that is adjusted to fit the measured saturation features. The $K_P^{vJ,v'J'}$ value is then easily extracted from the model. Since no polarisation of the fluorescence light has been observed, we assume that the emitting dipoles achieve an isotropic orientation distribution in a very short time compared to the observation time window.

Finally, the population of the $N_2(A,v)$ state is determined from the population of the single rotational level

$$N_{Av} \cong 35\, N_{AvJ}$$

in which the population ratio is calculated supposing Boltzmann rotational distribution at T_{rot} = 350 K. Specialisation to our case yields:

v = 4 , J = 9 and v' = 8 , J' = 8

N_{AvJ} = 2.6×10^{8} cm^{-3} $\qquad$ N_{Av} = 9.1×10^{9} cm^{-3}

4. Acknowledgements

This work has been partially supported by the Italian Space Agency (ASI). M. Simek undertook this work with the support of the " ITCP Programme for Training and Research in Italian Laboratories, Trieste, Italy".

5. References

[1] S. De Benedictis and G. Dilecce, *J. Phys III*, **6** (1996) 1189, and refs. therein.
[2] S. De Bendictis G. Dilecce, *sub. for pub* (1997)
[3] S. De Benedictis, G. Dilecce, M. Simek, *Chem. Phys.* **178** (1993) 547.
[4] M. Simek, G. Dilecce and S. De Benedictis, *Plasma Chem. Plasma Process.* **15** (1995) 427.
[5] S. De Benedictis and G. Dilecce, *J. Phys. D: Appl. Phys.* **28** (1995) 2067

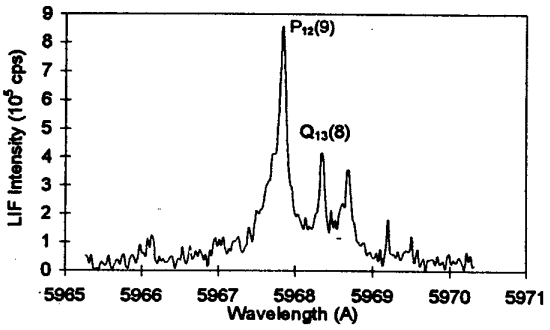

Fig.1 Laser excitation spectrum at $Q_{11}(8)$ line detection

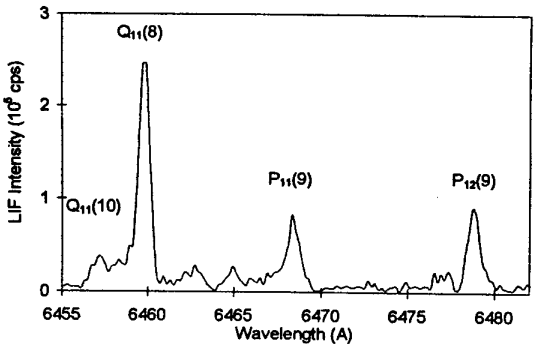

Fig. 2 Fluorescence spectrum with laser tuned on $P_{12}(9)$ line

Stark Profiles of Hydrogen Spectral Lines in Electric Fields of Plasma Turbulence

V. P. Gavrilenko
Center for Surface and Vacuum Research, Andreevskaja nab. 2, 117334 Moscow, Russia

Oscillating electric fields (OEF) play a decisive role im many physical processes in a plasma. The presence of OEF in a plasma is a feature of a host of experiments, including, e.g., the action of a powerful laser or microwave radiation and of electron or ion beam, reconnection of magnetic fields and passage of strong currents. One of the most commonly used methods for diagnostics of OEF in a plasma is spectroscopic method based on the modification of the emission spectra of atomic hydrogen under the influence of OEF. Calculations reported in [1] deal with the intensities of satellites of spectral lines of hydrogen atoms interacting with linearly polarized harmonic electric field of the form

$$\vec{E}(t) = \vec{E}_0 \cos(\omega t + \phi). \qquad (1)$$

These satellites appear at frequencies $\Delta\omega = \pm\omega$, $\pm 2\omega, \ldots$ measured relative to the unperturbed position of the spectral line. The phase ϕ is assumed to be fixed in (1). In [2] was calculated the modification of one Stark component of a hydrogen spectral line under the influence of linearly polarized stochastic oscillating electric field $\vec{E}(t)$ which is assumed to be a sample of a Gaussian process. The consideration in [2] was restricted to the case where $\vec{E}(t)$ is a quasimonochromatic field with the fix frequency ω_0. It was obtained in [2] that each Stark spectral component of hydrogen splits into a set of satellites. The total spectrum of these satellites is described by the expression

$$S(\Delta\omega) = \exp(-\kappa) \sum_{p=-\infty}^{+\infty} I_p(\kappa)\, \delta(\Delta\omega - p\omega), \qquad \kappa(\gamma < E^2 >^{1/2} /\omega_0)^2, \qquad (2)$$

where $I_p(\kappa)$ is the Bessel function, γ is the Stark constant, and $< E^2 >^{1/2}$ is the R.M.S. of the field. The profile of the envelope of $S(\Delta\omega)$ in the multisatellite case ($\kappa \gg 1$) is Gaussian

$$S_G(\Delta\omega) = \exp[-\Delta\omega^2/(2\gamma^2 < E^2 >)]. \qquad (3)$$

However, for a turbulent plasma the typical situation is that the OEF of plasma turbulence is a superposition of a large number of independent harmonics with random phases ϕ_j and different frequencies ω_j:

$$\vec{E}(t) = \sum_{j=1}^{N} \vec{E}_j \cos(\omega_j t + \phi_j), \quad N \to \infty. \qquad (4)$$

In the present work we consider the modification of spectral line profiles of hydrogen under the action of the field $\vec{E}(t)$ (4). Similar to [2] we assume that vectors $\vec{E}_j$ in (4) are parallel to each other, and thus, the field $\vec{E}(t)$ (2) is linearly polarized. In contrast with the work [2] in the present work the relation between ν and ω_0 can be arbitrary. In accordance with the central limit theorem the electric field $\vec{E}(t)$ (4) is a stochastic Gaussian process.

Let the field $\vec{E}(t)$ be a stationary Gaussian process with the correlation function

$$\vec{E}(t)\vec{E}(t+\tau) = B \cdot G(\tau). \qquad (5)$$

Here $\{\ldots\}_{av}$ means averaging, $B = \{E^2\}_{av}$ is the mean intensity of the stochastic field $\vec{E}(t)$, and the correlation coefficient $G(\tau)$ describes the time behaviour of the correlation function [G(0)=1].

The result of the calculation of the emission spectrum $S(\Delta\omega)$ of a hydrogen atom for the transition $a \to b$ in the "Gaussian" field $\vec{E}(t)$ is the following:

$$S(\Delta\omega) = \pi^{-1} \sum_{\alpha\in a, \beta\in b} Re \int_0^\infty \exp(-i\Delta\omega\tau)\Phi_{\alpha\beta}(\tau)d\tau,$$
$$\Phi_{\alpha\beta}(\tau) = |< \varphi_\alpha|\vec{r}\cdot\vec{e}|\varphi_\beta >|^2 P_{\alpha\beta}(\tau),$$
$$P_{\alpha\beta}(\tau) = \exp[-\gamma_{\alpha\beta}^2 B \int_0^\tau (\tau - t)\, G(t)\, dt], \quad \tau \geq 0. \qquad (6)$$

In (6) φ_α and φ_β are "parabolic" wave functions of the hydrogen atom, $\vec{e}$ is the unit vector of the photons emitted, and $\gamma_{\alpha\beta}$ is the Stark constant: $\gamma_{\alpha\beta} =< \varphi_\alpha|z|\varphi_\alpha > - < \varphi_\beta|z|\varphi_\beta >$ (the axis $z \parallel \vec{E}(t)$). We use the atomic units $\hbar = m_e = e = 1$.

The calculations were performed for the model in which the field $\vec{E}(t)$ represents a band noise with Lorentzian spectrum. For such model the correlation coefficient can be represented in the form

$$G(\tau) = exp(-\nu|\tau|)\cos(\omega_0\tau). \qquad (7)$$

The value 2ν is the halfwidth of the spectrum corresponding to the function $G(\tau)$. Substituting (7) in (6) we obtain

$$P_{\alpha\beta}(\tau) = \exp\{-\gamma_{\alpha\beta}^2 B\{[(\nu^2 - \omega_0^2)\cos(\omega_0\tau) - 2\nu\omega_0 \sin(\omega_0\tau)]\exp(-\nu\tau) + \nu\tau(\omega_0^2 + \nu^2) + \omega_0^2 - \nu^2\}(\omega_0^2 + \nu^2)^{-2}\}. \qquad (8)$$

In the case when $\nu/\omega_0 \to 0$ the result of [2] can be derived from (8):

$$P_{\alpha\beta} = \exp\{-(\gamma_{\alpha\beta}^2 B/\omega_0^2)[1 - \cos(\omega_0\tau)]\}$$

From (8) it follows that for $\nu/\omega_0 \ll 1$ each satellite in the spectrum (2) excepting a few satellites near $\Delta\omega = 0$ has a Lorentzian profile with the halfwidth $\Delta\omega_{1/2} = 4\nu\gamma_{\alpha\beta}^2 B/\omega_0^2$. In the case $\Delta_{1/2} > \omega_0$ the profiles of satellites are overlapping, and the resultant profile is described by the Gaussian function coinciding with (3). Now let us assume that the following conditions are valid

$$\nu/\omega_0 \gtrsim 1, \quad \gamma_{\alpha\beta}^2 B/\omega_0^2 \gg 1, \quad \gamma_{\alpha\beta}^2 B/\nu^2 \gg 1. \quad (9)$$

Under these conditions the profile of the spectral component is also Gaussian. A simple result can be also derived from (8) for the case

$$\gamma_{\alpha\beta}^2 B/(\omega_0^2 + \nu^2) \ll 1. \quad (10)$$

Under the condition (10) the profile of the spectral component is Lorentzian with the halfwidth $2\gamma_{\alpha\beta}^2 B\nu/(\omega_0^2 + \nu^2)$. Figs.1,2 show the spectrum of hydrogen spectral line H_δ with the polarization parallel to the vector $\vec{E}(t)$ (Fig.1) and orthogonal to the vector $\vec{E}(t)$ (Fig.2). Let γ_1 and γ_2 be mean Stark constants for a hydrogen spectral line with polarizations parallel $\vec{E}(t)$ and orthogonal $\vec{E}(t)$ respectively. Then $\gamma_2 < \gamma_1$. For the line H_δ the satellites are visible clearly for the polarization orthogonal to the field $\vec{E}(t)$ (cf. Fig.2). The disappearance of the most of satellites in Fig.1 (excepting a few satellites near the center of the line H_δ) is due to the fact that the formally calculated halfwidths of such satellites are greater than the separation between them ω_0.

The results of the present work give an opportunity to determine simultaneously two parameters of the turbulent electric field $\vec{E}(t)$ in a plasma: the R.M.S. strength $B^{1/2}$ and the spectral width ν. For this it is necessary to record spectral line profiles of hydrogen with two polarizations: parallel to the vector $\vec{E}(t)$ (the profile $S_1(\Delta\omega)$) and perpendicular to the vector $\vec{E}(t)$ (the profile $S_2(\Delta\omega)$). The profiles $S_1(\Delta\omega)$ and $S_2(\Delta\omega)$ may differ from each other not only in their halfwidths, but also qualitatively (as is shown, e.g., in Figs.1,2). Let us assume that the frequency ω_0 is known beforhand (or is measured by using the separation between satellites of a hydrogen spectral line). Then the values $B^{1/2}$ and ν may be obtained by comparing the experimental profiles $S_1(\Delta\omega)$ and $S_2(\Delta\omega)$ with a set of the theoretical profiles calculated for different values of B and ν by using the formulas (6), (8).

This work was supported by the Alexander von Humboldt Foundation, which sponsored the author's research stay at the Institute of Experimental Physics II of the Ruhr University at Bochum, Germany. The author is grateful to Professor H. Schlüter for his hospitality.

[1] D. I. Blochinzew: Phys. Z. Sowjet., **4** (1933) 601.
[2] E. V. Lifshitz: Sov. Phys. JETP, **26** (1968) 570.

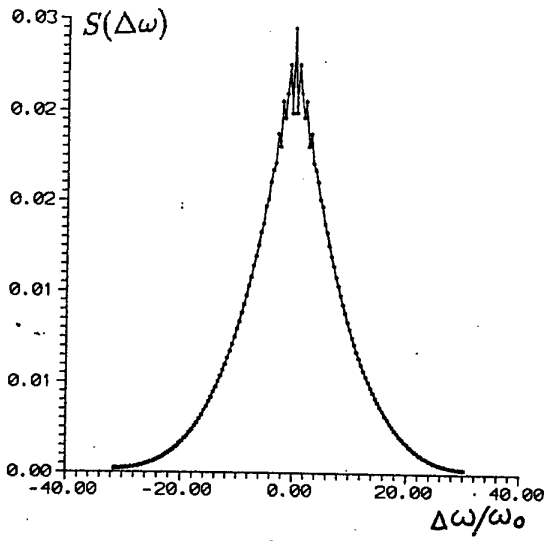

Fig.1

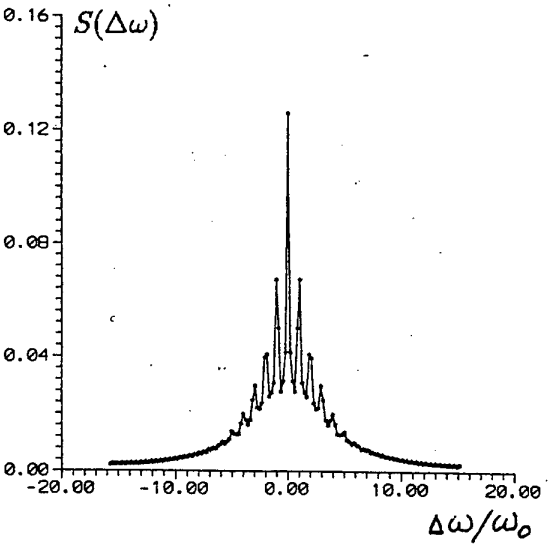

Fig.2

The analytic model for ion-dynamic effects in Stark-broadening theory of hydrogenic emitters.

I.O.Golosnoy
Institute for Mathematical Modeling, Miusskaya sq. 4-A, Moscow 125047, Russia
E-mail: golosnoy@imamod.msk.su

1. Introduction

The problem of calculating optical properties of hot, dense plasmas (the shape and intensity of spectra lines, the opacity) and Stark-broadening diagnostics of these plasmas arise in various physical experiments and technical processes and in astrophysics. The computation of the line shapes is an important task in this problem, because of the profiles of spectra lines, broadened mostly by Stark effects from electric microfield of plasma, have been long used for determining electron and ion densities and for calculating photoemission and photoabsorption by hot matter.

Plasma broadening of spectra lines arises from interaction of the radiator with electric microfield both electrons and ions of plasma. It is assumed to distinguish two types of electric fields, a high-frequency field of electrons and low-frequency field of shielded ions. It is now customary to treat the electrons with an impact theory and to obtained the ions contribution by quasistatic approximation. This assumptions allow to describe the far wings of spectra lines. However, the motion of ions can produce significant discrepancy near line center. The experiment [1] have shown that this ion-dynamic effects can change the halfwidth of the lines with unshifted components, such as $Ly_{\alpha,\gamma}$, $H_{\alpha,\gamma}$, by a factor of 2 or more with respect to quasistatic approximation for ions. Computer simulations [2] were performed to study the effects of ion dynamics on spectra line shape of charged hydrogenic emitters. It was shown [2] that considerably large effects due to ion motion are observed near the line center at this case.

It was shown in [3] that the main factor of broadening near the line center is the rotation of the ionic microfield. The perturbation theory was used for calculations of the corrections on thermal motion of ions [3,4]. That is why this corrections are suitable for the low temperature plasma only, when they are small. The influence of ions motion on the line broadening in hot plasma is so hard that the perturbation theory is not suitable. The difficult model [5] was constructed for this case. In spite of its difficult, this model gives rather accurate results only for Ly_α lines. For more complicated lines, such as Ly_β its accuracy falls off.

Often the models mentioned above not suitable for practical applications, because the simple, suitable for large scale numerical calculations, applied at wide rang of temperature and densities models are needed for plasma diagnostics and opacity calculations.

2. The model of ion-dynamic broadening

The new universal analytic semiempirical model of ion-dynamic broadening for all intermediate region between the impact limit and the perturbation theory corrections to the static approximation of ion broadening was obtained. This model was constructed by to steps:
1) Simple physical model was used for extracting the general functional relation between the broadening and the plasma temperature and density. We used the one-particle approach [6] for determining this relation. The line profile is reduced to quadratures with special functions at this case. The analytic approximation for this quadratures have been constructed. This model gives only the general proportions between the line halfwidth and the plasma conditions. So we have to determine the coefficient of this proportion, which due to many-particle effects in plasma.
2) The analytic approximation for this coefficient which connected the impact and quasistatic limits was constructed. The single free parameter at this model was selected to provide the best agreement of the results obtained with the experiment [1] or with calculations of the lines shape by molecular dynamic (MD) method [2].

3. Results

We tested our model to compare our results with experiments in hydrogen [1] at T~10^4(K), N_e~10^{18}(cm^{-3}) and with MD calculations [2,7] for hydrogen at the same conditions and for Al^{+12}, Ar^{+17}

at T~10^6(K), N_e~10^{22}(cm^{-3}). In spite of the very

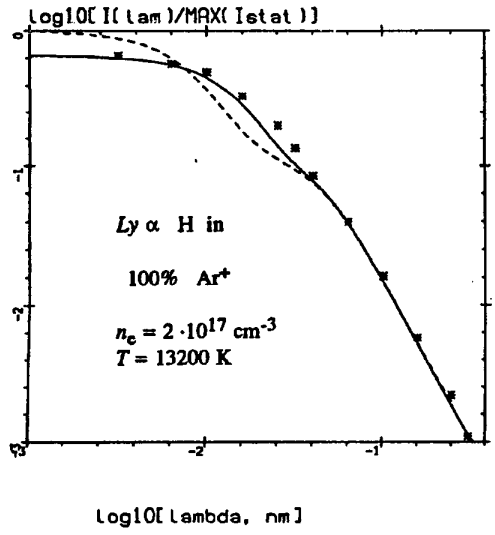

Fig.1. Comparison of measured (*, *, *) and calculated: the present model (——), static ions (– – –), Ly_α hydrogen Stark profiles. The intensity of the line calculated by the static model for ions is equal to 1 for $\Delta\lambda$=0. We use log-log coordinates for more detailed comparison as the line center as the far wings of the line.

different plasma conditions at this cases our model gave good accuracy (Fig.1,2,3). Emphasize that the quasistatic model is rather well for a far wings of spectral line (Fig.1,3), but there are significant deviations between this model and experiment or MD results near the line center. As opposed to this result, the model, presented here, describe well as the line center as the far wings of the line.

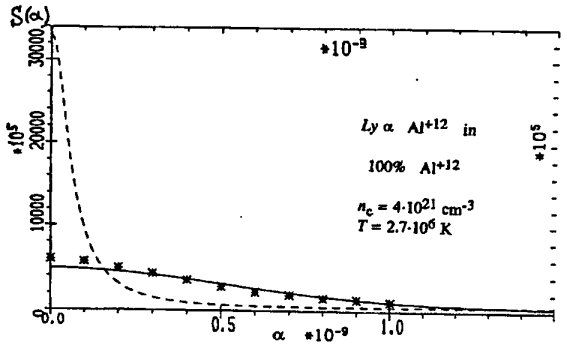

Fig.2. Ly_α spectral line of Al^{+12} for the present model (——), MD (*, *, *) and static ions (– – –); $\alpha=\Delta\lambda/E_0$, $E_0=e/R^2$, $(4\pi/3)N_eR^3=1$.

Also we tested the variation of the line profile with changing the reduced mass of radiator–perturbing-ion pair. It was founded in experiment [8] that the ratio I_D/I_H of the profiles Ly_α of D in Ar^+ and H in Ar^+ respectively, at the line center is equal to 1.17 for T=15500(K), N_e=$2 \cdot 10^{17}$(cm^{-3}). The proposed model give the close result (1.18) for this conditions. So the discrepancy is less than 1%.

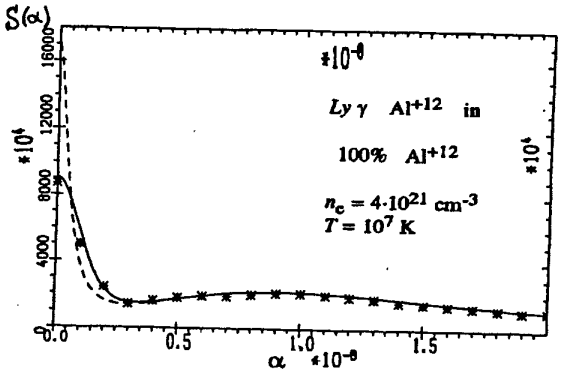

Fig.3. Ly_γ spectral line of Al^{+12}. The markings are the same as Fig.2.

4. References

[1] K.Gruntzmacher, B.Wende: *Phys.Rev.A*, **16** (1977) 243.

[2] R.Stamm, B.Talin, E.L.Pollock, C.A.Iglesias: *Phys. Rev. A*, **34** (1986) 4144.

[3] A.V.Demura, V.S.Lisitsa, G.V.Sholin: *Zh. Eksp. Teor. Fiz. (in Russia)*, **73** (1977) 400.

[4] R.Gauble, H.R.Griem: *Phys. Rev. A*, **27** (1983) 3187.

[5] D.B.Boercker, C.A.Iglesias, J.W.Dufty: *Phys. Rev. A*, **36** (1987) 2254.

[6] V.S.Lisitsa, G.V.Sholin: *Zh. Eksp. Teor. Fiz. (in Russia)*, **64** (1973) 2097.

[7] R.Stamm, E.W.Smith, B.Talin: *Phys. Rev. A*, **30** (1984) 2039.

[8] M.Geisler, K.Gruntzmacher, B.Wende: in *Spectral Line Shapes II*, ed. by Burnett (1983) 37.

Measurement of Particle Densities in Ar-Hg Discharge Plasma Used for Liquid Crystal Display Backlighting

Miki GOTO, Kiyoshi OHTANI and Toshihiko ARAI
Department of Electrical and Electronic Engineering, Kanagawa Institute of Technology, 1030 Shimo-Ogino, Atsugi 243-02, Japan

1. Introduction

The positive column of a low-pressure Ar-Hg discharge has been applied as an excitation source for a fluorescent lamp for illumination. Many studies on the diagnostics and fundamental mechanisms have been carried out on both the classical fluorescent lamp (d=36mm)[1-3] and a compact fluorescent lamp (d=12mm) [4-6].

On the other hand, a lamp of extremely narrow inner diameter (usually below 6mm) has been recently developed for liquid crystal display (LCD) backligting and its importance is undoubtedly increasing. Ar filling pressure (a few ten Torr) of LCD is higher than that of classical and compact fluorescent lamp (3Torr). Some characteristics or mechanisms of the narrow-diameter lamp may be similar to those of the 36mm one; however, the similarity rule does not hold between them due to the contributions from a stepwise ionization process taking place in the 36mm lamp[3]. Therefore, in order to clarify the excitation mechanism in the narrow-diameter lamp quantitatively, various parameters must be measured directly and some analysis must be done.

The $Hg6p^3P_{0,1,2}$ state densities and Hg^+ ground state density are important parameters for clarifying the excitation mechanism quantitatively. In this work, using a modified absorption method[7], we have measured the $Hg6p^3P_{0,1,2}$ state and Hg^+ ground state densities in the Ar-Hg discharge of tube diameter 4mm Ar filling pressure 20Torr and discharge current 5mA and 10mA on bath temperature.

2. Experiment

The $Hg6p^3P_{0,1,2}$ state and Hg^+ ground state densities were measured with the modified absorption method.

The principle of this method is described in detail in Ref. [7]. The discharge tube was made of quartz glass of 4mm inner diameter and has one anode; A, and two cathodes; K_1 and K_2. The discharge could be obtained at A-K_1 (ℓ =3cm) and A-K_2 (2ℓ =6cm) by changing the switch SW. The Ar filling pressure was 20Torr. The tube was placed in a water bath to control Hg vapor pressure by controlling the water temperature.

First, a discharge was obtained between anode A and cathode K_1 and the endlight intensity I_1 of the Hg(I) line ($7s^3S_1 - 6p^3P_{0,1,2}$) from the plasma I was measured with monochromator. Next, the discharge was switched from A-K_1 to A-K_2 and the endlight intensity I_2 of the line from the plasma I+II was measured. Then, the ratio of the two light intensities is given by

$$\frac{I_2}{I_1} - 1 = G(k_o l) = \frac{\int [1-\exp(-k_o l f(\nu))]\exp(-k_o l f(\nu))d\nu}{\int [1-\exp(-k_o l f(\nu))]d\nu} \quad (1)$$

Here, k_o is the absorption coefficient at the line center of the Hg^{202} isotope component, l is the plasma length, and $f(\nu)$ is the function giving the profile of the 404.7, 435.8 or 546.1nm line. Since the transmissivity of the window is not included in eq. (1), the absorption coefficient of an ultraviolet or visible line can also be measured exactly with this method. When $k_o\ell$

is known from the measured I_2/I_1 and eq. (1), the Hg6p $^3P_{0,1,2}$ state densities can be obtained. The Hg^+ ground state density is determined with the same procedure as that the Hg 6p $^3P_{0,1,2}$ state densities.

3. Results and Discussion

Figures 1 (a) and 1 (b) show the bath temperature dependences of the Hg6p $^3P_{0,1,2}$ state and Hg^+ ground state densities obtained on the tube axis at the discharge current of 5mA and 10mA, and the Ar filling pressure of 20Torr. They increase with the bath temperature. Hg^+ ground state density shows the trend of saturation above 70℃. This trend is similar to that obtained in the Ar filling pressure 3Torr[8]. The value of Hg^+ ground state density is higher than that obtained at Ar pressure 3Torr.

4. References

[1] For example, W. Verweij: Philips Res. Rep. Suppl. 2 (1961) 1.
[2] M. Koedam and A. A. Kruithof: Physica 28 (1962) 80.
[3] L. Vriens, R. A. J. Keijser and F. A. S. Ligthart: J. Appl. Phys. 49 (1978) 3807.
[4] T. Lin, T. Goto, T. Arai and S. Murayama: J. Appl. Phys. 66 (1989) 2779.
[5] T. Lin, T. Goto, T. Arai and S. Murayama: J. Appl. Phys. 67 (1990) 4012.
[6] T. Lin, T. Goto, T. Arai and S. Murayama: J. Appl. Phys. 69 (1991) 4201.
[7] T. Goto, M. Mori and S. Hattori: Appl. Phys. Lett. 29 (1976) 358.
[8] M. Goto and T. Arai: Jpn. J. Appl. phys. 34 (1995) L1074.

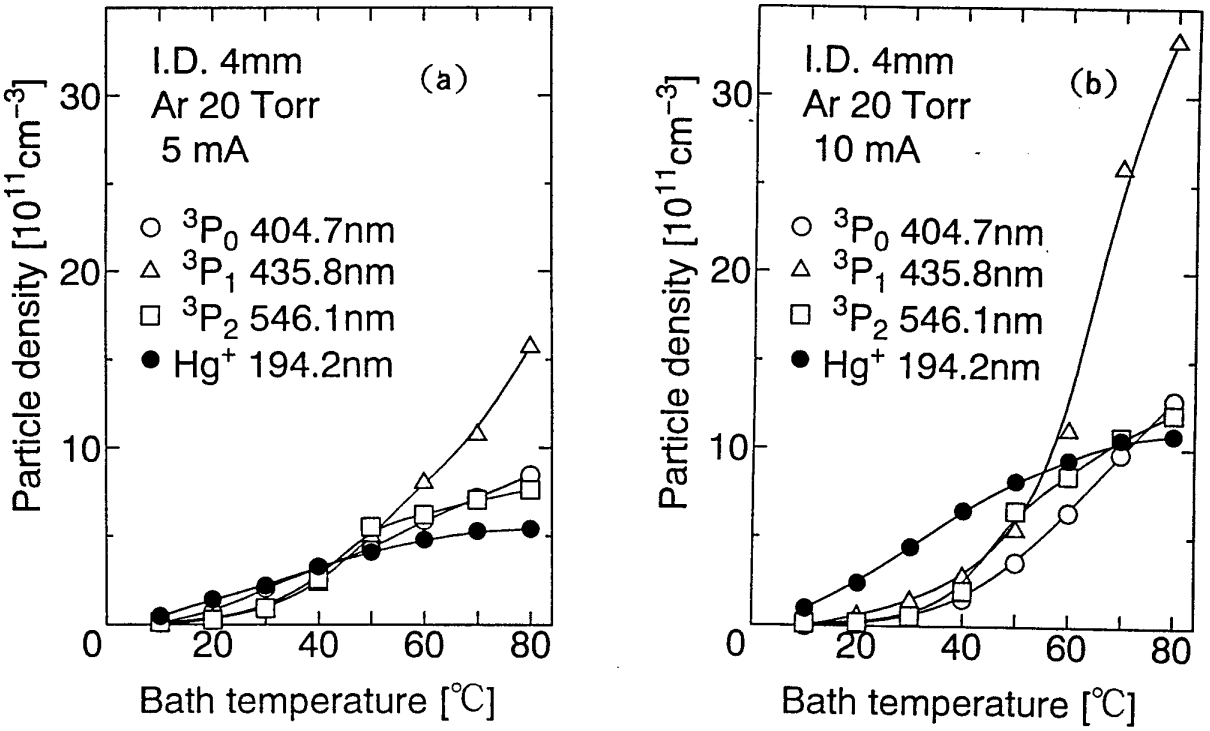

Fig. 1. Bath temperature dependences of Hg6p $^3P_{0,1,2}$ state and Hg^+ ground state densities at the discharge current of (a) 5mA and (b) 10mA.

Measurements of CF, CF_2 and CF_3 Radicals in a DC CF_4 Etching Plasma

Toshihiko ARAI, Miki GOTO, Hiroyuki FUJIOKA, Keita HORIKOSHI and Souichi MASHINO

Department of Electrical and Electronic Engineering, Kanagawa Institute of Technology, 1030 Shimo-ogino, Atsugi 243-02, Japan

1.Introduction

When CF_3, CF_2 and CF radicals are used as the reactive gas for dry etching of semiconductors, contribution of radicals of CF_3, CF_2, CF and F, the etchant, in the etching processes has been regarded important and widely studied. However, the details of the chemistry and physics in the etching reactors are not fully understood since measurements of free radicals in CF_4 plasma are very difficult.

CF and CF_2 radicals have been detected by a laser induced fluorescence technique[1-4] and also by an infrared diode laser absoption technique. [5] On the other hand, CF_3 and CF_2 radicals have been measured by a threshold ionization mass spectrometry in a CF_4 rf plasma. [6] These radicals are employed for modeling analysis and others in the computer simuration, and useful to clarify the etching mechanisum in a CF_4 plasma. Therefore, systematic measurement must be carried under the same condition because CF_3, CF_2 and CF radicals have been reported under different conditions of discharge plasma.

In this study, we have used the threshold ionization mass spectrometry[6-8] to determine absolute densities of CF_3, CF_2, CF and have compared these densities.

2.Experiment

The used discharge tube is made of pyrex glass of 3cm inner diameter with cold cathode. The CF_4 gas at flow rate of 10sccm was supplied to the discharge tube by a mass flow controller. The pressure in the discharge tube was measured with a capacitance manometer. The CF_4 gas was pumped through the discharge tube. The excitation of the discharge was made by DC discharge (20mA). The neutral species effusing from the plasma were introduced into a quadrupole mass spectrometer (QMS) through orifice of a diameter of 200 μ m at the cathode side. Pressures of 6×10^{-6} and 7×10^{-7} Torr were obtained in the quadrupole housing and discharge tube, respectively, under differential pumping with two turbo molecular pumps. Even with 0.4Torr pressure in the discharge tube, the pressure in the quadrupole housing did not rise above 5.1×10^{-5} Torr. The orifice is off plasma to minimize the background of discharge plasma. The neutral species is ionized by an electron beam energy from a filament in the ionization chamber.

3.Results and Discussion

A threshold ionization technique is based on several eV difference in threshold energies for electron-impact ionization of parent molecule and the radical. Figuer 1 shows the semilogarithmic plot of the QMS output current I_{QMS} for CF_3^+ (m/e=69) as a function of electron beam energy E_e. Here, the electron beam energy was calibrated by measuring the ionization threshold of Ar gas(15.75eV). There is a difference of about 6eV between the dissociative ionization threshold of $CF_4 \rightarrow CF_3^+$ (E_3=16.3eV) and the CF_3 radical ionization thershold of $CF_3 \rightarrow CF_3^+$ (E_3'=10.4eV)[9]. When the discharge is turned off, electron-impact dissocitation of CF_4 gives rises to fragment ion CF_3^+ at energy higher than this threshold ($CF_4 \rightarrow CF_3^+$: E_3 = 16.3eV).

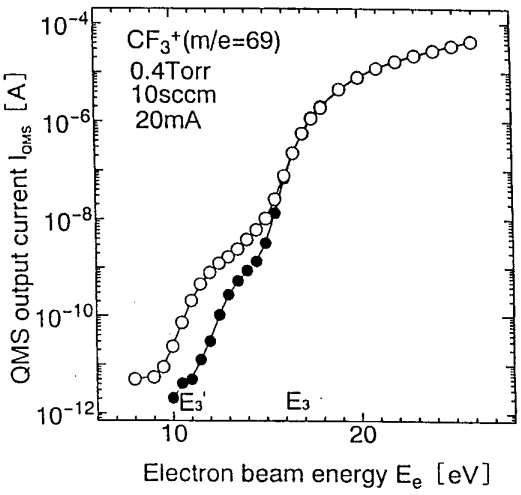

Fig. 1. Quadrupole mass spectrometer output current for CF_3^+ (m/e=69) as a function of electron beam energy, with the discharge on (open circles) and the discharge off (closed circles).

As seen in Fig. 1, the data taken with the discharge off has small residual signal below the threshold, probably due to dissociation of impurity gases. The observal difference between upper and lower curve in Fig. 1 is attributed to electron impact ionization of CF_3 effusing from the plasma when the discharge is on. Therefore, the CF_3 density n in the plasma is proportional to the difference between both QMS output current I'_{QMS} below 16eV and it can be obtained from the equation[6]

$$I'_{QMS} = I_{QMS}(discharge\ on) - I_{QMS}(discharge\ off) = A\,\sigma\,(E_e)n, \qquad (1)$$

where σ (E_e) represents the CF_3 ionization cross section for each value of electron impact energy and A is a constant which depend on the vacuum conductance of the orifice and the QMS sensitivity.

A can be obtained from the discharge off CF_3^+ signal due to CF_4 fragment ion if eq. (1) is applied replacing n by CF_4 density and σ (E_e) by the dissociative ionization cross section. Eq. (1) can be transformed as shown in the following equation

$$\frac{\Delta I'_{QMS}}{\Delta E_e} = An\frac{\Delta \sigma (E_e)}{\Delta E_e}. \qquad (2)$$

By substituting the slope $\Delta I_{QMS}/\Delta E_e$ (dischagre off) when E_e above E_3 in Fig. 2 is plotted on the linear scale, and the slope $\Delta \sigma (E_e)/\Delta E_e$ of the dissociative ionization cross section ($CF_4 \rightarrow CF_3^+$)[10] into eq. (2), we can determine the value of A, Using this value of A, and substituting the slope $\Delta I_{QMS}/\Delta E_e$ when the E_e between threshold E'_3 (10. 4eV) and E_3 (16. 3eV) in Fig. 2 is plotted on the linear scale and slope $\Delta \sigma (E_e)/\Delta E_e$ of the ionization cross section ($CF_3 \rightarrow CF_3^+$)[10] into eq. (2), we can obtain CF_3 density.

Using the data for dissociative ionization cross section($CF_4 \rightarrow CF_2^+$, $CF_4 \rightarrow CF^+$)[10] and the ionization cross section ($CF_2 \rightarrow CF_2^+$, $CF \rightarrow CF^+$)[11], we determined CF_2 density and CF density with the same procedure as that the CF_3 density. The following value were obtained for $n(CF_3)$, $n(CF_2)$ and n(CF) : $n(CF_3) = 2.6\times10^{12}\ cm^{-3}$, $n(CF_2) = 1.5\times10^{12}\ cm^{-3}$, $n(CF) = 1.3\times10^{12}\ cm^{-3}$. The radical density ratio is estimated to be $n(CF_3) : n(CF_2) : n(CF) \simeq 2 : 1 : 1$.

Reference

[1] For example, J. P. Booth, G. Hancock, N. D. Perry and M. J. Toogood: J. Appl. Phys. **66** (1989) 5251.

[2] T. Arai, M. Goto, D. Takayama, T. Shimizu and M. Murakami: Jpn. J. Appl. Phys. **33** (1994) 4170.

[3] T. Arai, M. Goto, D. Takayama, T. Shimizu, M. Murakami, H. Fujioka and K. Horikoshi: Jpn. J. Appl. Phys. **34** (1995) L1392.

[4] M. Murakami, H. Fujioka, K. Horikoshi, M. Goto and T. Arai : Proceeding of 8th Symposium on Plasma Sience for Materials, University of Tokyo. (1995) 1.

[5] M. Magame, N. Itabashi, T. Goto, C. Yamada and E. Hiroto: Jpn. J. Appl. Phys. **29** (1990) L829.

[6] Y. Hikosaka, H. Toyoda and H. Sugai: Jpn. J. Appl. Phys. **32** (1993) L353.

[7] R. Robertoson, D. Hils, H. Chatham and A. Gallagher: Appl. Phys. Lett. **43** (1983) 544.

[8] H. Toyoda, H. Kojima and H. Sugai: Appl. Phys. Lett. **54** (1989) 1507.

[9] T, Nakano and H, Sugai: Jpn. J. Appl. Phys. **31** (1992) 2919.

[10] K. Stephan, H. Deutsch and T. D. Mark: J. Chem. Phys. **83** (1985) 5712.

[11] V. Tarnovsky and K. Becker: J. Chem. Phys. **98** (1993) 7868.

MEASUREMENTS OF DIFFUSION COEFFICIENT OF CF RADICAL IN CF_4/H_2 DISCHARGE PLASMA

S.Mashino, K.Horikoshi, H.Fujioka, M.Goto and T.Arai
Department of Electrical and Electronic Engineering, Kanagawa Institute of Technology
1030 Shimo-Ogino, Atsugi 243-02, Japan

1. Introduction

Low-pressure CF_4 discharge plasmas are used extensively for dry etching of semiconductor devices. Mixing CF_4 with O_2 or H_2 provides etching selectivity between Si and SiO_2. Laser-induced fluorescence (LIF) has been used as a diagnostic technique in such plasmas, due to its high sensitivity and selectivity in measurement.[1] This LIF technique has been applied to obtain information on the buildup and decay of CF_2 and CF radical densities in pulsed CF_4 discharges.[2-5]

The diffusion coefficient of a radical is one of the important parameters needed to clarify the etching mechanism in CF_4 plasma. Measurements of the diffusion coefficient have been carried out for the CF_2 radical in Ar,[6] CF_4[7] and O_2[8] and for the CF radical in CF_4 and H_2.[9]

In this study, we have used LIF to probe the decay of transient CF radical density in pulsed CF_4/H_2 plasma and have determined the diffusion coefficient of the CF radical in CF_4 and H_2.

2. Experimental

The discharge tube was a hollow cathode tube consisting of a stainless steel cylindrical cathode (10cm inner diameter, 30cm long) with optical access parts and two tungsten pin anodes (1.5mm diameter). CF_4 was supplied to the discharge tube by a mass flow controller at a flow rate of 2sccm. The pressure in the discharge tube was measured with a capacitance manometer. Then H_2 gas was added to the CF_4 gas and the H_2 pressure was obtained from the capacitance manometer reading based on the increase in pressure. The CF_4/H_2 gas mixture was pumped through the discharge tube. A DC pulsed voltage with a repetition frequency of 10Hz, a width of 0.5ms and a discharge current of 300mA was applied between the electrodes. After 0.5ms, the current falls to a zero level within 1 μs. Digital delay generators provided precise timing control of the discharge, laser, and detection equipment. Laser excitation was provided by a Nd^{+3}:YAG pumped dye laser (Quanta Ray DCR-3G/PDL-2) with a wavelength extender (WEX-1).

Fluorescence was collected at 90° from the incident beam using a quartz lens, focused onto the entrance slit of a monochromator (Nikon G-250), and detected with a photomultiplier. The signals were averaged over 300 samples in 50ns gate using a boxcar integrator (Stanford Research Systems SR250).

The 232.9nm laser beam of 0.05mJ/pulse was used to excite CF radicals from the ground state $X^2\Pi(v=0)$ to the excited state $A^2\Sigma^+(v'=0)$.[10] The relative density of CF radicals was determined from an intensity change of the emission band at 255.5nm, which corresponds to the $A^2\Sigma^+(v'=0) \rightarrow X^2\Pi(v=3)$ transition.

3. Results and Discussion

In a simplified model of the discharge afterglow, the CF radical density N will vary roughly as

$$N = No\ exp\left(-\frac{t}{\tau}\right), \quad (1)$$

where No is the initial CF radical density, and the lifetime of CF radical τ [11] is provided by

$$\tau = \frac{1}{Kwall} = \frac{\Lambda^2 P}{D} + \frac{V}{A}\cdot\frac{2(2-\alpha)}{\bar{v}\alpha} \quad (2)$$

$Kwall$ is the effective loss-rate constant, Λ is the diffusion length of the container, P is the pressure in Torr, D is the diffusion coefficient of CF radical in the CF_4/H_2 gas mixture at 1Torr, V/A is the volume to surface area ratio of the container, $\bar{v}$ is the kinetic mean velocity of CF radical, and α is sticking coefficient. The first term in eq.(2) is proportional to the gas pressure, and assuming that the α is constant, the second term is constant.

Figures 1 and 2 show the dependences of lifetime of the CF radical on the H_2 partial pressure and the total pressure, respectively. The lifetime increased with H_2 pressure under constant CF_4 pressure and total pressure. These linear increases show that gas phase recombination riactions are much smaller than the diffusion to the chamber walls and can be neglected under the conditions of Figs.1 and 2. The radial distribution of the CF radical density in the discharge decreased gradually along the direction of radius under the present discharge conditions. This distribution curve was approximated to the zeroth Bessel function. Therefore, the lifetime τ in the CF_4/H_2 discharge

plasma is given by eq.(2).

The linear relationship shown in Figs.1 and 2 indicates that the diffusion coefficient in eq.(2) can approximately satisfy Blanc's law:

$$\frac{P}{D} = \frac{P(CF_4)}{D(CF \text{ in } CF_4)} + \frac{P(H_2)}{D(CF \text{ in } H_2)} . \quad (3)$$

Here D(CF in CF_4) and D(CF in H_2) are the diffusion coefficients of CF in CF_4 and H_2 at 1Torr, respectively. When eq.(3) is substituted into eq.(2), we obtain

$$\tau = \Lambda^2 \frac{P(CF_4)}{D(CF \text{ in } CF_4)} + \frac{V}{A} \cdot \frac{2(2-\alpha)}{\bar{v}\alpha} + \Lambda^2 \frac{P(H_2)}{D(CF \text{ in } H_2)} . \quad (4)$$

The first and second terms on the right of eq.(4) become constant and the third term is proportional to H_2 partial pressure under the present conditions. From the slope of the straight line in Fig.1, D(CF in H_2) is estimated to be

$$D(CF \text{ in } H_2) = 660 \text{ cm}^2 \cdot \text{Torr} \cdot \text{s}^{-1}$$

at room temperature. From the value of D(CF in H_2) and the slope of the straight line in Fig.2, D(CF in CF_4) is estimated to be

$$D(CF \text{ in } CF_4) = 240 \text{ cm}^2 \cdot \text{Torr} \cdot \text{s}^{-1}.$$

These values were in good agreement with that obtained in infrared diode laser absorption spectroscopy.[9]

Reference

[1] R.A.Gottsho and T.A.Miller : Pure Appl. Chem. 56 (1984) 189

[2] J.P.Booth, G.Hancock and N.D.Perry : Appl. Phys. Lett. 50 (1987) 318

[3] S.G.Hansen, G.Luckman and S.D.Colson : Appl. Phys. Lett. 53 (1988) 1588

[4] J.P.Booth, G.Hancock, N.D.Perry and M.J.Toogood : J. Appl. Phys. 66 (1989) 5251

[5] S.G.Hansen, G.Luckman, G.C.Nieman and S.D.Colson : Appl. Phys. Lett. 56 (1990) 719

[6] S.E.Bialkowski, D.S.King and J.C.Stephenson : J. Chem. Phys. 72 (1980) 1156

[7] T.Arai, M.Goto, Y.Asoh, D.Takayama and T.Shimizu : Jpn. J. Appl. Phys. 32 (1993) L4169

[8] T.Arai, M.Goto, D.Takayama, T.Shimizu and M.Murakami : Jpn. J. Appl. Phys. 33 (1994) 4170

[9] M.Magane, N.Itabashi, N.Nishiwaki, T.Goto, C.Yamada and E.Hirota : Jpn. J. Appl. Phys. 29 (1990) L829

[10] T.L.Porter, D.E.Mann and N.Acguista : J. Mol. Spectrosc. 16 (1965) 228

[11] J.P.Booth and N.Sadeghi : J. Appl. Phys. 70 (1991) 611

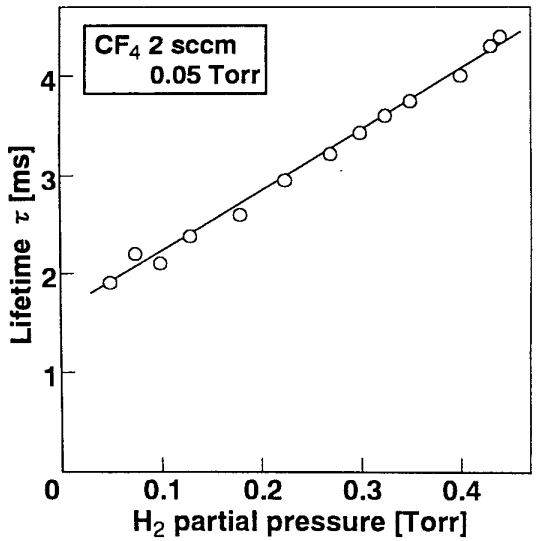

Fig.1 Lifetime of the CF radical as a function of the H_2 partial pressure at the CF_4 partial pressure of 0.05 Torr and the flow rate of 2 sccm.

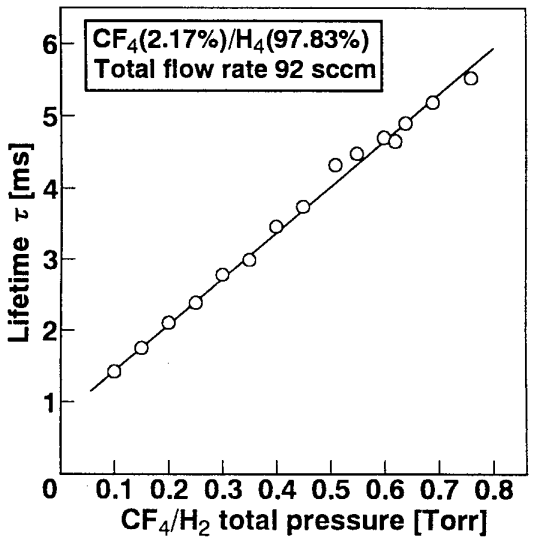

Fig.2 Lifetime of the CF radical as a function of the CF_4(2%)/H_2 total pressure at the total flow rate of 92 sccm.

Time resolved temperature measurements in a H_2 high density pulsed discharge

A Rousseau, E Teboul, G Gousset, P Leprince
Laboratoire de physique des gaz et des plasmas, Université Paris-Sud, Bat 212, 91 405 Orsay Cedex,France

1. Introduction

Low pressure plasmas (about 1 Torr) are very efficient sources of active species (radicals, excited neutrals, ions) and their applications increase continuously (thin films deposition and etching, polymer treatments, environmental applications). For these processes, the neutral temperature is an important parameter. In hydrogen plasma, it was recently reported that the H atom temperature T_H is higher than the molecular temperature, both in the positive column of a DC discharge [1] and in surface wave discharges [2]. Up to now, these measurements have been performed at the steady state.

For example, it was shown that the H atom temperature does not depend on the gas velocity in a flowing surface wave discharge, suggesting that the heating of the gas occurs in very short time. In the present study, we investigate the heating of the gas (H and H_2) during a short pulse (10 µs) in a microwave discharge created in a cavity. Three distinct temperatures are determined at the same time: the kinetic temperature of the H atoms and of the molecules, and the rotational temperature of the molecules. The purpose of this study is to evaluate the power balance in order to understand the mechanisms and the time caracteristics of the heating of the gas.

2. Experiment

The discharge is created in a quartz tube (inner diameter = 16 mm), set in a microwave cavity excited at the frequency = 1.12 GHz. The microwave generator supplies 10 µs pulses, with a duty cycle equal to 10^{-3}. Two distinctive microwave powers are studied: 4 kW and 8 kW. In both cases, the cavity length is set so that all the incident power is absorbed by the plasma at the end of the pulse (critical coupling). The mechanisms of the breakdown in this cavity are described in ref [3]. In the following, results presented have been obtained after the gas breakdown (t > 0.1 µs).

Temperature measurements are performed using a JY HR1000 spectrometer, providing a resolution of 0.005 nm at the 2° order of the 1200 lines/mm grating. Atomic and molecular temperatures (T_H and T_{H2}) are deduced from Doppler broadening of H_α, H_β lines for the H atoms and of $B^1\Sigma_u^+ \rightarrow G^1\Sigma_g^+$ (v' = v = 0) 462.8 nm line for the molecules. For the atomic lines, the fine structure is deconvoluted: $T_{H\alpha,\beta}$ is determined by comparing the experimental atomic line spectrum with a calculated spectrum taking into account altogether the fine structure, Doppler broadening and apparatus broadening. The rotational temperature is deduced from the Fulcher α band ($a^3\Sigma_g^+$ (v'=1) -> $d^3\Pi_u$(v=1)) (N=1,3,5). As discussed in [1], the rotational constant to be considered is the rotational constant of the ground state B_v=60 cm^{-1}. The intensity line signal, averaged along the tube axis, is time resolved using a boxcar averager EGG 4420.

3. Results

Rotational temperature.

In the following, the time t=0 is refered to the beginning of the pulse. Figure 1 presents the rotational distribution (F_α band) for different time t after the beginning of the pulse. It appears that at t=0.8 µs the rotational distribution is very far from the Boltzmann law. Even at the end of the pulse (t=9.5 µs), the rotational distribution is not completely relaxed. However, a mean rotational temperature T_{rot} can be defined by fitting the rotational distribution by a linear regression. At t=9.5 µs, Trot increases from 1580 K to 1820 K , when the microwave power increases from 4 kW to 8 kW.

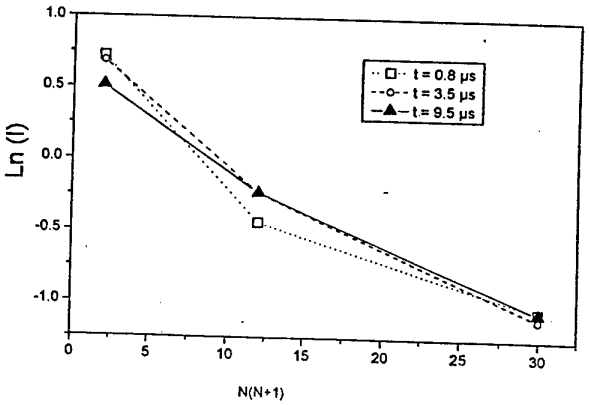

Figure 1. Rotational distribution for different instant of the pulse . p=1Torr, P=4kW.

Kinetic temperatures and gas temperature.

The molecular singlet-singlet transition $B^1\Sigma_u^+ \rightarrow G^1\Sigma_g^+$ is considered because no fine structure complicates the determination of the temperature by Doppler broadenning. In this experiment, the dissociation degree is supposed to remain very low, due to low duty cycle ratio (1/1000), and the shortness of the pulse duration (t=10 µs). Indeed, It was previously shown by laser induced stimulated emission that the effective dissociation time of the H_2 molecule by electron impact, is typically 10 ms at 1 torr for an

electron density $n_e=10^{12}cm^{-3}$ [4]. Therefore, T_{H2} is expected to be the kinetical temperature of the neutrals. Figure 2 represents the time evolution of the kinetic temperature; T_{H2} increases sharply during 2.5 µs from 300 K to about 900 K.

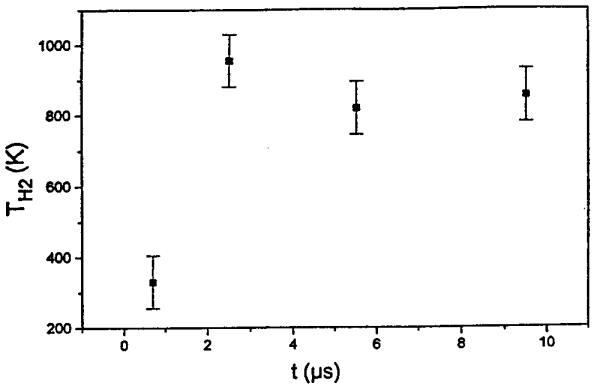

Figure 2: Time evolution of the molecular temperature T_{H2}. p=1Torr, P=4kW

The determination of the atomic temperature from balmer lines must be discussed in detail. Figure 3a and 3b present the H_α line at the begining (t=0.9 µs) and the end (t=9.5 µs) of the pulse respectivelly. At the beginning of the pulse, the experimental spectrum H_α can not be fitted by a simple theoretical calculation (figure 3a). In such cases, a non doppler broadening of balmer lines are generally attributed to dissociative excitation ($e + H_2 \rightarrow e + H + H(n)$). However, figure 3a exhibits a splitting of the line which can also be attributed to a strong stark effect (l mixing of the J=1/2 and 3/2 components); indeed, at the beginning of the pulse (just after the breakdown), the electric field is still very high. Work is in progress in order to understand this phenomena. At the contrary, at the end of the pulse, the theoretical spectrum fits perfectly the experimental one (the corresponding temperature is $T_{H\alpha}$=1950 K), which shows that the determination of the H atom temperature is perfectly valid in this case. The temperature $T_{H\beta}$ determined in the same way by deconvoluating the H_β line is equal to $T_{H\beta}$ =1800 K at the end of the pulse. The difference between $T_{H\alpha}$ and $T_{H\beta}$ is within the error bars.

Heating of the H atoms.

These results show that the H atom temperature is considerably higher (about 1900 K) than the molecular temperature (900 K), after a 10 µs pulse. This was attributed to the fact that the thermal energy of the neutral particules is provided by the dissociation of the molecules by electron impact $e + H_2 \rightarrow e + H + H$ (3.5 eV per atom), which creates hot H atoms. The H atoms lose part of their energy by very efficient momentum transfer on the molecules.

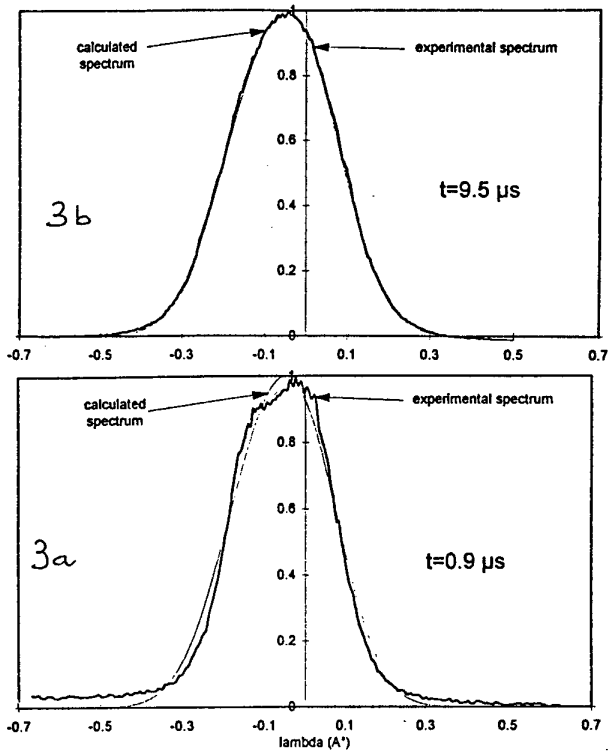

Figure 3: Experimental and calculated spectra of the Hα lin, at the beginning of the pulse (3a) and at the end of the pulse (3b). p=1Torr, P=4kW.

Heating of the molecules :

T_{H2} increases from 300 K to 900 K in less than 2.5 µs. The heating of the molecules is sustained by two main mechanisms:

- Dissociation of the molecules and creation of energetic neutrals as described above.
- electron neutral elastic collisions.

Work is in progress in order to quantify these two mechanisms.

[1] J Amorim, G Baravian, J Jolly and M Touzeau, *J. Appl. Phys.* **76** (1994) 1

[2] L Tomasini, A Rousseau, G Gousset, P Leprince, *J. Phys. D: Appl. Phys.* **29** (1996) 1006

[3] A. Draghici-Lacoste, L Alves, C M Ferreira, P Leprince and G Gousset, ICPIG XXIII Contrib. Paper

[4] L Tomasini, A Rousseau, G Baravian, G Gousset, P Leprince, *Appl. Phys. Let.* **69** (1996) 1553

Franck-Condon factors calculation for the A $^3\Sigma_u^+ \rightarrow$ C $^3\Pi_u$ and A $^3\Sigma_u^+ \rightarrow$ B $^2\Sigma_u^+$ transitions of N_2.

H.Champain, D.Djermoune, G.Hartmann

Laboratoire de Physique des Gaz et des Plasmas, E.D.E.E., ESE., plateau de Moulon, F.91190 GIF-sur-Yvette.

Abstract

Electron impact cross sections for non radiative transitions A $^3\Sigma_u^+ \rightarrow$ C $^3\Pi_u$ and A $^3\Sigma_u^+ \rightarrow$ B $^2\Sigma_u^+$ are unknown. Nevertheless, for calculations, it is often assumed that Franck-Condon factors can be used as a substitute. These calculations are proposed here; they are justified by the lack of reference in spectroscopic tables, since they mainly concern radiative transitions.

Taking into account a partial excitation starting from the metastable state A $^3\Sigma_u^+$, the use of the Franck-Condon factors enables us to compute spectra of the second positive system and the first negative system of nitrogen N_2. The calculated spectrum is compared with an experimental one, as it appears in the next paper.

Introduction

An abnormal distribution of the intensity of the molecular band of the second positive system of N_2 is observed in the light from the cathodic region of a low current electric arc (see next paper).

This suggests that a partial excitation of the electronic level C $^3\Pi_u$ is possible, starting from the metastable level A $^3\Sigma_u^+$. At this time, the cross sections for this electron impact transition are unknown. Similarly, the Franck-Condon factors are omitted in the tables, since this transition is non radiative.

The cross sections values cannot easily be theoretically evaluated, but the Franck-Condon factors can be accessed by computation following the method given by Nicholls [1].

Calculation results

Computation are made for the transitions A $^3\Sigma_u^+ \rightarrow$ C $^3\Pi_u$ and A $^3\Sigma_u^+ \rightarrow$ B $^2\Sigma_u^+$ with the constants given by Nicholls [1].

The computed values of the Franck-Condon factors are given in tables 1 and 2.

Simulated spectra

The computed factors are then introduced in the simulation code for the second positive system of N_2 already made by Hartmann et Johnson [2], further used for spectra simulations, [3-6]. Simulation of the first negative system of N_2 was made later.

The present simulated spectra are obtained assuming 5000K for the rotation and vibration temperatures. The entrance and exit slits of the assumed monochromator are of .1 and .5 nm equivalent width respectively. The displacement is by .5 nm steps.

We show the simulated spectra of the second positive system of N_2 on figures 1 and 2, respectively, assuming a 100 % production either from ground or metastable states. On figures 3 and 4, are show the same simulated spectra for the first negative system of N_2.

v''\v'	0	1	2	3	4
0	.023	.110	.252	.363	.311
1	.071	.181	.148	.013	.068
2	.120	.139	.008	.085	.170
3	.148	.056	.028	.132	.009
4	.151	.006	.088	.040	.050
5	.134	.004	.090	.001	.106
6	.108	.031	.049	.041	.054
7	.081	.059	.011	.079	.003
8	.058	.076	-	.072	.014
9	.039	.079	.013	.039	.051
10	.026	.072	.034	010	.068
11	.017	.060	.051	-	.055
12	.011	.047	.061	008	.028
13	.007	.035	.062	.025	.007
14	.004	.026	.057	.041	-
15	.002	.018	.049	.052	.005

Table 1 - Franck-Condon factors for A $^3\Sigma_u^+(v'') \rightarrow$ C $^3\Pi_u(v')$

v''\v'	0	1	2	3	4	5	6	7	8	9	10	11
0	-	.002	.013	.050	.134	.235	.341	.347	.281	.177	.082	.030
1	.001	.012	.052	.135	.221	.186	.071	-	.091	.248	.295	.227
2	.003	.033	.104	.175	.143	.022	.025	.139	.135	.018	.040	.214
3	.007	.063	.142	.137	.029	.020	.122	.074	.001	.102	.133	.017
4	.014	.096	.144	.061	.003	.089	.073	.001	.091	.077	.001	.110
5	.024	.121	.111	.008	.049	.085	.003	.062	.070	.001	.092	.053
6	.036	.132	.064	.004	.085	.029	.024	.077	.002	.067	.047	.013
7	.048	.126	.023	.031	.074	-	.067	.024	.029	.064	.001	.081
8	.060	.107	.002	.059	.036	.018	.062	-	.065	.007	.050	.033
9	.070	.080	.002	.069	.006	.048	.024	.027	.042	.011	.056	.001
10	.077	.052	.017	.058	.002	.056	.001	.052	.005	.046	.013	.039
11	.081	028	.035	.036	.018	.040	.009	.044	.005	.048	.002	.051
12	.082	.011	.050	.015	.037	.017	.031	.018	.028	.019	.028	.019
13	.081	.002	.057	.002	.049	.002	.044	.001	.042	-	.042	-
14	.078	-	.055	.001	.047	.002	.040	.004	.034	008	.029	.014
15	.072	.004	.047	.007	.035	.012	.024	.019	.015	.026	.007	.033

Table 2 - Franck-Condon factors for A $^3\Sigma_u^+(v'') \rightarrow$ B $^2\Sigma_u^+(v')$

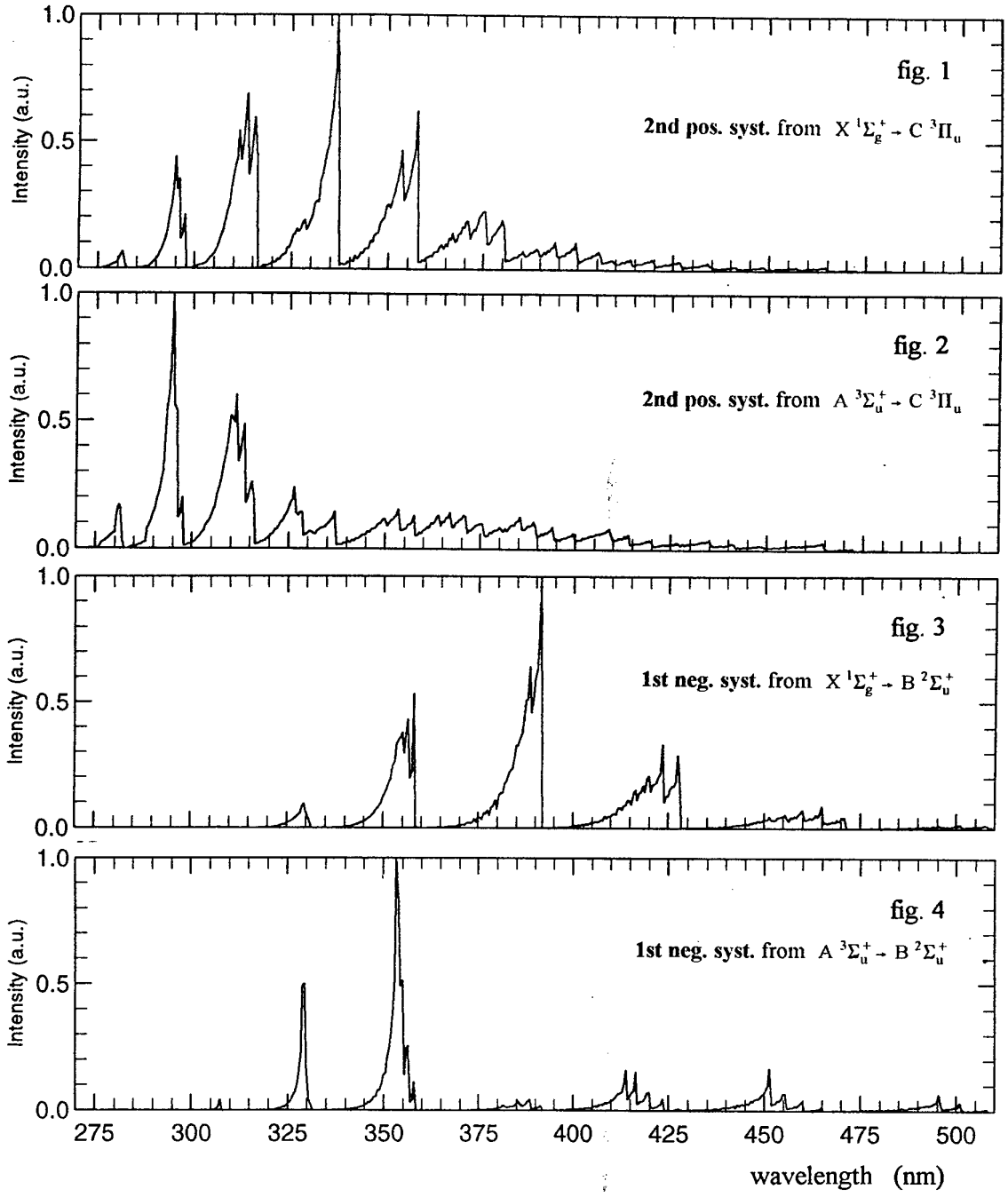

Conclusion

The influence of the excitation of the C $^3\Pi_u$ and B $^2\Sigma_u^+$ states starting from the A $^3\Sigma_u^+$ métastable state is clear and evident. Of course, for a thermodynamically equilibrium state plasma, this influence is negligible, but for cold plasmas or arcs in extinction, which are of interest here, this can become important. The electrons present at the spontaneous extinction of a low current arc have an evaluated kinetic energy higher than 40 eV, far from thermal equilibrium.

References

[1] Nicholls R.W. J. Res. Nat. Bur. of Stand.-A Phys.& Chem. 65A, 5,(1961) p.451 - 460.
[2] Hartmann G. Johnson P.C. J. Phys. B :Atom. Molec. Phys, 11, 9,(1978) p.1597 - 1612.
[3] Hartmann G. Marode E. ESCAMPIG 90 Orléans (1990) p.423 - 424.
[4] Chelouah A. Marode E., Hartmann G. J. Phys. D Appl. Phys. 27,(1994) p.770 - 780.
[5] Chelouah A.. Marode E., Hartmann G. Achat S. J. Phys. D Appl. Phys. 27,(1994) p.940 - 945.
[6] Champain H.,Hartmann G.,Lalmas M., Goldman A. 11th Intern. Conf. on Gas Discharges and their Applications.-Tokyo, 11-15 sept.,(1995) p.152 - 155.

The role of the metastable state A $^3\Sigma_u^+$ in the excitation mechanism of molecular nitrogen. Application to the spontaneous extinction of the low current arc.

*M.Tioursi, R. Haug, G.Hartmann

L.P.G.P., E.D.E.E., SUPELEC., plateau de Moulon, F.91192 GIF-sur- Yvette Cedex.
*Institut d'Electrotechnique - Université des Sciences et de la Technologie d'ORAN B.P. 1505 Oran El-Menouar ALGERIE

Abstract

The influence of the metastable state A $^3\Sigma_u^+$ of N_2 on the excitation mechanisms is experimentally solved by study of the emitted light from the cathodic region during the spontaneous extinction of the low current electric arc. A theoretical approach is proposed on the basis of Franck-Condon factors and is in agreement with the experimental results.

Introduction

The cathodic region plays a major role in the self-sustaining arc discharge. The low DC current arc between metallic electrodes exhibits internal instability, leading to complete extinction.

The electrical study of this phenomenon in the air at atmospheric pressure [1],[2] shows that these arc instabilities result in voltage fluctuations and sharp rises of the voltage, due to the total extinction of the current.

This electrical phenomena are correlated with an intense and brief emission of NII, OII, AgII and N_2, and by a decrease of the emission of Ag I coming from the region close to the silver cathode.

A previous spectroscopic study [1],[3] allowed us to show the excitation mechanisms of the different species. We proposed a detailed analysis of the resulting spectra, namely the intensity of the heads of the N_2 molecular bands. We assume that, at the time of the extinction, two groups of electrons exist in the plasma : a group of electrons with thermal energy and a group of fast electrons (>40 eV) emitted by the cathode and accelerated in the sheath. This last group is involved in the intense light emission from the region close to the cathode.

Here, our attention is focused on the results concerning the N_2 and N_2^+ emission, in particular, the intensity of band's heads of the second positive system and the first negative system.

The experimental data are presented using time resolved spectroscopy as a investigation means. In a second step, the data are compared to the computed ones derived from Franck-Condon factors calculations.

Experimental set-up

A DC current supply allows the re-ignition of the arc by thermal breakdown after an extinction. The circuit was described in previous work [1],[2],[3] allows us to record numerous observations of extinctions and subsequent re-ignitions with external intervention.

To be analysed, the light emitted by a thin part of the arc located at a known distance from the cathode, is focused by means of concave mirror on the entrance slit of the monochromator followed by a photomultiplier. The trigger of the time sorting of the light pulses is taken from the arc voltage fast rising slope dV/dt of the long pulses fig.1. The recording appararatus was described in a previous studies [1],[2],[3].

Experimental results

We established the histograms of the light emitted in the cathodic region for Ag electrodes from 210 nm to 510 nm by steps of 0.5 nm.

An interesting phenomenon appears as a short and intense light emission coming from the region close to the cathode at moment of extinction (channel 80). The detailed results of this phenomena are presented in our previous works [1],[3].

For molecular nitrogen N_2, the typical shape of the histograms obtained is displayed on fig.2.

The stationary spectrum [1],[4] shows that the molecular bands of the second positive system are permanently excited. In fact, if we subtract from the histogram of N_2 (λ = 295.3 nm for example), the histogram of very near continuum (λ = 299.0 nm), the result on fig.3, shows the existence of an emission of molecule nitrogen before the extinction of the arc. The light pulse observed at the moment of extinction therefore corresponds to a reinforcement of the emission of N_2.

At the moment of extinction (channel 80), the recorded spectrum represented on fig.4 , shows that the intensity of band's heads is disturbed with respect to the structure of the molecular spectrum when the population of the excited states C $^3\Pi_u$ and B $^2\Sigma_u^+$ are done starting from the fundamental state X $^1\Sigma_g^+$, [5].

Discussion

The first electronic excited state A $^3\Sigma_u^+$ of N_2 is a metastable state, for which the life span for the isolated molecule is about 12-13 s [6], [7]. The second metastable state is the excited state B $^3\Pi_g$ for which the life span for the isolated molecule is about 2 to

8 µs. [6]. [7]. However, at the atmospheric pressure, we obtain a quenching effect of this state by collisions with the gas species [8]. The life span of such state becomes of the order of one nanosecond. On the contrary, the metastable state $A\ ^3\Sigma_u^+$ is more stable at atmospheric pressure (life span of the order of some millisecond) [9]. It results that the radiating levels $C\ ^3\Pi_u$ and $B\ ^2\Sigma_u^+$ are probably populated in cascade using the metastable level $A\ ^3\Sigma_u^+$, which requires electrons of lower energy.

Theoretical approach

The collisional cross sections of transitions $(A\ ^3\Sigma_u^+ \rightarrow C\ ^3\Pi_u)$ and $(A\ ^3\Sigma_u^+ \rightarrow B\ ^2\Sigma_u^+)$ being unknown, we used the method developed by Nicholls [10] for the computation of Franck-Condon factors. To our knowledge, this calculation was never done, because of the non radiating character of this transition. The results of such calculation are presented in previous paper.

By the use of Franck-Condon factors, calculated for the fundamental state to $C\ ^3\Pi_u$ and to $B\ ^2\Sigma_u^+$ states transition, we could simulate the spectrum of the second positive and the first negative systems. For the $C\ ^3\Pi_u$ state, we assume that populating is starting, 30% from fundamental and 70% from metastable states $A\ ^3\Sigma_u^+$. For the $B\ ^2\Sigma_u^+$ state (75% and 25%, respectively). Finally, the spectrum is formed by 60% of $C\ ^3\Pi_u$ and 40% of $B\ ^2\Sigma_u^+$ as showed on fig.5. *vs.* fig.4

Note that this result agrees with our interpretation of the experimental results.

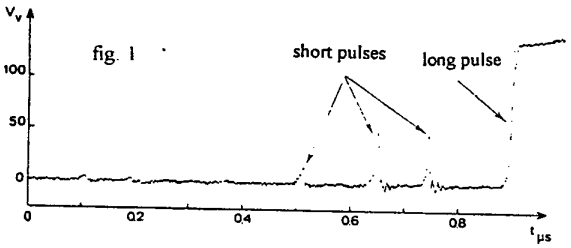

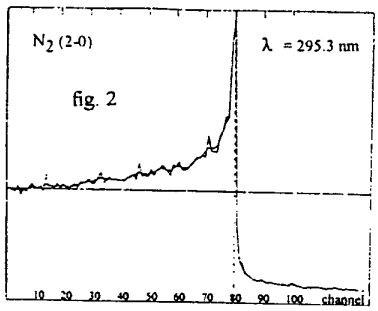

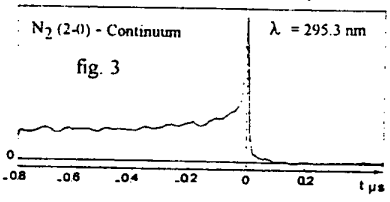

Conclusion

During the transient which happens just at the extinction of a low current arc in air, the nitrogen molecular spectra is strongly anomalous, compared to that of the steady arc discharge.

The hypothesis of a cascade excitation mechanism using the metastable level $A\ ^3\Sigma_u^+$ and the computation of the related Franck-Condon factors, for the populations of the excited states $C\ ^3\Pi_u$ and $B\ ^2\Sigma_u^+$ are in agreement with the observed spectrum at the moment of extinction.

References

[1] Tioursi M., Thèse de doctorat de l'Université Paris VI (1990)

[2] Tioursi M., Haug R. Proc. XIXth Int. Conf. Phen. Ion. Gases, Belgrade (1989)

[3] Tioursi M., Hartmann G., Haug R. J. Phys. III France 2 (1992) 2267-2286

[4] Maftoul J. Thèse de doctorat d'Etat, n° 3429, Orsay (1987)

[5] Hartmann G. Thèse de doctorat d'Etat, n° 1783, Orsay (1977)

[6] Brennen W. J.Chem.Phys. vol.44 (1966) 1793-1796

[7] Wentink T.Jr, and Isaacson L., J.Chem.Phys., vol. 46 (1967) 822-823

[8] Wright A.N., Winkler C.A. Active Nitrogen, Academic Press, N.Y. and London, (1968)

[9] Carleton N.P., Oldenberg O., J.Chem.Phys. vol.36 (1962) 3460-3463

[10] Nicholls R.W. J.Res.Nat.Bur.of Stand.-A Phys.& Chem. 65A, 5,(1961) 451-460

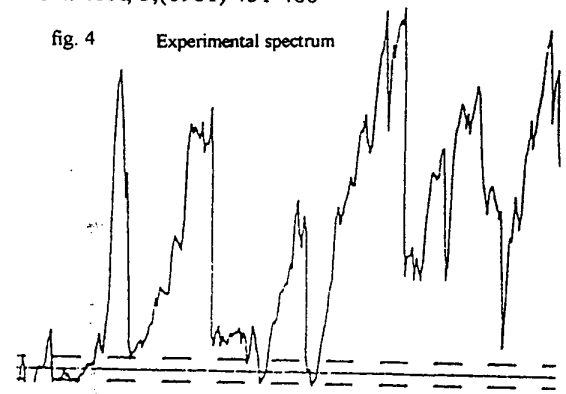

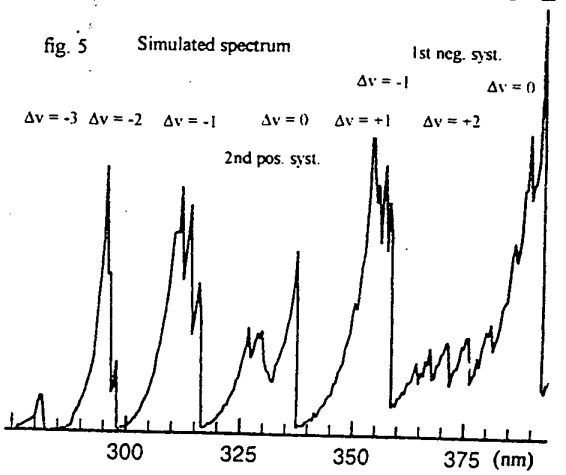

Spectral diagnostics of glid-arc up to 1.1 MPa

J.Janča and C. Tesař
Department of Physical Electronics, Faculty of Science,
Masaryk University, 61137,Brno, Kotlářská 2, Czech Republic

1. Introduction

Spectral analysis of gliding low frequency glow discharges in air as the carrier gas, under atmospheric and increased pressures up to $1.1 MPa$, may demonstrate the utilisability of discharges for ignition of various organic mixtures, [1].

The present paper concerns the determination of vibrational and rotational temperatures and tentative determination of the electron temperature of parts of the gliding discharge using spectral methods. Gliding discharges were excited under atmospheric and increased pressures at various rates of air flow in horn-shaped Cu electrodes, [2].

The utilisability of the standard spectral diagnostic methods depends on the working gas used in which a given type of discharge is excited. When exciting discharges in air, we may preferably make use of the spectral methods elaborated for molecular nitrogen N_2 and OH radicals. The abrasion of the electrode material permits, under specific physical conditions, to employ also atomic spectra for the determination of the electron temperature.

2. Experimental

Primary very short arc discharges were excited in a pressure vessel between horn-shaped Cu electrodes according to Fig. 1. The minimum distance of electrodes was 0.25 to 0.40 mm. This arc discharge was blown out by a stream of air from a jet of a dia. of 1 mm at flow rates of 10 to 70 l/min. The blowing-out of the ionised plasma of the arc upwards in between the extending horns caused the short arc to change into a spark discharge. The plasma of the spark discharge then faded out in a vague form of coronal discharge.

Having analysed its spectra, we called this type of discharge occurring in flowing air the "high-pressure glow discharge", [2].

The thin and flat discharge area between the horn-shaped electrodes is thus filled out with two types of discharges. In the narrowest part and immediately over it is the region of spark discharges with a high intensity of the electric field in the spark channel at a high current density. Sparks are excited in each half-period of the alternating voltage at a frequency of $100 Hz$. In the extended part of horn-shaped electrodes, there prevails the plasma of sparks disintegrating into coronal discharge.

The spectral analysis of the individual parts of a discharge under various physical conditions was performed by means of the monochromator Jobin-Yvon HR 640.

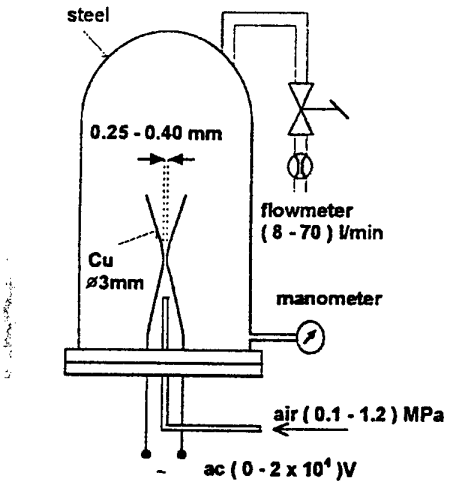

Figure 1: The pressure vesel and the arrangement of horn-shaped Cu electrodes for the excitation of gliding glow discharges.

The electrical parameters of discharge U, I, $cos\varphi$ were monitored by placing an elctrostatic voltmeter and an A.C. ammeter in the secondary circuit of leaked transformers of Italian product, 10 000/100 CM, (prim 230 V/4.8 A; sec 2 x 5000 V/100 mA). The primary side contained, in addition to a voltmeter and an ammeter, a wattmeter. The $cos\varphi$ in a discharges on the secondary side of the transformer was determined on accont of minimal heat losses of the transformer.

The electrical parameters U, I and $\cos\varphi$ excited discharges are given in Fig. 2.

3. Measurement

The vibrational temperature T_{VX} of the ground electron state $X^{'}\Sigma_g^+$ of the N_2 molecule was determined by means of the "effective" vibrational temperature T_{VC} of the excited electron states $C^3\Pi_g$ measured from transition $C^3\Pi_g \rightarrow B^3\Pi_u$, (2nd positive system). The effective vibrational temperature T_{VC} was calculated by means of the relative intensity of heads of vibrational bands of the sequence $\Delta v = +2$, $(2-0,\ 3-1,\ 4-2)$, of the N_2 band system mentioned above. The determination of T_{VC} was performed by the method used in [5]. The transition probabilities and corrections on $R_e(v'v'')$ centroide were taken over from [4]. In accord with the paper [5] , the vibrational temperature T_{VX} of the electron

	$N_2 = (X^1\Sigma_g^+)$			Cu		
air	$T_{VX}[K]$			$T_E[K]$		
pressure	air, flow ~ [l/min]			air, flow ~ [l/min]		
MPa	25	34	48	25	34	48
0.1	2400	3500	3470	-	-	-
0.2	5000	5130	3630	8200	-	8600
0.3	-	-	-	9200	8460	9400
0.5	-	-	-	9050	9300	8870
0.7	-	-	-	8600	9400	8830
0.9	-	-	-	11050	9900	9950
1.1	-	-	-	10400	11100	-

Table 1: The vibrational temperatures T_{VX} and electron temperatures T_E.

ground state $X^1\Sigma_g^+$ was then determined based on the functional dependence of $T_{VX} = fce(T_{VC})$.

The rotational temperature T_{R1} of the molecule N_2 was determined from the relative intensities of rotational lines of the R-branch of the vibrational band $0-0$ of the N_2 molecule. The relation of rotational line intensity and intensity factors publisted in [6], [7] were applied in our calculations.

The rotational temperature T_{R2} of the OH radical was determined from the relative intensities of the first five rotational lines of branch Q_1, of the vibrational band $0-0$ of the transition $A^2\Sigma^+ \rightarrow X^2\Pi$ of a system of 306.4 nm. The rotation lines with the following values of quantum rotation numbers of the lower electronic state $X^2\Pi$ are involved : $J = (3/2,\ 5/2,\ 7/2,\ 9/2,\ 11/2,\ 13/2) \sim$ the "cold group" of rotational lines [8]. This rotational temperature T_{R2} has been corrected according to paper [9] to a temperature $T_{RN} = T_{R2}(1-\gamma T_{R2})^{-1}$ where $\gamma = 3.24\times10^{-5}$, which is in very good approximation with the temperature of neutral gas $T_N \leq T_{RN}$.

The electron temperature T_E was determined by means of the relative intensity of the atomic lines of Cu of wavelengths $\lambda = (521.82,\ 515.32,\ 510.55)\ nm$, [10].

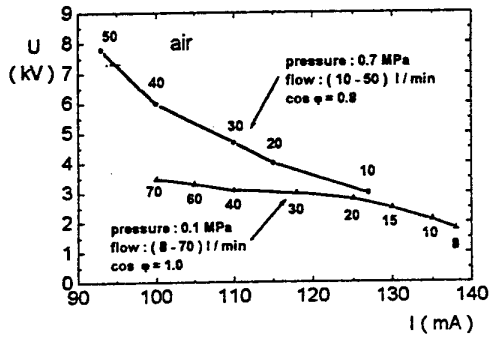

Figure 2: The V-A characteristic of the discharge $U = f(I)$. The flow of air is an independet parameter.

The molecular spectra of N_2, N_2^+, and OH were recorded only up to a pressure of $((0.3 \sim 0.4)MPa$ with varying intensity in various parts of the discharge. For pressures of $(0.5-1.1)MPa$ the intensities of N_2 and OH molecular spectra were very

	$N_2 = (C^3\Pi_u - B^3\Pi_g)$			$OH = (A^2\Sigma^+ - X^2\Pi)$		
air	$T_{R1}[K]$			$T_{RN}[K]$		
pressure	air, flow ~ [l/min]			air, flov ~ [l/min]		
MPa	25	34	48	25	34	48
0.1	3080	3060	3080	1140	1290	960
0.2	4960	4620	4330	1300	890	740
0.3	5500	5220	4080	1250	810	740
0.4	5850	5700	4200	-	-	-
0.5	-	-	-	-	-	-

Table 2: The rotational temperatures T_{R1} and T_{RN}.

weak in the preserved form of discharge and thus Cu atomic lines may be used for the T_E determination only. The temperatures presented in Table 1. and Table 2. were measured in the position where the light irradiation in the plasma is maximal. The measured values of the T_{VX}, T_{R1}, T_{RN} show that the gliding discharge plasma is nonisothermic in the whole interval of investigaeted pressures.

4. Acknowledgment.

This work was performed under the auspices of the Grant Agency of the Czech Republic, contract 202/96/0139.

5. References

[1] Czernichovski A. : Pure & Appl.Chem., Vol. 66, No.6, pp. 1301-1310, 1994.

[2] Tesař C., Janča J., Kapička V. : Proceedings XIth Symp. on Physics of Switching Arc, Brno, Sept. 26-30,(1994), p. 74-76.

[3] Floyd A.L. and King R.B. : Jour. opt.soc. Am., 45 (1955) p.249.

[4] Gilmore F.R., Laher R.R. and Espy P.J. : J. Phys. Chem. Ref. Data, Vol.21, No.5, 1962

[5] Kosoruchkina A.D. and Trekhov E.S. : ZhTF, Vol. XLV, No. 5, (1975), p. 1082.

[6] Kovacs I. : Astrophys. J. 145,(1966),p. 634.

[7] Kovacs I. :Rotational Structure in the Spectra of Diatomic Molecules, Akadémiai Kiadó, Budapest (1962).

[8] Meinel H. and Krauss L. : J.Quant. Spectrosc. Radiat. Transfer., Vol. 9, (1969), p. 443.

[9] Crosley D.R. and Lengel R.L. : J. Quant. Spectrosc. Radiat. Transfer., Vol. 15, (1975), pp. 579-591.

[10] Corliss Ch.H. and Bozman W.R. : Experimental transition prbabilities for spectral lines of seventy elements, Izd." Mir", Moskva 1968.

Detection of Desorbed Hydrocarbons by CN Chemiluminiscence in N_2 Flowing Afterglow at Low Temperatures

F. Krčma[1], J. Janča[2]
[1] Institute of Plasma Physics, Czech Academy of Science
Za Slovankou 3, 182 00 Praha, Czech Republic
permanent address: Faculty of Chemistry, Technical University
Veslařská 230, 637 00 Brno, Czech Republic
[2] Department of Physical Electronics, Faculty of Science,
Masaryk University, Kotlářská 2, 611 37 Brno, Czech Republic

1. Introduction

Emission of the CN red (A $^2\Pi$ - X $^2\Sigma^+$) and violet (B $^2\Sigma^+$ - X $^2\Sigma^+$) systems has been widely observed in the reaction of active nitrogen with hydrocarbons [1, 2, 3] and with partially or fully halogenated hydrocarbons [4]. In these systems electronically excited CN is formed preferentially in selected vibrational states of the upper electronic states (A $^2\Pi$, B $^2\Sigma^+$). Simultaneously the strong emission from the lowest CN(B $^2\Sigma^+$) vibrational levels is observed due to the resonance excitation energy transfer from the vibrationally excited ground state nitrogen molecules [5].

2. Experiment

In our experimental arrangement the flowing plasma reactor given in Fig. 1 was used.

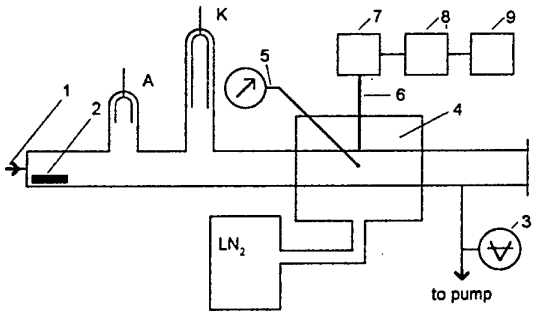

Figure 1: Plasma reactor and optical diagnostic setup
1: pure nitrogen inlet; 2: studied sample; 3: Pirani gauge; 4: cooled part of the reactor; 5: thermocouple; 6: optical fibre; 7: monochromator Jobin Yvon HR 320; 8: optical multichanell analyzer; 9: PC

Before the start of the observations the reactor has been prevacuated to pressure better then 10^{-3} Pa for more then 1 hour and thereafter we purified it by plasma combined with heating the reactor walls because the heavy hydrocarbon chains it was impossible to pumped. The polyhydrocarbon sample was placed inside the reactor before an active DC discharge so the desorbed hydrocarbon (fluorocarbon) molecules and the fractions of polymeric chains were thereafter disintegrated in the active discharge. By consequent recombination of C, N, and H atoms electronically excited simple radicals as CN and NH were created. The emitted spectra were recorded by optical multichanell analyzer. Due to the fact that in our previoused experimental works we observed very strong dependence of the CN band intensities on the reactor wall temperature at measuring point [6], this part of the reactor has been cooled by liquid nitrogen vapour down to 77 K. The effect on the spectra is demonstrated in Fig. 2. There it can be seen that at low temperature the CN and NO bands can be clearly visible though at room temperature they can not be resolute.

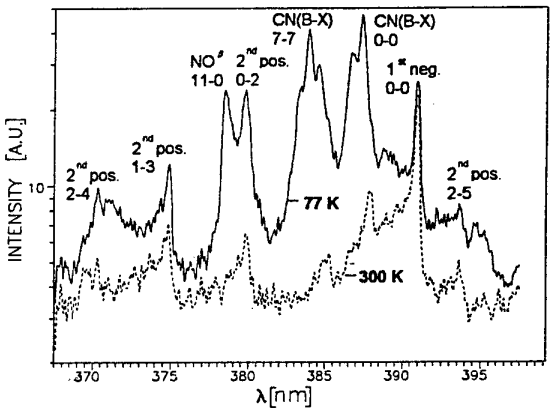

Figure 2: The spectra obtained at different reactor wall temperature with presence of a sample

3. Results

An experimental spectrum example of polyethylene sample inside the reactor is shown in Fig. 3 in comparison with the spectrum without presence of any hydrocarbon inside the reactor. It can be clearly seen the strong CN emission at sample presence. Due to the fact that both CN bands are overlapped by nitrogen 1st negative and 2nd positive bands it is necessary to study the intensities of CN bands with respect to a nonoverlaped nitrogen band. The nitrogen 2nd positive 0–2 band could be overlapped by one branch of NO$^\beta$ 11–0 band (see Fig. 2) so

we chose the nitrogen 2nd positive 1–3 band as a referential.

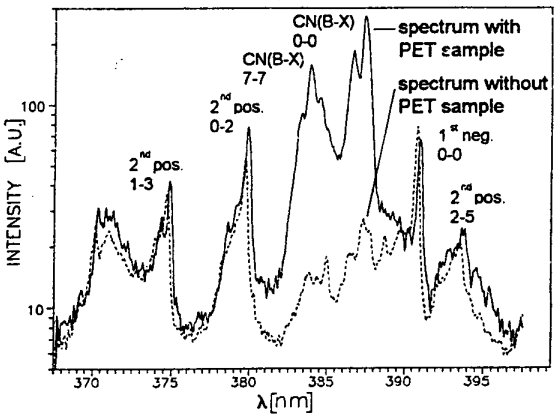

Figure 3: The spectra with and without presence of the PET sample at low wall temperature

It is clear that the desorbtion from the polymeric sample is not constant during the time; the light fractions are dominant during the first minutes while the heavy molecules are more stable. The time evolution of the destruction of different materials are given in Fig. 4 and 5.

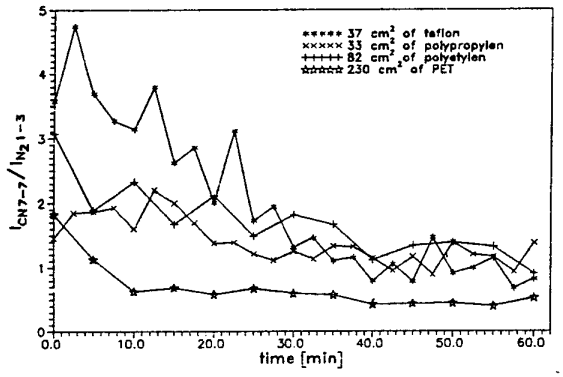

Figure 4: Intensities of the CN violet 7–7 band related to the intensity of nitrogen 2nd positive 1–3 band for different samples

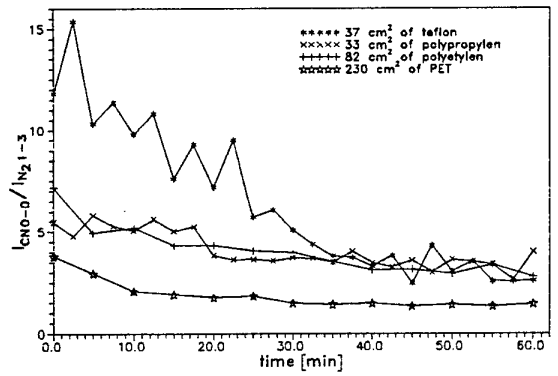

Figure 5: Intensities of the CN violet 0–0 band related to the intensity of nitrogen 2nd positive 1–3 band for different samples

It can be seen from these figures, that the related CN band intensities are quenched nearly exponentially during the first a few minutes and later they are nearly constant. In the case of teflon sample the higher initial intensities can be observed probably due to the not long enough initial purification (before this sample we tested a common gum which shows very high disintegration rate).

4. Conclusion

The intensities of the CN violet band system ($B\ ^2\Sigma^+ - X\ ^2\Sigma^+$) emitted from the cooled part of the flowing nitrogen afterglow can be used as a "fingerprint" for density determination of the desorbed hydrocarbon (fluorocarbon) trace species. The new method of chemiluminiscent spectroscopy at low temperatures is a relatively simple technique that is inexpensive, both in terms of initial expense and operating costs. It has detected molecular concentrations of hydrocarbons down to 10^{10} molecules·cm^{-3}. The method described can be used for fast determination of the desorption rate from solid polymer surfaces. Thus it can be applied in the food and packing industry as the test of stability of protective polymeric thin films on various substrates.

This work has been supported by Grant Agency of Czech Academy of Science, contract No. C 104 3601.

5. References

[1] N. Washida, D. Kley, K. H. Becker, W. Groth: J. Chem. Phys. **63** (1975) 4230

[2] F. Krčma, L. Hochard, A. Ricard: Acta Phys. Univ. Comenianae **35** (1994) 197

[3] A. Oumghar, J. C. Legrand, A. M. Diamy, N. Turillon: Plasma Chem. Plasma Process. **15** (1995) 87

[4] S. Cavadias, J. Amouroux, L. Hochard, A. Ricard: Plasma Chem. Plasma Process. **15** (1995) 221

[5] F. Krčma: Thesis, Brno 1995

[6] J. Janča, A. Tálský, F. Krčma, L. Hochard, A. Ricard: Plasma Chem. Plasma Process. **14** (1994) 197

Electron energy distribution functions spatially resolved in the expansion of a microwave discharge containing Ar-CH_4 gas mixture.

M. J. Cinelli, J. L. Jauberteau, I. Jauberteau, J. Aubreton and A. Catherinot.
URA 320 CNRS, UER des Sciences, 123 av A. Thomas, 87100 Limoges (France).
P. Lasgorceix.
Laboratoire d'Aérothermique du CNRS, 4 ter Route des Gardes, 92190 Meudon (France).

Expanding plasma can be obtained using different types of discharges (dc, ac, Rf, ...) [1], [2].
It can be used to generate and to carry out simple radicals without loss on the reactor wall. So the interest of such a plasma is both fundamental and technological.
The purpose of this work is to study the electron energy distribution function (EEDF) in a discharge sustained by a surface wave.

I. Experimental setup.

The experimental setup is schematically shown in figure 1. The microwave discharge (surface wave at 2.45 GHz) is produced within a surface-wave launcher connected to the entrance of the stainless steel expansion chamber. An Ar-CH_4 gas mixture is fed through a fused silica tube (external diameter = 24 mm, internal diameter = 20 mm) passing through the surface-wave launcher. The total pressure is maintained constant in the range 1 to 5 Torr using a Roots blower (70-700 m^3/hour) which allows a gas drift velocity of about 20 to 50 m/s. A stainless steel disk (diameter 60 mm) is located downstream in the expansion reactor and can be moved along the discharge axis. It is grounded and is used in order to delimitate sustained discharge region. At the end of the expansion, the plasma is covering all the disk surface.
Spatially resolved measurements are performed using both simple and double electrostatic probes. Simple probes are used to determine the EEDF, which are derived from the Druyvesteyn expression [3]. Double probes are used to determine both electron temperatures and densities. These parameters are deduced from the theory given by Johnson and Malter [4]. However, this convenient method is more appropriated for uncollisional sheath.
In order to obtain spatially resolved results, an horizontal clip with four probes fixed at 10 mm from each other is moved vertically along the expansion chamber axis, from the exit of the quartz tube (80 mm below the discharge center) to a downstream position (130 mm below the discharge center). The whole region contained between the quartz tube exit and the metallic disk can be observed.

II. Results and discussion.

Investigation have been performed in order to study the plasma propagation conditions in the expansion region when plama parameters are changing.
In a first approximation [5], the wave propagation (plasma propagation) is obtained when the electron density is larger than a critical value given by the condition

$$\omega_p > \omega.(1+\varepsilon_v)^{1/2}$$

where ω and $\omega_p = (n_e e^2 / m_e \varepsilon_0)^{1/2}$ are respectively, the microwave angular frequency and the electron plasma angular frequency. ε_v is the relative permittivity of the tube wall.
In our case ($\omega/2\pi$ = 2.45 GHz) the plasma propagation condition is obtained for $n_e > n_{ec} = 3.6.10^{11}$ cm^{-3}.
Results show that when this condition is complied, the probe signal is undisturbed and the EEDF deduced from the probe characteristic curves (I=f(V)) is generally quite well described using a Maxwell distribution function (see figure II). However, when the electron density is lower than n_{ec}, the probe signal is very noisy and also strongly decreasing. The EEDF is now corresponding to high energy electrons and cannot be described using a Maxwell distribution function. Consequently, the electron temperature and density measured using a classic method [4] are not available in this case.
Figure III shows the change in EEDF with increasing % CH_4 mixed to Ar. The total pressure is kept constant and equal to 2 Torr and the microwave power is fixed to 300 Watt. Measurements are performed at 120 mm downstream below the discharge center. For a low % CH_4, the EEDF can be described using a Maxwell distribution function. The mean electron energy is low (lower than 0.3 eV) and decreases with increasing % CH_4, because of inelastic collisions between electrons and methane molecules. When the % CH_4 is larger than 0.6%, the EEDF is strongly disturbed and cannot be described using a Maxwell distribution function.

[1] R. Darchicourt, E. Bloyet, C. Boisse-Laporte, A. Granier, Ph Leprince , J. Marec : 8th International Symposium on Plasma Chemistry, Tokyo, September 1987.

[2] M. J. de Graaf, R. P. Dahiya, J. L. Jauberteau, F. J. de Hoog, M. J. F. van de Sande, D. C. Schram : J. Phys. Colloq. 18, C5-51 (1990).
[3] R. I. Cherry, T. D. Whitmore : Diamond and related Materials 4, 524-527 (1995).
[4] E. O. Johnson, L. Malter : Phys. Rev. A80, 1 (1950).
[5] L. Thomas, J. L. Jauberteau, J. Aubreton, A. Catherinot, A. R. de Souza, M. J. Cinelli : Appl. Phys. Lett. 64, 20, (1994).

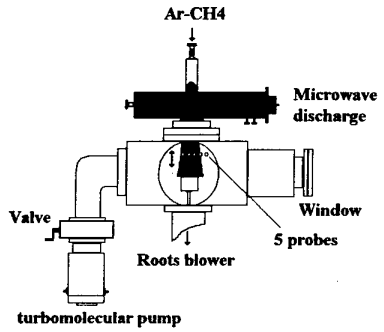

Figure 1 : Experimental setup.

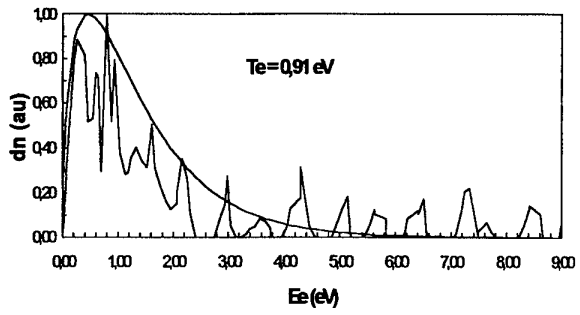

Figure 2 : EEDF measured in a pure argon plasma expansion (1 Torr, 180 Watt); The distribution function can be described (in a fisrt approximation) using a Maxwell distribution with Te=0.91 eV (smooth curve).

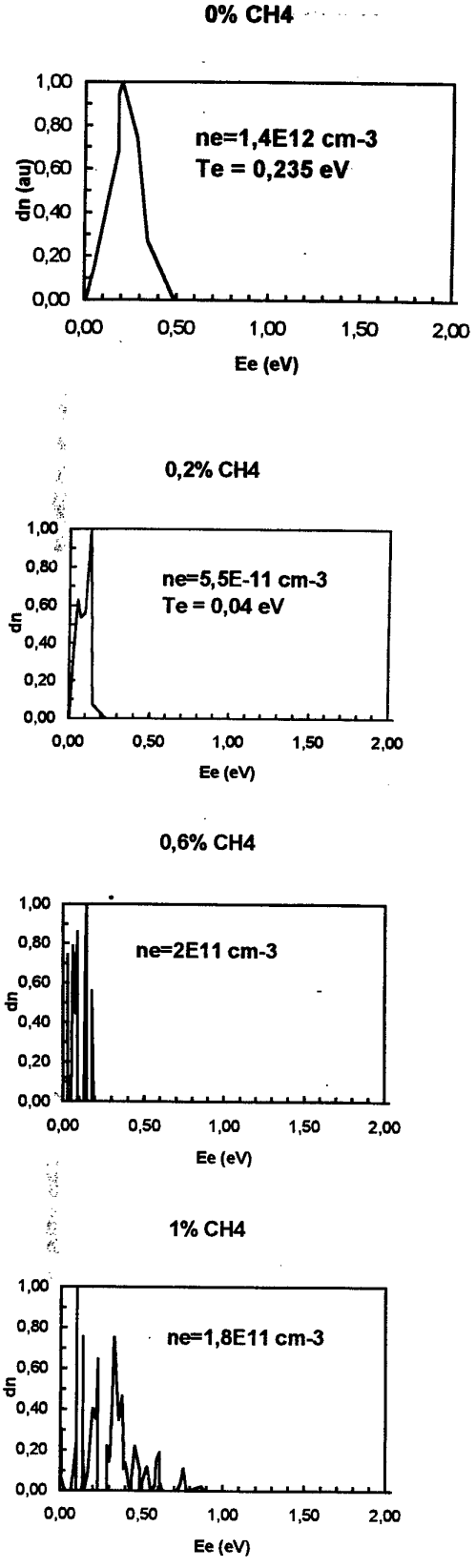

Figure 3 : EEDF measured in an Ar-CH_4 gas mixture (2 Torr, 300 Watt), versus % CH_4.

Plasma parameter measurement from the probe temperature

Masashi Kando, Yoshinori Kinoh and Akihiro Etoh
Department of Electrical and Electronic Engineering
Shizuoka University
Johoku 3-5-1, Hamamatsu 432, Japan

1. Introduction

The probe temperature is considered to reflect the plasma parameters such as electron temperature, plasma density and plasma potential because the probe in the plasma collects or emits the electrons, which transport their kinetic energy to the probe, depending on the probe bias potential. This permits to measure the plasma parameters from the probe temperature.

In the present paper, we will propose to adopt the probe temperature to determine the plasma potential and electron temperature. The main advantage of the present method is the reduction of the disturbance caused by the displacement current which flows into the probe together with the conduction current in RF discharge plasmas. To confirm the possibility of this method, the numerical calculation of the probe temperature is carried out by solving the equation of the heat conduction as a function of probe bias voltage. As a result, it is clarified that the probe can be heated by electron bombardment in the plasma with the density higher than 10^{11} cm^{-3} up to enough high temperature to emit thermionic electron from the probe and that there exist two abrupt changes in the probe temperature with respect to the probe bias voltage. It is concluded that the probe temperature measurement will provide the reliable data concerned with electron temperature, density and plasma potential in the plasma.

2. Calculation of the probe temperature

2.1 Fundamental equation

The temperature of the probe in the plasma is governed by the well-known equation of the heat conduction. In the present calculation, the heat convection loss is neglected because the plasma is assumed to be excited at the pressure lower than a few Torr. Since the probe is immersed into the high density plasma, the probe will be able to be heated by the electron bombardment to such a high temperature that the electronic cooling will dominate over the other loss processes like radiation and heat conduction losses.

As for the power gain that the probe will obtain from the plasma, the electron and ion bombardment are taken into account as follows:

a) in the case that the probe potential V_b is higher than the plasma potential V_p, electrons will be collected by the probe together with kinetic and potential energies. Thus, the probe obtains the power presented by $J_eS(V_b - V_p + \phi + \kappa T_e/e)$, where J_e is the electron saturation current density, S is the probe surface, ϕ is the work function of probe material, T_e is the electron temperature, κ is Boltzmann constant and e is the electronic charge.

in the opposite case of a), i.e., $V_b < V_p$, the bombardment heating by the ion, expressed by $J_iS(U - V_b + V_p - \phi + \kappa T_i/e)$ should be considered in the calculation in addition to that by the electron, modified by multiplying Boltzmann factor $\exp\{e(V_b-V_p)/\kappa T_e\}$, where J_i is the ion saturation current, U is the ionization potential of the atom of the gas species and T_i is the ion temperature.

2.2 Numerical calculation and results

The equation of heat conduction in the steady state has been numerically calculated by Newton-Raphson method under the following assumption.

1) the electrons reaching on the probe surface from the plasma are perfectly absorbed into the probe.

2) the ions coming on the probe recombine with the electrons inside the probe material.

3) thermionic electrons are not depressed to emit from the probe surface by the plasma potential around the probe.

4) collisions of electrons in the probe sheath are neglected.

The numerical calculation are carried out for the probe of 5 mm in diameter and 0.1 mm in thickness and a Cu lead wire of 0.5 mm in diameter and 20 cm in length, assuming the emissivity of the probe made of thoriated tungsten of 0.6.

In Fig.1, the relation between the probe temperature T and V_b-V_p for T_e of 5.0 eV is shown as a function of the plasma density n. It is found that there exist two steps in the curve with V_b increasing, i.e., one is V_b-V_p = -5 V and the other is V_b-V_p = 0 V. The first step in the curve is originated by the remarkable change of the power which the electrons in the plasma with T_e > 5.0 eV carry to the probe, while the second step is caused by the electronic cooling. The heights of both steps increase with n increasing and ϕ decreasing since the amount of power transported to the probe by the electrons in the plasma is proportional to n. Therefore, it is possible to determine the plasma potential, electron temperature and density by measuring T-V_b characteristics.

As a matter of fact, the unnatural discontinuous changes in the T-V_b curve will be relaxed by the

fluctuation of the space potential in the plasma. The slope in the curve around the steps may give the information of the plasma potential fluctuations.

By the way, the conventional emissive probe is heated by external power to enough high temperature to emit the thermionic electrons. To compare it with the present method, the effect of external probe heating on the T-V_b curve has been examined. As shown in Fig.2, the first step becomes obscure, while the second step becomes clearer, when the external power to the probe P increases. These mean that the conventional emissive probe is limited to the measurement of the plasma potential.

Finally, the amount of thermionic electron density is estimated to discuss the effect of space potential caused by themselves, which may prevent the thermionic electron emission. The thermionic electron density is around 10^{13} cm^{-3} at the maximum, which is one order higher than the plasma density. However it is considered that most thermionic electron will be immediately recombined with ions because of the small size of the probe. Thus, the negative space potential created by the thermionic electron will not seriously affect on T-V_b curve.

In conclusion, the emissive probe made of the low work function material can be a simple and promising tool for the plasma parameter measurement, if it is applied in the plasma with a high density. The main advantage of the present method exists in fact that the probe temperature measurement is not disturbed by RF electric field as much as the probe current measurement.

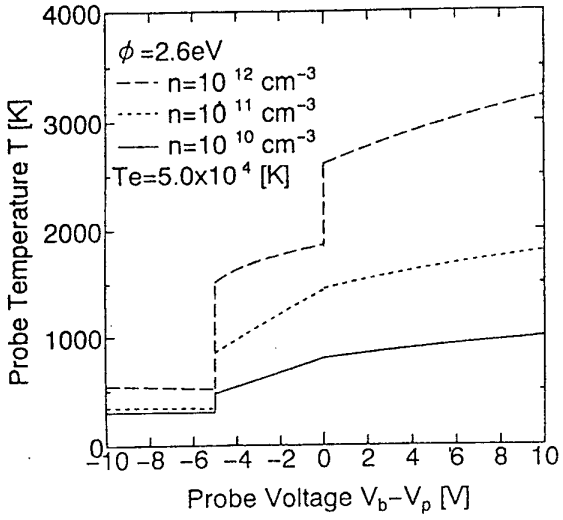

Fig.1 Probe temperature T versus probe voltage V_b-V_p as a function of plasma density n. Probe size is 5 mm in diameter and 0.1 mm in thickness.

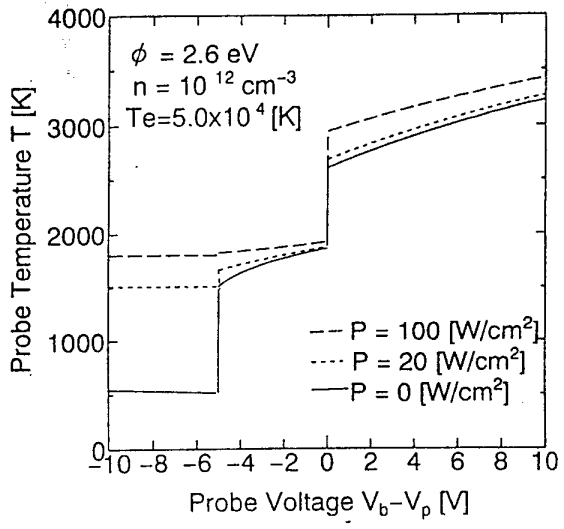

Fig.2 Probe temperature T versus probe voltage V_b-V_p as a function of external input power for probe heating. Probe size is same as in Fig.1.

Influence of the retarding potential of a collector and parameters of a plasma flow on the deposition of accelerated isotope ion component for ICR-separation method

A.I.Karchevsky, E.P.Potanin

Kurchatov Institute Russian Research Centre, Moscow, 123182 Russia

1.Introduction

The influence of the retarding potential of collector and plasma flow parameters on extracting of the accelerated ion component in ICR-isotope separation method is considered. The idea of ICR-method is based on the isotopically selective resonant acceleration of ions of a target isotope in plasma flow with the help of the special RF-antenna (2) (Fig.1) at presence of the homogeneous

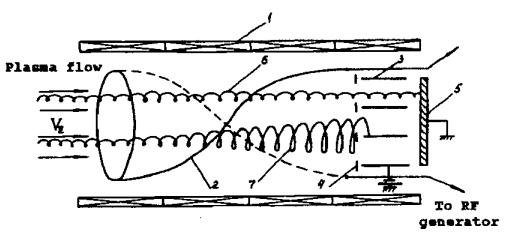

Fig.1. Principal scheme of separation.

longitudinal magnetic field, created by coils (1) [1]. The separation of the accelerated ions (7) from cold ions (6) can be achieved by means of the specific collectors of "heated" particles (3), which consist of plates placed parallel to both the magnetic field and the longitudinal plasma flow [2].

2. Method of calculation

In [3] the technique of calculation of ion flows on collecting plates was offered. The transverse-energy distribution functions of particles were calculated first, then the ion flows onto the collector were numerical integrated over longitudinal (v_z) and transverse ($v_\perp$) (with respect to the magnetic field) velocities and also over the transverse coordinates of ion guiding centres y_0 in the plane of the forward screen of the collector (4). The plate (5) is used for extraction of the waste. In [4] this technique was modified in such a manner that originally it were defined the ion effective temperatures and then the flows were calculated. Besides, unlike [3], the analytic determination of the allowable range of ion guiding centre coordinates y_0 was made. In the given work the influence of the positive retarding potential U is taken into account on the extraction of accelerated ions from the plasma flow for the isotope mixture and case of "shifted" longitudinal velocity distribution functions is considered. The value of the ion flow on a collector j is calculated by integration over allowable range of particle velocities and over guiding centre coordinates of ions

$$j = \int f \omega_c v_\perp dv_\perp dv_z dy_0 , \qquad (1)$$

where ω_c is the ion cyclotron frequency.

The calculations were carried out for the next parameters of ICR-installation: the natural ^{6}Li -^{7}Li isotope mixture with the initial concentration C_0=0.08; the magnetic induction is B_z=0.25 T; electric-field amplitude in the bulk plasma is E_0=54 V/m; the heating system length L is 0.8 m; the wave-length of RF-field is 0.8 m, the initial ion temperatures $T_{\perp 0}$ and $T_{||0}$ are 5 eV and 10 eV, accordingly.

3. Results and discussion

Fig.2 shows the dimensionless flow of $^6Li^+$ ions j/j_0 versus longitudinal coordinate z for the various retarding potentials U.

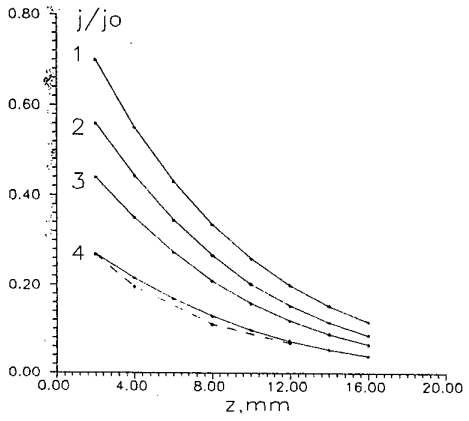

Fig.2. Dimensionless ion flow j/j_0 versus longitudinal coordinate z (in millimeters) for various retarding potentials U: 1 - U=0; 2 - U=10V; 3 - U=20V; 4 - U=40V. The dashes line - evaluation of work [3].

The calculation dependences agree with experimental results [5,6].
Fig. 3 shows average on the length 15 mm of the lighter isotcpe concentration versus retarding potential U.

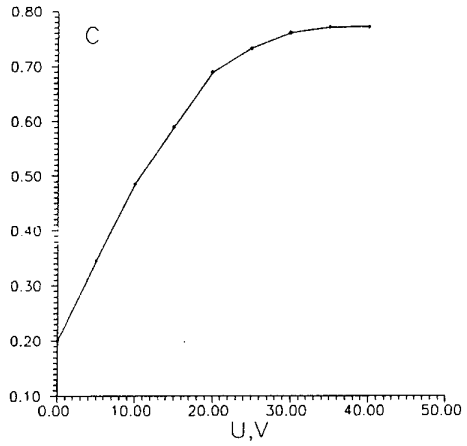

Fig.3. The concentration of ^6Li C versus the retarding potential U.

It was supposed above, that the longitudinal -velocity distribution function is Maxwellian and there are not enough ions, moving in the opposite direction to a source. In a real source due to of possible action of acceleration mechanisms the most approached in practical situation is the "shifted" Maxwellian distribution [2].
Fig.4 shows the z-coordinate profiles of the ratio j/j_0 for various "longitudinal"temperatures.

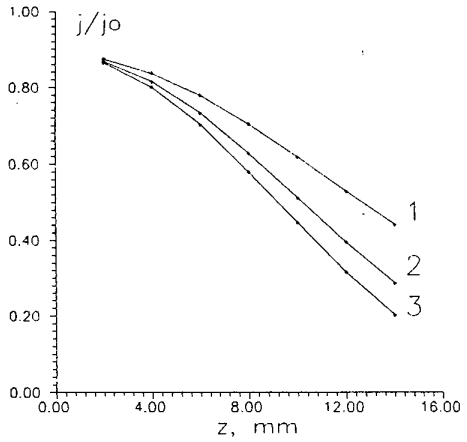

Fig. 4 The dimensionless ion flow j/j_0 versus the longitudinal coordinate z at various values of the parameter $T_{||}/T_{||0}$ for shift parameter $v_0=10^4$m/c.(1 - $T_{||}/T_{||0}=1$; 2 - $T_{||}/T_{||0}=0.25$;3 - $T_{||}/T_{||0}=0.1$).

Figure 5 shows z-coordinate dependences for the flow of $^6Li^+$ ions onto the collecting plate for $T_{||}/T_{||0}=1$ and various v_0:. 1 - $v_0=10^4$ m/c; 2- $v_0=2500$ m/c; 3 - $v_0=0$.

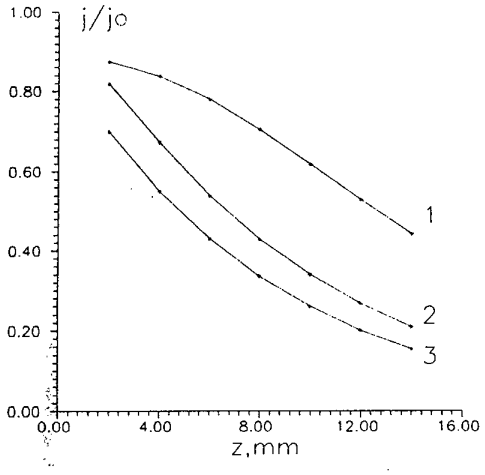

Fig.5. Dimensionless ion flows j/j_0 versus longitudinal coordinate z for various v_0.
(1 - $v_0=10^4$ m/c; 2- $v_0=2500$ m/c; 3 - $v_0=0$)

References

[1] J.M. Dawson., H.C. Kim., D. Arnush. et al. Phys.Rev.Lett., 37 (1976) 1547
[2] P.Louvet., Separation phenomena in liquids and gases. Second Workshop, Versailles, 1 (1989) 5
[3] A.L.Ustinov, Preprint of Kurchatov Inst. Russ. Res. Centre, Moscow, N5354/6 (1991)
[4] A.I.Karchevsky, E.P.Potanin., Fiz.Plazmy, 21 (1995) 416
[5] A.I.Karchevsky, V.S.Laz'ko, Yu.A.Muromkin et al., in: Proc.20th IGPIG, Pisa , 1 (1991) 331
[6] A.I.Karchevsky,V.S.Laz'ko,Yu.A.Muromkin et al., Plasma Phys, Rep.19(3), March (1993)

DETERMINATION OF TEMPERATURE PROFILES AND PARTICLE NUMBER DENSITIES IN HIGH-PRESSURE MERCURY AND MERCURY IODIDE PLASMAS

E. Kindel, C. Schimke, H. Schöpp and M. Kettlitz
Institute of Low Temperature Plasma Physics e.V. Greifswald, Robert-Blum-Str. 8-10, D-17489 Greifswald, Germany

1. Introduction

The knowledge about the radial temperature distribution in high pressure discharge lamps is of great importance for the physical understanding of this discharge type. It is for example necessary for the calculation of particle density distributions, the radiative transfer as well as the radiation output.
This paper presents two independent methods for the determination of temperature distributions in such discharges.

2. Experimental methods

2.1 Emission spectroscopy

Frequently the temperature profile is spectroscopically determined from the absolute measurement of the spectral emission coefficient of the optically thin mercury lines at 577/579 nm. Assuming local thermodynamic equilibrium (LTE) the emission coefficient reads:

$$\varepsilon_{ik} = \frac{1}{4\pi}\frac{hc}{\lambda} g_i A_{ik} \frac{p_0}{kT} \exp\left(\frac{-E_i}{k_B T}\right)$$

h - Planck's constant, T - temperature, g_i, A_{ik}, E_i - statistical weight, transition probability, excitation energy of the upper level, p_0 - pressure, k_B - Boltzmann constant, c - velocity of light, λ - wavelength.

Besides the atomic data, information about the pressure is essential to determine ε_{ik} . The information is received by a laser interference method. Finally, if the pressure is known the temperature is calculated by an iterative procedure from the emission coefficient of the lines at 577/579 nm [1].

2.2 Hook method

The hook method is an interferometric measurement of absolute population densities of excited atoms and atoms in the ground state. The physical background of this method is the interferometric measurement of the anomalous dispersion in the vicinity of an absorption line, that causes a rapid change of the refractive index. In this region distortions in the interference fringes occur. They form the so-called hooks. The wavelength distance Δ between these hooks (from minimum to maximum) at the absorption wavelength λ_0 depends on the population density and has to be measured.
The population density of the lower level is given by:

$$n_k = \frac{\pi K \Delta^2}{r_0 l f_{ik} \lambda_0^3}$$

r_0 - classical electron radius, l - absorption length, f_{ik} - oscillator strength, K - hook constant.

A more detailed description is given in [2].

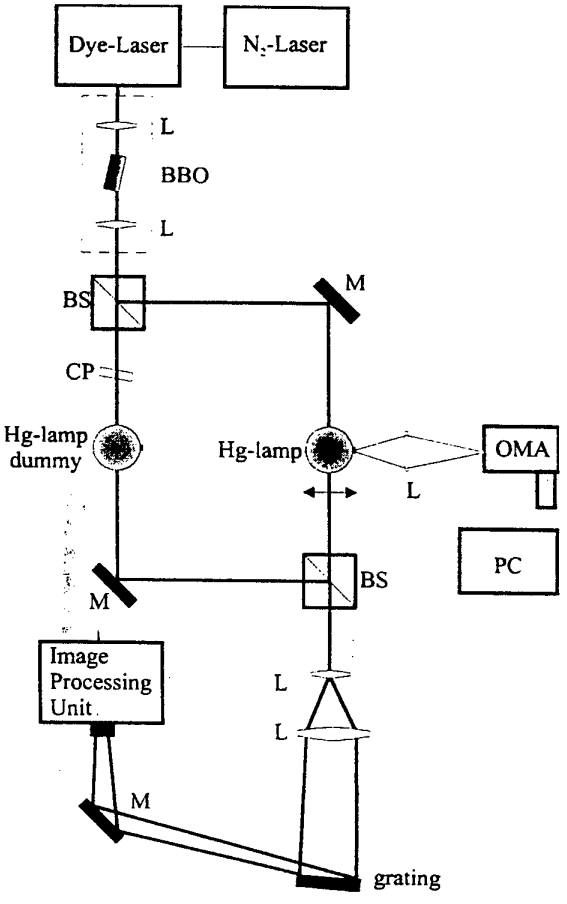

Fig. 1 Experimental set-up, BS - beamsplitter, L - lens, M - mirror, CP - compensating plate

By measuring the population densities of the ground (n_0) and metastable (n_k) states and using the Boltzmann formula we can calculate the temperature distribution:

$$T(r) = \frac{E_k}{k}\left[\ln\left(\frac{n_0(r)\, g_k}{n_k(r)\, Q}\right)\right]^{-1}$$

Q - partition function.

2.3 Experiment

The experiments were performed in two different discharge systems: mercury and mercury-iodide arcs. Figure 1 shows the experimental set-up. In the centre the observed mercury discharge is seen which was operated with 50 Hz and a power of 240 W. The lamps consist of quartz and have a diameter of 18 mm.
The radiation of the lamp was imaged to a spectrograph with a gated CCD-array as detector. In both cases from the recorded side-on intensity distribution of the optically thin Hg lines at 577/579 nm ε_{ik} was determined carrying out an Abel inversion.
The main part of the arrangement consists of an Mach-Zehnder interferometer and a dye laser as a background light source. The discharge lamp can be moved in radial direction via a translation element to investigate different zones of the discharge.
For the determination of the density of mercury atoms in the ground state the transition 6^3P_1 - 6^1S_0 (λ = 254 nm) is used. A BBO II crystal is applied to create radiation in the UV-region at 254 nm.
The population densities $n_k(r)$ in the metastable 6^3P_2 and 6^3P_0 levels of mercury are measured as a function of the radius and the discharge current. That can be done using the Hg transitions at 7^3S_1 - 6^3P_2 at 546 nm as well as the 7^3S_1 - 6^3P_0 at 405 nm.
The whole interferogram is achieved in scanning the line profile in steps of 0.2 nm width (see fig. 2).

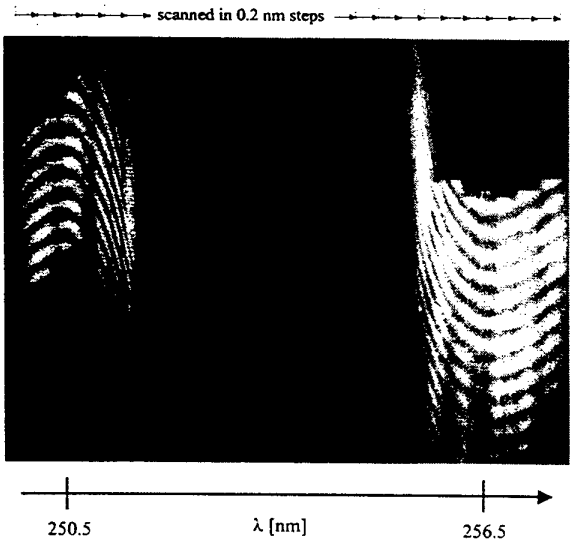

Fig. 2: Typical interferogram close to the 254 nm absorption line in a mercury high pressure lamp at 240W.

3. Results

From the uv measurement we got a radial averaged density of the ground state $n_0 = 6.1*10^{18}cm^{-3}$ for the Hg lamp, which is in good agreement with the calculated value of $7.1*10^{18}cm^{-3}$ from the ε_{ik} measurements.
Fig. 3 shows the results of the temperature measurements of the Hg and HgI_2 discharges obtained for the two applied methods. The circles (HgI_2) and the squares (Hg) stand for the hook method and the full (HgI_2) and the dashed line (Hg) for the emission method. It can be seen that the curves of both methods agree quite well concerning the absolute values as well as the shape of the temperature profiles. The measured temperatures in the discharge axis are between 6000 and 7000 K. They differ for both discharges in their height as well as in their shape. The discharge containing iodides is more constricted but has a higher temperature in the axis. The temperature profile of the pure mercury discharge is flatter than that with iodide. That's why this arc is a bit more extended to the wall and can be observed closer to the wall.

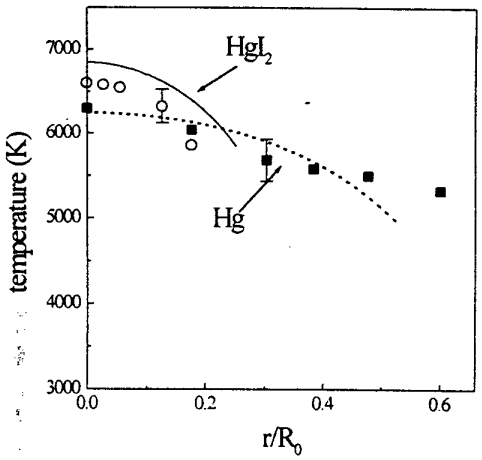

Fig. 3: Plasma temperature of Hg and HgI_2 arcs versus the reduced radius. The lines refer to the emission measurements and the points to the hook method.

[1] G. Hartel, H. Schöpp, J. Phys. D: Appl. Phys. **29** (1996), 2881
[2] E. Kindel, C. Schimke, Contrib. Plasma. Phys. **36** (1996) 6, 711

RADIATIVE SPECTRUM OF HYDROGEN IN THE NONEQUILIBRIUM GAS-DISCHARGE PLASMAS AND ITS APPLICATION FOR GAS TEMPERATURE DETERMINATION

A.V.Chebotarev, I.A.Kossyi, D.K.Otorbaev*, V.P.Silakov
General Physics Institute of Russian Academy of Sciences, Moscow, 117942, Vavilov Str. 38,
* Eindhoven University of Technology, Eindhoven, Netherlands.

The possibility for direct measurements of the gas temperature by recording the radiation spectrum of the atomic lines is of considerable interest for studying fast nonequilibrium discharges in dense gases. This possibility arises owing to the fact that very efficient inelastic interactions involving highly excited atoms lead to the equalization of the temperatures for the distribution function of the electronically excited atoms at upper levels. In the case of two-temperature plasma, the problem of whether it is possible to identify the temperature for the corresponding distribution function is questionable and requires additional investigations, because both light and heavy plasma components take part in the formation of the distribution function of the excited atoms. Estimates show that, in a hydrogen plasma, inelastic interactions between excited atoms and heavy plasma particles can occur as efficiently as those between excited atoms and background electrons. In this connection, using a hydrogen plasma as an example, we consider the effect of inelastic collisions of the excited hydrogen atoms with electrons, atoms and molecules on the formation of the distribution function of electronically excited H(n) atoms.

For this purpose we use the kinetic scheme have been described in [1] for the plasma-chemical processes occurring in a nonequilibrium discharge in hydrogen. In order to find distribution function of the electronically excited H(n) atoms,we use a set of balance equations in which we take into account cascade radiative transitions, inelastic collisions of the excited hydrogen atoms with electrons, H_2 molecules and hydrogen atoms H(n=1) in the ground electron state, the ionization of the excited hydrogen atoms by electron impact and the processes of the excitation of H(n) levels through reactions of three-particle recombination of H^+ ions and of photorecombination and dissociative recombination of H_2^+ and H_3^+ ions. We took into account 25 levels of a hydrogen atom.

We have analyzed the effect of the quenching of the excited levels of hydrogen atoms by heavy plasma particles on the distribution function of H(n) in a purely atomic system in the post-discharge period. This situation was studied by de Graaf in [2], where the absolute concentrations of the excited H(n) atoms in the atomic flux of a recombinative plasma were measured by recording the radiation from the Balmer series of atomic hydrogen lines. It was noted that, in some cases, the effective temperature for the distribution of the H(n) atoms (calculated from the slope angle of the distribution function for $n \geq 8$) can differ substantially from the electron temperature obtained by Langmuir probe.

In order to identify the mechanisms for the formation of the distribution of H(n) atoms whose effective temperature T_{eff} differs markedly from the electron temperature, we calculated the quasisteady distribution function of the excited H(n) atoms by using the "atomic" model (model which incorporates as a heavy particles only atoms).

In calculations the unknown values of the gas temperature, the concentration of heavy particles $n_{(H(n=1))}$ and the electron concentration were varied in a wide range. A comparison between the calculated and experimental dependencies of the population of electronically excited levels of hydrogen atoms is made in Fig.1, in which $H(n)/g_n$ are plotted as a function of E_{ni} (where E_{ni} and g_n are, respectively, the ionization energy and the statistical weight factor of the atomic level with quantum number n). In this case, the measured temperature and concentration of the electrons were T_e = 0,31 eV and $n_e \cong 2{,}8.10^{12}$ cm^{-3}

The best agreement between the calculated and experimental distribution of H(n) atoms at n = 3,....,13 levels was obtained for T_g = 850 K, $n_H = 3{,}42.10^{15}$ cm^{-3} and $n_e = 4{,}3.10^{12}$ cm^{-3}. In this case, the effective temperatures for the both distributions at n = 8-13 levels are the same (0,1 eV) and are lower than the electron temperature by a factor of three.

The effective temperature for the calculated distribution of H(n) atoms is $T_{eff} \equiv T_g$ because the excitation and quenching of hydrogen atoms at levels higher then n=6 are primarily governed by their collisions with heavy particles.

Analysis of the mechanisms for the formation of the distribution function of excited hydrogen atoms allows us to draw a conclusion that the proposed method of measuring the temperature from the radiation spectrum of the atomic lines of hydrogen atoms can be used in a fairly wide ranges of the gas temperatures and of the electron concentration.

This work was supported by INTAS (Project INTAS-94-2922), by the Russian Foundation for Fundamental Investigations (Project No 96-02-16419) and NATO (NATO HTECH.LG 951514).

References.

[1] A.A.Matveyev and V.P.Silakov, Plasma Sources Sci. Technol., v. 4, 1995, pp 606-617

[2] M.J. de Graaf, A new hydrogen particle source, Technical University of Eindhoven, Eindhoven, Netherlands, 1994, 130 p.

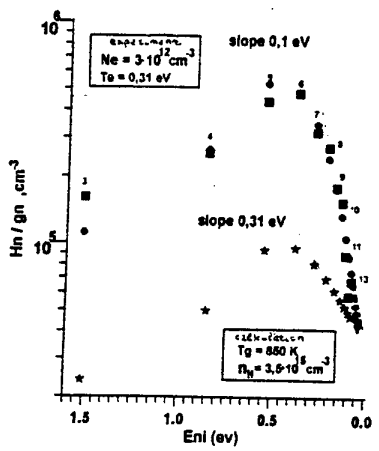

Fig.1.
Population of the excited states of hydrogen atom: ■ - experimental data [2]; ● - results of calculations made in the framework of "atomic" model with taking into account of the inelastic collisions of excited atoms with heavy particles for $n_H = 3{,}42.10^{15}$ cm^{-3}, $T_g = 850$K, $T_e = 0{,}3$ eV and $n_e = 4{,}3.10^{12}$ cm^{-3}; ★ - the similar calculations made without taking into account of inelastic collisions with heavy particles.

A diagnostics laser apparatus for investigation of plasma in a wide range of electron densities

O.A. Bashutin, E.D. Vovchenko, V.A. Kurnaev, A.S. Savjolov, and Lee Zh. H.
Department of Plasma Physics, Moscow State Engineering and Physics Institute
115409, Moscow, Russia

Results of a work on development of laser diagnostics complex for plasma investigation in wide range of electron densities are presented. Diagnostics apparatus consists of two laser units with the ratio between the laser wavelengths ≈10. They can be used independently or simultaneously.

1. Infrared He-Ne laser interferometer

For investigation of low density plasma or a lowdensity part of ingomogeneous plasma we have succesfully used an interferometer based on He-Ne laser with soft competition of two normal axial orthogonal modes of the resonator with homogeneous line of amplification (λ_1=3.39 μm). It's main merits are: linearity of the working part of the apparatus function and possibility of control of the sensitivity of measurements with the factor of 10^2 without replacement and readjusting of optical elements. The schematic diagram of the two-mode interferometer is presented in fig. 1. Its resonator is formed by the mirrors M_1 and M_2. Between them there are placed an active element with He-Ne mixture, a phase anisotropy element K and the investigated plasma. One of the competition modes is selected by the polarized P_1 and radiation of this mode is registrated by the photodetector D_1. Plasma inside the resonator M_1M_2 having linear electron density N_el causes proportional changing of the optic length of the resonator Δ(nL) and changing of the electric signal on the detector D_1 that equals ΔV (where n is refractive index and L is distance between mirrors M_1 and M_2). In regime of soft two-mode competition $N_el = k\cdot\Delta V$. Coefficient k depends on resonator phase anisotropy, that can be changed using two wedges (K in fig.1). Improvement of the interferometer was made to enhance the measurement sensitivity and to make the control of the device characteristics more convenient. To protect the resonator M_1M_2 from influences of outer factors, the regulation system of its length L based on highly stabilized visible He-Ne laser (λ_2=0,63 μm) was developed. Red radiation reflected back from the resonator M_1M_2 is registrated by the photodetector D_2, voltage signal is amplified and applied to piezocorrector that changes L. The feature of this system is in frequency modulation of reference radiation with the wave length λ_2. To decrease the level of the gas discharge tube noise of the infrared laser, simultaneous exitation of its active media by direct current and UHF-radiation with frequency ~360 MHz was used. The noise level of the output laser radiation was decreased by the factor of 10^2 and the radiation intensity was increased by 30%. Change of laser interferometer sensitivity is connected with change of resonator phase anisotropy. The later is usually achieved either by mutual rotation of two quarter-wave phase plates (placed between M_1M_2) around their own axis or by mutual transportation of two phase wedges. The phase-anisotropy remote controlled element based on electro-optical crystal made of $LiNbO_3$ has been proposed and developed for these experiments. An general ellipsoid of refractive indexes of this crystal in major rectangular coordinate system is defined by an equation of the form:

$$a_{10}(x^2+y^2) + a_{30}z^2 = 1,$$

where a_{ij} - polarization constants (optic axis lies in axis Z). There are three alternative of mutual orientation of axis Z, electric field strength E and laser axis, when major ellipsoid axis are not swung by electric field. One of them was choosen in the way that the crystal optic axis and the optical laser axis were aligned, but the electric field was perpendicular to both of the axis. In this case the equation reduces to the following form:

$$(a_{10} - r_{22}E)x^2 + (a_{10} + r_{22}E)y^2 + a_{30}z^2 = 1,$$

where r_{22} - linear electro-optical affect coefficients.

As we can see an anisotropy is not introduced in the resonator if the electric field E = 0. The dependence of the frequency splitting of own axial resonator mode on the electric strength is described of expression:

$$\nu_{12} = (cd/L\lambda)n_o^3 r_{22}E,$$

where d- crystal length in direction of optic axis and n_o - refractive index of crystal for 0-wave.

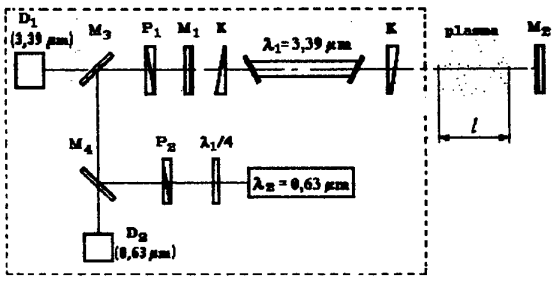

Fig. 1. The schematic diagram of the two-mode laser interferometer

Voltage variation between 0 - 1,5 kV lead to variation of sensitivity within the factor of 40 for the crystal used. The value $N_e l_{min} = 10^{12}$ cm^{-2} was achieved using a two-mode laser interferometer. We can note that the two-mode laser can be used as a two-frequency source of radiation for various interferometer types with controlled difference of the two frequencies in the interval of ~ 100 MHz.

2. Ultraviolet pulse diagnostics

Along with infrared diagnostics we discuss some results dealt with application of ultraviolet nitrogen laser (337 nm) for investigation of rapidly changing dense plasma. Such laser apparatus with either Mach-Zehnder or Bates interferometers is able to measure plasma electron densities in the range $N_e = 10^{16}$-10^{21} cm^{-3}. However, only shearing interferometer system is promising for investigation of nonhomogeneous plasma with the electron densities higher than 10^{19} cm^{-3}. As early as in 1990, we developed a diagnostic TEA N_2 laser and investigated its performance. Then, this laser was used in our experiments as a light source with the subnanosecond pulse width [1,2]. Its design is simple as well as inexpensive and especially useful for multichannel apparatus. TEA N_2 laser consists of a low impedence Blumlein pulse generator and transverse HV-discharge system. Some efforts were made to improve efficiency of the laser. For this purpose physics of formation of nanosecond glow discharge in TEA N_2 laser was investigated [3]. We obtained experimental data about the regimes of transition between spark and glow discharge as well as about dependence of the laser output on the overvoltage between the electrodes. As a matter of fact, fast risetime of the discharge circuit leads to increase in N_e and this is the main factor which determines the efficiency. In previous nitrogen laser designs electrodes were made of copper or brass. However, in order to achieve the maximum power at a given cavity length and overvoltage, we tested various electrode materials and modificated the cathode discharge surface by plasma technology.Use of this cathode with large electron emissiviti led to two-fold increase in power. Also we investigated post - breakdown prosesses which conditioned the highest repetition rates. Results of behavior of the N_2 atmospheric pressure discharge at its late stages as well as gas movement at the stage when the discharge current is over were obtained using shadow photography. Fig. 2 illustrates these results.

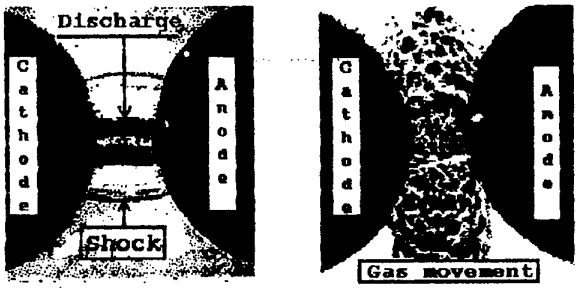

Shock formation (τ=1,6 μs) Turbulent cooling (τ=74 μs)

Fig. 2 Imaging of post-breakdown processes in TEA nitrogen laser.

3. References

1. Bashutin O.A., Vovchenko E.D., Savjelov A.S. et al. Dynamics of plasma jet formation using a quasistationary discharge at atmospheric pressure/ Proc. XX Conf. on Phenomena in Ionized Gases.Pisa, Italy, 1991, vol. 6, 1375-1376.

2. Vovchenko E.D., Korolev L.V. et al. Investigation of plasma dynamics and post-discharge processes in the pulse arc at atmospheric pressure / Proc. XX Conf. on Phenomena in Ionized Gases,Pisa, Italy, 1991, vol. 6, 1327-1328.

3. Basutin O.A., Vovchenko E.D., Savjelov A.S., Kurnaev V.A. Studies of the transversal discharges in atmospheric pressure nitrogen laser / Proc. XXII Conf. on Phenomena in Ionized Gases, Hoboken, New Jersey, USA, 1995, vol.3, 79-80.

Electron density and Electron Distribution Function measurements in Copper Vapour Laser

L. GIGANT, P. LEMAIRE, J. MAURY

Direction du Cycle du Combustible
Département des Technologies de l'Enrichissement
Service Laser et Chimie
CEA Pierrelatte
BP 111 26702 PIERRELATTE CEDEX, FRANCE

We have done high resolution electron density and electron temperature time variations during the discharge period in a Copper Vapour Laser. These measurements are based upon spectroscopic diagnostics and results obtained are one of the keys to understanding the electrodynamic behaviour of this kind of lasers.

Copper Vapor Lasers, mainly used in S.I.L.V.A. (Atomic Vapor Laser Isotope Separation) have been often studied. But a deep hole in their knowledge comes from a lack of plasma state variables set, as electronic density and electronic temperature, with enough temporal resolution. At the power level reached yet [1], performance improvement needs to manage electronic energy at any times during the discharge period. As far as we know, this paper presents the first temporal results related to plasma parameters direct characterization in the discharge period with high time resolution.

Electronic temperature and density on axis are measured from incoherent Thomson scattering [2]. The attractiveness of this diagnostic derives from two main features. First, it is, a non perturbing method, requiring only an access to the plasma radiation. Second, it offers the potential of determining detailed information about the component of the Electron Distribution Function (EDF) on the laser axis and sometimes even on the ions too. These advantages are sufficient to forget the fact that the measurements are generally very difficult to perform mainly because the scattered light intensity is so low, more than ten orders magnitude smaller than the incident laser power.

Ionic density is measured from Stark broadening of the Balmer emission lines of atomic hydrogen on the quasistatic approximation [3]. This method has already be applied in time integrated measurements or with poor resolution [4] but never with the time resolution we have brought into operation in the discharge period. The results obtained by these two methods will be successively presented.

1 : Thomson backscattering

The C.V.L. is a 20 W, 42 mm bore commercially available triggered at a pulse repetition frequency of 6000 Hz, for a buffer gas pressure of 25 mbars. Electrical circuit is a classical resonant one. The injected Q-switched Nd:YAG laser delivers 0.5 J at 532 nm at a 20 Hz repetition rate. The optical pulse duration is about 7 ns full width at half maximum (FWHM) which is naturally the time resolution and this allows us to use a lidar set up. For this reason, the C.V.L. was lengthened by 1 m to prevent window diffusion of the YAG probe. The scatered light at 180° is then carried in a Faraday cage by successive imagery to prevent electromagnetic noise, dispersed in a double monochromator for high rejection rate and analysed by a low noise, high dynamic Princeton Instrument C.C.D. camera. The camera is driven by a controller which operates the intensification during 10 ns for limiting noise. Figure 1 presents results of the electronic temperature during the discharge period of the C.V.L extracted from the EDF analysis. We give two temperature for each time step relating to the two wings of the scattered light of the incident YAG beam. Those results are compared with Boltzman equation resolution and Maxwell EDF numerical calculations [5]. The time t=0 corresponds to the maximum of the green laser fluorescence.

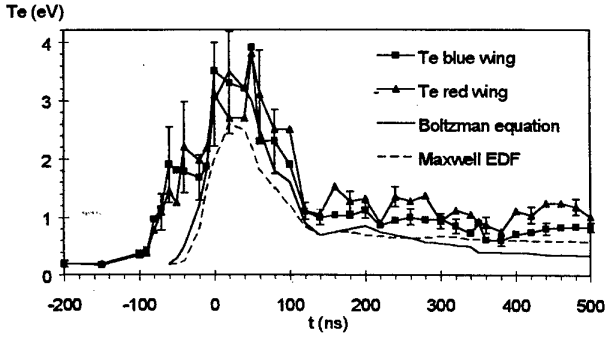

Figure 1 : Time resolved electronic temperature

Measurements show good correlations with Boltzmann calculations excepted before the time origin (t = 0). The EDF is not maxwellian during that first period of time in a C.V.L. The temperature of the main part of the EDF grows up about 2 eV and radiative emissions show that a lot of copper states of high energy are involved. A further paper in preparation will describe the EDF behaviour and the importance of the high lying levels during that first period. Then, electronic energy reach 4 eV with a maxwellian EDF and upper laser state are populated. After lasing, this temperature falls rapidly at about 1 eV and reaches gas temperature after 10 µs as

already mentionned [6].
Electronic density (Ne) deduced from EDF integration over all energies is presented on figure 2 in arbitrary units.

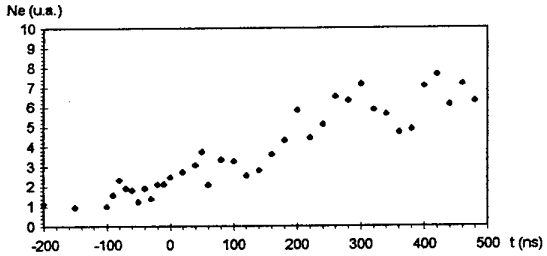

Figure 2 : Time resolved electronic density on the tube axis.

2 : Quasistatic Stark broadening of hydrogen Balmer lines

The light emitted from the C.V.L. is focused onto a set of 14 optical fibers of different length to discretise precisely (for derivative analysis) the time resolved acquisition and again is carried in the Faraday cage. The detection set up is the same as for Thomson scattering. The radial translation of the fibers bundle, statistically arranged on the front of the laser and after two diaphragms, allows the measurements of Ni for three independant radial positions (one only is used here). More than 2500 spectra were handly analysed to verifie the good reproductibility and to obtain a temporal resolution smaller than 5 ns.
Figure 3 shows results on ion density measurements for H_δ spectra in the discharge period.

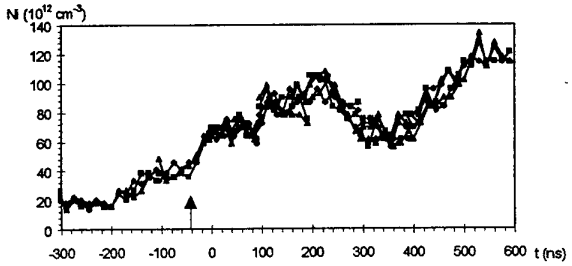

Figure 3 : Ionic density determined from Hδ (410.2 nm) broadening on the tube axis. The three differents points represent three successive acquisitions.

In a first step, from H_β width measurements we have verified that H_δ was not reabsorbed by the plasma. In a second step, by a fit at t = -200 ns (late post-discharge) of both Ne and Ni (Figures 2 and 3), we have verified that space charge, negative ions and multicharged ions densities are less than a few 10^{13} cm^{-3} and confirmed the drop at 350 ns (figure 4).
After this verifications, we can conclude to a singular behaviour of the electronic density. Firstly, the density is already high 2.10^{13} cm^{-3} in the begining of the discharge period and the plasma is highly conductive. Then electron density behaviour at t less or equal to 0 (the arrow) shows a strong copper ionisation by a factor of 2.

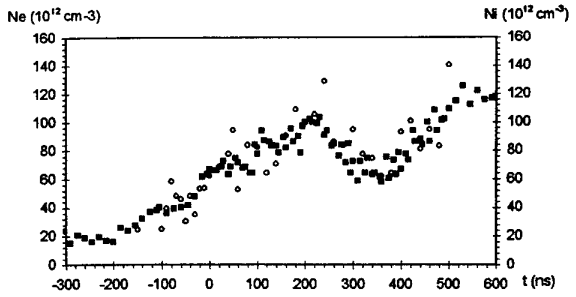

Figure 4 : Ionic density (circles) on the tube axis deduced from Stark broadening and comparaison with electronic density (squares) obtained from Thomson scattering.

The Ne drop between 200 and 300 ns is not due to neither three body nor radiative recombination nor ions and electrons transportation, but for us, it seems to be attributed to autoionizing states kinetic through dielectronic recombination (capture) combined with trapping, ion levels and stepwise ionization. By introduction of the $3d^9 4p^2$ [7] state in a kinetic code [8] it is possible to confirm a Ne 50 % drop at that time.

3 : Conclusion

Ionic density, electronic density and electronic temperature are measured in the discharge period in a C.V.L with high temporal resolution lower than 7 ns. Results on density measured by Stark broadening were confirmed by Thomson scattering. No measurable space charge is observed, and it is the same for negative ions or positively multicharged one. Results on EDF show from row data a non maxwellian EDF during the period preceeding laser emission. The main way for excited ions recombination seems to be dielectronic one.

[1] C. Konogai, Y. Sano, N. Aoki, Pulsed Metal Vapour Lasers (Kluwer Academic Publishers), 371-376, 1996.
[2] J. Sheffield, Plasma Scattering of Electromagnetic Radiation (Academic Press, New York, 1975)
[3] H. Griem, Spectral Line Broadening By Plasmas (Academic Press, New York, 1974)
[4] P. Blau, I. Smilanski, S. Rosenwaks, J. Appl. Phys.. 72, **3**, (1992)
[5] J. Maury, P. Lemaire, J. P. Goossens, E. Le Guyadec, J. M. Borgard, Pulsed Metal Vapour Lasers (Kluwer Academic Publishers), 221-226, 1996.
[6] J.P. Goossens, Thèse Université Joseph Fourier, Grenoble-France, 1995
[7] M. Martins, P. Zimmermann, Z. Phys. D, **23**, 115-119, 1992.
[8] J. M. Borgard, Private Communication.

Transition Probabilities of NI Lines from Laser Induced Breakdown Spectroscopy

P. MATHERON*, I. DEHA**, R. REDON* and J. RICHOU*
* Laboratoire d'Optoelectronique, Université de Toulon et du Var, BP 132, 83957 LA GARDE France
** Institut de Physique, USTHB ALGER, Algerie

1. Introduction

Transitions probabilities are relevant for atomic studies, applications to astrophysics and laser physics. However, a few papers treated this subject using laser induced breakdown spectroscopy (LIBS). Indeed, pulsed focused laser is a simple way for plasma creation. Emission spectra treatment allows transition probabilities determination.

In this work, transition probabilities are experimentally determined with branching ratios of some spectral lines arising from $2s^2 2p^2 3p$ levels from multiplet. Emission spectra are deconvolved by a iterative method [5] to remove apparatus function effect. Electron density and temperature are calculated. Transitions probabilities are deduced from relative total intensity ratios in deconvolved spectra by combining experimental lifetime. Finally, our results are compared with previous values of other authors [1,2] and discussed.

2. Experimental Setup

A Nd:YAG laser operating at its fundamental wavelength λ_0 = 1064 nm generates pulses of 310 mJ maximal energy and 10 ns duration. The laser beam is focused in a N_2 gas by a 7,56 cm focal length lens. The spot diameter is about 0,5 mm large and gives a light flux equal to $1{,}7.10^{11}$ W/cm^2. The laser intensity may be reduced using a polarization device. Nitrogen gas was inside a vacuum cell and maintained at 0,5 bar pressure. Plasma emission is focused onto the entrance face of an optical fibber at right angle to the path of the laser pulse. This fibber is specially carried out IR and visible transmission. The light is focused onto the entrance slit of a Chromex spectrometer coupled to a 512 pixels detector. The diffraction device used is 1200 grooves/mm grating yielding a spectroscopic resolution of 0,4 Å/pixel. An optical multichannel analyser system (OMA 3) allows time resolved analysis of emission spectra. Temporal delay between the laser pulse and spectrum acquisition is controlled. We check the detector linearity in the spectral range of interest using a tungsten lamp.

3. Method

The used method is based on relative line emission intensities measurement. In the local thermodynamic equilibrium and optically thin plasma assumption, line intensities ratios are obtained using Boltzman law and emission line intensities for two transitions [3]. Branching ratios method is suitable when studying transition probabilities of lines multiplet. In this method, all transitions from the same level are considered. Absolute density number, absolute line intensity and temperature are not needed [6]. Branching ratios are given by :

$$R_{mn} = \frac{I_{mn}}{\sum_m I_{mn}} = \frac{A_{mn}}{\sum_m A_{mn}} \qquad (1)$$

Using the known upper state lifetime τ_m, we deduced individual transitions probabilities by :

$$A_{mn} = \frac{R_{mn}}{\tau_m} \qquad (2)$$

4. Results and discussion

4.1. Emission spectrum

Spectrum identification shows that at early time (< 300 ns), continuum radiation dominates. NII ionized lines appear up to 1,5 µs delay after laser pulse. Neutral lines becomes evident after 1 µs. NI lines intensities and linewidths decrease considerably after 3 µs delay. Fig. 1 shows a typical spectrum for NI lines studied and obtained for *2 µs* delay and for 5.10^{10} *W/cm^2* laser intensity. Under these conditions, optically thin plasma assumption is made to calculate transition probabilities.

Line intensity analysis was carried out by making deconvolution of the experimental profile by the apparatus system determined by registering a spectral line from mercury calibration lamp at λ = 4358.4 Å. This line is quite narrow in comparison with plasma lines. The deconvolution method is used on real and positive signals as line spectrum [5]. Working on deconvolved spectrum allows to improve continuum and line intensity estimation by resolving the overlapped lines. Line intensities are calculated by integrating each line from the deconvolved spectrum. The relative error on these parameters is 4 %.

4.2. Diagnostics

In an optically thin plasma, excitation temperature is given by line intensities ratios from two same ionization states elements [3]. The selected lines are NI lines at 7442.3 Å and 8242.4 Å respectively. From the deconvolved spectrum, the electronic temperature is calculated to be 3.10^4 °K. In order to support the Local Thermodynamic Equilibrium (LTE) assumption, we used the Mc Whirter criterion [4]. From simplified expression of full width at half maximum [4], electron density of the plasma is about 2.10^{17} cm^{-3}. This value derived from Stark broadening

parameter of NI line. These results support the LTE assumption for considered levels.

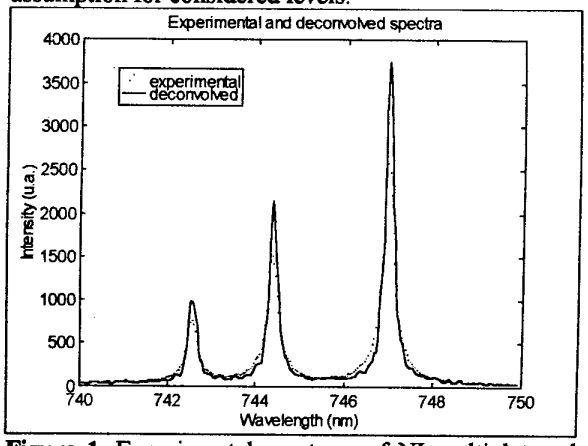

Figure 1. Experimental spectrum of NI multiplet and deconvolved one.

4.3. Results and discussion

We have measured the atomic transition probabilities of NI multiplet lines and obtained experimental reference values of $2s^2\ 2p^2(3P)\ 3p(^4S_{3/2})$ -- $2s^2\ 2p^2(^3P)\ 3s(^4P_{1/2,3/2,\ 5/2})$ transitions at 7423.64 Å, 7442.3 Å and 7468.31 Å respectively with available lifetime data for their upper states. We applied the measurement of [1] who take an experimental average value determined by state selective laser excitation techniques. They obtain τ_m = 24.7 ns ± 5 %. All the results are shown in table 1; branching ratios, transition probabilities and standard uncertainties are given for each multiplet line. For comparison, we present in table 1 the theoretical results for transition probabilities calculated by Weiss (this result is given by Musielok) and the experimental results obtained by Musielok [1] and Zhu [2].

The uncertainties listed in table 1 have been estimated by taking into account the following contributions : a) systematic uncertainties of the line profile after deconvolution method, give a line intensity measurement error of ± 4 % for each line, b) uncertainty in the lifetime data is estimated to be ± 5 %, c) possible deviation from linearity of the photoelectric detection system, estimated to be less than 1 % in our wavelength interval. Integrated intensity computation error is also negligible. Finally, uncertainty on atomic transition probabilities is estimated to ± 13 %.

Our results for the 3p - 3s NI transition are in good agreement with the experimental and theoretical values from other plasma sources. This experiment confirm LIBS as a good emission source for atomic transition probabilities determination.

5. Conclusion

In this work, it is proved laser produced plasmas are very interesting spectroscopic sources providing enough high temperature and density media. The advantages are the simple method to obtain spectrum and deconvolution method validity to more accuracy. If we used time resolved spectroscopy, the employed method to calculate atomic transition probabilities is a good reference to calibrate our system. Moreover, emission spectrum will be used for Stark parameter determination. At this time, experiments are carried in our laboratory to study other multiplet transitions in N_2 plasma. Other experiment will be conducted to study transition probabilities in Fe and Si laser produced plasma for abundance determination which is important in astrophysical applications.

References

[1] J. Musielok, W. L. Wiese and G. Veres : Phys. Rev. A, **51** (1995) 3588

[2] Q. Zhu, J. Bridges, T. Hahn, and W. L. Wiese., Phys. Rev. A, **40**, (1989) 3721

[3] H.R. Griem, *Plasma Spectroscopy*, Academic Press, New-York, (1974)

[4] F. Blanco, B. Botho and J. Campos, Physica Scripta, **52** (1995) 628

[5] R. Redon, B. Ferhat and J. Richou, GRETSI '97, (submitted)

[6] M. C. Huber and R. J. Sandeman, Physica Scripta, **22** (1980) 373

Table 1 : *Atomic transition probabilities of NI with experimental branching ratios*

Transition levels		Line (Å)	Branching ratios	Atomic transition probabilities (10^8 s^{-1})			
Upper	Lower			This work	Ref. [1]	Ref. [2]	Ref. [1]
$2s^22p^23p(^3S_{3/2})$	$2s^22p^23s(^4P_{1/2})$	7423.64	0.1425	0.0591 ±13%	0.0563 ±11%	0.062	0.0638
$2s^22p^23p(^3S_{3/2})$	$2s^22p^23s(^4P_{3/2})$	7442.3	0.309	0.125 ±13%	0.123 ±11%	0.12	0.0127
$2s^22p^23p(^3S_{3/2})$	$2s^22p^23s(^4_{5/2})$	7468.31	0.548	0.221 ±13%	0.19 ±11%	0.185	0.188

Application of a Digital Camera to Imaging Spectroscopy of TPD-S Plasma

M. Mimura, T. Uneyama, T. Hamada, A. Ishida, and K. Sato*
Faculty of Engineering, Osaka City University, Sumiyoshi-ku, Osaka 558 Japan
*National Institute for Fusion Science, Oroshi-cho, Toki 509-52 Japan

1. Introduction

TPD-S of National Institute for Fusion Science stands for Test Plasma with Direct current discharge for Spectroscopy. As shown in Fig. 1, the TPD-S machine creates a stationary plasma by discharge between cathode and anode. The plasma flows out of the hole in the anode into the vacuum vessel where there is no magnetic field. It was found that a very sharp boundary plasma is created even without magnetic field. Depending on discharge parameters, the plasma takes various shapes. To study the plasma shape and its creation mechanism, a measurement with a spatial resolution is necessary

For such spatially resolving measurement, the following two types of image detector have been prepared. Each of them will be used as a detector of a visible, VUV, or soft X-ray polychromator.

(1) Hamamatsu C4880-92 Intensified Cooled CCD camera with a software HiPic (High Performance Image Controll System) to process the image data.

(2) FUJIX DS-505 Digital Camera, which is not manufactured for physical measurement. So to process its image data, we should develop a computer program for ourselves.

The purpose of this research is to analyze the data format of the digital camera and make a computer program to read the image data. Process of the image data will be made by modifying the computer program already developed in our group[1].

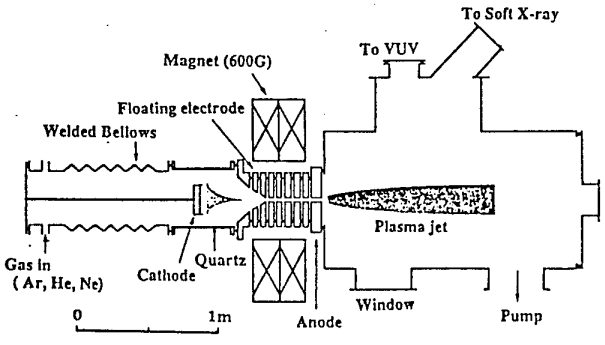

Fig. 1. Schematic Drawing of TPD-S machine.

2. Data Format of Digital Cameras

Recently performance of digital cameras has been improved extensively. Various digital cameras can be purchased. To use one as a detector of spectroscopy, the most important thing is its data format. Because the image data file is very big, several techniques are used to reduce the file size. After applying such a size reduction technique, the information of the light intensity is lost. Usually this fact is not paid attention because the major purpose of digital cameras is to display a good image for human vision, where physical exactness is not needed. For the light detector, however, it is essentially important. Therefore the selection of a digital camera should be made very carefully.

Many digital camera use JPEG format because of its small file size. But it should be noted that a digital camera with such format as JPEG, PCX, EPSF etc, cannot be used as a light detector. A digital camera which uses the uncompressed mode of TIFF (Tag Image File Format) or BMP (Microsoft Window Bitmap Format) can be used because they contain the light intensity in the form of red, green, and blue components.

3. Reading Image Files

The digital camera DS-505 which we prepared has the uncompressed TIFF format (24 bit color mode). So what we need is to make a computer program for reading the TIFF format file. We found that the TIFF format is very complicated and many versions exist.

According to a literature[2], "TIFF has garned a reputation for power and flexibility, but it is considered complicated and mysterious". So we gave up to read the general TIFF file and will be satisfied with reading

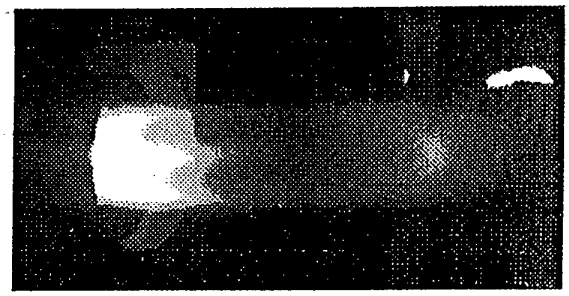

Fig. 2. An example of plasma image taken from the window.

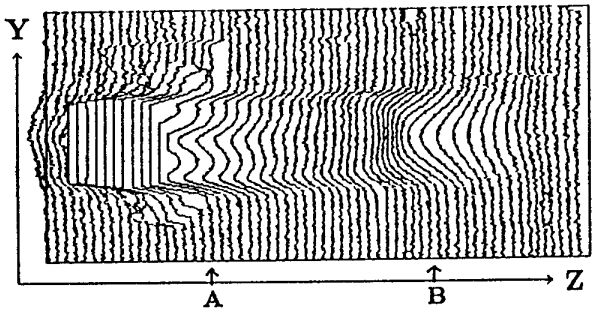

Fig. 3. Bird's eye view like plot of red component of light intensity.

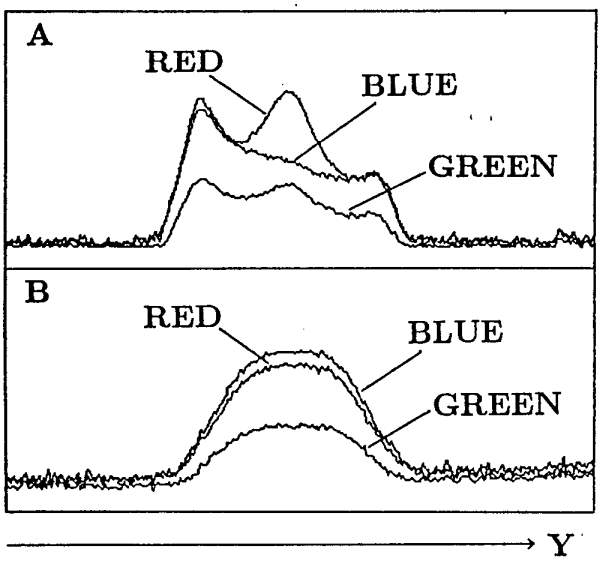

Fig. 4. Vertical distribution of red, green, blue component of light intensity at positions A and B.

only the TIFF file created by DS-505.

TIFF files are organized into three sections, the Image File Header, the Image File Directory, and the bitmap data. We analyzed the location of image data and made a reading program using Quick Basic.

4. Light Intensity Distribution

As is described before, the shape of TPD-S plasma changes variously depending on the discharge parameters. So before setting the digital camera to a polychromator, several plasma images were taken as usual photographs through the window shown in Fig.1. Figure 2 shows an example of plasma shape, where the color image taken by the digital camera is converted to a monochromatic image and printed out by a laser printer. In this example, the plasma light is bright near the anode, then decreases, and appears again.

Using the Quick Basic program, the data file is read and the red component of plasma light is plotted in a bird's eye view like plot in Fig.3. It is seen that the plasma light near the anode is so bright that the CCD detector of the digital camera was saturated.

Although the digital camera is to be used with the combination of a polychromator for spectroscopy, a very simple separation of wavelength is made by the digital camera itself because it has red, green, and blue filters. Using these filters we check the plasma light intensity distribution at two positions A and B. The vertical distribution of the red, green, blue components are plotted in Fig. 4. It is found that the red component of the plasma light has a peak at the axis near the anode (position A), while the blue component shows a hollow distribution. In contrast, at the position B, all of red, green, blue component show the similar parabolic distribution. This suggests an interesting plasma creation mechanism, the details of which will be made clear in near future using a polychromator.

Acknowledgment

This work was carried out under a collaborating research program at the National Institute for Fusion Science.

References

[1] M.Mimura, T.Kakeda, A.Inoko, E.Ishiguro and K.Sato, Proc. XXII Int. Conf. Pheno. Ion.Gas.,1 (1995) 105.

[2] J.D. Murray and W. van Ryper, *"Encyclopedia of Graphics File Formats"*, O'Reilly Inc. 1994, p880.

Measurement of electron density in dielectric barrier discharges

E. Gerova and S. Müller
Institut für Niedertemperatur-Plasmaphysik e.V., Robert-Blum-Strasse 8-10, 17489 Greifswald, Germany

1. Introduction

The usual fields of technical application for dielectric barrier discharges (further called DBD) are radiation sources (excimer radiation) and plasmachemical reactors in the range of medium or atmospheric pressures [1].
DBD are initiated by ac-voltages in gaps where one or both electrodes are covered with dielectric layers which separate them from the gas. The dielectric barrier inhibits the flow of direct current. The basic principle in most cases is to produce a plasma in which a majority of the electrical energy is used for the production of energetic electrons, rather than for gas heating.
In spite of a widespread use of DBD, our understanding of the plasma is still incomplete and insufficient. Consequently, it is very important to diagnose the plasmas to make clear and control the physical and chemical processes working in the plasma.
The aim of the present paper is to have a more detailed view in the nature of DBD on the basis of new experimental data concerning the electron component. Here we present investigations of the electron density in He, obtained from the Stark broadening of the profiles of the H_β line.

2. Experimental setup

The discharges were performed in a single discharge arrangement [2]. This way, spatial jitter effects have been minimized. The typical geometrical dimensions were: glazed Mo-electrodes with a front surface diameter of 1 mm and glazings with a diameter of 4 mm, thickness of the front surface dielectric d_i= 0.4 mm and gas space thickness (electrode distance) d= 1.6 mm.
In the experiments we have used He as working gas with traces of hydrogen (ppm range). The total pressure range was 300 - 1005 Torr. The discharge was driven by square waves at a frequency of 10 kHz (fast high voltage transistor switch). At this stage of investigations no Abel inversion was applied.
The spectra emitted were analyzed by means of a 0.5 m double monochromator equipped with a grating of 2400 g/mm. At the outlet slit an optical multichannel analyzer (OMA) was used, consisting of a CCD (576x483 pixels) and proximity-focused micro channel plate (MCP) image intensifier fiber-optically coupled to the CCD array. The MCP can be gated in less than 5 ns. This way a time resolved measurement was possible. The effective spectral resolution of the optical system was about 0.06 Å. The discharge is imaged onto the entrance slit so that discharge areas of 0.5-0.3 mm x 5.6 μm could be analyzed.

3. Diagnostics and results

To estimate the electron density we measured the profile of H_β patially resolved for different delay times. The profile of a line is the result of many factors. When the Stark broadening dominates, this provides a method for the estimation of charged particle density. Stark broadening is a perturbation of the energy levels of an atom or ion by changing electric fields occurring in a collission with a charged particle.
Before the measured line width is used to calculate densities, it is necessary to make sure that the Stark effect is really the most important line broadening mechanism. At first, the Doppler broadening and the shape of the whole profile were checked. A typical result for the full width at half maximum (FWHM) is 0.06 Å. Compared with measured profiles this width is significantly smaller so that one may completely neglect Doppler broadening. However, corrections of the measured profiles by deconvolution of Doppler profile and apparatus function have been done. The resulting line shape is approximately Lorentzian as can be seen from Fig. 1. In our case the main contribution to the line width arises from the Stark effect.
The electron density was determined using the following formula [3]:

$$n_e = C(n_e,T_e) \cdot \Delta\lambda_S^{3/2} \qquad (1)$$

where $\Delta\lambda_S$ is the full Stark width and $C(n_e,T_e)$ a coefficient that is only a weak function of the electron density n_e and has a slight temperature (T_e) dependence. The values of the coefficients C were taken from [3], too. A theoretical profile for $n_e = 10^{15}$ cm^{-3} and 10^4 K [4], considering the quadratic Stark effect and the ion quadrupole shift due to the ionic microfield and its gradients, was compared with the deconvoluted experimental profile at the same density obtained from (1). The FWHM of the theoretical profile was 3% larger than that of the experimental profile.
Typical experimental results for a gas pressure of 600 Torr are illustrated in Fig. 2-4. Figure 2 represents the axial time development of electron densities at the anode and cathode. The first discharge activities were observed at the anode with densities of the order of 10^{13} cm^{-3} (The precision and sensivity decreases for values of electron densities smaller than 10^{14} cm^{-3}). The electron density reaches its maximum at 80 ns, whereas a strong rise of ~1.5 orders of density is observable within ~5 ns. Nearly the same strong rise of density occurs at the cathode, but starting 5 ns earlier then at the anode. The breakdown at

higher pressures occurs in this case streamer-like simultaneously with a cathode directed discharge development. The high plateau of the electron density at the anode at delay times of 60 -70 ns, resulting from a Townsend phase of the discharge development acts as precursor on the streamer phase due to field perturbations by space charges.

Fig. 3 shows the radial resolved densities of the filament. The radius of the He filament is relatively large compared with intensity profiles of other gases (s.[5]). The centre of the filament shows a slight radial dependence of density, whereas the other part kept constant. Compared with intensity profiles of a single discharge [5] the density profile is shaped more like a square.

The density profiles show a much more spreading effect at the electrodes. In addition, as one can see from Fig.4, the anode profile is characterised by a central dip of nearly 20% compared with the maximum of density. It could be due to repulsive electrostatic forces and/or surface discharges.

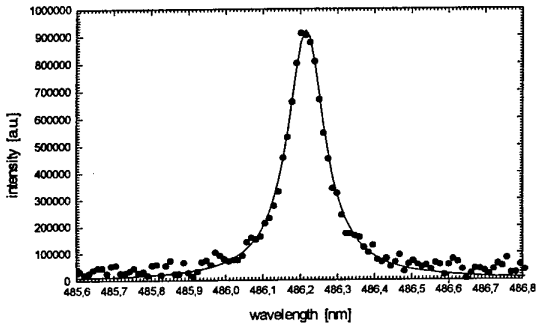

Fig. 1 Deconvoluted profile and its Lorentzian fitting

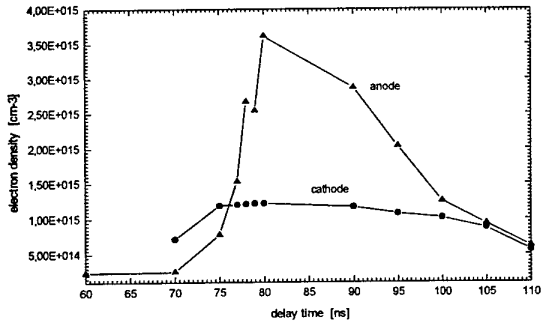

Fig. 2 Axial time development of the electron densities at the anode and cathode

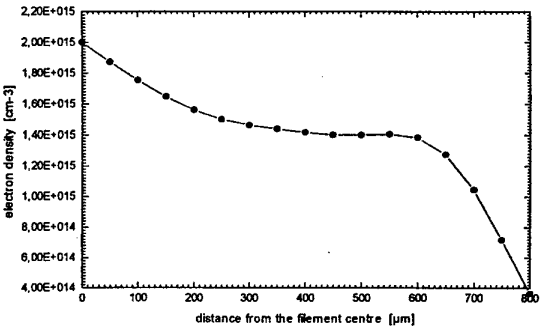

Fig. 3 Radial filament electron density distribution

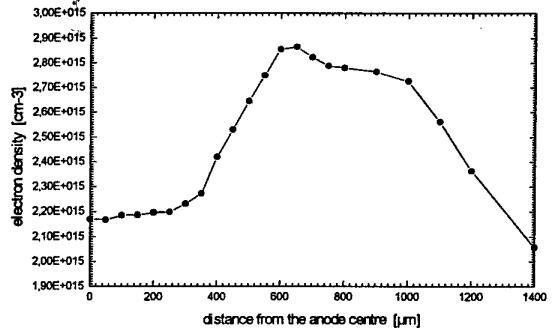

Fig. 4 Radial electron density distribution at the anode

4. References

[1] U.Kogelschatz: X Int.Conf. on Gas Discharges and their Applications, Swansea, 13. - 18. Sept. 1992

[2] S.Müller, R.-J. Zahn: Contr. Plasma Phys .**36**(1996)697

[3] H.R.Griem: Plasma Spectroscopy, New York 1964

[4] S.Günter, A.Könies: Private communication

[5] S.Müller, R.-J. Zahn: 7th Int. Symp. on the Science & Techn. of Light Sources, Kyoto, 27. -31. Aug. 1995

Determination of the Spatial Distribution of the Electron Density in an Argon Arc by Digital Speckle-Pattern-Interferometry

M. Hipp, W. Fließer, T. Neger, H. Jäger

Institut f. Experimentalphysik, Technische Universität Graz, Petersgasse 16, A-8010 Graz, Austria

1. Introduction

Digital Speckle-Pattern-Interferometry (DSPI) [1] can be applied to investigate plasmas like classical and holographic interferometry [2]. It belongs to the methods of speckle-pattern-correlation and is rather known as a fast and cheap technique for determination of surface displacement and deformation. As an advantage compared to conventional interferometry, DSPI allows optical components of non-interferometric quality in the setup. On the other hand the statistical properties of the speckle-pattern result in an unavoidable background noise of the phase-signal. Holographic methods are free of this shortcoming and provide the same advantage, however, they require expensive and time-consuming photographic processing techniques.

The different spectral contributions of the plasma to its refractivity due to electrons, atoms and ions can be used to determine the electron density by measuring the phaseshift of a wavefront in the plasma at two different wavelengths.
We applied this two-wavelengths method to a stationary argon *mini-arc* [3] end-on diagnosted at atmospheric pressure, assuming a homogeneous plasma. The phase shift was measured with DSPI spatially resolved to demonstrate its applicability.

2. Principle

Electron densities can be measured by determining the total refractivity of a plasma at two different wavelengths, which is the sum of the refractivities of all the plasma components [2]. The contribution of the electrons according to their density N_e

$$(n-1)_e = -const\ \lambda^2 N_e \qquad (1)$$

is characterized by a completely different spectral dependence compared to that of the ions and atoms (indices refer to sort of particle)

$$(n-1)_{a,i} = \frac{1}{2\varepsilon_0}\alpha_{a,i}(\lambda)N_{a,i}\,. \qquad (2)$$

Here $N_{a,i}$ denote the number density and $\alpha_{a,i}$ the polarizability. According to this different spectral behaviour one is able to determine the density of electrons, provided the used probing wavelengths are far off-resonant.

Assuming only one species of atoms, equal density of electrons and ions (single ionization) and the relation

$$\beta = \frac{\alpha_a(\lambda_2)}{\alpha_a(\lambda_1)} = \frac{\alpha_i(\lambda_2)}{\alpha_i(\lambda_1)}, \qquad (3)$$

being equal for both probing wavelengths, the electron density in a homogeneous plasma of length L may be described by

$$N_e = \frac{4\pi\varepsilon_0 m_e c^2}{e^2 L}\cdot\frac{\beta\Delta\psi_{\lambda 1}\lambda_1 - \Delta\psi_{\lambda 2}\lambda_2}{\lambda_2^2 - \beta\lambda_1^2}\,. \qquad (4)$$

Here $\Delta\psi_{\lambda 1}$, $\Delta\psi_{\lambda 2}$ are the interferometrically measured total phaseshifts after the wavefronts with wavelengths λ_1, λ_2 have passed the plasma. The relation β can be determined by using the Cauchy-formula; values for argon are tabulated in [4].

The basic optical setup for DSPI can be considered as a modified *Mach-Zehnder* interferometer [5]. Two speckle-patterns, produced by two diffusors, establish a third one (*primary interferogram*), which is imaged onto a CCD camera. The resulting intensity pattern is digitized before changing the object (e. g. displacement, deformation) in one of the partial beams, as well as after it. A so called *secondary interferogram* is obtained by subtracting these two primary interferograms pixel by pixel and taking the absolute value of the difference. The resulting picture shows fringes with same spacing as in conventional interferometry [1].

3. Experiment and results

As can be seen by inspecting (4), the precision of density-measurement strongly depends on the spectral separation of these wavelengths. Therefore we used a Nd-YAG-laser in the near infrared spectral range at 1064 nm, and an Argon-Ion laser with 456 nm. Both wavelengths could be detected by standard CCD-cameras, such as Hitachi KP-160 and Sony XC75/CE in our case.
The setup consists of two nested *Mach Zehnder* interferometers with two reflecting diffusors. The arc column with at length of (20 ± 5) mm and a diameter

of approximately 4 mm is transmitted by both object beams of the interferometer. After that, the beams are separated again by a filter reflecting at 1064 nm. The arc column is imaged onto the diffusor to minimize decorrelation effects due to ray deflection.
To reduce the amount of detected light from the arc itself, a spatial filter procedure is used in addition to the reflecting filter.
Both reference beams hit a common piezo-mounted mirror in an additional Michelson interferometer, which is part of a computer-controlled feedback-system for temporal phase-shifting [6].

After ignition of the arc one primary interferogram with 512x512 pixels is recorded by the camera for each wavelength simultaneously. The discharge is cut then, about 30 seconds later primary interferograms are recorded after distinct phaseshifts. With each of these frames together with the corresponding interferogram of the discharge, secondary interferograms are produced. Their noisy signal can be dramatically enhanced by applying low-pass filters and convolution [7] to rescale intensity. The results are quasi-classical interferograms.
Considering the time consumption for the phaseshift procedure including frame-grabbing, the *Four-frame-technique* at 458 nm and the *Carré-technique* [6] at 1064 nm turned out be the best choice for the evaluation of the two-dimensional distribution of the phase shift caused by the arc. Values with modulation of intensity below 3% are masked.
Figure 1 shows the obtained phaseshifts in the mini arc multiplied with the wavelengths versus the radius for an electrical current of 35 A. The argon flow rate was 4.8 l/min. Figure 2 shows the corresponding radial electron density determined using (4) and fitted by polynomial regression of 2nd order.

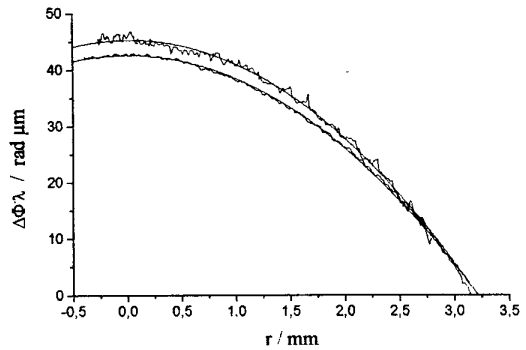

Figure 1. Radial dependence of the phase shift $\Delta\Phi$ multiplicated with corresponding wavelength λ of 1064 nm (curve 1) and 458 nm (curve 2).

The highest electron density in the plasma column is about $3\times10^{22}\,m^{-3}$. This result is in good agreement with those obtained by a nonlinear Fizeau interferometer [8] and by interferometry using holographic elements [9].

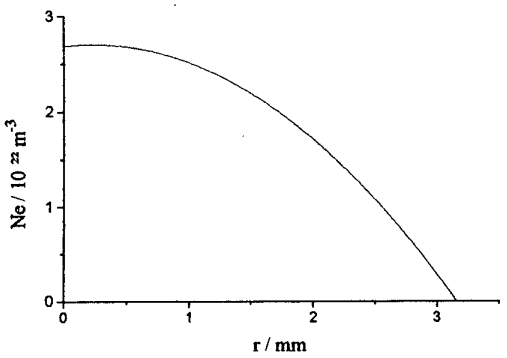

Figure 2. Radial distribution of the electron density N_e

The spectral separation of the used wavelengths, the comparatively short length of this plasma and the given particle density represent a lower detection limit of the electron density using two-wavelength interferometry by DSPI. Since no refractive index value of the undisturbed surrounding medium is available, which strongly effects the precision of the fit-parameters, the noisy signal in the infrared leads to an overall error of more than 70%. The error of the longitudinal size of the plasma column is also taken into account.

4. Reference

[1] R. Jones, C. Wykes: *Holographic and Speckle Interferometry,* Cambridge University Press, Cambridge (1983)
[2] R.A. Alpher and D.R. White: *Optical Interferometry* in *Plasma Diagnostic Techniques* ed. R.H. Huddlestone and S. L. Leonhard, Academic Press, New York -London (1965)
[3] M. Bridges and W.R. Ott: Appl. Opt., **16** (1977) 367-376
[4] W. Allen: *Astrophysical Quantities* 3rd ed (London: Athlone) (1976)
[5] K. Creath: *Digital speckle pattern interferometry (DSPI) using a 100x100 imaging array,* Proc SPIE **501** (1984) 292-298
[6] K. Creath: *Temporal Phase measurement methods* in *Interferogram Analysis* ed D.W. Robinson and G.T. Reid, IOP Publishing (1993)
[7] R.C. Gonzales, R.E. Woods: *Digital Image Processing,* Addison Wesley, Reading, Massachusetts (1992)
[8] J. Flieser, Diploma Thesis, Technische Universität Graz (1994)
[9] K. Widmann, G. Pretzler, J. Woisetschläger, H. Philipp,T. Neger and H. Jäger: Appl. Opt., **35** (1996) 5896-5902

A nonlinear Fizeau interferometer for real-time determination of spatial distributions of electron densities in a mini-arc plasma

J. Flieser[1], A. Morozov[2], T. Neger[1], and H. Jäger[1]

[1] Institut für Experimentalphysik, Technische Universität Graz, Petersgasse 16, A-8010 Graz, Austria
[2] Institute of Physics, St. Petersburg State University, Ulianovskaya 1, 198904 Petrodvoretz, St. Petersburg, Russia

1. Introduction

A new experimental technique for real-time measurements has been developed which permits the determination of the spatial distribution of the electron density of a plasma with a time resolution commensurate with the 6 ns duration of a single laser pulse. Electron densities of 3×10^{22} m^{-3} can be measured at 1 cm plasma length. The possibilities of this method were demonstrated by studying a steady state mini-arc argon plasma at atmospheric pressure.

By measuring refractivities of a plasma, particle densities can be determined. As the spectral behaviour of the refractivity due to atoms and ions differs principally from that of free electrons, one can selectively determine a plasma constituent by choosing appropriate probing wavelengths. Provided the difference in refractive indices of a plasma is measured at two far separated visible or near infrared off-resonant wavelengths, electron densities can be determined. Usually the refractivities are measured interferometrically at these two wavelengths separately and the electron density is calculated then. In 1970 a holographic method for a direct measure of the refractivity dispersion of phase objects was suggested [1] and applied to plasmas later on, e. g. [2]. Ten years later [3] and independently [4,5] described a number of interferometers based on second harmonic generation (SHG); the so-called nonlinear Fizeau interferometer allows a direct measurement of the difference in the refractive indices for the fundamental and second harmonic wavelengths.

By introducing a polarizing filter after the second SHG crystal (see Fig. 1) we were able to cancel the inhomogeneity of the carrier fringes introduced by the crystal. Since all relevant information is carried by the second harmonic waves, dielectric mirrors could be used to suppress the light from the arc itself.

2. Principles of measurements

In case of non-resonant conditions the refractivity $(n\text{-}1)$ of a plasma at visible and infrared wavelengths λ may be described by

$$(n-1) = -CN_e\lambda^2 + (a + b/\lambda^2)N_a. \qquad (1)$$

The first term considers the influence of free electrons of number density N_e, the second term gives the contribution of the atomic constituents of density N_a. C comprises some physical constants, a and b are material parameters. For argon they are tabulated in Ref. [6].

Assuming a plasma length l the fringe shift k in a nonlinear Fizeau interferometer is given by

$$k = \frac{3}{2}C\lambda N_e l + \frac{6b}{\lambda^3}N_a l. \qquad (2)$$

For many plasmas the second term in Eq. (2) is small and may be neglected. So the fringe shift k is proportional to the electron density and the interference pattern yields lines of equal electron densities.

In the case of a mini-arc plasma [7] as used in our experiments both terms in Eq. (2) are of the same magnitude. To avoid errors introduced by the second term we measured N_a independently by means of a Mach-Zehnder interferometer. As the fringe shift in the nonlinear Fizeau interferometer is much smaller than unity, we used heterodyning and Fourier transform methods as described in Ref. [8] and discussed in Refs. [9-12].

A scheme of the real-time interferometer is shown in Fig. 1. Light of the fundamental λ and second harmonic $\lambda/2$ wavelength of a Nd:YAG laser equipped with a SHG crystal SHG_1 penetrates the plasma *Pl*. Due to the plasma dispersion the optical paths for infrared and green light are slightly different. A part of the infrared light is frequency doubled by SHG_2 and interferes with the green light from SHG_1, such forming the dispersion interferogram.

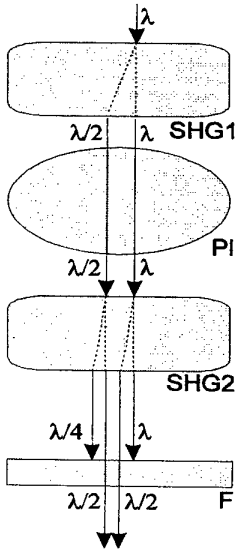

Figure 1. Principal set-up of a nonlinear Fizeau interferometer. SHG_1, SHG_2 second harmonic generating crystals; *Pl* plasma source; *F* filter.

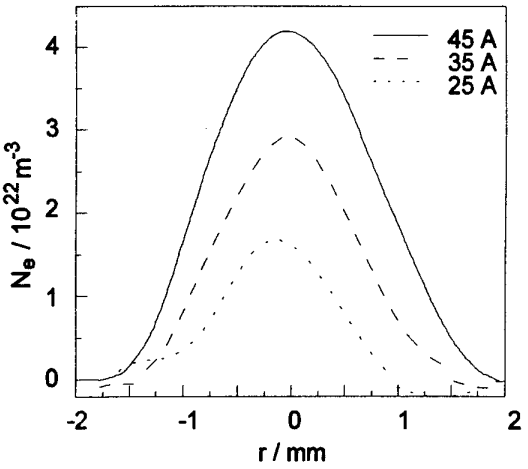

Figure 2. Radial distributions of the electron density N_e in a mini-arc plasma at an argon flow rate of 4.8 l/min and various electric currents. The overall error is estimated to 30%.

3. Experiments, results and discussion

For our experiments we used an injection-seeded Nd:YAG laser (Spectra-Physics GCR 170-10) in long pulse mode with a built in KD*P crystal for SHG. As plasma source we used a mini-arc in argon at atmospheric pressure [7]. The plasma length was (20±5) mm, the diameter of the cascade approximately 4.5 mm.

The centre of the arc column was imaged onto a CCD camera (Hitachi KP 160) and digitized by a frame grabber card (Imaging Technology PCVision Plus). Quantitative evaluation was done by means of fast Fourier transform algorithms on a personal computer (Intel i486). The carrier frequency for the heterodyne evaluation procedure was introduced by a BK7 glass wedge. The light from the arc itself was supressed by multiple reflection on dichroic mirrors optimized for the second harmonic wavelength and by spatial filtering.

The KD*P crystal SHG_2 produced some additional light which was polarized orthogonally to the original probing beams. These additional beams disturbed the final interference pattern, so a polarizing filter was introduced to remove this unwanted influence.

Measurements of the electron density have been carried out for three values of electric current (25 A, 35 A and 45 A) at an argon flow rate of 4.8 l/min. The radial distributions of the electron densities typically obtained are shown in Fig. 2, no smoothing algorithms have been used. The electron densities at the plasma column axis were 1.7×10^{22} m^{-3} at 25 A, 2.9×10^{22} m^{-3} at 35 A and 4.2×10^{22} m^{-3} at 45 A. The behaviour of the experimental curves shows a reasonable growth of electron density with the electric current and an axial symmetry corresponding to the discharge geometry. These results correspond within 7% with those obtained by speckle metrology [13]. They are also in good agreement with measurements done by two-wavelength interferometry on a similar arc [10] using holographic optical elements [12].

The main contributions to the overall error of 30% are to equal amounts due to (i) the signal-to-noise ratio typically obtained in the sub-fringe domain, (ii) the evaluation procedure based on heterodyning and fast Fourier transform methods, (iii) the not exactly known longitudinal size of our mini-arc plasma column.

4. References

[1] Ostrovskaya G V and Ostrovskii Yu I 1970 *Zh. Tek. Fiz.* **40** 2419-22; 1971 *Sov. Phys.-Tech. Phys.* **15** 1890-2

[2] Radley R J Jr. 1975 *Phys. Fluids* **18** 175-9

[3] Hopf F A, Tomita A, and Al-Jumaily G 1980 *Opt. Lett.* **5** 386-8

[4] Alum Kh P, Koval'chuk Yu V, and Ostrovskaya G V 1981 Zh. Tekh. Fiz. **51** 1618-23; 1981 *Sov. Phys.-Tech. Phys.* **26** 928-31

[5] Alum Kh P, Koval'chuk Yu V, and Ostrovskaya G V 1984 *Zh. Tekh. Fiz.* **54** 896-904; 1984 *Sov. Phys.- Tech. Phys.* **29** 534-8

[6] Allen W 1976 *Astrophysical Quantities* 3rd ed. (London: Athlone) ch. 5, p. 92

[7] Bridges M and Ott W R 1977 *Appl. Opt.* **16** 367-76

[8] Pretzler G, Jäger H and Neger T 1993 *Meas. Sci. Technol.* **4** 649-58

[9] Takeda M, Ina H, and Kobayashi S 1982 *J. Opt. Soc. Am.* **72** 156-60

[10] Widmann K 1992 *Diplomarbeit* Technische Universität Graz

[11] Widmann K, Pretzler G, Woisetschläger J, Neger T, and Jäger H 1993 Holographics International '92 ed Y Denisyuk and F Wyrowski *Proc. SPIE* **1732** 712-8

[12] Widmann K, Pretzler G, Woisetschläger J, Philipp H, Neger T, and Jäger H 1996 *Appl. Opt.* **35** 5896-902

[13] Hipp M, Fließer W, Neger T, and Jäger H to be published

Spatially-resolved determination of the electron density in a high pressure mercury lamp using two-wavelengths speckle-interferometry

W. Fließer, M. Hipp, T. Neger and H. Jäger

Institut für Experimentalphysik, Technische Universität Graz
Petersgasse 16, A-8010 Graz, Austria

1 Introduction

Experimental data of electron densities in plasmas of high pressure lamps are needed to improve computer simulation models to understand fundamental properties of these light sources. Optical two-wavelengths interferometry is a common tool for the determination of electron densities in plasmas [1]. It is based on the different wavelength dependences of the refractivity of electrons and heavy particles. For high sensitivity of the electron density determination one of the two waves should have a large wavelength.

We used the method of Digital-Speckle-Pattern-Interferometry (DSPI) [2,3,4] in connection with a temporal phase-shifting-technique [5,6] to evaluate the phase distribution of a wavefront after passing the plasma. In contrast to conventional interferometers the use of DSPI allows a compensation of the influence of the glass-bulb of the lamp on the phase of the wavefront. The advantage of DSPI against holographic interferometry is the direct detection of intensities by CCD-cameras instead of using photographic materials for storing the wave fronts without plasma. So we were able to use the 1064 nm line of a Nd:YAG-Laser (beside an Ar^+-Laser at 488 nm) to increase the sensitivity of the measurement.

2 Principle of measurement

The total refractivity $(n-1)$ of a plasma can be considered as the sum of the refractivities of its different particles [1]. Assuming a plasma containing only electrons and one sort of neutral and singly ionized atoms the measured phase shift of an electromagnetic wave of wavelength λ traversing the plasma is related to the number densities of the atoms N_a, the ions N_i and the electrons N_e by

$$\Delta\phi(x,y) = \frac{2\pi}{\lambda}\Big[\frac{1}{2\epsilon_0}\alpha_a(\lambda)\int_L N_a(\boldsymbol{r})\,ds + \\ + \frac{1}{2\epsilon_0}\alpha_i(\lambda)\int_L N_i(\boldsymbol{r})\,ds - \\ - k\cdot\lambda^2\int_L N_e(\boldsymbol{r})\,ds\Big], \qquad (1)$$

with the factor of physical constants being $k = e^2/8\pi^2\epsilon_0 m_e c^2$. x and y are spatial coordinates in the interferogram, $\boldsymbol{r}$ is the position vector in the plasma. L is the geometrical path length of the light beam through the plasma, α_a and α_i are the polarizabilities of atoms and ions involved.

Because of the weak wavelength dependence of the polarizabilities it is possible to calculate the electron density in the plasma by producing two interferograms at different wavelengths λ_1 and λ_2. Assuming radial symmetry for the plasma arc of the lamp and interferometric side-on diagnostics the radial distribution of the electron density $N_e(r)$ in one cross section (with constant coordinate x in the two dimensional interferogram) can be calculated from the two measured phase shifts $\Delta\phi_1(y)$ and $\Delta\phi_2(y)$ by an *Abel*-inversion using a *Fourier*-algorithm [7]:

$$N_e(r) = \frac{4\epsilon_0 m_e c^2}{e^2(\lambda_2^2 - \beta\lambda_1^2)}\cdot \qquad (2)$$
$$\cdot\int_r^R \frac{d(\beta\Delta\phi_1(y)\lambda_1 - \Delta\phi_2(y)\lambda_2)}{dy}\cdot\frac{dy}{\sqrt{y^2-r^2}}$$

β is defined as $\alpha_a(\lambda_2)/\alpha_a(\lambda_1)$.

3 Measurements and results

The optical setup can be considered as two speckle-interferometers of MACH-ZEHNDER-type for the wavelengths of 488 nm and 1064 nm (Fig. 1). This arrangement allows a digitization of the two interferograms for both wavelengths at the same time. To reduce the radiation of the plasma, diaphragms and interference filters were used in the optical paths of the object arms.

A common phase shifting device in the reference arm of the two interferometers allowed the digitization of primary interferograms at defined reference phase shifts. The phase shift was controlled by measuring the intensity at the exit of an additional MICHELSON-interferometer in the reference arm of one of the two speckle-interferometers. The phase distributions

were calculated from four phase-shifted frames of primary interferograms in the two object states.

Figure 2 shows the electron density in one cross section of the lamp calulated using eq. 2.

An error of $0.8 \cdot 10^{22}$ m^{-3} was estimated because of the accuracy of the phase determination (about $2\pi/20$). The lowest electron densities which can be measured depend on difference of the wavelengths choosen and are in the range of $2 \cdot 10^{22}$ m^{-3} at 1 cm plasma length.

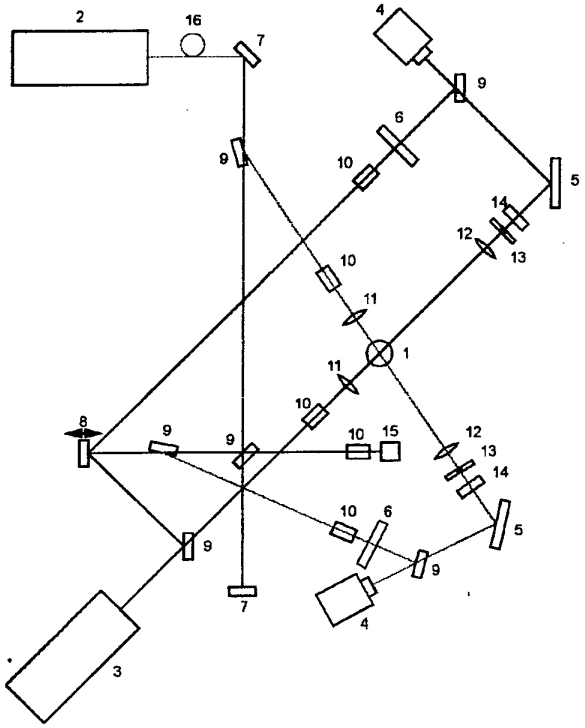

Figure 1: *Schematic optical setup for the spatially resolved determination of the electron density in a high pressure mercury lamp by DSPI.* **1** high-pressure mercury lamp, **2** Ar^+-laser, **3** Nd:YAG-laser, **4** CCD-camera, **5** reflecting diffusor, **6** transmitting diffusor, **7** laser mirror **8** phase shifting mirror, **9** beamsplitter, **10** beam expander, **11** cylindric lens, **12** collecting lens, **13** diaphragm, **14** interference filter, **15** photodiode.

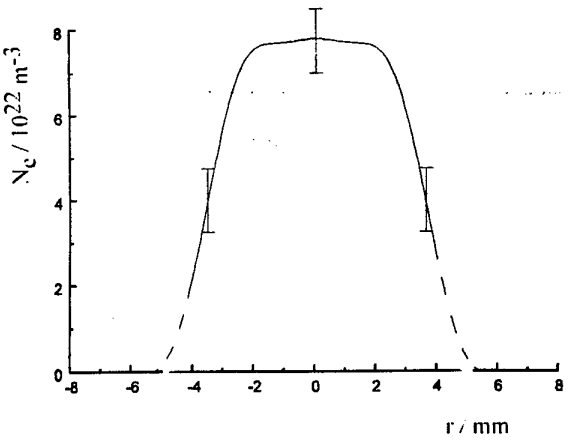

Figure 2: *Radial distribution of the electron density in one cross section of the mercury lamp.* $I_{eff} \approx 3A$.

4 References

[1] Alpher R. A. and White D. R.: *Optical interferometry* in *Plasma Diagnostic Techniques*, ed. Huddlestone R. H. and Leonhard S. L., Academic Press, New York (1965)

[2] Butters J. N. and Leendertz J. A.: Opt. Laser Technol., **3**, (1971) 26

[3] Nakadate S., Yatagai T. and Saito H.: Appl. Opt., **19** (1980) 1879

[4] Creath K.: Proc. SPIE, **501** (1984) 292

[5] Creath K.: Proc. SPIE, **556** (1985) 337

[6] Creath K.: *Temporal phase measurement methods*, in *Interferogram Analysis*, ed. Robinson D. W. and Reid G. T., IOP Publishing (1993)

[7] Pretzler G.: Z. Naturforsch., **46a** (1991) 639

Optical Diagnostics of Plasma Produced in Laser Beam Welding Process

J. Pavlík*, S. Novák*, R. Hrach*, P. Kuba*, A. M. Koseček**, P. Fodrek**, F. Kolenič**
* Department of Physics J. E. Purkyně University, České mládeže 8, CZ - 400 96 Ústí nad Labem, Czech Republic
**Welding Research Institute, Račianská 71, 832 59 Bratislava, Slovakia

1. Introduction

Laser welding proved to be a great success in the research laboratory as well as in industry. The high power laser welding is performed with very complex physical phenomena. In order to expand practical applications of high power laser welding, it is important to understand the basic phenomena of laser welding. These physical phenomena should be observed using several method of diagnostics to get a highly reliable welding process.

In this paper we described an experiment, a laser-induced plasma plume during laser welding of steels was investigated using a method of optical emission spectroscopy. A high power CO_2 laser (λ = 10.6 μm, output laser power P = 2 to 4 kW) was used for various processing applications, such as the heat treatment of metal surfaces or welding and cutting metals in the Welding Institute in Bratislava. In a laser machining the shield gas atmosphere plays an important role in determining the quality of the work sample. Argon, Helium or their mixture are used as a shield gas for welding. Nitrogen is applied as a shield gas for the heat treatment of metal surfaces and Oxygen for cutting metals. The purity of gas ranged from 99.996% to 99.998 %.

The material was heated by the interaction between the focused laser beam and the treated material during material processing (the temperature of the processed material T= 1200 to 1400 °C [1]), and the surface will be melted instantly to form plasma. The metal plasma will conflict with the shield gas. At the same time the ionization of the shield gas occurs. The plasma plume of the size of magnitude of a few cm is formed near the surface processed. There are both the shield gas and the vapours of the material processed in the plume.The laser-induced plasma plume affects deeply the processing results. It is an important parameter on which the quality of laser welding depends. Experimental and theoretical work on this kind of plasma is rare [2, 3 and 4]. However, it is obvious that it is necessary to know the different plasma parameters as well as the plasma-chemical reactions taking place in order to explain the behaviour of these media and to optimize their effectiveness during the process laser welding.

2. Observation Method of Plasma

We have made an analysis of the possibility of acquiring basic data of that type of plasma. The suitable methods for analyzing on of the laser-produced plasma parameters seem to be non-contact methods. We have chosen the method of the optical emission spectroscopy.

It is necessary to use either a system of collimating lenses or an optical coupling by an optical fibre cable with an fibre optic probe for collecting the from plasma-emitted radiation to the entrance slit of the spectrometer. We have used the second way. We have prepared a simple system of the fibre optic cable with the fibre optic probe, see Fig. 1. The fibre optic probe system is arranged so that the entrance of the fiber optic cable pipe (circular profile, diameter 2.8 mm) is located at the focal plane of the probe lens. In this way the light emitted from the plasma was introduced to the entrance pipe of the fiber optic cable (60 fibers, diameter: 250 μm).

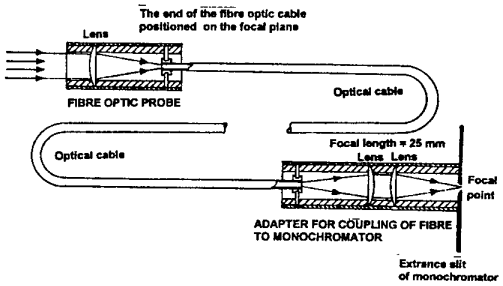

Figure 1: The optical arrangement of the fiber optic cable with a fiber optic probe

Because the probe consists of the focusing and receiving optics in one compact unit, it allows us right to position the probe to the plasma plume.The solution chosen makes it possible to complete the fibre optic probe together with the technological head of the laser, in the future.

The farther end of the bundled fibre optic cable is connected to a fibre optic adapter which transforms the aperture of fibre to the aperture of the monochromator.

Although optical fibres have enormous advantages, they have one drawback since of their small diameter they collect a limited amount of light.

As a spectrometer (in the wave length range of 450 - 700 nm) we used the mirror monochromator SPM-2 (produced by Zeiss Jenna, entrance slit width: 0.25 or 0.46 mm) with photodiode detector.

The scheme of the optical emission spectroscopy setup is shown on Fig. 2.

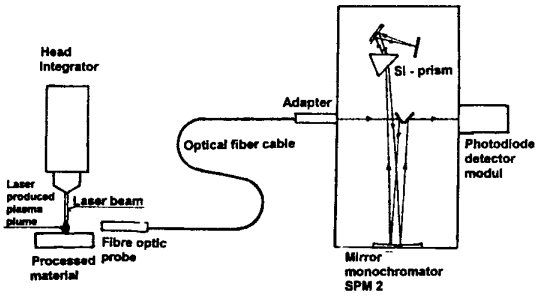

Figure 2: The schematic diagram of optical arrangements for spectroscopic measurement

3. First results of Observing Plasma Plume

The typical examples of our first results of the measured line emission spectra are shown on Fig. 3 (for shield gases - Ar, He) and in Fig. 4 (their mixture) and in Fig. 5 (for different output laser powers, 2kW and 4 kW), where the left side the values of reference spectral lines [5, 6] and the right represents spectra emitted from the laser plume.

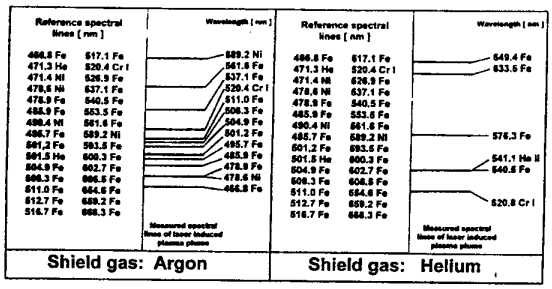

Figure 3: The emission spectra of plasma plume induced during the laser welding of austenitic steel. As a shield we applied the argon and helium gases.

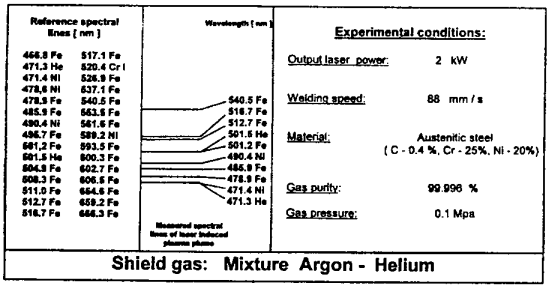

Figure 4: The emission spectrum of plasma plume induced during the laser welding of austenitic steel. As shield gas the mixture of argon and helium (75% - Ar and 25%-He) was used.

The intensity of the measured light emitted from the plasma plume was varying. That fact complicates the further quantitative measurements of chosen spectral lines. Therefore these first measurements have been only qualitative and we prepare a system consisting of the imaging spectrograph Jobin Yvon - CP 200 and the CCD imaging camera SBIG - ST - 7I.

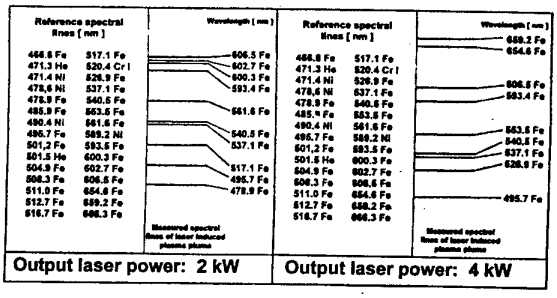

Figure 5: The emission spectra of plasma plume induced during laser welding of low carbon steel (C - 0.2%, Mn - 0.5%, Si - 0.3%) for different output laser powers. As shield gas we applied argon.

It is evident that our emission spectra include the emission lines mainly from the processed material components such as Fe, Cr and Ni. The emission lines of the working gases were observed, too.

4. Conclusion

The present study leads to the following conclusions:

An occurence of the particular emission lines depends on both the experimental parameters (laser power) and the laser-processed material parameters (according to the quality of steel and shield gas).

Our goal is to find out correlations between the metallurgical characteristics of the laser processed material and the properties of the laser produced plasma. Both aims seem to be possible.

We can assume that the analysis of chosen characteristic emission lines makes it possible to optimize the material laser processing technology.

5. Acknowledgement

This work has been supported by the European Community through the COPERNICUS Grant No. CIPA - CT94 - 0183.

6. Reference

[1] A. M. Koseček and P. Fodrek: private information

[2] S. Kimura, Y. Makino and m. Ikeda: Proc. of the 6th Int. symp.- Nagoya - JWS, (1996) 185

[3] T. Maede, T. Maiwa, E. Ohmura and I.Miyamoto: Proc. of the 6th Int. symp.- Nagoya- JWS, (1996) 191

[4] T.Ohji, T. Shiwaku, Y.Hirata, and K. Hiraoka: IIW in Stockholm document - Doc. 212-881-95, (1995)

[5] H. Scheller: Einführung in die angewandte spektrochemische Analyse, VEB Verlag Technik Berlin, (1957)

[6] A. N. Zaidel, V. K. Prokofev and S. M. Raiskii: Tables of Spectrum Lines, Pergamon Press, Berlin, (1961)

Characterization of a multi-component plasma in an ionospheric plasma simulation chamber

Jean-François Roussel, Virginie Viel, Jacques Bernard
ONERA-CERT 2 Av. Edouard Belin 31055 Toulouse Cedex, France

Introduction

Simple plasma diagnostics, such as Langmuir Probes (LP) or Retarding Potential Analysers (RPA), are usually used to characterize one-component plasma, either drifting or at rest in the diagnostics' frame. However, some plasmas involve several distinct components, one at rest and the other drifting at supersonic velocity for instance. Such is sometimes the case in space: the ambient ionospheric plasma is drifting with respect to the spacecraft frame, and a second plasma component can sometimes be emitted at rest by the spacecraft. In ionospheric plasma simulation chambers, a drifting plasma is emitted to simulate ambient plasma flowing at spacecraft speed. It is yet impossible to avoid the generation of slow ions through Charge EXchange (CEX) between fast drifting ions and slow neutrals. The density of this CEX plasma at rest depends closely on the neutral pressure, but is usually higher that in orbit and can sometimes even exceed the drifting plasma density. In this context, the classical interpretation of I-V characteristics, either for drifting plasma or at rest, does not apply, especially concerning LP. The outcome of this paper is to show that a proper analysis of LP characteristics allows to distinguish between the two components of the plasma and determine (at least) their densities. The method used in this study is to perform numerical simulations and use their results as an abacus to compare with experience, but it should lead to faster methods generalized from classical ones for one-component plasmas. We give the experimental results in a first section and their interpretation and comparison to numerical simulations in a second section.

Experimental Results

We performed measurements of plasma parameters with LP and RPA in an ionospheric plasma simulation chamber called JONAS that is a cylinder of 1.8 meter in diameter and 3 meters in length. The Kaufman ion source located at one of its ends generates an Ar^+ ion flow neutralized by an electron emitting filament. We obtain a plasma flow drifting at velocity v_i depending on the acceleration voltage V_{acc} applied on ions. Neutral (Ar) pressure is 3 10^{-6} hPa. LP and RPA are located at 1 meter from the source. Measurements were performed using different acceleration voltage values i.e. different drift velocities for the ions. The bias of a spherical LP of diameter 1 cm was swept from -10 V to +10 V. Current-tension characteristics for different V_{acc} are given in Fig. 1 (due to the source nature, the density varies with V_{acc}). The RPA retarding potential was swept around the potential V_{acc} corresponding to the drifting ion energy. Classical analysis of RPA current and LP characteristics in drifting plasma — extrapolated ion current at plasma potential gives the product of LP cross-section, ion density, speed and charge — yielded two values for plasma density. Density from LP characteristics exceeded the one from RPA approximately by a factor of 3 as can be seen on table 1.

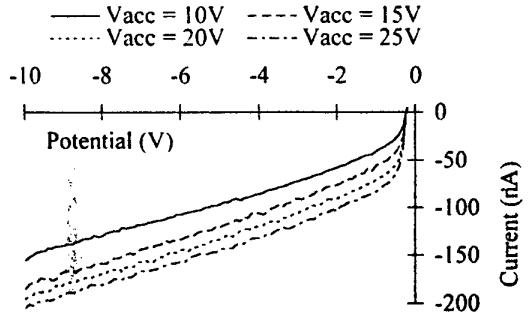

Fig. 1 : LP experimental characteristics (ionic branch).

V_{acc}	v_i	LP density	RPA density
10 V	6.9 km/s	4.4 10^5 cm^{-3}	1.2 10^5 cm^{-3}
15 V	8.5 km/s	5.1 10^5 cm^{-3}	1.5 10^5 cm^{-3}
20 V	9.8 km/s	5.8 10^5 cm^{-3}	2.1 10^5 cm^{-3}
25 V	11 km/s	5.9 10^5 cm^{-3}	2.3 10^5 cm^{-3}

Table 1 : Experimental densities obtained from classical treatment of LP and RPA characteristics.

Interpretation - Numerical simulaions

The discrepancy between RPA and LP values for density had to be understood. We first eliminated the possible causes constituted by secondary electrons and photo-electrons. We then examined the possibility that it originated in the slow CEX plasma component. In spite of its lower velocity, it is collected on a much larger surface — the one of the sheath — than the drifting component. A first hint that the experimental LP characteristics cannot be due only to a drifting plasma is the slope of its ionic branch : it is much larger than the one given by numerical simulations, either our (see below case C1) or from literature [1] — which are in good agreement together.

Consequently we modelled this two-component plasma thanks to a 3D Particle-In-Cell code for various densities of drifting plasma and CEX plasma at rest and swept the probe potentiel form -10 V to 0 V — electronic density is given by Boltzmann distribution which is faster than modelling electron dynamics but does not allow positive potentials. The densities of the seven simulated cases are given in table 2 and the corresponding LP characteristics in Fig 2 (now V_{acc}=15V always). In a numerical simulation, currents from drifting ions, CEX ions and electrons can be distinguished and both ion currents are given separately in Fig 3. This figure and the potential and density distributions around the probe — not given here — make it easy to understand that :

1- The fast drifting ions cannot easily be deflected by the probe potential that is lower than their kinetic energy, they are not very sensitive to the potential: the slope of drifting ion characteristics in Fig 3 is small.
2- On the contrary, slow CEX ions are collected at the surface of the sheath of which radius rapidly increases with probe potential: this yields larger slopes for CEX characteristics of Fig. 3.
3- As a consequence, one could roughly say that the slope of the total current is related to the CEX plasma density whereas the linear interpolation to zero potential of the characteristics is related to the drifting plasma density.

↓CEX Drift →	1.5 10^5 cm^{-3}	2.5 10^5 cm^{-3}	5 10^5 cm^{-3}
0			case C1
1.25 10^5 cm^{-3}			case C2
1.75 10^5 cm^{-3}	case A3	case B3	case C3
2.5 10^5 cm^{-3}		case B4	case C4

Table 2 : Drifting ion density (1st line) and CEX ion density (1st column) of numerical simulations

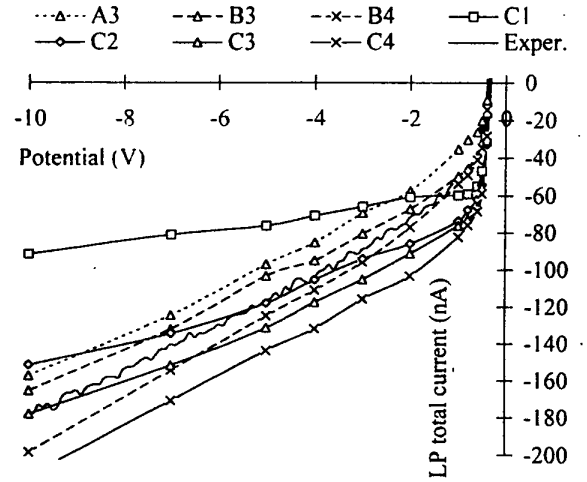

Fig 2 : numerical simulation LP characteristics (cases A3, B3-B4, C1-C4 of table 2) compared to experiment.

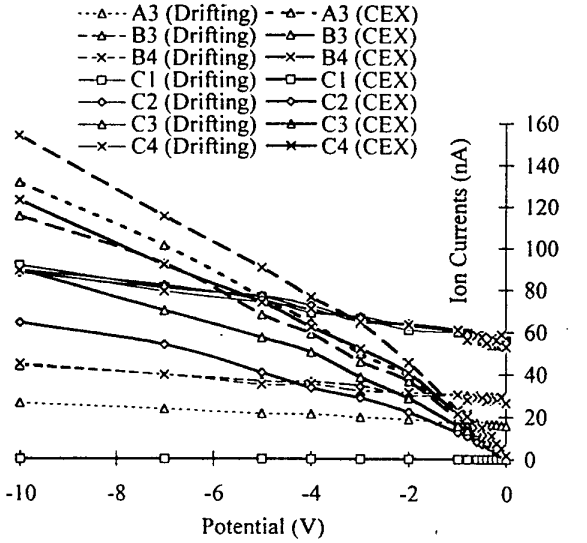

Fig 3 : Contribution from drifting and CEX plasma to LP current in numerical simulations (see table 2).

The point 3 is still too approximate and this needs further analysis. For the time being, we simply compare experimental results to several simulations in Fig 2. Clearly, the small voltage part of the characteristics (-2 to 0 Volts) is consistent with the dashed lines (B series, drifting density = 2.5 10^5 cm^{-3}) and not with full lines (C series, drifting density = 5 10^5 cm^{-3}) or the dotted line (A series, drifting density = 1.5 10^5 cm^{-3}). The high voltage part of the characteristics, or its slope, is between B3 and B4 simulations. The densities consistent with simulations are then intermediate between B3 and B4 : about 2.1 10^5 cm^{-3} for CEX plasma, and 2.5 10^5 cm^{-3} for drifting plasma.

The drifting plasma density deduced from this analysis, 2.5 10^5 cm^{-3}, is much lower than the one obtained from the standard analysis assuming no slow plasma (5.1 10^5 cm^{-3}, see table 1). Although not in perfect agreement, it is much closer to the value given by the RPA, 1.5 10^5 cm^{-3}. Of course, the external grid of the RPA is grounded and so no sheath is present to collect more slow ions : the ratio of speed makes then the RPA almost insensitive to the slow plasma component and 1.5 10^5 cm^{-3} is only the fast drifting ion density.

One could be surprised by the high density of slow CEX plasma in spite of the relatively low neutral pressure. However, studies in similar conditions [2] gave high densities too. Moreover, we performed an extra experiment in which we protected the LP from the direct drifting flux by a shield. It was only exposed to the slow plasma, although perturbed by the shield's presence and wake. The result, about 1.10^5 to 2.10^5 cm^{-3}, although very approximate, confirms the presence of a high density of slow ions.

As a last remark, let us note that we really have to perform a simulation to obtain the characteristics of Fig 2. They cannot be simply given by a sum of standard characteristics in a drifting plasma on the one side and in a plasma at rest on the other: an increase of drifting ion density results in a lower Debye length, a smaller sheath and so a lower collection of slow CEX ions. It is very clear in Fig 3 on the series A3-B3-C3 or B4-C4 with fixed slow plasma density, where the increase of drifting plasma density results in a lower collection of slow plasma.

Conclusion

New analysis of Langmuir probe characteristics in a two-component plasma allowed us to obtain the densities of both the drifting plasma and the plasma at rest. This was confirmed by RPA results and complementary LP measurements. This analysis was carried out by direct comparison of experimental and simulated characteristics but direct treatment of experimental characteristics should be possible in future.

References

[1] R. Goddard, Thesis, 1975, University of Toronto.
[2] A. Soubeyran, Thesis, 1991, Ecole Nationale Supérieure de L'Aéronautique et de L'Espace, Toulouse, France.

Measurement of Line Intensity Ratios from Low-Pressure, Weakly-Ionized Helium Plasmas

Tamotsu Sasada, Mamoru Matsuoka and Motoichi Kawaguchi
Department of Industrial and Technical Education, Mie University, Tsu, Mie 514, Japan

1. Introduction

The measurements of electron temperature (T_e) using line intensity ratios of helium have been proposed and performed on the basis of the LTE (Local Thermal Equilibrium) model for high electron density (n_e) plasmas [1], or the CORONA model for low electron density plasmas [2] with $T_e > 10$ eV. Recently, more general treatment is proposed for plasmas with wide range of density but with $T_e > 20$ eV on the basis of the CR (Collisional-Radiative) model [3]. We studied experimentally whether T_e measurements from these line intensity ratios are applicable for low n_e ($\sim 10^{17}$ m^{-3}) and low T_e (< 10 eV) plasmas.

2. Experimental Setup

Figure 1 shows the experimental setup. The discharge tube was a pyrex glass sphere filled with helium of 133 Pa. When a 13.56 MHz rf wave of 20 W$\sim$70 W was applied with an antenna coil of 3 turns wound around the tube, the doughnut-shaped plasma was formed. Line intensities of visible light from the plasma were measured using a monochrometer.

We evaluate five line intensity ratios appeared in references[1-3] ;

468.7 nm/587.6 nm	(L)	LTE	[1]
443.7 nm/412.1 nm	(C)	CORONA	[1]
492.2 nm/471.3 nm	(R1)	CR	[2]
501.6 nm/471.3 nm	(R2)	CR	[2]
504.8 nm/471.3 nm	(R3)	CR	[2]

Grotrian diagrams including these lines are shown in Fig. 2. Four ratios (C. R1, R2 and R3) are the ones of singlet to triplet lines of He I . while one pair (L) is the one of a doublet line of He II to a triplet line of He I.

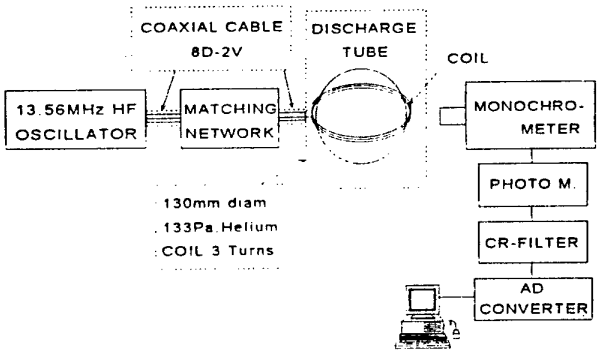

Fig.1. Experimental setup.

3. Experimental Result

Two typical spectra at 30W and 60W are given in Fig.3 where light intensity is normalized so that the intensity of the line of 587.6 nm takes the value of 0.5. Smooth lines in the figure indicate the sensitivity of the measuring system, including the transparency of the glass tube, the characteristics of the monochrometer and the photo-multiplier. Shown are the spectra before calibration using this curve. It is clear that the line intensity ratios are varied depending on the rf power.

From C-pair data, the electron temperature is evaluated to be less than 10 eV, which is the lower limit of the conversion curve based on the CORONA model [1]. If the curve is extrapolated, the electron temperature is evaluated to be about 2 eV, which is a reasonable value for such a low-powered plasma.

As for R1, R2 and R3-pairs, however, the electron temperature is evaluated to be as high as about 20, 100 and 50 eV, respectively. Here we used the conversion

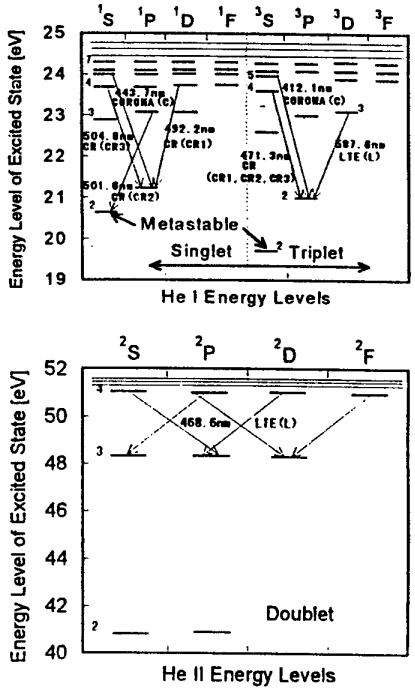

Fig.2. Grotrian diagrams of He I and II.

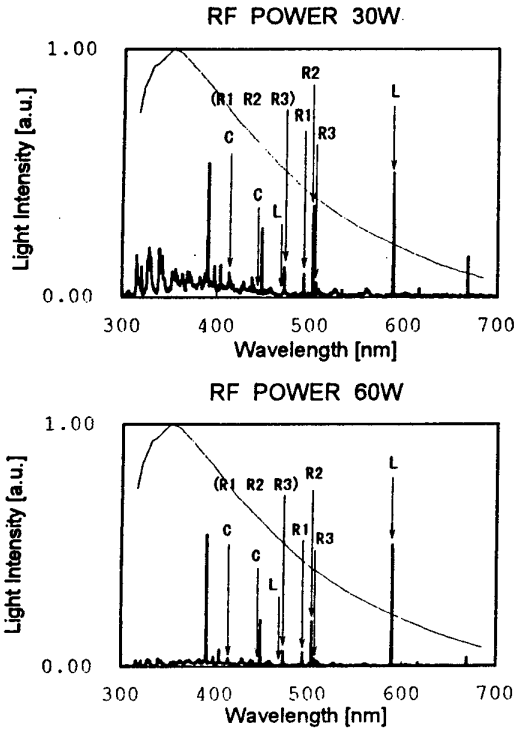

Fig.3. Spectra for 30W and 60W.

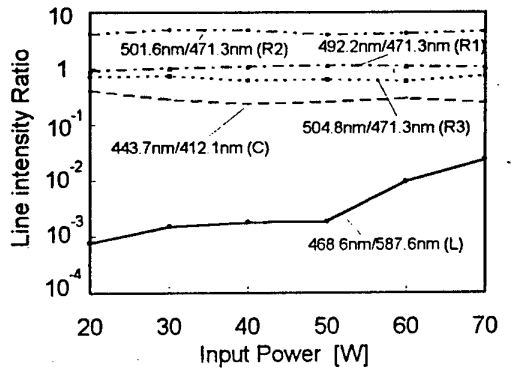

Fig.4. Dependence of the line intensity ratios on the rf power.

curve based on the CR model for $n_e=10^{18}$ m^{-3} [1]. There are two possible reasons for too high T_e results. In such an rf discharge as this experiment, high-energy electrons can be easily produced. These high-energy electrons mainly determine the line intensity ratios. The other reason is the influence of the metastable state of helium. In this experiment, the gas density is 2×10^{23} m^{-3} (133 Pa). This is much higher than 5×10^{19} m^{-3}, above which the resonance absorption becomes significant. In our experiment, both contributions would give high electron temperatures.

In our experimental result, however, the ratio for L-pair showed a monotonous increase with the rf power and seems to reflect the variation of T_e though the other plasmas parameters, such as n_e may contribute, too. This ratio varies by several orders of magnitude in the range 3 eV$\leqq T_e \leqq$10 eV, while the others vary only by a factor. Thus L-pair seems still the best one to deduce T_e in the range less than 10 eV. To this end, re-calculation with recent atomic data and re-consideration would be required.

[1] R. Mewe : Brit. J. Appl. Phys, **18** (1967) 107
[2] R. J. Sovie : Phys, Flulds, **7** (1964) 613
[3] S. Sasaki, S. Takamura, S. Watanabe, S. Masuzaki,T. Kato and K. Kadota : Rev. Sci. Instrum, **67** (1996) 3521
[4] M. Monte, M. Matsuoka and M. Kawaguchi : Proc. 7th Intern. Symp. Sci. &Tech. Light Sources, 22P, Illm. Eng. Inst. Jp, Kyoto (1995).

AN ELECTRON ENERGY ANALYSER IN MAGNETISED PLASMAS

V. Antoni, M. Bagatin, D. Desideri, E. Martines, G. Serianni, F. Vallone, Y. Yagi*

Consorzio RFX
Padova, Italy
*Electrotechnical Laboratory, Tsukuba, Japan

The electron energy distribution function (EEDF) in magnetised plasmas can be measured using the electrostatic Electron Energy Analyser (EEA) [1].

An electrostatic EEA is made up, in its basic form, of a front plate with a pinhole, aimed to stop the ions, a repeller electrode, used to discriminate the electron energy, and a collector. The less energetic electrons entering the probe through the pinhole are restrained by the repeller, which is polarised negative with respect to the local plasma potential, whereas the higher energy component is captured by the collector. Measuring the collector current for different repeller voltages yields the dependence of the electron flow on the parallel energy.

If $f(v_{//},v_{\perp})$ is the electron distribution function averaged on the fast cyclotron motion and V_{rep} is the repeller potential, the collector current I_{col} is given by:

$$I_{col}(V_{rep}) = -eA \int_{v_{//min}}^{\infty} v_{//} dv_{//} \int_{0}^{\infty} 2\pi v_{\perp} dv_{\perp} W(v_{//},v_{\perp}) f(v_{//},v_{\perp})$$

where $v_{//min} = (-2V_{rep}/m)^{1/2}$, m is the electron mass and A is the area of the pinhole. The function $W(v_{//},v_{\perp})$ is a transparency function which accounts for the selection in perpendicular velocities caused by the radius and thickness of the pinhole.

An electrostatic EEA has been used to study the EEDF in the outer region of plasmas magnetically confined in the RFX reversed field pinch experiment [2], with particular emphasis on the detection of the field-aligned superthermal tail [3]. The EEA equipment used in RFX has been originally developed for the TPE-1RM20 experiment [4], and is schematically shown in fig.1.

The EEA has been operated in 600 kA discharges with on-axis densities in the range $2\text{-}8\cdot10^{19}$ m^{-3} and on-axis electron temperatures T_0 = 200-350 eV. The outer region plasma where the EEA was inserted has a typical density of $5\cdot10^{18}$ m^{-3} and typical temperature of 20 eV [5].

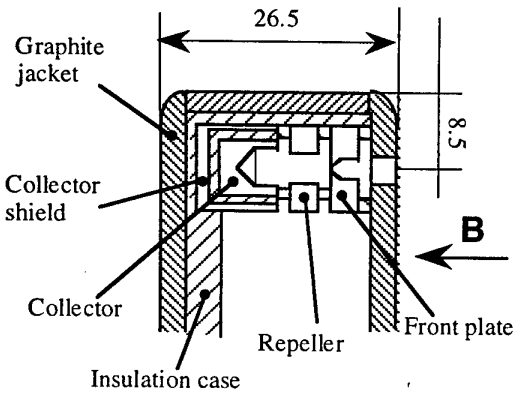

Fig.1: Scheme of the EEA used on RFX.

The front plate is a disk made of molybdenum, while the repeller ring and the collector cup are made of a W/Cu alloy. The front plate has a 2.5 mm diameter channel with a 0.1 mm diameter pinhole (0.05 mm thick). Typical Larmor radii of bulk electrons and hydrogen ions in the edge of RFX for 600 kA discharges are 0.07 mm and 3 mm respectively and the Debye length is of the order of 10-20 μm. The pinhole radius is thus comparable to the Debye sheath thickness. In order to survive the high energy fluxes (100 MW/m^2), the equipment is protected by a graphite jacket 3 mm thick. The diameter of the entrance hole in the graphite is 3 mm. While in TPE-1RM20 the jacket was electrically connected to the vacuum vessel, on RFX it has been kept floating, in order to avoid large currents to be driven through the insertion system.

The transparency function $W(v_{//},v_{\perp})$ has been evaluated analytically considering the equations of the orbits of electrons with random initial position. We consider in our model a magnetic field parallel to the pinhole axis, while neglecting the effects of the induced electric field due to the charging of the electrodes. If the thickness of the aperture is neglected the transparency function turns out to be equal to 1, which is not the case when the finite thickness of the entrance is taken into account.

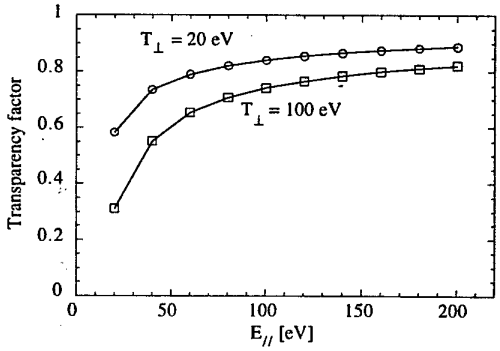

Fig.2: Transparency factor as a function of parallel energy.

The value of the transparency function, averaged in the perpendicular velocity space over a maxwellian with temperature lower than or equal to 100 eV, is always greater than 0.75 for all electrons with parallel energy above 100 eV (those typically collected by the EEA), and shows a small dependence on parallel energy in the range 100-600 eV, as shown in fig.2. For this reason it has been decided to assume in the data analysis $W(v_{//},v_{\perp})$ always equal to one, which implies that the collected current values could be underestimated by 25% in the worst case.

The Laplace equation has been numerically solved to calculate the potential profile inside the EEA, where no

ions are present. The on-axis potential in the repeller hole (3 mm diameter) is found to be ~ 95% of the applied voltage. The collector is usually kept to a voltage of +70 V (referred to the RFX vacuum vessel, like all the voltages reported in the following) in order to avoid the loss of secondary electrons. Anyway, no significant change in the data has been observed when the collector has been kept at the vessel potential.

A linear power supply has been developed in order to apply a variable voltage waveform to the repeller down to -1 kV, with a rise and fall time of a few milliseconds. Since a typical pulse in RFX lasts 100 ms, this has allowed to make multiple measurements of the I_{col}-V_{rep} characteristic during a single discharge.

Three different configurations of the EEA have been tested. In the first one (A) the front plate was electrically floating, in the second one (B) it was connected to the vacuum vessel through a 2.3 Ω, 50 W resistor and in the third one (C) it was in electrical contact with the graphite jacket. With configuration (A) the front plate potential was systematically lower than -100 V, leading the collector current signal to saturate for repeller voltages higher than -100 V. This made it impossible to obtain the low energy portion of the I_{col}-V_{rep} characteristic. In fact the Debye sheath thickness was comparable to the pinhole diameter, causing the front plate to act as an effective repeller. To overcome this limitation, configuration (B) was adopted. With this configuration, the front plate voltage was around -50 V, so that the lower energy part of the characteristic could be explored. However, this configuration resulted in high currents (~ 10 A) flowing from the front plate to the vacuum vessel, increasing the noise level on the signals. A reduced noise level was found with configuration (C), in which the front plate was at the same potential as the graphite jacket. Such potential was typically -50 V, resulting from an average of the floating potential over the whole jacket. Results obtained with configuration (C) are reported in the following.

Figure 3 shows different typical potentials of the electrodes and of the plasma. When considering the effect of the voltages applied to the various EEA components on electrons entering the device, it is important to note that they must be referred to the potential V_p of the unperturbed plasma away from the diagnostic. Thus, for instance, the effective potential barrier given by the repeller will actually be V_{rep}-V_p.

Generally speaking, due to the small pinhole radius, the first potential barrier encountered by an incoming electron is that originated by the front plate, V_{fp}-V_p. In the case where the front plate is kept electrically floating, this potential difference will be equal to the Debye sheath voltage drop, that is of the order of $-3T_e$ for a maxwellian plasma with local electron temperature T_e. Indeed, the experimental I_{col}-V_{rep} characteristics show a saturation for repeller voltages higher than V_{fp}, confirming the presence of this potential barrier. The consequence of this effect is that with a floating front plate only repeller voltages lower than V_{fp} are useful for deducing the properties of the electron distribution function, so that only the portion of distribution function with energies higher than $3T_e$ can be explored. In the presence of a superthermal tail the sheath potential drop rises, depending on the relevance of the tail with respect to the bulk of the distribution function having temperature T_e.

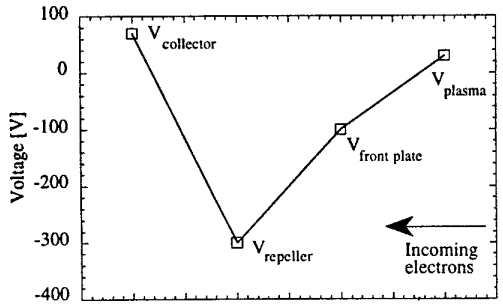

Fig.3: Potentials encountered by incoming electrons.

In order to detect the superthermal tail on RFX, the repeller voltage V_{rep} has been linearly swept in 10-20 ms from 0 to -600 V (below this value the signal to noise ratio was too small), several times per discharge. Figure 4 shows an example of the resulting I_{col} -V_{rep} characteristic, fitted with a half-maxwellian model for the superthermal tail, indicating in this case that such tail has a temperature of the order of 100 eV.

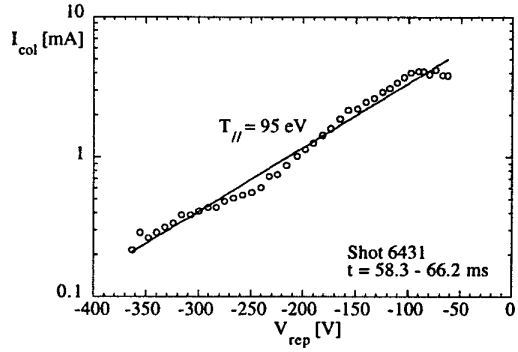

Fig.4: Typical I_{col}-V_{rep} characteristic.

The extensive use of the EEA has allowed to detect and characterise the field-aligned unidirectional superthermal electron flow in the outer region of RFX. The diagnostic has proven to be very resistant to the interaction with the plasma, and no sign of perturbation have been observed over the discharge.

References

[1] J. C. Ingraham et al., Phys. Fluids B **2**, 143 (1990).

[2] L. Fellin, P. Kusstatscher, G. Rostagni, Fusion Eng. Des. **25**, 315 (1995).

[3] Y. Yagi, V. Antoni, M. Bagatin, D. Desideri, E. Martines, G. Serianni, F. Vallone, "First measurements of electron energy distribution in RFX edge plasma", to be published in Proceedings of the 23rd EPS Conference on Controlled Fusion and Plasma Physics, Kiev, 1996.

[4] Y. Yagi, Y. Hirano, Y. Maejima, T. Shimada, Japanese J. of Applied Phys. **35**, 4064 (1996).

[5] V. Antoni E. Martines, M. Bagatin, D. Desideri, G. Serianni, Nucl. Fusion **36**, 435 (1996).

Vibrational and translational temperature measurements in nitrogen and air glow discharge by 2λ-CARS spectroscopy method.

O.A. Gordeev, K.A. Vereshchagin, V.V. Smirnov, V.A. Shakhatov.

Russian Academy of Sci., Moscow Radiotechnical Institute, Varshavskoe shosse 132, Moscow, Russia.

Introduction

The last several years scanning CARS - spectroscopy (coherent anti - Stokes Raman scattering spectroscopy) is widely used for many of the investigative and of the practical tasks of the gas thermometry in discharges. One of essential lack of this method is rather long time of spectrum record. In our paper there is suggested and applied for research of discharges alternating method two - wavelength coherent anti-Stokes Raman scattering spectroscopy (2λ-CARS-spectroscopy). It combines the high sensitivity of scanning CARS - method and high speed of spectrum record. In the present work these methods are used for the determination of the gas temperature T_g, vibrational and rotational excited molecules populations of N_2 in the ground state (VP) in a positive column of glow discharge in the molecular nitrogen and in the air.

Experiment

The discharge was realized in quartz tube (1) (see Fig.1). It was characterized by following parameters: the distance between platinum electrodes was 58 cm; the tube radius was 1.8 cm; the discharge current was varied from 30 to 50 mA. The measurements were carried out in N_2 at 3.5, 7.0, 9.5 Torr and in the air at 20 Torr. The tube had a water and liquid nitrogen cooling loops. The reduced electric field (E - is average electric field strength in the positive column, and N is the molecule concentration at the discharge axis, defined with due regard for the drop of density as result of heating) varied from 40 to 80 Td.

The following methods were used for direct measurements of the degree of the vibrational - translational nonequilibrium in a discharge: the scanning version of CARS spectroscopy; and the two-wave version of CARS. The scanning CARS spectrometer has been described in detail in [1].

In the two-wave version of CARS, a 2λ-CARS spectrometer was used, whose scheme is shown in Fig.1. Its laser system consists of a single-mode YAG:Nd laser (2) with frequency doubling and a dye laser (3) generating the two-wavelength radiation. For this purpose, the resonator scheme was used with a common diffraction grating (4) and two "plug" mirrors (5) tuned separately. The master oscillators work in the pulse-periodic mode with the repetition frequency of 10 Hz and generated pulse duration of 25 ns. In the course of the experiment, the intensities of nonoverlapping Q - lines were measured that correspond to two vibrational - rotational transitions v,J=6→v+1,J=6, and v,J=16→v+1,J=16 (v and J are the vibrational and rotational quantum numbers). To normalize the radiation intensities of the CARS signals obtained simultaneously in two different transitions of the Q-branch, a reference channel was used in experiments. The CARS signals, corresponding to the two above mentioned transitions and obtained in the investigated (1) and reference (6) channels, were filtered by the monochromator (7) and registered by the optical multi-channel analyzer (OMA-III) (8). Procedures of data acquisition and processing (9) were automated on the basis of an IBM PC (10) and were described in more detail in [2].

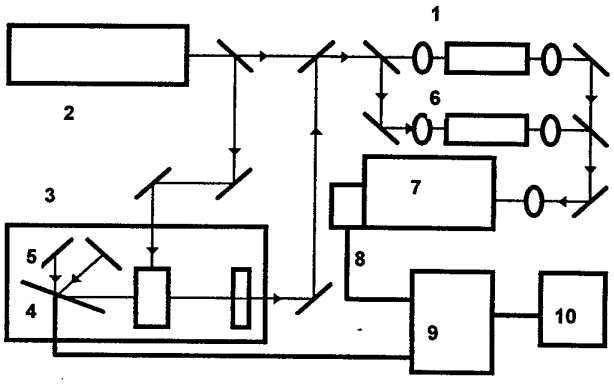

Fig.1

Theory

The numerical model is in detail described in [3,4]. The rate constants for excitation and deexcitation of first ten vibrational levels (v=1-10) by electron impact were calculated by averaging of corresponding cross sections using electron energy distribution function (EEDF) which was received by numerical solving of Boltzmann equation. The Boltzmann equation was completed by collision integrals taking account the superelastic electron-molecule collisions for vibrational levels v=1-10. Populations of the first five vibrational levels of N_2 in the ground electron state were determined from measured CARS spectra. However information about populations of vibrational levels v>4 is also necessary for correct calculation EEDF. The approximation of VP by the Boltzmann or Treanor distribution may result in considerable errors. Therefore calculations were carried out of the VP in

glow discharge under conditions of our measurements and the experiment [5].

Results and discussion

Fig.2 (a) shows the histogram of values of the rotational temperature resulted from 170 of impulses N for the room temperature at pressure 20 Torr.

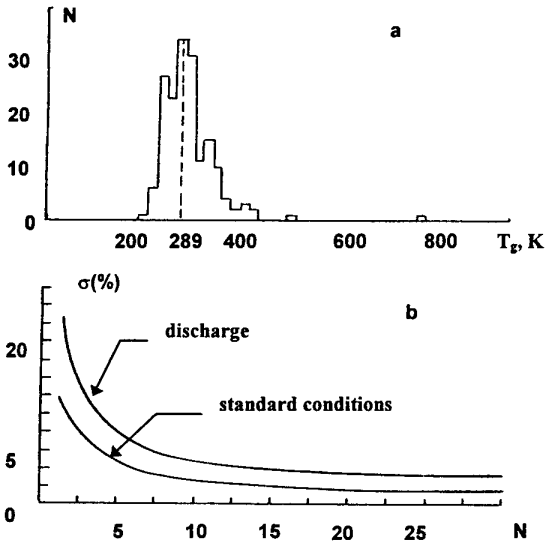

Fig.2

One can show (see Fig.2 a), that the data are grouped around on the most of possible value which is equal to 289 K. On the base of experiments the air temperature measurements for standard conditions in the probe volume and also in the discharge which was cooled of liquid nitrogen for it stability, we were determined the standard deviation of measurement σ(%) versus number of N (see Fig.2 b). Using results above considered analysis the rotational temperature in the discharge was measured for 1 s. The average temperature was equal to 525 K with the standard deviation of 26 K. Notice that achieved accuracy 5 % at averaging of 10-15 impulses at repetition rate 10 Hz requires 1-1.5 s for the temperature measurement as for version of scanning CARS for measurement with analogy of accuracy it has 5 minutes and 3000 impulses respectively.

In the Table there are compared the results of measurements T_g and T_v , carried out in the present work. Also there are presented the T_v values received from the VP, which were calculated on the basis of master equations for nitrogen glow discharge using the above mentioned experimental parameters.

Table

Experimental data					Calc
E/N	scanning CARS		2λ CARS		T_v
Td	T_g, K	T_v, K	T_g, K	T_v, K	K
80	480±35	4470±350	460±25	4450±220	4415
45	530±35	4940±360	510±25	4920±245	4750
60	600±40	4770±370	580±30	4750±240	4700

From the Table it is evident that the values T_g and T_v, measured by two above mentioned CARS-methods are in good agreement among themselves and so they are with the values predicted by theory. We can conclude that the suggested in [2] the 2λ-CARS - spectroscopy method permit us to measure parameters of glow discharge plasma with good accuracy. The essential advantage of this method is the spectrum record time reduction about of two order of magnitude.

Fig.3 illustrates a good agreement between calculated and measured by probe method [5] EEDF at E/N=70 Td.

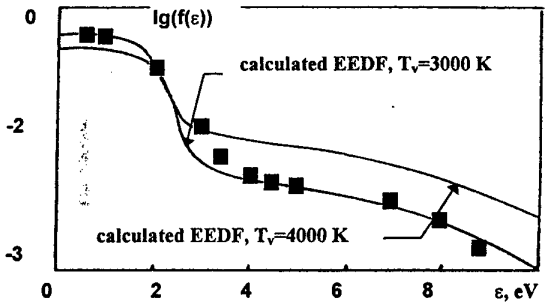

Fig.3

Note that it is only the inclusion of the superelastic collisions of electrons with vibrationally excited molecules, as well as of the decrease of the population with level v=0, that makes it possible to reach a consistent description of the electron component and vibrational kinetics.

Thus the performed analysis of possibilities of scheme 2λ-CARS shows that such approach let essentially to decrease the time registration of temperature and to be perspective for research of the rapid processes and also of the impulse discharges.

References

1. A.V. Bodronosov, K. A. Vereshchagin and et. al.: Sov. J. Tech. Phys. 64 (1994) 47. (in Russian)

2. A.V. Bodronosov, K. A. Vereshchagin and et. al.: Sov. J. Quantum Electronics 21 (1994) 891. (in Russian)

3. O.A. Gordeev, V.A. Shakhatov: Sov. J. Tech. Phys. 65 (1995) 40. (in Russian)

4. A. V. Bodronosov, K. A. Vereshchagin and et. al.: High Temperature. 34 (1996) 656.

5. Yu. A. Ivanov, L. S. Polak et. al.: Teplofiz. Vys. Temp. 9 (1971) 1151.

Probe Diagnostics of Strongly Ionized Noble Gas Plasma at Atmospheric Pressure

F.G.Baksht, N.K.Mitrofanov, A.B.Rybakov and S.M.Shkol'nik
A.F.Ioffe Phys.-Techn.-Inst. Rus.Acad.Sci., Polytechnicheskaya 26, St.Petersburg 194021, Russia

1. Only the probe methods permit to determine a plasma potential - a parameter which is very essential for the investigation of near-electrode phenomena in gas discharges. This is the most important stimulus to expand the field of application of probe diagnostics. The probe measurements were applied to strongly ionized high pressure plasma for a long time (e.g. see [1,2]). But the procedure of such measurements is not enough elaborated up to now.

The purpose of the present investigation is the elaboration of the methods of probe diagnostics of strongly ionized plasma at atmospheric pressure. The spectroscopic measurements were used as a control method. The experiments were performed in a free burning argon arc which is of common use for a plasma production in a lot of applications. The results of probe characteristics calculation for xenon plasma are described in [3]. In the present paper the theory developed in [3] is applied to calculation of probe characteristics in Ar plasma.

2.. An arc was vertically oriented. A tungsten stick cathode of diameter D=2 mm with a semispherical tip was disposed at a bottom of the arc. A flat copper water-cooled anode was disposed at a top of the arc and at 12 mm distance from the cathode. A thermionic emission of the cathode was supplied by the cathode self-heating by a duty arc current I_d = (50-70) A. A pulse generator of single rectangular pulses (I≤ 1000 A) with a duration up to 5 ms was connected in parallel. A pulse front depended upon the transient arc processes and was about 1 ms long. The measurements were carried out in a quasistationary mode of operation, i.e. in 3 -4 ms after the beginning of a pulse discharge. A flying spherical probe of d ≡ 2a = 0.5 mm in diameter moved at a velocity ≥ 1 m/s across the arc core zone. The probe position uncertainty was estimated to be less than 0.3 mm. Time dependences of floating probe potential V_f and ion current I_i were measured, I_i being measured at negative probe potential (5 - 15) V with respect to V_f. For each operation mode the measurements were performed in sets of 8 - 10 oscillograms. Then the results were averaged. To record an arc emission spectrum the monochromator was jointed to the multichannel optical analyzer. An enter slit width of the monochromator was 0.15 mm to provide an adequate record of intensity across the emission spectrum. During a single exposure the spectral range of 25 nm was recorded.

In a plane of an enter slit of the monochromator the reduced horizontally oriented arc image was formed which was scanned across the slit. On the discharge axis the spatial resolution was ≤ 0.3 mm. The exposure was varied in a range (0.2 - 0.5) ms.

3. Previously a probe operation in a dense collisional plasma was analyzed theoretically at various degrees of ionization but mainly for comparatively low plasma pressures when collisions between electrons and heavy particles did not affect an electron temperature T_e in a near-probe layer. In the present investigation the calculations are performed for the other case when a common temperature T of electrons and heavy particles is established due to frequent collisions between them in a near-probe layer. The temperature T is not equal to the temperature T_∞ of undisturbed plasma. This case is typical for high pressure plasma.

The calculations were performed for a spherical probe with radius a = 0.25 mm which was inserted in argon plasma at atmospheric pressure. The method of calculation was described before [3]. The near-probe layer was divided to several layers according to effects dominating in each layer [4,5]. The following hierarchy of characteristic lengths is supposed to be fulfilled : $L_o << l_i << L_r^+ << L_T << a$, where L_o is Langmuir sheath dimension, l_i is an ion free path, L_r^+ is Ar^+ recombination length and L_T is a temperature relaxation length [4,5]. We consider the case in which the plasma is fully ionized at the distance, where $r > L_r^+$. According to these unequalities it is possible to separate the phenomena in each of the above mentioned regions and to consider the inner layers, where $r \le L_T$, as planar ones. This hierarchy of the main physical layers takes place only at sufficiently high T_∞. It may be shown that undisturbed plasma consists only of electrons and double charged ions Ar^{++} at this temperature. The temperature range in which a transition occurs from Ar^+ to Ar^{++} corresponds to the distance that is significantly greater than Ar^{++} recombination length. Therefore the local

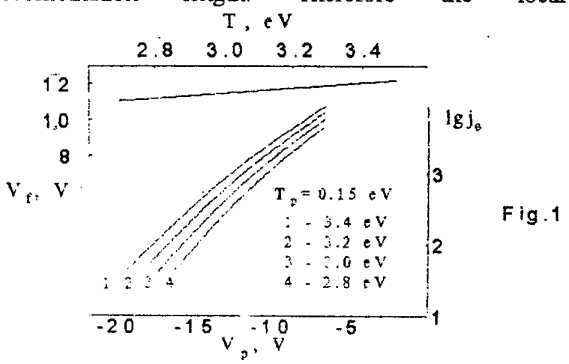

Fig.1

thermodynamical equilibrium (LTE) exists in all the regions where $r \geq L_r^+$. The LTE condition was used in the determination of plasma composition. Some results of calculations are shown in Fig.1 where floating probe potential V_f is plotted versus T_∞ and electron component j_e of a probe current density - versus probe potential V_p at a set of T_∞ values (listed in Fig.1).

4. It was necessary to carry out the probe measurements at high enough plasma temperatures ($T_\infty \geq 2$ eV) to compare the experimental and theoretical data. Such temperature can be obtained in the near-cathode region of free burning atmospheric arc. According to the previous experimental results [6] the typical size of region, where $T > 2$ eV, is of the order of 2 mm at $I \geq 250$ A. While the arc current increases this size grows. So the measurements were performed at $I \geq 250$ A and at the distance ≤ 1 mm from cathode surface. According to the theory [3] the disturbances of plasma parameters by a probe relax at the distance $L_T \sim 0.1$ mm. Because L_T and probe radius 'a' are significantly less than z, the probe measurements may be used for determination of plasma parameters in the case investigated. Also it is essential for a validity of probe diagnostics that near the cathode, at $z < D$, a stagnation zone exists and a cathode plasma jet is formed at the distance $z \geq D$ from the cathode. Therefore the probe measurements are correct and the results of the rmeasurements may be compared with the theoretical those which are obtained for the plasma at rest.

The dependence of current I_p of the moving probe upon time has a flat maximum corresponding to a probe position near the axis of an arc plasma column. The maximum current value at the oscillogram was considered as the probe current on the arc axis. Then the ion probe current I_i was determined at various negative potentials with respect to the floating potential V_f. A distinct ion current saturation was observed.The plasma temperature T_∞ was also measured by the spectral line relative intensities technique at the distance z_∞ from the cathode surface. Spectral lines of ArIII with known transition probabilities were used for T_∞ determination in the near-cathode layer. The dependence of ion saturation probe current density j_{iS} upon T_∞ obtained by this technique is shown in Fig.2.

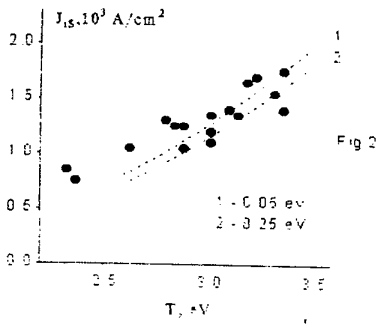

Fig.2

5. According to the theoretical results which are shown in Fig.1 the dependence of a logarithm of a probe current density j_e upon the probe voltage V_p is essentially non-linear in a strongly ionized argon plasma at atmospheric pressure. A similar result was obtained in xenon plasma [3]. This is a consequence of a diminution of the electron temperature near the probe surface, which occurs simultaneously with a growth of j_e. This effect was investigated experimentally and theoretically in [7] in strongly ionized plasma of considerably low pressure.

A strong distortion of a transient branch of probe characteristics in a strongly ionized plasma of atmospheric pressure as well as a diminution of ion probe current as compared with the saturation ion current at $j_e \geq j_{iS}$ does not allow to use the measured voltage-current (VC) probe characteristics for the direct determination of j_e by means of the extrapolation of j_{iS}. Therefore the transient branch of VC probe characteristics is not suitable for diagnostic purposes. But the plasma temperature T_∞ can be measured by means of the j_{iS} measurement. According to the calculations, j_{iS} is a sufficiently strong function of T_∞ and depends slightly on the probe temperature T_p (see dotted curves for two T_p values in Fig.2). This weak dependence is essential for diagnostics because T_p varies in some unknown manner during the measurement.

In Fig.2 one can see a good agreement between the theoretical and experimental data. An uncertainty of T_p does not affect essentially the accuracy of T_∞ determination, this accuracy being better than 10 % as estimated. So it may be concluded that the theory [3] describes correctly the processes in near-probe layer and VC probe characteristics. The experimental confirmation of the developed theoretical model proves the possibility of the correct determination of plasma potential by a probe method in a strongly ionized high pressure plasma.

The research described in this publication was made possible in part by Grants N^0 R5D000 and R5D300 from the International Science Foundation.

References

[1] W.Finkelnburg und H.Maecker: Elektrishe Boegen und thermisches Plasma, Handbuch der Physik, XXII (1956) 254

[2] B.S.Gavrjutshenko, R.Ya.Kucherov,A.V.Pustogarov et al.: J. Tech. Phys., 45 (1975) 2119

[3] F.G.Baksht, A.B.Rybakov: J.Tech. Phys., 67 (1997))

[4] F.G.Baksht, V.G.Yur'ev: J.Tech.Phys., 49 (1979) 905

[5] F.G.Baksht,A.B.Rybakov: J.Tech.Phys., 64 (1994) 42

[6] G.A.Djuzhev, N.K.Mitrofanov, S.M.Shkol'nik: J. Tech. Phys., 67 (1997) (in Russian)

[7] F.G.Baksht, G.A.Djuzhev, S.M.Shkol'nik, V.G.Yur'ev: J. Tech. Phys., 47 (1997) 2280 (in Russian)

Primary electrons influence to the plasma parameters in multipolar magnetic-confined device

Eugen Stamate*, Kouji Inagaki and Kazuyuki Ohe

Department of Systems Engineering, Nagoya Institute of Technology
Showa-ku, Gokiso-cho, Nagoya-466, Japan

1.Introduction

Diffusion plasma confined in a multipolar-magnetic system is one of the most uniform and low fluctuation level plasmas. The plasma is generated by the so-called primary electrons, which are emitted by a thermionic filament, and energized by the negative bias in respect with the wall. The presence of multipolar magnets results in a localization of ionization at the plasma periphery due to the primary electrons trapping in a cusp magnetic configuration.

Measurements with electric probes have shown that the electron distribution function (EDF) is not always Maxwellian, and is mostly approximated to a bi-Maxwellian one [1]. Using a more sensitive method to obtain the two electron group parameters [2,3], three electron groups were separated in a recent work for the well understanding of magnetic-confined plasma properties [4], a primary electron group and two Maxwellian ones. The anisotropy due to the primary is too strong to be neglected, and results in modification of plasma parameters especially in the vicinity of the filament. The probe geometry may integrate the anisotropy induced by the primary electrons, eventually loosing some information related to the electrons.

In the present work, the anisotropy induced by primary electrons and their influences to the magnetic-confined plasma are investigated with a spherical and planar probe in the vicinity of the filament.

2.Experimental setup and processing of probe characteristics

Experiments were performed in a multipolar magnetic-confined cylindrical chamber with 26 cm in diameter and 46 cm in length. Plasmas with its density about 10^{13}-10^{15} m^{-3} were produced by a DC discharge between the chamber wall and a spirally wound filament with 10 mm in diameter made of a tungsten wire with $\varnothing$=0.2 mm. The discharge current I_d and its voltage U_{AC} were typically 150 mA and -50 V, respectively. Ar gas, of which pressure was ranged from 10^{-2} to 10^{-4} Torr, was used. In order to keep the plasma axially symmetrical, the filament was installed at a position of 40 mm from one of the cylindrical chamber ends, where the magnetic field due to the magnets was neglected. A planar probe with 2.5 mm in diameter and a spherical one with 1.2 mm in diameter were movable to the axial and radial directions.

A -60 V + +10 V ramp bias voltage was applied to the probe. Detected probe current, after averaged 700 times, was amplified and converted into digital data with 12 bit resolution. A numerical program to obtain the bi-Maxwellian parameters [2,3], primaries [5] and ion density [6] was used.

3.Experimental results and discussions

Radial profiles of n_p at p=5x10^{-4} Torr and different distances d, obtained by planar and spherical probe are presented in Fig. 1. The presence of primary electrons result in strong anisotropy even at d=100 mm, for the

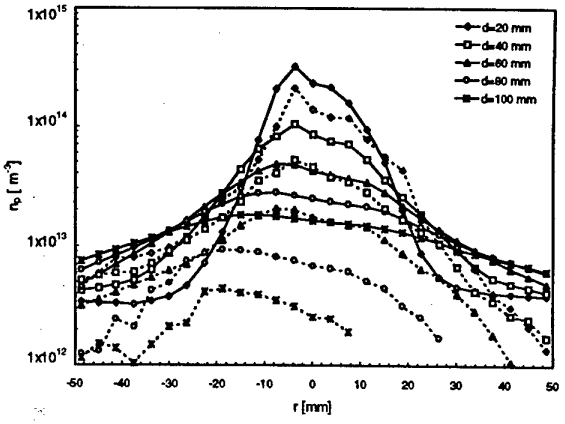

Fig. 1 Radial profiles of primary electron density, at p=5x10^{-4} Torr, by the planar (___) and spherical (_ _ _) probes.

planar probe measurement, but not for the spherical probe one by an integrating effect over the surface. In Fig. 2 is presented the radial profile of the probe current's second derivative I_e", at d=60 mm, by planar probe, where the ion and primary electrons

*Permanent address: Faculty of Physics, "Al.I.Cuza" University, Copou No.11, Iasi-6600, Romania

contributions were subtracted. The primary electrons influence causes a double-hump structure of the I_e" profiles. The influence de creases with d and p increasing,

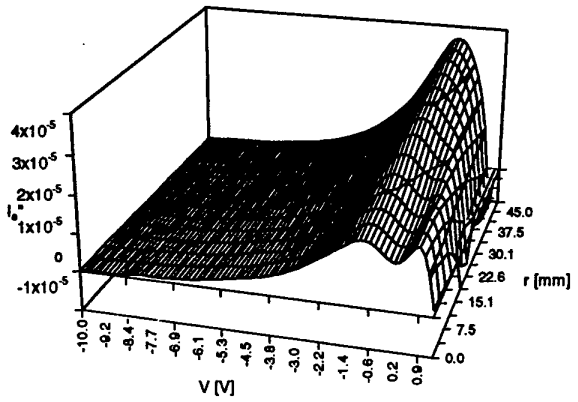

Fig. 2 Radial profiles of I_e", at p=5x10^{-4} Torr, and d=60 mm, by the planar probe

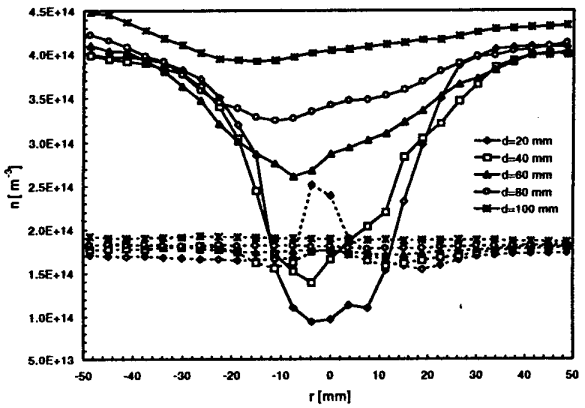

Fig. 3 Radial profiles of electron (___) and ion (_ _ _) densities , at p=5x10^{-4} Torr, by the planar probe

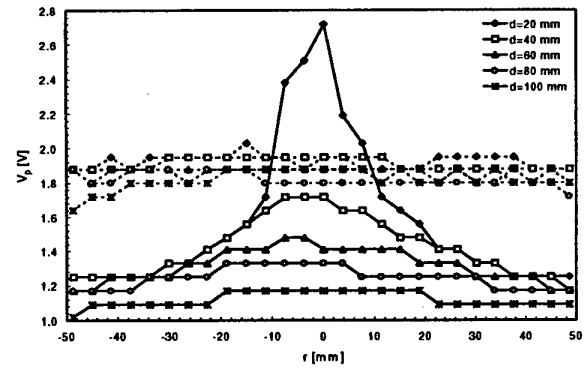

Fig. 4 Radial profiles of plasma potential, at p=5x10^{-4} Torr, by the planar (____) and spherical (_ _ _) probes.

while can not be detected by the spherical probe. The electron density (by integration of EDF) and ion density (by using the OML in the ionic saturation part [6]) radial profiles, at p=5x10^{-4} Torr, by the planar probe, are presented in Fig. 3. The primaries influence result in decreasing of plasma electron density and increasing of ion density in the filament vicinity. Such an electron kinetics explain the appearance of positive space charge in the vicinity of filament, which can be understood from the result of Fig. 4, where the radial profiles of plasma potential, by the planar and spherical probes, are presented.

4.Conclusions

The anisotropy due to the primary electrons induce modification of plasma parameters in the filament vicinity and then a space charge appears there. The primary electrons influence cannot be detected by the non-directive probes, its producing ambiguity in estimation of another parameters, like floating potential and hot electron group temperature. The filament position and its shape have to by take in account for the anisotropy.

References

[1] M.B.Hopkins and W.G.Graham, Rev.Sci.Instrum. 57(9), (1986) 2210

[2] D.Ruscanu, G.Popa and E.Stamate 1992 Int.Conf. on Plasma Physics, Innsbruck, vol.II, (1992) 1179

[3] E.Stamate and G.Popa, ICPP'96, 9-13 Sept. Nagoya, Japan, (1996)

[4] E.Stamate, K. Inakagi and K.Ohe, 1997 Int.Conf. on Reactive Plasmas, (1997)-87

[5] K.N.Leung, N.Hershkowitz, and K.R.MacKenzie, Phys.Fluids, 19(7), (1976) 1045

[6] J.G.Laframboise, Report No 100, University of Toronto, Institute of Aerospace Studies, (1966)

Evolution of the vibrational energy carried by $N_2(X\ ^1\Sigma^+_g)$ from a microwave discharge

P. Supiot*, D. Blois*†, M. Barj†, A. Chapput†, O.Dessaux* and P. Goudmand*
* Laboratoire de Physico-Chimie de l'Energétique et des Plasmas, (*E.A.M.E.N.E.S.R. n°1761*)
† Laboratoire de Spectrochimie Infrarouge et Raman (LASIR) (*U.P.R. C.N.R.S. n°2631*)
Bat C5, Université des Sciences et Technologies de Lille
59655 Villeneuve d'Ascq Cedex, FRANCE

1. Introduction

The nitrogen is often used for chemical applications involving plasmas. The energy carried both by the ground state molecules and the atomic species can be used both in the early afterglow and in the far remote afterglow either for surface treatment or thin films deposition [1]. Under microwave discharges conditions, the vibrational and the rotational energies stocked by the $N_2(X\ ^1\Sigma_g^+)$ molecule is known to be quite large [2] especially at moderate and hight reduced electric field (E/N) values.

In a previous paper [3], we presented first results concerning a Raman Stokes Scattering study of the first vibrational levels of the ground state molecules (v=0-5) for pressures down to 1 hPa. This analysis tool provides the possibility to determine the relative population of each level and so the Treanor temperature (θ_1) [4]. We present here results obtained from the early afterglow to the far remote afterglow. The former is the siege of the well known Short Lived Afterglow [5], where a second ionization of the gas occurs without further electric field application.

The strong deviation from the Boltzmann equilibrium observed in the case of N_2 under plasma conditions has been already described on the basis of the work of Treanor [4]. This author describes the near resonant Vibration-Vibration (V-V) energy exchanges. The main feature of the model is that there is a strong interdependence of θ_1 and the kinetic gas temperature (T_g). The V-V processes are particularly favored when θ_1 is larger than T_g and lead to an overpopulation of the medium levels. To make a more complete description of the Vibrational Distribution Function of N_2 (VDF), Gordiets [6] has developed an additional analytical expression to account for the effect of Vibration-Translation (V-T) exchanges occurring essentially on the population of the highly excited levels. On the contrary, the V-T exchanges leading to a relaxation of the highly excited levels are enhanced when T_g increases with regard to θ_1. A modified Gordiets model [5] is used jointly with our experimental data to evaluate the amount of energy transported by the $N_2(X\ ^1\Sigma_g^+)$ molecule and the results are discussed.

2. Experiment

The N_2 plasma is ignited in a Pyrex discharge tube (inside diameter : 38 mm) by a coaxial resonant cavity at 2450 MHz. The microwave power absorbed by the plasma is equal to 300 W. The nitrogen (Air Liquide «U» grade) pressure is set at a value of 3.3 hPa with a flowrate equal to 1.46 slpm. The Raman scattering signal collected via two conjugated lenses is recorded owing to a home made spectrometer equipped with a gated intensified CCD detector synchronized with laser pulses. The acquisition procedure requires 3or 4 averaged records with duration equal to 4 min with regard to the ration signal to noise. The relevant experimental setup is described more extensively in the reference [3].

The kinetic gas temperature is evaluated by optical emission spectroscopy with help of a HR460 JY monochromator equipped with a liquid N_2 cooled CCD detector. The transition used is the ionic N_2^+ ($B^2\Sigma^+_u$ v'=0,1$\rightarrow X^2\Sigma^+_g$ v''=0,1) $\Delta v = 0$ sequence. A 0.5 Å bandwidth allows to resolve the rotational structure of this first negative system (1^-) transition. Comparison with computed spectra with the relevant bandwidth finally gives the rotational temperature with an accuracy of about 50 K. The kinetic temperature and the latter one are close to each other under our experimental collisional conditions.

3. Results and discussion

The Raman scattering data after calculation of θ_1 are shown on the figure 1. The abscissa scale (L) describes the axis tube from the gap center (L=0) to the far remote region. It appears that the θ_1 values in the L range of measurement are still decreasing from about 4300 K to 2600 K. The calculation is achieved with a typical standard deviation of 300 K. The monotonous decrease of θ_1 suggests us to fit the data by an exponential law. More data are nevertheless needed to confirm this tendency. With this assumption the law has been extended up to L = 0 giving hence a maximum estimation of θ_1 in the discharge (4700 K). The θ_1 value in the short lived afterglow is close to

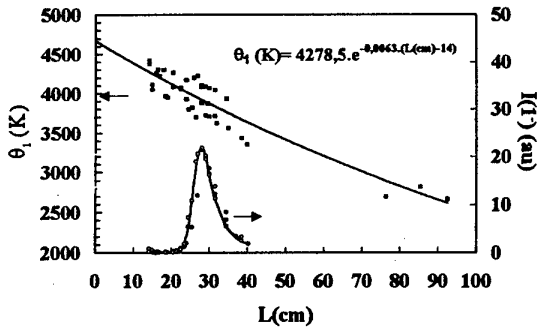

Fig. 1 : Profile of θ_1 and of the signal amplitude of the (0,0) head band of the 1^- emission system.

4000 K around the maximum of amplitude emissions of the 1^- system. We hence notice that this value is much less than the vibrational temperature deduced from the emissions of the transitions $N_2(B^3\Pi_g \rightarrow A^3\Sigma^+_u)$ for the levels $v'<9$ (~ 9500 K) and than the Treanor vibrational temperature of $N_2^+(B^2\Sigma^+_u)$ deduced from the emissions of the transitions $N_2^+(B^2\Sigma^+_u \rightarrow X^2\Sigma^+_g)$ (~10000 K) measured at the same position. Furthermore the constant decrease of θ_1 is in contrast with the corresponding ionic emission intensity variation.

The figure 2 presents the profile of the gas temperature T_g for a smaller L range than in fig. 1. The result is similar to previous data obtained at 433 MHz under the same experimental conditions [5]. The two

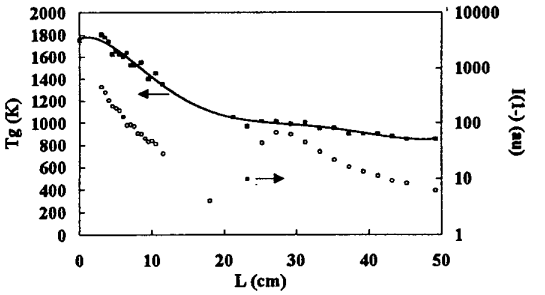

Fig. 2 : Profile of the kinetic temperature and of the signal amplitude of the (0,0) head band of the 1^- emission system.

profiles of θ_1 and T_g allow to calculate the vibrational distribution function of $N_2(X\ ^1\Sigma^+_g)$ by the modified Gordiets model and so to follow its evolution along the axis. The total vibrational energy is calculated by the expression:

$$E_v = \sum_{v=1}^{v^{**}} [N_2(X\ ^1\Sigma^+_g)_v]\varepsilon_v \qquad (1)$$

where [ ] denotes the volumic concentration of the species, v** is the v value beyond which the population

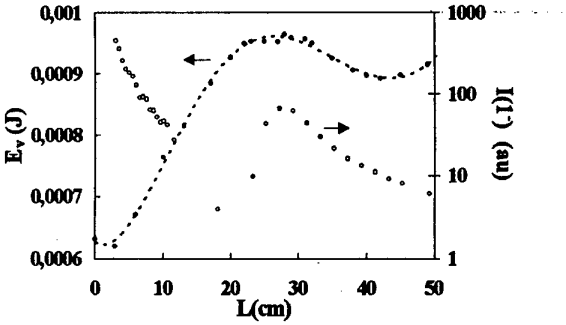

Fig. 3 : Profile of the calculated total vibrational energy E_v and of the signal amplitude of the (0,0) head band of the 1^- emission system.

is negligible and ε_v is the energy of the level considered. The result can be seen on fig.3. The calculation assumes that the pressure is almost constant along the studied region. The E_v value starts from about 0.6 mJ in the gap region and rises when living the discharge. A flat maximum (0.95 mJ) is observed in coincidence with the maximum of amplitude of the 1^- emissions. This result is remarkable because both data are obtained independently. The decrease of E_v following this maximum is moderate and let the place to a further increase. Despite an decrease of θ_1, the vibrational energy increases when the gas leaves the discharge. The increase of about 58 % of E_v needs to be faced with the 55 % increase of $[N_2(X^1\Sigma_g^+)]$. A conclusion is that E_v is controlled by the drop of T_g and its effect on $[N_2(X^1\Sigma_g^+)]$. The maximum of E_v corresponds to the area where the drop of T_g and so the increase of $[N_2(X^1\Sigma_g^+)]$ are stopped. The ratio of θ_1 to T_g therefore favors the V-T relaxation. The T_g drop is strongly slowed by the heat release induced by ionization. The slight rise of E_v beyond L=45cm is a calculation artefact of this simplified model which takes only into account the V-V and V-T exchanges but not the wall deactivation occurring when θ_1 and T_g are low. An improved model should involve the density effect on kinetic rates and also the collisions with electrons and electronic states .

[1] E. Baclez, B. Mutel, O. Dessaux, P. Goudmand, J. Grimblot and L. Gengembre, Thin solid Films (in press)

[2] J. Anketell and B. Brocklehurst, J. Phys. B, Atom. Molec. Phys., 7, 14 (1974) 1937; J. Loureiro and C.M. Ferreira, J. Phys. D:Appl. Phys., **19** (1986) 17

[3] A. Chapput and M. Barj, P. Supiot, D. Blois, O. Dessaux and P. Goudmand, J. Ram Spec.,**27**(1996) 863

[4] C.E. Treanor, J.W. Rich and R.G. Rehm, J. Chem. Phys., **48**, 4 (1968) 1798

[5] P. Supiot, O. Dessaux and P. Goudmand, J. Phys.D: Appl. Phys. **28** (1995) 1826

[6] B.F. Gordiets, S.S. Mamedov and L.A. Shelepin, Sov. Phys.-JETP, **40**, 4, (1975) 640

Density measurement of OH free radical in a magnetized sheet plasma crossed with vertical gas-flow

Akira Tonegawa, Yukihiro Kobayashi, Kazutaka Kawamura* and Kazuo Takayama*

Department of Physics, School of Science, Tokai University
*Institute of Research & Development, Tokai University
1117 Kitakaname, Hiratsuka, Kanagawa, 259-12 Japan.

We demonstrated the production of OH free radicals in an argon magnetized sheet plasma crossed with vertical gas-flow mixed with an oxygen gas O_2 and a hydrogen gas H_2. The density of the OH free radicals were measured by a laser-induced fluorescence (LIF). The density of OH free radicals reaches its peak with changing the argon gas flow. When the density of OH free radicals is the maximum value ($3.6 \times 10^9 cm^{-3}$), the high part of the electron-energy-distribution-function $f_e(E)$ above 8 eV decreases. These results suggest that the high energy part of $f_e(E)$ is contributed to the dissociation of O_2 and the production of OH free radicals.

1. Introduction

The effect of collisions of neutral gas on the plasma behavior is considerably interesting in connection with many fields of application, such as plasma processing, environmental problem, and divertor plasma in recent years. In particular, an important role of free radicals is mainly due to their outstanding physical and chemical properties. The characteristics of the free radicals in the plasma are very complex in commonly used plasma device, such as RF, ECR and so on, because the cascade type of collision process takes place in the plasma column.

For a better understanding of the relation between the plasma parameters and the properties of the free radicals, we have proposed to use a newly designed system of a magnetized sheet plasma crossed with vertical gas-flow system [1-3]. In this system, the parameters of radicals and plasma, such as the reactive gas-flow, the plasma density, the electron temperature are controlled independently. This system is capable of measuring the plasma and radical parameters by the electrical probe and a laser induced fluorescence (LIF), respectively.

We demonstrated the production of the hydroxyl (OH) free radicals in an argon magnetized sheet plasma crossed with vertical gas-flow (H_2+O_2). The OH free radical has been recognized as the most commonly studied combustion species and important species from the view of environment.

2. Experimental setup

The magnetized sheet plasma crossed with vertical gas-flow system is shown in Fig. 1. The advantages of the magnetized sheet plasma with vertical gas-flow system are: (i)the plasma parameters and conditions of the reactive gas are controlled independently because the part of the plasma source is separated from the part of the production of the radicals in this system, (ii)the plasma density and the electron temperature can be widely changed with changing a discharge current and a discharge gas flow, (iii)since the geometry of this system is estimated to be nearly 1-D on the scale of the plasma thickness the experimental results could be compared with the expected results based on 1-D models, (iv)free radicals and ionized charged particles can be separated into the different space because the reactive gas is vertically fed to the magnetized sheet plasma, and (v)the influence of the process of the ion collision in addition to that of the electron collision can be examined in the plasma, such as the charge exchange, and so on. Therefore, this system is capable of making some complex phenomena between the plasma and neutral gas species as the simple model.

The reactive gases for the production of the OH free radical were the hydrogen gas H_2 and the oxygen gas O_2. When reactive gas is vertically fed to the sheet plasma, OH free radicals produce in the plasma and

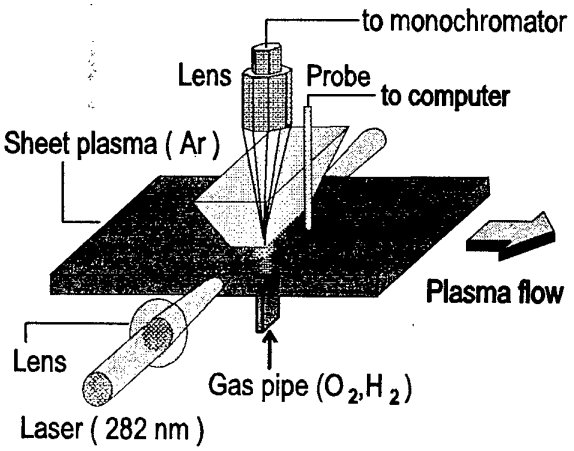

Fig.1 The magnetized sheet plasma crossed with vertical gas-flow system.

pass through its above space because the mean free path of neutral-neutral collision is much longer than the thickness of the sheet plasma. The plasma parameters (the electron density, the mean electron energy, the space potential and the electron-energy-distribution-function $f_e(E)$) in the gas contact region were measured by the Langmuir probe. The density and the rotational-vibrational temperature of the OH free radicals were measured by the laser-induced fluorescence (LIF)[4-7]. The uv laser light for the fluorescence excitation of the OH molecule is provided by a Nd:Yag pumped dye laser system with subsequent frequency doubling using a KDP crystal. A 5 ns laser pulse with 2 mJ energy is tuned in wavelength that corresponds to an transition of the (0,0) band of the $A^2\Sigma^+$-$X^2\Pi$ near 282 nm at a repetition rate of 10 Hz. The LIF signal entered in the entrance slit of a monochromator with both a focused lens and optical fiber was detected by a multichannel analyzer (SMA). The rotational-vibrational temperature of the OH free radicals decided from the slope of a straight line that is obtained by plotting the fluorescence intensity of a given laser-excited transition divided by the transition strength for that absorption against the energy of the absorbing rotational state in the $X^2\Pi$ electronic state.

3. Experimental Results

The typical experimental parameters are as follows: the discharge current I_d is 16 A, the magnetic field B_z is 0.03 T. The H_2 gas flow rate as a reactive gas Q_{H2} is fixed at 10 sccm.

Figure 2 shows the density of OH free radical n_{OH} as a function of the Ar discharge gas flow Q_{Ar}. The density of OH free radicals initially increases with

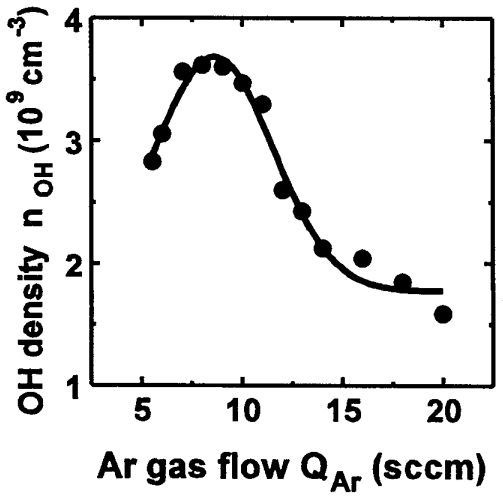

Fig. 2 The LIF intensity (308 nm) corresponding to the relative density of OH free radical as a function of the Ar discharge gas flow Q_{Ar}.

increasing Q_{Ar}. After the maximum value (n_{OH} = 3.6 x $10^9 cm^{-3}$, Q_{Ar} = 10 sccm) is obtained, n_{OH} decreases with increasing Q_{Ar}. When the density of OH free radicals reaches its peak at Q_{Ar}=10sccm, the high energy part of the electron-distribution-function $f_e(E)$ above ~8 eV decreases from a result of probe measurement. This value of the high energy part of $f_e(E)$ corresponds to the dissociation energy of oxygen (~8.8 eV). In the collisions of electrons in molecular gases, electron-neutral collisions may occur the dissociation.

The rotational-vibrational temperature of the OH free radicals T_{OH} was determined by the plot of LIF spectrum per transition strength vs energy of initial rotational state. The T_{OH} deduced from the slope of plot is 4000 K ± 200 K.

4. Conclusions

We demonstrated the formation of the OH free radicals in the magnetized sheet plasma with vertical gas-flow system. The density of OH free radicals reaches its peak with changing the Ar gas flow. At the same time, the electron density and the high energy part of the electron-energy-distribution function $f_e(E)$ above the energy of ~ 8 eV decrease. These results suggest the production of OH free radicals is contributed to the dissociation of O_2 in electron-neutral collisions.

The authors wish to express their gratitude for the financial assistance from Grant-in-Aid for Grant-in-Aid for Scientific Research (C), No.08680513, the Ministry of Education, Science, Sports and Culture.

References

[1] K.Sunako, K.Yamauchi, T.Noguchi, T.Nihei, T.Tsugueda, H.Watanabe, T.Tanikawa and K.Takayama, Nucl.Instrum & Methods,**B77/3738**, 636(1989).

[2] T.Noguchi, T.Tanikawa, K.Yamauchi, T.Nihei, H.Watanabe, K.Sunako, and K.Takayama, Nucl.Instrum & Methods, **B77/3738**,632 (1989).

[3] M.Matsumoto, M.Shibagaki, A.Tonegawa and K.Takayama, VACUUM, **47**, 1039(1996).

[4] D.Stepowski and M.J.Cottereau, Applied Optics, **18**,354(1979).

[5] C.C.Wang and L.I.Davis,Jr.,Phys.Rev.Letters,**32**, 349(1974).

[6] L.D.Pfefferle, T.A.Griffin and M.Winter, Applied Optics,**27**,197 (1988).

[7] G.H.Dieke and H.M.Crosswhite, J.Quant.Spectrosc. Radiat.Transfer.,**2**,97 (1962).

On the hydrogen Balmer H_α line shapes in an abnormal glow discharge operating in helium-hydrogen mixture

I. R. Videnović, M. M. Kuraica and N. Konjević
Faculty of Physics, University of Belgrade, P.O.Box 368, 11001 Belgrade, Yugoslavia

Abstract

The shapes of the hydrogen Balmer H_α line are studied in the modified Grimm-type abnormal glow discharge, operating with iron and copper cathode, in helium with small admixture of hydrogen. For comparison, the H_α profiles in pure hydrogen and in neon-hydrogen mixture are recorded as well. The magnitude of the lower broadened part of the profiles is related to the efficiency of scattering and excitation of hydrogen atoms, reflected from the cathode.

1. Introduction

Recent studies of atomic-hydrogen line shapes in various types of glow discharges [1-7] has shown Balmer lines shapes with an extraordinary wings development. The extensive far wings indicate the presence of excited hydrogen atoms with very high velocities. As shown by both theory and experiment ([8] and Refs. [4,10] therein), those energetic hydrogen neutrals originate from incident H^+, H, H_2^+, H_2 and H_3^+, whose backscattered fragments from the cathode are almost entirely H atoms. On their way back through the discharge, they collide mainly with matrix gas and excite [9].

In the preceding paper [9], the hydrogen Balmer H_α line shapes, emitted from the Grimm-type abnormal glow discharge operating in pure hydrogen and in neon-hydrogen mixture (3% H_2), with cathodes made of several different materials, are studied. Most of the end-on recorded H_α profiles, showed more developed blue wing of the lower part of the profile, than the red one, see Fig. 1. These line shapes testify on the higher energies and larger number of hydrogen atoms traveling from the cathode surface towards observer. As a quantitative measure of the wings broadening effect, the value $\delta = (A_b+A_r)/A$ is introduced, as a ratio between sum of areas under the blue A_b and red A_r wing of lower, broader part of the profile, and whole profile area A, where $A=A_b+A_r+A_0$ (see Fig. 1). Concerning cathode material influence, it is revealed that sputtering processes play an important role in the line shape formation. Namely, the wings broadening effect is more pronounced in discharges with cathodes made of material with high sputtering yield coefficient (such as Cu, Ag and Au [9]). In the light of these results, one would expect that the influence of the operating gas would be also related to the sputtering efficiency, i.e. that the effect should be more pronounced if the cathode is bombarded with heavier particles. The results were, however, quite opposite: in comparison with pure hydrogen discharge, in neon-hydrogen mixture, the wings development was considerably depressed [9]. This result lead to the conclusion that the role of the operating gas is related mainly to the efficiency of scattering and excitation of reflected hydrogen atoms, i.e. to the matrix transparency for energetic hydrogen neutrals.

In order to check the above conclusion, in this work we extend our study to the H_α line shapes emitted from the Grimm glow discharge operating in helium-hydrogen (5% H_2) mixture, and compare them with the results obtained in pure hydrogen and neon-hydrogen mixture, under similar experimental conditions.

2. Experiment

Our plasma source is laboratory made modified Grimm-type glow discharge, described in details elsewhere [10,11]. Here we shall mention only few important details. Unlike the original Grimm design [10], the cathode is mounted inside the hollow anode (30 mm long with inner and outside diameters 8.00 and 13 mm), The water-cooled cathode holder has an exchangeable iron or copper electrode, 18 mm long and 7.60 mm in diameter, which screws tightly onto its holder to ensure good cooling. The gas flow 500 cm^3/min through the discharge was sustained at 250 Pa by means of a needle valve and a two stage mechanical vacuum pump. To run the discharge a 0-2 kV and 0-100 mA current stabilized power supply was used. A ballast resistor of 10 kΩ was placed in series with the discharge and power supply. The end-on radiation from the discharge source was focused with unity magnification onto the entrance slit of the scanning monochromator-photomultiplier system with 0.74 nm/mm inverse linear dispersion. The signals from photomultiplier were A/D converted, collected and processed by PC.

3. Results

Typical results of Balmer H_α spectra recordings in three different gases, with iron and copper cathode are shown in Fig. 1. The new results in helium-hydrogen mixture confirm the previously noticed regularities [9]: (a) the blue wing of the lower, broader part of the H_α profile is more developed then the red one and (b) the

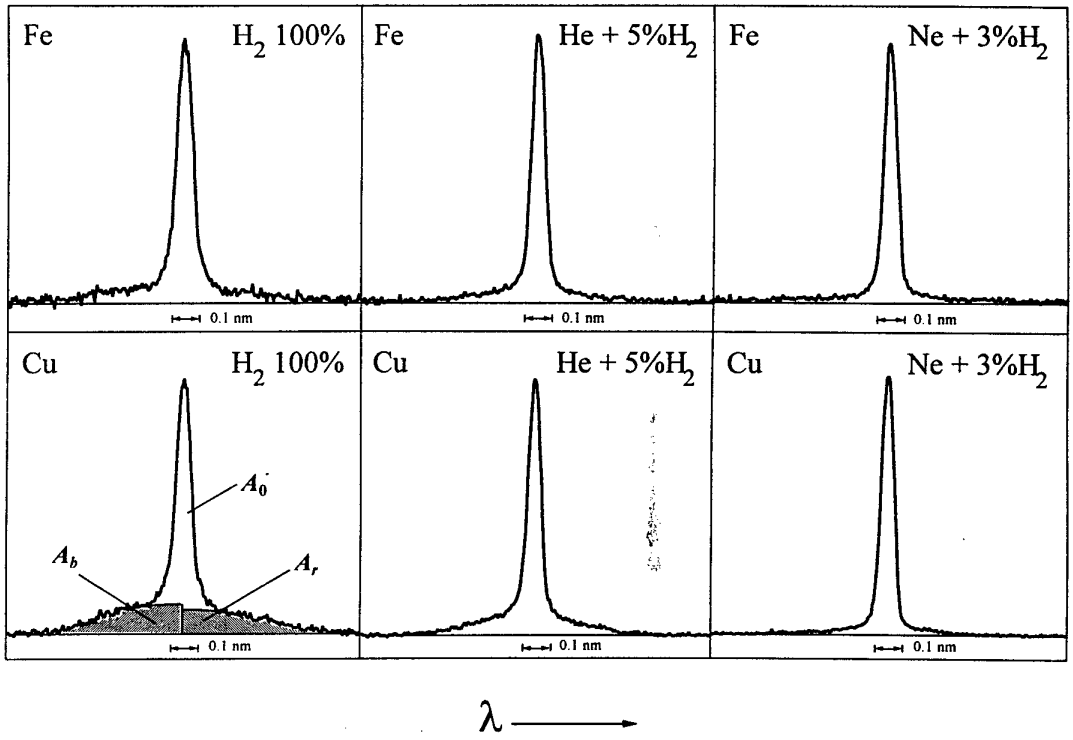

Fig. 1. Typical end-on H_α spectra recordings (with relative intensities) in Grimm glow discharge with iron and copper cathode, in three different gases. Discharge conditions: 25 mA, (16±2) W. In the Cu-H_2 graph are defined areas A_b, A_r and A_0.

wings broadening effect is more pronounced with copper than with iron electrode.

Considering influence of the operating gas, the effect in helium-hydrogen mixture is between those in pure hydrogen and in neon-hydrogen mixture. Furthermore, by plotting the obtained δ values vs. mass ratio of atomic hydrogen and matrix gas (in logarithmic scale), see Fig. 2, one obtains apparent linear dependence. This supports our previous conclusion [9] that the role of the operating gas is related to the efficiency of the scattering and excitation of hydrogen neutrals in collisions with matrix gas. These processes

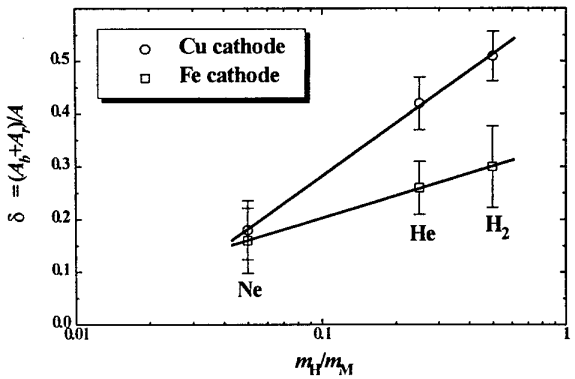

Fig. 2. The wings-broadening effect (δ values) vs. mass ratio of atomic hydrogen (m_H) and matrix gas (m_M).

are the most efficient in pure hydrogen (mass ratio 1:2), while neon matrix (1:20) is the most transparent for energetic hydrogen atoms, reflected from the cathode.

References

[1] W. Benesch, E. Li, *Opt. Lett.* **9,** (1984) 338.

[2] A. Cappelly, R. A. Gottscho, T. A. Miller, *Plasma Chem. Plasma Process.* **5,** (1985) 317.

[3] G. Baravian, Y. Chouan, A. Ricard, G. Sultan, *Appl. Phys.* **61,** (1987) 5249.

[4] E. Li Ayers, W. Benesch, *Phys. Rev. A* **37,** (1988) 194.

[5] C. Barbeau, J. Jolly, *J. Phys. D* **23,** (1990) 1168.

[6] M. Kuraica, N. Konjević, *Phys. Rev. A* **46,** (1992) 4479.

[7] B. P. Lavrov, A. S. Melnikov, *Opt. Spectrosc.* **75,** (1993) 676.

[8] Z. Lj. Petrović, B. M. Jelenković, A. V. Phelps, *Phys. Rev. Lett.* **68,** (1992) 325.

[9] M. Kuraica, N. Konjević, *Phys. Scripta* **50,** (1994) 487.

[10] W. Grimm, *Spectrochim. Acta* **23B,** (1968) 443.

[11] M. Kuraica, N. Konjević, M. Platiša, D. Pantelić, *Spectrochim. Acta* **47B,** (1992) 1173.

Langmuir-probe measurements in the afterglow of rf-discharges

A. Remscheid, S. Rudakowski, K. Wiesemann
Ruhr-Universität Bochum, Experimentalphysik, inbes. Gaselektronik, 44780 Bochum, Germany

We present Langmuir-probe measurements in the afterglow of pulsed rf-discharges. The pulsed plasma is expected to contain negatively charged particulates having large masses. The aim is to determine the ratio of mean negative and positive masses of ions in the plasma. First measurements in Ar/C_2H_2 and $Ar/H_2/W(CO)_6$ discharges will be presented.

Introduction

It is well known that clusters and dust are formed in rf-plasmas containing carbon and hydrogen. While heating the discharge continuously particulates can grow in the plasma and charge up negatively like a floating probe. Small particulates beyond a certain size (roughly up to about 20nm) can be expected to bear only one charge. If the plasma is pulsed the particulates growing inside the plasma have sizes depending on the plasma-on time, t_{on}. When the plasma is switched off the electrons escape very fast due to their high mobility on a time scale shorter than 1ms. After roughly 1ms one can assume a quasi neutral plasma consisting of positive and negative ions. In this electron free plasma it is possible to measure the saturation currents of positive and negative ions using cylindrical Langmuir-probes. From the saturation currents the mean mass ratio of positive and negative charge carriers can be deduced as suggested by the group of Watanabe [1,2,3]. They determined the ratio of the mean masses in a silane rf-discharge. We extended this method in order to get information on the time dependence of the mean mass ratio in the afterglow of an argon/acetylene discharge.

Theoretical considerations

When a Langmuir probe is immersed in a plasma with negative ions, its saturation current above the space potential is given by [1]

$$I_S=eS[n_e(kT_e/2\pi m_e)^{1/2}+(Q/e)n_-(kT_-/2\pi M_-)^{1/2}],$$

where e is the electronic charge, S the probe area, k the Boltzmann constant, Q the number of charge of a negative ion, and further, n_e, m_e, T_e are the density, mass, and temperature of electrons respectively, and n_-, M_-, T_- those of the negative ions. For the current I_S measured at a time >1ms after rf-discharge-off the contribution of electrons can be neglected compared to that of the negative ions.

The positive ion saturation current of a probe immersed in such an afterglow plasma composed of negative and positive ions is given by

$$I_+=eSn_+(kT_+/2\pi M_+)^{1/2}.$$

One can assume thermal equilibrium $T_+=T_-$, because of the small mass ratio and because there is no rf-heating in the afterglow. In this case the mass ratio, M_-/M_+, can be expressed by

$$M_-/M_+=(I_+/I_S)^2\equiv R_{-/+}.$$

This expression suggests that information on growth processes of subnanometer sized particles in rf-discharges can be obtained by measuring I_+ and I_S as a parameter of the rf-discharge-on period, t_{on}, with a Langmuir probe in afterglow plasmas. Fukuzawa *et al* measured $R_{-/+}$ at fixed probe voltages of ±27V: $R_{-/+}=I(U=-27V)/I(U=+27V)$.

However, if there are no electrons, heavy particles are not necessarily negatively charged.

Experimental

The measurements have been performed in a capacitively coupled parallel plate device with a heatable ground electrode. We used also a heatable probe which was not compensated for the rf-modulation. In the experiments with Ar/C_2H_2 the probe was placed near the centre of the discharge volume and in the experiments with $Ar/H_2/W(CO)_6$ it was placed a few mm in front of the rf-electrode. During the measurements in $Ar/H_2/W(CO)_6$ a conducting film of WC was deposited on a substrate and on the probe.

We have measured the probe current I as a function of the probe voltage U and the afterglow time t. This leads to a matrix $I(U,t)$ which is obtained in the following way: For fixed voltages U_n we measured the "time-characteristics" $I_n(U_n,t)$. From these time-characteristics the probe-characteristics $I_n(U,t_n)$ can be obtained at a certain time t_n in the afterglow.

Results

Fig. 1 shows the probe current measured in an Ar/C_2H_2 plasma (20W rf-power, t_{on}=3.2s, t_{off}=0.32s). The measurement starts 0.2ms after plasma-off and extends 4.2ms in the afterglow. The voltages range from -100V to +100V in 1V steps. During the first 0.2ms after turning off the plasma the maximum saturation current of negatively charged particles I(+100V) drops very fast from 6mA to 0.5mA while I(-100V) decreases from 0.2mA to 0.034mA. As shown in Fig. 1 these values decrease to I(100V,4.2ms) = -150nA and I(-100V, 4.2ms) = 3.6μA, respectively, in a time range of 4ms.

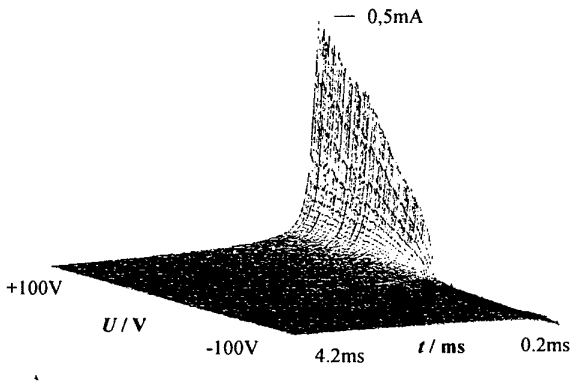

Fig. 1

In the case of Ar/C_2H_2 we varied t_{on} from 0.1s up to 6.4s while the plasma-off time t_{off} has been kept constant at t_{off}=0.32s. In Fig. 2 the data obtained for t_{on}=3.2s and 6.4s are shown. In all cases a significant increase of $R_{-/+}$ can be observed indicating that the mean masses change during the afterglow. Either M_+ decreases or M_- increases, or the negative particles are cooled.

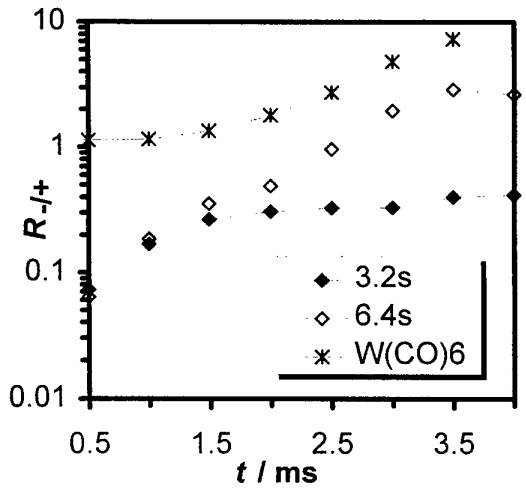

Fig. 2

$R(t)_{-/+}$ is obtained from the mean value of the ratio of $[I(U,t)/I(-U,t)]^2$ averaged over the voltage range 30V-90V. At t=0 the plasma was switched off.

For t_{on}=3.2s the ratio $R_{-/+}$ increases from 0.06 at t=0.5ms to 0.3 at t=4ms indicating that the mean mass of positively charged particles is much larger than the mean mass of the negatively charged species. Between 0.5 ms and 1ms one can see the same behaviour for $R_{-/+}$ at 6.4s. But at larger afterglow times this curve seems to reach a saturation value of about 2 showing that M_- becomes larger than M_+ during the afterglow.

In the $W(CO)_6$ containing plasma we found a different behaviour. During the afterglow the ratio $R_{-/+}$ increases from a nearly constant value 1 to a value of about 7 at 3.5ms.

A more detailed analysis and discussion will be given on the poster.

This work was supported by the Deutsche Forschungsgemeinschaft, Bonn, under grant Wi-461-10-3.

References

[1] T. Fukuzawa, M. Shiratani, Y. Watanabe: App. Phys. Lett. 64 23 (1994) 3098-3100

[2] Y. Watanabe, M. Shiratani: Plasma Sources Sci. Technol. 3 (1994) 286-291

[3] M. Shiratani, T. Fukuzawa, Y. Watanabe: IEEE Trans. Plasma Sci. 22 2 (1994) 103-109

Optical absorption techniques used in diagnostics of a rotating arc in an electrical circuit-breaker

C. Fleurier, D. Hong, S. Ciobanu and C. Fiévet#

GREMI, Université d'Orléans - CNRS. BP6759, 45067 Orléans Cedex 2, France
Centre de Recherche Merlin Gerin, 38050 Grenoble Cedex, France

In a previous paper [1], we reported about the time resolved electron density and temperature measurements of a rotating arc in a SF_6 electrical circuit-breaker with a peak current of 4.8kA. Measurements on this turbulent, non-reproducible and moving arc were performed by differents methods of emission spectroscopy with the assistance of photography using interference filters. This SF_6 plasma is strongly polluted by copper ablated from electrodes. Time resolved total number of the atomic species present in the arc, including copper, were measured. Spatial information was also deduced from the measurements allowing concentration estimates for the different atoms.

In order to confirm the emission measurements, we used also three different optical absorption techniques: i) self-absorption of two FI lines belonging to the same multiplet, ii) absorption of a line emitted by the arc core by the peripheral plasma and, iii) absorption of an external Z-pinch radiation [2] by the arc.

i) The electron density and temperature of this plasma are of about $4.10^{17}cm^{-3}$ and 18000K [1], respectively. In these conditions, the line broadening is mainly caused by the Stark effect which depends mainly on the electron density. However the measured line profile depends also on the self absorption of the line in the plasma. The detailed study of this process for two line profiles from the multiplet FI $3s^4P$-$3p^4D°$, which have very different absorption coefficient makes possible to obtain good estimates of plasma thickness and plasma apparent surface. An absolute calibration renders also the plasma temperature.

ii) In specific conditions, some CuI lines emitted by the arc core are absorbed by the cold peripheral plasma. The spectral profile of such lines shows an absorption dip in the line peak. Calculation of the profile with a model allows to determine the copper linear density in the peripheral zone.

iii) Absorption measurements of an external radiation by this plasma are very difficult to realize because of the refractive index fluctuations in the arc chamber. Indeed, the laser beam is strongly and randomly deflected by the arc and the gas. Nevertheless such an experiment was successfully achieved with the aid of a high current Z-pinch discharge instead of a laser thanks to its brightness, its short duration, its spatial expanse and its spectral expanse. Spectral absorption profiles of the copper resonance lines were directly obtained. Copper concencentration could be subsequently inferred from these measurements.

References:

1. S.S. Ciobanu, C. Fleurier, D. Hong, C. Fievet, to be published in *J. High Temp. and Chem Proc.* (1997)
2. V. André, C. Fleurier and D. Hong, XXIth Int. Conf. Phys. Ion. Gases, Bochum, (September 1993).

Comparison of Electron Energy Distributions Determined by Spectroscopic and Electrostatic Probe Methods

J. McFarland*, C.M.O. Mahony*, E. I. Toader[+] and W.G. Graham*

* Department of Pure & Applied Physics, The Queen's University of Belfast,Belfast, N. Ireland. BT7 1NN
[+]Department of Plasma Physics, The Bucharest University- Faculty of Physics, Bucharest-Magurele, Romania.

1. Introduction

An understanding of electron energy distribution functions (eedfs) is fundamental to characterising plasmas and plasma phenomena. Electrons with energies greater than 10 eV are of particular interest since they drive processes such as ionisation, excitation and the production and excitation of radicals. Electrostatic probes have been used for such measurements for many years but are intrusive and can be difficult, if not impossible to use in some plasma environments. Optical emission spectroscopy appears to offer a simple and non intrusive technique for determining electron energy distributions [1]. Here we compare measurements made using a spectroscopic technique with those made using an electrostatic probe technique.

2. Experiment

Measurements were made on helium in a capacitively driven, GEC (Gaseous Electronics Conference) reference reactor. Four spectral lines were chosen by virtue of their relative intensities: 471.3 nm, 492.2 nm, 504.8 nm and 587.6 nm. The values for the ratio of the intensities of the spectral lines 504.8 nm and 587.6 nm (R_1), 504.8 nm and 471.3 nm (R_2) and 492.2 nm and 587.6 nm (R_3) were obtained experimentally using a spectrometer with a photomultiplier tube detector. Based on a theoretical calculation of the dependence of R on the electron temperature (kT_e), values for kT_e were obtained. The results were compared to measurements made under the same conditions using a compensated Langmuir probe technique.
The experiments were performed, at a power of 40 Watts, for a range of pressures from 50 mTorr through to 500 mTorr. Above 500 mTorr the plasma can no longer be considered optically thin, a condition required by the theoretical model.

2. Results

The spectroscopic results generated from R_1, R_2 and R_3 show a decrease in kT_e with increasing pressure. However the values of kT_e obtained using R_2 were consistently greater than those determined using R_1 and R_3. The R_2 determination might be expected to be the more accurate since the excited states are populated only through electron impact. Results obtained using Langmuir probe techniques demonstrated the same pressure dependence. However, the probe-determined values of kT_e lay between those obtained from R_2 and R_3. Typical of the results are those at 300 mTorr. Values of 1.3, 5.6 and 2.7 eV were derived for kT_e from R_1, R_2 and R_3 respectively. The probe measurement was 4.2 eV.
The spectroscopic data was generated using spectral lines originating from states requiring a threshold electron energy for excitation from the ground state of 21 eV. The measured eedfs were basically Maxwellian. However at energies greater than 15 eV, they dropped more rapidily than would be expected for a Maxwellian distribution. This may account for the discrepancy in the magnitude of the values for kT_e determined by the two procedures. More work is planned to modify both techniques through further experiment and computational modeling, to look specifically at high energy electrons.

4. References

[1] E.I. Toader J. Phys.D: Appl.Phys. 28 (1995) 75.

Topic 9

Plasma wall interactions, electrode and surface effects.

Experimental investigation of the interaction of a C-SiC wall with a low pressure CO_2-N_2 plasma jet

P. Boubert, L. Robin, P. Vervisch
UMR 6614 CNRS CORIA - 76821 Mont-Saint-Aignan Cedex, France

Currently, information on chemical reaction processes and radiative properties around hypersonic flight vehicles is very scarce for atmospheres different from the earth atmosphere. The present paper investigates the interaction of a CO_2-N_2 low pressure plasma flow with a C-SiC material. The aim of this work is to identify the main processes contributing to the heating of a thermal protection material during a Martian atmospheric entry.
Measurements were performed in a laboratory wind tunnel. An equal mass-fraction CO_2-N_2 gas mixture is heated up by an electric arc between a cooled carbon cathode (in the heating chamber) and a carbon insert sintered into a copper nozzle that serves as anode. Thus metallic pollutions are eliminated. The arc current is 100 A corresponding to a 9 kW power for a flow rate of 12 l.min^{-1} at STP. The pressure inside the vacuum tank is 1 mbar. The C-SiC material is located on the axis of the expanding flow, perpendicular to the velocity field, 10 cm downstream from the nozzle exit.

For the characterization of the plasma different measurement techniques have been used.
In the 350-800 nm spectral range, the intensity of the plasma is measured with a 1.5 m Sopra spectroscope using a grating with 2500 grooves per mm coupled with a multichannel array of photodiode detectors.
The main spectral features are provided by the violet and red systems of the CN radical. For those systems a vibrational and rotational temperature is determined by the comparison of the experimental evolution with a calculated spectrum. The 777 nm atomic oxygen line is the only atomic line detected.
Working in monochromator mode with an EMI photomultiplier in detection gives a greater sensitivity. This has allowed us to detect small signals due to the usual N_2^+ first negative system and the C_2 Swan system, which indicate that there are traces of these elements, but no atomic nitrogen lines have been detected.
A 1 m Jobin-Yvon UV scanning monochromator (4500 grooves/mm grating) with a Hamamatsu UV photomultiplier detection was employed to analyze the 190-300 nm spectral range.
In emission, the strong radiation at 193 and 248 nm, which increases near the C-SiC sample, is well identified as associated to transitions of atomic carbon. Also close to the C-SiC sample, a large emission from the $3p^2\ ^3P$-$4s\ ^3P^0$ Si atom transitions near 250 nm is detected ($Si(^3P)=3x10^{12}$ part.m^{-3}) accompanied by the $A^1\Pi$-$X^1\Sigma^+$ emission band of the SiO radical. The remaining spectrum is dominated by the ε, γ, δ systems of NO.
LIF spectroscopy of the (D-X) NO electronic transitions has been applied to detect NO species.

The light source was a LPX150T Lambda Physik tunable ArF excimer laser which produces 15 ns halfwidth 150 mJ pulses. The laser is tunable over 320 cm^{-1} with a bandwidth of 0.3 cm^{-1}. The spectral filter used for fluorescence detection was a 0.5 m Jobin-Yvon spectrometer.
In the present low pressure experiment, quenching processes are negligible and a good confidence in the NO population density measurements can be expected. The rotational temperature is deduced from the two lines thermometry method.
An order of magnitude of the CO population density was also derived at 193 nm by three photon photolysis. This multiphotonic process which dissociates CO is enhanced by the coincidence between the laser wavelength and the spin forbidden $a^3\Pi$-$X^1\Sigma^+$ one photon transition. Atomic fragments which are produced in the ArF photolysis of CO are detected by monitoring the 248 nm resulting line of the carbon atom.
Usual Langmuir probe devices were implemented to determine electron temperature and density.
Finally the local distribution of the sample temperature is deduced from the intensity field measured by an infrared thermography system. On the axis of the plasma jet, the surface temperature of the C-SiC sample is 1600 K.

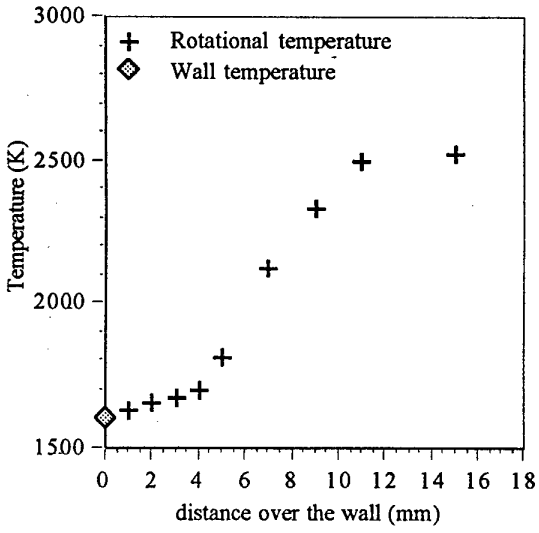

Fig. 1. Measured temperatures in the boundary layer

The main species present in the free stream of the plasma are CO_2, CO, N_2 and O. The absence of atomic nitrogen lines in the spectrum seems to indicate that the concentration of nitrogen atoms is low.

The orders of magnitude for the CN, NO and CO mole fractions in the mixture are respectively $5x10^{-3}$, 10^{-4} and $3x10^{-1}$.
The NO(X) rotational temperature is about 2500 K in the free stream above the sample. In the boundary layer this temperature decreases with the distance over the plate and tends toward the measured surface temperature indicating a rotational equilibrium at the kinetic temperature (Fig. 1).

In opposition, the evolution of rotational population density of CN electronic levels $B^2\Sigma^-$ (T_{rot}=7500 K) and $A^2\Pi$ (T_{rot}=4000 K) indicates a thermal nonequilibrium of their rotational degree of freedom.
Similarly, a large vibrational temperature excitation for these two electronic levels is observed: the vibrational temperatures are respectively 12500 K and 6000 K for the $B^2\Sigma^-$ and $A^2\Pi$ levels, remaining unchanged in the boundary layer.
The ionization degree is about $1.5\ 10^{-4}$ and the electrons are in thermal nonequilibrium with heavy particles. In the plasma free stream, the electron temperature is about 5500 K and has no significant change in the boundary layer. The corresponding electron population density remains constant down to two millimeters above the surface (the location of the last point of measurement).
The CO mole fraction has no significant change in the boundary layer, indicating either a low catalytic efficiency or the result of the competitive opposite processes:

$$CO + O_s \rightarrow CO_2$$
$$C_s + O2 \rightarrow CO + O$$
$$C_s + O \rightarrow CO$$

where s denotes atoms present in the solid phase, all other species are in the gas phase.
Conversely, in the extension of the boundary layer (1 cm) the O, CN and C population densities increase of about one order of magnitude as the distance to the wall decreases (Fig. 2). This cannot result from homogeneous reactions and has to be imputed to wall reactions.

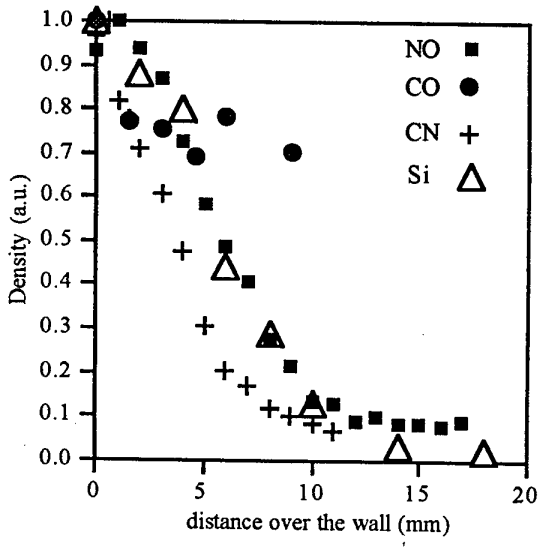

Fig. 2. Measured species evolution in the boundary layer

The first result is the carbon atom production at the wall: the calculated equilibrium vapor pressure of the carbon compound at the actual wall temperature is favorable to the carbon atom sublimation rather than the formation of C_3 and C_2 radicals. However, the equilibrium concentration of carbon atoms is far much smaller than the measured one. Then, adsorbed atoms on the surface are probably responsible for the enhancement of carbon ablation. Nevertheless, in contrast to a graphite sample which showed an extreme erosion due to its strong catalycity, the C-SiC sample was found to have a very low erosion rate caused by the detected free carbon and silicon. There is nearly no mass loss during the test. The amount of SiO molecules detected close to the wall owing to the oxidation process $Si_s + O \rightarrow SiO$ shows that passive oxidation by SiO_2 is not predominant.
NO and CN are the main nitrogen compound species created on the C-SiC material. The NO mole fraction near the wall is about 10^{-3}. This small amount of NO is expected to be due to the recombination of O atoms with nitrogen atoms adsorbed on the sample:

$$O + N_s \rightarrow NO$$

The large value of the CN mole fraction measured close to the wall (about 5.10^{-2}) is more difficult to explain. First, in current experiments the concentration of carbon atoms in the gas phase is too low to have an efficient production by the reaction channel:

$$C + N_s \rightarrow CN.$$

Second, the CN molecules could result from the process:

$$N + C_s \rightarrow CN$$

But, an excessively high concentration of nitrogen atoms would be required to explain the high concentration of CN measured.
In fact, an explanation may be found if the dissociative sticking probability of N_2 is significantly enhanced by the vibrationaly excited N_2 molecules impinging on the surface. With this hypothesis the CN radical would be created by the two step reaction:

$$N_2(v) + wall \rightarrow N_s + N_s$$
$$N_s + C_s \rightarrow CN$$

Future measurements in the 120-190 nm spectral range, where the nitrogen and oxygen atom concentration can be obtained by absorption measurements on the resonant lines, will provide more information.

In conclusion, this note emphasizes the interest of accurate measurements of species concentrations to study in detail the interaction processes on a thermal protection material.
Further measurements are underway to obtain an exhaustive analysis of the interaction of the CO_2-N_2 plasma with the C-SiC sample. However, current results underscore the diversity of species behaviors at the wall and the importance of an accurate knowledge of the plasma composition in catalycity tests in high enthalpy wind tunnels.

BOUNDARY WALL EFFECTS ON NEUTRAL DYNAMICS IN MICROCAVITIES IN AIR

O.Eichwald, M.Jugroot, M. Yousfi , P. Bayle*

CPAT, ESA du CNRS n°5002, 118 Rte de Narbonne, 31062 Toulouse Cédex, FRANCE
*CEMES-LOE, 29 Rue J.Marvig, 31055 Toulouse Cédex, FRANCE

1. Introduction

The spatio-temporel evolution of a discharge in a micro-cavity is influenced by the proximity of the walls: the energy injected is confined in a small volume and cannot be dissipated by pressure waves as in an unbounded discharge. Therefore, temperature and neutral density heterogeneities created by the discharge is not only conserved but are also amplified due to reflections on the walls. The energy is dissipated by viscous effects and thermal exchange at the surface. Hence, the geometry of the micro-cavity plays a significant role on neutral dynamics induced by the discharge. We study the influence of walls in micro-discharges observed [1] in two different geometries: i)cylindrical with a diameter of 0.5mm and a gap distance of 0.5mm ii) cubic of side 0.5mm. The discharge occur in air at atmospheric pressure and at ambiant temperature. The duration of current impulsion is 120ns with a maximum of 5mA corresponding to a maximum power of 12Watts.

2. Description of the model

The evolution of the neutral gas is described by the hydrodynamic equations for a compressible and viscous fluid coupled to the equation of state of a perfect gas [2-3]. The gas-solid interface take into account thermal exchange in the boundary layer. The walls and neutral particles on them are assumed to be cold. The assumption of flow resistance on the surface of micro-cavity gives a viscosity which increases with velocity gradients [4]. The effects of the discharge on the fluid particles are simulated by a thermal energy injection function and by a direct transfer momentum function. The system of transport equations is solved by a powerful and optimized tri-dimensional MUSCL method [5] (with a rotational symmetry in the cylinder microcavity) with no Time Splitting and a non-uniform meshes.

3. Resultats

Under the thermodynamic effect of the discharge (which presents rotational symmetry), the gas is set into motion. During a first phase, short in time and before the impact with the lateral surfaces, the gas moves freely and the processes are identical for the two geometries because the injection conditions are the same. The neutral gas temperature increases sharply with a maximum of 600K ,at the end of injection (120ns). The thermal shock is accompanied by an increase in pressure (1500Torr) in the core of the discharge. The pressure gradients are mainly radial and as soon as there are sufficiently high there initiate a radial motion of the gas. It is superimposed to the axial motion created by momentum transfer. Near the electrode surfaces boundary effects appears rapidly (fig1) with high temperature gradients and an increase of neutral density. In the formed boundary layers, there is a heat exchange between gas and surface. Furthermore, viscous effects and high pressure gradients parallel to the electrode induce a slip along the walls (fig2). In a second phase, after the energy injection and before the return of equilibrium, the gas perturbation is a result of wave propagation and successive reflections on the walls more particularly on the lateral ones. During this phase, the geometry of the micro-cavity plays an important role in the state of the gas. In the cylindrical micro-cavity, the rotational symmetry is conserved during the successive reflections. At every time, the combined parameters of the gas (temperature, density and velocity field) have this symmetry and we observe a globally uniform movement of return waves after each impact on the wall (fig3-4). In a cubic micro-cavity, the cylindrical symmetry vanishes immediately with the first reflection on the wall. The rupture of symmetry is accentuated by a mechanism of delayed reflection in the corners which increases the heterogeneity of the gas since this effect appears at each arrival of pressure waves on lateral walls. Hence, this delay in reflection induces an accumulation of neutral density in the corners (fig5), even though the movement of return toward the axis is initiated (fig6). The neutral accumulation in the corner is redistributed both in the volume of the cavity towards the axis and along the wall by slip effect.

In the two geometries, the memory effect of the discharge is conserved with a minimum in neutral density and a maximum in temperature in the injection zone.

4. References

[1] R.Bartnikas, J.P.Novak, 1993, IEEE Tran. on Elec. Ins., 28, 456.

[2] O.Eichwald, M.Jugroot, P.Bayle, M.Yousfi, 1996, J. Appl. Phys., 80, 694

[3] O.Eichwald, M.Jugroot, M.Yousfi, P.Bayle 1995, ICPIG XXII, Hoboken, USA

[4] O.Eichwald, M.Jugroot, P.Bayle, M.Yousfi, To be published.

[5] C.D.Munz, 1988, J.Comp.Phys., 77, 18

Section of view

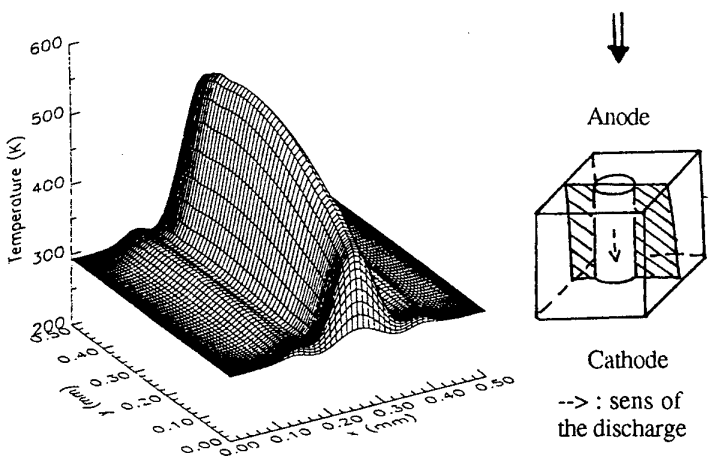

Fig1: Temperature profile in a cubic and cylindrical micro-cavities for t=360ns.

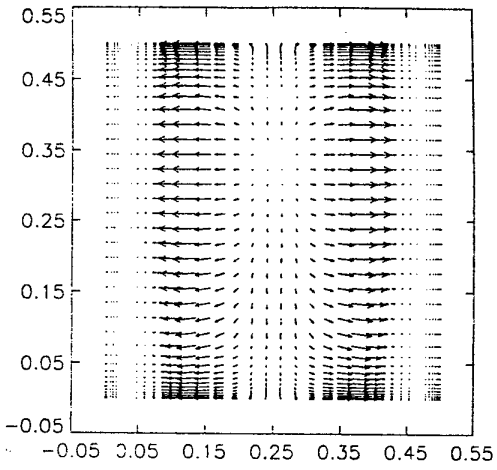

Fig2: Velocity field in a cubic and cylindrical micro-cavities for t=360ns and vmax=40m/s.

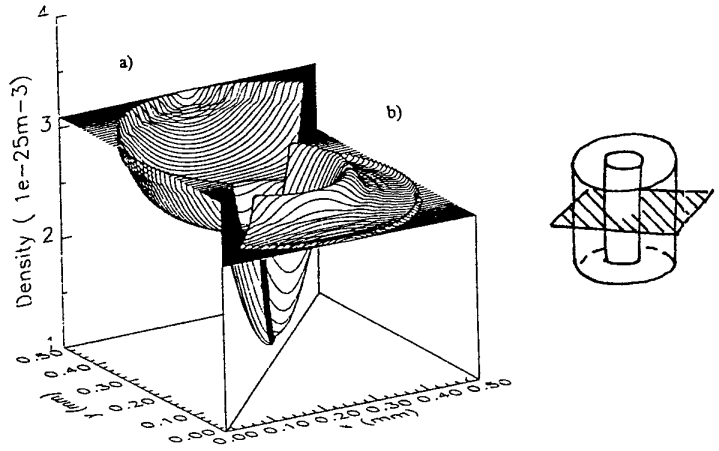

Fig3: Density of neutral for two different times in a cylindrical micro-cavity: a) t=640ns, b) t=960ns.

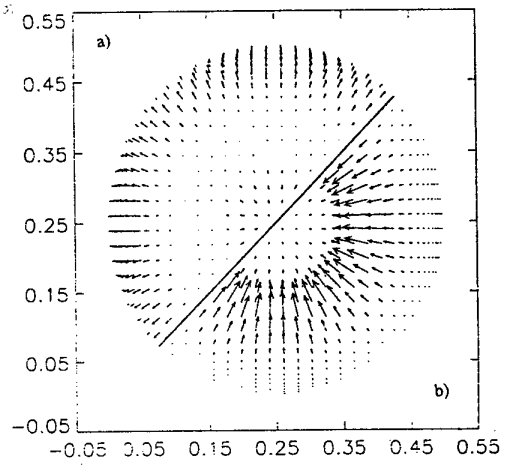

Fig4: Velocity field for two different times in a cylindrical micro-cavity: a) t=640ns and vmax=19m/s, b) t=960ns and vmax=49m/s.

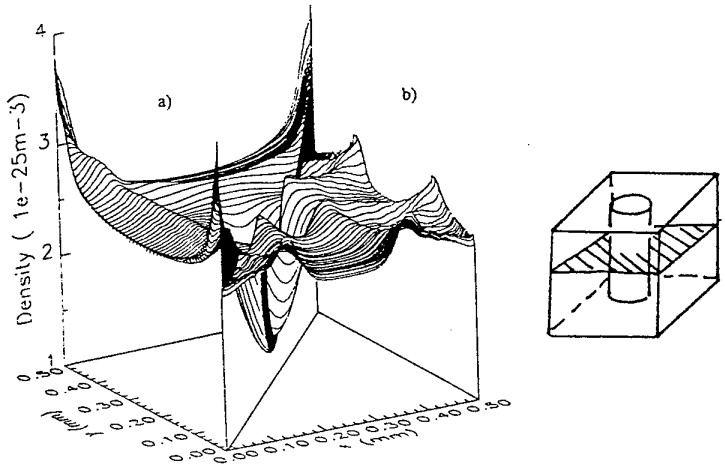

Fig5: Density of neutral for two different times in a cubic micro-cavity: a) t=820ns, b) t=1200ns.

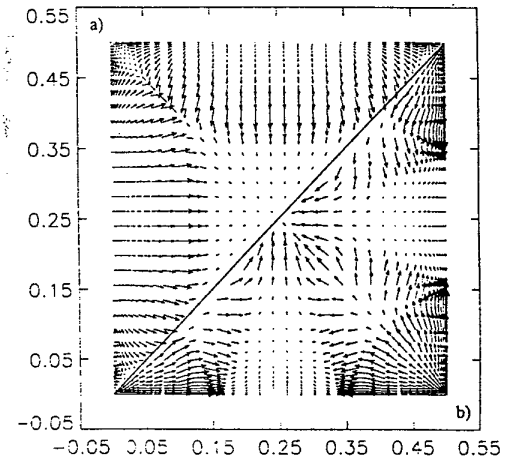

Fig6: Velocity field for two different times in a cubic micro-cavity: a) t=820ns and vmax=35m/s, b) t=1200ns and vmax=45m/s.

Distributions of Plasma Parameters in a Sputter Discharge

Y.Funato, C.Kiyooka, K.Akaishi*, Y.Kubota*, M.Mushiaki**,
Suzuka National College of Technology,Suzuka 510-02, JAPAN
* National Institute for Fusion Science, Nagoya 464-01
** Kawasaki Medical School, Kurashiki 701-01.

1. INTRODUCTION

It ie well known that a sputter discharge is one of the most useful technique for thin film fabrications. Many types of cathode materials are used usually for these purpose in the discharges. It is important to obtain the high quality films with large area for industrial applications. The requirement for the film properties depends on strongly the spatial distributuion of the plasma parameters. In sputter processing,therefore it is necessary to monitor and control externally the plasma parameters during the discharge. Here we investigate experimentally the sputter discharge, in which, lanthanum hexaboride(L_aB_6) is applied for the cathode material. The application of L_aB_6 for the cathode was proposed at first to obtain a low outgassing wall for a plasma vacuum chamber. The experimets showed that the L_aB_6 coating by the sputter discharge on a stainless steel wall is apparently effective to reduce the oxygen impurities in discharge gases. To control oxygen amounts in the discharge is expected for the wall conditioning for various clean vacuum devices. It is obvious that the cathode materials depend strongly on the created film properties and vacuum conditions.Many studies and developments have been carried out on these problems[1]. Here,we inves- tigate experimentally properties of plasma parameters during a sputter discharge.

II. EXPERIMENTAL DEVICE

The cross sectional view of the experimental apparatus is shown schematically in Figs.1.The sputter discharge experiment is done in the chamber, which is made of a stainless steel and has a diameter of 98 mm,300 mm in length. In the center of the main chamber the

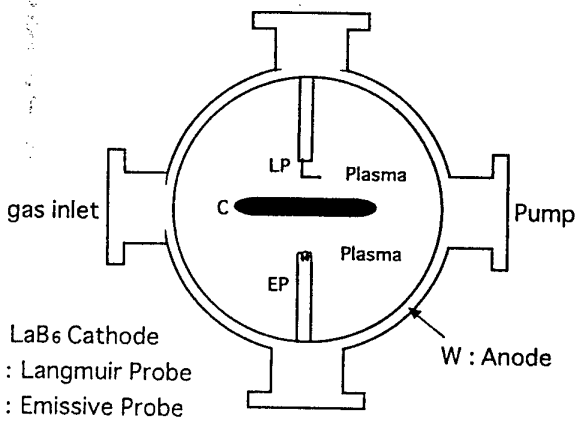

Fig.1. Experimental Device

lanthanum hexaboride(LaB_6) disk with a diameter of 50 mm and 5 mm in thickness is arranged for the cathode electrode. The anode electrode is the stainless-steel wall surface of the discharge chamber. The sputter discharge occurs between the LaB_6 disk cathode and the chamber wall. The applied DC voltage is 300-2000 Volts. The experiments were carried out in pressures of 5-200 Pa Argon gase. The sputter discharge parameters of the electrode voltage V_d and the total discharge current I_d are monitored with usual methods. In the chamber, elecrostatic probe(Langmuir probe) for measurements of the plasma parameters is set and can be moved externally along the plasma region. From the probe measurements, local electron density, electron temperatute are deduced. The plasma space potential of the sputter discharge is measured by using an emissive probe. The small sample substrate for XPS measurements is also installed near the wall electrode. Corellations between partial pressures and plasma parameters are also analyzed by QMS measurements.

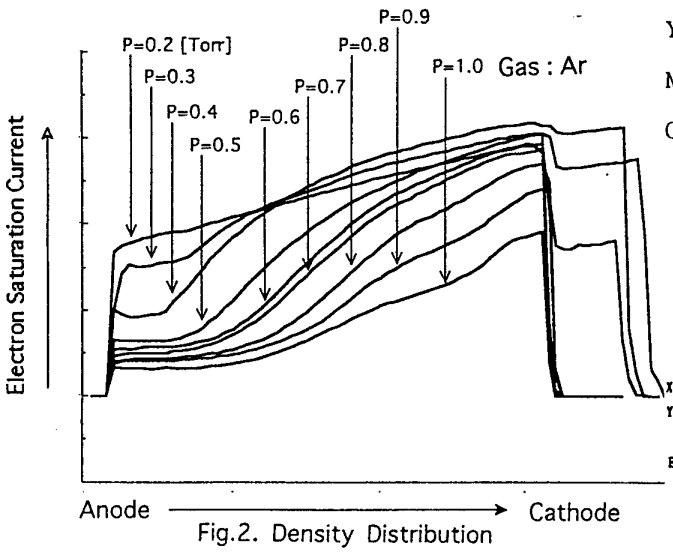

Fig.2. Density Distribution

III. EXPERIMENTAL RESULTS

The most characteristic point of this experiment is to apply the LaB_6 electrode for the sputter discharge. We use the LaB_6 cathode to sputter the boron and create the boron like films on the chamber wall. Figure 2 indicates the electron density distributions which is plotted the saturatin current I_s, where the electron temperature is almost constant in this case. The discharge conditions of the initial argon pressure is P=10 Pa. The discharge parameters obtained here are V_d=0.9-1.2 kV, discharge current I_d=30-70 mA. The electron density near the cathode is estimated to be $(3\text{-}5)\times10^{10}$ particles /cm^3. The electron temperature is 3-4 eV and is not affected remarkably by the discharge conditions. Figure 3 shows the XPS signals. The signals of La4p3/2, B1s, O1s and C1s are detected from the sample after the exposure to the sputter discharge plasma with LaB_6 cathode.

REFERENCES (1) F.Waelbroeck, Vacuum, 39, 821(1989). (2) J.Winter, J. Nuclear. Materials, 176&177, 14(1990). (3) T.Mori, K.Akaishi, Y.Kubota, O.Motojima, M.Mushiaki, Y.Funato; J. Nuclear Materials, 200, 385(1993). (4) M.Mushiaki, K.Akaishi, T.Mori, Y.Kubota, Y.Funato and O.Motojima, Material Science and Engineering,A163,177(1993).

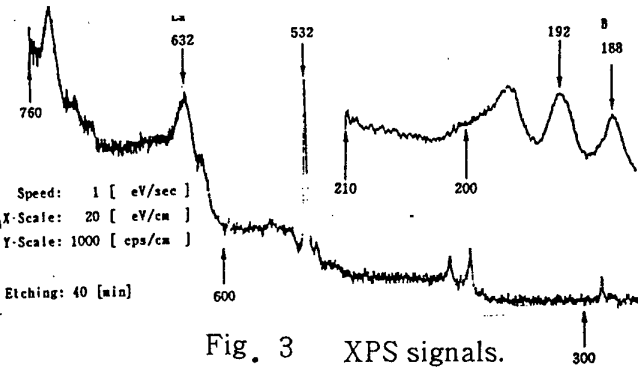

Fig. 3 XPS signals.

Near-electrode layers originating at magnetized plasma acceleration

S. F. Garanin

All-Russian Research Institute of Experimental Physics, 37 Mir Avenue, Sarov, 607190, Russia

1. Introduction

The magnetohydrodynamic (MHD) approach is widely used for describing various dynamic plasma devices. MHD approach validity is determined, generally speaking, by a smallness of the parameter $\xi \equiv \frac{c}{\omega_{pi} L}$ (L is a characteristic spatial scale of the flow). For $\xi << 1$ the plasma flow can be described by the ideal MHD equations and the effect of the electrodes confining the plasma region by the boundary conditions that for the magnetic field parallel to the electrodes reduces to an ideal sliding condition. Near the electrodes the plasma moves therewith along them accelerating or decelerating under the Lorentz force action $\frac{1}{c}[\vec{j}\vec{B}]$ (plasma is considered cold, $\beta \equiv \frac{8\pi p}{B^2} << 1$). Near the plasma-surface interface near-boundary layers arise (see [1,2] and references herein) where plasma viscous heating and cooling due to heat conduction take place. The Hall effect can play an important role in these layers bringing a magnetic flux to the anode that leads to plasma rarefaction in the near-anode region and bringing it off the cathode that results in plasma compression in the near-cathode region.

2. 1D problem

Assume that the near electrode layer thickness is small as compared to the characteristic dimensions of the complete MHD problem. Then for this layer a time-dependent one-dimensional problem can be considered where all values depend only on the coordinate perpendicular to the surface and on time.

Assume that far from the electrodes plasma is homogeneous and has the density $n_0 = 1.5 \cdot 10^{17}$ cm^{-3}, the temperature $T_0 = 2$ eV, the magnetic field $B_0 = 10^5$ Gs parallel to the electrode surface and constant current density $j = \pm 2.4 \cdot 10^{13}$ (the signs + or - correspond to the anode or the cathode) perpendicular to the surface. These conditions approximately correspond to those in the region of the MAGO plasma chamber [3] nozzle.

Denote the coordinate perpendicular to the surface as x, assume the magnetic field as directed along z, then the electric field and velocity attained by plasma will be directed along y.

As the layer under consideration is assumed sufficiently thin, one may assume that along x the total pressure has time to become uniform, i. e.

$$p + \frac{B^2}{8\pi} = P_0 , \qquad (1)$$

the total pressure P_0 depends only on time (we will actually solve the problems where P_0 is constant, while density n_0, temperature T_0 and magnetic field B_0 slightly change due to Joule heating and thermal expansion). Besides (1), the near-wall layer dynamics will be determined by the following MHD equations: the equation of motion for the velocity along y taking into account the action of force $\frac{1}{c}[\vec{j}\vec{B}]$ and viscosity, the equation for magnetic field and equations for heat transport for ion and electron plasma components taking into account finite electrical conductivity, Hall and Nernst effects, ion and electron heat conduction, heat transport by current and electron-ion energy exchange. These effects depend on the plasma magnetization degree and are determined by formulas [4].

At distances from electrodes less than the ion Larmor radius we also took into account the kinetic ion flows into the wall and thereby additional "abnormal" viscosity and heat conduction.

3. Near-cathode layer

The plasma mass which looses the magnetic flux and is squeezed to the cathode is determined by the relation

$$\int n \, dx = \frac{|j| t}{e} . \qquad (2)$$

For small times, as long as plasma viscosity and viscous heating are insignificant, this mass will accumulate in the layer whose thickness is determined by magnetic diffusion and electron heat conduction. Equating these coefficients and taking into consideration (2), one can obtain self-similar dependencies of the basic plasma characteristics on the problem parameters and time, with plasma density and thickness of this layer increasing with time as

$$n \sim t^{3/8} , \qquad x \sim t^{5/8} . \qquad (3)$$

At the next stage when viscous heating becomes essential the ion temperature is determined by viscous heating due to plasma friction against the wall and increases as the square of time, while the viscous zone

scale will be determined by the ion Larmor radius. For illustration of this stage of the near-cathode layer evolution in our 1D problem Fig. 1 presents profiles of the values pertaining to time $t = 1$ μs, when the bulk plasma velocities equal $v_\infty = 1.6 \cdot 10^8$ cm/s.

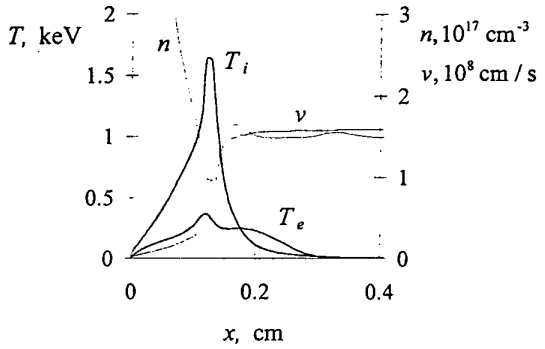

Fig.1. Near cathode plasma ion and electron temperatures, density and velocity

4. Near-anode layer

At the initial phase of the near-anode layer evolution in the MHD approximation plasma is pushed out of the electrode surface due to the magnetic flux coming to the surface. The time dependence of the principal plasma parameters will be described for small times, like in the near-cathode layer, by self-similar formulas (3) with the difference that instead of t we have to substitute $|t_0 - t|$, where t_0 is some time, i. e. in this approximation density drops down to zero during a finite time. However, according to the problem conditions, current continues to flow through this layer. A way out from this contradiction is only by attaching additional kinetic effects and considering small problem scales for which the MHD approximation, strictly speaking, is not valid. We do this taking into account electron inertia, i. e. considering the scales $\sim c / \omega_{pe}$.

Then the near-anode region will contain plasma of a low, but non-zero density.

The ion viscous near-anode plasma heating may lead to appearance near the anode of considerable electric fields proportional to ion pressure and perpendicular to the surface. Voltage differences along the surface may lead to magnetic flux flow along the anode and bring the magnetic flux out of the near-anode layer. This 2D effect was qualitatively taken into account in our 1D computations in the form of magnetic flux losses through the anode surface (a relevant electric field on the boundary was set).

Fig. 2 presents profiles of temperatures, density and velocity for the same time $t = 1$ μs, as for the near-cathode layer (Fig. 1). Fig. 2 shows that the density decrease in the near-anode layer is not very significant (due to the magnetic flux bringing out along the electrode) and, as a result, for large times plasma velocities in the near-anode layer are not higher than those for the bulk plasma. For large times the characteristic ion temperatures in the near-anode layer are determined, like for the near-cathode layer, by squared plasma velocity and characteristic spatial scales by the ion Larmor radius.

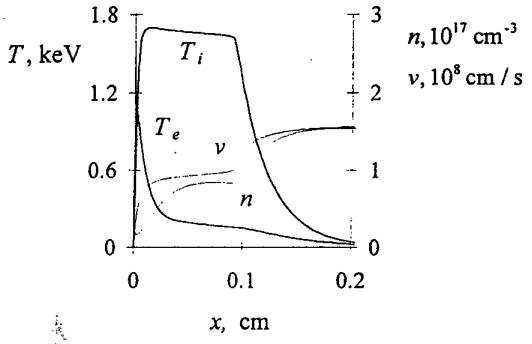

Fig. 2. Near anode plasma ion and electron temperatures, density and velocity

5. References

[1] K. V. Brushlinsky and A. I. Morozov, "Calculation of 2D Plasma Flows in Channels," *Reviews of Plasma Physics*, Vol. 8 (Atomizdat Publishers, Moscow, 1974), p. 88.

[2] S. F. Garanin and V. I. Mamyshev, *Fiz. Plazmy*, 16, 1218 (1990).

[3] A. M. Buyko, G. I. Volkov, S. F. Garanin et al., *Dokl. Akad. Nauk*, 344, 323 (1995).

[4] S. I. Braginsky, "Transport Processes in a Plasma," *Reviews of Plasma Physics*, Vol. 1 (Consultants Bureau, New York, 1965), p. 205.

Surface and Volume Kinetics of O(^{3}P) atoms in a Low-Pressure O_2-N_2 Microwave Discharge

V. Zvoníček*, V. Guerra†, J. Loureiro†, A. Tálský* and M. Touzeau‡
*Masaryk University Faculty of Science, Kotlárská 2, 611 37 Brno, Czech Republic
†Centro de Electrodinâmica, Instituto Superior Técnico, 1096 Lisboa Codex, Portugal
‡Lab. de Phys. des Gaz et des Plasmas, Université de Paris-Sud, 91405 Orsay Cedex, France

1. Introduction

A renewed interest has been devoted to the study of low-pressure discharges in pure O_2 and in O_2 with N_2 impurity, due to the broadening use of oxygen plasmas in several fields, such as etching and surface treatment of polymers, nitric oxides synthesis or silicon oxidation. For instance, the plasma-assisted oxidation of silicon using microwave-excited O_2 is one of the most promising methods to form SiO_2 films with very small damages on the substrate produced by the charged particles [1]. Moreover, since O atoms are the active species in most of the applications, the study of dissociation of molecular oxygen is a field of current interest. The concentration of O atoms has been found to be enhanced by the addition of N_2 impurity into O_2 gas, either in the case of microwave discharges [1,2] or in DC discharges [3,4]. Here, measurements of O-atom concentrations in a O_2-N_2 microwave discharge are compared to the predictions of a self-consistent kinetic model including both surface and volume processes. It is shown that wall atom reassociation is the dominant process to control the degree of dissociation, so that rather than an increase of the rate of dissociation, the dependence of O-atom concentration on N_2 impurity is due to a surface phenomena.

2. Experiment and kinetic model

A microwave discharge at $\omega/2\pi$=2.45 GHz was created in a quartz tube 100 cm long and 0.8 cm inner radius. The discharge input power was kept constant at P=100 W, which corresponds to a plasma length of approximately 5 cm. The concentration of O atoms has been measured near of the end of the discharge by using the electron spin resonance method [5], with a spectrometric calibration as described in [6].

A kinetic model for a low-pressure microwave discharge was developed by coupling the homogeneous electron Boltzmann equation, under the effective field approximation, to a system of rate balance equations governing the populations of the dominant neutral and charged species in a O_2-N_2 discharge, which includes the self-consistent determination of the maintenance reduced electric field.

Both volume and wall processes are considered in the model. In what concerns the latter, catalytic surface effects are taken into account for the heterogeneous deactivation of the vibrationally excited molecules $N_2(X\ ^1\Sigma_g^+,v)$ and for the wall recombination of O and N atoms. Whereas the processes of vibrational deactivation and recombination of N atoms are assumed first-order with constant probabilities independent of the composition of the mixture due to the small percentage of N_2 impurity, the probability for wall losses of O atoms, γ_O, is derived here using a statistical Monte Carlo like simulation of a sequence of elementary surface processes.

3. Surface kinetic model

The model includes steps for adsorption and desorption of O and N atoms, irreversible adsorption on active sites of O and N atoms and of O_2 and N_2 molecules (that is dissociative chemisorption), surface diffusing of reversibly adsorbed atoms, and both recombination due to the direct impingement of atoms from the gas phase on chemisorbed atoms (Eley-Rideal mechanism) and recombination of diffusing atoms with chemisorbed atoms (Langmuir-Hinshelwood mechanism). A reversibly adsorbed atom can either diffuse to the nearest site or can be desorbed back to the gas phase. The surface is covered with a small fraction of active sites of two types, which can bound irreversibly O and N atoms separately. The independent occupation of the active sites by O and N atoms can occur as a result of dissociative chemisorption of O_2 and N_2 molecules, by atomic flows comming directly from the gas phase, or by surface diffusing of a reversibly adsorbed atom.

In practice, due to lack of data the coverage of active sites is governed by two independent Langmuir adsorption isotherms. In the present conditions, the L-isotherm for the occupation of irreversible sites by O atoms is found saturated, while for the atomic impurity it stands in its increasing part. In this latter case, the occupation of the irreversible adsorption sites with N atoms is mainly governed by dissociative chemisorption. On the other hand, the reversibly adsorbed atoms are trapped in an adsorption well of energy E_d, which is assumed to decrease in the vicinity of dislike atoms due to a

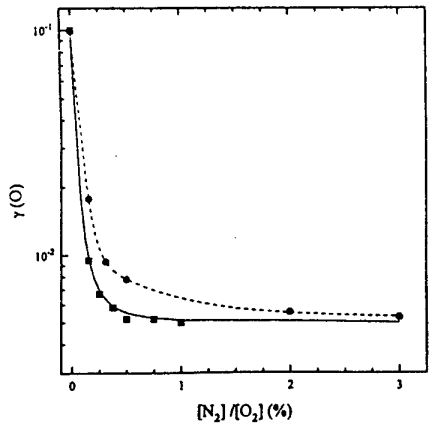

Fig.1 - Probability of O-atom recombination on quartz for two L-isotherms (see text).

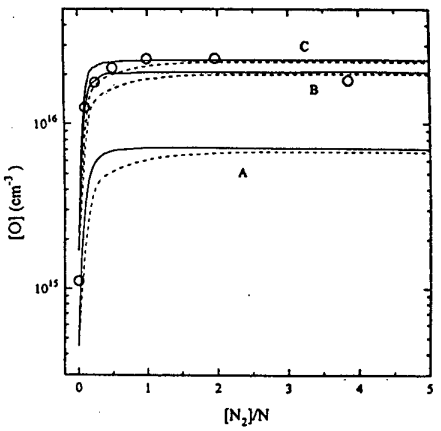

Fig.2 - Measured and calculated [O] concentrations for p=5 Torr, and n_e=10^{11}(A), 3.8×10^{11}(B), 5×10^{11}cm^{-3}(C) (theory), for the two L-isotherms as in fig.1.

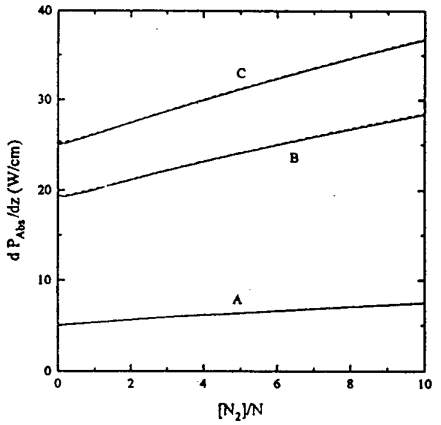

Fig.3 - Predicted power absorbed per length unit as in fig.2.

lateral repulsive interaction. This effect has been proposed for interpretation of experiments involving the adsorption of O and H atoms on Ni(110) [7]. Thus, the desorption energy for a O atom surrounded by a N atom is significantly lower than that corresponding to a O-O interaction between two neighbouring cells, which originates a higher probability for desorption in the first case. The probability γ_O rapidly decreases with the concentration of N_2 impurity due to a smaller efficiency of the Langmuir-Hinshelwood mechanism. This interpretation is suported by [8], where the decrease of γ_O due to the adsorbed N atoms at a glass wall is evidenced in the afterglow of a O_2 pulsed discharge. Finally, this model also includes formation of NO molecules on the wall.

4. Results

Fig.1 shows the probability γ_O calculated using two L-isotherms for irreversible occupation of N active sites. The sharp decrease of γ_O in the range 0–0.5% $[N_2]/[O_2]$ is governed by the magnitude of the repulsive potential for the O-N lateral interaction, whereas the position of the minimum is mainly determined by the L-isotherm. Both functions along with the final magnitude found for γ_O are obtained from a fit of the model predictions for the concentration of O atoms to the experiment. Fig.2 shows the measured [O] concentrations obtained in a $\omega/2\pi$=2.45 GHz microwave discharge in a quartz tube of inner radius R=0.8 cm at p=5 Torr and P=100 W, and the predicted concentrations calculated for the same values of $\omega/2\pi$, R and p, three different values of the electron density in the discharge n_e=10^{11}, 3.8×10^{11} and 5×10^{11}cm^{-3}, and T_g=800 K and T_w=400 K for the gas and wall temperatures, respectively. Using the present formulation the power absorbed by the electrons per length unit, P_{Abs}/dz, is derived from the model. The magnitude of γ_O has been obtained by fitting the calculated [O] concentrations using the central value n_e=3.8×10^{11}cm^{-3}. This choice has been dictated from the comparison between the predicted values of dP_{Abs}/dz, shown in fig.3 as a function of the fractional N_2 concentration, and those estimated in the discharge $\simeq$20 Wcm^{-1}.

[1] - Y. Yasuda et al 1990 J. Appl. Phys. 67 2603; [2] - A. Granier et al 1994 J. Appl. Phys. 75 104; [3] - A.R. de Souza et al 1993 J. Phys.D: Appl. Phys. 26 2164; [4] - B. Gordiets et al 1996 J. Phys.D: Appl. Phys. 29 1021; [5] - S. Kronbelg and H.W. Stranberg 1959 J. Chem. Phys. 31 1196; [6] - S.S. Westenberg and N. de Haas 1964 J. Chem. Phys. 40 3087; [7] - P.T. Sprunger et al 1995 Surf. Science 344 98; [8] - G. Cartry et al, in this conference.

Two of us (V.G. and J.L.) thank the support of a PRAXIS XXI Research Grant (Portuguese Ministry of Science and Technology).

Collector floating potentials in a two-electron temperature plasma

M. Čerček[1], J. Rovtar[1], T. Gyergyek[2] and M. Stanojević[1]
[1]) J. Stefan Institute, University of Ljubljana, Jamova 39, POB 100, 1000 Ljubljana, Slovenia
2) Faculty of Electrical Engineering, University of Ljubljana, Tržaška 25, 1000 Ljubljana, Slovenia

1. Introduction

In the contribution we report on our study of a two-electron temperature plasma flowing to a floating collector surface. Specifically, we are investigating its floating potential dependence on various plasma parameters.The analysis should apply to the exposed surfaces in any low pressure, low temperature hot cathode discharge plasma.

2. Theoretical analysis

The plasma system, bounded by a plasma source (x=0) and a collector (x=L) is modelled after Schwager and Birdsall [1]. We add in the system a second hot electron component characterised by a truncated full Maxwellian velocity distribution function, f_{eh}, given by:

$$f_{eh}(\psi,V)=\frac{n_{0eh}}{\sqrt{\pi t}}\exp\left(\frac{\psi}{t}\right)\exp\left(\frac{-V^2}{t}\right)\mathrm{H}\left(V-V_{Me}(\psi)\right) \quad (1)$$

In Eq.(1) n_{0eh} is the hot electron density of the full Maxwellian source, ψ is the normalised potential $\frac{e\phi}{T_{ec}}$; V is normalised electron velocity $v\sqrt{\frac{m_e}{2kT_{ec}}}$; t is the ratio between hot electron temperature T_{eh} and cold electron temperature T_{ec}; and H is the Heaviside step function with $V_{Me}(x)=-\sqrt{\psi(x)-\psi_C}$ as the normalised velocity of the fastest returned electron; ψ_C is the floating potential of the collector. In order to calculate the collector potential ψ_C and source sheath potential drop ψ_P, we characterise the potential between the source and collector sheaths by $\nabla^2\psi_P=0$. Setting the net charge to zero, $n_i(\psi_P)=n_{ec}(\psi_P)+n_{eh}(\psi_P)$, we obtain the expression which relates ψ_C and ψ_P:

$$\gamma_0\exp\left(-\frac{\psi_P}{\tau}\right)\mathrm{erfc}\left(\sqrt{-\frac{\psi_P}{\tau}}\right)=\exp(\psi_P)\times$$
$$\times\left[1+\mathrm{erf}\left(\sqrt{\psi_P-\psi_C}\right)\right]+\beta_0\exp\left(\frac{\psi_P}{t}\right)\times$$
$$\times\left[1+\mathrm{erf}\left(\sqrt{\frac{\psi_P-\psi_C}{t}}\right)\right]. \quad (2)$$

We obtained the ratio γ_0 of the ion and cold electron plasma source densities from the assumption of zero net electric current (floating collector):

$$\gamma_0=\frac{n_{0i}}{n_{0ec}}=\frac{1}{\sqrt{\mu\tau}}\left[\exp(\psi_C)+\beta_0\sqrt{t}\exp\left(\frac{\psi_C}{t}\right)\right]. \quad (3)$$

In Eq. 3 μ denotes ion to electron mass ratio and $\tau=\frac{T_{0i}}{T_{0ec}}$; β_0 is the hot electron to cold electron plasma source density ratio.

A second equation relating ψ_C and ψ_P is obtained by assuming zero electric field at ψ_P. According to Poisson equation we integrate the zero net charge expression:

$$\int_{\psi_P}^{0}\left[n_i(\psi)-n_{ec}(\psi)-n_{eh}(\psi)\right]d\psi=0. \quad (4)$$

The resulting relation is:

$$\gamma_0\tau\left[1-2\sqrt{\frac{-\psi_P}{\pi\tau}}-\exp\left(\frac{-\psi_P}{\tau}\right)\mathrm{erfc}\left(\sqrt{\frac{-\psi_P}{\tau}}\right)\right]= \quad (5)$$
$$=\left[\begin{array}{l}-1-\mathrm{erf}\left(\sqrt{-\psi_C}\right)+\exp(\psi_P)\left\{1+\mathrm{erf}\left(\sqrt{\psi_P-\psi_C}\right)\right\}+\\ +\frac{2}{\sqrt{\pi}}\exp(\psi_C)\left(\sqrt{-\psi_C}-\sqrt{\psi_P-\psi_C}\right)\end{array}\right]+$$
$$+\beta_0 t\left[\begin{array}{l}-1-\mathrm{erf}\left(\sqrt{\frac{-\psi_C}{t}}\right)+\left\{1+\mathrm{erf}\left(\sqrt{\frac{\psi_P-\psi_C}{t}}\right)\right\}\times\\ \times\exp\left(\frac{\psi_P}{t}\right)+\frac{2}{\sqrt{\pi}}\exp\left(\frac{\psi_C}{t}\right)\left(\sqrt{\frac{-\psi_C}{t}}-\sqrt{\frac{\psi_P-\psi_C}{t}}\right)\end{array}\right]$$

The simultaneous solutions of Eqs. (4) and (5) are shown as plots of ψ_C and ψ_P as functions of mass ratio for temperature ratio $\tau=0.1$, in Fig.1. For comparison the curves from [1], β_0=0, are added. In Fig .2 the dependence of both potentials on temperature ratio τ is shown for argon plasma with cold electrons , β_0 = 0, and with hot population added, β_0=0.1.It can be observed that the potential drop through the source sheath varies very little with composition ratio and mass ratio, while it depends slightly on temperature ratio. The collector floating potential as a function of hot to cold electron composition ratio in argon plasma, for two values of electron temperature ratio, is shown in Fig.3. It is mainly dominated by hot electrons, since already a small value of hot electron

current is sufficient to compensate the ion saturation current .

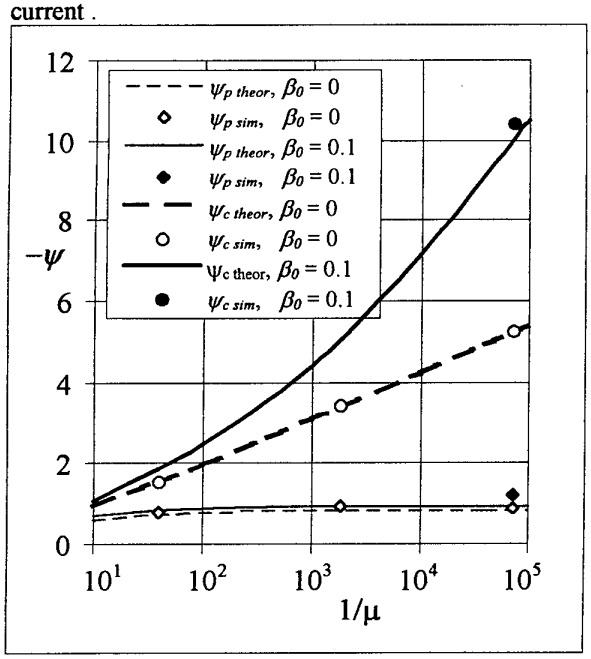

Fig.1. The potentials ψ_C and ψ_P as functions of ion mass ratio.

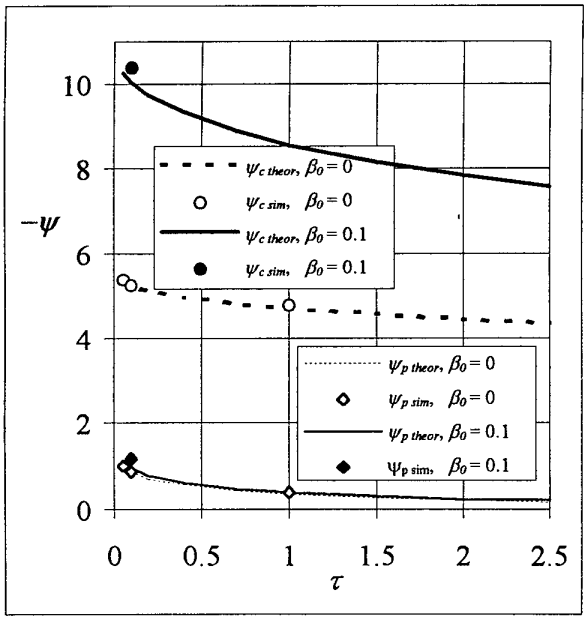

Fig.2. The potentials ψ_C and ψ_P as functions of ion to cold electron temperature ratio for argon plasma.

3. Simulation and experiment

A PIC simulation code XPDP1 composed at Berkeley [2] was used to study the plasma system. The set of fixed and variable parameters were similar to those used in [1]. A second hot electron population was added to the input file and the mass ratio for argon plasma was utilised. A typical potential profile which evolved in these simulations is shown in Fig.4. It is the collector potential which is strongly influenced by

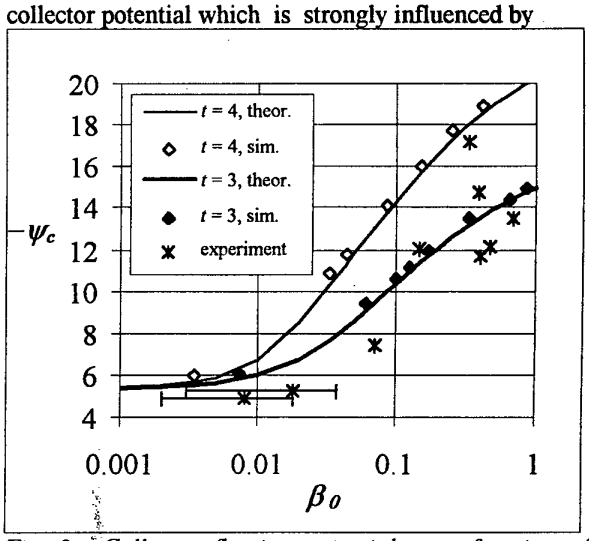

Fig. 3. Collector floating potential as a function of electron density ratio for argon plasma.

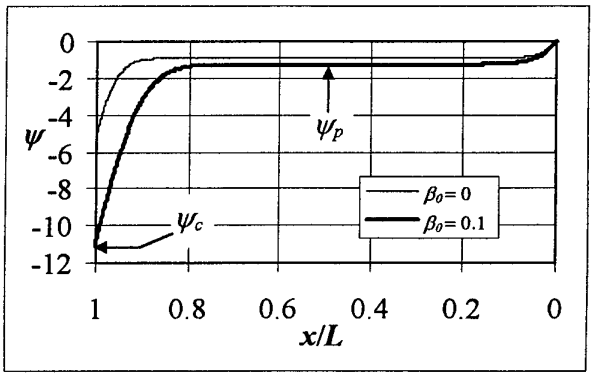

Fig.4. Simulated potential profile in argon plasma

the addition of hot electrons to the plasma.The values of potentials obtained from simulations for various of parameters μ, τ, β_0 are included in Figs. 1., 2., 3. They are in accordance with the results from theory. Also included in Fig. 3. are the measured floating potentials of a collector electrode in our laboratory hot cathode discharge plasma described already elsewhere [3]. By changing the working gas pressure in the system, we were able to control the partial density of primary (hot) elektrons in the plasma. The experimental values fit the theoretical and simulation results very well.

References

[1] L.A. Schwager, C.K. Birdsall: Phys. Fluids B **2** (1990) 1057.

[2] V.Vahedi, J. Verbocoeur and C.K. Birdsall: *XPDP1 Plasma Device 1 Dim Bounded Electrostatic Code* University of California, Berkeley (1992).

[3] T. Gyergyek, M. Čerček and M. Stanojević: Contrib. Plasma Phys. **36** (1996) 647.

INTERACTION OF CATHODE MICROTIPS AND DENSE PLASMAS

Rudolf Schmoll*, and Werner Hartmann**
*: Institut für Theoretische Physik, Ruhr Universität, P.O.Box 102148, 44780 Bochum, Germany
**: Siemens AG Corporate Research Center, P.O. Box 3220, 91050 Erlangen, Germany
**Phone: +49-9131-7 31623; Fax: +49-9131-7 24709
e-mail: werner.hartmann@zfe.siemens.de

Introduction

The interaction between a plasma and microprotrusions on cathode surfaces is modelled numerically [1]. Taking into account the statistical nature of protrusion geometries, this kind of cathode-plasma interaction is thought as to be the key to the understanding of cathode spot ignition in glows and diffuse arcs, and the motion (prograde and retrograde) of cathode spots in vacuum arcs. The 3-dimensional time-dependent model used in this work allows a detailed investigation of the nature of this interaction. Of particular interest are the ignition of emissive behaviour as a function of tip geometry and plasma density, and the physical processes governing emission and erosion. The rôle of the physical processes can be used to classify four major types of emitters, with smooth transitions between their emissive and erosive behaviour, respectively.

Description of the model

The heating of ellipsoidal three-dimensional (3-D) model microprotrusions in contact with a hydrogen plasma is simulated in order to achieve the time-dependent behaviour in terms of electron emission and erosion. Use is made of the rotational symmetry in order to reduce the computational problem essentially to a 2-dimensional one. The electron density is varied in the range of 10^{14} to 10^{17} cm^{-3} in order to account for many technically relevant plasmas, including the vicinity of cathode spots. The electric field in the cathode fall region and at the surface of the protrusion is calculated from the MacKeown and Poisson's equations, assuming a plasma bias (≈ cathode fall voltage drop) on the order of 300 V.

The emission processes considered are: secondary electron emission due to ion impact; field and thermo-field (Schottky) emission as formulated by Murphy and Good [2]; and evaporation of neutral atoms.

Heating of the tip is taken care of by considering the energy balance of the following processes: heat conduction cooling; Nottingham cooling or heating, respectively; evaporation cooling; ion bombardment heating from the plasma-cathode interaction; and Joule heating. Melting and erosion of the protrusion are taken care of by different approximation methods, i. e. like the stability of the molten tip against Rayleigh-Taylor instabilities under the balance of surface tension and different pressure components. Under this assumption, an unbalanced pressure leads to the instantaneous removal of the molden surface layer at the top of the protrusion, thus leading to an additional erosion in the form of droplets.

Results

The behaviour of a protrusion heated by ion bombardment from a plasma boundary can be best understood by comparing the heat flux inside the tip with that of a planar surface (1-D simulation). Figure 1 shows the development of the temperature along the vertical axis for both the 1-D and the 3-D case just prior to the onset of strong erosion of the protrusion.

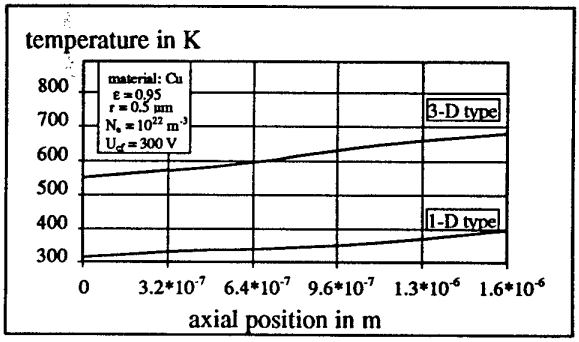

Figure 1) Comparison of the temperature along the vertical axis of a 3-dimensional tip (parameters: see legend) and the 1-D case (planar surface).

Due to the spatial concentration of the energy flow in the 3-D case as compared to the planar surface, the heating is much more effective and rapid for spatial inhomogeneities on cathodes than for a plane surface under identical conditions (compare e. g. [4]).

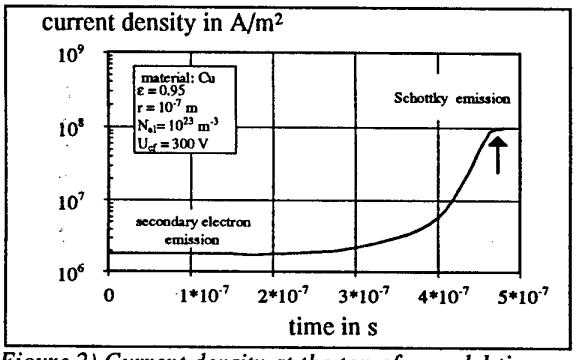

Figure 2) Current density at the top of a model tip as a function of time. The arrow indicates breakdown.

It is found that the comprehensive 3-D treatment of the interaction of a plasma and a "realistic" cathode surface microprotrusion leads to an emission behaviour (figs. 3, 4) which is in accordance with experimentally observed breakdown times and fields [3].

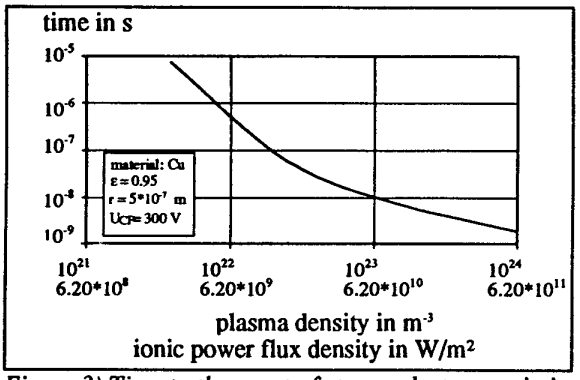

Figure 3) Time to the onset of strong electron emission and tip erosion ("breakdown") as a function of the plasma electron density (ionic power flux density), for an ellipsoiaal Cu tip of eccentricity ε = 0.95 and a base radius r of 0.5 μm.

Electron emission is governed by secondaries in the early phase, and particularly Schottky emission during the later stages. For the protrusions investigated, the field enhancement factor ß at the tip of the protrusion is only moderately enhanced (by a factor on the order of 30) over the macroscopic field strength. Therefore, the macroscopic electric fields necessary for ignition of emissive behaviour are considerably lower than those responsible for pure field emission. For a high eccentricity of the tip ε > 0.95, however, breakdown occurs very rapidly (figure 4), indicating the early onset of strong field emission and, hence, Joule heating, as is expected for typical field emitters ("explosive emission" [4, 5]). A comparative study was made to evaluate the significance of ion bombardment heating during the heating process leading to the ignition (triggering) of breakdown. For this purpose, the ion current was intentionally "switched off" during the calculations; the results are shown in figure 5 in comparison to those with the ion current "switched on".

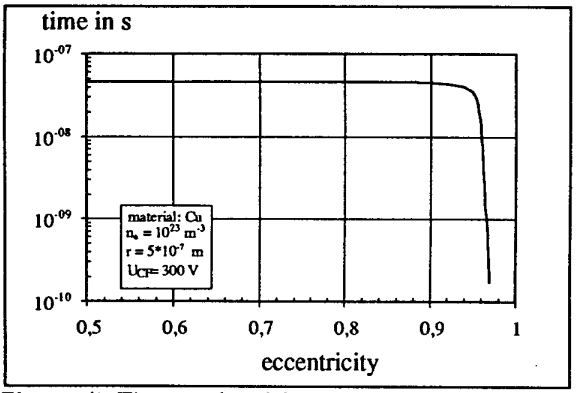

Figure 4) Time to breakdown as a function of the eccentricity of the emitter of figure 2.

It is obvious, for the tip geometry and parameter range investigated, that ion bombardment heating is essential for the ignition of emissive (and hence, erosive) behaviour for a large range of densities.

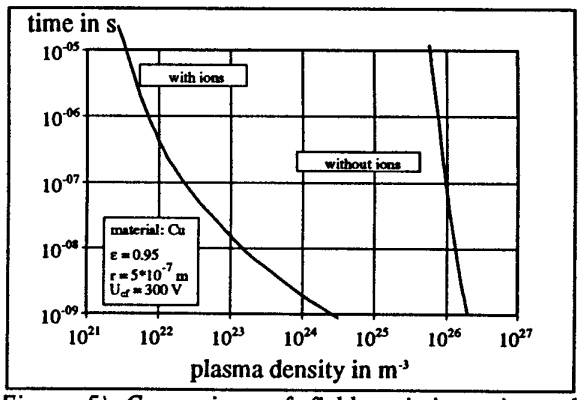

Figure 5) Comparison of field emission triggered breakdown ("without ions") and ion heating triggered breakdown of a model Cu protrusion.

From the temporal development of the emissive and erosive behaviour, a classification can be made as to the prevailing physical processes for a specific tip and a distinct set of parameters. In essence, four different kinds of emitters can be distinguished:

- o quasi-stationary (>μs) thermionic emission with slow evaporation
- o non-stationary thermionic emission with strong evaporation and loss of liquid phase material
- o quasi-stationary field-emission dominated; slow evaporation, no loss of liquid phase material
- o non-stationary, extremely fast explosive destruction of the emitter, field-emission dominated in early phase.

In effect, quasi-stationary and explosive emission and erosion, respectively, are included as extreme cases.

Conclusions

The interaction of cathode protrusions and a plasma has been simulated for ellipsoidal model tips. It is shown that ion bombardment heating of cathode protrusions immersed into a biased plasma is essential in cathode spot ignition. It leads to emissive behaviour of microprotrusions in a wide range of parameters where field emission alone fails. The numerical results concerning breakdown delay and electric field strength/plasma density are in good agreement with experimental results from different authors.

References

[1] R. Schmoll, "Plasma-Wand-Wechselwirkung strukturierter Oberflächen", PhD thesis, Ruhr-Universität Bochum, Germany 1995

[2] E. L. Murphy, R. H. Good, Phys. Rev. 102, 1965, pp. 1646 ff

[3] V. F. Puchkarev, IEEE Trans. Plasma Sci. 21, 1993, pp. 725-730

[4] J. Mitterauer, P. Till, "Computer simulation of the dynamics of plasma-surface interaction in vacuum arc cathode spots", IEEE Trans. Plasma Sci PS-15, 5, 1987, pp. 448-501

[5] G. A. Mesyats, D. I. Proskurovskii, "Pulsed Electric Discharges in Vacuum", Springer-Verlag Heidelberg, Germany, 1989

Relation between crater dimensions and voltage fluctuations in low current cold cathode electric arcs

*M.TIOURSI, **R.HAUG
*Université des Sciences et de la Technologie, ORAN, ALGERIE
** EDEE, LPGP, SUPELEC 91190 GIF-SUR-YVETTE, FRANCE

Abstract

We present a study of instabilities and of spontaneous extinctions which occur in low current DC arcs between metal electrodes. Two theoretical models for the behaviour of emitting sites on the cathode surfaces are proposed. Both models are in agreement with experimental results and yield equal values for the charges required for crater formation on a given cathode. This charge is roughly proportional to the third power of the crater dimension revealed by SEM observation.

Introduction

Phenomenological studies of the instabilities of arcs burning in air have been made [1-5]. Thus, it is important to distinguish forced extinctions provoked by external causes, such as current vanishing, from natural extinctions (self extinctions) which happen without any change in external conditions. Natural arc instabilities and spontaneous extinctions in low current free burning arcs appear as voltage pulses, and the observation of this fluctuations with fast recorders shows that, when the average time between individual phenomena becomes sufficiently large, the noise resolves in short unipolar voltage pulses [4].

In other studies [5], the shape of the voltage increase is significantly dependent of the cathode material. In particular, the presence of oxide mixed with a silver matrix yields a slope change in the voltage increase. A consistent hypothesis, [4-5], assumes that each pulse is related to a spot extinction. The voltage pulse associated with this extinction, whose mechanisms are strongly related to the cathode thermal and electrical properties, is reproducible and exhibits a standard shape for the voltage increase.

The statistics of self extinctions and instabilities are established by means of electrical high speed devices.

At low current and without care, the first self extinction blows out the arc. But by using a constant current circuit which reignites the arc after extinction, we can have an apparently steady arc. Thank to repetitions, we are able to cumulate data on many individual events. With a well defined trigger, given by the voltage pulse, we record the fast evolution of physical parameters as functions of time.

Experimental set-up

The electrodes are cylinders 3 mm in diameter and 5 mm long. the inter-electrode gap is 1-6mm long, the electrode axis is horizontal and the electrode holders are water cooled. the electrical circuit is especially designed for decoupling the arc from the electrical DC power supply (fig. 1.). a capacitor c (5nF) is sufficient to achieve this decoupling for fast signals. the low inductance resistor r is an air cooled carbon cylinder. the inductance of the fast response part of the circuit, including the arc, is less than 30 nH. the stray capacitance of the arc electrodes is equal to 60 pF. the dc power supply has 2 kV, 4 A power capability. this high voltage is necessary to induce, through the decoupling circuit, subsequent reignition after arc extinction. due to the circuit configuration, at the extinction, the arc voltage jumps with an amplitude equal to the resistance voltage drop R.I. later, the capacitor c charges with an initial slope of voltage equal to i/c. with the chose value of capacitance, the elapsed time between extinction and the subsequent reignition is of the order of microseconds. the arc voltage is measured through a fast voltage divider (probe Tektronix p 6057) with 1.3 GHz bandwidth and 50 Ω input resistance in series with a 10 nF capacitor. for the measurement of the arc voltage, we use a fast recorder (Tektronix DSA602) 400 MHz bandwidth. for statistical measurements, we use a fast counter (Racal Dana) having 6 ns dead time. Fig. 2 shows a typical voltage pulse related with an arc extinction. Due to the time constant of the fast recorder input circuit (10 nF, 500 Ω, high pass filter), some differentiation occurs, changing the baseline of the record. This appears on fig. 2 as a baseline lowering of 0.3 V at the end.

Experimental results

Silver (Ag) and Gold (Au) electrodes materials are tested.

1- The voltage appears as DC superimposed with unipolar pulses. Physical recordings are shown on fig. 3. The recorded voltage shows many pulses with randomly distributed amplitudes but the resolution of the recorder does not enable us to see fluctuations of very low amplitudes. On the right side of the fig., the large amplitude step corresponds to a complete self-extinction of the arc.

With a faster recording speed, in accumulation mode, fig. 4 shows that the voltage increase rate is almost the same for all pulses, either short or long extinction voltage pulses.

2- Using a fast response current transformer (0.5 GHz bandwidth) in series with the arc enables us to record the arc current evolution, fig. 5. The comparison with the voltage measurements shows the ohmic behaviour of the arc supply circuit as stated above. The current drops near zero in less than 20 ns.

3- For pulse statistics measurements, the voltage divider is connected to a variable threshold counter. The threshold is set to zero, but due to input hysteresis circuit, it corresponds to an effective 20 mV threshold, thus rejecting the arc voltage noise.

Statistical approach

1- A previous study [4] allowed us to propose a theoretical model which explains the experimental results obtained in arc duration measurements. We have proposed a model for the emitting site temporal behaviour in the low current cold cathode arc, freely burning in atmospheric air. The mean arc duration is proportional to $\exp(I/I_0)$:

$$< T >= \tau_0 \cdot \left[\exp \left[\frac{I}{I_0} - 1 \right] \right]$$

where I is the arc current, τ_0 is the spot life span and I_0 the mean current per spot.

If $I >> I_0$, we can write :

$$\log < T >= \log \tau_0 + \left[\frac{I}{I_0} \right]$$

On fig. 6, the logarithm of the mean life time of an arc is plotted vs. arc current for Ag and Au. Table I collects the values for I_0, τ_0 obtained from the fit of experimental results to the model. We introduce $q0 = I_0 \tau_0$ as a characteristic parameter for the cathode material.

Material	τ_0 [μs]	I_0 [A]	q_0 [C]
Ag	60	0.58	$3.48\ 10^{-5}$
Au	2.4	0.52	$1.25\ 10^{-6}$

Table I

2- The average frequency of spots extinctions can be defined as :

$$f = \frac{n}{\tau} = \frac{I}{I_0 \tau_0} = \frac{I}{q_0}$$

where n is the mean number of emitting spots.

From the slope of plotted curves (fig. 7), we deduce the $q0$ parameter. Table II collects the results for both Ag and Au.

Material	q_0 [C]
Ag	$3.26\ 10^{-5}$
Au	$1.13\ 10^{-6}$

Table II

Discussion

The values of q corresponding to both models for one metal are in agreement. The differences between values of q for Ag and Au are mainly due to spot life span differences. For both metals, the average currents per spot I are relatively close.

We assume that the thermodynamical properties of both metal (Ag, Au) are close (latent heat of fusion and vaporisation, heat conduction, ...) as well as the energy of ions impinging the cathode. Therefore, the value of the ratio of electric charges is close to that of eroded masses.

Assuming a geometrical similitude in the craters shape for both metals, the atomic volume being almost the same, the ration of crater radius is the third root of the charge ratio :

$$r_{0Ag}/r_{0Au} = \left[q_{0Ag}/q_{0Au}\right]^{1/3}$$

Both models yield a ratio of radius values near 3. By observation with a scanning electron microscope, the ratio of the diameters of craters is close to that value : 3µm for Ag and 1 µm for Au. See photographs 1-2. This is agreement with the hypothesis of an equal erosion rate as expressed in volume per charge.

The current densities are deduced from the observed craters dimensions by the relation :

$$j = I_0/\pi r_0^2$$

We obtain for Silver (Ag), j=8 10^{10} Am^{-2}, and for Gold (Au), j=6.4 10^{11} Am^{-2}

Conclusion

Comparison of the erosion characteristics of two metals having close properties, chemical or atomic, yields a common mechanism for the interaction with the arc plasma in the cathode spot, and the same eroded volume of material per charge unit. This is confirmed by two evaluations methods of charge per spot and by microscope observation of cathode spot trace.

Bibliography

[1] GRAY F. W., PHARNEY J. R., *Proc. LX th. ICECP*, CHICAGO, USA, 1978, p57.

[2] BEN JEMAA N. *Ph. D. Thesis*, RENNES University, FRANCE, 1977.

[3] BARRAULT M. R., HAUG R., MAFTOUL J., *IEEE Trans.*, PS10, 1982.

[4] M. TIOURSI M., *PhD Thesis*, PARIS XI University, FRANCE, 1990

[5] TIOURSI M., HAUG R., *Proc. XIXth, Int. Conf. Phen. Ion. Gases*, BELGRADE, YU, 1989

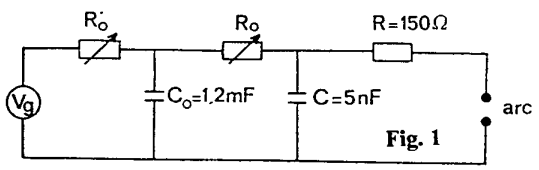

Fig. 1

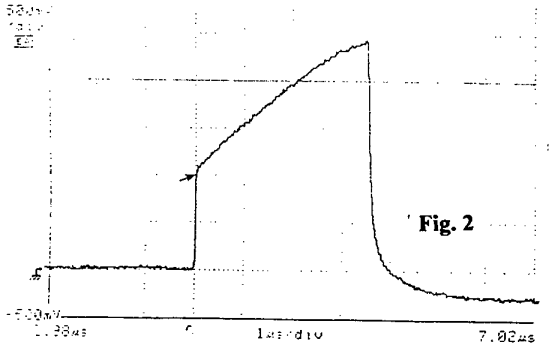

Fig. 2

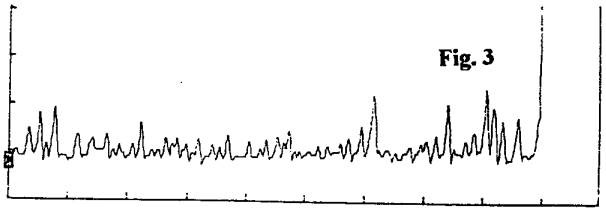

Fig. 3

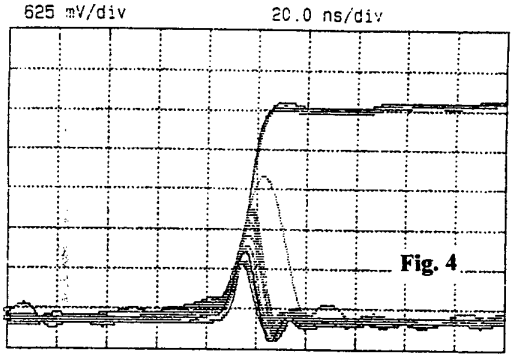

Fig. 4

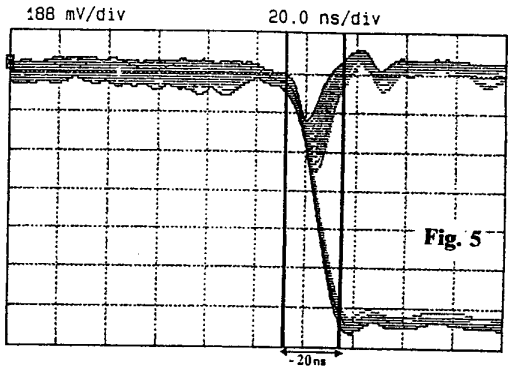

Fig. 5

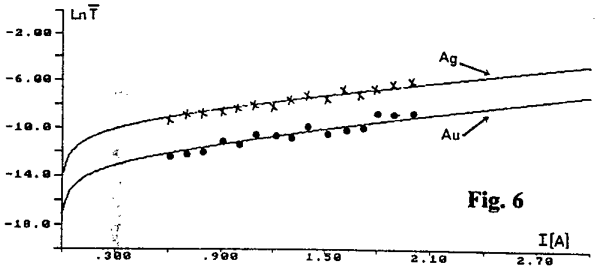

Fig. 6

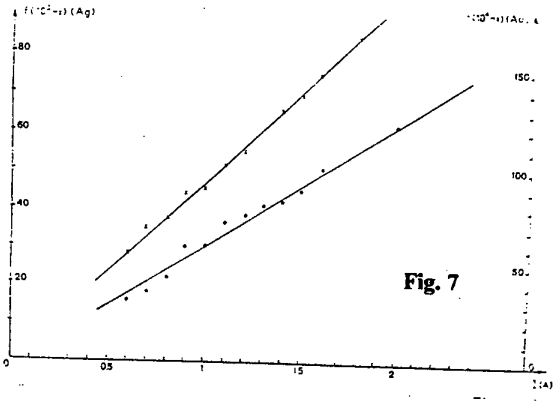

Fig. 7

BREAKDOWN PHENOMENA BETWEEN A HYDROGEN PLASMA BEAM AND THE DISK AS A WALL

TATSUZO HOSOKAWA, MAKOTO FUKUDA, TERUO KANEDA*

Department of Electrical and Electronic Engineering, Hosei University
Kajino-cho, Koganei-shi, Tokyo 184, JAPAN
*Department of Electronic Engineering, Tokyo Denki University,
Kanda-Nishiki-cho, Chiyoda-ku, Tokyo 101, JAPAN

INTRODUCTION

The breakdown phenomenon observed between a plasma and a wall is an arc discharge. This phenomenon has been investigeted by many researchers [1]-[5]. In this paper, the breakdown phenomena between the plasma beam and the plate electrode were investigated, and its results were compered with a theoretical analysis.

It has became clear that the breakdown characteristics depend on the discharge conditions and the developments of craters produced by the arc discharge on the cathode surface retrograded to the drift direction of $E \times B$. This breakdown characteristics is very similar to the property of a unipolar arc observed in the nuclear fusion device.

EXPERIMENTAL APPARATUS

The hydrogen plasma beam was formed through a 2 mm diameter orifice by the differential evaporation as shown in Fig.1. The density of plasma beam was $\sim 10^{11}$ cm^{-3}. The gas pressure was in the range of $10^{-3} \sim 10^{-4}$ Torr. The plate electrode consisted of 10 cm length and 7 cm width, and this electrode held to the distance of 1.5 cm from the plasm beem to the radial direction, and was electrically floated.

The electrode material was aluminium. The magnetic field of 500 G was applied to the plasma beam direction. A negative DC voltage was applied on the electrode. The current pulse due to an arc discharge was observed by a current probe.

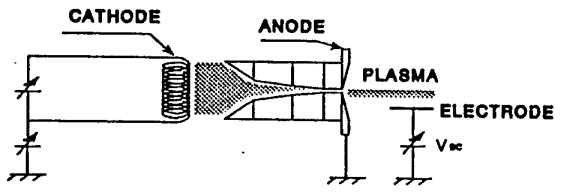

Fig. 1 Experamental apparatus

EXPERIMENTAL RESULTS

When the DC applied voltage reaches 50 ~ 300 V, the breakdown occurs and the breakdown characteristics depend on the plasma beam current, gas pressure, magnetic field and electrode materials. The typical oscillograms of current and photon pulses of the arc are shown in Fig. 2, and the time variation of appearances of arcs is shown in in Fig. 3. The frequency of appearances decreased with time, but increased again after stoppage of applied voltage on the gap. And the more stoppage time, the more the frequency of appearances.

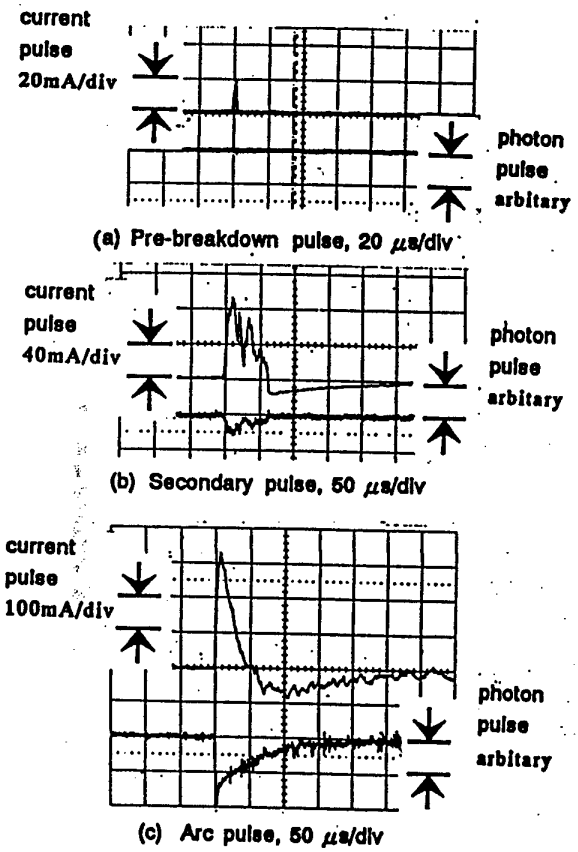

Fig. 2 Typical oscillograms of the arc

The space potentials in the gap are shown in Fig.4. The space potentials are about constant from plasma beam to near cathode and the vicinity of cathode forms a sheath. The craters due to the arc were observed on the cathode surface.

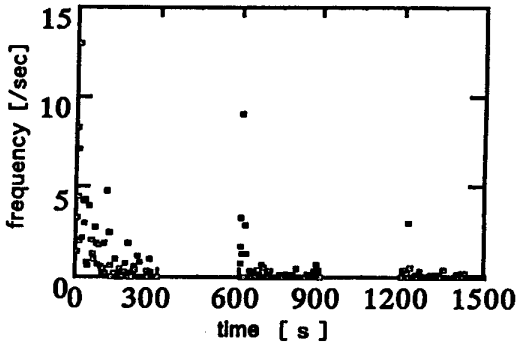

Fig. 3 Time variation of appearances of arcs

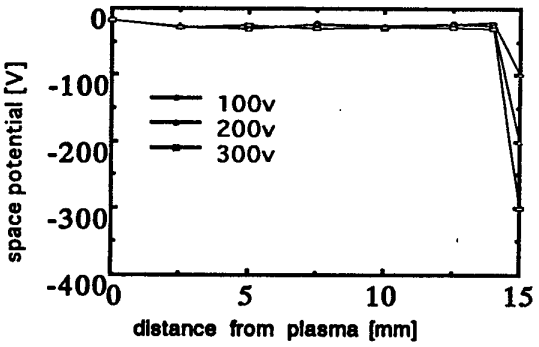

Fig. 4 Distributions of the space potentials in the gap

DISCUSSIONS

From a unipolar arc theory of the discharge mechanism between a plasma and a wall, the ion current density ji at the boundary of the plasma and the ion sheath is,

$$j_i = n_i q_i \sqrt{\frac{k T_e}{m_i}} \qquad (1)$$

where ni is ion density, qi is ion charge, k is Boltzmann constant, Te is electron temperature and mi is ion mass, respectively.

On the other hand, if the voltage difference of the plasma beam and the plate electrode is Vsf, the electron current density je to the wall direction is,

$$j_e = n_e q_e \sqrt{\frac{k T_e}{2\pi m_e}} \exp\left(\frac{q_e V_{sf}}{k T_e}\right) \qquad (2)$$

where ne is electron density, qe is electron charge and me is electron mass, respectively.

The unipolar arc is, however, monopolar arc, and is electrically float. So, the sum of je and ji becomes 0 by offsetting each other.

From equations (1) and (2), Vsf is,

$$V_{sf} = \frac{k T_e}{e} \frac{1}{2}\left[\ell n\left(\frac{m_i}{2\pi m_e}\right) - \ell n\left(\frac{1+\delta_i}{1-\delta_e}\right)\right] \qquad (3)$$

where δ_e and δ_i are ratios of secondary electron emission on the cathode surface by the electron and the ion[6].

If it is assumed that unipolar arcs generate at the voltage of Vsf, the electron emitted from the cathode surface return to the cathode again. And this electron circulation forms a circulation current, that is,

$$I_c = A n_e e \sqrt{\frac{k T_e}{2\pi m_e}}\left[\exp\left(-\frac{e V_c}{k T_e}\right) - \exp\left(-\frac{e V_{sf}}{k T_e}\right)\right] \qquad (4)$$

The density of a cathode spot can be calculated numerically from the value of experimental results by the equation (4). The results of the calculation are shown in Table 1. From the results, the density of the cathode spot is 10^{17} cm^{-3}, and this value is nearly equal to that of the vacuum arc spot.

Table 1. Results of calculation

sheath potential	7.58 V
circulation current	60 A
cathode spot plasma density	10^{17} cm^{-3}

(1) G.Ecker : Proc. ICPIG, Duseldolf (1983)
(2) D.E.Post, R.Behrisch : Physics of Plasma-wall Interractions in Controlled Fusion, 495, NATO Series, Series B : Physics Vol. 131 (1986)
(3) F.R.Schwirzke : Vacuum Breakdown on Metal Surfaces, IEEE Trans. Plasma Science, 19,690(1991)
(4) T.Hosokawa, T.Kaneda : Proc. ICPIG XXI, Bochum, 423 (1993)
(5) T.Tanaka, M.Fukuda, T.Hosokawa, T.Kaneda : Proc. ICPIG XXII, Hoboken, 1-29 (1995)
(6) J.Karlau, C.Martin, K.G.Uller and H.tuczek : J.Nucl.Mater. 76/77 (1978)

MOMENTUM ACCOMODATION AT LOW ENERGY IONS-SOLID SURFACE INTERACTION.

V.YU. Kolosov, V.S. Sukhomlinov

Department of Optics , Institute of Physics, St.-Petersburg State University, Ulyanovskaya 1, 198904, St.-Petersburg, Russia.

Introduction

Last time due to hypersonic airdynamics rapid development and plasma applications to airdynamical characteristics improvement [1], the consideration of the process of keV- charged particles momentum accommodation at their collision with surface becomes actual. In proposed work an attempt of development of the theory for accommodation coefficient of normal and tangential momentum projections of light low energy ion under their oblique incidence on the amorphous solid body surface is presented.

General

The developed theory based on the approximate analytical solution of Boltzmann kinetic equation for ion distribution function in solid body obtained in [2] which takes into account both electron and nuclear stopping. The analytical formulas for the calculation of the accommodation coefficients of the normal and tangential momentum projections α_n and α_{tg}, respectively have been obtained.

The calculations of these values for the case of protons collision with surfaces of various elements from Be to Pt have been performed. The simple approximation formulas describing obtained results (with 1-2 % accuracy) in the wide region of incident ion energy - from several hundreds of eV to several keV - and for incident slopes - from 0^0 to 70^0 - have been evaluated.

It appeared that under the considered conditions $\alpha_{tg} \approx 1$, which is caused by high isotropization of the ion in the solid body due to elastic collisions with atoms. The value of α_n increases at incident slope increase (Fig.1) and ion energy decrease (Fig.2, 3) which is caused by back-scattering coefficient and average energy increases. As the example in Fig. 1 given the cases : 1 a), 1 b) $H^+ \rightarrow W$; 2 a), 2 b) $H^+ \rightarrow Ag$; 3 a), 3 b) $H^+ \rightarrow Ti$; 4 a), 4 b) $H^+ \rightarrow Si$ where a) and b) represents the results of calculations α_n as the function of angle of protons incidence ϑ_0 by analytical and approximation formulas respectively. In Fig.2 the value of α_n is plotted against energy of the incident protons E_0 for the cases: 1 a), 1 b) $H^+ \rightarrow W$; 2 a), 2 b) $H^+ \rightarrow Ag$ where a) and b) represents the results of calculations α_n as the function of energy of incidence E_0 by analytical and approximation formulas respectively.

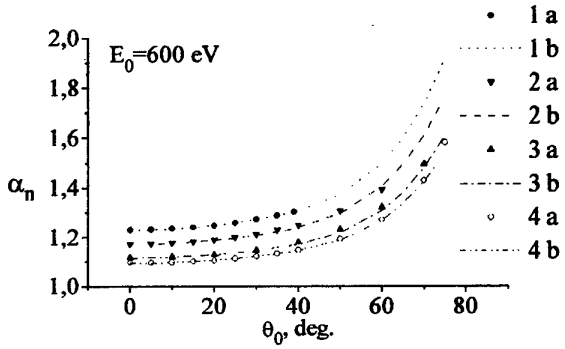

Fig. 1

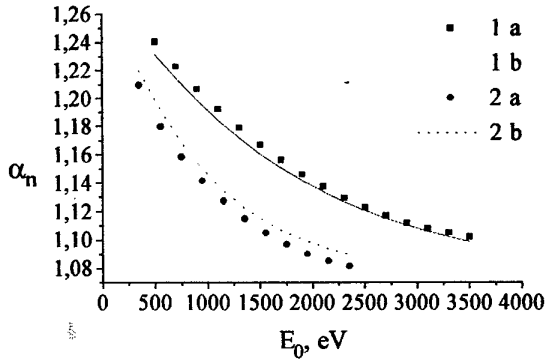

Fig. 2

The Fig.3 shows the same value for cases: 1 a), 1 b) $H^+ \rightarrow Si$; 2 a), 2 b) $H^+ \rightarrow Ti$. For all considered cases under the obtained conditions $\alpha_n(E_0)$ lies between 1.25 and 1.05.

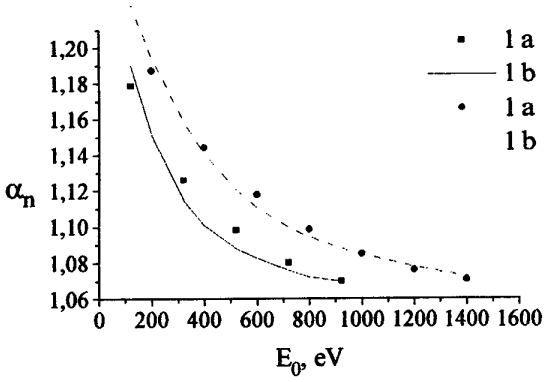

Fig. 3

References

[1] V.V.Vitkovsky, L.P.Grachev, N.N.Gritsov *at al.*, Materials of TSAGI, **v.2505**, Moskva, (1991), 27 p.
[2] V.S.Sukhomlinov, Zn. Tech. Fiz., **40(12)**, (1995), pp. 1214-1217.

BACKSCATTERING BY A SOLID SURFACE OF ITS OWN IONS IN THE CASE OF THEIR NORMAL INCIDENCE.

V.Y.Kolosov, V.S.Sukhomlinov

Department of Optics , Institute of Physics, St.-Petersburg State University, Ulyanovskaya 1, 198904, St.-Petersburg, Russia.

Introduction

The processes of interaction of a plasma with a surface play an important role in the formation of plasma properties. In particular, this concerns the processes of the mass transfer through a plasma-wall boundary, namely, of the sputtering and backscattering, as a result of which atoms of the wall materials enter into the plasma and undergo the ionization . At a sufficient intensity of such a process, the quantity of these ions grows so that self-sputtering becomes the main factor of entering impurities into a plasma. The present work is devoted to the development of the analytical theory of backscattering by the surface of an amorphous solid of its own low-energy ions at their normal incidence. This theory will allow one to take into account a role of backscattering in a self-sputtering process and enable one to develop the adequate theory of this process.

General

The theory is based on the approximate analytical solution of the Boltzmann kinetic equation:

$$\eta\frac{\partial\varphi(z,v,\eta)}{\partial z}+\Sigma(v)\varphi(z,v,\eta)=$$

$$=\frac{1}{\pi}\int_0^{2\pi}d\psi'\int_{-1}^{1}d\eta'\int_v^{v_0}\frac{v}{v'^2}\delta(\mu_0-\frac{v}{v'})\Sigma(v')\varphi(z,v',\eta')dv'$$

where $\varphi(z,v,\eta)$ is the distribution function of the ion flux in a solid; $\Sigma(v)$ is the inverse mean free path of the ion relative to elastic collision with atoms at the given velocity v; z is the coordinate measured from the surface along the inward normal to this surface ; μ_0 is the cosine of the angle of scattering; η , ψ and η' , ψ' are polar and azimuth angles before and after a collision, respectively. The solution of this equation was obtained by the known method of "generations" [1] and permitted us to calculate the distribution function for the flux of backscattered ions. The integral and differential characteristics of the backscattering (the reflection coefficient of the particles R_N and the energy reflection coefficient R_E, the distribution function of the ion flux over the angles $F(\theta)$ and energy $F(E)$ of outgoing particles), as well as the twice differential characteristics (their calculation even by the method of computer simulation is a sufficiently difficult task) were obtained in terms of the distribution function of the flux. The conducted analysis showed that the particles scattered in the first monatomic layer of the solid are completely absent in the flux of backscattered ions at any type of the surface barrier. The backscattering flux is formed only owing to the particles penetrated into the depth of the solid. Note that the developed theory does not involve fitting parameters. Comparison of the integral and differential characteristics of the backscattering calculated in this work with those obtained in [2] by the computer simulation based on the Monte-Carlo method for different elements was performed. Our results proved to be in the satisfactory agreement with these data (Figs.1-4) over a wide range of the initial parameters (the energy of incident ions, the charge of the atom nucleus , the surface binding energy) :

1) Fig.1. - R_N for C^+, 1) - Ref. [2], 2) - this work;
2) Fig.2. - R_E for Si^+, 1) - Ref. [2], 2) - this work;
3) Fig.3. - F(E) for C^+ at E_0=100 eV: 1) - Ref. [2], 2) - this work;
4) Fig.4. - F(E) for C^+ at E_0=1000 eV: 1) - Ref. 2, 2) - this work.

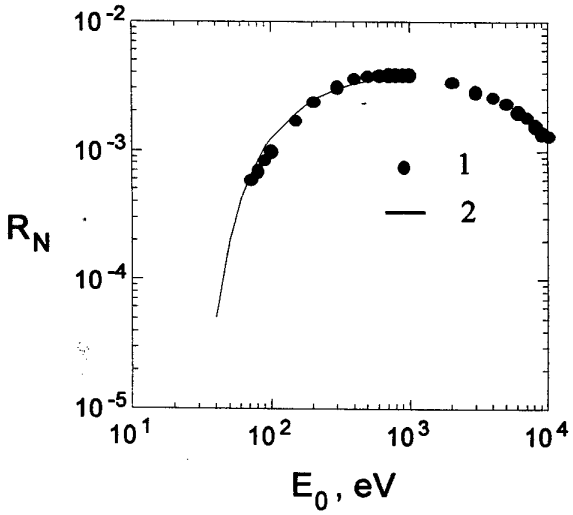

Fig. 1

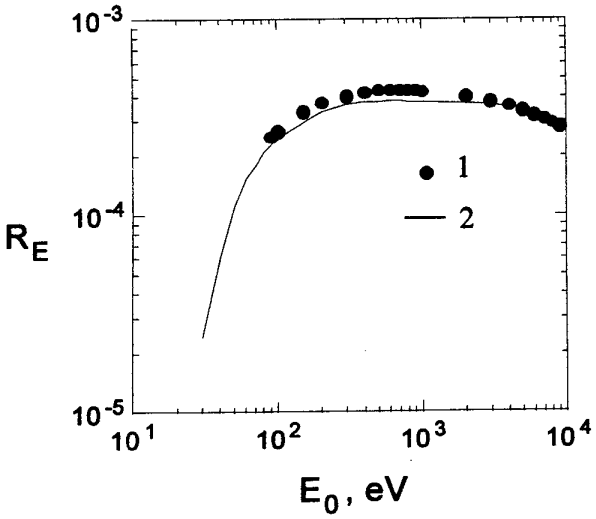

Fig. 2.

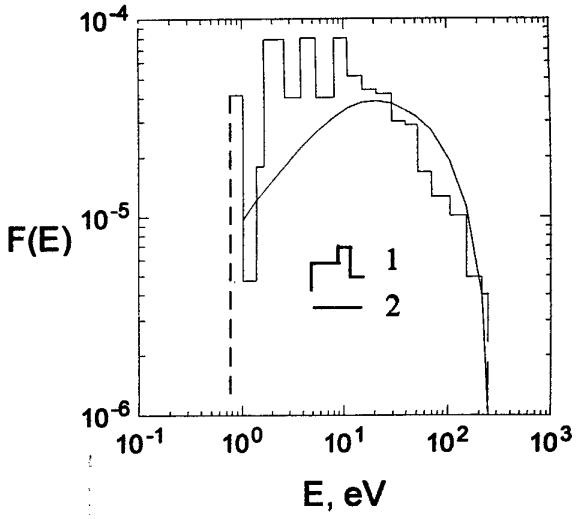

Fig. 4.

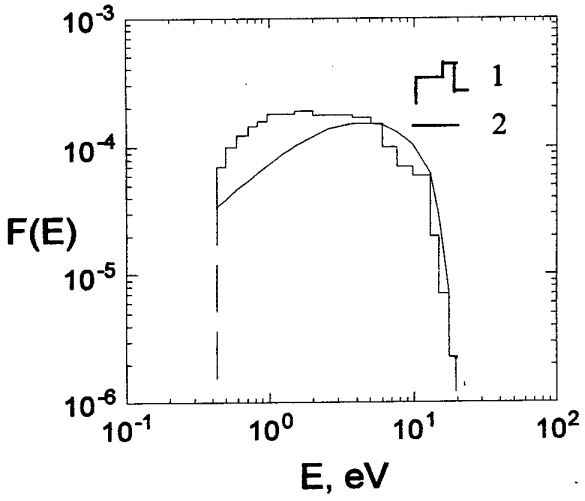

Fig. 3.

References

[1] V.V.Pletnev,D.S.Semenov,V.G.Telkovsky, Sov.Surface, **5, 5**, (1983).
[2] W.Eckstein., Z.Phys.B. (Germany), V.**63**, No.**1**. (1986), pp.109-120.

Formation of supersonic atom flux in the cathode region of vacuum arc.

Yu.D. Korolev and A.V. Kozyrev

High Current Electronics Institute of RAS, Russia, 634055, Tomsk

Introduction

In this paper it is called attention to an original mechanism for formation of neutral atom flux at the cathode voltage drop boundary, which may be realized in some types of vacuum arcs. It is possible when a neutral atoms vaporize from the cathode surface, and after that its ionization occurs in the cathode voltage drop region. In particular, a low-current-density arc or so called "diffuse vacuum arc" satisfies this condition [1,2].

In [1] it was shown that an electrical potential profile can be nonmonotonic at the near-cathode regions. This profile and particle fluxes are shown schematically in Fig.1.

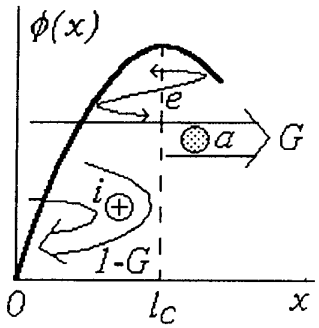

Fig.1

The length of the cathode voltage drop region, l_c , is certainly shorter than all mean free paths. However, the ionization of the atoms moving through this region in the x-direction may occur since it is produced by chaotic energetic electrons from the cathode flare plasma, which may enter the region $0l_c$. The probability for the ionization is determined by the electron temperature in the plasma, T_e, and the time required for an atom to fly through the layer $0l_c$. Ionized atoms as an ion current will be returned to the cathode surface by the strong electric field.

At first, let us consider the ionization of a unit atom evaporated from the cathode surface in its motion through the space charge layer of l_c. Since l_c is much shorter than the mean free path of the atom untill its collision with another heavy particle, the atom velocity, v, will not change within the lenth l_c . However, the atom can be ionized by one of the thermal electrons presented in the potential well. The average number of ionizing collisions, q, that may occur throughout the length l_c is determined from equation:

$$q(v) = (k_i/v)\cdot \int_0^{l_c} n_e(x)dx, \qquad (1)$$

where $k_i(T_e)$ is the ionization constant. It is important that the number q varies in inverse proportion to the velocity v. If q is the average number of collisions within the distance $0l_c$ then the probability for collisionless passing of this way $P(v)$ is

$$P(v) = \exp(-\text{const}/v).$$

It means that the slow atoms will be largely ionized within the layer $0l_c$, and the fast atoms will largely pass this region without ionization. Thus, at the outer boundary of the cathode space charge layer a flux of the fast atoms will be formed. Below the simple 1-D theory of this process is presented.

Theory

It is known that the velocity distribution function of the evaporated atoms is 1-D Maxwellian:

$$f(v_x) = A\cdot\exp(-Mv_x^2/2kT_c).$$

At the evaporative surface the average atom velocity of mass M is

$$\langle v\rangle = v_{at} = (2kT_c/M)^{1/2}.$$

Then it is convenient to write all equations using the dimensionless velocity $V = v_x/v_{at}$. So that the normalized 1-D Maxwell distribution function is

$$f_0(V) = (2/\pi)\cdot\exp(-V^2/\pi). \qquad (2)$$

The probability for collisionless passing of the cathode layer is

$$P(V) = \exp(-Q/V), \qquad (3)$$

where $Q = q(v_{at})$ is determinated by (1). Then at the outer boundary of the cathode space charge layer, $x=l_c$, the deformed distribution function $f_Q(V)$ is

$$f_Q(V) = P(V)\cdot f_0(V) =$$

$$= (2/\pi)\cdot\exp[-(V^2/\pi) - Q/V]. \qquad (4)$$

In Fig.2 these functions for the some different Q are shown. The distribution function shows a supersonic particle flux because the slow particles are completely absent. As evident from the figure, the value of V, which corresponds to maximum of distribution function, grows as Q rises. This growth is correlated to decreasing of the total number of atoms. Only the some part G of initial atom flux can reach a point $x=l_c$ without ionization:

$$G(Q) = \int_0^\infty f_Q(V)\, dV \cong \tag{5}$$

$$\cong exp\{-3(Q^2/4\pi)^{1/3}\}.$$

The average velocity $W(Q)$ of this part of flux can be found from equation:

$$W(Q) = (1/G)\int_0^\infty V f_Q(V)\cdot dV \cong \tag{6}$$

$$\cong (1/G)\cdot exp\{-Q/\pi^{1/2}\}.$$

In order to find $G(Q)$ and $W(Q)$ in an explicit form the dependence $n_e(x)$ which is present in equation (1) must be known. It is rather complicated task. However, for some problems it is quite sufficient to know a dependence $W(G)$ which can be used as one of the boundary conditions for the plasma expansion theory.

The equations (5) and (6) can be considered as the function $W(G)$ which is given in parametric representation (Q is parameter). Such a function is shown in Fig.3. Of particular value is the universal character of this function because it does not depend on either a potential profile $\varphi(x)$ or an electron distribution $n_e(x)$ within the cathode layer. Of special note is the very convenient approximate analitical form of the relationship $W(G)$, which has the relative accuracy within ± 10%.

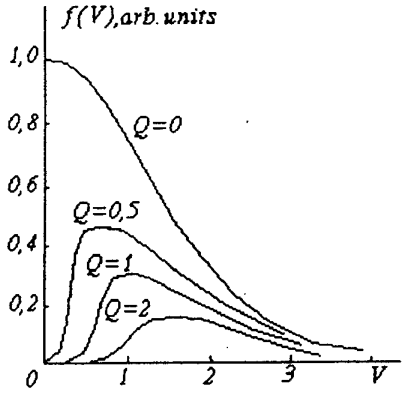

Fig.2.

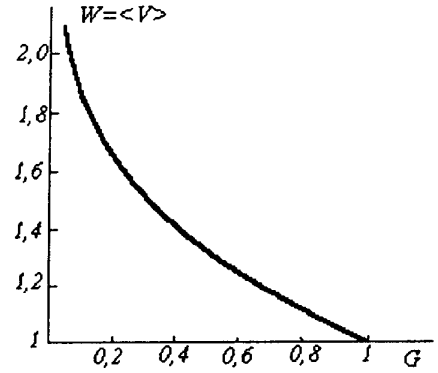

Fig.3.

Acknowledgement

This work is supported by Russian Foundation for Basic Researches (projects No 95-02-03504a and 96-02-16669)

References

[1] A.V. Bolotov, A.V. Kozyrev, Yu.D. Korolev. "A Physical Model of the Low-Current-Density Vacuum Arc". — *IEEE Trans. on Plasma Science*, 1995, v.23, No.6, pp.884-892.

[2] S.N. Paranin et al. "Experimental study of the thermal regime of a heated evaporated cathode in a stationary vacuum arc with a diffuse spot". — *High Temperature*, 1986, v.24, pp.307-313.

The Benefits Of Using A Steered Arc In The Continuous Mode Over Graphite Cathodes

Munther Kandah and Jean-Luc Meunier
Chemical Engineering Department (McGill University)
Plasma Research and Technology Center (CRTP)

1. Introduction

In the past decade, there has been increasing interest in the deposition of a special form of carbon films which are hard, dense, electrically insulating and optically transparent. These films have been called "diamond-like" [1] and have been obtained essentially through ion-beam deposition techniques. The Arc Ion Plating (AIP) process is considered as one of the most advanced processes among the ion and plasma assisted vacuum coating technologies.

The generation of micron-sized particles in such systems prevents the widespread applications of the diamond-like carbon (DLC) films produced using this technique. Therefore, this work aims at the control of the emission of these macro-particles from the cathode using combined magnetic field configurations in a continuous AIP system and without the use of any filtration system. Radial magnetic field (Br = 0.03 T) was applied parallel to the erosion surface, using permanent magnets, to rotate the arc spot in a circular pattern. At the same time, Helmholtz coils were fixed around the electrodes, generating constant axial magnetic field intensity of 0.14 T between the electrodes to confine the arc and increase the plasma density over the cathode surface.

At constant radial magnetic field intensity, various graphite cathode materials show different spot velocities, ion flux and macro-particles emission due to the changes in their surface properties. Surface property effects of the various of all graphite cathode used in this work were described previously [2].

2. Results

2.1 Cathode erosion rate

From the previous study [2], the arc spot velocity was found to be increasing with the decrease in cathode pore size at constant magnetic field intensity. In this work, the effect of material porosity on the cathode erosion rate is investigated for two cases, with and without Helmholtz field. In both cases, the erosion rate was found to increase with the increase in the pore size. With the case of using Helmholtz field (BH = 0.14 T), the erosion rate is found to be lower than that without the magnetic field confinement (BH = 0). The study of the major erosion rate components (i.e., ions and macro-particles) is necessary to know which one has stronger effect.

2.2 Particles number density

Figure 1 illustrates that cathodes showing higher spot velocities due to the difference in their surface properties emit smaller number of particles. This indicates that various graphite types will emit different quantities of particles towards the substrate under similar operating conditions. Comparing with the results of [3], one can notice the huge reduction in the number density of the emitted particles using a steered arc over graphite cathodes. The number density of particles shown in Figure 1 was measured at a 9 cm distance between cathode and substrate, 70 A arc current and 1.5 minute arc duration time. At a distance of 52 cm between the cathode and the substrate, with Br = 0.03 T and BH = 0.14 T, no particles were observed in the produced DLC films.

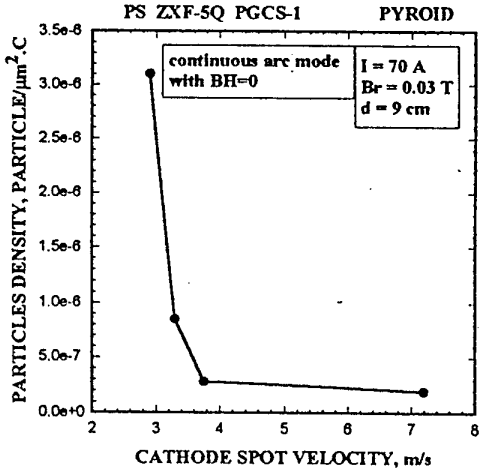

Figure 1 : Effect of cathode spot velocity on the number density of emitted particles over silicon wafer substrate for various cathode materials (continuous mode).

2.3 Ion current flux

Figure 2 shows the effect of cathode spot velocity as a function of total ion current emitted from the cathode spot and reaching a 7 cm diameter probe at 52 cm distance from the cathode with the presence of Helmholtz field. The change in velocity is imposed here by a change in the material properties of the graphite cathode at constant radial magnetic field intensity of 0.03 Tesla, driving the arc into rotation.

The radial ion current flux emitted from the cathode spot to a probe at 52 cm distance opposite to

the cathode is also measured for different graphite types. It is found that various graphite types emit different ion fluxes. The arc trace is found to be always at a radial distance between 2.1 and 2.3 cm from the center of the cathode (i.e., at the location of arc rotation and zero axial magnetic field intensity).

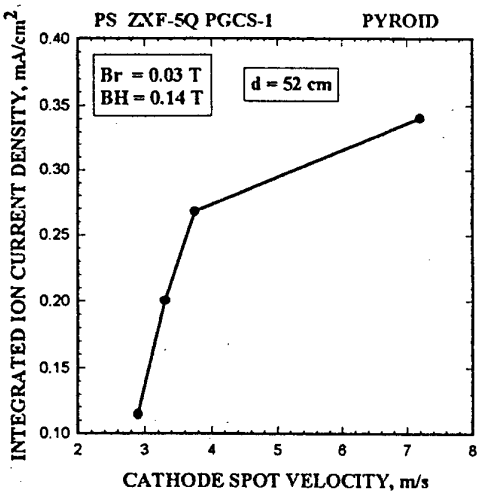

Figure 2 : Effect of material induced cathode spot velocity on total ion flux.

3 Discussion

Structural considerations of the graphite material used is shown here to be very important and strongly affecting the actual behavior of the cathode spot. The control of the heat load input to a given site of the electrode is found to be very important in view of macro-particles reduction. Therefore, the effort was focused in this work at the design of the vacuum arc ion plating system that works in a continuous arc mode using permanent magnets behind the cathode and a pair of Helmholtz coils around the electrodes. The idea behind this configuration is to rotate the arc spot over the cathode surface, confine the arc plasma and increase the spot velocity. As a result, the residence time of the spot at any given location is decreased and the stability is increased. Decreasing the residence time of the arc spot on a given site of the cathode should result in a reduced heat load on that site, hence reducing the particles emission.. The objective of using Helmholtz field is to create higher plasma density on the cathode surface, thus increasing the probability to create new emission sites. Confining the arc also increases the deposition rate significantly through the reduction in the ions losses.

The observed deposition rate in the absence of a Helmholtz field was a strong function of cathode to substrate distance. The ions were not able to reach the substrate when placed at a distance larger than 9 cm from the cathode. The deposition rate increased as the Helmholtz magnetic field increased, and at a close distance (less than or equal to 9 cm), the flux emitted was too strong in this design and resulted in the melting of the substrate.

Figure 1 shows that lower number of particles can be emitted from the cathode if the arc spot velocity is increased. The increase in the arc spot velocity can be achieved by increasing the radial magnetic field intensity (Br) over the cathode surface and/or using graphite types with small pore size, low electrical resistivity, high density and high grain size [2].

From Figure 2 the ion flux emitted from the cathode is found to be increasing with the increase in the cathode spot velocity. At the same time, it is found that various graphite types show different cathode spot velocities at fixed operating conditions (especially the applied magnetic field and arc current). Therefore, a good choice of graphite cathode material shows high spot velocity, low or no macro-particles emission and shows a more intense ion flux emission.

4 Conclusions

It is found that rotating the arc spot over graphite surface is much more difficult compared to metallic electrodes under same conditions. The rotation of the arc spot over graphite surface was achieved using permanent magnets behind the cathode. The arc was found to be rotating in a circular pattern at the radius where the perpendicular magnetic field component is equal to zero. Increasing the radial component results in an increase in the spot velocity. Different types of graphite showed different cathode spot behavior and emitted different number of particles and ions. The ion flux is peaked in the perpendicular direction to the cathode surface and the arc trace. The rotation of the arc spot over the graphite surface generates a more uniform erosion over the cathode surface, reduces the emission of particles and chunks and prevents any local overheating. Shifting the arc emission to a more stable emission mode was achieved by rotating the arc spot, confining the plasma and cooling the cathode. The control of the plasma flux, ion current and ion energy were possible through the change in the axial magnetic field component induced by Helmholtz coils. As a result of using the permanent magnets and Helmholtz coils, the cathode spot velocity and the ions flux emission are enhanced, while the number of particles emitted from the cathode spot decreased. Diamond-like thin films , free of particles, were produced using graphite in a continuous arc ion plating system without using any filtering tube.

5. References

[1] S. Aisenberg and R. Chabot, J. Appl. Phys., 42 (7) (1971) 2953.

[2] M. Kandah and J.-L. Meunier, Plasma Sources Sci. Technol., 5 (1996) 349.

[3] M. Kandah and J.-L. Meunier, J. Vac. Sci. Technol. A, 13 (5) (1995) 2444.

Temperature dependence of the surface recombination coefficient of nitrogen atoms on copper oxide

V. Lj. Marković*, M. M. Pejović† and Z. Lj. Petrović*

* Department of Physics, University of Niš, P.O. BOX 91, 18001 Niš, Yugoslavia

† Faculty of Electronic Engineering, P.O. BOX 73, 18001 Niš, Yugoslavia

* Institute of Physics, P. O. BOX 57, 11000 Belgrade, Yugoslavia

1. Introduction

The surface recombination of nitrogen atoms on copper oxide in afterglow is studied by measuring the dependence of the mean value of the breakdown time delay on afterglow period $\overline{t_d} = f(\tau)$ (the memory curve) and fitting of the data by the approximate gas phase model. The cause of the secondary electrons initiating the breakdown is the energy of the surface recombination of nitrogen atoms on the electrode surface and the surface recombination on container walls is the main loss channel. The breakdown time delay method is shown to be very efficient in nitrogen atom detection, and accompanied by the developed models of afterglow kinetics, in study of surface reactions [1-3].

In paper [1], we have shown that the nitrogen atom recombination on the glass container walls is second-order in number density, and determined the value of the surface recombination coefficient. Furthermore, we derive the adsorption isotherm of nitrogen atoms on molybdenum glass, the type of recombination mechanism and the dependence of the activation energy for desorption on the fractional coverage.

By fitting the experimental data on the basis of an approximate gas phase and exact diffusive model [2] it has been shown that the surface recombination on the iron electrode is of the second order and on the molybdenum, aluminum and gold-plated electrode it is of the first order. In addition, the analytical form of the recombination coefficient as a function of the adsorption characteristics of surfaces and the pressure of the parent gas has been derived.

In a recent paper [3] the adequacy of the gas phase model for a representation of the surface losses and comparison with the exact diffusive model are studied. It was found that diffusion should not be neglected as application of the gas phase coefficients to represent surface losses gives an error in the value of the recombination coefficient.

2. Experiment

The time delay dependencies were measured for a gas tube made of molybdenum glass with inserted copper cylinder (Fig. 1) with volume $V = 77\,cm^3$ and area $S = 88\,cm^2$. Copper oxide had been dark-red and was formed when the electrode was exposed to the atmosphere. The electrodes are rounded and polished copper rods of 99.98% purity. The electrode diameter was $D = 5\,mm$, area $S_E = 1\,cm^2$ and gap $d = 2.5\,mm$. The static breakdown voltage was $U_s = 400\,V$ DC.

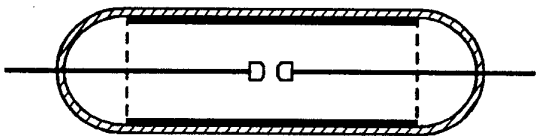

Fig. 1. Schematic cross section of a discharge tube

The tube was evacuated down to $10^{-3}\,mbar$, then filled with nitrogen of technical purity at $6.6\,mbar$ pressure, detected impurities O_2 being below 0.1%. The mean values of time delay were established from series of 300 measurements. The time delay measurements were carried out at overvoltage of $\Delta U/U_s = 50\,\%$, glow current of $I_g = 0.5\,mA$, glow time $t_g = 2\,s$, by an automatic system [4]. More details on the conditions, schematics of the experiment and more on experimental procedure can be found in [1-4].

3. Results and discussion

If we treat surface recombination of atoms as an effective gas phase process and if the number density of nitrogen atoms $[N](\vec{r}, \tau)$ during the afterglow decays due to the second order recombination on the copper oxide surface, its temporal evolution is given by equation

$$\frac{1}{[N]} = \frac{1}{[N_0]} + \gamma_w \tau, \qquad (1)$$

where $[N_0]$ is the initial number density of nitrogen atoms and γ_w represents an apparent recombination rate coefficient on the copper oxide. The volume recombination in three body collisions and surface recombination on the electrode surface can be neglected under our conditions.

The electron yield in the interelectrode space in this approximation [1-3] is given by equation:

$$Y = \gamma_e^{eff}\,[N]\,V_C, \qquad (2)$$

where γ_e^{eff} is the effective recombination coefficient on the electrode surface multiplied by the probability that one secondary electron is emitted on the basis of the recombination energy, and V_C is the volume of the interelectrode space.

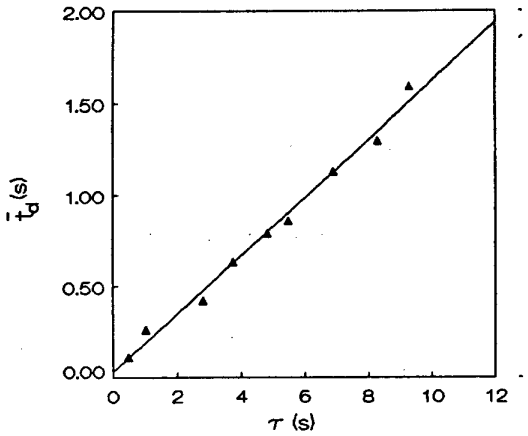

Fig. 2. The breakdown time delay dependence on afterglow period for technical purity nitrogen

On the other hand, the statistical time delay of electrical breakdown can be expressed as [5]:

$$\overline{t_s} = 1/Y\,P, \quad i.e. \quad Y = 1/\overline{t_s} \approx 1/\overline{t_d}, \qquad (3)$$

where P is the probability of starting a discharge from a single charged particle, and $P \approx 1$ at overvoltage of 50 % [1]. By combining the equations (1), (2) and (3), the value of the γ_w and γ_e^{eff} can be obtained from Fig. 2, in the form:

$$\gamma_e^{eff} = \frac{1}{\overline{t_{d0}}\,[N_0]\,V_C}, \qquad (4)$$

$$\gamma_w = \frac{\overline{t_d} - \overline{t_{d0}}}{\overline{t_{d0}}}\,\frac{1}{[N_0]\,\tau}. \qquad (5)$$

Since the time constant for the second order process is $\overline{\tau_d} = 1/\gamma_w\,[N_0]$, we obtain the following formula for the probability of recombination P_w:

$$P_w = \frac{4\,V}{\overline{\tau_d}\,\overline{v}\,S} = 4 \cdot 10^{-4}, \qquad (6)$$

where $\overline{v}$ is the mean thermal velocity.

For other temperatures (Fig. 3) we obtain the following values of the recombination probability $P_w(350K) = 3.5 \cdot 10^{-4}$ and $P_w(400K) = 5 \cdot 10^{-5}$. In our analysis gas phase model is used to obtain the coefficients so only apparent values are obtained but other data in the literature are obtained by a similar procedure so the results are generally comparable (provided that overall conditions are similar) [6-8].

The results presented here were obtained for technical grade nitrogen that has a large amount of oxygen which would decrease the recombination rate [9] due to interaction of nitrogen and oxygen atoms in the adsorption layer. Our work will proceed to obtain results for research grade nitrogen and also to extend the temperature range. In addition exact numerical diffusion model is applied that can provide recombination coefficients which are not subject to uncertainty due to inadequacies of the gas phase kinetic model.

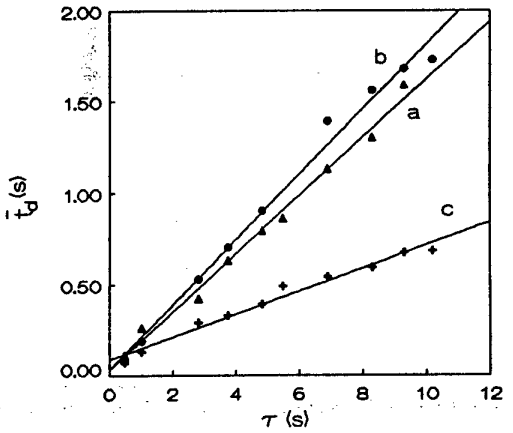

Fig. 3. The breakdown time delay dependence for a) 293 K, b) 350 K, c) 400 K

4. References

[1] V. Lj. Marković, Z. Lj. Petrović, and M. M. Pejović, J. Chem. Phys. **100** (1994) 8514

[2] V. Lj. Marković, M. M. Pejović i Z. Lj. Petrović, Plasma Chem. Plasma Process. **16** (1996) 195

[3] V. Lj. Marković, Z. Lj. Petrović and M. M. Pejović, J. Phys. III France **6** (1996) 959

[4] V. Lj. Marković, M. M. Pejović, and Z. Lj. Petrović, to be published

[5] J. M. Meek and J. D. Craggs, *Electrical Breakdown of Gases* (Oxford at the Clarendon Press, 1953).

[6] R. A. Young, J. Chem. Phys. **34** (1961) 1295

[7] A. N. Wright and C. A. Winkler, *Active Nitrogen* (Academic Press, New York, 1968).

[8] B. Brocklehurst and K. R. Jennings, in *Progress in Reaction Kinetics* (Pergamon Press, Oxford, 1967).

[9] A. Talsky and V. Zvoníček, Proc. of the XIII ESCAMPIG (Poprad, Slovakia, 1996) 325

Influence of a polymer sample on wire-to-plane corona discharge regimes

L. GRESSER, R. PEYROUS, N. SPYROU*, B. HELD.
Laboratoire d'électronique, des gaz et des plasmas, Université de Pau, 64000 PAU, FRANCE
* Electrotechnic Materials Laboratory, Patras University, Greece

1 Introduction

The surface treatment of polymers by plasma discharges is a well known mean of increasing their adhesion energy [1]. This kind of treatment is an interesting dry process in these days of environmental preoccupations, so it is marked out for a brilliant future.
The presence of the plasma implies great changes on the polymer surface, as shown by many works [2, 3], but the presence of the sample has a great influence on the discharge regimes and it is interesting to investigate this influence in order to improve the treatment efficiency.

2 Experimental setup

The figure 1 shows the reactor and the electrical and gas supplies.

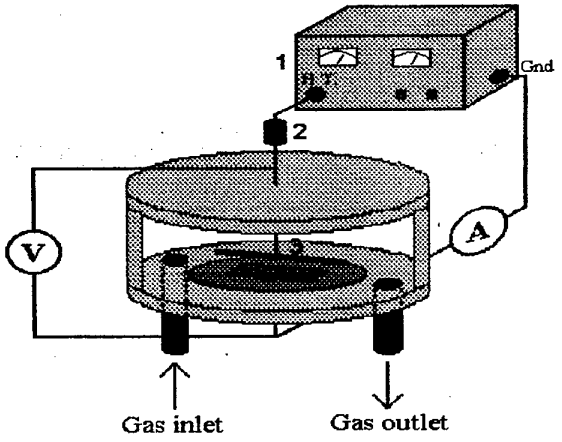

Fig.1: Experimental setup

The reactor consists in a cylindrical surrounding wall in Pyrex of 12 cm high, 22.5 cm of inner diameter and 1.5 cm thick. Being transparent, it allows the observation of the electric discharges which take place between the electrodes. The wall is placed between two P.M.M.A. plates of 1.5 cm thick. This system permits to attain pressures around 2.10^{-2} Torr.
The electrical supply is a DEL D.C. high voltage generator (1) which delivers voltages between 0 and 10 kV current stabilized. A loading resistor (2) of 100 MΩ is placed in serie with it and the upper electrode (3) which is placed inside the reactor. This electrode is a Monel 400 wire, 0.5 mm in diameter, placed parallely to the grounded electrode which consists of a stainless steel plane. A teflon ring ensures the parallelism of the wire with the plane and fastens the gap. Several rings with various distances have been made.
A polymer sample (P.M.M.A.) 1 mm thick is placed on the grounded electrode, as shown in fig.1, so that it is parallel to the wire.

3 Diagnostics materials

We want to characterize, prior to the treatment efficiency itself, the discharge and the influence of the polymer sample on the discharge. This is why we plot the V(I) characteristics at the same time we display with the oscilloscope the current impulses characterizing the evolution of the discharge regimes.
The electrical measurements are made with a Metrix MX 56 voltmeter and a Metrix MX 309 A ammeter. A 50 Ω resistor is placed in serie between the grounded electrode and the ammeter.
The visualisations of the current impulses are made with a LeCroy 9400 oscilloscope.

4 Results and discussion

The main aim of our works is to study polymer corona treatment using intermediary working pressures (5-700 Torr) this is why we chose a 10 Torr pressure of N_2.
Firstly, we measured the interelectrode potential (V) as a function of the discharge current (I) in order to obtain the electrical characteristics without sample. The V(I) curves obtained for different gaps (d) are shown in figure 2.

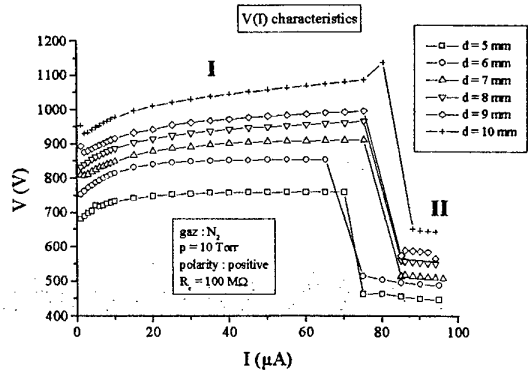

Fig.2 : V(I) characteristics without polymer sample

In a second time, we plotted the V(I) characteristics for the same working conditions but in the presence of a sample. We made the measurements with the grounded

electrode surface being 20% and 30% covered by the polymer. The curves obtained for these ratios are respectively shown in figures 3 and 4.

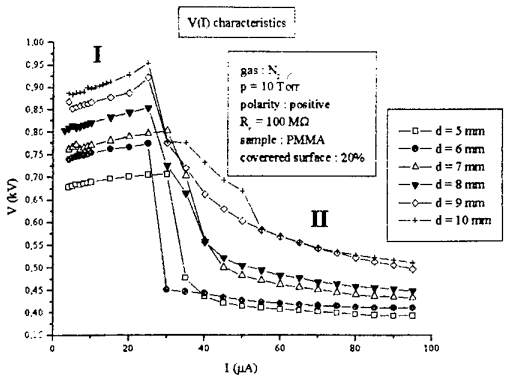

Fig.3 : V(I) characteristics with polymer sample (20% electrode surface covered)

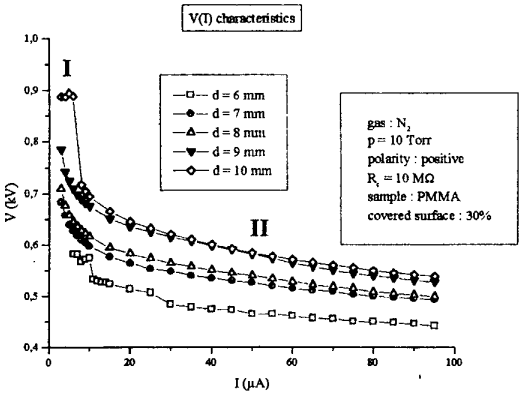

Fig.4 : V(I) characteristics with polymer sample (30% electrode surface covered)

In figure 2, without sample, the discharge remains in the same regime, named regime I, until a certain amount of current allows the transition to another regime, the regime II, the transition being marked by a drastic potential drop.

As we can see by comparing figures 2 and 3 the presence of the sample modifies significantly the transition conditions of the discharge regimes as does the percentage of surface covered (comparison between figures 3 and 4). In effect, the more electrode surface is covered by the sample, the less current is sufficient to pass from regime I to regime II. This evolution of the transition current value is related to the amount of charge needed to form the cathodic sheath.

The second step of our survey was to determine what are the two regimes that we could observe on the characteristics, by attempting to visualize the corresponding current impulses with an oscilloscope.

For the regime I, we were not able to see any impulse during our observations. In the transition zone characterised by the potential drop we can observe short current impulses that are unstable and non repetitive in time. When the regime II is reached, we obtain repetitive current impulses as shown in figure 5.

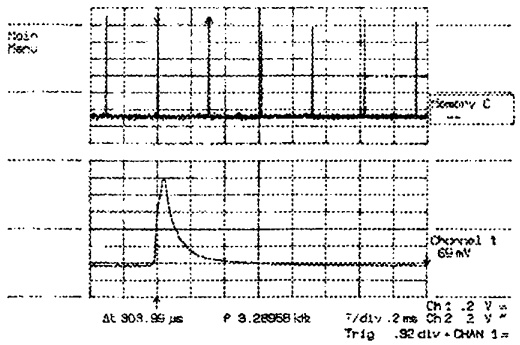

Fig.5 : Current impulses in regime II (d=10 mm, I=47µA, 20% electrode surface covered)

From these results, we might say that the regime I is related to the dark Townsend discharge. The regime II is, for itself, akin to a "glow-like" discharge [4] where a cathodic sheath is formed and the discharge becomes self-sustained.

The polymer, being a dielectric, promotes the formation of the sheath by non evacuating the charges that collide on its surface. This can explain why the more electrode surface is covered, the less charges are needed to create a sheath that allows the discharge to be self-sustained.

5 Conclusion

The study of the influence of the polymer sample presence on corona discharge regimes is a preliminary stage in the determination of the discharge treatment regimes. Both presence and area of the polymer seem to promote a regime that we may call " glow-like". It is then important to take into account those parameters in order to optimize the process.

6 References

[1] LISTON E.M., MARTINU L., WERTHEIMER M.R.; *J. Adhesion Sci. Technol.* 7(10); 1091-1127 (1993)

[2] PODHAJNY R.M.; *J. of Plastic Film and Sheeting* 4; 177-188 (1987)

[3] YOUXIAN D., GRIESSER H.J., MAU A.W-H., SCHMIDT R., LIESEGANG J.; *Polymer* **32**(6); 1126-1130 (1991)

[4] ERCILBENGOA A., LOISEAU J.F., SOULEM N., HELD B.; *Proc. 13th ESCAMPIG, Poprad (Slovakia), Europhysics Conference Abstracts* **20E**, part **A** (1996)

Intensive Stationary Electric Discharges with the Electrode Homogeneously Evaporated in Vacuum (ISEDEHEV)

V.A.Saenko
Scientific Center "Institute for Nuclear Research"
47 Prospect Nauki, Kyiv 252028, Ukraine
Phone : (0-44) 265-38-39,
Fax : (0-44) 265-44-63
e-mail : kinr2@riskaudit.kiev.ua

A review of one of the modern trends in the development of physics, engineering and technological applications of electric discharges is given [1]. From a variety of intensive stationary electric discharges with a vacuum-evaporated electrode we exclude only a well-studied vacuum arc with local (inhomogeneous) evaporation in cathode and anode spots. The theories of classical low pressure electric discharges form the foundation for ISEDEHEV physics. The presense of an evaporated electrode in a discharge gap greatly complicates these theories and causes new physical effects, so it becomes impossible to make strict calculations of practical constructions and their techological parameters. Thus, primary attention is focused on the construction of physical discharge models and the analysis of the experimental results (see review [2]).

The discharges with an evaporated cathode.

As to their physical properties,they are close to a well-studied discharge with an incandescent cathode in a rarefied gas. The discharges are supported by thermoemission of electrous from a working substance in case of high-melting substances and from refractory crucible in case of low-melting substances. The discharge with a working substance evaporated from a hollow cathode is of great importance. The mechanism of its arcing is analogous to the arcing of the discharge with the gas flowing out through the pipe or the nozzle into vacuum. The only difference is that the consumption of the working substance dm/dt in the first case is associated with discharge conditions and the thermal condition of a cathode operation, and in the second case dm/dt, is an independent parameter. Vapour pressure over the working substance surface during the discharge arcing is 1 - 100 Pa. The discharge is mostly used in the technology of deposition precious metals (Au, Ag) and Cu.

The discharges with an evaporated anode.

Here we can distinguish between diode and triode discharges. The diode discharge gap consist of a cathode and an anode heated to thermal emission, the material of which is evaporated by electron bombardment from the cathode. The discharge characteristics are similar to those of the non-self-maintained arc discharge with an incandescent cathode in a rarefied gas, in case the discharge power W considerably exceeds the critical power W* at which the discharge in the anode material vapour occurs. At W≈W* and gas pressure in a discharge chamber $p_1 \le 3 \cdot 10^{-3}$ Pa, volt-ampere characteristics of a discharge corresponds to the function of $I_a V_a = W^* = Const$, but not to $V_a \sim V_i = Const$. At high vacuum on intense cooling of a anode V_a can exceed 10^3 V. The diode discharge with an evaporated anode, at a free mode of operation of a cathode with a space charge of electrons near the cathode surface, can be put out (extinguished), in case we put the potencial $V_c > V_a$ to the additional electrode surrounding diode discharge gap, or if we increase gas pressure in a discharge chamber to $p > p_1$ at W≈W*.

The effective means of stabilizing the breakdown of a diode discharge at $V_c > V_a$ we found and the use of an additional electrode with $V_c > V_a$ was shown to be an effective means of intensifying the vapour ionization of an anode material.

In this case, when thre is an additional electrode with $V_a > V_c$, we can speak about a triode discharge with a vacuum-evaporated electrode. Further increase in ionization coefficient α of the anode material vapours in diode and triode discharges way be possible due to induction B≥0.0050 T applied to the discharge gap of the cathode-anode magnetic field longitudinal to the axis and the transition to the forced mode of operation of the cathode without a space charge of electrons near the cathode surface, when V_a and the electric field E in the discharge plasma increase. The increase in B and I_a and the decrease in the current of cathode heating lead to the stabilization breakdown of the discharge by the current of an additional electrode I_c. The mechanism of the breakdown is due to the fact that at a free mode of operation of the cathode, at $V_c > V_a$, the plasma potencial near the cathode, the current emission of the electrons from the cathode, and plasma conductivity σ in the discharge "cathode-anode" gap increase, while V_a decrease even if I_a=Const and at W≤W* the discharge breaks down. In much the same way we can explain the discharge breakdown at $p > p_1$, when the degree of relaxation of the electron beam from the cathode increases, σ also increases, V_a decreases at I_a=Const, W becomes less then W* and the discharge breaks down.

The main advantage of diode and triode discharges in comparison with other ISEDEHEV is that the first two ones generate accelerated charge-compensated plasma flow with the mean ion energy $E_i \approx eV_a$ for the diode and $eV_a \le E_i \le eV_c$ for the triode with an earthed cathode. Plasma accceleration takes place at $p \le 5 \cdot 10^{-1}$ Pa at low rate of deposition q of the

anode working substance on a substrate, when it is placed at a distance of 15 cm from the anode, plasma acceleration takes place at $q \leq 1 \cdot 10^{-9}$ m/s. From this it follows that the above discharges are used first all for deposition high-adhasive qualitative thin films from the material of any conductivity on the substrates deposition of any conductivity in particular for deposition dielectrics, synthesizign oxides, nitrides, carbides, etc.

Electrion-beam discharges.

Here the evaporation of the working substance of any conductivity from the electrode-crucible with an electron beam is used. To increase α, an additional incandescent cathode is placed into a vapour flow at a negative potential to a crucible. At the same time this makes it possible to provide the highest purity of the working substance plasma vapour. The properties of this discharge, of course, are similar to those of non-self-maintained arc discharge in a rarefied gas. The use of such discharge for ionizing the vapours is restricted due to a restricted emission capacity of cathodes. It is used for electron guns with a power of $W_e \leq 2 \cdot 10^4$ w. For electron guns with greater power, the only ionizer is a beam-plasma discharge which is ignition at vapour pressure over the working substance $p^* \geq 1$ Pa in the induction magnetic field $B \geq 0.05$ T longitudinal to the electron beam. In this case plasma with $\alpha \sim 1$ is formed. The distribution of ions over charges z in this plasma to a first approximation is described by the Gaussian function with a mean charge $z_m > 1$. The most possible mechanism of supporting a beam-plasma discharge in this case in an electron-cyclotron resonance which should be studied in more detail. If a beam-plasma discharge is not ignision,a beam-magnetron discharge is sometimes used [3]. For this purpose an electron beam in longitudinal magnetic field is surrounded by a cylinder with a positive potential $V_c > 0$ relative to the earthed crucible. The best effect can be achieved in high-temperature materials with high thermoelectron emission.

Technological advantages of all the ISEDEHEV over a vacuum arc as follows :

1) the absence of the working substance microdrops in a plasma flow,

2) the ability of evaporating a substance of any conductivity,

3) a wider range of varying technological parameters.

Thus, ISEDEHEV considerably extends practical possibilities of a vacuum arc. Technological advantages of ISEDEHEV over a magnetron discharge, in particular, to a flat magnetron, consist in : 1) considerably larger $\alpha \sim 1$; 2) possibility of supporting discharge arcing in a pure vapour of a working substance without a ballast gas; 3) high rate of deposition q. The above advantages lead to a considerable improvement, in thin films on thermoionic deposition using ISEDEHEV.

Thus, the physical properties of ISEDEHEV are studied well enough to be used in practice. But a number of physical aspect of ISEDEHEV arcing are still unknown, specifical, a beam-plasma discharge is little investigated. The problem of plasma production of any chemical element is practically solved. But the study of ISEDEHEV to improve physical models, plasma devises and technologies will be continued.

References.

1. Saenko V.A.// High Temperature. 1997.(to be published).

2. Saenko V.A.// Instrum. and Exper. Techn.1985,N3, P.9-21.

3. Sayenko V.A.// Proc. XII ICPIG. Part 1. Contrib. papers. Eindhoven.1975. P.107.

Secondary electron emission due to hydrogen ion and neutral bombardment

T. Šimko*, J. Bretagne and G. Gousset

Laboratoire de Physique des Gaz et des Plasmas, Bât. 212, Université Paris XI, 91405 Orsay Cedex, France
*Permanent address: Dept of Plasma Physics, Comenius University, Mlynská dolina F2, 84215 Bratislava, Slovakia

1. Introduction

The liberation of electrons from the cathode surface in a DC glow discharge is vital for maintaining the discharge operation as a supply of charge carriers for the discharge region. The emission of these secondary electrons occurs due to the bombardment of the cathode by ions, metastables, neutrals and photons coming from the discharge region [1].

Ion bombardment usually provides a major contribution to secondary emission [1]. In hydrogen, several kinds of ions co-exist (H^+, H_2^+ and H_3^+) and bombard the cathode concurrently. Moreover, in the cathode sheath they efficiently create high-energy neutrals (H, H_2) via charge-transfer and collision-induced dissociative reactions. These fast neutrals have similar energy distribution functions and particle fluxes, especially at high electric fields [2]. The bombardment of the cathode is therefore a joint action of the above-mentioned species, which complicates the understanding and modelling of the emission process. Moreover, emission details concerning all the species involved in bombarding are not sufficiently known, therefore one often avoids to use the emission in hydrogen discharge models [3].

In this paper, we propose a simple emission model for heavy-particle-induced secondary electron emission in hydrogen glow discharges. The proposed model is tested against various available experimental data for the low-pressure Townsend discharge.

2. Emission model

An individual emission process is characterized quantitatively by the secondary electron emission coefficient or yield $\gamma_\alpha(\varepsilon)$ defined as an average number of liberated electrons per incident particle of type α having energy ε [1]. It depends on the material of the cathode, the incident particle nature and energy.

In discharge physics, one makes often use of the overall secondary electron emission yield γ which characterizes the emission process as a whole: it represents the average number of electrons liberated per incident ion [1]. The advantage of such a formulation is that γ is directly equal to the ratio of electron to ion current at the cathode, a macroscopic boundary condition of discharge models [1].

The two definitions are related as follows: provided that the $\gamma_\alpha(\varepsilon)$ is known for species α, the overall γ_α emission coefficient of species α is given by

$$\gamma_\alpha = \int_0^\infty \gamma_\alpha(\varepsilon)\, F_\alpha(\varepsilon)\, d\varepsilon, \qquad (1)$$

where $F_\alpha(\varepsilon)$ is the energy distribution function of particles of species α incident on the cathode (normalized to 1). Here, γ_α represents the γ coefficient as if only the α species take part in bombarding.

The overall γ coefficient as used in discharge physics and as defined above is given as the weighted sum of contributions of all the species involved in the bombardment [4]

$$\gamma = \frac{\sum_\alpha \gamma_\alpha(\varepsilon) N_\alpha}{\sum_{\alpha'} N_{\alpha'}}, \qquad (2)$$

where N_α represents the particle flux of the species α at the cathode and α' denotes only the ionic species in the denominator.

Using the above formulae, one can calculate the γ coefficient supposing that (i) the emission yields $\gamma_\alpha(\varepsilon)$ are known for each incident species and that (ii) the energy distributions of bombarding species at the cathode are known.

There are only a few experimental data for hydrogen ion- or neutral-induced secondary electron yields [5,6]. Fig. 1 presents measurements for incident H and H^+ on gas-covered Cu surface [5]. It can be seen that the secondary yield is virtually the same for H atoms and ions. In addition, assuming the independent action of each nucleus of incident molecular particle, the secondary electron emission yield is given by:

$$\gamma_{H_k}(\varepsilon) = k\,\gamma_H(\varepsilon/k), \qquad (3)$$

where k numerates the number of incident nuclei. The hypothesis (3) gives the $\gamma_\alpha(\varepsilon)$ for all the other species as shown in Fig. 1. Note that the molecular species have much lower yields in the low-energy region, which is consistent with the Auger emission mechanism [4].

The distributions $F_\alpha(\varepsilon)$ can be obtained from the kinetic model of the discharge as described below, so that the γ value can be calculated using Eqs (1)–(3).

3. Kinetic model

The kinetic model of the Townsend discharge is similar to [2]. Further details can be found in [7] which is a paper at this conference and are therefore not described here. The simulation provides the energy distribution function of bombarding ions and neutrals.

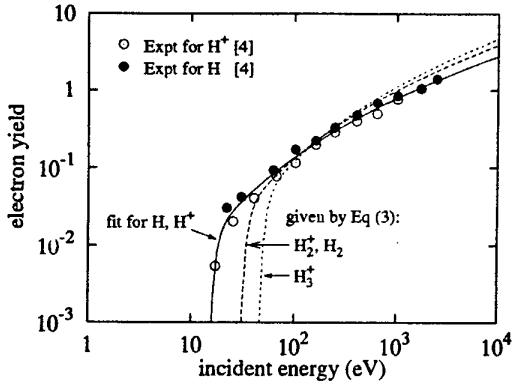

Fig. 1: The secondary electron emission yields for various hydrogen projectiles used in the model.

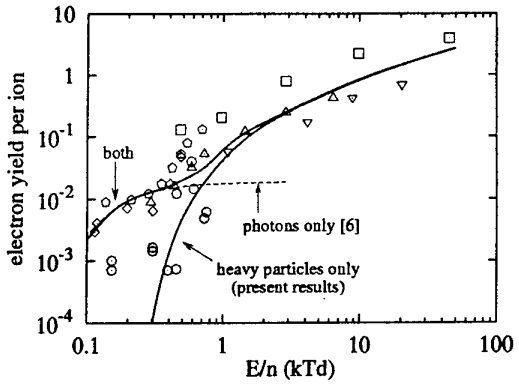

Fig. 2: The overall γ coefficient over a large E/n range. Various experimental results are plotted as points [6,8,9].

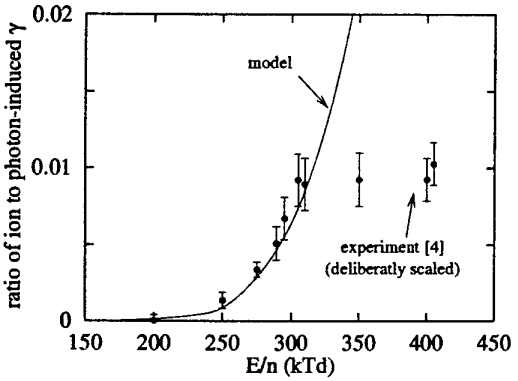

Fig. 3: The overall γ coefficient for low E/n. Error bars are the experimental results of [4] deliberately scaled (see text).

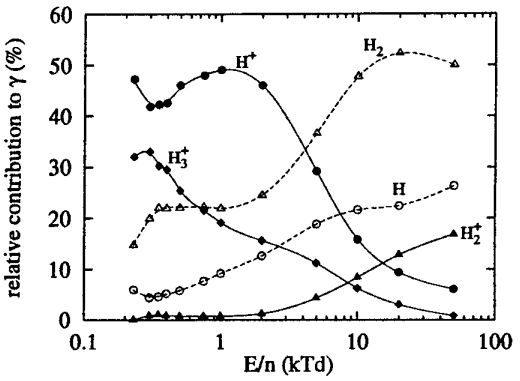

Fig. 4: The contribution of various species to overall γ as a function of E/n.

4. Results

Fig. 2 compares the present model and various experimental results [6,8,9]. We have not treated the photon-induced emission but used the results of Phelps [6]. The figure shows a very good agreement over all the E/n range and indicates the importance of photon-induced emission in majority of low-field experiments.

The γ values at low E/n are plotted in Fig. 3 together with deliberately scaled experimental results of [4] with the purpose to show the threshold-like behaviour of the emission. The onset is situated at around 300 Td both in the model and the experiment. The model results suggest that the onset appears when molecular species and especially H_3^+ (the most abundant species in this E/n region [2]) gain sufficient energy to pass the emission threshold (see also Figs 1,4). The model results in Fig. 3 do not saturate at 300 to 400 Td as observed in [4].

The species responsible for emission at various E/n can be inferred from Fig. 4. Neutral-induced emission becomes dominant at several kTd. Note that in [4], H^+ was identified as the sole species causing emission at around 400 Td, while present results show also a significant contribution of H_3^+. The experimental method of identification used in [4] discriminated high-energy H_3^+ due to the possibility of its collisional breakup to H^+.

Acknowledgments

The authors acknowledge A. V. Phelps for suggesting the subject of this work, helpful discussions and for sending us his valuable data. One of us (TŠ) was supported in part by the Bourse du Gouvernement Français and the Slovak Grant Agency (grant No 1/2312/95).

References

[1] M. J. Druyvesteyn and F. M. Penning: Rev. Mod. Phys. **12** (1940) 87

[2] T. Šimko, J. Bretagne, G. Gousset, M. V. V. S. Rao, R. J. Van Brunt, J. K. Olthoff, Y. Wang, B. L. Peko and R. L. Champion: Bull. Am. Phys. Soc. **41** (1996) 1332

[3] A. C. Dexter, T. Farrel and M. I. Lees: J. Phys. D **22** (1989) 413

[4] J. Fletcher and H. A. Blevin: J. Phys. D **14** (1981) 27

[5] J. A. Ray, C. F. Barnett and B. Van Zyl: J. Appl. Phys. **50** (1979) 6516

[6] A. V. Phelps: private communication (1994)

[7] T. Šimko, Z. Donkó and K. Rózsa: this conference.

[8] M. A. Folkard and S. C. Haydon: Aust. J. Phys. **24** (1971) 527

[9] M. Shimozuma, Y. Sakai, H. Tagashira and S. Sakamoto: J. Phys. D **10** (1977) 1671

Magnetic presheath in front of an Oblique End-Plate in a Magnetized Sheet Plasma

Akira Tonegawa, Masataka Ono*, Masahiro Shibamoto, Sigeyasu Sakamoto* ,
Kazutaka Kawamura** and Kazuo Takayama**

Department of Physics, School of Science, Tokai university
* Department of Nuclear Engineering, School of Engineering, Tokai university
**Institute of Research & Development, Tokai university
1117 Kitakaname, Hiratsuka, Kanagawa, 259-12 Japan.

To investigate the effect of an oblique end-plate on the transition layer between a plasma and an absorbing wall, we measured the space potential at the end-plate in a magnetized sheet plasma from the view of the two-dimensional boundary-like plasma. The magnetic presheath increases with increasing the angle of the end-plate. The thickness of magnetic presheath is several times as larger as the ion Larmor radius. The potential drop at the magnetic presheath is of the order of T_e/e.

1.Introduction

The transport of charged particles along with the magnetic field lines dispersed at the walls is important for the researches on the laboratory plasma, divertor plasma and so on. In particular, when a wall is placed at an angle to the magnetic field, the particle diffusion toward the wall deviates markedly from the uniformity by the electric field, the density and the temperature gradients. Such imbalances are expected to give some remarkable effects on plasma parameters, the edge potential and particle flow along the magnetic field[1-3]. In the magnetic field intersecting the surface at a shallow angle, Chodura showed that the transition layer has a double structure composed of the magnetic presheath and the Debye sheath. Using a kinetic analysis by K.Sato et. al., he found that an oblique magnetic field provides two presheath mechanisms; one is due to the ion polarization drift and another is due to finite ion-gyraradius effects[3]. These processes at the plasma-wall boundary are very complex.

In order to investigate the effect of the plasma-wall boundary with the oblique end-plate, we use a magnetized sheet plasma produced by a TP-D type discharge apparatus [4]. We can consider the sheet plasma as a "two-dimensional boundary-like" plasma that still preserves an overall charge to be neutral. The study of the thin plasma column, whose thickness is the order of the ion Larmor radius ρ_i, is important from the view points, such as the effect of dc electric fields on particle dynamics and the effect of the potential wall in sheet plasma on ion Larmor radius and so on. Thus, we measured the space potential to investigate the effect of an oblique end-plate, on plasma parameters.

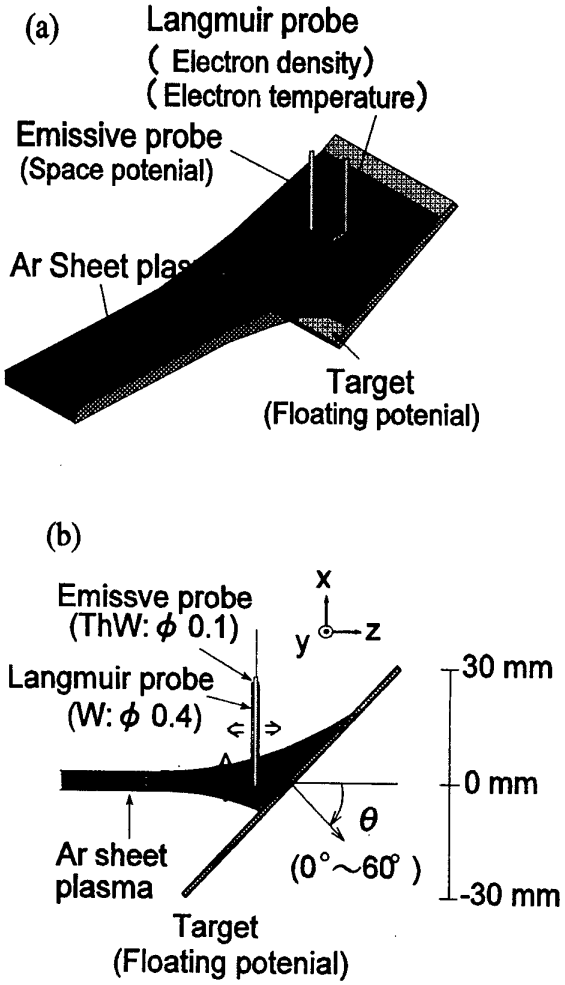

Fig. 1. Schematic drawing of (a)the plasma at end-plate and (b)measuring system.

2.Experimental apparatus

Schematic drawing of the plasma at end-plate and measuring system are shown in Fig.1 (a) and (b),respectively. The sheet plasma device is divided into two regions: the discharge region and the experimental region. A TP-D type plasma source, which was originally developed at the Institute of Plasma Physics in Nagoya University, is in the discharge region. This plasma source is composed of a cathode, an anode combined with a floating electrode system having a hole of rectangular cross-section. The dimensions of the anode slit are 1.5mm in thickness and 30mm in width. The strength of the magnetic field in the experimental region formed by ten rectangular magnetic coils is $\leqq$ 1kG, and the pressure in the experimental region is $\sim 10^{-4}$ Torr.

The oblique end-plate was placed at 70 cm away from the anode slit along the axis of the device in an open-magnetic-filed (~0.1 kG). The potential of end-plate is floating potential. In the plasma-wall transition layer, the direction of the magnetic field is parallel to the plasma flow (z direction) and the electric field is perpendicular to the oblique end-plate. The angle between the magnetic field and the electric field θ is changed 0°, 30°, and 60°. The oblique end-plate is perpendicular to z expressed in $\theta = 0°$.

A Langmuir plane probe (W:ϕ 1 mm) was employed to measure basic plasma parameters, such as the electron density and the electron temperature. The plasma potential, ϕ_p, was measured with an emissive probe (0.1 mm in diam, 2 mm long) heated with dc power supply. The potential measurements were performed in the Z direction from the end-plate at the center of the magnetized sheet plasma.

3.Experimental Results

The experimental conditions are as follows: the discharge current is 16 A, the strength of the magnetic field is about 0.1 kG. Fig. 2 shows the potential profiles for the various angles of the end-plate as functions of the Z/ρ_i: ρ_i is the ion Larmor radius. When the argon gas flow rate for sheet plasma production is 9 sccm, the electron temperature is 6.5 eV. At the same time, the floating potential of the end-plate is about -32 V. When the oblique end-plate is perpendicular to z, i.e., $\theta = 0°$, the ϕ_p shows a sudden drop in front of the end-plate. For $\theta \neq 0°$, the profile of ϕ_p is composed of two parts: a slowly falling part that is called "magnetic presheath" succeeded by the sharp fall of the sheath region at the wall. With increasing angle the potential drop in the presheath increases. The scale length of the magnetic presheath is several

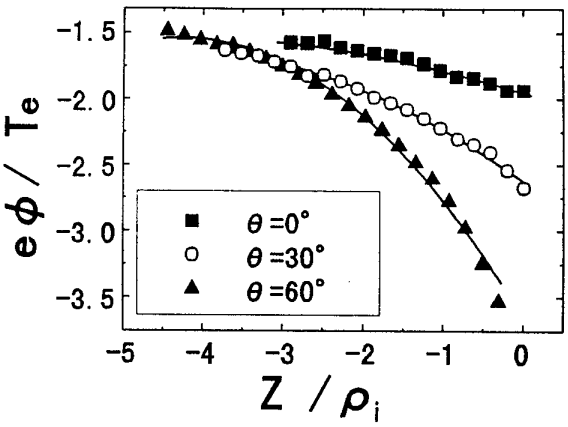

Fig.2. The potential for the various angles of the end-plate in a magnetized sheet plasma as functions of the Z/ρ_i : ρ_i is the ion Lamor radius.

times as larger as the ion Larmor radius. The potential drop at the transition layer is of the order of T_e / e.

4.Conclusions

We have investigated the effect of an oblique end-plate on plasma parameters by using the sheet plasma designated as the two-dimensional boundary-like plasma. With increasing angle the potential drop in the magnetic presheath increases. The total potential drop between plasma and wall is insensitive to the angle of the end-plate. The magnetic presheath is increases with increasing the angle of the end-plate. The magnetic presheath scale is several times as larger as the ion Larmor radius. The potential drop at the transition layer is of the order of T_e / e.

The authors wish to express their gratitude for the financial assistance from Grant-in-Aid for Encouragement of Young Scientists, No.08780459 and general Scientific Research(c), No.08680513, the Ministry of Education, Science, Sports and Culture.

This work has been carried out in the collaboration with the National Institute for Fusion Science.

References

[1] R.Chodura, Phys.Fluids, 25(1982)1628.
[2] R.Chodura, in Physics of Plasma-Wall Interaction in Controlled Fusion, eds.D.E.Post and R.Behrisch (Plenum Press, New York, 1986)P.99.
[3] K.Sato, H.Katayama and F.Miyawaki, Plasma Phys. (to be published)
[4] K.Sunako, K.Nanri, T.Noguchi, E.Yabe and K.Takayama,Nucl.Instr.and Meth.,B111(1996)151.

Investigation of the $1s_j$ Densities in the Vicinity of the Electrodes of a Neon Glow Discharge

A. Dinklage, H. Deutsch, H. Scheibner and C. Wilke
Institut für Physik, Ernst-Moritz-Arndt Universität Greifswald, Domstr. 10a, D-17489 Greifswald, Germany

1. Introduction

Excited state atoms in inert gas discharges play an essential role for the principles of plasma formation. They are well known to take part in spatial and temporal relaxation processes which are considered to be outstanding features for a detailed understanding of the discharge processes [1] and the dynamic behavior of glow discharges (e.g. [2]). Therefore it is extraordinaryly desirable to know exactly the spatial distributions of the excited species.

In this paper, we present axial density measurements of excited neon atoms consisting of both metastable ($1s_3$, $1s_5$) and resonant ($1s_2$, $1s_4$) states in a glow discharge in the vicinity of the electrodes by laser induced fluorescence, yielding state selective results of a high spatial resolution . Owing to the principles of this method an optical method employing light pulses of short duration will not affect the plasma itself as it should be expected in probe measurements, especially in the vicinity of the electrodes.

2. Experimental results

The experiments were performed in a neon glow discharge (r_0= 1 cm, p_0= 1.5 Torr, $d_{electrodes}$ = 0.75 cm) driven by a current source (i<25mA). Densities were measured by laser induced fluorescence spectroscopy employing a pulsed dye-laser system (τ = 10 ns) operated at visible wavelengths in order to cover $1s_j \rightarrow 2p_k$ transitions (Paschen notation) of neutral neon (NeI). The wavelengths of the observed fluorescence were chosen to be distinct from the pumping wavelength in order to suppress scattered light from the discharge tube (3-level pumping scheme). The pulse energy of the laser yields high saturation parameters S. Thus, the excitation process will be governed by coherent processes that have to be treated by a time dependent Schrödinger equation for the density matrix [3]. In order to suppress the influence of coherent excitation effects, a large number of the fluorescence experiments (n=200) for a given axis position (x) and discharge current (i) were performed with slightly varying pulse energies fulfilling the condition of large saturation (S>>1). Thus, the mean value of the signal corresponds to the pulse-energy averaged expectation value of the atomic state yielding the classical limit. In order to prove this method of energy-averaged saturation spectroscopy we compared our results with independent density measurements in the positive column formerly derived by absorption spectroscopy [4]. Our results agree very well with the absorption measurements for different currents (discrepancy less than 20 %).

Here, we present axial density measurements at a discharge current of about i=1.6mA. The laser light was irradiated perpendicularly to the discharge axis; observation was both perpendicular to the discharge axis and the laser beam. The axial resolution was better than 1.5 mm.

Qualitatively the densities of all species investigated decayed in the direction of the ASTON dark space. We have to mention that in front of the cathode density measurements were restricted due to a decrease of transparency of the discharge tube as depicted by hollow symbols in Fig. 1. At longer distances from the cathode densities rose to values which are typical for the positve column. We observed a spatially damped periodicity at the head of the positive column. Quantitatively the portion of the $1s_3$ atoms of all excited atoms was less in the cathode region than in the positive column. The relation of densities in the positive column at i=1.6 mA was given by $n_{s2}:n_{s3}:n_{s4}:n_{s5}$=1:44:16:220 with a density of $1s_5$ atoms of about $n_{s5}=4.2 \times 10^{11}$ cm^{-3} in the positive column. Absolute experimental uncertainities due to the calibration procedure were less than 30 %, while relative errors between different species were less than 5 %.

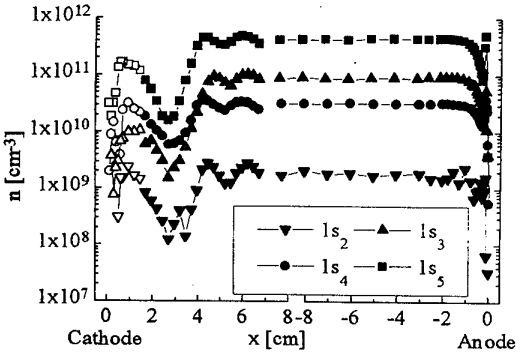

Figure 1: Axial density distribution of excited neon atoms in a glow discharge (r_0= 1 cm, p_0 = 1.5 Torr, i = 1.6 mA). Hollow symbols belong to the cathode region, where the transparency of the discharge tube was reduced due to the sputtering of the cathode.

In the vicinity of the anode a decay of $1s_j$ densities with a typical scale of about 1.5 cm was observed. Close to the anode (approximately 2mm) densities increase strongly corresponding to the anode glow. Figure 1 displays the axial behavior of 1s densities from the cathode to the anode of the discharge.

Figure 2 depicts the densities in the vicinity of the anode for the predominantly populated metastable ($1s_5$) and resonant ($1s_4$) states in detail. The relative distribution of less populated metastable ($1s_3$) and resonant states ($1s_2$) were found to be similar; their absolute values correspond to the portion in the positive column. In detail it was found that the decay of resonant state atoms is slightly smoother than the decay of metastable atoms.
Physically the decay in front of the anode may be understood as a spatial relaxation phenomenon of the metastable and resonan state atoms in the discharge.

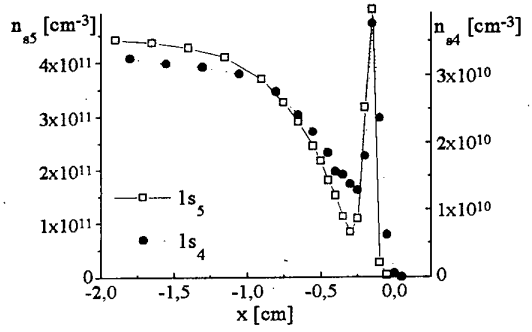

Figure 2: Axial density distribution of excited $1s_4$ and $1s_5$ neon atoms in the vicinity of the anode (x=0cm). The sharp decay in front of the anode (-1.5mm<x< 0mm) corresponds to the cut laser diameter in front of the anode. For discharge parameters see Fig. 1. Note the different scales for the metastable ($1s_5$) and the resonant ($1s_4$) states.

3. Conclusions

Axial density distributions of excited $1s_j$ state atoms in a low pressure neon glow discharge were measured in front of both a plane cathode and plane anode. The results are consistent with former results of absorption measurements in the positive column. Minima correspond to the well known dark spaces. It should be remarked that light emission in the dark spaces (corresponding to $2p_k \rightarrow 1s_j$ transitions owing to collisional excitation processes) is nearly vanishing, although the $1s_j$ densities decay only to a value of about 1/20 of the positive column value. Experimental results suggest that the transition regions of the positive column (column head and anode region) are governed by spatial relaxation processes.

This work was funded by the Sonderforschungsbereich 198 'Kinetik partiell ionisierter Plasmen', Projekt A7 of the Deutsche Forschungsgemeinschaft.

4. References

[1] F. Sigeneger and R. Winkler: Phys. Rev. E, **52** (1995) 3281

[2] K.-D. Weltmann, H. Deutsch, H. Unger and C. Wilke: Contrib. Plasma Phys., **33** (1993) 73

[3] B.C. Shore: *The Theory of Coherent Atomic Excitation,* Wiley Interscience: New York (1990)

[4] J. Behnke: Beitr. Plasmaphys., **11** (1971) 23

Topic 10

Physical aspects of plasma chemistry, plasma processing of surface, plasma wall interaction and thin film technology.

Effects of H_2 Dilution on Surface Loss Probability of CH_3 on a-C:H in CH_4+H_2 RF Discharges

H. Videlot[1], M. Shiratani[1, 2], J. Jolly[1], and J. Perrin[1, 3]
[1]Laboratoire PRIAM, Unité Mixte de Recherche CNRS-ONERA, Fort de Palaiseau, 91761 Palaiseau cedex, France
[2] School of Information Science and Electrical Engineering, Kyushu University, Hakozaki Fukuoka, 812-81, Japan
[3]BALZERS Process Systems, 5 rue Léon Blum, Z.I. Les Glaises, 91124 Palaiseau cedex, France

1. Introduction

Hydrogenated amorphous carbon (a-C:H) films have great potential in industrial applications such as hard protective coatings, electrical insulator and passivation layers and are commonly deposited using radio frequency (RF) plasma enhanced chemical vapor deposition (PECVD) method. H_2 dilution of CH_4 has been often used to produce a-C:H films, because their properties strongly depend on the hydrogen content of the films [1]. Recently Naito et al. have studied the correlation between the deposition rate of a-C:H and CH_3 density measured using infrared diode laser absorption spectroscopy in CH_4+H_2 RF discharges [2]. The results suggested a possible decrease of the sticking probability of CH_3 with an increase of the H_2 partial pressure. Therefore, it is important to get information about the surface reaction probabilities for CH_3 on a-C:H films in CH_4+H_2 RF discharges to improve understanding and control of the deposition process.

Previously, we reported on measurements of absolute radical densities in SiH_4, CH_4, and H_2 RF discharges by using the threshold ionization mass spectrometry (TIMS) technique [3,4]. Time-resolved TIMS was used to obtain surface loss probability β of SiH_3 on a-Si:H films in SiH_4 RF discharges, β of H on stainless steel, a-Si:H and oxidized silicon in H_2 RF discharges, and β of CH_3 on a-C:H in CH_4 RF discharges [5,6]. We report here on the β value of CH_3 on a-C:H in RF discharges in CH_4 diluted with H_2.

2. Experimental

The experimental set-up and measurement method have been described in detail elsewhere [3-5]. The 13.56 MHz RF discharge was confined in a cylindrical volume between two parallel-plate electrodes (R = 6 cm radius and L = 3.3 cm interelectrode distance) and a grounded grid. In this study, an isothermal and electrical symmetric reactor was employed instead of the non-isothermal asymmetric one used previously, in order to facilitated the interpretation of the results. Both electrodes were heated at 523 K. The self-bias voltage is less than 10% of the discharge voltage (250 V) for an effective RF power coupled to the discharge of 5 W. Reactive gases CH_4+H_2 were supplied through the RF shower electrode at a total flow rate of 50 sccm, and the filling pressure was 20 Pa. A Si wafer was placed on the lower grounded electrode.

The mass spectrometer was mounted under the grounded electrode to measure the radical density near the substrate. The absolute CH_3 density was detected using TIMS. The time evolution of the radical density in the afterglow was determined with a multichannel scaler connected to the output of the mass spectrometer. The discharge was turned on and off at about 5 Hz (50% duty cycle), and the signals were accumulated synchronously.

3. Kinetics of the Radical-Surface Interactions

In the post-discharge, the conservation equation for CH_3 is $\partial n/\partial t = -2kn^2 + D\nabla^2 n$, where n is the CH_3 density, k the recombination reaction rate (3×10^{-12} cm^3/s at 523 K and 20 Pa [7]), and D the diffusivity. The boundary condition is $|\partial n/\partial q| = n/\lambda$, with

$$\frac{1}{\lambda} = \frac{1}{D}\frac{v}{4}\left(\frac{\beta}{1-\beta/2}\right),$$

where q is a generalized spatial coordinate, v the thermal velocity of CH_3.

Under the present experimental conditions, the characteristic length λ for CH_3 is much larger than the dimensions of the discharge. In addition, gas phase loss of CH_3 is small compared to diffusion and surface reaction losses. Therefore, a 0-dimension approximation can be applied for the conservation equation of CH_3, i. e.

$$\frac{\partial n}{\partial t} = -2kn^2 - \frac{A}{V}\frac{v}{4}\frac{\beta}{1-\beta/2}n,$$

where A and V are the surface area and the volume of the discharge. Using this equation, the time evolution of β is deduced from that of the CH_3 density.

4. Results and Discussion

Figure 1 shows the time evolution of β deduced from the density decay of CH_3 with the CH_4 concentration as a parameter. In the post-discharge, the β values rapidly decrease, from initial values of 0.6-1% to about 0.2% in 7-10 ms. They further continued to decrease down to less than 10^{-5} (probably to 0) for $t > 0.2$ s. The initial β value increases with decreasing the CH_4 concentration.

Now we consider the surface reaction kinetics leading to the results in Fig. 1. Important species involved in the kinetics are ions, CH_3 radicals and H atoms. CH_n^+ (n=0-5) and $C_2H_n^+$ (n=0-6) ions creates the active

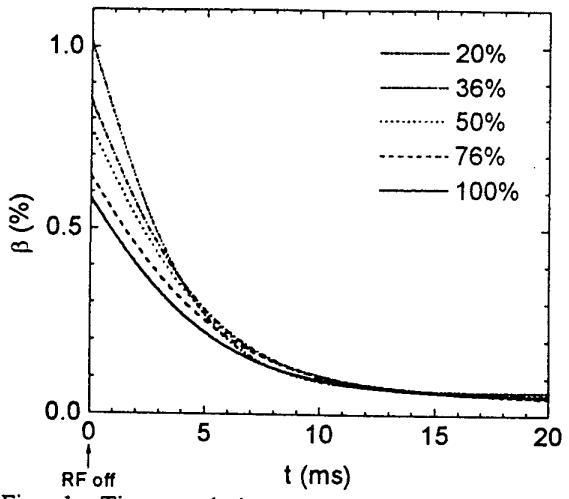

Fig. 1. Time evolution of the surface reaction probability β of CH_3 on a-C:H with CH_4 concentration as a parameter.

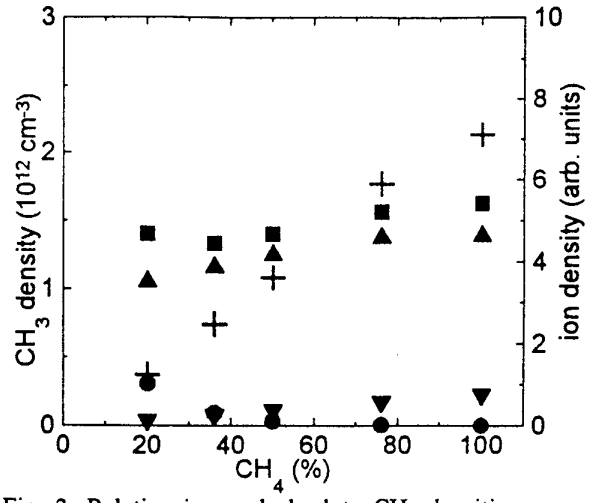

Fig. 2. Relative ion and absolute CH_3 densities as a function of CH_4 concentration. ■: total ion density, ●: H_n^+, ▲: CH_n^+, ▼: $C_2H_n^+$, +: CH_3.

chemisorption sites on the surface during the discharge, while H_n^+ (n=1-3) are less efficient, due to their light mass. CH_3 radicals are incorporated into the film at the activated sites. H atoms also are expected (1) to create the activated sites due to H abstraction reaction, (2) to react with CH_3 on the surface and desorbed as CH_4, and (3) to terminate the activated sites. The reactions (1) and (2) enhance the β value of CH_3, while the reaction (3) reduces it.

To get information about the production of the activated sites due to ions and the annihilation due to CH_3, relative ion densities and absolute CH_3 density were examined as functions of the CH_4 concentration. Results are shown in Fig. 2. The total ion density is nearly constant, the CH_n^+ density decreases by about 25% for CH_4 concentration from 100% to 20% and CH_n^+ ions remain the predominant ionic species. As the H_2 concentration increases from 0 to 80%, H_n^+ density increases by two orders of magnitude and $C_2H_n^+$ decreases by a factor 4. The sum of CH_n^+ and $C_2H_n^+$ densities increases slightly (by about 35%) with the CH_4 concentration. Then, the production rate of activates sites due to ions is considered to remain constant for all the gas mixtures. The CH_3 radical densities increase almost linearly from 3.8×10^{11} to 2.1×10^{12} cm^{-3} with the CH_4 concentration. If we neglect the surface reactions of H, β should be proportional to $[C_iH_n^+]/n$ (where $[C_iH_n^+]$ is the total density of CH_n^+ and $C_2H_n^+$). Then, from the ion densities shown in Fig. 2, we should obtain an increase of β, with decreasing CH_4 concentration, much faster than what is observed. Therefore, other species principally H atoms, the density of which increases with H_2 concentration, have to be taken into account to reduce the β value. This hypothesis is consistent with the fact that an estimated reaction rate for mechanism (3) is larger by more than two orders of magnitude than for (1) [8].

Measurement of H atom density is necessary for further discussion.

The time evolution of β, can be understood as follow. The ions mainly create activated sites on the surface during the discharge and then enhance the β value. After turning off the discharge, the activation becomes negligible in few ms due to the rapid decay of the ion density. Therefore, in the afterglow the sites are rapidly occupied initially by both H and CH_3 and then only by CH_3, since H is expected to be more reactive on the surface than CH_3 [8]. Thus the β value, for the low CH_4 concentration, decreases first rapidly due to the higher H density, and then more slowly due to the lower CH_3 density. In the far afterglow, the final value $\beta = 0$ agrees with the result of molecular dynamics simulations which give zero sticking probability on a diamond surface completely terminated with H [9].

References

[1] A. Pastol and Y. Catherine: J. Phys. D: Appl. Phys. **23** (1990) 799.
[2] S. Naito, N. Ito, T. Hattori and T. Goto: Jpn. J. Appl. Phys. **34** (1995) 302.
[3] P. Kae-Nune, J. Perrin, J. Guillon and J. Jolly: Jpn. J. Appl. Phys. **33** (1994) 4303.
[4] P. Kae-Nune, J. Perrin, J. Guillon and J. Jolly: Plasma Sources Sci. Technol. **4** (1995) 250.
[5] P. Kae-Nune, J. Perrin, J. Jolly and J. Guillon: Surf. Science, **360** (1996) L495.
[6] M. Shiratani, H. Videlot, J. Jolly and J. Perrin: Jpn. J. Appl. Phys. (to be published).
[7] D. L. Baulch, C. J. Cobos, R. A. Rox, G. Heyman, Th. Just, J. A. Kerr, T. Murrels, M. J. Philling, J. Troe, R. W. Walker and J. Warnatz: J. Phys. Chem. Ref. Data, **23** (1994) 847.
[8] S. J. Harris: Appl. Phys. Lett. **56** (1990) 2298.
[9] D. R. Alfonso and S. E. Ulloa: Phys. Rev. B, **48** (1993) 12235.

Doppler broadening of atomic lines in a low pressure radio frequency discharge of Ar-tetramethylsilane

J.M. Badie*, M. Andrieux, M. Ducarroir, C. Bisch

IMP-CNRS, BP5, F- 66120 Font Romeu cédex, France
IMP-CNRS, Université, Av de Villeneuve, F- 66860 Perpignan cédex, France

1. Introduction

Radio frequency glow discharges are commonly used in plasma assisted CVD processes in order to get growth of coatings at relatively low temperatures. The present study is part of a larger research program on the deposition of silicon carbide based films on steel substrates from Ar-H_2-$Si(CH_3)_4$ (tetramethylsilane: TMS) gaseous mixtures [1-3]. The input gas flows from downward to upward in a cold wall tubular vertical reactor. The discharge is created by an external coil which is connected to a radio frequency generator (2MHz). A fundamental goal was to investigate the process by optical emission to contribute to the understanding of the deposition process which leads to hard coatings of different compositions even in a narrow range of the deposition conditions.

2. Experimentals

The substrate on which deposition occurs was grounded through an embedded thermocouple and was located outside the coil. In such a device, the substrate temperature is essentially governed, for a given input power, by its distance to the coil and also by the convective exchanges with the plasma. The experiments were carried out at a steady state temperature of 850K. Nevertheless, whatever the total presure (300-3000 Pa) and the substrate coil distance (8-36 mm) are, the glow discharge aspect is identical. It is constituted by a very luminous sheath surrounding the substrate followed downward by a dark space and then by a weak luminous volume inside the coil.
Optical emission is sampled parallel to the discharge axis or perpendicularly by means of an optical fiber equipped with an afocal system. A high resolution spectrometer (focal length 1m, double pass) with a 1800 lines/mm grating and a slit entrance of 50μm was used. A CCD detector cooled with liquid nitrogen allows the analysis of the dispersed light. With such a device, the spectral lines emitted by a low pressure argon lamp exhibit linewidths (FWHM) of 0.011nm

3. Results

The profiles of the emission lines and their widths depend strongly on the nature of the emitting species.

- The Ar and Ar^+ lines are purely gaussian with FWHM values which correspond to the apparatus function. The result is independent of the way to sample the optical signal either perpendicular or parallel to the discharge axis.

- The molecular hydrogen (Fulcher system) behaves quite similarly: only a slight doppler broadening can be observed.

- The atomic hydrogen lines H_α, H_β, are significantly broadened. Their profiles are no longer ascribed to a Voigt function and they change with the distance to the substrate. For Ar-H_2 mixtures the line profiles are the convolution of two gaussian components centered on the same wavelength meanwhile they result of the combination of three gaussian components when TMS is added in the input gas. In all cases the energy of the narrow component (NC) is about 0.25 eV; the broad component (BC) reaches 24 eV close to the substrate. The third component called intermediate component (IC) which is characteristic of the TMS dissociation exhibits an energy value of 1 eV at the substrate interface.

- The Si^+ lines have a pure gaussian profile when sampled perpendicularly to the discharge axis. The measurement of their width leads to energies up to 40 eV. When the observations are parallel to the discharge axis these lines are splitted in two « components » shifted from their standard position in wavelength. But the Doppler shifts lead to identical energies.

4. Discussion

The excitation mechanisms responsible of the formation of low energy excited hydrogen atoms are known to result from electronic collisions with molecular hydrogen [4-8] . The energy of the third component could be explained in the same way by the dissociative excitation of radicals issued of the TMS molecules.
On the other hand, the only way to explain high energy atoms such as Si^+ and the broad component of H (BC) is to consider mechanisms in which the ions are accelerated in the electric field [7,9] of the sheath surrounding the substrate. The observed values for Si^+ are a direct proof of this kind of mechanism. As, even with our optical system of high resolution , Ar^+ does not appear to be accelerated one can deduce that the reduced electric field E/n is always lower than 800 Td. For such values it is impossible to observe the doppler broadening due to the drift velocity [10] which

can be calculated from the charge exchange cross section of Ar^+ in Ar [11].

For the Si^+ line profiles, when they come from observations perpendicular to the discharge axis, a good fit is obtained with one unshifted gaussian profile which denotes a distribution with a single temperature. The splitting of the lines observed in the direction parallel to the axis indicates that there is a flux of ions moving away from the substrate and a flux of ions moving towards the surface. The Si^+ energy does not depends on the way of sampling. Therefore, there is no directional velocity effects due to the applied electric field. In all cases the line intensities reflect the emission of all the excited silicon ions.

In same conditions, the drift velocities of H^+, H_2^+, H_3^+ in Ar [12] and also in H_2 [13] can be calculated. The analysis of these calculations in relation with the charge transfer cross sections lead us to conclude that the energy of hydrogen atoms result mainly from collisions of H^+ with H_2.

5. References

[1] M. Lelogeais , M. Ducarroir . Thin Solid Films, 197 (1991) 257-267

[2] J.M. Agullo, M. Ducarroir, F. Clemendot, A. Lina. IX Euro Conf on CVD,Tampere, Finland. Colloque C3 J de Physique Suppl n° 8 (1993) 163-170

[3] M. Andrieux, J.M. Badie, C. Bisch, M. Ducarroir, F. Teyssandier. X Euro Conf on CVD, Lido de Jesolo, Italia. Colloque C5 J de Physique II Suppl n°5 (1995) 607-614

[4] K. Ito, N. Oda,Y. Hatano,T. Tsuboi. J. Chem. Phys 17 (1976) 35-43

[5] S.Freund, J.A. Schiavone, D.F. Brader. J. Chem. Phys 64 (3) (1976) 1122-1127

[6] A. Capelli, R.A. Gottscho, T.A. Miller. Plasma Chem - Plasma Processes 5 51985) 317-331

[7] C. Barbeau, J. Jolly. J. Phys. D 23 (1990) 1168-1174

[8] S. Djurovic, J.R. Roberts. J. Appl. Phys 74 (11) (1993) 6558-6565

[9] G. Sultan, G. Baravian. J. High. Temp. Chem. Proc, 1, Coll Suppl n° 3 (1992) 525-532

[10] J.E. Lawler, Phys. Rev . A 32 (5) (1958) 2977-2980

[11] A.V Phelps. J. Phys. Chem. Ref. Data 20 n° 3 (1991) 557-573

[12] A.V Phelps. J. Phys. Chem. Ref. Data 21 n° 4 (1992) 883-897

[13] A.V Phelps. J. Phys. Chem. Ref. Data 19 n° 3 (1990) 653-675

The effect of hydrogen admixtures on the nitriding of AISI-316 stainless steel

Matthew Baldwin,† Sunil Kumar,† Matthew Fewell,† Syd Haydon,†
George Collins,‡ Ken Short‡ and John Tendys‡

†Department of Physics, University of New England, Armidale, N.S.W. 2351, Australia
‡Australian Nuclear Science and Technology Organisation, Private Bag 1, Menai, N.S.W. 2234, Australia

1. Introduction

In the past decade, plasma-nitriding has emerged as a viable commercial tool for increasing the load bearing capacity and surface hardness of steel through the incorporation of sub-surface nitrogen into the metal. In commercial nitriding, treatment is usually conducted in an abnormal glow discharge through a nitrogen-hydrogen mixture at elevated temperatures (~500° C). However, despite commercialisation of the plasma-nitriding procedure, the precise mechanism allowing the incorporation of nitrogen into the metal surface and the role played by hydrogen within the discharge remains unclear [1].

More recently, rf discharges in low-pressure nitrogen have been shown to be a convenient medium for plasma nitriding [2,3]. These plasmas are convenient since process parameters such as workpiece temperature and bias are independent of the plasma generation. Furthermore, these plasmas provide a technique for nitriding stainless steel at relatively low temperature, so avoiding the loss of corrosion resistance that generally occurs above 450° C [4,5] and distortion of the workpiece brought about by higher treatment temperatures. However, the reduction of treatment temperature, despite the advantages that it offers, results in nitrided layers that are in general thinner than those obtained with higher temperature treatments.

We report here improvements in the nitrided layer thickness of low-temperature nitrided AISI-316 stainless steel by the introduction of admixtures of hydrogen to the nitriding environment. We also discuss these effects in the light of fundamental studies concerning surface effects in pre-breakdown regimes involving hydrogen.

2. Experimental Techniques

Polished disks of AISI-316 stainless steel, 25 mm in diameter and 4 mm thick, were treated in the PI^3 nitriding facility at the Australian Nuclear Science and Technology Organisation [6]. These treatments were conducted with various admixtures of hydrogen to the nitriding regime, keeping the partial pressure of nitrogen within the gas mixture constant. Table I lists the process parameters used.

After treatment, the microhardness of the nitrided surfaces were examined using a Nano-instruments IIs micro-indenter [7]. The nitrided layer thickness was measured by examining a transverse section of the nitrided sample, etched in Marble's solution, with a JEOL JSM-5800LV scanning electron microscope. The optical emission from these plasmas was explored using a SPEX 270M spectrometer.

Pre-breakdown investigations were conducted separately using the techniques and equipment described by Ernest *et. al.* [8] and Haydon *et. al.* [9].

3. Results

Figure 1 displays the measured thickness of the layer formed during the nitriding process as a function of percentage hydrogen admixture. Addition of hydrogen to the discharge dramatically enhances the thickness of the formed layer: layer thicknesses were approximately double for admixtures of hydrogen in the

Table I. *Process parameters used in this work.*

sample temperature	400° ± 10° C
rf power	300 W
rf frequency	13.56 MHz
N_2 partial pressure	180 mPa
admixture H_2	0-75 %
sample bias	0 V dc (ground)
treatment time	3 hr

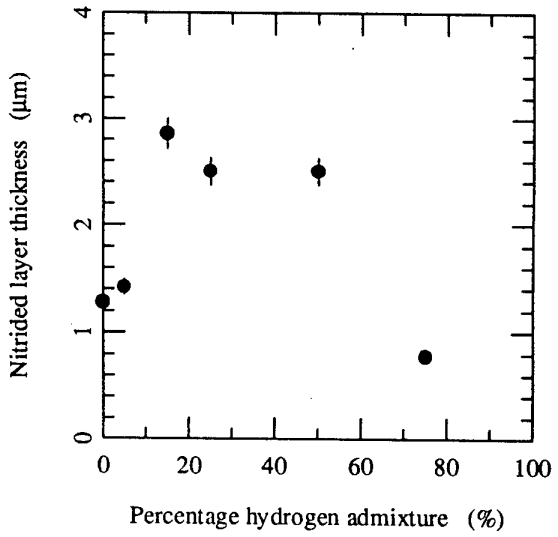

Figure 1. *Nitrided layer thickness as a function of hydrogen admixture.*

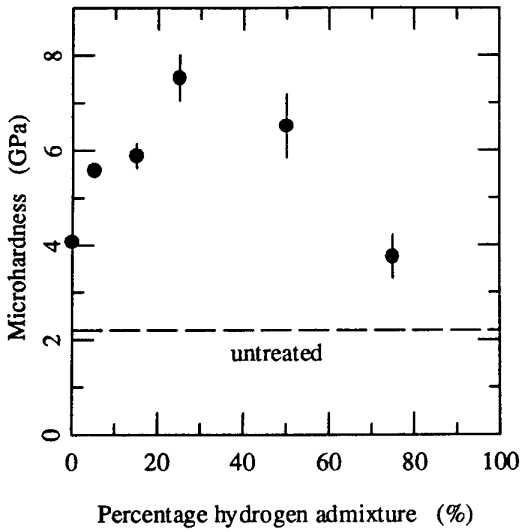

Figure 2. Microhardness as a function of hydrogen admixture. The indenter load was 50 mN.

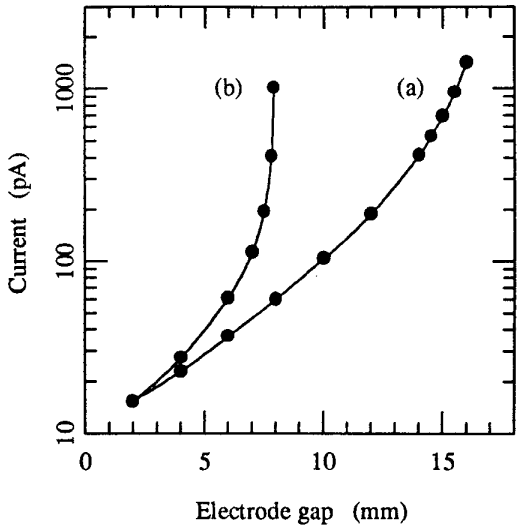

Figure 3. Spatial growth of current measurements in nitrogen using an AISI-316 stainless steel cathode, (a) after baking, (b) after hydrogen treatment.

range 15–50 %. A similar trend is observed in the microhardness of treated samples as a function of the hydrogen content, as shown in Figure 2. Increases in the microhardness of similar proportions are observed compared to the micrhardness of the sample treated in pure nitrogen alone.

We are currently exploring the spectral features of these plasmas using an optical spectrometer in order to establish the roles of both neutral excited species and ions in the plasma. Correlation of these spectral aspects of the plasma chemistry with the enhancements produced in the nitrided layer properties by hydrogen admixtures will be reported at the conference.

In complementary studies we examined the surface properties of AISI-316 stainless steel when used as a cathode in a pre-breakdown discharge. Measurements of the spatial growth of current under conditions of constant reduced electric field *E/N* provide a means for examining the condition of the cathodic surface.

Figure 3 displays two spatial growth of current measurements in nitrogen at a pressure of 5 Torr with *E/N* set to 283 Td. The first measurements (a) were made after extensive out-gassing of the vacuum system by baking at a temperature of 200° C. Following this, the second set of measurements (b) were recorded after further treatment of the cathode with a dc hydrogen glow. It is evident from the dramatic reduction in the critical breakdown distance that hydrogen bombardment of the cathode has enhanced the efficiency of the cathode to release new electrons into the pre-breakdown discharge. This more efficient response to the pre-breakdown discharge can be attributed to a greater interaction of the steel surface with the secondary mechanisms in the pre-breakdown nitrogen such as long-lived neutral excited states. Indeed, such species of nitrogen are well known to play an important role in nitriding [10]. Hence, surface effects of this nature may be related to the enhancements produced by hydrogen admixtures in nitriding.

Acknowledgments

This research is supported by the Australian Research Council, the Australian Institute of Nuclear Science and Engineering and by an Australian Post-graduate Research Award.

References

[1] H. Michel, T. Czerweic, M. Gantois, D. Ablitzer and A. Ricard: Surf. Coat. Technol **72** (1995) 103–111

[2] F. El-Hossary, F. Mohammed, A. Hendry, D.J. Fabian and Z. Szaszne-Csih: Surf. Eng. **4** (1988) 150–4.

[3] G.A. Collins, R. Hutchings, K.T. Short, J. Tendys, X. Li and M. Samandi: Surf. Coat. Technol. **74–5** (1995) 417–24.

[4] Z.L. Zhang and T. Bell: Surf. Eng. **1** (1985) 131–6.

[5] P. Gröning, S. Nowak and L. Schlapbach: Appl. Surf. Sci. **52** (1991) 333–7.

[6] G.A. Collins, R. Hutcchings, K.T. Short, J.Tendys and C.H. Van Der Valk: Surf. Coat Technol. **84** (1996) 537–43.

[7] R. Hutchings, K.T. Short, and J. Tendys: Surf. Coat. Technol **83** (1996) 243–9.

[8] A. Ernest, S.C. Haydon and M.T. Elford: Aust. J. Phys. **39** (1986) 479–96.

[9] S.C. Haydon, M.P. Fewell, A.D. Ernest and M.J. Baldwin: Chem. Phys. **206** (1996) 245–56.

[10] G.G. Tibbets: J. Appl. Phys **45** (1974) 5702–3.

Ions and Neutrals in the Ar-Tetraethoxysilane (TEOS) RF Discharge

R. Basner, R. Foest, M. Schmidt, F. Hempel*, K. Becker**
Institut für Niedertemperatur Plasmaphysik, Robert Blum Str. 8 - 10, 17489 Greifswald, Germany
*Institut für Physik der Ernst Moritz Arndt Universität Greifswald, Germany
**Dep. Physics, Stevens Institute of Technology, Hoboken, NJ, USA

1. Introduction

Capacitively coupled RF discharges are important in low pressure plasma processing for etching, thin film deposition techniques like plasma polymerization or for SiO_x deposition [1]. Silicon-organic compounds are proved precursors. Among them tetraethoxysilane (TEOS, $Si(OCH_2CH_3)_4$) is often used for plasma polymerization and with O_2 admixtures for SiO_x deposition [2]. An effective optimization of the process techniques demands an understanding of the plasma reactions and properties which can be investigated by plasma diagnostic like optical spectroscopy, Langmuir-probe measurements and mass spectrometry. With the mass spectrometry it is possible to investigate the neutral components as well as the ions in the plasma.
Mass spectrometric investigations of TEOS plasmas are known only for the neutral gas [2,3]. In this paper are presented results of the mass spectrometric measurements of the ions and neutral gas in a capacitively coupled Ar-TEOS RF discharge (13.56 MHz). These measurements are completed by mass spectrometric determination of the partial and total electron impact ionization cross sections for electron energies between threshold and 100 eV using a method described recently [4].

2. Experimental

The RF reactor (Fig.1) consists of a stainless steel vacuum chamber with two planar steel electrodes of 128 mm diameter and spacing of 40 mm. The upper electrode is capacitively coupled through a matching network to an RF generator (ACG-5, ENI) while bottom electrode and the chamber wall are grounded. The RF power transmitted to the matching network was measured by the VI Probe (ENI), it varies from 15 to 120 W. Moreover the sustaining RF voltage, the DC-self bias and the thickness of the dark space in front of the powered electrode were measured.
The vacuum system is evacuated by a turbomolecular and a rotary pump. The gas flow rates are regulated by the Multi Gas Controller 147 (MKS Baratron) with mass flow controller (MFC).
The plasma monitor (SXP 300H, VG Instruments) with ion transfer optics, electron impact ion source, cylindrical mirror analyzer (CMA) and quadrupole field enables the determination of neutral and ion composition of the plasma including the energy distribution of the ions hitting the wall (IED). The ion sampling orifice (d = 0.1 mm) is located at the chamber side wall equidistant to the electrode surfaces. The TEOS admixture was held at 2% to keep the deposition rate low, the Ar pressure was 5 Pa, the flow rate 5 sccm.

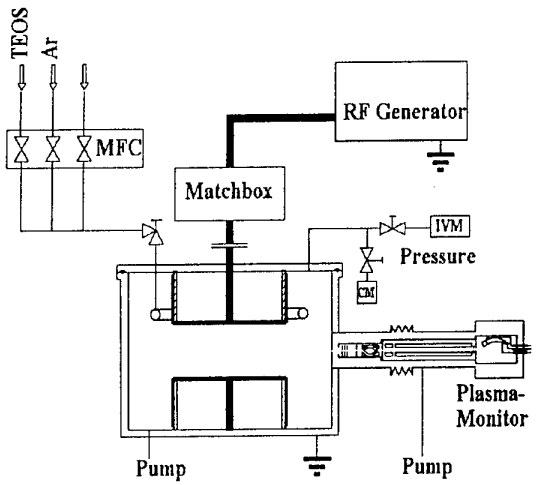

Fig. 1. Scheme of the reactor with plasma-monitor.

3. Results and Discussion

The electron impact ionization cross section measurement shows that the TEOS molecule decomposes into more than 40 fragment ions with intensities >1% of the base peak (m/z 193). The appearance energies and relative intensities of selected ions are presented in Table 1. The rate constants for electron impact ionization of TEOS for formation of these ions are calculated with the measured cross sections and a Maxwell distribution of the electrons (Fig. 2).

m/z	formula	rel. int.%	app.energy eV
208	$SiO_4C_8H_{20}$	26.1	7.2
193	$SiO_4C_7H_{17}$	100	8.4
179	$SiO_4C_6H_{15}$	24.5	8.2
149	$SiO_3C_5H_{13}$	80.5	11.4
119	$SiO_2C_4H_{11}$	31.4	15.2

Table 1. Mass number, sum formula, intensity in relation to the base peak, and appearance energy of the molecular and selected fragment ions of TEOS.

With the electrical data (input power 50 W, RF voltage 810 V_{PP}, DC self bias -360 V, thickness of dark space 0.9

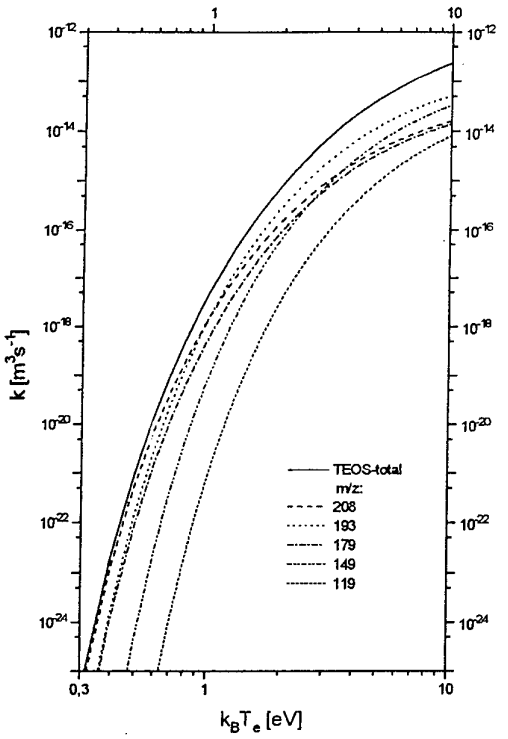

Fig. 2. Rate constants for electron impact ionization of TEOS in relation to electron temperature

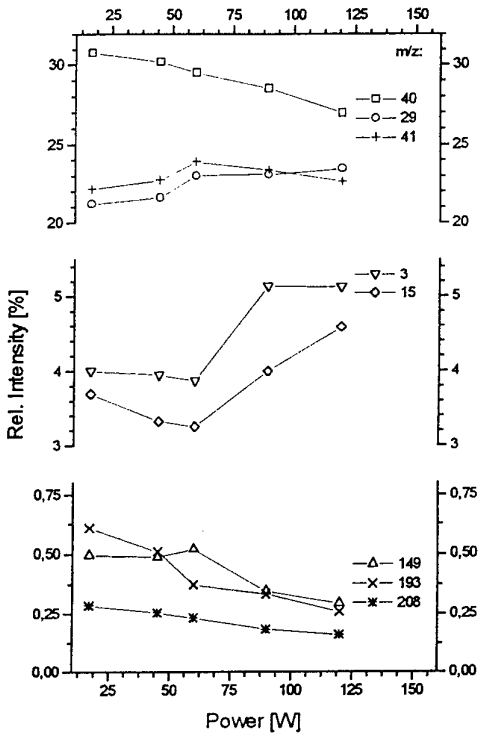

Fig. 3. Relative intensities (related to the total intensity) of selected ions of the Ar-TEOS RF discharge (5 Pa, 2% TEOS) over RF power received by integrating the IEDs over the energy range.

mm) an estimation of electron temperature (2.7 eV) and mean electron density ($7*10^{15}$ m^{-3}) was possible by a charge carrier balance assuming direct ionization of Ar and using Langmuir Child law [1], the sheath equation [5] andischarge model [6].

The main observation concerning the neutral gas is the strong decay of the TEOS concentration after the ignition of the discharge. In the neutral gas spectrum the base peak (m/z 193) was not detectable, whereas a plasma ion m/z 193 was measured. An estimation of the TEOS concentration assuming direct electron impact ionization only and using the rate constants for the TEOS ion production (Fig. 2) and for Ar ions [1] with an electron temperature of 2.7 eV results in a value of $N_{TEOS}/N_{Ar} = 2*10^{-4}$. The main neutral gas components besides Ar are H_2 ($3*10^{-2}$), CO ($2*10^{-1}$). Lower hydrocarbons are observed in the spectrum too, but with smaller intensities.
The ion current to the grounded reactor wall is determined (Fig.3) by the Ar^+, ArH^+, COH^+, $C_2H_2^+$, $C_2H_3^+$, H_3O^+, CH_3^+ and H_3^+ ions. Ions of the TEOS molecule are observed, but the intensities are two orders of magnitude smaller than the Ar^+ ion signal. The dependence of the relative intensities on the RF power is small, however with increasing power the relative intensity of the heavier TEOS ions is lowered whereas the portion of the smaller ions is slightly increasing. The comparison of the intensity of the TEOS ions with the results of ionization cross section measurements shows, that the intensity of the plasma ions with decreasing mass number is higher than the expected intensity after calculating the ion production rate with the rate coefficients (Fig. 2) for electron temperatures between 2 and 3 eV. This behaviour may be explained by secondary processes, including ion-molecule reactions and plasma induced decomposition of the plasma polymer films. ArH^+, COH^+, H_3O^+ and H_3^+ are also products of ion-molecule reactions preferably with the molecular hydrogen. The maximum kinetic energy of the ions hitting the grounded wall is nearly 30 eV. The shape of the IED shows the influence of collisions in the sheath.

This work is partially supported by the US National Science Foundation.

4. References

[1] M.A. Liebermann, A.J. Lichtenberg, Principles of Plasma Discharges and Materials Processing, John Wiley & Sons, New York, 1994
[2] F. Fracassi, R. d'Agostino, P.Favia, J.Electrochem. Soc. 139(9) (1992) 2636
[3] C. Charles, P. Garcia, B. Grolleau, G. Turban, J. Vac. Sci. Technol. A 10(4) (1992) 1407
[4] R. Basner, R. Foest, M. Schmidt, F. Sigeneger, P. Kurunczi, K. Becker, H. Deutsch, Mass Spectrom. Ion Proc.153 (1996) 65
[5] R.T. Bettinger, E.H. Walker Phys. Fluids 8 (1965)748
[6] K.Köhler, J.W.Coburn, D.E. Horne, E. Kay, J.H. Keller J.Appl. Phys. 57 (1985) 59

B ATOMS REACTION WITH OXYGEN IN Ar-BCl_3-(O_2) FLOWING MICROWAVE DISCHARGES

T. Czerwiec [a], J. F. Pierson [a], T. Belmonte [a], H. Michel [a], A. Ricard [b]

[a] *Laboratoire de Science et Génie des Surfaces (Unité de Recherche Associée au CNRS 1402), Institut National Polytechnique de Lorraine, Ecole des Mines de Nancy, parc de Saurupt, 54042 Nancy Cedex, France.*
[b] *CPAT , Université Paul Sabatier, 118, route de Narbonne, 31062 Toulouse Cedex, France.*

Introduction

Plasma borizing of stainless steels and titanium alloys has been achieved in mixtures of Ar-H_2-BCl_3 [1]. Also, Plasma Enhanced Chemical Vapour Deposition (PECVD), has been performed with BCl_3 and $TiCl_4$ gas mixtures to obtain TiB_2 thin films [2,3]. Plasma diagnostic had been reported by Optical Emission Spectroscopy (OES) in Ar-BCl_3 gas mixtures in a microwave flowing discharge for deposition of borides on metal surfaces, located downstream the plasma [4]. In this paper, particular attention is paid to the reaction of oxygen with boron species when O_2 is introduced into the reactor in discharge or in post-discharge conditions.

The experimental set-up

The experimental setup is reproduced in fig. 1. A microwave discharge (2.45 GHz) is produced in a quartz tube (inner diameter 5 mm) in Ar-BCl_3 gas mixtures at a standard gas pressure of 700 Pa (5 Torr) and a total flow rate of about 1 slm. Oxygen can be introduced either in the Ar-BCl_3 gas mixtures (process 1 in fig.1) or downstream the plasma to analyse the chemiluminescent reactions with B atoms (process 2 in fig.1). The radiative species have been analyzed by emission spectroscopy in the plasma and the post-discharge conditions by means of a movable optical fibre which is connected to a Jobin-Yvon HR 640 spectrometer (1200 grooves mm^{-1} grating) equipped either with a photomultiplier tube (PM) (Hamamatsu R636) or with an Intensified Photodiode Array Detector (IPAD) (IRY / 1024 G/B). A spectral resolution of 0.1 nm is obtained with slits of 100 µm width.

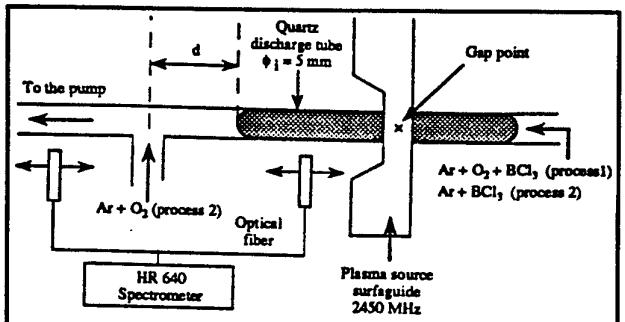

Figure 1 : Experimental set-up

Detection of radiative species in discharge and post-discharge conditions

The emission spectra between 320 and 500 nm of an Ar-0.4%O_2-1.5%BCl_3 plasma at 700 Pa, 1 slm, 140 Watts and 4.5 cm downstream the surfaguide gap are reproduced in figure 2 a. Spectral lines and bands from radiative states of Cl and BO are identified in this figure in addition to few argon lines. This emission spectrum is very different to those of an Ar-1.5%BCl_3 plasma produced in the same experimental conditions. As a matter of fact, the emission spectrum of such discharge with high dilution of BCl_3 in argon is very rich in atomic lines (Ar, Cl, B^+, Si) and molecular bands (BCl, B_2, BO) [4].

By introducing an Ar-10%O_2 (Q = 0.11 slm) gas mixture into the Ar-1.5% BCl_3 (Q = 1 slm) post-discharge at 10 cm from the gap (process 2 in fig. 1), three different situations can occur depending the distance d between the plasma end and the Ar-O_2 inlet. This distance d can be adjusted by varying the microwave power. The total pressure is always 700 Pa.

* **Case I** : for d > 5-6 cm, no emission is observed downstream the Ar-O_2 inlet.

* **Case II** : for d ≤ 5 cm, a blue light only composed of BO* band emission is observed downstream the Ar-O_2 inlet as shown in fig. 2b. Such BO ($A^2\Pi \rightarrow X^2\Sigma^+$) band emissions are the result of chemiluminescent reactions between the B atoms and O_2 as reported in references [5-8].

* **Case III** : for d ~ 0 cm (i.e. discharge beyond the Ar-O_2 inlet), a very intense green light is observed close to the Ar-O_2 inlet. The previously observed blue light is always present,as shown in fig. 2c, downstream the green light region . In addition, Cl* and Ar* are also detected in this case, and it must be noted that no O* emission lines are observed. The green light zone arises from BO_2 ($A\,^2\Pi_u \rightarrow X\,^2\Pi_g$) bands [9]. The (000-000) band of this BO_2 system (not shown in fig. 2c) is twelve time higher than that of the (100-000) band.

Excitation processes

Excitation processes leading to the formation of BO ($A\,^2\Pi$) and BO_2 ($A\,^2\Pi_u$) states will now be discussed by analysing the experimental results. Implications of B atoms reactions will also be considered.

For BO ($A\,^2\Pi$) production in case II (process 2 in fig. 1), the situation is rather clear since BO* is the only observed excited state. BO* emission results from the following reactions :

$$B + O_2 \rightarrow BO\,(A\,^2\Pi) + O \qquad (a)$$

with $k_a = 5.7\ 10^{-14}\ cm^3\ s^{-1}$ for BO ($A\,^2\Pi$, v' = 2) production[10]. The BO ($A\,^2\Pi$, v' = 2) state has a

radiative loss frequency $\nu_r = 7.3\ 10^5\ s^{-1}$ [11] and are quenched by Ar and O_2 :

$$BO\ (A\ ^2\Pi) + Ar \rightarrow \text{products} \quad (b)$$
$$BO\ (A\ ^2\Pi) + O_2 \rightarrow \text{products} \quad (c)$$

with $k_b = 1.3\ 10^{-12}\ cm^3\ s^{-1}$ [11] and $k_c = 2.1\ 10^{-11}\ cm^3\ s^{-1}$ [11]. The pseudo-stationary density of BO ($A\ ^2\Pi$, $v' = 2$) is then given by :

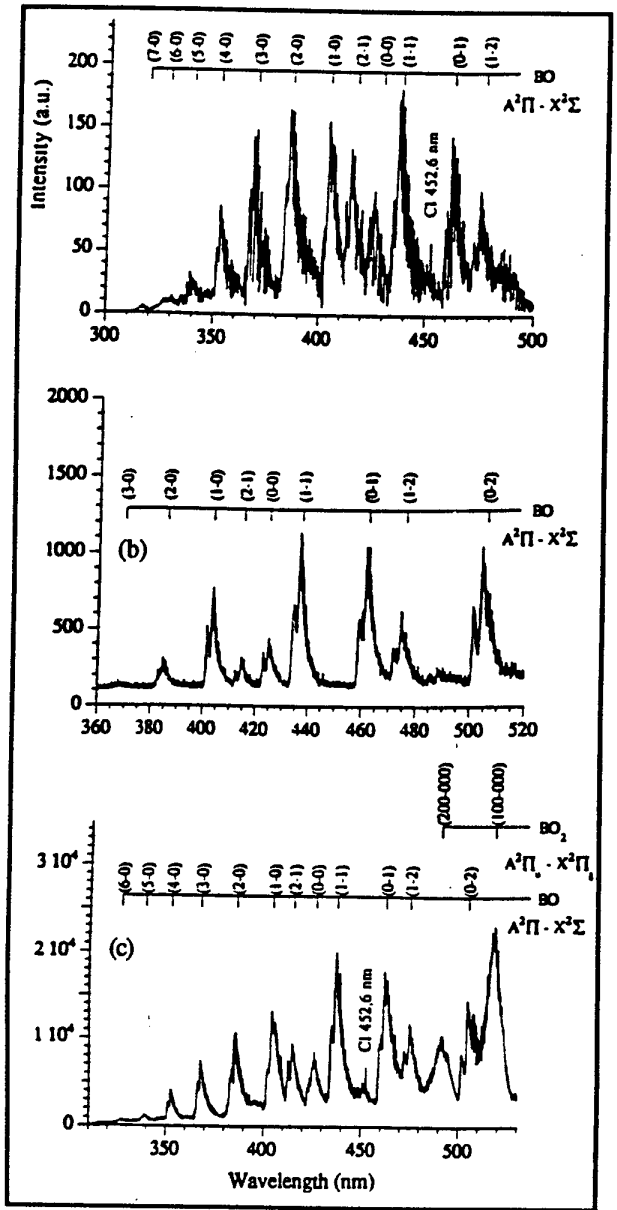

Figure 2 : Emission spectra of various Ar-BCl_3-O_2 plasmas at 700 Pa : a) Ar-0.4%O_2-1.5% BCl_3 at 140 Watts (process 1 in fig. 1), measured at 4. 5 cm from the gap. b) Ar-1.5% BCl_3 discharge at 70 Watts with an Ar-10%O_2 gas mixture introduced in post-discharge at 10 cm from the gap (process 2 in fig. 1). Measurements are performed at 13 cm from the gap. c) Same as (b) but at 100 W. Measurements are performed at 10 cm from the gap near Ar-O_2 inlet.

$$[BO\ (A\ ^2\Pi, v' = 2)] = 6\ 10^{-19}\ [B]\ [O_2] \quad (1)$$

where the densities are in cm^{-3}.

The BO ($A\ ^2\Pi$) production in case III (process 2 in fig. 1) is much more difficult to explain. Nevertheless, similarities can be found by comparing emission spectra of BO ($A\ ^2\Pi \rightarrow X\ ^2\Sigma$) emission in case III and the one from an Ar-O_2- BCl_3 plasma (fig. 2a). Moreover, as evidenced in fig. 2a, the upper vibrational levels of the $A\ ^2\Pi$ state are more highly populated (up to $v' = 7$) than those resulting from chemiluminescent reaction (a) ($v' \leq 3$). As a matter of fact, the exoergicity of reaction (a) with thermalized B atoms is only sufficient to populate the four vibrational levels in the $A\ ^2\Pi$ state [12]. Then, electronic excitation of BO ($X\ ^2\Sigma$) must be a key channel to produce BO ($A\ ^2\Pi$) in this case.

BO_2 ($A\ ^2\Pi_u$) production in case III would be produced by the two possible reactions :

$$BO\ (X\ ^2\Sigma) + O \rightarrow BO_2 \quad (d)$$
$$BO\ (X\ ^2\Sigma) + O_2 \rightarrow BO_2 + O \quad (e)$$

with $k_e = 4.4\ 10^{-12}\ cm^{-3}\ s^{-1}$ [13] and k_d being unknown. However, the exoergicity calculated for these two reactions [14] is to low to produce BO_2 in the $A\ ^2\Pi_u$ state. Then, these two possible reactions should be followed by electronic excitation of the produced BO_2 ($X\ ^2\Sigma$) to form BO_2 ($A\ ^2\Pi_u$).

REFERENCES

1) A. Raveh, A. Inspektor, U. Carmi and R. Avni, Thin Solid Films, 108 (1983) 39-45.
2) L. M. Williams, Appl. Phys. Lett., 46 (1985) 43.
3) H. Karner, J. Laimer, H. Stori and P. Rodhammer, Surf. Coat. Technol., 39/40 (1989) 293.
4) J. F. Pierson, T. Czerwiec, T. Belmonte, H. Michel, to be published in Surf. Coat. Technol.
5) S. E. Johnson, P. B. Scott, G. Watson, J. Chem. Phys. Lett., 60 (1978) 102.
6) A. Brzychcy, J. De Haven, A. .T. Prengel, P. Davidovits, Chem. Phys. Lett., 60 (1978) 102.
7) G. Green, J. L. Gole, Chem. Phys. Lett., 69 (1981) 1946.
8) T. G. Digiuseppe and P. Davidovits, J. Chem. Phys., 74 (1981) 3287.
9) J. W. C. Johns, Can. J. Phys., 39 (1961) 1738.
10) De Haven, M. T. O'Connor, P. Davidovits, J. Chem. Phys., 75 (1981) 1946.
11) J. J.Hinchen, J. Chem. Phys., 99 (1993) 4403.
12) A. W. Hanner, J. L. Gole, J. Chem. Phys., 73 (1980) 5025.
13) I. P. Llewellyn, A. Fontijn, M. A. A. Clyne, Chem. Phys. Lett., 84 (1981) 504.
14) M. W. Chase, C. A. Davies, J. R. Downey, D. J. Frurip, R. A. Mc Donald and A. N. Syverud, J. Phys. Chem. Ref. Data, Suppl. I, 14 (1985).

Nitrogen active species in a microwave flowing post-discharge reactor

S. Bockel (1)(2), D. Ablitzer (2), H. Michel (1) and A. Ricard (3)

(1) LSGS - Ecole des Mines de Nancy, Parc de Saurupt, 54 042 Nancy cedex
(2) LSG2M - Ecole des Mines de Nancy, Parc de Saurupt, 54 042 Nancy cedex
(3) CPAT - Université Paul Sabatier, 118 route de Narbonne, 31 062 Toulouse

1. Introduction :

A growing interest in the use of flowing N_2 post-discharge has recently appeared in the field of surface treatments processes. For steel surface nitriding, thick nitride layers (10 µm thickness) have been obtained in Ar-N_2-H_2 HF post-discharges [1] where a few H_2 (less than 1%) was introduced into the Ar-N_2 gas mixture in order to remove the Fe_3O_4 oxide layer which inhibits the nitriding reaction. In flowing N_2 post-discharges, the N atoms and the $N_2(X,V)$ vibrationally excited molecules are the dominant active species [2].
The N atom density can be measured by NO titration and the $N_2(X,V)$ vibrational distribution can be deduced from these of $N_2(C)$ and $N_2^+(B)$ [3]. In the present communication, the N atom density and the $N_2(X,V)$ characteristic temperatures are reported in a flowing nitriding post-discharge reactor of industrial scale (100 liters).

2 . The experimental setup :

The flowing post-discharge reactor is reproduced in Fig. 1.

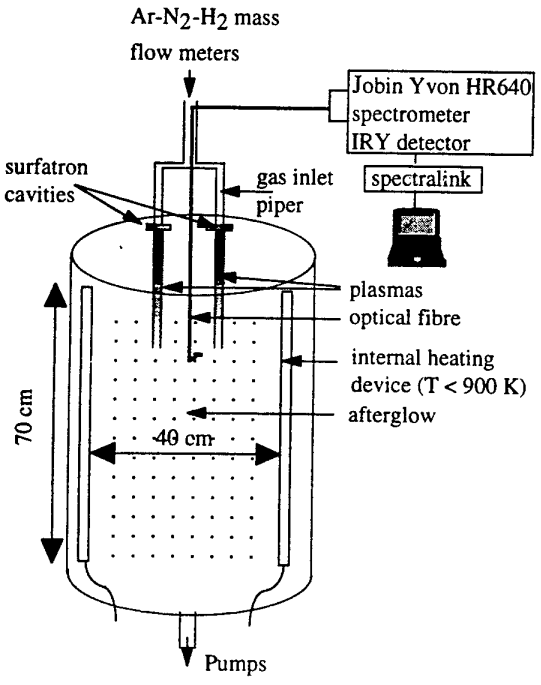

Fig. 1 : Post-discharge reactor

Two Ar-N_2-H_2 plasmas are created in a 0.6 cm diameter quartz tube with two surfatron cavities at a transmitted power of 100-500 Watts, a flow rate of 1 - 3 Slm^{-1} and a gas pressure of 10 - 25 hPa. The post-discharges run into a cylindrical reactor of diameter 40 cm and length 70 cm where the substrates can be introduced. The reactor chamber is heated by internal resistances up to 850 K to obtain the ε, γ' and α diffusion layers on the iron substrates.
The emission spectra of the discharge and of the afterglow are analysed by a Jobin-Yvon HR 640 spectrometer (grating 1200 grooves/mm) equipped with an OMA (IRY) detector which is connected to the discharge and post-discharge by means of a quartz optical fiber. The optical fiber can be located inside the reactor as reproduced in Fig. 1.

3 . Emission of radiative species and N atom titration :

3. 1 . Plasma radiative species :

In a previous study [4], it has been concluded that the best gas mixture to obtain maximum density of N and H atoms was 0,5 Ar - 0,5 (N_2-0,5%H_2). In these conditions, the radiative species in the microwave discharge came from Ar and H atoms, from N_2, N_2^+ molecules and NH radical. The $N_2(C\text{-}B)$ and $N_2^+(B\text{-}X)$ 2^{nd} positive and 1^{st} negative bands were easily detected. From the $\Delta V = -2$ vibrational sequence of the 2^{nd} positive, it has been found a Boltzmann distribution of the $N_2(C, v'=0\text{-}3)$ states with a vibrational temperature of $T_{v'}^{C} \cong 6000 \pm 500$ K in a N_2-0,5%H_2 discharge at 500 Pa, Q = 3 Slm^{-1} and a transmitted power of 500 W. By assuming a direct excitation of $N_2(C)$ from the $N_2(X)$ ground state, the θ_1 ground state characteristic temperature can be deduced by using the Franck-Condon factors which relate these two states [3]. It is then calculated that $\theta_1 \cong 6000$ K.
The N atom density has been determined at the outlet of one of the gas pipes inside the reactor (see Fig. 1). The obtained results are reported in table 1 for four experimental conditions.
The results reported in table 1 clearly show an increase of N atoms density with less than 1% H_2 into N_2 and a maximum value with about fifty-fifty Ar-N_2 gas mixture.

Experimental conditions	N atom density (10^{15} at. cm^{-3})
0,8 Ar - 0,2 N_2, 250 W, 2000 Pa, 1 Slm^{-1}	0.6
0,4 Ar - 0,6 (N_2-0,25%H_2) 250 W, 2000 Pa, 1 Slm^{-1}	1.1
N_2-0,25%H_2, 150 W, 1500 Pa, 1 Slm^{-1}	0.6
N_2-1%H_2, 150 W, 1500 Pa, 1 Slm^{-1}	0.45

Table 1 : N atom density as determined by NO titration with four experimental conditions. Gas temperature : 400K - Outlet of gas pipes : about 10^{-3}s after the discharge

3. 2 . Afterglow emission :

In previous studies, it has been reported that the N_2, 1st pos. intensity from the $N_2(B,V'=11)$ level in the afterglow is well related to the square of N atom density [4]. Also this afterglow emission is considered as a signature of N atoms in the post-discharge, giving the density of these active species after NO titration. If this relation was verified at low gas temperature (400 K) in the reactor, it was observed a sharp decrease of the N_2 1st pos. intensity as the gas temperature inside the post-discharge reactor was increasing up to 850 K. None 1st pos. emission was detected beetween 450 and 850 K. Inversely, a new light emission appeared after 650 K, which was identified as coming from Na and K atoms. Such effects have been previously observed [5,6] and was used as Na probe of the $N_2(X)$ vibrational temperature. The Na line emissions are coming from upper levels which are in resonance with vibrational levels of $N_2(X)$. In Table 2 are reported the three Na lines that we have clearly identified.

Na line (nm)	Optical transition	Upper level energy (eV)
589.2	3s1/2 - 3p3/2	2.11
569.0	3p3/2 - 4d5/2	4.29
498.4	3p3/2 - 5d5/2	4.59

Table 2 : Na line transitions and upper levels energies

A Boltzmann distribution of Na (4d to 8d) upper levels has been previously observed [5,6] as resulted from the following resonance transfer :

$N_2(X, V\geq 16) + Na \rightarrow N_2 + Na(n\geq 4d)$ (a)

The two Na 569 and 498.4 nm line intensities have been compared to determine the T_{Na*} temperature which is equal to the $\theta_{X,16\text{-}17}$ vibrational temperature.

In the following conditions : 0.8 Ar - 0.2 (N_2-0.5%H_2), 800 Pa, 3 Slm^{-1}, 200 W, it has been determined at 800 K the following intensity ratio $\frac{I(4d-3p)}{I(5d-3p)} = 6$ which is related to $T_{Na*} = \theta_{X,16\text{-}17} \cong 2500$ K. By using the Gordiets distribution [7], the θ_1 characteristic vibrational temperature (between the two first vibrational levels of T_X) is deduced : $\theta_1 \cong 2000$ K.

The decrease of the 1st pos. $N_2(B,11\text{-}A,7)$ when the gas temperature was increasing can be analysed by considering the following equation :

$$I_{N_2(11-7)} = K\ [N]^2\ \frac{k_{N+N}}{k_{Q,11}} \qquad (1)$$

where k_{N+N} ($cm^6\ s^{-1}$), $k_{Q,11}$ ($cm^3\ s^{-1}$) are the rates of N atom (density [N]) recombination and quenching respectively.

By assuming a constant value of the quenching cross section between 300-800 K, the k_Q quenching rate is varying as $T^{1/2}$. The k_{N+N} recombination rate is decreasing with T : $k_{N+N} = 4$ and $2.5\ 10^{-33}\ cm^6\ s^{-1}$ at 300 and 450K [8].

In the above discharge conditions, an increase of T from 300 to 450 K has produced a decrease of the $N_2(B,11\text{-}A,7)$ total intensity by a factor 3, giving a decrease of N atom density by a factor 1.2.

4 . Conclusion :

In flowing Ar-N_2-H_2 microwave discharge, it has been determined a characteristic vibrational temperature $\theta 1 = 6000$ K in discharge conditions (N_2-0,5%H_2, 500 W, 500Pa, 3 Slm^{-1}) and $\theta 1 = 2000$ K in the post-discharge (0,8 Ar - 0,2(N_2-0,5%H_2), 200 W, 800 Pa, 3 Slm^{-1}, T = 800 K).

The N atom density reached a maximum value at the discharge pipe exit of about 10^{15} cm^{-3} at 300 K, decreasing by a factor 1.2 at 450 K.

The decrease of $N_2(X, V)$ vibrational temperatures and of N atom density as T increased up to 850 K could come from several processes :

- $N_2(X, V)$ quenching by neutral gas,
- $N_2(X, V)$ and N destruction on the reactor walls,
- $N_2(X, V)$ destruction by impurities (Na, K) which are outgazing.

References :

[1] H. Malvos, H. Michel and A. Ricard : J. Phys D 27 (1994) 1328
[2] A. Ricard, G. Henrion, H. Michel and M. Gantois : Pure Appl. Chem. 60 (1988) 747
[3] J. Loureiro and A. Ricard : J. Phys. D 26 (1993) 163
[4] S. Bockel, J. Amorim, G. Baravian, A. Ricard and P. Stratil : Plasma Sources Sci. Tech. 5 (1996) 567
[5] E.L. Milne : J. Chem. Phys. 52 (1970) 5360
[6] L.D. Schearer : J. Chem. Phys. 84 (1986) 1408
[7] B.F. Gordiets, S.S. Mamedou and L.A. Shelepin : Sov. Phys. JETP 40 (1975) 640
[8] A. Ricard, J. Deschamps, J.L. Godart, L. Falk and H. Michel : Materials Sc. and Eng. A139 (1991) 9

CF_x radical surface production and loss mechanisms in fluorocarbon RIE plasmas

Jean-Paul Booth, Gilles Cunge, Pascal Chabert, François Neuilly, Walter Schwarzenbach, Jacques Derouard and Nader Sadeghi

Laboratoire de Spectrométrie Physique, Université Joseph Fourier-Grenoble, BP 87, 38402 St Martin d'Hères, France

Absolute CF and CF_2 radical concentration profiles have been determined in a CF_4 RIE plasma with Al, SiO_2 and Si substrates on the powered electrode, using laser induced fluorescence and absolute calibration techniques. The results show that net *production* of these species occurs at the substrate surface under many conditions, an effect which is particularly marked with Si. Time resolved experiments in pulsed plasmas show that the phenomenon is linked to energetic ion bombardment. Absolute produced radical fluxes are compared to incident ion fluxes to distinguish between different potential mechanisms. Mass analysis of the positive ions shows the presence of heavier ions in fluorine poor conditions, suggesting that gas phase polymerisation takes place. The implications of these results for the polymer formation mechanism will be discussed.

1. Introduction

Selective etching of SiO_2 over Si in fluorocarbon plasmas depends on the formation of polymer layers. The exact mechanism by which this polymer is formed is still poorly understood, but the deposition rate is well correlated with high concentrations of CF_x radicals. Previous work in this laboratory, using laser induced fluorescence (LIF) to detect CF and CF_2 radicals with high spatial resolution, has shown that, contrary to expectations, the *net* flux of these species is often *away* from the substrate surface at the RF electrode, especially with an Si substrate [1]. Thus these species are produced predominantly at this surface, rather than by gas phase fragmentation of the parent gas. In this study we have now put the concentration profiles (and thus the net fluxes) on an absolute scale, and compared them with the incident ion flux.

2. Experimental

The experiments were carried out in a modified 30cm diameter Nextral RIE reactor with a thermostated 10cm diameter powered electrode surrounded by a co-planar grounded guard ring and separated by 3.3cm from the grounded counter-electrode. The plasma was sustained by 13.56MHz power, which could be modulated on and off in 5μs, applied though an L-type matching network. Si and SiO_2-coated substrates placed on the aluminium RF electrode were kept in good thermal contact by a layer of silicone vacuum grease.

Relative radical concentration profiles were determined by the laser induced fluorescence technique combined with translation of the reactor relative to the optics [2]. The CF_2 profiles were put on an absolute scale by a UV absorption technique using a broad-band Xe lamp source [3], whereas the CF LIF signal was compared with that from a known concentration of NO gas, using a new method to allow for optical saturation effects [4]. The ion flux to the counter-electrode was measured using a novel Langmuir probe technique that is tolerant of insulating deposits [5].

3. Results and Discussion

Typical steady-state concentration profiles in a 50mTorr CF_4 plasma are shown in Figs 1 and 2. The CF radical was produced at the RF electrode and lost at the counter-electrode for all substrates studied, with net sticking coefficient, α, of about 0.2. The almost linear nature of the profiles indicates that little reaction occurs in the gas phase at this pressure.

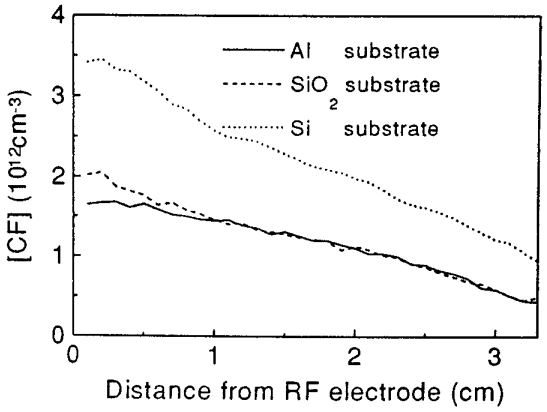

Fig. 1. CF concentration profiles in a 100W 50 mTorr CF_4 plasma with different substrates on the RF electrode.

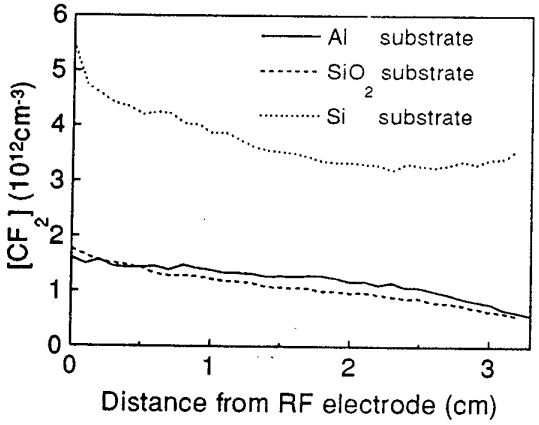

Fig. 2. CF_2 concentration profiles in a 100W 50 mTorr CF_4 plasma with different substrates.

The CF_2 results are rather more complex: small production occurs at Al and SiO_2 substrates, with loss occurring at the counter-electrode ($\alpha \approx 0.15$). The profiles are slightly convex, indicating some net gas-phase production. With a Si substrate the CF_2 concentration is much higher, and small net production occurs even at the counter-electrode. A similar phenomenon was observed when C_2F_6 gas was used (even without Si), strongly suggesting that it is linked to low [F] conditions.

The net flux of radicals produced at the substrate can be calculated, using Fick's law, from the concentration gradient and the diffusion coefficients in CF_4: $90cm^2s^{-1}$Torr for CF (estimated from the values for NO and CF_4, after allowing for the difference in reduced mass [6]) and $65cm^2s^{-1}$Torr for CF_2 [7]. The fluxes are summarised in Table I.

Table I. Neutral fluxes leaving the substrate, and incident ion fluxes (measured at the counter-electrode) in a 50mTorr CF_4 100W plasma. Units of $10^{15}cm^{-2}s^{-1}$

Substrate	CF	CF_2	Ion flux
Al	0.5	0.2	2.2
SiO_2	1.0	0.8	0.9
Si	2.2	1.5	0.9

The ion fluxes to the sidewalls were an order of magnitude smaller, indicating a strong radial gradient in the plasma density. Further information is obtained from concentration profiles taken after plasma extinction. The Al substrate becomes a net sink for both species as soon as ion bombardment has stopped. The SiO_2 substrate continues to produce both for several milliseconds, whereas Si produces CF_2 and consumes CF.

In experiments at the higher pressure of 200mTorr, strong production of both radicals occurs at all substrates, but gas-phase reactions become important, leading to concave profiles.

Several mechanisms can be proposed to explain the observed radical production. Energetic ion bombardment is a necessary component, as the phenomenon only occurs at the powered electrode (except for the CF_2/Si case). Neutralisation, reflection and dissociation of the CF_x^+ ion flux is one possibility. However, the neutral flux exceeds the ion flux when Si and SiO_2 substrates are present, so this cannot account for the whole flux unless either i) the ion flux to the powered electrode is significantly greater than that measured at the counter electrode, or ii) there is more than one carbon atom per incident ion. Another mechanism is sputtering of fluorocarbon polymer film present on the substrate. In this case we must account for the flux of carbon-containing material to the surface to form this polymer: it is not formed from CF_x radicals (which have a net flux away from the surface) or from ions (whose flux is too low). We propose that gas phase radical recombination reactions, e.g.

$$CF_3 + CF_2 + M \rightarrow C_2F_5 + M \quad (1)$$

$$CF_3(CF_2)_n + CF_2 + M \rightarrow CF_3(CF_2)_{n+1} + M \quad (2)$$

lead to the formation of heavier molecules, and that these are the polymer precursors. Under atomic fluorine poor conditions (with Si or SiO_2 substrates or with C_2F_6 gas) the CF_2 recombination rate with gaseous F and at the walls becomes small, the $[CF_2]$ rises and these otherwise slow reactions become significant.

References

[1] J.P.Booth, G.Cunge, P.Chabert, N.Sadeghi and J.Derouard: Abstracts of the IUVSTA International Workshop on Plasma Sources and Surface Interactions in Materials Processing, September 20-22 1995, Fuji-Yoshida, Japan.

[2] J.P.Booth, G.Hancock, N.D.Perry and M.J.Toogood: J. Appl. Phys: **66**, (1989), 5251.

[3] J.A.O'Neill and J.Singh: J. Appl. Phys. **77**, (1995) 497.

[4] G.Cunge, J.P.Booth and J.Derouard: Chem. Phys. Lett. (accepted, 1996).

[5] N.St J.Braithwaite, J.P.Booth and G.Cunge: Plasma Sources, Sci. Technol. **5**, (1996), 677

[6] A.Boushehri, J.Bzowski, J.Kestin and E.A.Mason: J. Phys. Chem. Ref. Data: **16**, (1987), 445.

[7] T.Arai, M.Goto, Y.Asoh, D.Takayama and T.Shimizu: Jpn. J. Appl. Phys. **32**, (1993), 1470.

NANOCRYSTALLINE THIN FILMS ELABORATION USING Ar-SiH4 LOW PRESSURE PULSED RF DISCHARGES

L. Boufendi, A. Hadjadj, S. Huet,
GREMI, UFR Sciences, Université d'Orléans; BP 6759, F-45067 Orléans cedex 2, France.
e-mail : boufendi@univ-orleans.fr

and P. Roca i Cabarrocas
L.P.I.C.M. Ecole Polytechnique, 91128 Palaiseau cedex, France.

1. INTRODUCTION

In our previous work on particle nucleation and growth, we identified four phases: i) molecular phase leading to the formation of 2 nm mean size crystallites, ii) crystallites formation and accumulation up to a critical concentration, iii) coalescence of the crystallites to form more and more big particles, iv) particle growth by molecular sticking on there surface [1].

Focusing our interest on the first phase of this phenomena, we showed that the coalescence of the crystallites starts, at room temperature, at about 150 ms after the ignition of the discharge. We showed also that the occurrence of the crystallites can be delayed just by varying the gas temperature. For example, at 100°C, these crystallites appear at about 1 s after the ignition. Therefore, if we switch on the discharge for a laps of time leading to the formation of the crystallites and to avoid the beginning of the coalescence phenomena, we can elaborate nanocrystalline or, for high temperature, amorphous thin films.

2. EXPERIMENTAL DETAILS

We used a 13.56 MHz rf discharge reactor with a cylindrical grounded stainless steel box of 130 mm in diameter. A grid of 20% transparency at its bottom allows a laminar gas flow [2]. The gas mixture was 1.2 sccm of silane and 30 sccm of Ar which results on a total pressure of 110 mTorr. The growth films was deposited by pulsed discharge with various T_{on} of the discharge on 7059 Corning glass. Several techniques have been used to investigate the structure of the films (Micro-Raman scattering, UV-visible ellipsometry, infrared transmission, X ray diffraction and XPS). In this paper we shall mostly present the results obtained by Micro-Raman scattering and spectroscopic ellipsometry characterization.

3. RESULTS AND DISCUSSION

3.1. Micro-Raman characterization

In order to avoid any laser modification of the film structure by the Ar-laser beam source, we fixed the laser power on the sample surface at a very low level of 0.03 mW. The spot size on the film is about 1 μm^2. The measurements were performed on films prepared at different gas temperatures. At room temperature (Fig. 1) the spectrum reveals two contributions: a crystalline one (I_c) and an amorphous one (I_a).

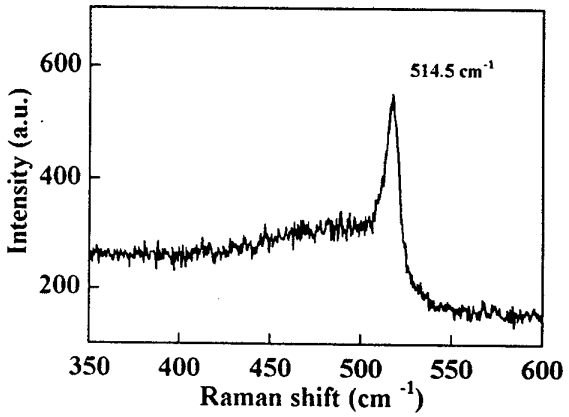

Fig. 1: Micro-Raman spectrum of a film deposited at room temperature. The spectrum reveals two contributions : a crystalline one (I_c) and an amorphous one (I_a).

The volume fraction (X_c) of the crystallites (d) from the relative magnitude of these two contributions:

$$X_c = \frac{I_c}{I_a + I_c} \qquad (1)$$

The shift $\Delta\omega$ of the crystalline peak with respect to its position of for a bulk crystalline silicon leads to the size (d) of the crystallites in the film:

$$d = 2\pi\sqrt{\frac{B}{\Delta\omega}} \qquad (2)$$

where B = 2.0 cm^{-1} nm^2. The results are summarized in Table 1.

These results are in good agreement with those obtained by grazing incidence X ray diffraction. For T = 100°C, the film is completely amorphous.

T (°C)	X_C (%)	d (nm)
0	50	5.6
25	46	3.6
50	20	2.9
100	0	-

Table 1: Volume fraction (X_C) and size (d) of the crystallites in the film, deduced from Raman measurements, as a function of the gas temperature.

3.2. Laser crystallization

In order to confirm the role of the crystallites as seeds in the crystallization of the film, we studied the crystallization of the produced thin films with different T_{on} (different crystallites size), under laser irradiation. We used an XeCl excimer laser (λ = 308 nm, pulse duration 40 ns). The laser beam was focused on a 2 cm^2 area of the sample surface. In these conditions the maximum laser fluence obtained is 190 mJ/cm^2. The laser fluence was progressively increased from mJ/cm^2 and the crystallization was controlled by UV-visible ellipsometry.

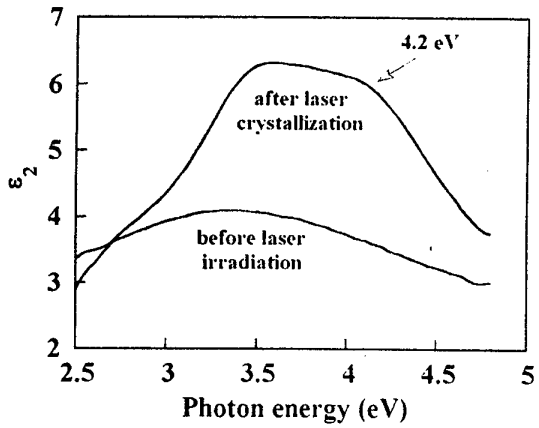

Fig. 2: ε_2 spectra of a film deposited with T_{on} = 100 ms before and after laser crystallization. Note the broad shoulder at about 4.2 eV which occurs after crystallization.

First, when the laser fluence increases the ε_2 of the film increases gradually, indicating a densification of the material. When the threshold of crystallization (E_{cryst}) is reached, a drastic change in ε_2 spectrum occurs with a broad shoulder at about 4.2 eV [3]. This behavior is a characteristics of microcrystalline material where a crystalline phase is embedded in an amorphous matrix. Preliminary quantitative exploitation of these results indicates that the laser crystallization concerns 200 to 300 nm of the film thickness. More quantitative information, such as the optical gap and the morphology of the material, can be extracted from ellipsometric measurements and will be discussed in another paper. For example the volume fraction of the crystalline phase can be deduced from the ellipsometric measurements according to the effective medium theory which allows the dielectric response of a heterogeneous material to be described from the dielectric functions of its constituents [4].

In Fig. 2 are represented the ε_2 spectra of a film corresponding to T_{on} = 100 ms before and after laser crystallization.

The results summarized in Table 2 allow the following remarks: i) The values of the threshold energy of crystallization which are low than the one of the standart hydrogenated amorphous silicon (a-Si:H) which is near 145 mJ/cm^2 [4]. ii). The threshold energy of crystallization decreases when T_{on} increases.

T_{on} (ms)	E_{cryst} (mJ/cm^2)
100	103
200	103
400	78
1000	51
CW	125

Table 2: Threshold energy of crystallization (E_{cryst}) as a function of the T_{on} of the plasma deposition of the film. CW corresponds to a film deposited under continuous plasma. As a comparison, the threshold energy for a standard a-Si:H is 145 mJ/cm^2.

4. CONCLUSION

In this contribution we reported some results on a method based on low pressure RF discharge for the elaboration of new materials showing optoelectronic properties different from those of a-Si:H. They consist in an amorphous matrix encrusted with nanocrystallites which can play the role of seeds for the crystallization of such thin films.

Films obtained with H_2 and silane mixture are under investigation. Preleminary results show that these films show completely different optical, electrical and mechanical properties. They present a higher ε_2 and higher dark conductivity and photoconductivity and seems to be promising as photovoltaic materials.

REFERENCES

1. L. Boufendi, J. Hermann, A. Bouchoule, B. Dubreuil, E. Stoffels, W.W. Stoffels and M.L. Giorgi, J. Appl. Phys. 76 (1994) 148.
2. A. Bouchoule, A. Plain, L. Boufendi, J. Ph. Blondeau and C. Laure, J. Appl. Phys. 70 (1991) 1991.
3. N. Layadi, P. Roca i Cabarrocas, V. Yakovlev and B. Drévillon, Thin Solid Films 233 (1993) 281.
4. D.E. Aspnes Thin Solid Films 89 (1982) 249.

Super-pure plasma chemistry in non-equilibrium plasma processes

G. M. Chumak
Russian Scientific Center "Applied Chemistry"
St.Petersburg, Russia, 197198

An increasing interest both theoretical and experimental is currently devoted to the study of reactive plasmas in mixture continuing N_2 molecules, and in particular to the study of N_2-H_2, N_2-O_2, N_2-F_2 discharges. Special attention is given to the coupling between the electron and vibrational kinetics of $N_2(X,v)$ and $F_2(X,v')$ molecules due to the important role played by the e-V superelastic collision, as well as to the coupling between both vibrational kinetics.

In nitrogen discharge, the electron energy distribution function (EEDF) is strongly coupled to the vibrational distribution of the ground state. The evolution of this vibrational distribution shows of the EEDF evolution also slow. This evolution occurs during the starting of the discharge and during the post-discharge. The electronic rate coefficients for population of excited state are also dependent on the EEDF[1].

The results show a large deactivation on vibrational levels belonging to the plateau of nitrogen vibrational distribution with strong consequences on the dissociation and ionization rate of nitrogen plasmas.

The problem of absolute negative conductivity (ANC) of low temperature plasmas have being recently published[2]. The sign of the total conductivity depends on the concentration of negative and positive ions and their mobility. Estimates show, that the time interval exists in which the total conductivity will be negative from E/N = 0 to some critical E/N.

The experimental setup used for the present study is in two devices. The first investigation were carried out with a UV-preonized self-sustained discharge camera with length of active medium was 63 cm, the distence between electrodes was 2.2 cm, ratio of buffer volume and active volume was 10^3. The materials of this camera were selected in consideration of their stability in galogen medium for minimization of fluorine concentration decrease, and also in consideration of their chemical purity for impurities concentration reduction in camera, which were formed as a result of chemidesorption and UV stimulation desorbtion from the surface. In turned out possible for a number of materials to improve the surface properties by employment of fluoro-polimer coating. Discharge voltage was of 23 kV, current of 13 kA, pulse recurrence frequency of 10-20 Hz, pulse duration of 200 ns [3]. The main part of measurements was carried out for gas mixture of He/ N_2/ F_2 (1400/ 100/ 20 torr).

The second investigation were carried out with electrodeless induction glow plasma canal in toroidal insulation sections st. steel camera diameter of 7 cm, and length of 200 cm transformator plasmotrone[4], turn voltage of 200 V, total current in plasma of 200 A, gas temperature of 500 K, electrons temperature of 20 000 K, electrons concentration 1014 cm^{-3}, E/N=2 10^{-17} Vcm^2, temperature characteristics of cooling water in reactor (plasmotron chamber) jacket: at the inlet 10^oC, at the outlet 35^oC.

Experiment have been performed in the pressure range between 5 and 20 mbar with admixture of F_2 going partial pressure of 1 and 5 mbar for F_2.

Experimental confirm that F_2 full converted only into NF_3. The reaction products were detected by gaschromatography as well as by absorption spectroscopy. Experimental results is an chemical quasi-equilibrium in reactive non isothermical plasma. Chemical quasi-equilibria describe stationary states of a reactive plasmas which can be reacted from both sides of a reversible gross reaction and which are independent (sometimes only in restricted region) on the operation parameters of the reactor (e.g. the power input). The formation of such quasi-equilibria is experimental secured[5].

This device may be work out the process NF_3 producing from the N_2-F_2 under the atmosphere pressure of gas plasma chamber. It was developed the project of commercial plant with the follows characteristics: NF_3 capacity 1 000 ton per year with energy consumption per 1 ton of NF_3 4000 kWt hour.

Numerical modeling of the chemical reaction system has been done, using the LASKIN computer code[6].

Plasmochemical method annihilation and processing of different toxic substances, e.g. industrial waste of fluoroorganic products manufacture used engine and transformer oil, containing large spectrum of various

impurities, has been developed. Further processing consist in separation of non-toxic substances from toxic gases formed and in neutralization of last ones.

Reference

[1] Ed. M. Capitelli "Non-Equilibrium vibrational kinrtics", "Topic in Curent Physics", Vol.32, 1986, Springer Verlag
[2] N.A. Dyatko, I.V. Kochetov, A.P. Naportovich, ESCAMPIG, 1992, St. Petersburg, p.129-130
[3] G.M.Chumak, V.V.Nazarov, M.M.Smirnova, SPIE Vol.1835 pp.2034.
[4] V.A.Kogan, I.M.Ulanov, Sov.Thertophysics Heigh Temperature, Vol.31, # 1, 1993 pp. 105-110
[5] A. Rutscher and H.-E. Wagner, ESCAMPIG, 1992,St. Petersburg, p.32-35. W. Lucke, F. Niethke, A.Ruscher, H.-E.Wagner, ESCAMPIG, 1992 St.Petersburg, p. 439-440
[6] G.M.Chumak, V.V.Rizhov, A.A. Sapozhnikov, I.Yu.Turchanovskiy XI Symposium Heigh Current Electronics, 1992, Russia, p. 103

Physico-chemical and electrical properties of PECVD a-SiN_xH_y films

G.Dupont and B.Despax
LGET Université Paul Sabatier, 118 route de Narbonne, 31062 Toulouse Cédex France

I-Introduction

Plasma-enhanced chemical vapour deposition techniques (PECVD) are particularly attractive in microelectronics, as they permit material deposition at a relatively low temperature. They also provide the possibility of achieving an in-situ plasma cleaning of the semiconductor surface, before the insulator layer deposition.

Silicon nitride films prepared by PECVD have come to be widely used in III-V semiconductor device technology. They can be applied as an interlayer insulation, as the final passivation film in integrated circuits, and as a charge-storage layer of metal-nitride-oxide-semiconductor (MNOS) memory devices. Nowadays, silicon nitride is used as a gate dielectric for amorphous silicon (a-Si:H) thin film transistors (TFTs) [1], because it can offer low defect density when deposited under certain operating conditions.

II-Experiments

SiN_xH_y films were deposited by PECVD, at 300°C, using a gas mixture of ammoniac and silane, for different values of gas ratio R (ammoniac/silane) under variable radiofrequency (rf) power. Thereby the film composition could vary widely.

When rf power and gas ratio R values are quite low, silicon nitride films are silicon-rich. On the contrary, when synthesized under higher values of R and power, films are rather nitrogen-rich, in particular with no detectable Si-H bonds. These experimental results have incidentally been confirmed by modelling works of rf plasma SiN_xH_y deposition [2]. They have indeed shown that, under low silane percentage and high power, silane dissociation products react with NH_2, NH and H radicals, leading to the formation of aminosilane active species, and finally to a nitrogen-rich film. On the other hand, under higher silane percentage and lower power, silane dissociation products become dominant, leading to the formation of disilane (Si_2H_6), and finally to a silicon-rich film.

The effects of plasma deposition conditions on physico-chemical and electrical properties of SiN_xH_y films have been reported.

III-Results and discussion

III-1-UV/VIS spectroscopy

The Tauc optical bandgap, Eg, was graphically obtained for films deposited with R varying from 16.7 to 50 and at two different power densities. The variations of Eg with R and power density are illustrated in figure 1.

It appears that the optical bandgap increases with R and power density, until reaching a value close to the one obtained in case of stoichiometric CVD silicon nitride films. According to Robertson [3], the bandgap of silicon-rich films is controlled by Si-Si and Si-H bonds, whereas that of nitrogen-rich films is controlled by Si-N and N-H bonds.

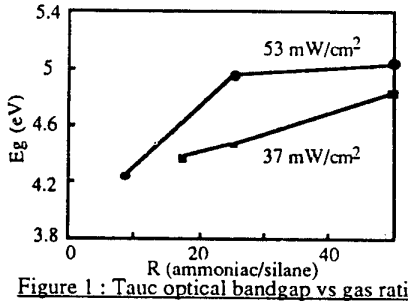

Figure 1 : Tauc optical bandgap vs gas ratio R

The bandgap broadening, with the increase of N amount, should thus result from the progressive replacement of Si-Si bonding and antibonding states by N atoms pπ states and Si-N and N-H antibonding states respectively (the latter being further away from the midgap than the former).

Furthermore, these results agree with X-ray photoelectron spectroscopy (XPS) analyses, which have confirmed the existence of Si 3p-Si 3p states in silicon-rich films. These states do not appear in nitrogen-rich films, and are replaced by new states identified as N $2p_z$ states.

III-2-Infrared spectroscopy

Infrared spectroscopy analyses have provided some accurate informations about different bonds present in SiN_xH_y films and about their surroundings.

In order to remove the ambiguity previously reported in literature [4] about the absorption peak at 840 cm^{-1}, direct transmission and reflection measurements have been carried out on SiN_xH_y films deposited onto intrinsic silicon substrate. Corresponding infrared spectra are reported in figure 2.

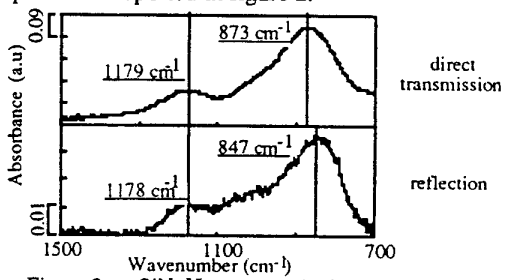

Figure 2 : a-SiNxHy spectra obtained by direct transmission and by reflection

On the spectrum of the film analysed by reflection, a wide abnormal reflection peak appears at 840 cm^{-1}, instead of the absorption peak expected and present in the other spectrum. This peak might be due to a strong reflectivity of the incident light at the interface air/silicon nitride (Reststrahlen Effect). Therefore, in case of direct transmission analysis, the peak generally observed could be mainly constituted by an abnormal reflection peak. In order to avoid a false interpretation of the peak amplitude, it is then suggested

to analyse films under specular reflection (with films deposited onto metallized substrate).

In order to understand precisely how the infrared incident beam interacts with material, the beam has been polarized on one hand , and inclined on the other. When it is polarized in a parallel way, the electrical field perpendicular component, $E_{\perp}$, is suppressed, and inversely when the beam is polarized in a perpendicular way, it is the electrical field parallel component, $E_{//}$, which is suppressed. This latter has two sub-components : $E_{//L}$, which is its projection in the direction perpendicular to the sample plane, and $E_{//T}$, which is its projection in the sample plane. It becomes apparent then, that when the light is perpendicular-polarized, longitudinal optical phonons of the material cannot be excited, whereas when the light is parallel-polarized, both longitudinal and transversal optical phonons can be excited, though the last ones are less excited than in the previous case (because of the absence of $E_{\perp}$). Spectra obtained in case of polarized light are shown in figure 3.

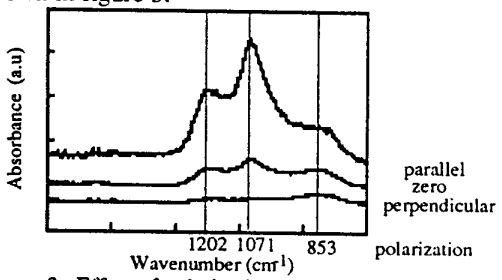

Figure 3 : Effect of polarization on a-SiNxHy spectra

The peak amplitude at 840 cm^{-1} decreases in case of parallel polarization and on the contrary, increases in case of perpendicular polarization. Inversely, the peak amplitude at 1070 cm^{-1} shows opposite trends. As these two peaks are both assigned to Si-N bond stretching modes [5], it seems then that the first and the second peaks are due to a transversal and a longitudinal optical mode respectively. Additional experiences carried out under variable infrared beam angle of incidence, lead to identical conclusions.

The effects of operating conditions on Si-H and N-H bonds, whose stretching modes appear respectively at about 2100 and 3330 cm^{-1}, have next been studied. It is observed that Si-H bond concentration decreases when films become richer in nitrogen, and at the same time, N-H bond concentration increases. These last results confirm the previously reported interpretation of the optical bandgap broadening.

III-3-Electrical measurements

Among different electrical characterization techniques, the fixed defect amount has been evaluated by means of capacitance/voltage measurements, for different operating parameters. The next figure (figure 4) represents the evolution of the amount of fixed charges with R.

It always corresponds to the presence of positive fixed charges and is found to decrease strongly with increasing R.

The influence of power on fixed charge amount, appears to be quite strange. Indeed, when power increases, silicon nitride films seem to own a smaller amount of fixed charges, though electronic and ionic

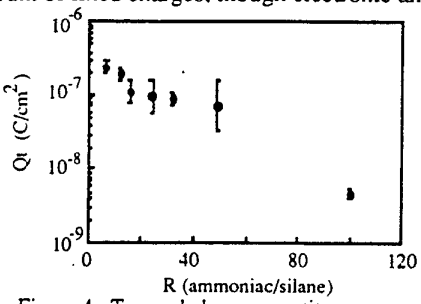

Figure 4 : Trapped charge quantity vs gas ratio R

bombardment increases and therefore should promote an increase in charge trapping. In fact, the power increase is directly related to the modifications in film composition, as when R increases. As already seen, according to modelling and spectroscopy results, the power increase corresponds to the formation of nitrogen-rich deposit precursors with respect to silyl radicals leading to a nitrogen-rich silicon nitride. Therefore, it can be concluded that electronic and ionic bombardment due to rf discharge does not play an important role for the experimental conditions considered, and that the trapping rate seems to be indirectly controlled mainly by physical and chemical mechanisms in gaseous phase, i.e. directly controlled by the chemical nature of bonding in the material.

IV-Conclusions

Plasma-deposited silicon nitride films have been analysed under different techniques. The results obtained are in good agreement with each other and with previous studies, and help to understand the mechanisms that determine material quality, in order to improve them.

UV/visible spectroscopy has shown an optical bandgap broadening when silicon nitride films become richer in nitrogen. This broadening is attributed to progressive replacement of Si-Si and Si-H bond states by Si-N, N-H and N atoms $p\pi$ states.

Infrared spectroscopy has in particular revealed an anisotropic effect probably due to short-range atomic arrangement in silicon nitride films. Thus, the absorption peaks at about 840 cm^{-1} and 1070 cm^{-1} are identified respectively as due to a transversal and a longitudinal optical Si-N stretching mode.

The amount of fixed charges determined by electrical characterization of silicon nitride films, decreases with increasing amount of N. The origin of charge trapping seems then rather due to the chemical nature of bonding than to the electrical character of the discharge.

References

[1] : Y.Kuo, J.Electrochem.Soc.142(1), 186-190 (1995)
[2] : H.Caquineau, G.Dupont, B.Despax, J-P.Couderc, J.Vac.Sci.Technol.A14(4), 2071-2082 (1996)
[3] : J.Robertson, Phil.Mag.B63(1), 47-77 (1991)
[4] : K-C.Lin, S-C.Lee, J.Appl.Phys.72(11), 5474-5482 (1992)
[5] : G.Lucovsky, D.V.Tsu, J.Vac.Sci.Technol.A5(4), 2231-2238 (1987)

Optical diagnostics of r.f argon and xenon magnetron discharges.

M.F. Dony, F. Debal, M.Wautelet, J.P.Dauchot, M. Hecq.
Laboratoire de Chimie Inorganique et Analytique Université de Mons-Hainaut, 23 Avenue Maistriau, B-7000 Mons, Belgium.
J. Bretagne, A. Ricard*.
Laboratoire de Physique des Gaz et Plasmas, Bt. 212, Université Paris-Sud-CNRS, F-91405 Orsay, France.
* CPAT-Université. Paul Sabatier, 118 route de Narbonne, F-31062 Toulouse, France.

1. Introduction.

Magnetron sputtering of various materials in Argon gas is widely used in thin film deposition technology [1]. Magnetron sputtering in Xenon gas is also of great interest to study the sputtering of BN ceramics in Xe ion sources for stationary plasma thrusters [2]. Previous studies in argon magnetron discharges with aluminium target have be devoted to the spectroscopic analysis of Ar, Ar^+, Al radiative states and to Ar ($^3P_{2,1,0}$,$^1P_1$) metastable and resonant states [3,4]. In the present work, the Xe, Al, B radiative states and Xe ($^3P_2$) metastable atoms are analysed for Al and BN targets by changing gas pressure and power of the RF magnetron discharge.

2. Experimental setup.

The experimental setup is reproduced in Fig.1. The magnetron cathode can be in Al (thickness 5mm) or in BN (thickness 3mm) of dia. 33mm. The cathode is surrounded by a guard ring at the ground potential. On the cathode surface, the magnetic induction (B = 400 gauss) confines the electrons which are producing a plasma at about 1 cm above the cathode surface. The 13.56 Mhz r.f power can vary from 1 to 50 watts, for a gas pressure between 3 and 150 mTorr. As shown in Fig.1, the plasma is analysed by emission and absorption spectroscopy via a quartz optical fiber with a spatial resolution estimated to be 2 mm. The spectrometer is a Chromex 2501 S with a CCD camera.

3. Intensities of radiative species (Xenon and sputtered atoms).

Intensity (I_λ) of xenon and sputtered atom lines have been recorded at 1 mm above the cathode, at the maximum of the negative glow. Variations of Log I_λ versus Log W (RF power) are reproduced in Fig.2 for the Al 396.1 nm and Xe 840.9 nm lines. It is deduced $I_\lambda=W^\beta$ variations with $\beta=0.5(\pm0.03)$ for Xe and $\beta=1.9(\pm0.5)$ for Al. In an argon plasma, it was also found $\beta=0.5$ for the argon lines[3]. By assuming as for Ar a direct electron excitation of Xe radiative states, it is deduced that $I_\lambda(Xe)\approx n_e$ with $n_e\approx W^{0.5}$.
The Al line intensity ratios in the two Ar and Xe discharge are reported in table 1 for the same plasma parameters : 25 and 100mTorr and a RF power between 5 and 50 watts. It is deduced that the Al line intensity is about 10 to 20 % lower in Xe than in Ar discharges. With the BN ceramic cathode, the B, λ=249.7 nm intensity was largely weaker in Xe than in Ar discharges. At 25 mTorr, 50 watts, the intensity ratio $I_B(Xe)/I_B(Ar)=0.27$. It is then concluded that the Xe^+ ions have a sputtering rate lower than the Ar^+ ions, by a factor 0.8-0.9 for Al and as low than 0.3 for BN.

4. Density of Xe($^3P_2$) metastable atoms.

The density of Xe($^3P_2$) has been determined by the resonant absorption method of Mitchell-Zemansky as it is detailed in ref 3,4. Briefly, the A_L-absorption coefficient: $A_L=1-I_t/I_0$ (I_t ,I_0 transmitted and incident intensity coming from a Philips lamp) is related to the $k_{\sigma 0}L$ optical thickness :

$$k_{\sigma 0}L = 8.2510^{-13}\, L \frac{f}{\delta\sigma_{1/2}^{\,p}} n_{Xe(^3P_2)}$$

(f-oscillator strength of the chosen absorbing line of Doppler broadening $\delta\sigma_{1/2}^p$ in the plasma, L-absorption length and $n_{Xe(3P2)}$ density of metastable atoms) through the factor : $\alpha = \dfrac{\delta\sigma_{1/2}^{\,s}}{\delta\sigma_{1/2}^{\,p}}$ ($\delta\sigma_{1/2}^S$ source line broadening). The factor α has be calculated by estimating that in the Philips lamp (R=1cm), the spectral lines are self-absorbed by their own metastable atoms of density between 10^{11} and 10^{12} cm^{-3} with a Doppler broadening of T_e=300K. It has been chosen the Xe 823.2 nm, Xe line has been chosen whose f=0.227 [5,6] and with $\alpha_{823.2}$=1.2-2.1. The L absorption length has been estimated by measuring A_L versus the Z-axial distance above the magnetron cathode [3]. It is obtained L=10 cm at 25 mTorr, 50W and L=8cm at 100mTorr, 50W. The Xe ($^3P_2$) metastable densities determined with Al and BN targets are reported in Table2. It was found constant values of Xe($^3P_2$) metastable densities between 5 and 50 watts, indicating that the Xe($^3P_2$) atoms have reached satured values as for the Ar($^3P_2$) atoms [3] as a result of production and destruction by electron collisions. It is also concluded from table 2 that the Xe($^3P_2$) metastable densities are not really affected by the Al or BN cathode material. In similar conditions with Ar discharges, it was found for the Ar($^3P_2$)

metastable atoms [3] : Ar($^3P_2$)=(3-6)10^{10}cm^{-3} at 25 mTorr and Ar ($^3P_2$)=(2-3)10^{10}cm^{-3} at 100mTorr which are in the same order of magnitude than for Xe($^3P_2$).

5. Conclusions.

Cathode magnetron discharges in Ar and Xe are working with similar electron kinetics. In the same conditions of pressure, power and with two cathode targets: Al and BN, it has been found about the same Ar and Xe metastable atom densities : (1-3) 10^{10} cm^{-3} and the same electron density variations with the discharge power: $n_e \approx W^{0.5}$. As it concerns the sputtering yields of Al and BN targets, lower rates have been determined in Xe as compared with Ar, by a factor of 1.1 to 1.2 with Al, droping to about 3 with BN. It can be concluded that Xe is a sputtering gas weaker than Ar on BN targets.

Table 1 :
Variations of the intensity ratio $r = I_{Al(Xe)} / I_{Al(Ar)}$ of Al I 396.1 nm versus the RF power in Xe and Ar discharges.

W_{RF} (Watts)	5	10	20	50
r 25 mTorr	0.6	0.8	0.86	0.91
r 100 mTorr	0.93	0.74	0.81	

Table 2 :
Xe ($^3P_2$) densities for two gas pressures and the Al and BN cathodes
d=1.5 cm

Xe ($^3P_2$) /p (mTorr)	25	100
Al cathode A_L	0.54	0.5
n (10^{10}cm^{-3})	1.2-2.6	1.3-2.6
BN cathode A_L	0.506	0.41
n (10^{10}cm^{-3})	1.1-2.2	1-1.8

References.

(1) A.Crill, Cold Plasma in Materials Fabrication, IEEE Press, N.Y C 1994
(2) 32nd AIAA / ASME / SAE / ASEE Joint Propulsion Conf. 1-3/07/1996 (Lake Buena Vista, USA)
(3) M.F. Dony, A.Ricard, J.P. Dauchot, M.Hecq and M.Wautelet, Surface and Coatings Tech. 74-75 (1995) 479
(4) M.F. Dony, A.Ricard, M.Wautelet, J.P. Dauchot and M. Hecq, submitted to J. Vac. Sci. Tech; (1996)
(5) M. Aymar and M. Coulombe. Atomic Data and Nuclear Data. Tables 21 (1978) 537
(6) J. Sabbagh and N Sadeghi, J.Q.S.R.T 17 (1977) 297

Fig.I: Experimental set-up of magnetron discharge with optical arrangement for emission and resonant absorption spectroscopy: 1. gas inlet; 2. turbomolecular pump; 3. cathode magnetron; 4. hollow cathode lamp; 5. optical fiber; 6. HR 1000; 7. photomultipliers; 8. PC control; 9. vernier; 10.cooling tubing; 11. female coaxial connector; 12. male coaxial connector (RF input: type " N"); 13. RG-393 coaxial cable; 14. copper conductor; 15. matching network; 16. 13.56 Mhz RF generator.

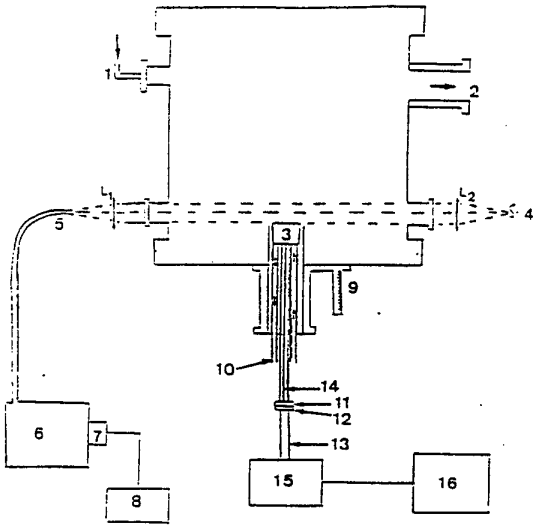

Fig.2. Variations of Ln I versus Ln W of Xe I 840.9 nm and Al I 396.1 nm lines at 25 and 100mTorr.

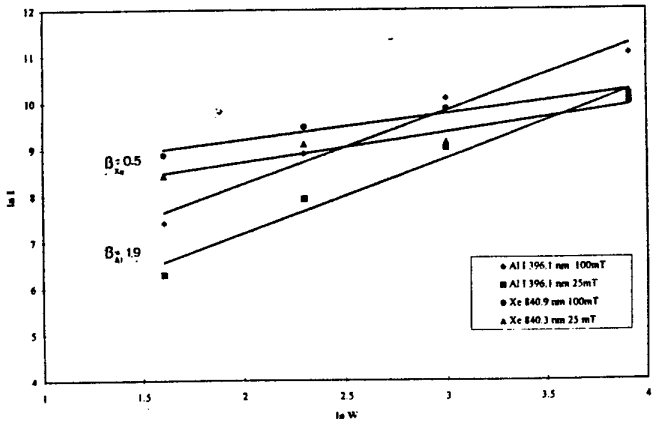

Reactions of Small Hydrocarbon Ions CH_3^+, $C_2H_3^+$ and $C_2H_5^+$ with Silane

G. Bánó[1], J. Glosík[1], A. Luca[1], W. Lindinger[2]

[1] Department of Electronics and Vacuum Physics, Mathematics and Physics Faculty, Charles University, V Holešovičkách 2, Prague 8, Czech Republic

[2] Institut für Ionenphysik der Universität Innsbruck, Technikerstr. 25, Innsbruck, Austria

Introduction and experiment

Many silicon-bearing ions, their structure, thermochemistry, and their reactions with neutral molecules have been the subject of a number of theoretical as well as experimental studies (see, e.g., [1], [2] and references therein). Investigations of ion-molecule reactions of different ions with silane and silicon ions with neutrals are mostly motivated due to their importance in plasmas for technological applications. The reactions of hydrocarbon ions with SiH_4 could be also of interest to the theoretical chemist because of fundamental aspects of the chemical bonding of carbon to silicon. In recent years our research has been directed towards understanding of ion-molecule reactions of this type (see, e.g., Refs. [3], [4]). The measurements have been carried out using the Innsbruck selected ion flow drift tube (SIFDT) apparatus of conventional design. Helium was used as a buffer gas. Ions were generated in an electron impact ion source from CH_4 and mass selected prior to injection into the drift tube. Mobility used for calculations of the drift velocity of ions CH_3^+ was taken from Peska *et al* [5]. Mobilities of $C_2H_3^+$ and $C_2H_5^+$ were measured in the present experiment. Operational pressure of the buffer gas was 0.16-0.26 Torr. Measured reaction rate coefficients and product distributions were independent on pressure.

Results

The reaction of CH_3^+ with SiH_4

In the covered energy range the reaction of CH_3^+ with SiH_4 is proceeding with rate coefficient close to collisional rate coefficient (approximated by Langevin rate coefficient, k_L). In Fig. 1 the measured reaction rate coefficient is plotted versus average kinetic energy in center-of-mass frame, KE_{CM}. SiH_3^+ is the dominant ionic product. Neutral products cannot be detected, nevertheless only energetically possible product is CH_4 (ΔH=-52.8kcal/mol, energetics of the reactions is calculated on the base of the i Refs. [6] and [7]). Reaction schema is:

$$CH_3^+ + SiH_4 \longrightarrow SiH_3^+ + CH_4 \qquad (1)$$

Formation of SiH_5^+ by proton transfer and consequent dissociation to SiH_3^+ and H_2 is endoergic and can be excluded.. Traces of $SiCH_3^+$ and $SiCH_5^+$ product ions, ($\leq$1%) were also observed in agreement with previous tandem mass spectrometer study (see compilation by Anicich *et al* [8]).

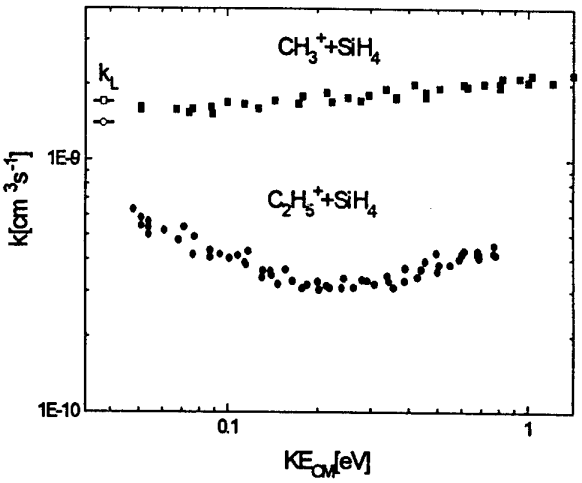

Figure 1. The reaction rate coefficients of the reactions of CH_3^+ and $C_2H_5^+$ ions with SiH_4.

The reaction of $C_2H_3^+$ with SiH_4

The reaction has three product ions as indicated in the reaction scheme (2). Indicated are energetically possible neutral products, there is not enough energy in the reaction for further dissociation of neutral molecules.
Reaction channel (2b) is thermoneutral and is the only one

$$C_2H_3^+ + SiH_4 \longrightarrow SiH_3^+ + C_2H_4 \qquad (2a)$$
$$\longrightarrow SiH_5^+ + C_2H_2 \qquad (2b)$$
$$\longrightarrow SiC_2H_5^+ + H_2 \qquad (2c)$$

in the present study, where production of SiH_5^+ was observed ($\leq$10% at low KE_{CM}). The partial reaction rate coefficients are plotted in Fig. 2. Note that with increasing KE_{CM} production of SiH_3^+ is increasing on expense of other two channels. The overall reaction rate coefficient (k) is nearly constant (note that $k \sim k_L/2$). Production of SiH_3^+ cannot be explained by formation of SiH_5^+ or $SiC_2H_5^+$ and their consequent dissociation, because in such case C_2H_2 and H_2 are formed and reaction is endoergic (ΔH=17.5kcal/mol). In study of Mayer and Lampe [9] only production of SiH_3^+ and SiH_5^+ was reported with reaction rate coefficient $2.8 \cdot 10^{-10} cm^3 s^{-1}$, this is corresponding to the sum of the partial reaction rate coefficients of channels (2a) and (2b) at near thermal energies.

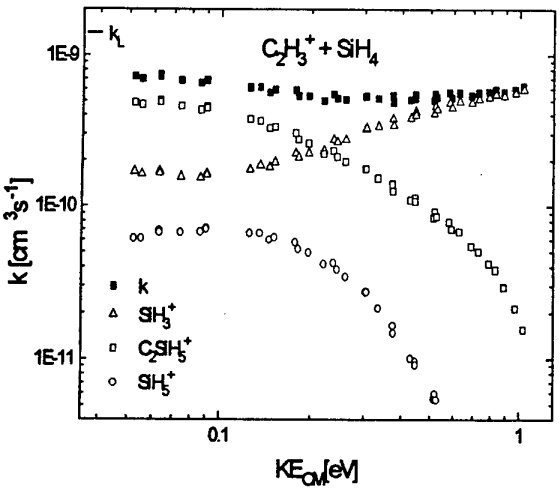

Figure 2. The partial reaction rate coefficient of the reaction of $C_2H_3^+$ ion with SiH_4.

The reaction of $C_2H_5^+$ with SiH_4

The reaction coefficient of the reaction of $C_2H_5^+$ ion with SiH_4 versus KE_{CM} is plotted in Fig. 1. Only SiH_3^+ was observed as a product ion. The reaction is exoergic (ΔH= -10kcal/mol) if the neutral product is C_2H_6. If two neutral molecules (H_2 and C_2H_4) are produced the reaction is endoergic (ΔH=22kcal/mol). This endothermicity rules out the formation of SiH_5^+ and its consequent dissociation. The reaction scheme is:

$$C_2H_5^+ + SiH_4 \longrightarrow SiH_3^+ + C_2H_6 \qquad (3)$$

Concluding Remarks

The siliconium ion SiH_5^+, an analog of the carbonium ion CH_5^+, is of considerable interest in understanding the nature of nonclasical bonding [10]. The dissociation energy of SiH_5^+ is approximately 14 kcal/mol (see calculation in ref. [11]). The aim of the presented study was the study of the production of SiH_5^+ ions by the proton transfer from hydrocarbon molecular ions in the drift tube. In order to avoid dissociation of eventually formed SiH_5^+, only the reaction of ions parent molecules of which have the proton affinity close to the proton affinity of SiH_4 (155 kcal/mol [12]) were studied. SiH_5^+ ions were produced only in the reactions of ions $C_2H_3^+$ at low KE_{CM}, channel (2b).

Acknowledgement

This work was supported in part by the Fonds zur Förderung der Wissenschaftlichen Forschung under project No. 10014, in part by Grant Agency of the Czech Republic under project No. 94/0449, and by Charles University Prague under project No. GA UK 179/96

References

[1] A.E. Ketvirtis, D.K. Bohme, and A.C. Hopkinson, J. Phys. Chem., **99**, 16121 (1995)

[2] J. Glosík, P. Zakouřil, and W. Lindinger, J. Chem. Phys., **103**, 6490 (1995)

[3] J. Glosík, P. Zakouřil and W. Lindinger, Int. J. Mass Spec. Ion Proc., **149/150**, 499 (1995)

[4] P. Zakouřil, J. Glosík, V. Skalský, and W. Lindinger, J. Phys. Chem., **99**, 15890 (1995)

[5] K. Peska, H. Stori, F. Hegger, G. Sejkora, H. Ramler, M. Kriegel and W. Lindinger, J. Chem. Phys. **70**, 5253 (1982)

[6] B.H. Boo and P.B. Armentrout, J. Am. Chem. Soc., **113**, 6421 (1991)

[7] S. Wlodek, A. Fox, and D.K. Bohme, J. Am. Chem. Soc., **113**, 4461 (1991)

[8] V.G. Anicich, J. Phys. Chem. Ref. Data, **22**, 1469 (1993)

[9] T.M. Mayer, F.W. Lampe, J. Phys. Chem. , **78**, 2433 (1974)

[10] D.W. Boo and Y.T. Lee, J. Chem. Phys., **103**, 514 (1995)

[11] Ching-Han Hu, M. Shen, and H. F. Schaefer III, Chem. Phys. Lett., **190**, 543 (1992)

[12] S.G. Lias, J.F. Liebman, R.D. Levin, J. Phys. Chem. ref. Data, **13**, 695 (1984)

Positive and Negative Chlorine Ion Kinetics in Inductively-Coupled Chlorine and Boron Trichloride Containing Plasmas*

G. A. Hebner and C. B. Fleddermann†
Sandia National Laboratories
Albuquerque NM, USA, 87185-1423

1. Introduction

Discharges in gas mixtures containing Cl_2, BCl_3, Ar, and N_2, are used by the integrated circuit industry for metal etching and definition. The large number of potential gas and surface phase reactions in these gas mixtures greatly reduces our capability to understand and model these plasmas from first principles. For example, a large number of the potential processes have unknown, or at best, incomplete sets of fundamental information such as cross sections, and gas and surface chemical reaction mechanisms. In such complicated chemical systems, measurements of plasma species can be critical to identifying the important chemical mechanisms, understanding the influence of additives to the gas mixture, and benchmarking model predictions. Many modern microelectronics plasma processing tools utilize high electron density sources such as inductively coupled discharges, electron cyclotron resonance (ECR) or helicon sources. This work will focus on a subset of the high density sources, the inductively coupled plasma (ICP). An essential parameter that must be measured in these plasmas is the density and spatial distribution of ions, both positive and negative, formed in the plasma.

In the work presented here, relative metastable chlorine ion (Cl^+*) and absolute Cl^- densities as a function of discharge parameters such as gas mixture, input power, and total gas pressure are presented. Laser induced fluorescence (LIF) was used to measure the spatially resolved Cl^+* temperature, radial drift velocity and relative density. The output from a cw ring dye laser was scanned across the $3p^3(^4S^0)4p^5P_3$ - $3p^33d^5D^0_4$ transition at 542.32 nm and the fluorescence was monitored on the $3p^3(^4S^0)4p^5P_3$ - $3p^34s^5S^0_2$ transition at 479.45 nm. The resulting lineshape was then fit to a sum of two Gaussian lineshapes to account for the relative abundance of the two Cl isotopes. Laser photodetachment spectroscopy was used to measure the Cl^- densities in the center of the plasma. A pulsed Nd:YAG laser operating at 266 and 355 nm was combined with a novel microwave interferometer to measure the excess electrons produced by photodetaching Cl^-. By varying the photodetaching laser wavelength, the identity of the negative ion could be inferred.

2. Cl^+* kinetics

The Cl^+* measurements indicate that the ion temperature in the center of the plasma varied from 2000 to 3000 K depending on discharge conditions. For example, Fig. 1 shows the temperature variation for BCl_3/Cl_2 and $BCl_3/Cl_2/Ar$ mixtures as a function of input power. This temperature is significantly hotter than temperatures of argon neutrals and argon ions measured in the same reactor[1]. In previous work, we suggested that the hot Cl^+* could be due to hot neutral chlorine atoms; Cl produced by dissociation of Cl_2 or BCl_3 could carry a small amount of energy into subsequent ionization and excitation[2]. The addition of BCl_3 to a Cl_2 plasma significantly decreased the chlorine ion density (Fig. 2) without causing a significant change in their temperature. A likely explanation for the decrease in Cl^+* density with increased BCl_3 fraction is the higher dissociation energy for BCl_3 compared with Cl_2. Addition of N_2 to a BCl_3 plasma caused a factor of three increase in the Cl^+* density (Fig. 3) suggesting that transfer of energy from long-lived nitrogen excited states can enhance the decomposition of BCl_3 [3]. Additional radial profiles of the Cl^+* temperature, relative density and radial drift velocity will be shown.

3. Cl^- kinetics

In discharges containing Cl_2 and BCl_3, Cl^- was the only negative ion detected. If present in the discharge, other negative ions have an estimated density below a few 10^8 cm^{-3}. Dissociative attachment to Cl_2 was the predominant Cl^- formation mechanism in Cl_2 discharges, and direct dissociative attachment to BCl_3 was found to be a potential source of Cl^- in BCl_3 plasmas. Interactions between Cl_2 and Ar (Fig. 4), and Cl_2 and BCl_3 altered the Cl^- formation kinetics, possibly due to enhanced dissociation of the parent molecules by argon metastables. Addition of N_2 to Cl_2 plasmas had very little effect on Cl^- density, but addition of N_2 to BCl_3

discharges caused an increase in Cl^- production (Fig. 5). This increase is similar to the increase in Cl^{+*} density with increased N_2 flow described above. It is concluded, that transfer of energy from N_2 metastables is responsible for the changes in the negative ion densities observed as well.

4. References

[1] G. A. Hebner, J. Appl. Phys. 80, 2624 (1996).
[2] G. A. Hebner, J. Appl. Phys. 80, 3215 (1996).
[3] F. W. Breitbarth, Plasma Chem. and Plasma Proc. 12, 261 (1992).

5. Acknowledgments

† Permanent address, University of New Mexico, Department of Electrical and Computer Engineering, Albuquerque NM, 87131

*This work was supported by the United States Department of Energy under Contract DE-AC04-94AL85000. Sandia is a multiprogram laboratory operated by Sandia Corporation, a Lockheed Martin Company, for the United States Department of Energy.

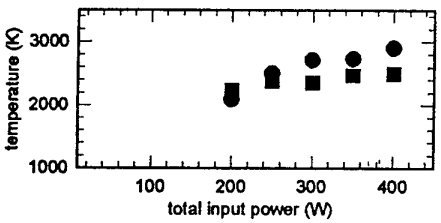

Fig. 1 Cl^{+*} temperature as a function of total input power for BCl_3/Cl_2 (●) and $BCl_3/Cl_2/Ar$ (■) mixtures at 10 mTorr.

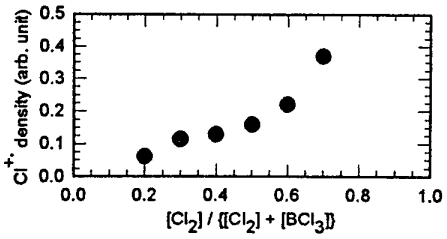

Fig. 2 Cl^{+*} density as a function of Cl_2/BCl_3 ratio at 10 mTorr and 400 W.

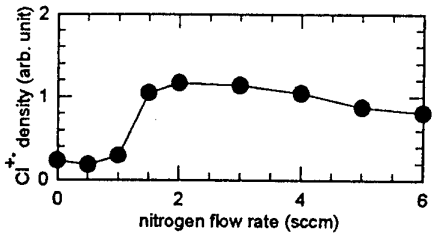

Fig. 3 Cl^{+*} density in a BCl_3 discharge as a function of added nitrogen flow rate at 300 W and 20 mTorr.

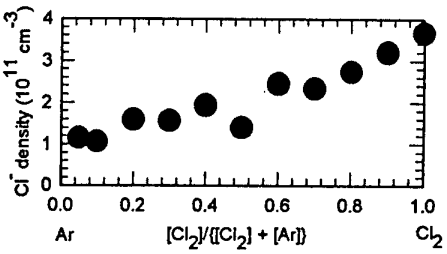

Fig. 4 Cl^- density as a function of Cl_2/Ar ratio at 300 W and 20 mTorr.

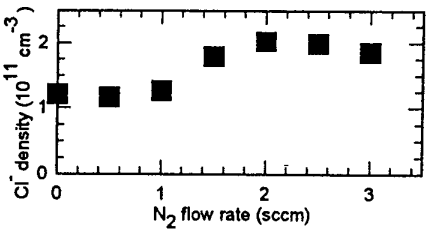

Fig. 5 Cl^- density in a BCl_3 discharge as a function of added nitrogen flow rate at 400 W and 10 mTorr.

Theoretical and experimental study of SiH radical density and thin film growth rate in PECVD H_2/SiH_4 radio frequency discharges

O. Leroy, N. Dorval, M. Hertl, J. Jolly, M. Péalat
Laboratoire PRIAM, Unité Mixte de Recherche CNRS-ONERA, Fort de Palaiseau, 91761 Palaiseau cedex, France

1. Introduction

Radio frequency (RF) discharges are extensively studied as they play an important role in plasma processing, such as surface treatment and thin film deposition. Amorphous hydrogenated silicon (a-Si:H) films are of special interest for the production of photoelectric cells and many efforts have been carried out to understand their deposition mechanism.

Recently we reported on numerical modelling of PECVD reactor plasmas and its experimental confirmation. A 1D thermal model has been developed and the calculated gas temperatures have been verified by CARS measurements [1]. The creation of radicals in the plasma has been treated by a 1D fluid model. We confirmed this model by spatio-temporal emission spectroscopy applied to the H_α transition [2]. In the present work we couple improved versions of these two models with a 2D model of plasma chemistry to predict absolute radical density profiles and deposition rates of a-Si:H films in different H_2/SiH_4 plasmas. The calculated SiH density profiles are compared with those measured by LIF, and the calculated film growth rate is checked by profilometry measurements.

2. Plasma chemistry model

The model [3] treats the chemistry and physics of the neutral radicals in the plasma. It is coupled with two other models developed previously: First, a 1D thermal model [1] calculates the axial temperature profile. The temperature is supposed to be uniform in radial direction. Then a 2D extension of the electrical fluid model is used to determine the source terms of radicals originating from electron impact on neutral molecules (we consider H_2, SiH_4, Si_2H_6 and Si_3H_8). The molecule densities have been measured by mass spectrometry and are used as input parameters. The radicals treated by the model are H, SiH_n (n=0..3) and Si_2H_m (m=2..5).The equation of transport for each radical species is

$$\vec{\nabla}.\vec{\Gamma} = \frac{1}{r}\frac{\partial}{\partial r}(r\Gamma_r) + \frac{\partial}{\partial z}\Gamma_z = S(z,r) \quad ,$$

where $\vec{\Gamma}$ is the particle flux and S the source term. We suppose that transport is governed only by diffusion, the diffusion coefficients D being calculated according to the theory of Chapman-Enskog [4]. S contains the source function for the creation of radicals due to dissociation of molecules by electron impact as well as creation and loss terms due to chemical reactions in the plasma volume. For each radical species the electrodes impose the boundary condition

$$-D\frac{\partial n}{\partial z} = \pm n\frac{v_{th}}{4}\frac{\beta}{1-\beta/2} \quad ,$$

which involves the radical loss probability β, the radical density n near the electrodes and the thermal velocity of the radicals v_{th}. A very similar condition holds for the particle losses at the plasma confining grid (see experimental setup). Due to the cylindrical symmetry of the plasma the 2D model calculates the radical densities at each point in the plasma volume. Furthermore, we can easily deduce thin film growth rates on the whole surface of the Si wafer. The contribution of each species to the film growth is proportional to its flux on the surface

$$\Phi = n\frac{v_{th}}{4}\left(\frac{\beta}{1-\beta/2}\right)\frac{s}{\beta} \quad ,$$

where s is the sticking coefficient.

3. Experimental setup

The experiment is performed in a PECVD reactor equipped with quartz optical ports for spectroscopic observations. The plasma is produced by a parallel plate RF discharge and confined to the interelectrode volume (diameter 12 cm, distance 3.2 cm) by a grounded grid. RF power is applied to the upper electrode, which is shower-like to allow gas injection. The grounded electrode is heated up to 523 K and is covered with a silicon substrate. The effective power P_{eff} coupled to the plasma, which is used as input parameter in the model, is obtained by the subtracting technique proposed by Godyak and Piejak [5].

The $A^2\Delta$ - $X^2\Pi$ transition of the SiH radical is used for the LIF measurements. A frequency-doubled single mode Nd:YAG laser (Quantel YG 780) delivers a 10 ns, 180 mJ beam at 532 nm which is used to pump a tunable dye laser (Quantel TDL IV). Radiation at 411 nm with pulse energies up to 2.5 mJ is obtained by mixing the dye laser radiation at 670 nm with the residual 1.06 μm radiation of the Nd:YAG laser. The 411 nm radiation has a linewidth of 0.08 cm^{-1} (FWHM). It enters the interelectrode region by a slit in the grid. The fluorescence radiation is collected at right angle to the laser beam through the grid (transmission about 50%) and is imaged on the entrance slit of a monochromator (Jobin Yvon H.20). Light detection is achieved by a photomultiplier (HAMAMATSU R212 UH) and a BOXCAR averager (Stanford SR250).

Absolute density of the $X^2\Pi$ state of SiH is deduced from the amplitude of a unique rotational line recorded in saturation regime. An estimate of the temperature, a

correction taking into account the effect of partial saturation in the wing of the laser beam and a calibration of the collection optics are successively applied. The transition $R_{1e}(N=7)$ in the $A^2\Delta$-$X^2\Pi$ band was selected because the population of the $X^2\Pi(N=7)$ state depends only weakly on the temperature ($\Delta n/n < 5\%$) between 400 - 600 K, typical temperature measured between the electrodes for various plasma conditions [1]. We suppose $T_{rot} = T_{gas} = 500$ K in all our calculations. A typical vibrational temperature of $T_{vib} = 2000$ K is also assumed to estimate the population on the vibrational states, but is actually without appreciable influence on the calculated absolute density.

The calibration of the optical transmission of the detection system and the multiplier response is obtained by a Rayleigh measurement using the same optical configuration as in the LIF measurements. By modelling the LIF saturation behaviour it is then possible to correctly normalize the LIF measurements over the whole laser energy range [6]. Strongly saturated LIF measurements have been carried out in order to maximize the fluorescence signal and to minimize incertainties due to laser energy fluctuations.

The uncertainty of the absolute SiH density is estimated to be about 70% (1σ). This large uncertainty is presently mainly due to the imprecise measurement of the laser energy by a calorimeter.

4. Results and discussion

In fig. 1 and 2 we show respectively the calculated and measured SiH density profiles and the growth rate of amorphous hydrogenated silicon on the silicon wafer for two different plasma conditions (see figure captions).

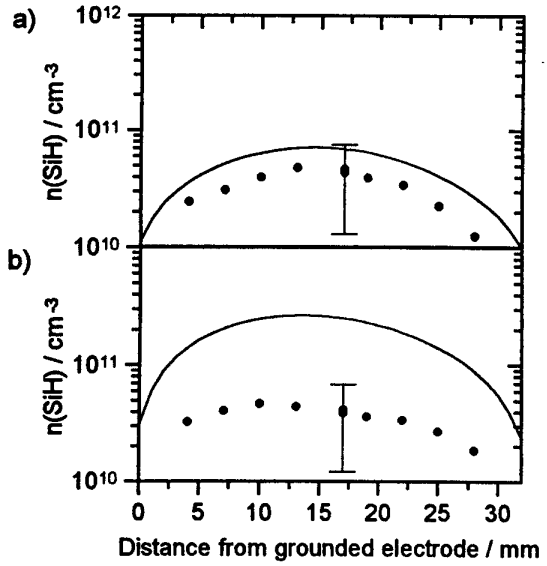

Fig. 1: Calculated (line) and measured (dots) axial SiH density profiles:
a) 5 sccm SiH_4, $p_{tot} = 68$ mtorr, $P_{eff} = 6$ W.
b) 5 sccm SiH_4 + 45 sccm H_2, $p_{tot} = 300$ mtorr, $P_{eff} = 15$ W

In both plasma conditions the shapes of the SiH density as well as of the film growth rate are well reproduced by the model.

The absolute values predicted by the model are in good agreement with the measured ones in the case of the pure silane plasma: they differ by less than a factor 2 (fig. 1a and 2a). If we consider the ab initio character of the model, this agreement of calculation and measurement is quite satisfactory.

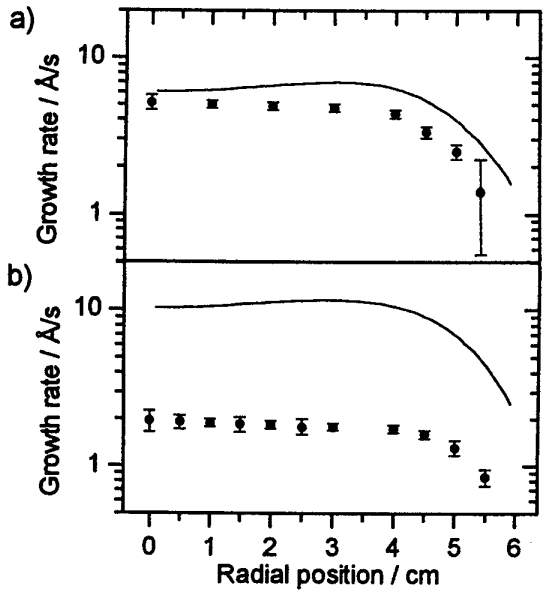

Fig. 2: Calculated (line) and measured (dots) radial a-Si:H growth rates on a silicon wafer. Plasma conditions a) and b) are the same as in fig. 2.

In the case of the hydrogen diluted plasma (fig. 1b and 2b), the model overestimates both the SiH density and the film growth rate by a factor of about six relative to the measurements. In order to investigate the origin of these discrepancies and to further increase the reliability of the model, density measurements of other radicals in H_2/SiH_4 plasmas are in progress.

5. References

[1] O. Leroy, J. Perrin, J. Jolly, M. Péalat and M. Lefebvre, J. Phys. D: Appl. Phys. **30** (1997) 1-11

[2] O. Leroy, P. Stratil, J. Perrin, J. Jolly and P. Belenguer, J. Phys. D: Appl. Phys. **28** (1995) 500-7

[3] O.Leroy, thesis, Université de Paris XI (1996)

[4] Hirschfelder, Curtiss and Bird, *Molecular Theory of Gases and Liquids*, Wiley, New York, 1954

[5] V. A. Godyak and R. B. Piejak, J. Vac. Sci. Techn. A **8** (1990) 3833

[6] T. Doerk, M. Hertl, B. Pfelzer, S. Hädrich, P. Jauernik and J. Uhlenbusch, Appl. Phys. B **64** (1997) 111-118

SPECTROSCOPIC STUDY OF METHANE CONVERSION IN THE FLOWING AFTERGLOW OF A DINITROGEN MICROWAVE PLASMA

Diamy A.-M. (*), Hrachová V. (°), Legrand J.-C. (*), and Hrach R. (°),

(*): Laboratoire de Chimie Générale et de Chimie des Surfaces. CNRS URA 1428.
Univ. Pierre et Marie Curie, Case 196, 4 place Jussieu, 75252 Paris Cedex 05, France.
Email jcl@ccr.jussieu.fr
(°) Department of Electronics and Vacuum Physics, Faculty of Mathematics and Physics,
Charles University, V Holešovičkách 2, 18000 Prague, Czech Republic.

1. Introduction

The conversion of methane to more useful chemicals or fuels has generated widespread interest because of important industrial applications. Many studies are still in progress. We have investigated the activation of methane in the flowing afterglow of a dinitrogen plasma by a spectroscopic method.

2. Experimental

The experimental setup was shown in [1]. A microwave generator (2.45 GHz) is connected to a rectangular waveguide cavity. Stationary waves produce a plasma in a cylindrical fused silica reactor (i.d. =2.8 cm ; o.d. = 3 cm) crossing the cavity.
Methane is introduced into the afterglow at distances d from the end of the cavity by means of four ports distributed all around the reactor.
All experimental results reported here are for the following experimental conditions : pressure = 13.2 mbar, N_2 flowrate = 200 mL(STP)/min, CH_4 flowrate = 150 mL (STP)/min, incident power = 370 Watt. The pressure is measured by means of a baratron and the gas flow rates F (in STP conditions, i.e. 298 K and 1 bar) by means of mass flowmeters.
Optical emission is analysed by a monochromator (Jobin-Yvon, HRS1, 1220 lines/mm, focal length 588 mm) and a photomultiplier (Hamamatsu, R928) by means of an optical fibre moving along the afterglow.
The emission intensity of the following bands is studied:
- N_2 First Positive System at 580.4 nm (B,v=11→A,v=7),
- N_2 Second Positive Syst. at 380.5 nm (C,v=0→B,v=2),
- N_2^+ Firt Negative Syst. at 391.4 nm (B,v=0→X,v=0),
- Violet System of CN at 388.3 nm (B,v=0→X,v=0).

3. Results and Discussion

Methane conversion is pointed out by emission of violet system of CN at the point of introduction of methane (Fig. 1). This emission shows that methane is converted as far as 150 mm in the afterglow.
Computations carried out by varying electron density as well as electron temperature [2] showed that electrons have a little influence in the mechanism of methane conversion in these experimental conditions. Fast decay of charged species occurs in the afterglow; electron density and energy are not high enough to dissociate methane.

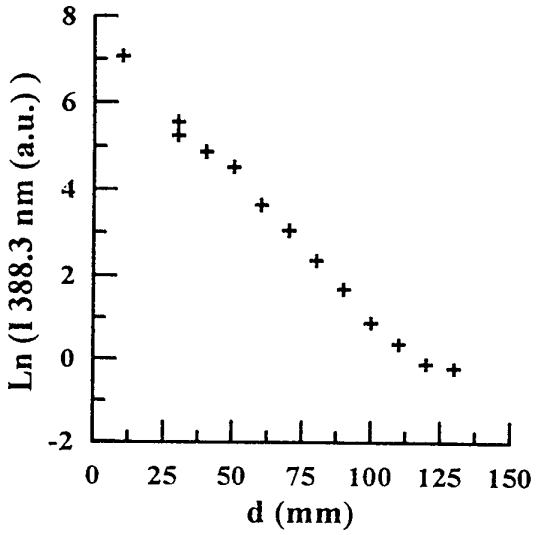

Figure 1 : Emission intensity I(388.3nm) versus methane injection point d in the afterglow.

The N_2^+(B,v=0→X,v=0) emission intensity (Fig.2) decreases with methane addition indicating the decay of excited ions: this is in good agreement with results of a previous paper where for injection of methane at d = 32 mm, charged species were no more measured with Langmuir probes [1].
If electrons do not play an important role in the methane decomposition, the initiation of the reaction could be due to active species of dinitrogen present in the afterglow

Figure 2 shows emission intensity I along the afterglow (Ln(I) versus distance x) for several bands of N_2 spectrum for pure N_2 and for a mixture N_2/CH_4 with introduction of methane at d = 9mm (i.e. x = 0).
Methane addition leads to an important decrease of the emission intensities of the First Positive System of N_2 and of the First Negative System of N_2^+ whereas the Second Positive System of N_2 is not changed.
Some information about nitrogen active species leading to methane activation can be deduced.

In the afterglow, N atoms mainly recombine on the $N_2(B,v)$ excited state according to the following reaction (a) [3]:

$$N + N + N_2 \rightarrow N_2(B,v) + N_2 \qquad (a)$$

This reaction leads to an enhancement of the $N_2(B,11\rightarrow A,7)$ band compared to the others bands of the sequence $\Delta v = 4$.

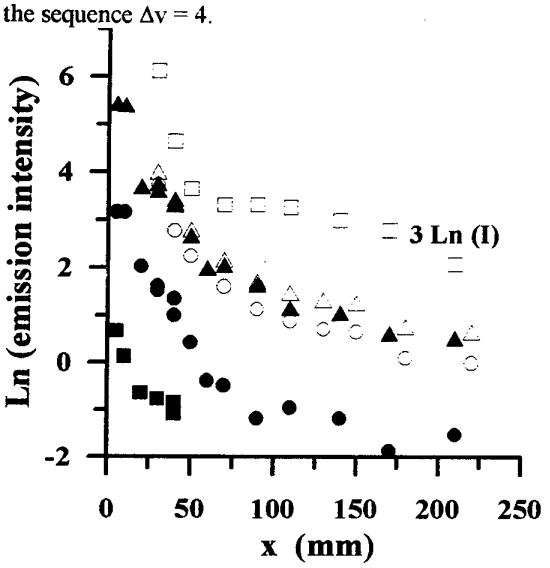

Figure 2 : Emission intensity of $N_2(B,11\rightarrow A,7)$: 580.4 nm (□, ■); $N_2(C,0\rightarrow B,2)$: 380.5 nm (Δ, ▲), and $N_2^+(B,0\rightarrow X,0)$: 391.4 nm (○, ●), along the afterglow for pure nitrogen (open symbols) and for a mixture of dinitrogen with 42.8 % of methane (black symbols) when methane is added at $d = 9$ mm (i.e. x = 0).

Another reaction can lead to $N_2(B,v)$ levels, especially in the near afterglow [4]:

$$N_2(A,v) + N_2(X,v\geq 6) \rightarrow N_2(B,v) + N_2 \qquad (b)$$

When this last reaction prevails against reaction (a), the $N_2(B,v=11\rightarrow A,v=7)$ emission is not enhanced with regard to the others. For B,v=11, we need:

$$N_2(A,v) + N_2(X,v\geq 12) \rightarrow N_2(B,v=11) + N_2 \qquad (b')$$

In our experimental conditions, the $\Delta v = 4$ band emission is significantly lowered in the mixture and the $N_2(B,11\rightarrow A,7)$ band is no more enhanced indicating a decrease of the rates of reactions (a) and (b). Quenching rate constant of $N_2(B,v)$ by CH_4 is only about 10 times higher than that by N_2 [5], so quenching cannot explain alone the large difference observed in Figure 2. When CH_4 is added, CH_x radicals are produced; these react with N atoms with a rate constant about 10^{+4}-10^{+5} times higher than that of reaction (a). Therefore there is a depletion of N atoms that can explain that $N_2(B,11\rightarrow A,7)$ band is no more enhanced.

The $N_2(C,v=0\rightarrow B,v=2)$ does not vary with methane addition. As studied in another paper [6], $N_2(C)$ state is formed from $N_2(A,v)$ metastable state:

$$N_2(A,v) + N_2(A,v) \rightarrow N_2(C,v) + N_2$$

Therefore, the observation of the $N_2(C,v)$ bands shows the presence of excited molecules $N_2(A,v)$ and allows one to follow their behaviour along the afterglow. It is well known that $N_2(A,v)$ is easily quenched by N atom; so one could expect an increase of $N_2(A,v)$ when atomic nitrogen concentration decreases. As this is not observed, we can deduce that CH_4, and radicals CH_x produced from CH_4 react with $N_2(A,v)$. Moreover Golde et al. [7] have detected H atoms during the quenching of $N_2(A,v)$ by CH_4. They reported that, although vibrational relaxation is the principal deactivation process for CH_4, deactivation by electronic quenching could reach about 10 % of the total quenching. As $N_2(A,v)$ density seems not affected by methane addition, decrease of reaction (b) could result of a decrease of $N_2(X,v\geq 6)$ density; so this species can also react with methane.

The creation of excited dinitrogen N_2^* in the afterglow is due to vibrational/vibrational transfer between molecules $N_2(X, v)$ when translational temperature of gas is going down [8]. Therefore, ground state dinitrogen molecules with high vibrational levels and excited molecules in electronic states (mainly A state) are present in the afterglow and can participate to methane activation.

The excited atomic nitrogen has some influence on decomposition of methane molecules too, but the concentration of excited nitrogen atom is much lower that the concentration of excited nitrogen molecule, therefore this channel of excitation is negligible.

Our results show the great influence of excited metastable dinitrogen molecules ($N_2(A,v)$ and $N_2(X,v)$) in the methane conversion. An absolute concentration of $N_2(A,v)$ of about 10^{+12} can be estimated from $N_2(C,v=0)$ emission as reported before in a previous paper [6].

4. References.

[1] A.M. Diamy, J.C. Legrand and V. Hrachová, *J. Phys. III Fr.*, **5**, 435-445 (1995).

[2] J.C. Legrand A.M. Diamy, R. Hrach and V. Hrachová, *Proc. 12th Intern. Symp. Plasma Chem.*, **2**, 601-606 (1995).

[3] H. Partridge, S.R. Langhoff, C.W. Bauschlicher and D.W. Schenke, *J. Chem. Phys.*, **88**, 3174-3186 (1988).

[4] L.G. Piper, *J. Chem. Phys.*, **91**, 864-873 (1989).

[5] L.G. Piper, *J. Chem. Phys.*, **97**, 270-275 (1992).

[6] J. Al Andari, A.M. Diamy, L. Hochard, J.C. Legrand and A. Ricard, *Proc. 12th Intern. Symp. Plasma Chem.*, **1**, 373-378 (1995).

[7] M.F. Golde, G.H. Ho, W. Tao and J.M. Thomas, *J. Phys. Chem.*, **93**, 1112-1118 (1989).

[8] M. Cacciatore, M. Capitelli, S. De Benedictis, M. Dilonardo and C. Gorse, in « *Non Equilibrium Vibrational Kinetics* », *Topics Curr. Phys.*, **39**, 5 (1986).

Acknowledgement : The financial support of the European Community (COPERNICUS Nr. CIPA-CT94-0183) for this work is gratefully acknowledged.

Carburation of steel performed in an Ar-CH_4 microwave expanded plasma. Correlations with plasma characteristics.

M.J. Cinelli, I. Jauberteau, J.L. Jauberteau, J. Aubreton and A. Catherinot
URA 320 CNRS, UER des Sciences, 123 av. A. Thomas, F-87100 Limoges (France)

M. Cahoreau
URA 131 CNRS, UER des Sciences, SP2MI, Bd 3, Téléport 2, BP179, F-86960 Futuroscope (France)

Plasma steel carburizing is used from many years because of the reduced process time and pressure in the furnace relatively to conventional process [1]. Moreover it produces no toxic or dangerous gases. The hydrocarbon molecules as CH_4 are dissociated in the plasma and the active species are probably adsorbed on the surface of the workpiece where they dissociate into carbon and hydrogen.
Our purpose is to study the plasma steel carburizing in an Ar-CH_4 mixture containing very low CH_4 content, where simple radicals as $CH_{x<3}$ are preserved. These radicals are very reactive and could play a role in the transfer of carbon from the gas to the surface.

I. Experimental set-up

The experiments where performed in a reactor which consists of a fused silica tube where a microwave discharge is produced by means of a power supply SAIREM GMP 12 kE operating between 0 and 1200 W. The base pressure is maintained at 10^{-5} Pa. The plasma is expanded out of the discharge center into the stainless steel vessel until the substrate surface (Figure 1).
During carburizing process, the total pressure of 1.3 kPa in the vessel is kept constant using an Alcatel Roots blower pump (70-700 m^3h^{-1}) which maintains a gas drift velocity of about 5-100 ms^{-1}.
The activated carbon species produced in the plasma are selected by moving the substrate along the axis of the reactor.
The steel is exposed to a mixture of Ar-1%, 3 %, 5% CH_4. The substrate temperature, the microwave power and the pressure are respectively held at 900 C, 300 W and 1.33 kPa.
Metallography, hardness, and SIMS (Secondary Ions Mass Spectrometry) measurements are carried out to investigate the carburized steel.

II. Results and discussion

The plasma carburizing of a 16MC5 steel is carried out in an (Ar-5%CH_4) mixture under the conditions previously described.

A surface layer of about 150 μm depth and containing 0.6 % to 0.8 % of carbon is builded after 1 h.
An (Ar-3%CH_4) exposure leads to analogous structure which remains deeper than in the former case.
These tendencies are also evidenced by hardness measurements investigated on a 16NC6 steel exposed to increasing doses from 1% to 5 % of CH_4 in Ar. The hardness decrease with increasing amount of CH_4 in Ar.
These results confirm the conclusions of previous investigations on carbon films that CHx<3 species which play a role in the formation of high densities carbon phases, are mainly identified for low CH_4 concentrations (Figure 2) [2, 3].
The influence of the substrate position with respect to the center of the discharge on the carburization of the 16MC5 steel is reported in figure 3 and 4. In that case plasma carburizing is carried out in an (Ar-5%CH_4) mixture for an exposure time of 15 minutes duration.
The steel hardness strongly decreases from positions close to the discharge center to positions far in the post discharge (Figure 3).
SIMS results show a strong surface carbon enrichment as the steel is carburised near the plasma discharge compared to the steel simply heated in vacuum or thermochemically carburised without plasma where a strong surface decarburization is observed. The surface carbon signal strongly decreases from positions close to the discharge center to positions far in the postdischarge (Figure 4). This means that the most important source of carbon for carburization is mainly localised near the plasma discharge where simple species as $CH_{x<3}$ and C ions are preserved.

[1] W.L. Grube and J.G. Gay : Metallurgical Transactions A, 9A, 1421 (1978).
[2] M.J. Cinelli, L. Thomas, I. Jauberteau, J.L. Jauberteau, J. Aubreton, A. Catherinot : Proceedings of the International Symposium on Heat Transfert under Plasma Conditions, Ed P. Fauchais, Turquie (1994).
[3] L. Thomas, I. Jauberteau, J.L. Jauberteau, M.J. Cinelli, J. Aubreton, A. Catherinot : Appl. Phys. Lett. 68, 12 (1996).

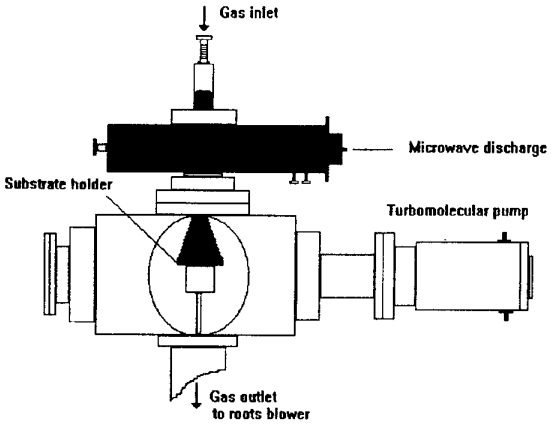

Figure 1 : Experimental set-up.

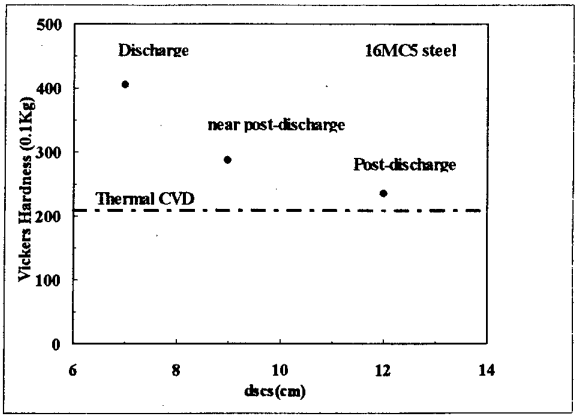

Figure 3 : Hardness measurements versus the length between the substrat and the discharge center (dscs).

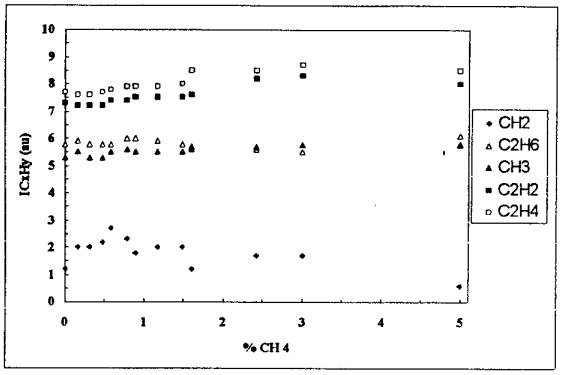

Figure 2 : mass spectrometer measurements of C_xH_y species versus the % CH_4.
Measurements are performed at 20 cm from the discharge center. The total pressure is 0.2 Torr and the power is 200 Watt.

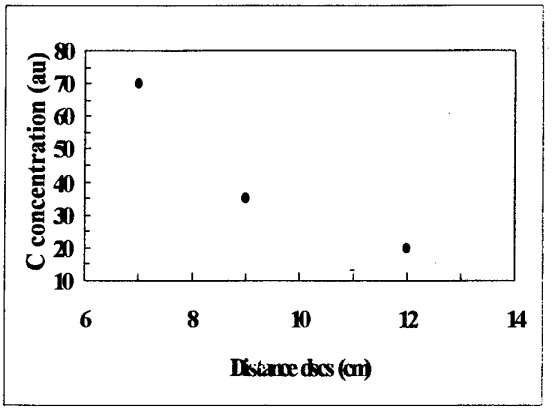

Figure 4 : Surface carbone concentration (SIMS measurement), versus the length between the substrat and the discharge center (dscs).

HIGH POWER RADIO FREQUENCY- AND MICROWAVE- DISCHARGES: COMPARISON UNDER A PLASMACHEMICAL TREATMENT OF HYDROGEN SULFIDE.

A.Bagautdinov, Yu.Eremenko, V.Jivotov, I.Kalachov, E.Konstantinov, A.Kosbagarov, S.Musinov, K.Overchuk, V.Rusanov, V.Zoller

Russian Research Centre "Kurchatov Institute"
Hydrogen Energy & Plasma Technology Institute
Kurchatov sqr.,123 182 Moscow,Russia

The investigation of energy characteristics for plasma chemical process of the treatment of hydrogen sulfide containing gases (H_2S+CO_2) with obtaining the synthesis gas (H_2+CO) and the sulfur as the products have been carried out at small industry plant .Two plasmatrons - microwave one (900 MGz, W= 300kW) and radio frequency one (440 kGz , W= 600 kW) - have used. The comparison of the process efficiency for both types of discharges has done.The influence of the gasodynamic parameters of discharges and the general macroscopic parameters of one (pressure,specific energy input) were investigated. The MCW discharge and HF discharge differ electrodynamically very much.The waveguide type of the discharge in microwave plasmotron and the inductive type of one in RF plasmotron,electric field distributions inside the discharges are different principally.The relations of "skin to radius" , of "wave length to radius" , of "emission frequency to collision frequency" are also different.At the same time the gasodynamic parameters of discharges (tube diameters, axial and linear gas velocities, gas flows Qin) and the general macroscopic parameters of one (pressures P and energy input E=W/Qin) could be chosen similar .

The general results.The hydrogen sulfide conversion degree (Qout/Qin) and the process energy expense A=W/Qout (Qout is the product flow) do not depend on the discharge type practically and are defined by the energy input value generally. The energy expense values are minimal (A is about 1.5 kW.h/ m^3 of synthesis gas + 1.4 kg of sulfur) under energy input about 0.2-0.3 kW.h/m^3 for both discharge types.The dependencies of A(E) and A(P) are similar for both discharge types too.The single difference , it is the constant low excess of energy expense for RF discharge (not more than 15 %) connected with the greater emission losses because of the greater temperatures in central area of RF discharge in comparison with microwave one.

So,the energy efficiency of the plasma chemical process of hydrogen sulfide dissociation is defined generally not by electrodynamic discharge properties but gasodynamic and energetic discharge parameters. More detailed investigation have shown that the general characteristics of the non-equilibrium plasma chemical process mechanism are connected with centrifugal effects in rotating gas and with inner recuperation of the energy giving out when realizing the sulfur recombination (S_2->S_8). Those effects take place at the discharge periphery and at the post-discharge area.

THE ROLE OF DISCHARGE PERIPHERY

The concentrations of hydrogen and carbon monoxide at the discharge periphery, were measured to make a specific conclusion about the process mechanism and to estimate the process product distributions at the after-discharge area. The product component concentrations are nearly linear with respect to the length along the discharge and reach such the values that can not be explained by usual diffusion and necessitate some non-equilibrium mechanisms refered above. Two region model was suggested for simulating the discharge. The model assumes that total gas flux after the discharge can be subdivided into two parts by convention.First - central "hot" flux and second - "cold" periphery flux.Processing experimental data has shown that hydrogen flux from periphery region must be about 40 % of the total hydrogen flux and CO flux from periphery region is about 20 % of the total CO flux .

Those experimental results lead to conclusion that commensurable parts of products emerge from "hot " central and "cold" periphery discharge regions.

THE ROLE OF POST-DISCHARGE AREA

Not only quenching of the obtained products but also the additional dissociation of the H_2S-CO_2 mixture, i.e. the additional synthesis-gas production,takes place at the post -discharge region. Radial distributions of gas temperature , of all the product concentrations and of gas flow velocity were measured by means of movable probes.This measurements allows to determine product compositions and energy expenses in different sections of post - discharge zone. It was established that the hydrogen concentration increases 1.4 times and CO concentration - 2.5 times in the distance between the outlet of plasmatron and the point laying 40 cm longer (at after-discharge area). The energy expenditures decreases accordingly.One of the possible reason for this fact is an effective inner recuperation of energy arising in the process of sulfur recombination (S_2 -> S_8).

THE PLASMA CATALYSIS EFFECT AT THE METHANE DISSOCIATION INTO HYDROGEN AND CARBON.

Babaritskiy A.I.[1], Baranov I.E.[1], Dyomkin S.A.[1], Etievant C.[2], Jivotov V.K.[1], Potapkin B.V.[1], Rusanov V.D.[1], Ryazantsev E.I.[1]

1 - RRC Kurchatov Institute, Russia, Moscow, 123182, Kurchatov sq.
2 - CIEE, France, Versailles, 78000, rue Saint-Charles, 44.

It is experimentally demonstrated the plasma catalysis influence on the endoergic process of the methane dissociation with the formation of hydrogen and carbon:

$$CH_4 = 2H_2 + C_{solid} \quad (1)$$

The plasma catalysis effect at this condition consists in the chemical process acceleration, due to the specific influence of the plasma active particles (ions, radicals) on the previously heated gas. The catalytic acceleration of the process is realized at the relatively low temperatures (about of 500 C), that allow to utilize the low potential heat.

The experimental installation consists of two blocks. The first is the gas heater. Gas (methane of expenditure 30÷250 ncm^3/s) at atmosphere pressure was heated up to temperature 400÷600 C. The heated gas entered the inlet of the plasmatron (the second block), in which the gas was exposureed by the pulse-periodic microwave discharge. The discharge transfered to the gas the additional energy input ε_{pl}, with the ratio ε_{pl} to the thermal energy input ε_{th} (due to the heater) being less than 20%.

The parameters registered experimentally were the follows: the gas temperature T at the inlet of the discharge zone; the methane expenditure Q; the microwave power W, absorbed by discharge; the gas product composition at the outlet of the plasmatron. The series of the experiments were performed with discharge and without one. The gas composition of products at the outlet of the plasmatron were analyzed and the increase of the methane conversion degree α due to the discharge influence was determined.

The experimental data and some calculated dependencies are presented in the Fig. 1.

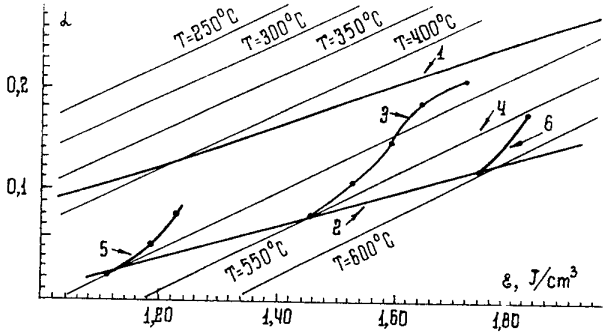

The methane conversion degree α into hydrogen and carbon (reaction (1)) lays off on the y-axis. The specific energy input ε in the system lays off on the x-axis. It corresponds to the thermal energy input ε_{th}, plus the energy input of the

discharge (if it exists):

$$\varepsilon = \varepsilon_{th} + \varepsilon_{pl}, \qquad (2)$$

where value $\varepsilon_{pl}=W/Q$, and the energy input ε_{th} is the function of the temperature T and the methane conversion degree α into hydrogen and carbon:

$$\varepsilon_{th}=\varepsilon_{th}(\alpha, T)=(1-\alpha)*\varepsilon_{CH_4}(T) + \alpha*\Sigma\varepsilon_{pr}(T)+\alpha*\Delta H(T_o) \qquad (3)$$

In (3) the first term is the thermocapasity energy input, due to the heating of the nonreacted part of methane from room temperature to T. The second term in (3) is the energy input, due to the heating of the process products from room temperature to T. The third term in (3) is the enthalpy of the methane dissociation reaction into products at the room temperature for the particular conversion degree α. The thermodynamic equilibrium calculation in coordinates α, ε_{th} is presented by the curve 1 in the Fig. 1. The experimental data under the thermal energy input only are presented by the curve 2 in the Fig. 1. The experimental data under heating the methane up to the temperature 550 C and with the microwave discharge of different power W (energy input ε is determined by (2)) are presented by the curve 3 in the Fig. 1. The comparison of the curves 1, 2, 3 in the Fig. 1 demonstrates evidently the great plasma catalysis effect.

Note, that the curve 4 in the Fig. 1 corresponds to the traditional thermocatalytic endoergic process, being performed at the constant temperature. The curve 4 is obtained by the transformation of the relation (3) relatively the value of the conversion degree α: $\alpha=F(\varepsilon_{th}, T)$, where the conversion degree α depends on energy input ε_{th}, and the temperature T is the parameter. This dependency for different temperatures T is presented by the series of parameter curves in the Fig. 1 (the temperature T=550 C corresponds to the curve 4). It is clear from the analysis of data in Fig. 1, that the plasma catalysis process leads to the gas temperature decrease due to the intensive energy consumption as a result of the reaction (1). It is principally important, that this temperature decrease doesn't influence on the plasma catalysis process efficiency, since the last one is not checked by the gas temperature, but by the electron temperature of the plasma. The plasma catalysis effect, being accompanied by the gas temperature decrease, was observed under different values of the previous heating of the gas too (the curves 5 and 6 corresponds to the temperatures of the initial heating 500 and 600 C).

The possible mechanisms of the acceleration of the methane conversion process in discharge were analyzed. It is shown, that the rational explanation of the observed effect is possible at the account of chain ion mechanism of the methane dissociation.

The Atmospheric Pressure Torch Discharge Plasma-Chemical Reactor

V. Kapička(a), M. Šícha(b), M. Klíma(a), M. Novák(c), M. Touš(b), P. Slavíček (a)

A. Brablec(a), L. Jastrabík(c), L. Soukup(c), J. Behnke(d), M. Tichý(b)

(a) Department of Physical Electronics, Faculty of Natural Science, Masaryk University, Kotlářská 2, 611 37 Brno, Czech Republic;

(b) Department of Electronics and Vacuum Physics, Faculty of Mathematics and Physics, Charles University, V Holešovičkách 2, 180 00 Prague 8, Czech Republic;

(c) Institute of Physic, Division of Optics, Academy of Sciences of the Czech Republic, Na Slovance, 2, 180 40 Prague 8, Czech Republic;

(d) Instiute of Physics, Ernst-Moritz-Arndt University, Domstrasse 10a, D-17487 Greifswald, Germany.

Introduction

In recent years there has been a considerable growing interest in the surface and coating technologies, in the treatments of various materials and in the deposition of thin films by the plasma-chemical processes. Various plasma-chemical systems (reactors) have been developed for the deposition of thin films which are able to deposit thin films on different materials and components. (For review see for example [1]). The disadvantage of most of these reactors is that they are not suitable for deposition of the thin films on the internal walls of cavities, holes and on substrates with complex shapes. Furthermore the reactors require a relatively low pressure of the working gas in the order of several Pa to several tens of Pa and therefore for some applications they are not suitable. For this reason it will be convenient to develop a plasma-reactor that will be able to work at higher pressures of the working gas closer or equal to atmospheric pressure.

In the present paper an attempt is made to develop the plasma-chemical reactor that will be able to work at higher pressures of the working gas up to atmospheric pressure. This reactor is based on the principle of the RF torch discharge.

The RF corona and the torch discharge

Generally the RF corona discharge is generated due to the strong intensity of the RF electric field in the neighbourhood of a sharp electrode edge where the discharge originates. This fact is confirmed by the spectrum of the discharge. Thus the main ionisation processes of neutral particles in the RF corona discharge are the ionisation collisions of the electrons accelerated in the strong electric field region.

When the RF power dissipated in the polyatomic working gas discharge increases then increases also the vibrational temperature of excited neutral molecules [2,3]. Due to increase of the vibrational temperature increases also the role of thermal ionisation of the excited neutral molecules (with higher vibrational temperature). This thermal ionisation causes the decrease of the electric field intensity in the neighbourhood of the electrode and as consequence decreases also the ionisation caused by accelerated electrons. In the case in which the difference between the electron temperature and the vibrational temperature of the excited neutral molecules is small then the corona discharge transits to the torch discharge. The transition between the corona and the torch discharge does not occur stepwise, but gradually [2,3]. At small RF power dissipated in discharge the discharge corresponds to the corona discharge while at higher power the torch discharge occurs. The plasma of the torch discharge in the monoatomic working gases differs from that burning in the polyatomic gas. The transfer of the electron energy to the neutral particles in this case has been studied in [4].

When the RF power which is dissipated in the torch discharge increases above a certain limit at which the temperature of the sharp electrode edge is so high that the electrode material is evaporated the plasma of the torch discharge is formed in the mixture of working gas and vapours of the evaporated electrode material. The properties of such torch discharge do not resemble those of a glow discharge but they are more like those of an arc discharge. For this reason it is necessary to consider such torch discharge as the arc torch discharge [3,5].

The plasma-chemical reactor with the arc torch discharge

The scheme of the experimental set up is shown in Fig 1. The powered electrode of the torch discharge is made from a thin pipe. The support for the electrode has been cooled by flowing water. The electrode is connected trough the matching unit to the RF generator the frequency of which was 13,56 MHz. The working gas which flows from the nozzle stabilises the arc torch discharge and well-defined plasma channel is created in the reactor chamber.

The pressure in the reactor chamber was maintained in the range of approx. 10^3 Pa up to atmospheric pressure. In such pressure range the powered electrode (thin pipe) cannot act as the hollow cathode [6] and only an edge of the electrode is involved in the discharge processes. This phenomenon is important from the point of view of the thin film deposition because only sputtered or evaporated material of the electrode edge is involved in the deposition processes of thin films.

The RF power dissipated in torch discharge has been adjusted for atmospheric pressure of the working gas above 100 W and so at the electrode edge the arc

torch discharge was created. At the lower pressure approx. 10^3 Pa the RF power which is necessary to create the torch discharge is in the order of several tens of watts.

Experiment

Experimentally the reactor with the torch arc discharge has been investigated by means of the system in which the active electrode has been created from the surgical needle. The photographic pictures have been scanned and computer processed to obtain lines corresponding to the equalight intensities (isointensities). An example of obtained results is seen in Fig.2. From the figure it is seen that in this case the velocity of the working gas flow is subsonic. The edge of the electrode is hot and due to this phenomenon the arc torch discharge is created in this case.

In order to increase the velocity of the working gas flow up to supersonic value the reactor chamber was continuously pumped by a rotary pump. In this case it was seen that near the electrode the velocity of the gas flow is supersonic and two barrel shock patterns have been observed. Furthermore the experimental results show that at this low pressure of the working gas inside the reactor chamber the RF power which is necessary for generation of the torch discharge is several tens of watts and it is roughly one order of magnitude smaller than in the torch discharge at the atmospheric pressure.

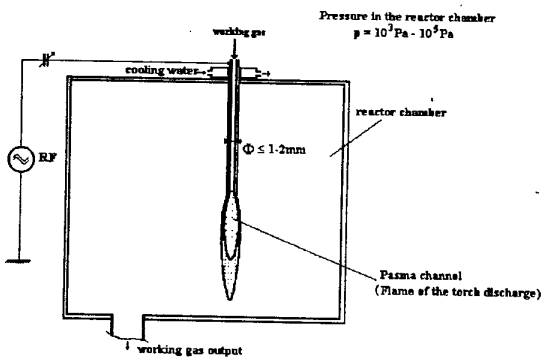

Fig. 1. The plasma-chemical ractor with torch discharge.

Discussion

The experimental results show that the plasma-chemical reactor which is based on the torch discharge is able to work in the high pressure region of the working gas up to atmospheric pressure. As it has been mentioned above in such pressure range the powered electrode (thin pipe) cannot act as the hollow cathode [6]. The experimental results show that in the investigated plasma-chemical reactors with torch discharge the thermal emission of electrons from the hot electrode edge should be taken into account and due to this phenomenon the arc torch discharge is created.

Acknowledgements

This work has been done in frame of the Association for Education, Research and Application in Plasma-Chemical Processes and was financially supported by grant 202/95/1222 of Grant Agency of Czech Republic and by project COST 515.50.

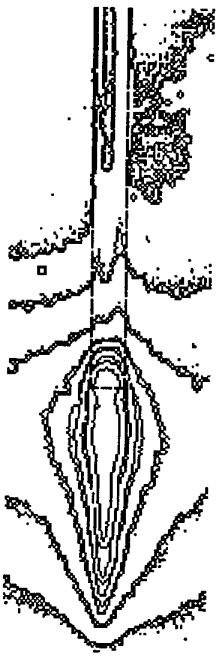

Fig.2. Curves of the equal light intensities (isointensities) obtained by scanning and consequent computer processing of the torch discharge photographic print (enlarged detail of the electrode edge). The outer contour of the electrode of the diameter 0,7 mm is illustrated by dashed line.

References

[1] L.Bárdoš.,Proc. Summer school of thin films, Skalský dvůr, (1988) 73.

[2] M.El Gammal, Proc. VIII ICPIG (Conrib papers) Vienna (1967) 237.

[3] V.Truneček, Proc. Conf. Unipolar Highfrequency Discharges, Brno (Folia Sci. Nat. University Brno, Physica) (1971) 3.

[4] J.Janča, Folia Fac. Sci .Nat. University Brno, 9 (1968) 31.

[5] Popov V., Stolov A. L., Učon. Zap. Kazan. Univerziteta, Kazan 113 (1953) 53 (in russian).

[6] H.I.Delcroix, H.Minoo, C.Popovici C., Proc. Int. Conf. Hollow Cathode Discharge
Appl. (1971) 18.

The RF Plasma-Chemical Reactor with the System of Multi-Hollow-Cathodes for the Surface and Coating Technologies.

Z. Hubička[a], M.Šícha[b], M. Novák[a], L. Soukup[a], L. Jastrabík[a], K. Kapoun[c], M. Šerý[c], V. Kapička[d]

[a] Institute of Physics, Division of Optics, Academy of Sciences of Czech Republic, Na Slovance 2, 180 40 Prague 8, Czech Republic
[b] Department of Electronics and Vacuum Physics, Faculty of Mathematics and Physics, Charles University, V Holešovičkách 2, 180 00 Prague 8, Czech Republic
[c] Department of Physics, College of Education, South Bohemia University, Jeronýmova 10, 371 15 České Budějovice, Czech Republic.
[d] Department of Physical Electronics, Faculty of Natural Science, Masaryk University, Kotlářská 2, 611 37 Brno, Czech Republic;

Introduction

In recent years there have been a considerable growing interest in the applications of plasma-chemical processes in the surface and coating technologies, treatments of various materials and deposition of thin films. The reason is that by means of plasma-chemical technologies it is possible to replace classical technologies that often have the harmful influence on the environment. Furthermore the plasma-chemical devices, reactors, can be used in novel applications. For example the surface treatment of polymers and materials that could be utilised in the medicine, ecological programs and biophysics. Recently for the deposition of thin films from the various materials different plasma-chemical reactors have been developed. The disadvantage of the most of them is that they are not suitable for deposition of thin films on the internal walls of cavities, holes and complex shapes of hollow substrates. For the novel applications it is necessary to develop the plasma-chemical reactor that should be able to deposit the composite thin films and multilayer structures.

The RF low pressure plasma-chemical reactors with one hollow cathode can in particular cases fulfil the mentioned requirements [1,2] (For review see for example [3] or [4]). In the plasma-chemical reactors with hollow cathode the working gas flows through the hollow cathode that acts simultaneously as a nozzle for the working gas. According to the working gas flow in the reactor chamber these reactors can be divided into two groups: The systems with the supersonic gas flow (plasma-jet reactor, RPJ) and with the subsonic one.

The results that have been obtained in the deposition of thin films by means of RPJ reactors with one hollow cathode [5,6] indicate, that the plasma-chemical reactor with multi-hollow-cathode system should be able to deposit the composite thin films and multilayer structures onto internal walls of cavities, tubes and on the components with complicated shapes. It can be also expected that by means of this system it will be able to deposit the composite thin films and multilayer structures from various materials in dependence on the sort of working gases and nozzles material.

In the present paper an attempt has been made to develop the plasma-chemical reactor with multi-hollow-cathode system.

The multi-hollow-cathode plasma-chemical reactor

In the present paper for sake of simplicity we developed the reactor with only two hollow cathodes. The schematic drawing of the experimental set up used in the present paper is shown in Fig. 1. The working gases that flow through both nozzles were adjusted in such a manner that flows from both nozzles are supersonic. Both nozzles are connected to the different RF generators (in Fig.1 generator RF1 and RF2). By means of these generators two plasma jets are created inside reactor chamber in the same way as in the one hollow cathode reactor. The advantage of such experimental set up is that both plasma-jet channels are created by independent sources and the working conditions of each hollow cathode discharge and primary plasma-jets can be independently adjusted.

The substrate is isolated from the metallic wall of the reactor chamber and it is connected with the output of the third RF generator (in Fig 1. RF3). Within certain limits by means of the output voltage of this generator it is possible to adjust the self-bias voltage of the substrate.

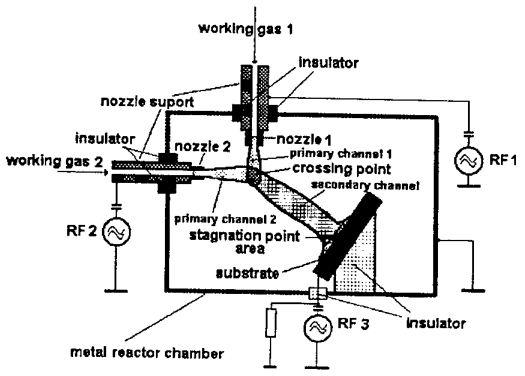

Fig 1. The scheme of the plasma-chemical reactor with the two-hollow-cathode system.

The plasma-chemical processes in the plasma channels.

In the primary plasma channels due to hollow cathode discharges there are both the neutral, excited and ionised particles of the working gas and the particles sputtered from nozzle surface. The plasma-chemical reactions between the mentioned particles take place in the hollow cathodes, in the primary plasma channels. In the crossing point, in the secondary plasma channel and in the stagnation point the intensive plasma-chemical reactions between the particles from both primary channels also could be expected. The scheme of the particles and the interactions between them inside the reactor with the two-hollow-cathode system is seen in Fig. 2

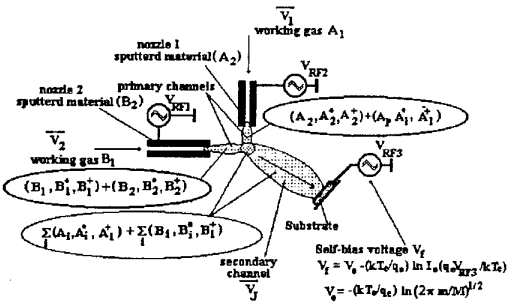

Fig. 2

As an example of plasma-chemical reactions the plasma-chemical ion-molecule reaction of ions from the first primary channel (A^+) with the neutral molecules from the second primary channel (B_n) inside the secondary plasma channel is presented here in more detail. The intensity of the particular plasma-chemical ion-molecular reaction of ions from the first primary channel (A^+) with the neutral molecules from the second primary channel (B_n) can be estimated under assumption that in the supersonic secondary channel the plasma is approximately in the condition of the flowing afterglow. The density of the neutral molecules $[B_n]$ is customary several orders of magnitude higher with respect to the density of ions $[A^+]$ so that the variation of the density $[B_n]$ due to reactions with ions (A^+) can be in our estimation neglected. Then for the variation of the ions density $[A^+]$ along the secondary channel can be written (diffusion losses do not play substantial role):

$$\frac{d\left[A^+(t)\right]}{dt} \approx -k_r\left[A^+(t)\right]\left[B_n\right] \qquad (1)$$

where $[A^+]$ and $[B_n]$ are the densities of ions and molecules respectively, k_r is the rate coefficient of the ion-molecule reaction between A^+ and B_n.
The solution of the equation (1) is:

$$\left[A^+(t)\right] \approx \left[A^+(0)\right] \exp\left\{-k_r\left[B_n\right]t\right\} \qquad (2)$$

where t is the reaction time and $[A^+(0)]$ is the density of the ions in the crossing point.

Because the plasma in the secondary channel is flowing with drift velocity V_D for the reaction time t can be approximately written:

$$t \approx \frac{x}{V_D} \qquad (3)$$

where x is distance from the crossing point where the reaction time is t.
By means of equation (2) it is possible to determine the decay of the ion density $[A^+]$ due to reactions with molecules (B_n) and from obtained results roughly estimate the intensity of the investigated ion molecular reactions. For example if we assume that the rate coefficient k_i of the investigated ion-molecule reaction is 10^{-9} cm^3s^{-1}, the density of the neutral molecules $[B_n]$ is between 10^{14}-10^{16} cm^{-3}, then the density of the ions $[A^+]$ in the secondary channel decreases downto 1% of the value at the beginning of the channel $[A^+(0)]$ after the reaction time $t \approx$ 0,5-50 μsec. For supersonic velocity of the particles in the secondary plasma channel the drift velocity is approx. $V_D \approx 3.3\ 10^4$ $cm.s^{-1}$. If we assume that the distance between substrate and crossing point is in the region of l≈2-3 cm the drift time of the particles in the secondary channel order of several tens till hundred μsec. For the exact calculations of the plasma-chemical reaction intensity along the channel it is necessary to take into account the recombination, the radial diffusion of the ions A^+ and also the variation of the drift velocity in the supersonic channel. Nevertheless from above presented simplified consideration it is seen that the density of the reaction product at the end of the secondary channel is of the same order of magnitude as the primary ion $[A^+(0)]$ density. It should be noted that the plasma-chemical processes inside the stagnation point also contribute to chemical activity inside the reactor.

Acknowledgements

This work has been done in frame of the Association for Education, Research and Application of the Plasma-Chemical Processes and was particularly financially supported by grant 202/95/1222 of Grant Agency of Czech Republic and by project COST 515.50

References

[1] L.Bardoš, V.Dušek, Thin solid films 159(1988) 256
[2] M.Šícha, L.Bárdoš, M.Tichý, L.Soukup, L.Jastrabík, H.Baránková, R.J.Soukup, J.Touš, Contrib.Plasma Phys. 34 (1994) 749
[3] L.Bárdoš, Proc.XXI ICPIG, Bochum Vol III(993)98
[4] L.Soukup, M.Šícha, L.Jastrabík, M.Novák, Proc. XXII ICPIG, Hoboken (1995) 299
[5] L.Soukup,V.Peřina,L.Jastrabík,M.Šícha,P. Pokorný, R.J. Soukup, M.Novák,J.Zemek, Surface and Coating Technology, (1996) 280
[6] L.Soukup,L.Jastrabík,M.Šícha,Z.Hubička,M.Novák, H.Šíchová,V.Valvoda, The deposition of the Cu_3N thin films by means of hollow cathode plasma-chemical reactor. (to be published)

Monoatomic Ion Rich Plasmas for Ion Implantation by Plasma Immersion : Ion Production Mechanisms in Distributed ECR Discharges

F. Le Coeur, Y. Arnal, R. Burke, and J. Pelletier
Laboratoire d'Electrostatique et de Matériaux Diélectriques, UMR C5517, CNRS & Université Joseph Fourier
BP 166, 38042 Grenoble Cedex 9, France

1. Introduction

In conventional ion implantation, mass separation is realized to select the ions to be implanted and to avoid the implantation of impurities. In contrast, to alleviate the implantation process, plasma-based ion implantation (PBII) does not apply mass selection. Therefore, it is of high interest to know the ion composition of the plasma to be able to predict the implantation profile. In addition, as the implanted ion depth range for monoatomic ions is much larger than for molecular ions of equal energy, plasmas with a high fraction of monoatomic ions are very attractive for applications in the high energy range.

2. Experimental

The chamber of our PBII reactor is a 60 cm diameter, 70 cm high cylinder. On a 50 cm diameter circle, the inside of the lateral wall is covered with an array of 24 tubular magnets, 2.45 GHz microwave power feeds, and wave propagators. Fast electrons, trapped in the magnetic field, oscillate along the field lines between the opposite poles of each magnet, and drift along the length of those magnets [1]. When the electrons reach the end of a magnet, they swing into the opposite lobe and continue their itinerary of plasma production. Hence, each individual magnet acts as a three-dimensional magnetron structure. The entire lateral wall of the cylinder, in excess of one square meter, constitutes a peripheral plasma source that produces a uniform distributed plasma (UDP) throughout the chamber, apt to treat the objects fastened onto the bottom platen. The platen has a 10 cm useful diameter, and may accomodate flat wafers, pipes, or objects of arbitrary form.

The 45 kV, 5 A high voltage pulse generator used in this study is of the conventional type [2]. The system includes a 60 kV, 2 mA high voltage power supply, connected to a 27 nF capacitor through a charging resistor of 200 kΩ. The high voltage pulse is obtained via the partial discharge of the capacitor by means of a tetrode high voltage tube, which switches the positive electrode of the capacitor to ground. The pulse duration can reach 100 μs with a repetition rate of up to 10 Hz.

The top cover on the PBII reactor can be replaced by a window, or by a support for electrostatic probes or a mass spectrometer. The plasma parameters (plasma potential V_p, floating potential V_f, electron temperature T_e, electron and ion densities n_e and n_i) were determined by analyzing the I(V) curves obtained with a cylindrical electrostatic probe.

The ion composition of the UDP plasmas was measured by quadrupole mass spectrometry. The mass spectrometer with its differential pumping system replaces the top cover of the PBII reactor. The quadrupole is separated from the UDP plasma by a 90° molybdenum cone. The base diameter of the cone is 10 cm, and ions are sampled from the plasma through a 1 mm diameter orifice at the cone tip. The quadrupole is equipped with a high efficiency electron impact source, with an extractor and a three-element ion lens. An additional cylindrical ion inlet lens is placed between the sampling cone and the ion source. It is possible to bias the quadrupole power supply by ± 10 V with respect to ground.

For plasma composition measurements, the sampling cone was grounded. Thus, the ions are driven into the mass spectrometer by the plasma potential. To obtain quantitative measurements, the quadrupole was run under high transmission, low resolution conditions. To obtain wide flat peaks, without notches, it was necessary to ground the inlet ion lens as well as the ion source elements. Then, it was feasible to obtain flat rectangular peaks by slightly retarding the ions during their trajectory in the quadrupole, through adjustment of the quadrupole bias with respect to the plasma potential.

3. Results and interpretation

The plasma parameters have been measured with a movable Langmuir probe in nitrogen, oxygen and hydrogen UDP plasmas. The radial and axial evolution of the plasma characteristics shows that the plasma is uniform radially, but exhibits a decrease in density at both the top and the bottom of the reactor, due to the absence of magnetic field confinement there. The plasma parameters (Table I) have been obtained at a pressure of 1 mtorr, and with 1.4 kW (N_2, O_2) or 1.6 kW (H_2) microwave input power distributed over the 24 microwave applicators. In nitrogen, oxygen and

hydrogen, the plasma and floating potentials are close to the ground potential. In such UDP's the electron temperature is rather low, and the ion densities are a few times 10^{10} cm^{-3}.

	Nitrogen	Oxygen	Hydrogen
V_p	10 V	9,5 V	6,4 V
V_f	7 V	5,7 V	4,3 V
T_e	1,2 eV	1,3 eV	0,95 eV
n^+	2×10^{10} cm^{-3}	$1,4 \times 10^{10}$ cm^{-3}	$4,5 \times 10^{9}$ cm^{-3}

Table I

The ion composition was determined by quadrupole mass spectrometry. The main result is that the atomic ions N^+, O^+, H^+ dominate over the molecular ions N_2^+, O_2^+, (H_2^+, H_3^+) by a factor of about three. That ratio depends only slightly on pressure in the 0.2-2 mtorr range.

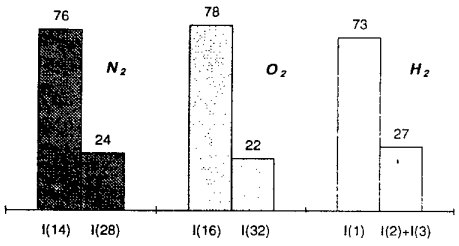

This result differs from what is observed in a classical electron impact ion source, or in less energetic plasmas. Here, we restrict the discussion to the phenomena that occur in the nitrogen UDP. Usually, the molecular ion N_2^+ prevails over the atomic ion N^+ in a ratio of ten to one or five to one [3]. This is due to the ratio of the cross-sections for the two ion formation processes by electron impact in the 50-100 eV electron energy range :

$$e^- + N_2 \longrightarrow N_2^+ + 2e^- \quad (1)$$
$$e^- + N_2 \longrightarrow N^+ + N + 2e^- \quad (2)$$

The reason why the atomic N^+ ion prevails in the UDP plasma cannot be attributed to the charge transfer from the molecular ion N_2^+ via the reaction

$$N_2^+ + N \longrightarrow N_2 + N^+ \quad (3)$$

Atomic nitrogen is likely to be an important constituent in the N_2 UDP plasma. However, in spite of the 1 eV exothermicity of this reaction, its rate coefficient has a low upper limit of 10^{-11} $molecule^{-1}$ cm^3 s^{-1} [4], so that the contribution of this reaction to the N^+ population can be neglected.

Dissociative ion-electron recombination (rate coefficient: 2.7 10^{-7} $molecule^{-1}$ cm^3 s^{-1} [5])

$$N_2^+ + e^- \longrightarrow 2\,N \quad (4)$$

is also too slow under our plasma density conditions to play a possible rôle in the (apparent) N_2^+ decrease. The only way to explain the N^+ overabundance is to take into account the electron impact dissociation of N_2^+ :

$$N_2^+ + e^- \longrightarrow N^+ + N + e^- \quad (5)$$

In the 50-100 eV electron energy range the cross-section for this process is roughly ten times larger than that for process (1) [6]. The importance of this molecular ion dissociation process is presumably linked to the trapping of the N_2^+ ions in the magnetic field region where they are produced, i.e. in the region where fast electrons are trapped [7]. Thus, a high dissociation rate of N_2^+ ions is easily obtained. Of course, ionization of the abundant N atoms :

$$N + e^- \longrightarrow N^+ + 2e^- \quad (6)$$

may also contribute to N^+ formation.

4 Conclusion

The uniform distributed plasma (UDP) is a powerful plasma source, which favors monoatomic ion over diatomic or molecular ion production. The high monoatomic to diatomic ion ratio in the UDP plasma will favor the effectiveness of the PBII process.

Acknowledgements

We thank J. Cocagne for technical assistance. This work is supported by a grant from the Région Rhône Alpes, France. F. Le Coeur acknowledges the financial assistance of the Région Rhône-Alpes for a doctoral fellowship.

References

[1] T. Lagarde, J. Pelletier and Y. Arnal, Plasma Sources Sci. Technol. **6** (1997) 1.
[2] J. Brutscher, Rev Sci. Instrum. **67** (1996) 2621.
[3] B.Y. Tang, R.P. Fetherston, M. Shamim, R.A. Breun, A. Chen, and J.R. Conrad, J. Appl. Phys. **73** (1993) 4176.
[4] E.E. Ferguson, Adv. Electron. Electron Phys. **24** (1968) 1.
[5] W.H. Kasner and M.A. Biondi, Phys. Rev. **A 137** (1965) 317.
[6] B. Van Zyl, G.H. Dunn, Phys. Rev. **163** (1967) 43.
[7] T. Lagarde, Dr Sc Thesis, Université Paris XI Orsay (1994).

Nitrogen Dissociation in a N_2-H_2 Glow Discharge

J. Amorim[1], J. Lino[1], J. Thomaz Jr[1], J. Loureiro[2], M. Pinheiro[2],G. Baravian[3], and G. Sultan[3].

[1] Depto de Física, Instituto Tecnológico de Aeronáutica - 12225-800 S. J. Campos - Brazil

[2] Centro de Electrodinâmica da Universidade Técnica de Lisboa, Instituto Superior Técnico, 1096 Lisboa Codex Portugal

[3] Laboratoire de Physique des Gaz et des Plasmas, Univ. Paris Sud, 91405 Orsay - Cedex France

The study of plasmas containing N_2 molecules currently motivates considerable attention as these mixtures are commonly employed for surface treatment. Nitrogen atoms are one of the most important species in metal surface nitriding, so that the study of N atom production and loss is of great interest. The theoretical model is based on the solution to the homogeneous Boltzmann equation for electrons coupled to a system of rate balance equations for the vibrational levels N_2 (X,v) and H_2 (X,v) for typical operating conditions of a low pressure, moderate current N_2-H_2 discharge[1]. The Boltzmann equation includes both inelastic and superelastic e-V collisions, while the rate equations system for the vibrational levels takes into account e-V, V-V and V-T exchanges as well as processes of dissociation, atom reassociation and vibrational deactivation on the wall of the container. In the calculations developed for this work we have considered the variations of the reduced electric field E/N, as a function of hydrogen concentration in the mixture[2]. The model considers that, under steady state conditions, the population of N atoms[3] are obtained by equating the production and loss mechanisms. The total dissociation rate, $\nu_{diss.}$, includes both dissociation by electron impact and dissociation by V-V energy exchanges. Only single quantum transitions are considered for the terms V-V, which are the most likely ones. The dissociation by a purely vibrational mechanism is assumed as a transition from the last bound level v=45 to a pseudo-level in the continuum(v=46), according to the following reactions:

$$N_2(X, v) + N_2(X, v=45) \rightarrow N_2(X, v-1) + N + N \quad (1)$$

and

$$N_2 + N_2(X, v=45) \rightarrow N_2 + N + N \quad (2)$$

The corresponding dissociation rate for this vibrational mechanism is given by:

$$\nu^{V}_{diss} = [N]^2\{\delta_{45}\sum_{v=1}^{45}\delta_v P^{v,v-1}_{45,46} + \delta_{45} P_{45,46}\} \quad (3)$$

where $P^{v,v-1}_{45,46}$ and $P_{45,46}$ denote the relevant V-V and V-T rate coefficients involving the last bound vibrational level and the pseudo-level into which dissociation is assumed to occur. The dissociation by electron impact $\nu^{e}_{diss.}$ is calculated by:

$$\nu^{e}_{diss} = n_e N_2 \langle \delta^{diss}_X \sqrt{\frac{2u}{m}} \rangle \quad (4)$$

where the quantity in brackets < > is rate coefficient for dissociation (the brackets mean the average over the electron energy distribution), δ^{diss}_X is the cross section for dissociation by electron impact, m is the electron mass, n_e is the electron density and u is the electron energy. In what concerns the destruction of N atoms, the mechanisms considered in this work are:

(i) three-body gas phase atom reassociation:

$$N_2+N(^4S) +N(^4S)\rightarrow N_2+N_2(A^3\Sigma_u^+, B^3\Pi_g, a^1\Sigma_u^+) \quad (5)$$

(ii) heterogeneous atom recombination on the wall:

$$N(^4S) \rightarrow \frac{1}{2}N_2 \quad (6)$$

(iii) destruction by electron impact:

$$e + N(^4S) \rightarrow e + N(^2D, ^2P) \quad (7)$$

(iv) collision with metastable molecules $N_2(A^3\Sigma_u^+)$

$$N_2(A^3\Sigma_u^+) + N(^4S) \rightarrow N_2(X) + N(^2D, ^2P) \quad (8)$$

The experimental apparatus was already described in details elsewhere [4]. Briefly, the gas flows in a Pyrex discharge tube of 1.6 cm i.d. at gas pressure of 2.0 torr and discharge current of 80 mA. The Laser Induced Fluorescence (LIF) diagnostics are performed by using a tunable (10Hz recurrence frequency, 7ns pulse duration)

[1] Supported by CNPq and FAPESP (Brazil).

pulsed laser, DATACHROM 5000 from Quantel The detection of LIF is obtained by imaging the interaction region onto the entrance slit of Jobin-Yvon HR640 monochromator. In atom LIF detection, two laser photons pumped ground state N atoms at λ=211 nm with fluorescence at λ=869 nm.

The density of N atoms as a function of de hydrogen concentration in the mixture is presented in figure 1. The concentration of nitrogen atoms increase when the gas mixture composition is varied N_2 - x%H_2 (0 < x < 15). The experimental results show that the N atoms number densities increase until 1%H_2 and decrease for the larger concentrations (experimental points are normalized to theoretical ones at N_2 pure discharge). When small %H_2 is added to the mixture, the high energy tail of the electron energy distribution function (EEDF) is enhanced (by the increase of the electric field) as compared to that in pure N_2 [1,2]. This change in the EEDF leads to an augmentation in the dissociation rates given by V-V and electron impact mechanisms. In the figure 1 the theoretical results are represented for three different conditions: the results in curve A were obtained for a metastable normalized density ($Q_a = \frac{N_2(A^3\Sigma_u^+)}{N_2}$) of 1.0 x 10^{-4} and a N atom wall reassociation probability γ_r = 3.2 x 10^{-6}. The curve B show that an increase in Q_a (5.0x10^{-3}) results in a lower density of atoms. The effect of augmentation in the γ_r value is shown in curve C.

The depopulation rates of N(^{4}S) atoms are presented in figure 2. The results reveal the importance of destruction of N(^{4}S) atoms by collision with metastable $N_2(A^3\Sigma_u^+)$ and by electron impact. These loss mechanisms are by far more effective than reassociation on the wall and by three-body collision.

We have presented results from a combined experimental and modeling study of N_2 dissociation mechanisms in a N_2-H_2 glow discharge positive column. We have shown that under the present experimental conditions, the value of Q_a is important in order to determine the N atom density. The influence of γ_r is less effective (see curve C in figure 2), because the coefficient for this reaction is two orders of magnitude lower than the coefficient for destruction by collision with triplet metastable state $N_2(A^3\Sigma_u^+)$.

References

[1] J. Loureiro and A. Ricard: J. Phys. D: Apply. Phys. 26 (1993), 163-176;

[2] R. Nagpal and A. Garscadden: Contrib. Plasma Phys. (35), 4-5 (1995), 301-330;

[3] J. Loureiro: Chem. Phys. 157 (1991), 157-168;

[4] S. Bockel, J. Amorim, G. Baravian, A. Ricard, and P. Stratil: Plasmas Sources Sci. Technol 5 (1996), 1-6.

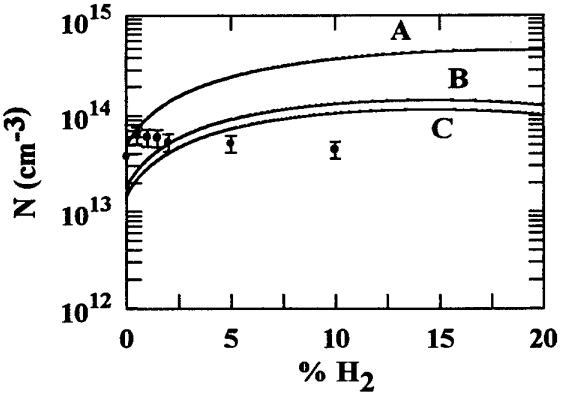

Fig. 1: Atoms density as a function of H_2 concentration in the mixture. (A): Q_a=1,0 x10^{-4} and γ_r=3,0x10^{-6}; (B): Q_a=5,0 x 10^{-3} and γ_r =3,0 x 10^{-6}; (C): Q_a=1,0x10^{-4} and γ_r=3,0x10^{-3}; • LIF experiments.

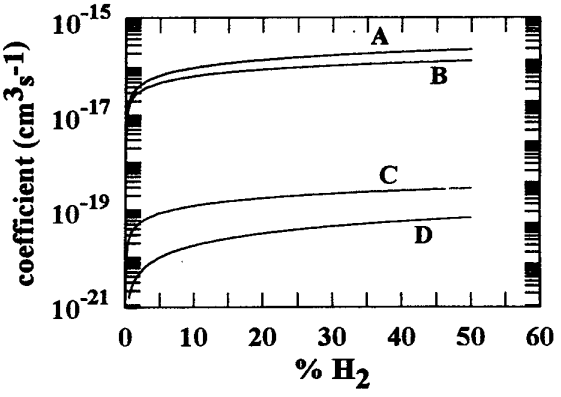

Fig. 2: Atoms depopulating rates as a function of %H_2. (A): destruction by electron impact, (B): destruction by collision with metastable N_2 ($A^3\Sigma_u^+$), (C) reassociation at the wall, (D): three body reassociation.

On forecasting materials properties obtained under ion bombardment conditions

A.A.Katkalo, A.I.Lyapin
The Mogilev Mechanical Engineering Institute
Lenin str.,70 , Mogilev , 212005 , Belarus

1. Introduction

One of the industrial applications of the processes taking place in gas discharge is surface treatment of materials in the presence of acce - lerating potential on the substrate , i.e. at ionic bombardment conditions. This is due to the fact that the material irradiation by the particles of keV energies substantially influences structure , electrical , magnetic , optical , mechanical and other properties of the materials surface layer. The method under consideration for obtaining materials with required properties needs a detail study of the implanted layer formation process.

The physical experiment is rather expensive. That is why preliminary theoretical calculations undoubtedly become actual. At present the sufficiently full picture of processes stipulated by the irradiation damage of material during it's ion implantation is composed. We have created a computer model which allows to investigate dynamics of structural transformation in an implanted layer. This model is based on general principles and contains modern theoretical and experimental data. In terms of cluster dynamics a system of integral-differential equations describing the dynamics of ion-stimulated processes in the implanted layer has been obtained. The parameters of which the system of equations is composed , are connected with the irradiation parameters (energy , intensity , temperature , dose) and the characteristics of the irradiated material (structure , the energy of atom binding and displacement , diffusion and sputtering coefficient and other parameters).

2. Results and discussion

Some calculation results of the probability of the occurrence of initial crystal phase I , amorphous phase A , intermediate phase S and new (impurity) crystal phase N in an implanted layer are given below. Calculation results are given for the implanted layer depth according Rp - average ion projective run in the material, ion energy E = 3 keV and irradiation intensity J = 5E+18 , m^{-2}.

It should be noted that initial conditions for the calculations are based on reliable experimental results. The dependence of I , A , S , and N on irradiation dose D under substrate temperature T = 300K are shown in Figure 1.

Figure 1. The probability of the occurrence of I , A , S , N as the irradiation dose function for B -> In combination. T=300K

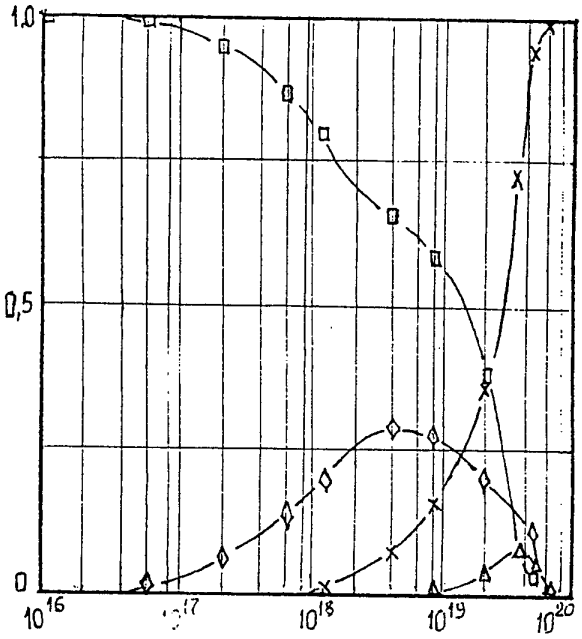

□ - initial crystal phase (I) ;
× - amorphous phase (A) ;
◊ - intermediate phase (S) ;
Δ - new crystal phase (N) ;

Figure 1 shows : from the beginning of irradiation the cored solid solution arises and develops. As diffusive processes are suppressed at the present temperature , the amorphous phase arises and progresses. During the following dose increasing the phase proportion changes to amorphous phase. The implanted layer becomes completely amorphous from D = 5E+19, m^{-2}. This result coincides with experimental data closely [1,2]. The fact of precipitates arising under the present irradiation conditions is very interesting in our opinion. The indicated result does not take place in the experiment at present. Possibly it is due to the fact that this effect arises in the narrow field of irradiation dose values. Figure 2 shows the dependence of I , A , S and N on irradiation dose D under substrate temperature T = 500K.

Figure 2. The probability of the occurrence of I , A , S and N as the irradiation dose function for combination B -> Ni. T = 500K.

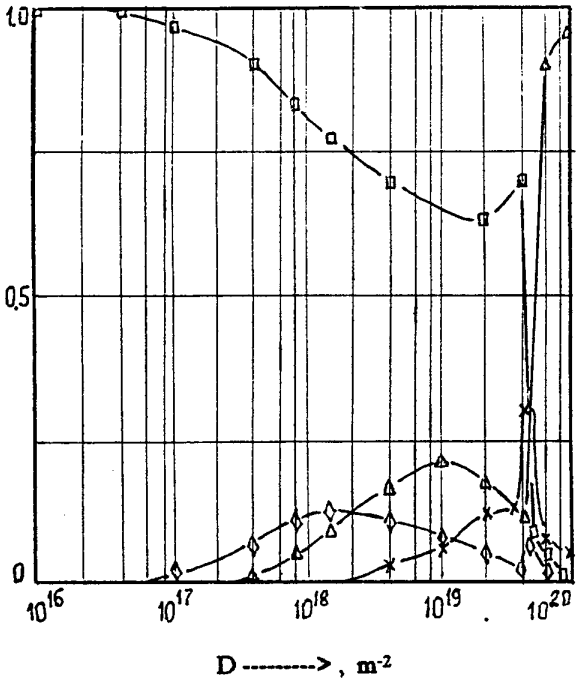

In this case initial crystallinity remains safety up to the dose value D = 4E+19 ,m^{-2}. It restorates because of diffusive processes. The proportion between S , A and N phases changes continuously during irradiation process in the dose interval D = (0.6 -4)E+19 , m^{-2}. The catastrophically destruction of initial crystallinity takes place from the dose value D =4E+19 , m^{-2}.

We can explain our results in the following way. Phase composition of the implanted layer is formed as a result of the development of the two rival processes - the process of atom mixing at the initial stage of irradiation (during atom penetration) and the process of atom segregation under the effect of chemical forces in the stage that follows (for the time between atoms hitting).The new phase (N) is constantly being destroyed during irradiation process. Dynamic equilibrium between phases in the layer is created arranges depending on irradiation conditions and thermo-chemical parameters.

Besides our calculations show that ion bombardment consequences depend on the irradiation intensity , substrate heat - conducting properties and the presence of temperature gradient in the substrate bulk. It is important that the structural and phase transformation dynamics in the implanted layer is determined by the velocity of the temperature increasing. As follows from it , at equal intensity , dose and temperature values the irradiation result must depend on the substrate size. This result differs from existing data which notes that irradiation of thick and thin specimens gives identical results.

3. Conclusion

Our results do not contradict the experimental data. These calculations may be used directly to plan the physical experiments. The model under consideration allows a ratio between crystal and amorphous phases to be calculated in the implanted layer under the irradiation conditions chosen or , on the other hand , it enables the required for it irradiation conditions to be determined using the given amorphism of the irradiated material. In addition to above mentioned possibility our model allows to investigate dynamics of structural transformation during nonisothermal implantation i.e. when specimen temperature increases in the course of irradiation process.

Finally, it should be noted that no other of model (except ours) can give suitable results if dose and temperature values change in wide range.

4. References

[1] L. Thomo, J.C. Pivin, F. Pons e.a.: Ibid , B19/20,(1987), 564

[2] A.I. Lyapin : ICPIG XXII , 2 , (1995), 200

Carbonitride hydrogenated deposition using various precursors

L. Ion, D. Marty-Dessus, B. Held, M. Trinquecoste*, P. Delhaès*
Laboratoire d'Electronique des Gaz et des Plasmas. IPRA- UPPA. Avenue de l'Université. 64000 Pau
* Centre de Recherche Paul Pascal. 33400 Pessac

1. Introduction

Theoretical papers [1,2] proposed hypothetical existence of a metastable phase with stoichiometric formula C_3N_4, structurally analogous to the β-Si_3N_4 phase. Our previous studies [3] have permitted to get an a:C-H(N) film with 14% nitrogen rate in a CH_4(0.2)-N_2(0.4)-Ar(0.4) RF discharge (P = 200 W, p = 1 mbar, total flow rate = 5l/h). Preliminary studies [4] concerning correlations between gaseous phase mechanisms and film characteristics suggest that the principal precursors of the deposition process seem to be the $C_xH_yN_z$ radicals (in particular CH_3N).

2. Experimental set-up

The experimental set-up used for PECVD method is a RF discharge (figure 1) obtained between two external electrodes surrounding a Pyrex reactor (a coil connected to the generator via a matching network and a metallic grounded electrode).

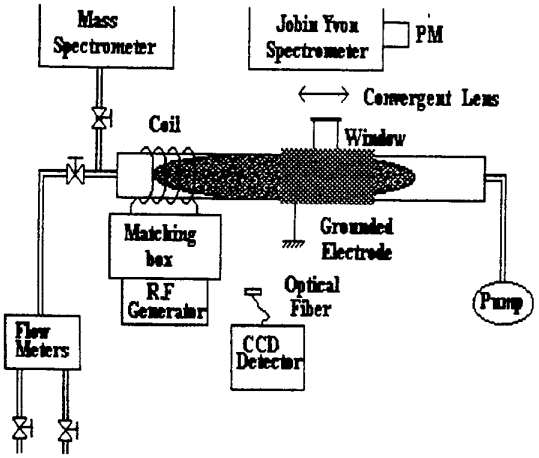

Fig.1: Experimental set-up

Light emission has been analysed using a Jobin Yvon monochromator with a high resolution and a CCD detector equipped with an optical fiber. A VG quadrupole gas analyser has permitted to detect stable species collected in different reactor regions. A substrate with or without external cooling and polarisation may be introduced perpendicularly in the gaseous flow.

3. Experimental analysis

Because of a strong asymmetric character of the discharge, the efficiency deposition in a CH_4-N_2-Ar mixture is limited by the methane destruction in the coil region and the formation of an a:CH film on the reactor walls.
In order to create a higher concentration of the carbonitride species in the gaseous phase, different methane and nitrogen partial pressures or other precursors were used in the same experimental conditions : CH_4-NH_3 (in the Ar or He presence), $C_6H_5N(CH_3)_2$, C_5H_5N and CH_3NH_2.
Principal dissociation and recombination mechanisms were analysed by optical emission spectroscopy (OES) and mass spectrometry (MS).
The most part of these diagnostics were associated with infrared spectroscopy (IRS) and chemical composition analyses of a:C-H(N) films deposited on SiO_2 or Zr substrates (with or without external cooling).
Oxygen and argon plasmas are created after deposition and the emission intensities ratios of the excited species obtained by sputtering inform on relative implantation rate evolution of C, N and H.
In the grounded electrode region, the mean rate deposition is directly estimated by mass measurements and in the coil region we have used the decrease of some argon lamp lines.

4. Results and discussions

4.1. a:C-H(N) deposition in a CH_4-N_2-Ar mixture

Changing the argon flow rate, it was remarked that the NH implantation rate in the film and the relative deposition velocity are favoured for a low partial pressure of methane (< 10%).
On the other hand, the relative intensities ratios I_{NH}/I_{CH} (OES) and I_{H2}/I_{CNH} (MS) present a strong increase for the same experimental conditions.

4.2. a:C-H(N) deposition using other precursors

The most interesting properties of a:C-H(N) film using the other precursors are obtained in CH_3NH_2 plasma (18% of implantation nitrogen rate in the film) and the presence of the CH_3N radical in the gaseous phase confirms our previous conclusions [4].
Several experimental results using different precursors are presented in table 1.

Experimental parameters	Experimental results Gaseous phase analysis	Deposition analysis
CH_3NH_2 **CH_3NH_2(0.2)-Ar(0.8)** P = 200 W p = 1 mbar	**OES :** N_2, N_2^+, CN,NH,Ar,H, CH **MS :** H_2, CH_4, N_2, N_2H_4, HCN, hydroc. in C_2,C_3	rate :1.0 mg/cm²/h density : 1.71 $C_{0.33}N_{0.18}H_{0.44}O_{0.042}$ (with cooling)
$C_6H_5N(CH_3)_2$ **$C_6H_5N(CH_3)_2$ Ar** P = 200 W p = 1 mbar T=Tgaz	**OES :** N_2, N_2^+, CN,NH,CH, H **MS :** H_2, CH_4, N_2, N_2H_4, HCN, hydroc. C_2,C_3 C_4,C_5,C_6,C_2N_2	rate: 8.43 mg/cm²/h density: 1.38 $C_{0.53}N_{0.04}H_{0.43}$ (P = 300 W)
C_5H_5N **C_5H_5N-Ar** P = 200 W p = 1 mbar	**OES :** N_2, N_2^+, CN, NH,H, CH **MS :** H_2, CH_4, N_2, N_2H_4, HCN, hydroc. in C_2,C_3 C_2N_2,fragments containing N in C_3,C_4,	rate:33 mg/cm²/h density: 1.33 $C_{0.53}N_{0.06}H_{0.40}O_{0.006}$
C_4H_5N	-	density : 1.25 $C_{0.51}N_{0.08}H_{0.43}O_{0.01}$
CH_4(0.2)-NH_3 (0.4)-Ar(0.4) 100≤P(W)≤300, 0.5≤p(mbar)≤7	**OES :** H_2, H,N_2, NH, NH_2,N_2^+,CN **MS :** CH_4, HCN,H_2,N_2, hydroc C_2,C_3	no deposition

Table 1

The I_{NH}/I_{CH} ratio is also important, in good agreement with the nitrogen implantation rate (the same ratio is very small with other precursors where the nitrogen rate is lower than 5%).
No evident correlation was established between the precursor nature and the deposition velocity.

5. Perspectives

The experimental set-up will be modified introducing the methane in the interelectrode region ; systematic OES and MS analysis were made for different partial pressures in order to verify the correlation between the I_{NH}/I_{CH} and I_{H2}/I_{CNH} ratios and the nitrogen implantation rate.
The strong hydrogen rate of all these depositions (nearly 50%) modifies their expected properties (in particular microhardness and thermostability). Recent works using cyanuric chloride as precursor have permitted to obtain a lower hydrogenated film (30%) containing 32% nitrogen rate.

6. References

[1] A.Y. Liu and M.L. Cohen, Phys. Rev. B 41, (1990) 10727-10729

[2] A. Y. Liu and M.L. Cohen, Science 245, (1989), 841-843

[3] L. Ion , M. Trinquecoste, R. Peyrous, C. Monge, B. Held, P. Delhaès, 11th Gas Discharge Congres, Tokyo (1995)

[4] L. Ion, D. Marty-Dessus, B. Held, R. Peyrous, 13th ESCAMPIG Congres, Slovakia, (1996)

Reactive species in SiH_4-NH_3 RF discharge

L. Ion, D. Marty-Dessus, B. Held
Laboratoire d'Electronique des Gaz et des Plasmas. IPRA- UPPA. Avenue de l'Université. 64000 Pau

1. Introduction

Many studies [1, 2] are devoted to the elaboration of the a:Si-H(N) deposition by PECVD using the SiH_4-NH_3 mixture. Its optimisation is prevented by the complexity of the reaction processes in the gaseous phase and different kinetic models are proposed in order to establish the precursor species. A previous theoretical model [3] suggests that the main responsible of the silane dissociation is the NH_2 radical. Systematic analysis of the gaseous phase by OS (optical spectroscopy) gives informations concerning the reactivity of the nitrogenated species in the SiH_4-NH_3 plasma.

2. Experimental set-up

The reactor used for the capacitive RF discharge (13.56 MHz) is presented in figure 1 (interelectrode distance 1.4 cm).

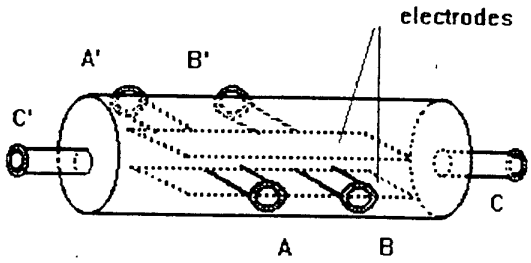

Fig.1. Experimental set-up

Mass flow regulators permit to introduce from 2 to 10% SiH_4 in a low energetic discharge (generally p=1 Torr, P=5 W). Actinometry analysis are realized introducing N_2 and Ar as impurities.
A CCD detector (two holografic gratings with 150 and 1200 grooves/mm) equipped with an UV optical fiber is used to made optical measurements in different reactor regions (named A, B and C windows).
A XeCl excimer laser (λ=308 nm) pumps a Dye laser using Rhodamine 6G and allows to explore the 560-630 nm spectral range.
The temporal signals are detected and explored by a Boxcar Integrator 4022.

3. Experimental analysis

The main species detected by optical absorption and emission spectroscopy in a SiH_4-NH_3 mixture (p= 1 Torr, p=5W, 5% SiH_4) are presented in table 1.

Optical analyse	Spieces	Transition
OES	$NH_{A,B}$	$A^3\Pi(0)\rightarrow X^3\Sigma^-(0)$ $A^3\Pi(1)\rightarrow X^3\Sigma^-(1)$
	$H_{A,B}$	$3d\rightarrow 2p$
	$H_{2\ A,B}$	$3p\ ^3\Pi\rightarrow 2s\ ^3\Sigma$
	SiN_B	$A^2\Sigma^+(0)\rightarrow X^2\Sigma^+(0)$
	SiH_B	$A^2\Delta^+(0)\rightarrow X^2\Pi^+(0)$
OAS	$SiH_{2\ A,B}$	$X^1A_1\rightarrow A^1B_1$

Table 1

(A-for window A ; B-for window B)

In contrast with an ammonia discharge analysed in the same experimental conditions, no NH_2 emission band was detected and the nitrogen emission bands are very low.
On the other hand, preliminary analysis of an ammonia discharge [4] allowed to point out by LIF (Laser Induced Fluorescence) that the reaction NH_2-NH is strongly favoured. But no induced fluorescence signal corresponding of NH(A) state was remarked in SiH_4-NH_3 mixture.
Emission spectra and actinometry measurements have informed us that in presence of silane, the ammonia dissociation is not inhibited and the tail of the EEDF is not perturbed.
These results suggest that the ammonia products (NH and NH_2 radicals) are very reactive in presence of Si_xH_y or $Si_xH_yN_z$. In order to establish correlations between ammonia and silane dissociation products, experimental conditions (total and partial pressures, electric incident power) were drastically modified.

4. Results and discussions

In figure 2 we present the evolution along the reactor of the emission intensities corresponding to excited species created at p = 1 Torr and P = 5 W.

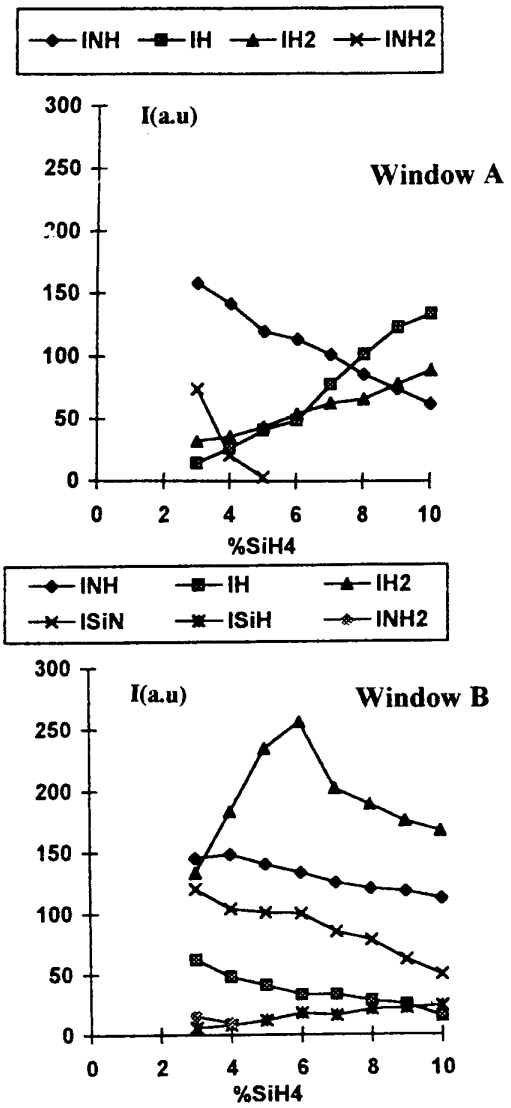

Fig. 2. Emission intensities

It is interesting to remark that the SiN and SiH radicals are detected only in the reactor exit (window B). On the other hand, the NH_2 bands appear only for the low SiH_4 partial pressures (<5%) and SiN radical creation is also favoured in the same experimental conditions. All experimental results suggest that the SiN radical is a dissociation product of the $Si_xH_yN_z$ neutral or radical species. In good agreement with the theoretical model [3], the deposition seems to be favoured for low energetic discharge and low SiH_4 partial pressure.

5. Perspectives

The selective creation of the NH_2 radical by photodissociation will permit to study the SiH_4-NH_2 reaction (with and without discharge). The electric characteristics will be correlated with the deposition rate and the a:SiH(N) film composition.

6. References

[1] D.L. Smith-Mat. Res., Soc. Symp., Proc., Vol. 165, (1990) 69-75

[2] T. Fuyuki, B. Allain, J. Perrin, J. Appl. Phys., No 7, (199), 3322-3328

[3] A. Dollet, J.P. Couderc, B. Despax, Plasma Sources Sci. Technol., (1995) 107-116

[4] L. Ion, D. Marty-Dessus, B. Held, C. Monge, 13th ESCAMPIG Congres, Slovakia, (1996)

Plasmachemical reactor for precision etching of elements with submicron size

V.N.Pavlenko, V.G.Panchenko, V.V.Ustalov, O.A.Fedorovich
Institute for Nuclear Research,
prospect Nauki 47, 252028, Kiev, Ukraine.

Elements of micron and submicron size are widely used now for production of computer integral systems, high-frequency techniques, TV-communication systems. Such elements usually are obtained due to precision plasmachemical etching in the F- and Cl-media. But most of plasmachemical reactors (PChR) has ion energy greater then 200-300 eV and receipt of submicron sizes on them is not possible due to small stability of resistive protective masks, essential overcoating of materials, small selection and anisotropy of etching, considerable radiation damages.

We have created PChR with the possibility of ion energy control from 50 eV up to 500 eV and more [1,2]. In the main working regime the ion energy is regulated in the range 50-150 eV. It is shown the etching velocity of Al films is $v_{et} \leqslant 0{,}5$ μm /min at the anisotropy coefficient $q > 7$ and the etching selection relatively Si~ 20 and he size of elements are nearly 0,3 - 0,5 μm.

These results are obtained due to utilization in PChR crossed magnetic and HF electric fields. The pressure of working gases in the chamber is $10^{-1} - 10^{-3}$ mm Hg.col. One of the electrodes is cooled trihedral prism with the size 110 × 340 mm. On this prism specimens are situated and HF voltage with the frequency 13,56 MHz is applied. The second electrode is cooled cylindrical case of the plant.

Mass-spectrometric and spectroscopic investigations of the plasma show that the molecule dissociation is very effective, - SF_6 dissociates up to S and CCl_4 up to atomic C (during this process all intermediate molecules are observed: SF_5, SF_4, SF_3, SF_2, SF ; CCl_3, CCl_2, CCl).

We have the possibility to obtain sufficiently large v_{et} due to high efficiency of the molecules dissociation and atoms ionization. The low ions energy allows to obtain a good

selection respectively the resistive masks and substrates, high anisotropy $q > 7$, and to avoid of radiation damages and to exclude the interlayer hafp.

To summarize,it is created the technology of etching of films from Al, Au, W, Mo, Ti and others with the elements of submicron size (the size of the superhigh frequency tranzistor is ~ 0,3 μm with the depth up to 0,6 μm) [2,3]. Silicon pillars with the diameter 0,1 mm and the height up to 0,5 μm are obtained. The velocity of the silicon etching is 0,6 μm /min for the anisotropic case and 1 μm/min for the isotropic case, when 9 plates are loaded (the diameter of each plate is 100 mm).

References

[1] A.Yu.Popov,V.V.Ustalov, O.A.Fedorovich: Contr. Papers of Conf."Thin films in the production of semiconduct. techniques and integral systems", Moscow (1990) 109.

[2] V.M.Konoval,V.V.Ustalov, O.A.Fedorovich: Proceed. of Ukr.Vacuum Soc., 1 (1995) 57.

[3] V.M.Konoval,V.V.Ustalov, O.A.Fedorovich: Abstr. of Intern. Conf. "HF techniques and Telecom. technologies",Ukraine (1996) 16.

Surface modifications of He-O_2 corona treated poly(ethylene terephtalate) (PET)

G. Placinta, D. Verdes, G. Popa
Plasma Physics department, "A.I.Cuza" University,
11, bd. Copou, RO-6600, Iasi, Romania

Introduction

In order to develop plasma techniques on an industrial scale, the surface modifications should be stable with time.

The exposure of polymer surfaces to ionic and metastable species of inert gases was shown to lead to the formation of a cross-linked layer with high cohesive strength, which isolates the bulk of the material. The layer formed by cross-linking renders the surface characteristics, obtained by introduction of functional groups, stable against ageing and would be indicated for further applications.

Actually, the obtention of treated materials for biomedical applications is of great interest. For this purpose the plasma technique is a versatile means to improve the blood compatibility of a polymer, by modifying the surface properties without affecting the bulk properties.

Blood compatibility means that a foreign surface in contact with blood should not induce adverse responses. An adequate value for the interfacial tension of blood-biomaterial can be established by taking into account the high compatibility degree and the interfacial stability of cellular elements with blood-plasma. The medium-cell interfacial tension is γ_{sl} = 1 - 3 mN/m. Thus it seems reasonable to consider that a good compatibility with a foreign surface and a mechanical stability of this interface can be insured when the interfacial tension of blood-biomaterial is in this range [1].

Poly(ethylene terephtalate (PET) has several desirable properties for blood contact applications, like good mechanical strength, chemical inertness to blood components and nontoxicity. In order to improve the blood compatibility of this material, any technique that increase the polar component of the surface energy, without affecting the material physico-mechanical characteristics, is of interest. The surface functionalization must also be stable in time, to prevent the ageing effect, which limits the practical uses of the treated polymer surfaces.

Experimental

The effect of a He-O_2 mixture on PET 25 μ films was performed using a corona-like discharge.

The experimental set-up consists mainly of an electric generator which supplies high tension pulses. A plasma beam is produced by ionization of the gas which is flowing in a glass tub at rather high pressure. The plasma beam thus formed, about 2 mm in diameter and 2 - 3 cm in length, allows for local surface treatment.

The discharge is a negative corona type.

The treatment conditions were: gas pressure about 10^5 Pa, gas flow rates 96, 144 and 180 sccm. Treatment times were 5 s and 30 s.

Different diagnostics allowed for plasma properties characterization and their correlation with the energetic and functional surface characteristics. Emission spectroscopy was used in order to characterize the plasma properties. Resulting modifications were analyzed via contact angle measurements and XPS technique.

Results and discussions

An evaluation of the electronic density in our discharge, by taking into account the current that flows in the discharge and the electric field, gives a mean value of about 10^9 cm^{-3}, while the peak value (during the pulse) is of about 10^{10} cm^{-3}.

The spectroscopic study of the discharge allowed us to identify the excited species in the discharge. Among these species, excited oxygen is particularly important, being an extremely reactive component at the polymeric surface.

The 468.5 nm emission line of ionized He was detected in the discharge. The observed species has an excitation energy of 50.2 eV. This fact indicates that very energetic electrons are present in our discharge, because even a two step ionization process necessitates high energies, which are not available in ordinary discharges used for materials processing (glow or RF), especially in presence of impurities. The ionic He species represents, beside the metastable ones, an important agent of cross-linking of the polymeric surface, due its high energy available for direct transfer.

An estimation of the electron energy available in the discharge was done following the ratio of the ion to atom lines intensities. A decrease in this energy with increasing gas flow rate is shown by the experimental data (Figure 1). This behaviour suggests a decrease in the electric field at higher gas flow rates. It might also be due to the shift of the high energies EEDF tail to lower energies in presence of increased amounts of oxygen which attach electrons with high efficiency.

This type of discharge induces important surface modifications.

The surface functionalization is emphasized by the decrease of the measured contact angle of water on treated samples as compared with the untreated substrate. Values obtained as a result of He-O_2 discharge treatment show an appreciable increasing in

the polar component of the energy γ_s^p and the interfacial work of adhesion, even for short treatment times (t = 5 s).

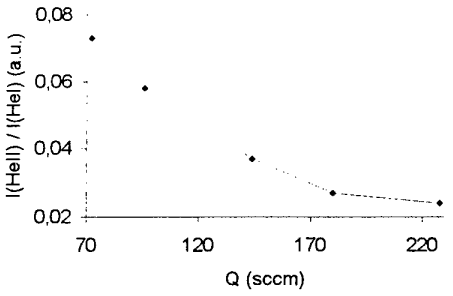

Figure 1. Ion to atom lines emission intensities ratio vs. gas flow rate.

The surface treatment of PET reduces the dispersive component of the surface energy γ_s^d as compared with untreated PET.

With increasing gas flow rate a saturation for the values of the surface energy arises, these are no longer depending on the treatment time.

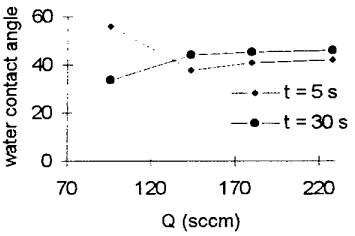

Figure 2. Water contact angle for treated PET (the value for untreated PET : 80°).

The evolution of the surface properties with the ageing time was studied by contact angle measurements made up to 10 days after the treatment. A good stability for γ_s^p is obtained for both short (t = 5s) and long (t = 30s) treatment times. Measurements showed practically no ageing with time (Figure 3). However, better stability is obtained for longer treatment times, and also for lower gas flow rates.

The surface analysis by XPS stood out the surface functionalization by introduction of oxigenated groups. The oxygen content of the treated PET surface is about 2 times larger than that of the untreated sample. Longer treatments times seem to allow for "saturation" of all reactive sites on the surface by reactions with oxygen species.

The two competitive processes which are taking place on the PET surface are cross-linking under the action of the inert gas and chain breaking and surface oxygenation under the action of the oxygen species. The stability of the treated surface suggests that in our treatment conditions the oxidized polymeric structure formes on a reinforced cross-linked layer. Formation of such a layer occurs even for treatment times of the order of a few seconds.

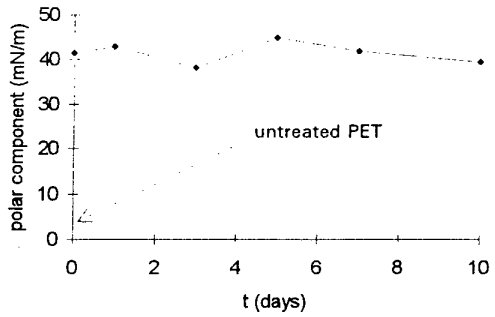

Figure 3. Polar component of the surface energy as function of the ageing time (Q = 144 sccm, t = 30 s).

Preliminary studies on the improvement of the He-O_2 treated PET compatibility with blood were realized by contact angle measurements.

An evaluation of the surface energy data leads to the conclusion that the He-O_2 treatment of PET materials can modify the surface energy components so that the interfacial tension PET film - blood is in the zone of biocompatibility (1 - 3 mN/m) (Figure 4).

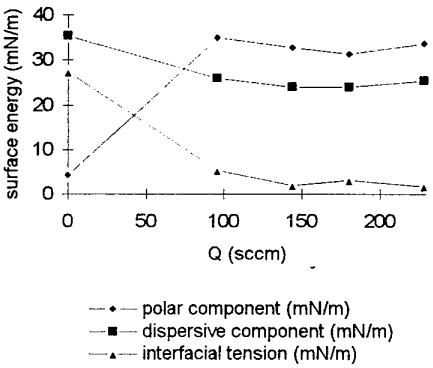

Figure 4. Surface energy components and interfacial tension for treated PET (t = 30 s).

This aspect, correlated with the very good surface stability, makes this type of treatment useful for practical applications.

The authors would like to acknowledge the Laboratory of Plasma Processing, Paris VI for support in recording the XPS spectra.

References

[1] E.Ruckenstein, V.Sathyamurthy, J.Coll.Interf.Sci., 101 (1984) 436.

USE OF DYNAMIC ACTINOMETRY FOR THE DIAGNOSTICS OF A MICROWAVE H_2 - CH_4 - N_2 PLASMA FOR DIAMOND DEPOSITION

Hassan CHATEI*, Jamal BOUGDIRA, Michel REMY and Patrick ALNOT
Laboratoire de Physique des Milieux Ionisés (CNRS URA 835); Université Henri Poincaré - Nancy I,
BP 239, F- 54506 Vandoeuvre les Nancy Cedex, France. Fax : + 33 3 83 27 34 98.

Microwave plasma assisted chemical vapour deposition is widely used for the growth of diamond films. Among the parameters that can affect the process the total gas pressure is an important one. It is known that at high pressure the discharge is a small plasma ball situated just above the substrate holder, without contact with the wall of the reactor and the carbon film is made of diamond [1]. At low pressure the discharge take up a larger volume, limited by the wall of the reactor (quartz tube) and the deposited film is made of graphite. We will point out, using dynamic actinometry, that the plasma chemistry in the gas phase as well as in the plasmas-film system is also modified by the pressure change.

The experimental device has been described elsewhere [2] and for each experiment a diamond film of standard quality is present on the substrate holder in the microwave discharge. The gas mixtures sustaining the discharge are : 98.6%H_2 - 0.4%CH_4 - 1%N_2 at 1.5 torr and 98%H_2 - 1%CH_4 - 1%N_2 at 60 torrs. The dynamic actinometry [3] consists in the study of the evolution with time of the relative concentration of some species after one of the gas lines feeding the reactor (CH_4 or N_2) has been cut off. The evolution of [H], [CH] and [CN] are shown respectively on figures 1, 2 and 3 at 1.5 torr and on figures 4, 5 and 6 at 60 torrs.

At low pressure the cut off of nitrogen in the gas mixture induces a decrease of the concentration of atomic hydrogen (fig 1a). We can speculate that vibrational excited states of nitrogen, as they have a sufficiently high energy, can promote the dissociation of the hydrogen molecule. After methane cut off [H] increases sharply and after 1 minute remains constant with a value 40% higher than its initial value. We have already observed [4], that at low pressure the introduction of methane in the discharge induces a sharp decrease in the electronic density. The elimination of methane from the discharge can thus be responsible of an increase of the density of electrons and, as electronic collisions is the main process for atomic hydrogen production, of an increase of [H].

At high pressure (fig 4) the evolution of [H] is different. The atomic hydrogen concentration increases (15%) after nitrogen cut off and decreases after methane cut off. In this case the effect of the gas mixture changes on the electronic density is not so drastic and chemical effects are more important than direct electron collisions in the process.

The relative concentration of the CH radical after cut off of nitrogen increase sharply and then stays constant (fig 2a and 5a). The atomic nitrogen reacts with carbonated species such as CH in order to produce CN, which is more strongly bound. Introducing nitrogen in the discharge results in a decrease of the relative concentration of carbon deposition precursors. After the cut off of methane, [CH] decreases sharply but, depending on the pressure, it vanishes (fig. 5b) at high pressure, but stays constant at 40% of its initial value at low pressure (fig 2b). Even if no gaseous carbon source is present in the reactor, CH can be produced by interaction of H with carbon films. At high pressure the plasma is close to the diamond film and far from the walls, as H is not an etchant of diamond the production of CH vanishes. At low pressure the plasma can interact with the walls of the reactor where non diamond carbon is unvoluntary deposited, which is etched by H to produce CH.

After the cut off of nitrogen, the relative concentration of CN decreases sharply and vanishes (Fig. 3a and 6a). This result shows that N or CN are not present on the carbon film : adsorption or incorporation of nitrogen in the film is thus not detectable.

After the cut off of methane, [CN] decreases sharply and then remains constant. Thus CN results both of interactions of nitrogen with carbonated species in the gas phase and of the etching of the carbon films by nitrogen. Contrary to hydrogen, nitrogen can etch both diamond and non diamond phases.

In order to prove our assumptions concerning the production of carbonated species without methane in the discharge by plasma-surface interactions, we have carried out an experiment at 60 torrs, after the cut-off of methane, and after removing the substrate holder out of the discharge (Fig 6c). In this case neither gaseous nor solid sources of carbon are present in the device. In this case the CN concentration decreases sharply during two minutes, corresponding to the elimination of the methane, the decrease is slow during 10 minutes corresponding to the elimination of solid carbon pollution in the reactor and then vanishes.

The dynamic actinometry is complementary to other diagnostics methods and allows us to point out the participation of plasma surface interactions in the production of some species, leading to a better knowledge of the global process of diamond deposition.

[1] C.P. Klages; Applied Physics A, **1** (1993) 513
[2] H. Chatei, J. Bougdira, M. Rémy, P. Alnot, C. Bruch, J. K. Krüger; Diamond and Related Materials, in press
[3] S.F. Durrant, E.C. Rangel, M.A. Bica de Moraes; J. Vac. Sci. Technol. A, **13** (1995) 1901
[4] J. Bougdira, H. Chatei, C. Simon, M. Rémy, P. Alnot; Le Vide : Sci. Techn. Appl., Suppl **275** (1995) 305

* on leave from LPTP, Faculté des Sciences, Université Mohamed I, Oujda, Marocco.

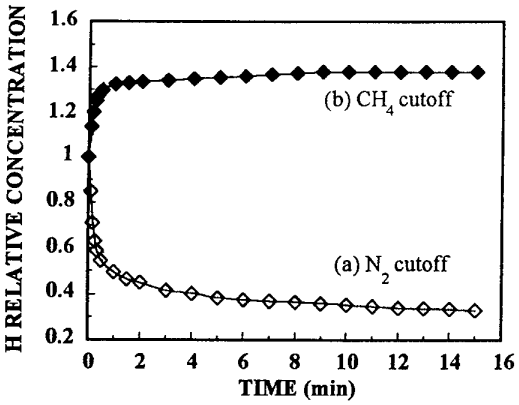

Fig 1: Evolution with time of [H] after cut off of a) nitrogen b) methane at 1.5 torr.

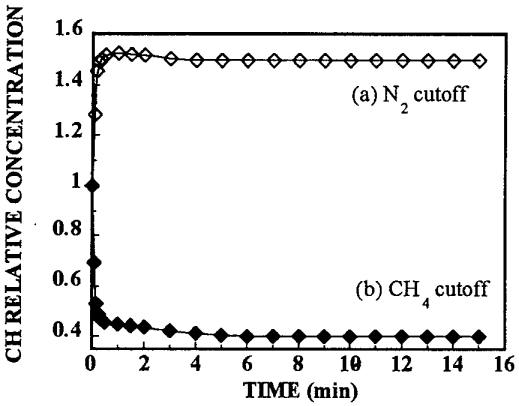

Fig 2: Evolution with time of [CH] after cut off of a) nitrogen b) methane at 1.5 torr.

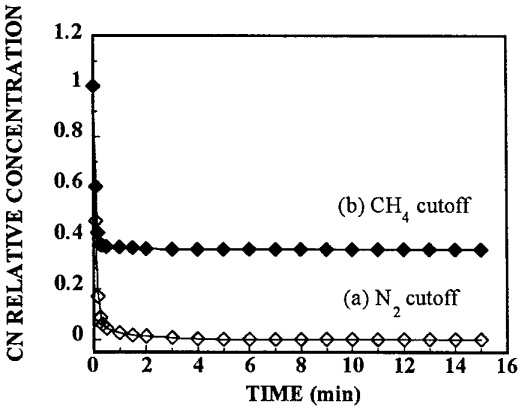

Fig 3: Evolution with time of [CN] after cut off of a) nitrogen b) methane at 1.5 torr

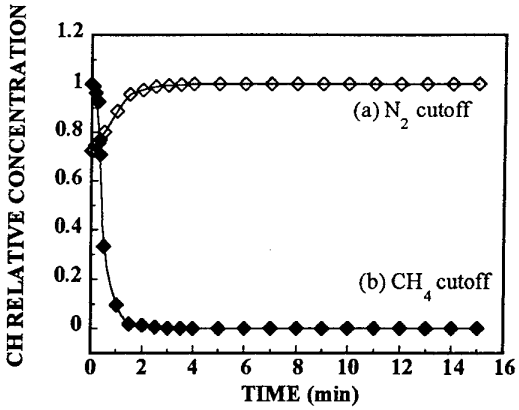

Fig 4: Evolution with time of [H] after cut off of a) nitrogen b) methane at 60 torr

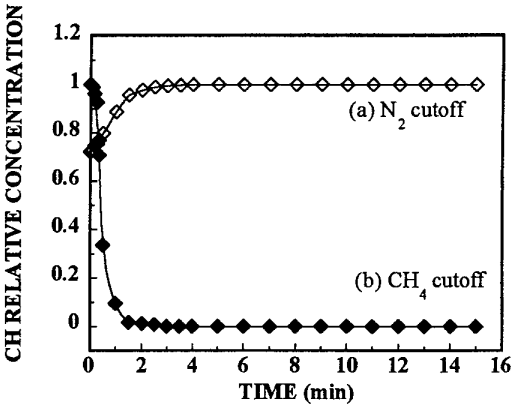

Fig 5: Evolution with time of [CH] after cut off of a) nitrogen b) methane at 60 torr

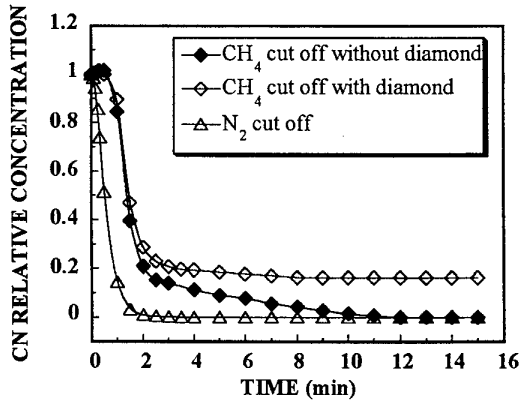

Fig 6: Evolution with time of [CN] after cut off of a) nitrogen b) methane with substrate c)methane without substrate at 60 torr.

Space resolved excitation mechanism and argon ion transport in a high density ICP Reactor

Nader Sadeghi#, Marc Van de Grift, Tarik Hbid Gerrit M. W. Kroessen, and Frits J. de Hoog

Eindhoven University of Technology, Department of Applied Physics,
P.O. Box 513, 5600 MB, Eindhoven, The Netherlands.
#Laboratoire de Spectrométrie Physique (CNRS UMR 5588), Université Joseph Fourier-Grenoble,
BP 87, 38402 St Martin d'Hères, France

1. Introduction

The need for rapid and large area wafer processing in the semiconductor industry has increased the interest in high density plasma sources and particularly in the inductively coupled plasma (ICP) reactors. To fully exploit the possibilities in these reactors, of independent control of plasma generation and wafer biasing, we need to understand how ions are formed and how they gain energy before impinging on the wafer surface.

In this work, we used the Doppler-Shifted-Laser-Induced-Fluorescence (DSLIF) technique to study the spatial evolution of the velocity distribution function (*vdf*) of the $Ar^{+*}(^2G_{9/2})$ metastable ions in an ICP device [1,2]. Both *vdf* parallel, $f(v_{//})$, and perpendicular, $f(v_{\perp})$, to the top glass plate have been determined. Space resolved emission spectroscopy is used to understand the excitation mechanisms of the excited states of argon ion. The space dependent electron density and temperature have also been obtained with a movable Langmuir probe. The experimental results are compared with a global model (for n_e and T_e) and a Monte Carlo model (for velocity distribution function).

2. Experimental set-up

Figure 1 shows a schematic diagram of the plasma reactor. The 3 turn, ϕ=10 cm, inductive coil is located below a 12 mm thick quartz window and is powered at 13.56 MHz with a 2 kW RF generator through an L-type capacitive matching network. The RF power

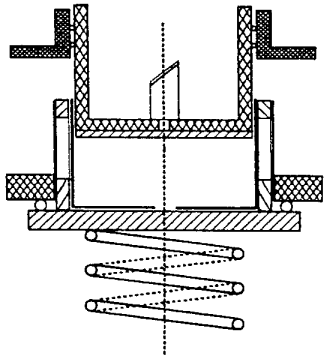

Fig. 1. Schematic of the ICP reactor.

dissipated in the plasma is estimated from the removal of the power absorbed in matching network/power cable [3]. The plasma volume is limited by a ϕ= 15 cm, l =3.8 cm Pyrex cylindrical bucket and a top glass plate. For the DSLIF measurements we use a continuous wave single mode Ar^+-pumped dye laser to excite the transition in Ar^+ ($4p'\ ^2F^0_{7/2} \leftarrow 3d'\ ^2G_{9/2}$) at 611.49 nm. The LIF signal, at 460.96 nm, is collected, with a combination of lens, ϕ=1 mm optical fiber, monochromator and PMT. The space resolution of the observed volume is therefore ±0.5 mm in both axial and radial directions. The *vdf* profile is obtained by tuning the laser frequency and recording the LIF signal.

3. Results and discussion

Given the 600 K gas temperature, measured from the Doppler width of an absorption line of the argon metastable atoms, for $p_{Ar} \leq 5$ Pa the mean free path of the electrons for inelastic collisions is larger than the high of the plasma column. Consequently, the electron temperature, T_e will be homogeneous within the plasma volume. Our probe measurements show that in fact T_e is constant along the reactor axis. This is also confirmed by the space dependence of the emission intensity which follows the variation of the electron density (Fig. 2). The measured values of T_e and n_e are in quite good agreement with those calculated by the 'global model' [3] for our experimental conditions.

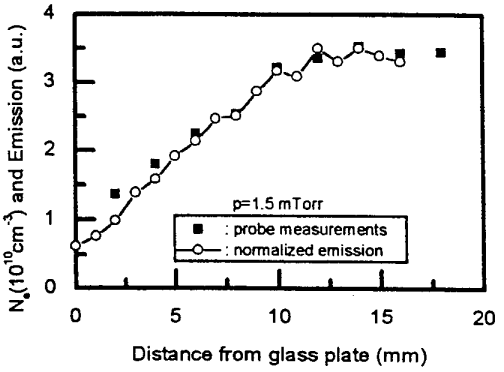

Fig. 2. n_e (square) and emission intensity of Ar 750 nm line (circle) vs distance from the glass plate.

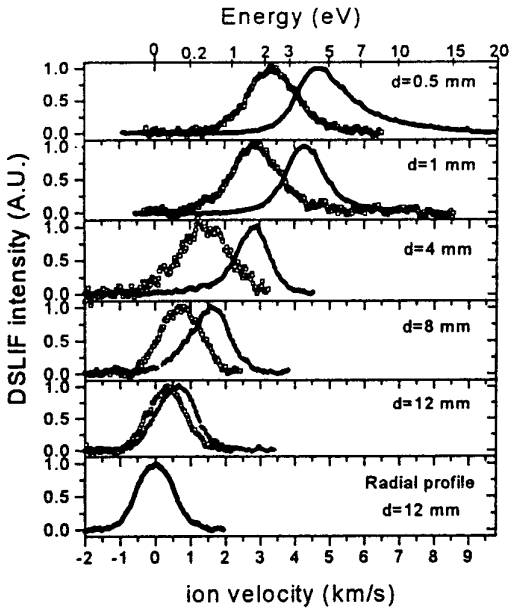

Fig. 3. Velocity distribution function of the $Ar^{+*}(^2G_{9/2})$ ions at different distances from the glass plate at 5 (solid circle) and 40 (hollow square) mTorr. All profiles are normalised to the unity. The five upper pair of curves are relative to the velocity component along the reactor axis, $f(v_\perp)$, and the lowest curve corresponds to the component parallel, $f(v_{//})$, to the glass plate.

Representative $f(v_\perp)$ distributions of argon metastable ions are shown in figure 3 for p=5 and 40 mTorr at different distances, d, from the top glass plate. Also shown is the $f(v_{//})$ at 5 mTorr and d=12 mm. We observe that the $f(v_{//})$ profile is symmetrical regarding the zero velocity and has almost a Gaussian shape, which can be expressed in terms of a temperature $T_{//}$. On the contrary, for both pressures, $f(v_\perp)$ profiles can not be fitted with a Gaussian. The shift to higher velocity of $f(v_\perp)$ when approaching the glass plate results from the acceleration of the ions by the electric field of the presheath. Considering the large cross-section, $\sigma = 1.1\ 10^{-14}$ cm^2, for the quenching of $Ar^{+*}(^2G_{9/2})$ metastable ions by argon atoms [4], the mean free path of these ions will be 12 and 1.5 mm at 5 and 40 mTorr, respectively. We therefore can conclude that, particularly at 40 mTorr, the $Ar^{+*}(^2G_{9/2})$ metastable ions we detect by DSLIF are not those formed outside the presheath and accelerated within it, but are produced by electron impact, a few mm before their respective observation points. If the main mechanism for population of the $Ar^{+*}(^2G_{9/2})$ metastable state was direct ionisation of the neutral atoms we should observe a large zero velocity component in all *vdf*s and particularly those recorded close to the glass plate. It is obvious that in our high electron density conditions, the $Ar^{+*}(^2G_{9/2})$ level is mainly populated by electron impact excitation of ground state argon ions. These ions have already gained kinetic energy by being accelerated by the ambipolar E-field of the presheath and their velocity is totally conserved during electron impact excitation of the ion.

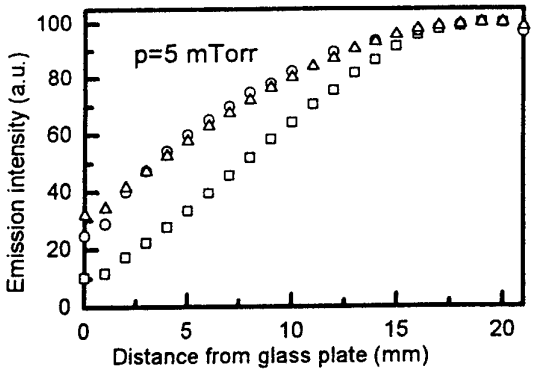

Fig. 4. Normalised emission intensity of Ar, 750 nm (circle), and Ar^+, 461 nm (square) lines, vs the distance from the glass plate. (triangle) square root of the 461 nm line intensity.

The fact that the excited states of argon ion are formed from the ground state Ar^+ ions is confirmed from the space dependence of the emission intensity of the 461 nm ionic line (Fig. 4). As pointed out before, the emission profile of the 750 nm atomic line corresponds exactly to the profile of the electron density along the reactor axis. Fig. 4. shows that in fact, the intensity of the 461 nm ionic line evolves proportional to the square of the electron density.

A 3D Monte Carlo model is developed to investigate the relation between the *vdf* of the ground state and metastable ions. The axial (z) dependent *vdf* of the ground state ions is calculated by assuming known p_{Ar}, $n_e(z)$, T_e, Ar^+-Ar charge exchange and elastic cross-sections and electric field, E(z), deduced from $n_e(z)$ by using the relation $E(z) = \partial [kT_e \log(n_e)]/\partial z$. Using this *vdf*, we can deduce the *vdf* of the metastable ions by applying the same technique to the metastable ions. These ions are assumed to be created by excitation from ground state ions and are quenched by collision with neutrals and electrons [4]. A satisfactory agreement is observed between the simulated and measured velocity distribution functions of the $Ar^{+*}(^2G_{9/2})$ ions.

4. References

[1] N. Sadeghi, T. Nakano, D.J. Trevor and R.A. Gottscho: J. Appl. Phys. **70** (1991) 2552.

[2] N. Sadeghi, M. van de Grift, D. Vender, G.M.W. Kroesen and F.J. de Hoog: Appl. Phys. Lett. **70** (1997) 835.

[3] P.N. Wainman, M.A. Lieberman, A.J. Lichtenberg, R.A. Stewart and C. Lee, J. Vac. Sci. Technol. A **13**, 2464 (1995).

[4] B. Pelissier and N. Sadeghi, Rev. Sci. Instrum, **67**, 3405 (1996).

The vacuum arc discharge in anode material vapour

A.G. Borisenko, V.N. Pavlenko,
V.G. Panchenko, V.A.Saenko
Institute for Nuclear Research,
prospect Nauki 47, 252028, Kiev, Ukraine.

Intensive investigations of stationary electric discharges with homogeneously evaporated anode are carried out now. These investigations are of interest due to possibility for utilization such type of discharge for vacuum deposition of high-adhesive thin films on various (metallic, semicondactor and dielectric) substrates.

Unlike the vacuum arc, the non-self-maintained arc discharge in the anode vapour may be realized when the diffusion current of discharge takes place on the anode. It allows to create dropless high-adhesive plasma flows of metallic vapour in vacuum and different gas environment [1-3].

In our experiments the discharge has lighted up between the thermionic cathode and water-cooled anode. Al, Cu, Ni, Cr, Ti, Ta, Mo, B, C, W are imbedded on the anode as a working substance. Using the cylindrical electrode and electromagnetic system we have the possibility for creation the transverse electric and magnetic fields. The discharge current I_D=(2÷10) A, the magnetic field induction $B \leqslant 400 \times 10^{-4}$ T. Our experiments show that for the case when the current of thermoelectronic emission from the cathode I_c exceeds the discharge current I_D, the current-voltage characteristics of the discharge may be presented in the form:

$$U_D = W_D / I_D \qquad (1)$$

where W_D is the discharge power, and U_D is the voltage of discharge. Thermoemission characteristics of cathode essentially influence on the discharge shape at $I_c \leqslant I_D$, and lead to the appearence of minimum and maximum on the curve $U_D(I_D)$.

In the regime of free burning ($I_c > I_D$) the film deposition rate q has linear dependence on the discharged current I_D, i.e. $q \sim I_D$.

In the regime of induced burning ($I_c < I_D$) we obtained that $q = A W_D$, where A is the constant. For example, using

Cu as a working substance we have $q \leqslant 45 \times 10^{-10}$ m/s at $W_D \leqslant 300$ W. Data presented indicate that the plasma flow at $q \leqslant 40 \times 10^{-10}$ m/s becomes charge-compensated and negative sound potential is equil 60 ÷ 100 V. The external magnetic field leads to decreasing of the discharge burning voltage and to increasing plasma-flow ionization coefficient even at the zero potential of the cylindrical electrode. The ion current dependence on the induction of the magnetic field has the form of the fluent curve with a maximum at $B \leqslant 100 \times 10^{-4}$ T. Note that for the case $B > 100 \times 10^{-4}$ T the ion current decreases with the growth of B, i.e. $I_i \sim 1/B$. It is shown that plasma-flow ionization coefficient α may reach the value up to 80%. Thus the data presented in this paper (high ionization coefficient, charge-compensated plasma flow) demonstrate the perspective of wide practical utilization of such type of discharge for creation of thin high-adhesive films.

References

[1] V.A.Saenko: Instrum. and Experim.Techn., 3 (1985) 9.

[2] A.G.Borisenko, A.V.Kravchenko,V.A.Saenko: Instrum. and Experim. Techn., 2 (1992) 257.

[3] G.Musa: Romanian Reports in Physics, 9 (1992) 917.

DC Negative Corona Discharge in Air + CCl_2F_2 Mixtures.

P. Cicman, M. Pavlík, J. Rahel, Š. Matejčík*, T.D. Märk** and J.D. Skalný

Plasma Physics Department, Comenius University, Mlynská dolina F-2, 842 15, Bratislava, Slovakia
*Institut für Physikalische Chemie, FU Berlin, Takustr. 3, D-14195 Berlin, Germany
**Institut für Ionenphysik, Leopold Franzens Universität, Technikerstr. 25, A-6020 Innsbruck, Austria

1. Introduction

The depletion of the ozone layer, protecting the Earth against the harmful UV radiation, by VOC (volantile organic compounds) is a very actual problem. Particularly important in this process are chlorofluorocarbons which destroy ozone very effectively. An efficient catalytic reaction of freon CCl_2F_2 (CFC12), one of the chlorofluorocarbons,, is initiated in the lower stratosphere by photons with ozone. Similar processes, but initiated by electrons, have been observed in gas discharges [1], [2], [3]. As we have shown earlier, the concentration of ozone produced by a negative corona discharge [4] is very sensitive to the presence of freon CFC12 molecules in oxygen [5]. The generation of ozone was substantially suppressed whenever the concentration of CFC12 in the oxygen was above 1%. The present paper studies the properties of the negative corona discharge in air + CFC12 mixtures at pressures slightly below 1 bar.

2. Experimental apparatus

A system of coaxial cylindrical electrodes (r_0 = 0.05 mm, R = 7.5 mm, L = 40 mm) was placed in a glass discharge tube ended by quartz windows. A UV light beam passing along the axis of the discharge gap allows us to measure the time dependence of the ozone concentration in the discharge tube. The time dependence of the ozone concentration as well as the corresponding current values at constant voltage on the electrodes have been recorded by on line PC system. The experiments have been carried out in the air + CFC12 mixtures at two values of gas pressure 800 and 900 mbar respectively. The concentrations of freon in the mixtures were changed over the range (0.1 - 2.0) by volume % at room temperatures.

3. Experimental results

The experiments have shown that the corona onset potential was influenced only by the pressure of the gaseous mixture. The content of the freon in air had a conspicuous influence both on the time dependence of ozone concentration as well as on the time dependence of mean corona discharge current. As we have mentioned earlier [6], the so called relaxing of negative corona current [7], observed in ambient air, is caused by the ozone generated by the discharge itself. Very effective attachment of free electrons by ozone molecules [8] is the reason for the observed decrease of the mean discharge current at increasing ozone density. The relation between ozone density and the mean discharge current in the clean air is evident from the comparison of the Fig. 1a and 1b or Fig. 2a and 2b. Moreover, the effect of addition of freon is remarkable from the mentioned dependencies. It must be noted that the pressure of the gaseous mixture has a significant influence on the effect of reduction of the ozone concentration at increasing freon density in the mixture.

4. Discussion

The dominate reaction in the formation of ozone is the three body reaction

$$O + O_2 + M \rightarrow O_3 + M \qquad (1)$$

The oxygen atoms are mostly (more than 90%) generated via the direct dissociation of molecular oxygen by electron impact

$$e + O_2 \rightarrow O + O + e \qquad (2)$$

The rest of them is produced via the dissociative attachment of electrons by oxygen molecules

$$e + O_2 \rightarrow O^- + O \qquad (3)$$

After the addition of freon CFC12 into the clean air the similar reactions of electrons with CFC12 molecules can occur

$$e + CCl_2F_2 \rightarrow CClF_2 + Cl + e \qquad (4)$$

$$e + CCl_2F_2 \rightarrow CClF_2 + Cl^- \qquad (5)$$

Both the atomic and ionic form of chlorine are active in reduction of ozone concentration. Chlorine atoms undergo predominantly the two step process

$$Cl + O_3 \rightarrow ClO + O_2 \quad (6)$$

$$ClO + O \rightarrow Cl + O_2 \quad (7)$$

which can be repeated many times. The negative chlorine ions lose the electrons in a very fast detachment process [3]

$$Cl^- + O \rightarrow ClO + e \quad (8)$$

The chlorine oxide ClO produced by reactions(7) and (8) reduces the density of oxygen atoms needed for ozone formation via the reaction (1). As it follows from our simple calculation of relative densities of negative ions and oxygen atoms on the boundary of the ionisation region created by one electron starting from the cathode, at 900 mbar and concentration of freon 1% these two are comparable. We suppose that presence of the freon molecules in air can reduce the ozone production via the reaction (1). The densities have been calculated by the use of data for electron attachment reaction (5) given by [9] and [10].At lower pressure of the mixture the rate of production of ozone by (1) is reduced because of three body character of reaction. Thus the effect of freon on the ozone formation can be observed at lower densities of freon. This is in accordance with the results shown in Fig. 1b.

6. Acknowledgement

This work was supported in part by Slovak Grant Agency

5. References

[1] Vicharev A.L. et all: J. of Tech. Phys. 66 (1996) 56
[2] Askaryan G.A. et all: Proc. of 11th GD, Tokyo (1995) II-438
[3] Alexandrov N.L.: Plasma Sources Sci. Technol. 3 (1994) 226
[4] Hadj-Ziane S. et all: J. Phys. D: Appl. Phys. 25 (1992) 677
[5] Sobek V., Lukáč P. and Skalný J.D.: CIP Colloquium, Antibes - France 1991, Le Vide, Les Couches Minces-Supplement N 256 (1991) 73
[6] Černák M. et all: Acta Phys. Slov. 29 (1979) 97
[7] Gagarin A.G.: Elektronnaja obrabotka materialov 3 (1984) 54
[8] Skalný J.D.: Chem. Phys. Lett. 255 (1996) 112
[9] Hayashi M.: private communication
[10] Kiendler A. et all: J. Phys. B: At. Mol. Opt. Phys. 29 (1996) 6217

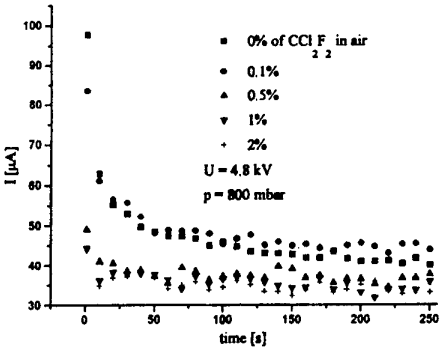

Fig. 1a. Time dependence of corona current.

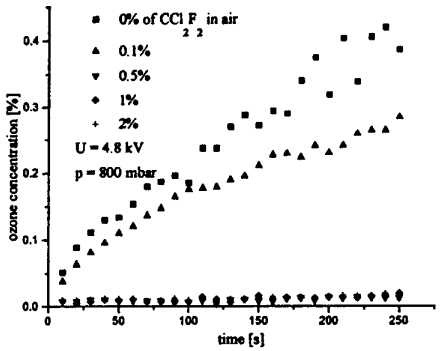

Fig. 1b. Time dependence of ozone concentration.

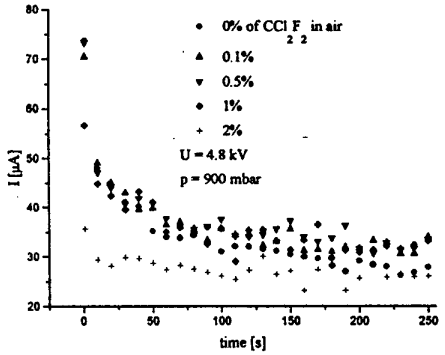

Fig. 2a. Time dependence of corona current.

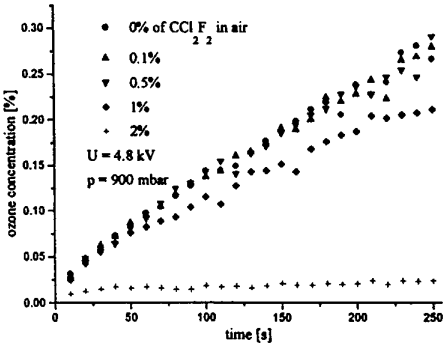

Fig. 2b. Time dependence of ozone concentration.

Catalyst synthesis by plasma assisted deposition

A.L. Thomann[§], C. Charles[*], P. Brault[§], C. Laure[§], C. Andréazza-Vignolles[#] and P. Andréazza[#]

[§]Groupe de Recherche sur l'Energétique des Milieux ionisés, CNRS-Université d'Orléans, BP6759, F-45067 Orléans Cedex 2, France.
[*]Plasma Research School, Australian National University, Canberra, Australia.
#Centre de Recherches sur la Matière Divisée, CNRS-Université d'Orléans, BP6759, F-45067 Orléans Cedex 2, France

1. Introduction

Many recent works have shown the great interest of supported metal aggregates in heterogeneous catalysis. These metal objects can exhibit higher activity than the bulk metal, as for example, in the case of butadiene hydrogenation catalyzed by palladium [1,2]. At present, we study the synthesis of such catalytic systems by a plasma process, which may allow to get rid of many problems encountered with methods commonly used as : long time duration and organic contamination (liquid phase methods), heavy UHV technology (atomic beam deposition). Compared to these techniques, the plasma process has many advantages : surface preparation before deposition by ion bombardment (cleaning or nucleation site creation) and catalyst postreatment before reaction. Our aim is also to characterize the metal aggregates or layer growth mode in plasma process in order to compare with the usually observed ones.

In previous work, the ability to synthesize by plasma continuous Pd layers or spaced-out aggregates with the size required for the catalysis application has been demonstrated[3]. First catalytic tests are encouraging, because they evidence the good activity of the plasma deposits, close to what is found with samples realized by atomic beam deposition. In this paper we present first results of the characterization of the deposition plasma as well as the main features of the deposits.

2. Set up and Plasma characterization

The set up has been widely describe in reference [4]. The chamber is filled with argon gas in the pressure range, 1 to 100 mTorr. The inner excitation antenna is connected to a HF (100 MHz) supply. A helicoidal Pd filament is set in the middle and is negatively biased with respect to the plasma potential so that the Ar ions produced in the antenna are attracted and sputter the metal wire. In deposition configuration, the substrate is located several centimeters away.

For plasma study, a Langmuir probe is placed instead of the sample holder. The current-voltage curves has been recorded at the substrate position at 1 mTorr and 100 mTorr Ar pressure. The values of plasma and floating potentials (V_p and V_f), electron density and temperature (N_e and T_e) are given in Table I : they do not depend on the Pd wire bias voltage.

	1 mTorr	100 mTorr
V_f (V)	60	90
V_p (V)	80	100
kT_e (eV)	3-4	2
$N_e 10^9$ (at.cm^{-3})	6	3

Table I : *current plasma parameters of the discharge*

It is observed that during the deposition process, the substrate is submitted to a high argon ion flux. Because the substrate is at the floating potential, the ion energy is low : 10 to 20 eV. Nevertheless, this flux may influence the growth regime. From Table I, it also appears that the plasma is less dense and hot at the substrate position along the experiment main axis, at high pressure. This is related to the ionization process that depends on the gas pressure as shown in Fig.1, where the Ar^+ density obtained from the ionic saturation current (Nsat) is presented versus the axial position.

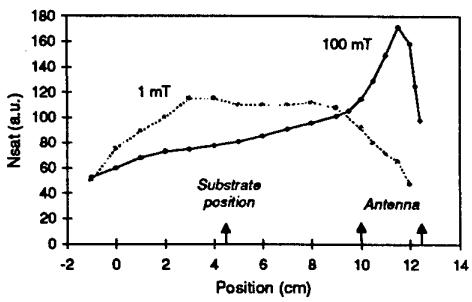

Fig. 1 : *Ion density in the plasma chamber.*

For these measurements the Pd wire has been removed from the chamber. At low pressures (1mTorr), the electron mean free path is large and then the ionization occur in a large volume. Conversely, at 100 mTorr a lot of collisions take place, and the ionization is confined in the antenna, only few Ar ions can to diffuse in the chamber.

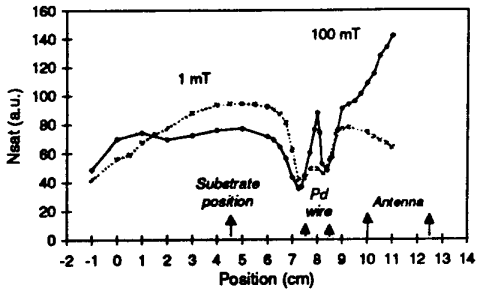

Fig. 2 : *Effects of the biased(-350 V) helicoidal Pd wire on the ion density.*

In Fig.2, the Ar^+ concentration variation with the position is given, the Pd wire being placed in the chamber and biased to -350V. Its influence on the Ar^+ concentration is well seen, and only deals with the filament close surroundings, i.e. does not reach the substrate position. The sharp decrease of NAr^+, at the wire sides is due to its attractive effect and exists at both pressures. However, a peak is visible at the wire center at 100 mTorr that does not exist at 1 mTorr. This is due to the presence of a secondary dc discharge (observable luminous area) inside the filament at high pressure and filament bias voltage. This auxiliary dc plasma has been evidenced in a previous work, its creation is expected to follow a shifted Paschen law[4]. From emission spectroscopy, in a zone close to the wire, this discharge has clearly been evidenced. Indeed, above 50 mTorr and -200 V, the Pd line emission abruptly increases whereas the Ar line intensity remains constant. Regarding to the Pd and Ar excitation energies (E_{Pd}=4.4 eV, E_{Ar}=11.47eV), this phenomenon may be due to a rise of the excitation level (electron density increase) inside the Pd wire when the secondary discharge occurs, and/or to an enhancement of the Pd sputtering process not only related to the Pd wire voltage but also to the large Ar^+ number detected in the wire center. The sputtering efficiency determines the deposition rate, which can be evaluated from the deposit analysis.

3. Deposit analyses

Number of analyses have performed on the deposits in order to determine their main features such as : chemical purity, cristallinity, morphology and Pd amount. From XPS (Xray Photoelectron Spectroscopy) analysis, metallic Pd (Pd-Pd bound) has been detected but no oxide or oxygen contamination have been evidenced, which is of great importance for catalysis application. GIXD (Grazing Incidence Xray Diffraction) experiments show that the deposits are polycrystalline with no preferential orientation. STM (Scanning Tunneling Microscopy) and TEM (Transmission Electron Microscopy) observations evidence the presence of Pd aggregates with spherical shape and diameter from 20 to 1000 Å depending on the experimental conditions : Ar pressure, Pd wire bias and deposition time. Owing to the Pd quantity, these aggregates are jointed or spaced-out, which are the requested morphologies for catalysis applications.

A first study of the growth mode has been carried out by TEM. Samples synthesized with increasing deposition times indicate a first step of nucleation and cluster size increase followed by coalescence. From RBS (Rutherford Bachscattering Spectroscopy) analysis results the deposition rates have been found to range from 0.5 to 60 layers/mn.

It is interesting to note that the samples synthesized in experimental conditions leading to the creation of the auxiliary plasma exhibit quite large deposition rates. Moreover, in these samples, the coalescence stage begins very early in times. Both trends confirm the hypothesis of an enhancement of the Pd sputtering process when the secondary discharge is created inside the Pd wire. Further work is under way to precisely characterize this discharge and to closely study the deposit features depending of the Ar pressure and the Pd filament bias voltage.

[1] J.C. Bertolini, P. Delichere, B.C. Khanra, J. Massardier, C. Noupa and B. Tardy, *Catalysis Letters*, **2** (1990) 215

[2] P. Hermann, B. Tardy, D. Simon, J.M. Guigner, B.Bigot and J.C. Bertolini, *Surface Science*, **307-309** (1994) 422

[[3] A.L. Thomann, P. Brault, C. Laure, B. Rousseau and H. Estrade-Szwarckopf, C. Andreazza-Vignolle, P. Andreazza and A. Naudon, Accepted for publication in *Surface and Coatings Technology*.

[4] C. Laure, P. Brault, A.L. Thomann, R. Boswell, B. Rousseau and H. Estrade-Szwarckopf, *Plasma Sources Science and Technology*, **5** (1996) 510

Optical Emission Spectroscopy on Ar/N_2 and $Ar/N_2/C_2H_2$ Expanding Thermal Plasmas

A. de Graaf, M.C.M van de Sanden, D.C. Schram
E. Aldea*, G. Dinescu*

Department of Applied Physics, Eindhoven University of Technology
P.O. Box 513, MB 5600 Eindhoven, The Netherlands
*Low Temperature Plasma Department, National Institute of Lasers, Plasma and Radiation Physics
P.O. Box MG 36, Bucharest-Magurele, Romania

1. Introduction

This work has been carried out in connection with the possibilities to deposit carbon nitride materials by Expansion Thermal Plasma Assisted Chemical Vapour Deposition (ETP-A-CVD). With the same technique high deposition rates and good quality a-Si:H and a-C:H materials have been obtained [1]. A study of the intensity of atomic lines and molecular bands in a Ar/N_2 and $Ar/N_2/C_2H_2$ expanding thermal plasma has been performed. In the case of the $Ar/N_2/C_2H_2$ mixture rotational and vibrational temperatures were obtained by comparing computer simulated spectra of the CN($B^2\Sigma$–$X^2\Sigma$, $\Delta v=0$) spectral system bands with the experimental spectra. Details on this computer procedure are given in [2]. The CN ground state density is determined by taking into account the self-absorption of the CN bands.

2. Experimental

The experimental set-up has been described in detail elsewhere [1]. It consists mainly of an arc plasma generated in a flowing gas between three cathodes and a nozzle and stabilised at wall by a cascade of cooled plates. The power injected in the arc can be varied in the range 0.6-5 kW. Gas fluxes up to a few hundred of sccs can be handled in the arc channel. The plasma expands in a vacuumed vessel (diameter 0.4 m, length 1.2 m). Additional gases can be added to the plasma directly in the main flow before the discharge, or in the middle arc channel, or injected some centimetres downstream the nozzle.The spectra have been recorded in the spectral range 350-650 nm by a spectral system consisting of a photomultiplier (Hamamatsu R 268) and a monochromator (Jobin Yvon THR 1000) working in the photon counting mode.

The conditions under which the experiments have been performed are: arc current 75 A, arc pressure 0.3-0.5 bar, background pressure 0.25 mbar, with two mixtures of gases:
a) Ar/ N_2 at fluxes of 95/5 sccs with addition of N_2 in the main flow.
b) $Ar/N_2/C_2H_2$ at fluxes 95/5/2 sccs, with nitrogen added in the main flow and C_2H_2 added in expansion through an injection ring.

The spectra have been recorded in expansion at two positions along the flowing axis:
1) In the mixing zone, at 7 cm from the arc nozzle, 2 centimetres downstream the injection point,
2) In the deposition zone at 62 centimetres from the arc nozzle.

3. Results

3.1 Ar/N2 plasma

a) The addition of nitrogen in the main gas flow produces a strong quenching of the plasma emission as comparing to the pure argon plasma. The spectra recorded near the nozzle (Fig 1a) are dominated by Ar neutral lines. The molecular nitrogen emission is present as well, the N_2^+ FNS spectral system and N_2 SPS spectral system bands having almost the same magnitude; however their intensity is only a few percent of the intensity of Ar lines.

b) For the same plasma settings, the spectrum recorded in the deposition region (Fig. 1b) is dominated by the molecular bands of the ionic molecular nitrogen (FNS); the SPS bands of N_2 are still present but in much lower measure. The Ar lines are hardly observed.

3.2 $Ar/N_2/C_2H_2$ plasma

a) In this case for the spectra recorded in the mixing zone the bands spectrum is much stronger than the line spectrum (Fig 2a). The CH($A^2\Delta$-$X^2\Pi$) and CH($B^2\Delta$-$X^2\Pi$, $\Delta v=0$ with maximum at 413.0 and 388.6 nm) bands and CN($B^2\Sigma$-$X^2\Sigma$, $\Delta v=0$ with maximum at 388.3 nm) bands are the most intense. There is also evidence for the radiation of C_2(A-X, $\Delta v=2$, transitions (2,0) at 438.2 nm, (3,1) at 437.1 nm and (4,2) at 436.5 nm) Swan system which appear in this spectral region superposed over the CH(A-X) bands. The nitrogen SPS and FNS bands have disappeared from the spectrum. The obtained values of rotational and vibrational

temperatures and of the CN ground state density have been: Trot=(5690 +/- 200) K , Tvib=(9200 +/- 400) K, [CN(X)]= (1.7 +/ - 0.1)x10^{19} m^{-3} .

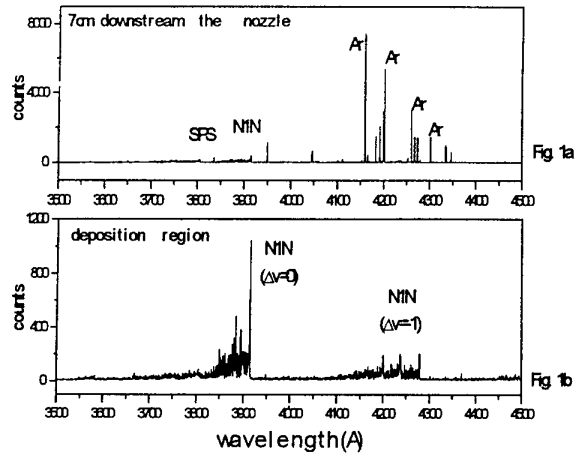

Fig. 1. *a) The spectrum of Ar/N_2 plasma recorded at 7 cm downstream the arc nozzle*
b) The spectrum of Ar/N_2 plasma recorded at 62 cm downstream the nozzle

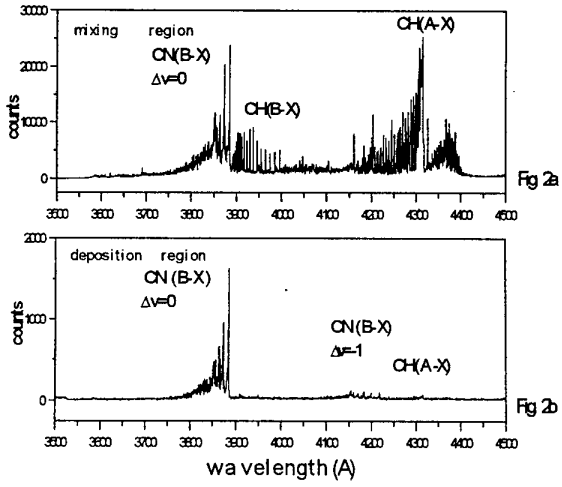

Fig. 2. *a) The spectrum of $Ar/N_2/C_2H_2$ plasma recorded at 7 cm downstream the arc nozzle*
b)The spectrum of $Ar/N_2/C_2H_2$ plasma recorded at 62 cm from the nozzle

b) In the deposition zone the spectrum (Fig. 2b) contains only molecular bands. The main characteristic is that the CN bands are dominating over CH bands which are very weak. The FNS bands are not present anymore. The obtained values of rotational and vibrational temperatures and of the CN ground state density have been: (T_{rot}=6710 +/- 200) K ,T_{vibr}=(6780 +/- 200) K, [CN(X)]= (4.8 +/- 0.2)x10^{18} m^{-3}.

4. Discussion

The observation of the atomic lines dissapearing after injection of C_2H_2 into Ar/N_2 plasma and the molecular bands being very strong indicates that the energy is transferred from the atomic excited species and ions to the molecules. The general behaviour that along the plasma flow axis the lines are disappearing faster than the bands is showing that this process of transfer of energy is also active out of the mixing zone. An explanation of this behaviour could be related to the process of charge transfer to molecular species followed in the case of the $Ar/N_2/C_2H_2$ mixture by a dissociation of the molecule and formation of CH and CN radicals.

A very interesting feature is the behaviour of CN and CH bands along the plasma flow. The spectra show that in the mixing zone both radicals are produced and excited and that only the CN radical survive in the late expansion. This could be related to a higher rate of deposition of the CH radical at the walls or to a higher diffusion of this radical away from the expansion axis towards the walls.
The lower value of the rotational temperature in the mixing zone compared to the deposition zone could be related to the plasma cooling due to the C_2H_2 injection. Along the plasma flow a tendency to equilibration of rotational and vibrational temperatures is noted. However these temperature values are unexpectedly high showing the non-equilibrium character of this plasma . The values of roto-vibrational temperatures in a $Ar/N_2/C_2H_2$ plasma are about twice of those obtained in a Ar/C_2H_2 plasma [2]. The disappearance of emission of FNS bands indicates the importance of the ionic molecular nitrogen in the energy transfer and excitation.

5. Conclusions

In Ar/N_2 and $Ar/N_2/C_2H_2$ expanding thermal plasmas the transfer of energy is from the atomic species towards the molecular species both in the mixing zone and along the expansion. The CN radical is produced in large quantities in the $Ar/N_2/C_2H_2$ expanding thermal plasma. Due to the importance of CN radical in the carbon-nitride deposition it results that Expansion Thermal Plasma Assisted Chemical Vapour Deposition technique is appropriate for this purpose.

6. References

[1] M.C.M. van de Sanden, R.J. Severens, J.W.A.M. Gielen , R.M.J. Pfaffen and D.C. Schram, Plasma Sources Sci. Technol. 5 (1996) 268
[2] E.Aldea, G.Dinescu, J.W.A.M. Gielen, M.C.M van de Sanden , D.C. Schram, ESCAMPIG **B** (1996) 239

Monte Carlo simulation of thin film deposition from low density jet excited by an electron beam.

A.V.Vasenkov, R.G. Sharafutdinov, and A.V. Skrynnikov

Institute of Thermophysics, Novosibirsk, 630090, Russia

Plasma processing for solar cell fabrication is moving towards achieving higher deposition rates. Recently, a new deposition method that satisfies this goal was developed [1]. In it thin films were deposited from low density jet excited by an electron beam (Fig.1). This deposition method is currently investigating using statistical techniques.

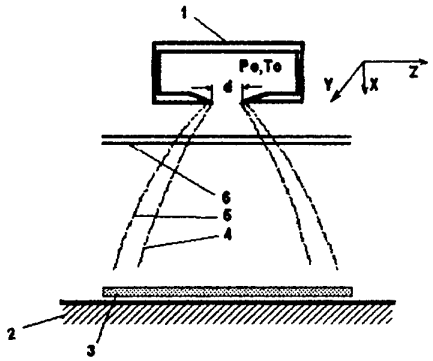

Fig.1 A schematic sketch of film deposition from low-density jet excited by an electron beam. P_0 and T_0 is total gas pressure and temperature within gas source, d is nozzle diameter, 1 - gas source, 2 - substrate, 3 - film, 4 - lateral shock wave, 5 - the boundary of the jet, 6 - electron beam.

To address conditions of thin film deposition from low density jet excited by an electron beam a hybrid model was developed. The model combines a Monte Carlo code for interaction of an electron beam with nonuniform gas flow [2] with direct simulation Monte Carlo (DSMC) techniques for the transport of molecules and gas surface interaction [3]. Chemical reactions in gas flow were not considered. This approach was justified by experimentally obtained linear dependencies of deposition rates on beam current and on pressure.

Calculations were performed for plasma jet of Ar with small portion of monosilane (10%). The model begins by solving for the electron distribution function (EDF) as a function of electron energy and position. Elastic scattering, ionization, and inelastic excitations were taken into account. The cross sections necessary for calculations have been discussed in [4,5]. No consideration is given to beam degradation, that is, the energy of the beam electrons is assumed to remain constant. Such an approximation is justified for a description of the interaction of high-energy beams with a low-density medium. The spatial distribution of the gas density in the jet in these computations was sampled from calculations, obtained using the DSMC code. By monitoring the position and velocity of each electron, the EDF in energies and space was obtained. To calculate the three-dimensional spatial distribution of total dissociation rates of monosilane, the simulation region was divided into cubic cells (primary electrons were incident along the Z axis):

$$F(x_i,y_i,z_i) = n_g(x_i,y_i,z_i)\, n_p(x_i,y_i)\, \sigma_d(E_p)\, E_p^{1/2} + \Sigma_k\, n_g(x_i,y_i,z_i)\, n_{sec}(x_i,y_i,z_i,u_k,v_k,w_k)\, \sigma_d(\varepsilon_k)\, \varepsilon_k^{1/2}$$

where the density of primary electrons is equal to

$$n_p(x_i,y_i) = n_s(x_i,y_i,z_i)/(\, n_g(x_i,y_i,z_i)\, \sigma_{ion}(E_p)\, E_p^{1/2}\, \Delta t)$$

where $n_g(x_i,y_i,z_i)$ is the gas density in position (x_i,y_i,z_i), $n_{sec}(x_i,y_i,z_i,u_k,v_k,w_k)$ is the distribution function of the electrons, σ_d and σ_{ion} are total cross sections of ionization and dissociation of monosilane, E_p is the energy of electron beam, $n_s(x_i,y_i,z_i)$ is the density of sources appearing during the time Δt. The summation was implicated over energies of electrons in the ith cell.

Finally, using information on spatial distribution of dissociation rates, deposition rates were obtained on the base of standard DSMC techniques for the transport of molecules and gas surface interaction [3]. In calculations, the variable hard-sphere model for molecular interaction potential and the diffuse reflection model with complete thermal accommodation were used.

In Fig.2 the computed thickness profiles of molecules adhering to the substrate are given. For comparison we present ellipsometry data on film thickness of a-Si:H in the same figure. The good agreement indicates that film thickness is proportional to the values of the flux of molecules.

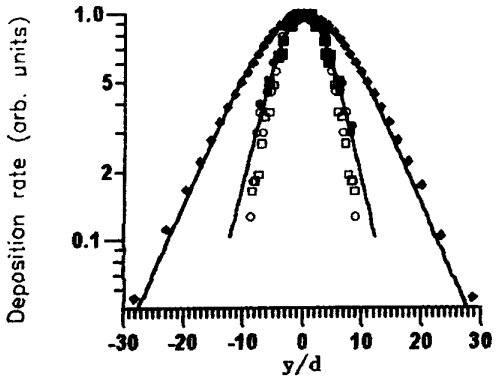

Fig.2 Euler equations - lines. Monte Carlo computations: ○ - P_0 d = 63 Topp mm, □ - P_0 d = 9.9 Topp mm. Measurements: ● - P_0 d = 63 Topp mm, ■ - P_0 d = 9.9 Topp mm, ◆ - P_0 d = 180 Topp mm; d=6.3 mm.

The dependencies of rate of dissociation of monosilane are given in Fig.3 as a function of position along the Y axis at different distances from the center of the beam (radius R_b) along the X axis. The results indicate that secondary electrons located at a distance from the beam were distributed more uniformly in space than primary electrons. It was found that this fact is the important reason for the formation of spatially uniform thin films deposited from the jet excited by an electron beam.

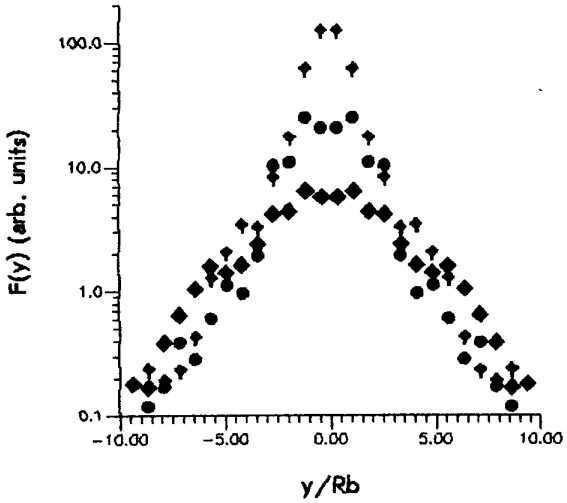

Fig.3 Rate of dissociation of monosilane vs distance from the jet axis: ● - x/R_b = -3, ✦- x/R_b =0, ◆- x/R_b = 3. E_p=16 keV, P_0=15.3 Torr, d=4.5 mm, R_b =2 mm.

It was shown that secondary electrons make an essential contribution to dissociation of monosilane and consequently to deposition of thin films of a-Si:H. From comparison of deposition rates calculated and experimental data effective sticking coefficient was determined. Its value 0.07 was compared favorably with those from the literature [6]. In fig.4 it is shown a comparison between computations and measurements of spatial dependencies of absolute deposition rate.

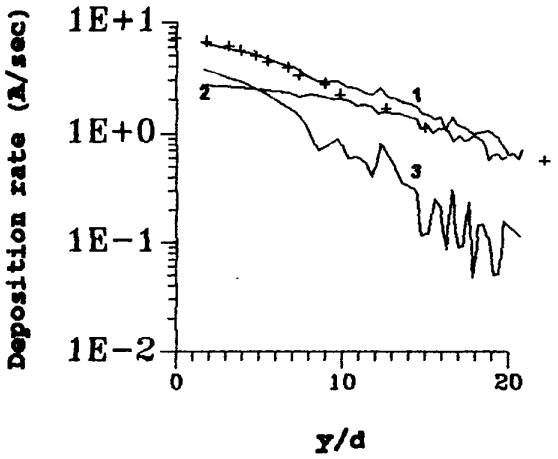

Fig.4 Dependencies of the a-Si:H film deposition rate on the distance from the jet axis X. Monte Carlo calculations - lines: 1 - total contribution, 2 - contribution from secondary electrons, 3- contribution from primary electrons. Experimental data - points. The conditions are the same as in Fig.3.

[1]. R.G. Sharafutdinov, A.V. Skrynnikov, A.V. Parakhnevich, B.M. Ayupov, A.M. Badalian, O.V. Polyakov, M.R. Baklanov, K.P. Mogilnikov, and S.A. Biryukov: J. Appl. Phys., **79** (1996) 7274
[2]. V.S.Malinovsky and A.V.Vasenkov: Phys. Rev. E, **52** (1995) R2175
[3]. A.V.Vasenkov, A.E.Belikov, R.G. Sharafutdinov, and O.V.Kuznetsov: J. Appl. Phys., **77** (1995) 4757
[4]. V.S.Malinovsky and A.V.Vasenkov: Phys. Rev. E, **50** (1994) 4969
[5]. J. Perrin, J.P.M. Schmitt, G.De Rosny, B. Drevillon, J. Huc, A. Lloret: Chem. Phys., **73** (1982) 383
[6]. A.Matsuda, K.Nomoto, Y.Takeuchi, A.Suzuki, A.Yuuki, J.Perrin: Surface Science, **227** (1990) 50

Emission spectroscopy in a deposition zone of the magnetron system for the preparation of carbon nitride films

J. Vlček, K. Rusňák and V. Hájek
Department of Physics, University of West Bohemia, Univerzitní 22, 306 14 Plzeň, Czech Republic

1. Introduction

The attempts to synthesize the superhard crystalline β-C_3N_4 phase [1] have resulted in several different kinds of carbon nitride (CN_x) compounds. In spite of the fact that a majority of the CN_x films prepared by a variety of sophisticated techniques (see e.g. [2] and the works cited therein) is amorphous and substoichiometric in nitrogen, these layers have interesting and potentially very useful mechanical properties for surface engineering [3, 4]. However, little is known today about the deposition mechanisms of CN_x materials.
The main aim of this work is to obtain reliable experimental data on the occurrence of the selected excited states of significant atoms, molecules and ions in a substrate region of the magnetron system used in the deposition of the CN_x films. The emitted light spectra have been measured in a dependence on the negative substrate bias voltage U_b, which is an important process parameter determining the chemical composition, structure and properties of the deposited films.
Motivation for this study came from a desire to understand better the mechanisms governing the production of excited states, which is strongly coupled with the complex physico-chemical phenomena on the surface of growing films.

2. Experimental details

The CN_x films were deposited on Si(100) substrates using DC magnetron sputtering of a high-purity 99.99 % graphite target in a pure 99.999 % nitrogen discharge at the pressure p in the range from 0.15 to 5 Pa and the constant gas flow of 75 sccm. The target-to-substrate distance was 100 mm. The discharge current on the cathode was held at 1 A, while the substrate temperature T_s was varied by an ohmic heater between 50 and 600 °C, and the negative substrate bias U_b induced by an RF generator operating at a frequency of 13.56 MHz was in the range from 0 to -1200 V.
Optical emission spectroscopy of the discharge was carried out using a computer controlled system comprising a Jobin-Yvon THR 1000S monochromator. The emitted light was studied in two positions characterized by the distances of 5 and 50 mm from the substrate. Spatial resolution along the axis of the discharge between a plane cathode and a paralell plane substrate was achieved by means of a fibre optic cable fitted with a 150 mm long and 4 mm wide collimating tube, pointing perpendicularly towards the axis. The spectrometer resolution was adjusted to 0.05 nm.

Table 1. Data characterizing the spectral lines investigated in this paper.

Species	Spectral lines [nm]	Transitions
N	493.5	$2p^24p \rightarrow 2p^23s$
N_2	337.1	$C^3\Pi \rightarrow B^3\Pi$ (0,0)
N^+	568.0	$2p3p \rightarrow 2p3s$
N_2^+	391.4	$B^2\Sigma \rightarrow X^2\Sigma$ (0,0)
CN	388.3	$B^2\Sigma \rightarrow A^2\Pi$ (0,0)
C	247.9	$2p3s \rightarrow 2p^2$

3. Results and discussion

The basic data characterizing the spectral lines investigated in this paper are given in table 1.
As we are interested here in an effect of the RF-induced negative substrate bias voltage U_b on the processes in a discharge near the substrate, figures 1 and 2 are included to illustrate a strong influence of this important parameter on properties of the layers deposited under the same conditions. In figure 1 we give our results for the N/C ratio in the CN_x films evaluated using elastic recoil detection analysis (ERDA). Figure 2 shows their hardness measured by a computer controlled microindentor Fischerscope H 100.
Increasing the U_b values at the substrate temperature of 600 °C and the pressures in the range from 0.15 to 5 Pa resulted in an increase in film density from 1.5 to 2.7 g/cm^3, and a decrease in surface roughness from 13 to 2 nm. This densification was accompanied by an increased hardness (from 2 to 27 GPa) and by higher adhesion to the silicon substrate. Tribological behaviour of these amorphous CN_x films, typically 1 to 2 μm thick, is studied in paper [4].
In figure 3 we present relative intensities of the selected spectral lines, which were measured in the position of 5 mm from a substrate as functions of the RF-induced negative substrate bias U_b at p = 0.5 Pa and T_s = 600 °C. As is shown, the populations in all excited states (see table 1) increase with a growing value of the applied RF power.
It is mainly due to enlarged values of the number density and kinetic temperature of electrons in the deposition zone, but the dissociative charge transfer between N_2^+ and N_2 might also play a role in producing the N atoms and N^+ ions near the substrate [5].

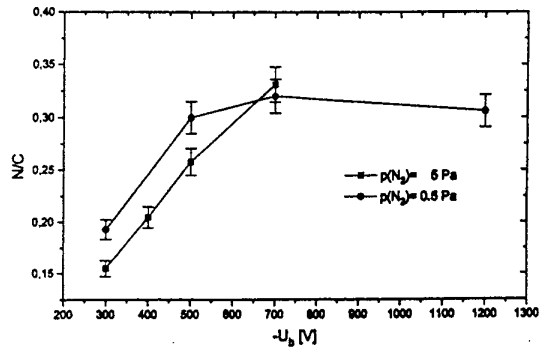

Figure 1. The N/C ratio in the CN_x films as a function of the RF-induced negative substrate bias voltage U_b at $T_s = 600$ °C.

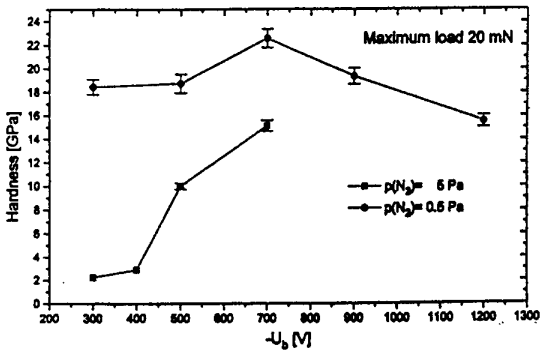

Figure 2. The hardness of the CN_x films as a function of the RF-induced negative substrate bias voltage U_b at $T_s = 600$ °C.

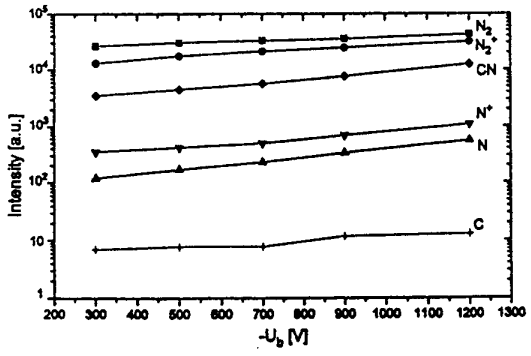

Figure 3. The relative intensity of the selected spectral lines measured in the deposition zone as a function of the RF-induced negative substrate bias U_b at $p = 0.5$ Pa and $T_s = 600$ °C.

Let us recall that CN radicals and N atoms are assumed to be the most appropriate precursors for the deposition of CN_x films and that a sufficient concentration of atomic nitrogen species in a discharge is required to ensure nitrogen incorporation in the growing layers [2, 6]. In figure 4 the intensity ratios of $I(N)/I(N_2)$ and I(N)/I(CN), measured in the deposition zone (5 mm from the substrate) and in the discharge plasma (50 mm from the substrate), are given as functions of the RF-induced negative substrate bias voltage U_b at $p = 0.5$ Pa and $T_s = 600$ °C to illustrate a tendency towards increased occurrence of N atoms in comparison with N_2 molecules in both investigated positions, and N atoms in comparison with CN molecules in the deposition zone, when the applied RF power increases.

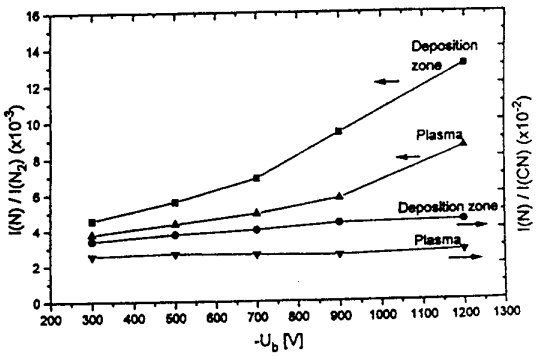

Figure 4. The ratios $I(N)/I(N_2)$ and I(N)/I(CN) measured in the deposition zone and in the plasma as functions of the RF-induced negative substrate bias U_b at $p = 0.5$ Pa and $T_s = 600$ °C.

As can be seen in figure 4, the growing influence of dissociation of N_2 molecules in the deposition zone leads to the increase in the ratio of the concentration of atomic nitrogen to that of CN species. It correlates with an increase in the N/C ratio in the CN_x layers (see figure 1) at lower values of the RF power, which are the most appropriate for the deposition process with regard to resputtering of the growing films.

This work has been partially supported by the Czech Grant Agency under Grant No. 106/96/K245 and by the Ministry of Education of the Czech Republic under Grant No. VS 96 059.

4. References

[1] A.Y. Liu, M.L. Cohen: Science, 245 (1989) 841
[2] S. Vepřek, J. Weidmann, and F. Glatz: J. Vac. Sci. Technol. A, 13 (1995) 2914
[3] H. Sjöström, L. Hultman, J.-E. Sundgren, S.V. Hainsworth, T.F. Page, G.S.A.M. Theunissen: J. Vac. Sci. Technol. A, 14 (1996) 56
[4] V. Hájek, K. Rusňák, J. Vlček, L. Martinů, H.M. Hawthorne: 11th Internat. Confer. on Wear of Materials, and Internat. Confer. on Metallurgical Coatings and Thin Films, San Diego (1997), submitted
[5] K.S. Fancey: Vacuum, 46 (1995) 695
[6] T. Okada, S. Yamada, Y. Takeuchi, and T. Wada: J. Appl. Phys., 78 (1995) 7416

Influence of Discharge and Substrate Parameters on PECVD of TEOS/Argon Mixtures

L. Zajíčková, V. Buršíková and J.Janča
Department of Physical Electronics, Faculty of Science, Masaryk University, Kotlářská 2, 611 37 Brno, Czech Republic,
e-mail: lenkaz@physics.muni.cz

1. Introduction

Tetraethoxysilane (TEOS) is an organosilicon compound widely used for CVD and plasma enhanced CVD of silicon dioxide films in the mixture with oxidant gases (O_2, N_2O, CO). These studies are applied in microelectronics. Beyond their dielectric properties, plasma deposited SiO_2-like films are characterized by other interesting properties which make them very promising material for many other applications (pigments and metal protection against photodegradation and corrosion, respectively, hardening of transparent plastics and polycarbonate etc.). These application do not always require $Si0_2$-like films. Polymers with an appreciable organic fraction, deposited without an oxidant gas in the feed, from several organosilicon compounds are usually suitable for many above applications (see for instance [1]). The advantage of TEOS compared with silane is its easy handling due to low flammability.

2. Experimental

The films were deposited by plasma enhanced CVD in a diode planar reactor described in [2]. The lower electrode capacitatively coupled to rf generator was used as a substrate holder. All films were deposited at rf power 100W (self bias -250V) and frequency 13.56MHz. TEOS vapour was introduced from glass bottle keeping liquid TEOS without any carrier gas. For all carried depositions the flow rate of TEOS was established by needle valve at 0.3 sccm. The flow rate of argon was regulated by Hastings HFC flow controller from 1.7 to 3.5sccm. The total pressure was from 12.8 to 20.1Pa in dependence on argon flow rate. The substrate electrode was a hard aluminum plate covered by plasma deposited film. The silicon substrates with different specific resistance (from 0.06 to 40Ω.cm) were putted on or sealed to the substrate electrode. To obtain more uniform films mixture of TEOS and argon was supplied by many inlets in the glass circle placed 7 or 4cm above the substrate electrode.

During the plasma processes we have measured the temperature of substrate electrode or silicon wafers by Raytek Thermalert LTCF2 pyrometer. Because of possible problems with object emissivity we have used the stickers with standard emissivity $\varepsilon = 0.95$ supplied by Raytek.

The reflectance of thin films on silicon substrates within the wavelength region 200 - 900nm were measured by an spectrophotometer ZEISS SPECORD M42. To find the thickness and the optical parameters of the thin films we have performed numeric minimization procedure of the least squared method (Marquardt - Levenberg) in the region 400 - 900nm. The model of a single homogenous film fitted well the measured values. Microhardness measurements were made using a Hanemann Vickers microhardness tester [3]. The film hardness was separated from the hardness of system film - substrate as described in [4].

3. Results and Discussion

In the arrangement with the reactant inlets 7 cm above the substrates we have deposited films changing the argon flow rate from 1.7 sccm to 2.5 sccm. The growth rate and the hardness of films deposited on silicon substrates 40 Ω.cm are in Fig. 1. The refractive a absorption indices did not show any clear dependence on deposition conditions. Refractive index at 650 nm was in range 1.72 - 1.77 and absorption index was in the range 0.01 - 0.05. This values are higher than for SiO_2-like films and differ from values declared in [5] for argon/TEOS mixtures.

To exclude the possible influence of temperature we have measured the temperature of electrode during 45min of argon and argon/TEOS discharges for argon flow rate from 1.7 to 3.5sccm starting from room temperature 25°C. Final temperature did not differ for various flow rates, mean value was (75 ± 4) °C. The temperature is not responsible for changes in films properties shown in Fig. 1. Mukherjee et. al. [6] supposed for argon/TEOS deposition that an increase of pressure causes a decrease of deposition rate because of electron energy decrease. Another explanation of deposition rate behaviour which could explain hardness dependence too is an increase of ion bombardment.

An interesting result is concerned to the temperature measured during deposition from argon/TEOS plasma. The electrode temperature is a little higher (88.9 °C)

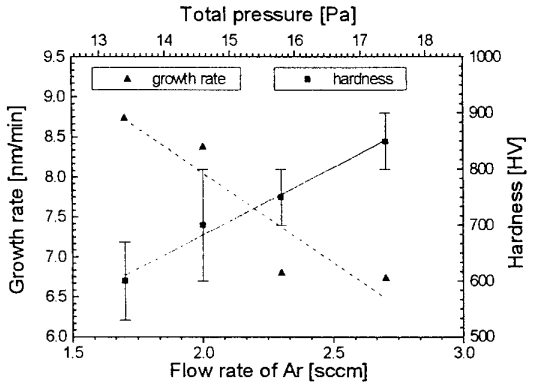

Figure 1 Influence of argon flow rate (total pressure) on growth rate and hardness of films deposited in argon/TEOS plasmas (P = 100W, U = -250V, TEOS flow rate 0.3sccm).

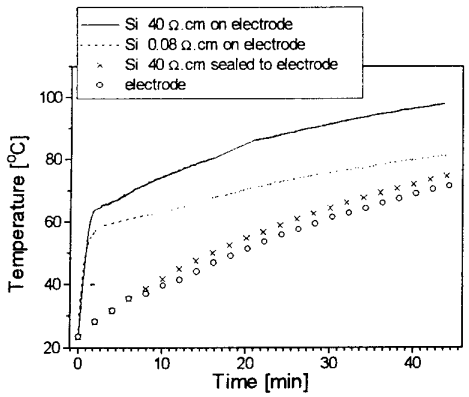

Figure 2 Temperature of various objects during argon discharge: P = 100W, U = -250V, argon flow rate 2.7sccm, pressure 17Pa.

than this one for pure argon plasma. We have check up the emissivity of the sticker after 45 minutes ofdeposition and find that emissivity decreased to 0.93. Such small change could not changed the true temperature and moreover it should decrease the measured temperature.

In the previous study we have found out that properties of films deposited from TEOS and TEOS/methanol mixtures depend on specific resistance of silicon wafer [2]. We have voiced that the temperature of different silicon wafers differs and causes unmistakable changes of film properties [7]. Optical properties and thickness of films deposited from argon/TEOS mixture again depend on specific resistance of silicon. The microhardness was in the range of experimental errors the same for different silicon substrates.

To confirm our assumption about temperature we have measured temperature of silicon wafers (40Ω.cm, 0.08Ω.cm) putted on electrode and temperature of silicon wafer 40Ω.cm sealed to the electrode by silver paste. We have sealed the stickers with ε = 0.95 to the silicon but the part of silicon surface was left uncovered. Temperature measurements in pure argon plasma (see Fig. 3) show that

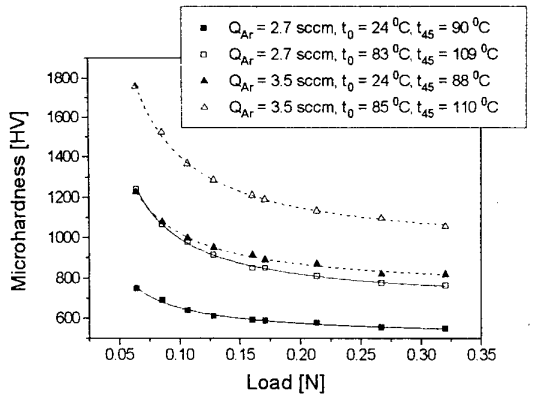

Figure 3 Dependence of microhardness on applied load.

pure thermocontact between silicon and electrode results in different surface temperatures. The silicon wafer is cooled mainly by radiation that depends on its emissivity. We have determined by pyrometer that the silicon 40Ω.cm has ε = 0.22, silicon 0.08Ω.cm has ε = 0.72 and the electrode covered by thick plasma deposited film has ε = 0.87. This is in perfect agreement with temperature measurements in Fig. 3. For discussed silicon the magnitude of absorption coefficients in infrared differ about several orders [8] and therefore differ emissivity too.

We have tested the influence of supply inlet position and starting electrode temperature on film properties. The films microhardness for reactant inlets only 3 cm above the substrates was generally lower than this one for the distance 7 cm. To achieved the same hardness it was necessary to use higher argon flow rate (see Fig. 3). To qualify the influence of starting electrode temperature we have heated electrode with substrates before the deposition by argon plasma to the temperature 90 °C. The increase of film microhardness is marked from Fig. 3.

4. Conclusion

We have found that the hardness of films deposited from argon/TEOS mixture is proportional to argon flow rate and is higher for higher distance between the substrates and supply inlets. Deposition rate is inversely proportional to argon flow rate and depends on the position of reactant inlets. Refractive and absorption indices are higher than for SiO_2-like films. Optical properties and deposition rate depend on specific resistance of silicon substrate because of temperature difference.

5. Acknowledgement

The authors wish to thank Dr. V. Navrátil for the reflectance measurements. The present work was supported by the Grant Agency of Czech Republic, contract 106/96/K245.

6. References

[1] N. Morosoff, in Plasma Deposition, Treatment, and Etching of Polymers, ed. R. d'Agostino, Academic Press, Inc., New York (1990), and references therein
[2] L. Zajíčková, I. Ohlídal, J. Janča, Thin Solid Films, 280 (1996) 26
[3] V. Navrátil, V. Stejskalová, Phys. Stat. Sol. (a), 157 (1996) 339
[4] J. Jönsson, S. Hogmark, Thin Solid Films, 114 (1984) 257
[5] M.G.J. Veprek-Heijman, D. Boutard, J. Electrochem. Soc., 138 (1991) 2042
[6] S.P. Mukherjee, P.E. Evans, Thin Solid Films, 14 (1972) 105
[7] L. Zajíčková, J. Janča, Proceedings of ESCAMPIG 96, Poprad, (1996) 315
[8] J. Humlíček, K. Vojtěchovský, Czech J. Phys. B, 38 (1988) 1033

Topic 15

Particle and laser beam interaction with plasmas.

Molecular admixtures role in the kinetics and radiation of helium beam plasma.

A.H.Amirov, O.V.Korshunov, V.F.Chinnov
Associate Institute for High Temperatures Russian Academy of Sciencies, Izhorskaya 13/19 127412 Moscow RUSSIA
B.N.Lomakin, A.A.Sunarchin, M.G.Tichonov
Keldysh Research Center Russian Space Agency, Onezhskaya 8/10 125438 Moscow RUSSIA

1. Introduction

Natural molecular admixtures (N_2, O_2, H_2O), inevitably presented in tank helium (for example, in commercial tank helium relative contents of O_2 and N_2 are about 10^{-6} and 10^{-5} respectively) rapidly change energy transfer processes in helium plasma. Due to their high excitation and ionization potentials, active helium species (excited atoms He^*, molecules He_2^*, atomic He^+ and molecular He_2^+, He_3^+ ions) effectively interact with molecules N_2, O_2, H_2O, and, if their contents correspond to the level, mentioned above, ionic constitution and radiative properties of such plasma mixture significantly differ from that properties of pure helium plasma.

This paper is devoted to analysis of the experimentally recorded spectra of beam helium plasma with molecular admixtures, noted above.

Experimental scheme.

It is shown in Fig.1.

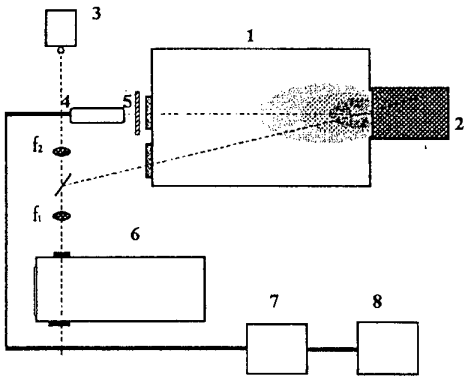

Fig.1

1 - chamber; 2 - electron accelerator; 3 - line spectrum source; 4 - PM; 5 - removable optical filter; 6 - diffractional spectrograph; 7 - analog to digital converter; 8 - computer.

Beam plasma was created in metallic chamber by impulsive electron accelerator. Accelerator produced impulses with following parameters: time of impulse $t_{imp} \sim 150$ ns, average electron energy $E_e \sim 220$keV, total energy in impulse $E_{imp} \sim 0.2$J, repetition frequency f =10Hz. The experiments were carried out in He at pressure 0.11 MPa. The radiation, emitted by plasma, was recorded photographically by diffractional spectrograph, wich permited measurements in wavelength range 260-620 nm, containing such molecular bands, as $N_2(2^+)$, $N_2(1^+)$, $N_2^+(1^-)$, $O_2(1^+)$, $O_2^+(1^-)$, OH(Meinel) and strong lines of He I (587.6, 447.1, 388.9 nm). In addition, time dependence of plasma radiation was recorded by photomultiplier with removable optical filters. Used in experiments filters had following transparency bands: 450–550 nm, 550-650 nm, 650–750 nm. Averaged by volume of chamber electron concentration was derived from microwave measurements.The near foil plasma region with concentration of $n_e \geq 10^{11}$ cm^{-3} was observed and analyzed.

3. Experimental results and their discussion.

Components, identified in spectra, are listed in Table 1.

Table 1.

N	Wavelength, nm	Belongs to
1	282.2	N_2^* (2^+, v' = 3, v'' = 0)
2	306.4	OH ($A^2\Sigma$ -$X^2\Pi$, 0-0)
3	306.8	OH ($A^2\Sigma$ -$X^2\Pi$, 0-0)
4	310.9	OH ($A^2\Sigma$ –$X^2\Pi$, 1-1)
5	312.2	OH ($A^2\Sigma$ -$X^2\Pi$)
6	313.6	OH ($A^2\Sigma$-$X^2\Pi$), N_2^+(2^+, 2-1)
7	315.9	N_2^* (2^+, 1-0)
8	333.9	N_2^* (2^+, 1-1)
9	337.1	N_2^* (2^+, 0-0)
10	350.0	N_2^* (2^+, 2-3)
11	353.7	N_2^* (2^+, 1-2)
12	367.2	N_2^* (2^+, 3-5)
13	375.5	N_2^* (2^+, 1-3)
14	380.5	N_2^* (2^+, 0-2)
15	391.4	N_2^+ (1^-, 0-0)
16	427.0	N_2^* (2^+, 1-5)
17	427.8	N_2^+ (1^-, 0-1)
18	470.9	N_2^+ (1^-, 0-2)
19	522.8	N_2^+ (1^-, 0-3)
20	587.6	HeI
21	594.7	N_2^* (1^+, 8-4)
22	611.4	N_2^* (1^+, 5-1)

The densitograms of helium spectra, obtained with diffractional spectrograph, are shown in Fig.2.

The most intensive components in spectrum of relatively pure helium are: OH^* bands (306-314 nm), N_2^+(1-st negative, 0-0, 0-1) bands and He I (587.6 nm) line. In helium with molecular admixtures OH^* bands slightly weaken, but remain considerable, intensity of N_2^+(1-st negative, 0-0, 0-1, 0-2, 0-3) increases and

intensity of He I (587.6 nm) significantly decreases. The bands of $O_2^+(1^-$; $\Delta v=2,-1,0$; $\lambda=529.6$, 563.2, 602.6nm) as well as He lines at 388.9, 447.2 and

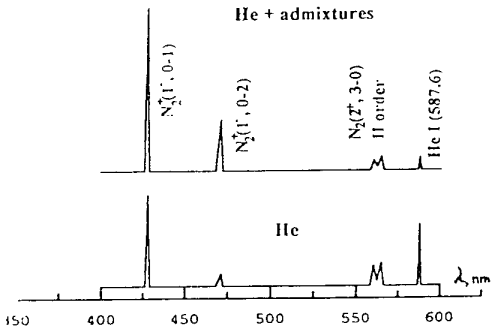

Fig.2

501.6 nm are very weak or absent. These facts, as we think, could be due to:

1) charge transfer reaction

$N_2^+(B^2\Sigma) + O_2 \rightarrow O_2^+(b^4\Sigma) + N_2^+$ (1) *

doesn't create sufficiently quantity of $O_2^+(b^4\Sigma)$ [1].

2) relatively low probabilities of radiative transisions from $O_2^+(b^4\Sigma)$ ($A_{ki} < 10^6 c^{-1}$, while for observed in spectra $N_2^+(1^-)$ $A_{ki} \sim 1.7\ 10^7\ c^{-1}$) [1].

3) high speed of nonradiative losses of He^* in reactions of conversion, charge transfer and assotiative ionization [1], [2]:

$$He^* + 2He \rightarrow He_2^* + He \quad (2)$$
$$He^* + N_2 \rightarrow N_2^{+\bullet} + He \quad (3)$$
$$He^* + He \rightarrow He_2^+ + e \quad (4)$$

All reasons, stated above are confirmed by the analisys of PM signals time dependences. Characteristic signals are represented in Fig.3. The ratio of admixtures in two cases, noted as "He" and "He + admixtures" is about 10. The behaviour of signals is following: in wavelength range 450-550 nm as the content of molecular gases in helium increases, the signal becames narrow, its amplitude significantly increases; signal in wavelength range 550-650 nm has two maximums in relatively pure He, while in He with molecular admixtures signal becames monotonouse and narrow, its amplitude increases, but not so sharply, as in range 450-550 nm.

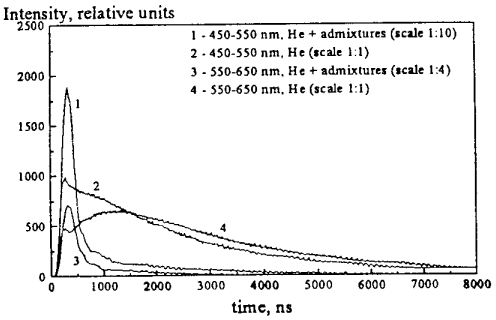

Fig.3

Radiation, registered in range 450-550 nm is due to $N_2^+(1^-, 0\text{-}3)$ (522.8nm), N_2^+ $(1^-, 0\text{-}2)$ (470.9nm). These species are formed in reactions [2], [3], [4]:

$$He_2^* + N_2 \rightarrow N_2^+(B,A) + 2He \quad (5)$$
$$He_2^* + N_2 + He \rightarrow N_2^+(B,A) + 3He \quad (6)$$

Then N_2^+ converts to N_4^+ in reaction

$$N_2^+ + N_2 + He \rightarrow N_4^+ + He \quad (7)$$

but radiation decay of $N_2^+(B^2\Sigma_u^+)$ proceedes with highier speed [1], [2].

After ~1.5μs radiation in this range follows $N_2^+(B)$ formation by Penning ionization of N_2:

$$He^*(2^3S, 2^1S) + N_2 \rightarrow N_2^{+\bullet} + He \quad (8)$$

The time (2μs) of signal decrease corresponds the $[He^*]$ decrease in (8), if $[N_2]$ ~5 $10^{15} cm^{-3}$. This value is in agreement with microwave measurements of $[O_2]$ and presumption, that $[O_2]$: $[N_2]$ = 1:4, as in air. In He with admixtures the same processes proceed, but their speed increases.

More interesting the behaviour of signal in 550-650nm. As this range embraces radiation of He I (587.6nm), He_2^* (640nm), $N_2^*(1^+, 8\text{-}4)$ (594.7nm), $O_2^+(1^-, 0\text{-}0)$ (602.6nm), $N_2^*(1^+, 5\text{-}1)$ (611.4nm), the interpretation of registered radiation is complicated. Unlikely He_2^* (640nm) line is beyond the range, registered by spectrograph, and we have no data about it's intensity. We assume, that behaviour of PM signal in this range is due to joint radiation of all species, mentioned above, but after ~3μs radiation of $N_2^*(1^+, 8\text{-}4)$ and $N_2^*(1^+, 5\text{-}1)$, formed in dissociative recombination of N_4^+, produced in (7):

$$N_4^+ + e \rightarrow N_2^* + N_2 \quad (9)$$

dominates. The time (3μs) of signal decrease corresponds the decrease of $N_2^*(1^+, 8\text{-}4)$ and $N_2^*(1^+, 5\text{-}1)$ due to vibrational relaxation and radiative decay.

In longer period of time ~15μs attachment of electron to O_2, conversion of simple ions to complex one [4]:

$$N_4^+ + H_2O + (He) \rightarrow H_2O^+ + 2N_2 + (He) \quad (10)$$
$$H_2O^+ + H_2O + (He) \rightarrow H_3O^+ + OH + (He) \quad (11)$$
$$H_3O^+ + H_2O + (He) \rightarrow H_3O^+(H_2O) + (He) \quad (12)$$
$$O_2^- + H_2O + (He) \rightarrow O_2^-(H_2O) + (He) \quad (13)$$

proceed, and finally charged particles recombine in reactions [4]:

$$O_2^-(H_2O) + H_3O^+(H_2O) \rightarrow \text{products} \quad (14)$$
$$O_2^-(H_2O) + H_3O^+(H_2O) + He \rightarrow \text{products} \quad (15)$$

References

[1] A.A. Radzig, B.M. Smirnov: Handbook on Atomic and Molecular Physics. M., Atomizdat, (1980).

[2] B.M. Smirnov: Complex Ions. M., Nauka, (1983).

[3] B.M. Smirnov: Ions and Exited Atoms in Plasma. Moscow, Atomizdat, (1974).

[4] H. Matzing: Chemical Kinetics of Flue Gas Cleaning by Electron Beam. Report KK4404, Karlsruhe, (1989).

C_2 emission of laser produced carbon plasma in an ambient gas

S. Abdelli, T. Kerdja, M. Si-Bachir and S. Malek
Laboratoire d'Interaction Laser-Matière
Centre de Développement des Téchnologies Avancées
128 chemin Mohamed Gacem, El-Madania, Alger, Algérie.

The interaction of high power laser beams with a graphite target in an ambient gas has become a subject of great interest since the first report on the existence of stable carbon clusters in laser ablated plumes[1]. Depending upon the time of observation, position of the sampled volume within the plasma, the relative abundance of the different type of carbon clusters has been found to change. In this paper, we report on experimental results on C_2 emission studies in laser vaporization of graphite target in three different gases environment. The relationship between the presence of these lines and the growth of diamond is always related to good quality diamond films and appears to be a "universal" feature[2].

The appearance of the high pressure Swan band ($v' = 6$) in helium is also reported.

I. Molecular Swan band emission.

In the presence of a background gas, the molecular emission at 516.5 nm corresponding to the well known Swan band emission will dominate the plasma emission.

As the surrounding gas pressure is increased, the molecular Swan band emission increases and the maximum intensity location moves to the left-hand side (target surface), the spatial profile becoming larger and sharper[3] (Fig.1). Beyond a some pressure depending on the gas nature (150 mbar, 100 mbar and 5 mbar for hydrogen, helium and argon respectively) the maximum emission comes very close to the target surface and then the Swan band emissivity will be masked by the continuum emission from the dense phase of the plasma. The consistency of the measured values for the three gases was tested by fitting the dependance of the maximum emission intensity of the Swan band at 516.5 nm, on the product of molar mass and the pressure of the foreign gas. The result is shown in Fig. 2. As the ambient gas pressure increase, the maximum emission intensity of the Swan band increases but the dependance of the Swan band intensity versus the gas pressure exhibit alike saturation at high pressure. The general behavior of the curve is the same for the three gases as seen in Fig. 2, but helium gives the highest intensity

II. Temporal evolution.

Fig. 3 shows the z-t plot of CII* transition at 426.7nm, CI* transition at 247.8nm and C_2 emission at 516.5nm. Fig.3 shows that at earlier time all the transitions involved have approximatively the same space-time behavior. Above 0.3μsec the time delay between the C_2* emission and CI* emission increases but the slope of C_2* emission remains constant suggesting the same production mechanism for C_2* emission over 0.3 μsec. At earlier time, C_2 are probably produced by the strong recombination occuring in the vicinity of the target surface, the recombination rate being strongly dependent on electron temperature increases as the plasma is cooled by expansion[4]. Cooling of the vapor by the surrounded gas results in condensation and the ultrafine particle creation[5]. Collisional ionization and three body recombination are the mains process occuring in the vicinity of the target surface, so we get excited state C_2 formation slightly away from the target surface.

Another possible mechanism of C_2 production is the dissociation of large clusters in the expanding plasma[6]. Clusters of carbon (C_n , $n>2$) along with electrons are ejected from the graphite target and C_2 could be formed by the dissociation of C_n due to collisions with energetic electrons. However, at large distance ($\cong$ 0.6 cm) from the target surface, the plasma is colder, but the confinment caused by the shock wave enhance the temperature exciting molecular vibrations which can cause molecular or clusters dissociation.

III. High pressure band appearance.

Spectral and kinetic observation by others support two classifications for C_2 emission : normal Swan band associated with $v' = 0$-6 and high pressure Swan band associated with an excess population in $v' = 6$ level[7]. Vibrations $v' > 6$ correspond to headless or tail bands which are not always evident. Fig. 4 shows microdensitometer traces of the plasma emission around 470.0 nm representing the vibrational excitation of the C_2 molecule in the $\Delta v = +1$ sequence in helium gas at 10mbar, at different distances from the target surface. The Swan band heads of (v',v'') i.e. (3-2) at 469.7nm, (4-3) at 468.4nm and (5-4) at 467.9nm are well identified. In addition to the vibrationnal excitation, the trace representes also the helium line at 468.6nm (0.2 nm to the red of the 4-3 band head). From the trace c taken at 0.25cm from the target surface, to the trace a (0.4cm) one can show an important enhancement of the vibrationnal excitation . This increase may be due to the shock wave produced by the plasma expansion in the gas and also may be due to the recombination process making the number of C_2

emitter increasing with distance. An important feature observed in the trace c is the red shift observed in the 5-4 band head corresponding to the (6-5) high pressure band, and the apparition of a tail at 466.6nm. The red shift is 0.2nm from the 5-4 band head and the tail is at 466.6nm. These effects are attributed to the excitation of the high pressure Swan band leading to an excess population in the v' = 6 level. The same feature is observed in argon below 1mbar. The tail band and the red shift are not still visible above 0.4 cm from the target surface corresponding to the maximum line enhancement observed earlier for CI* transition at 247.8nm[8].

Comparison in time evolution and spatial extension of the normal Swan band system represented by the intense (0,0) band head at 516.5nm and as an example of high pressure system the (6,8) band head at 589.9nm which is better isolated than the (6,5) band head, suggests a common intermediate or parallel production mechanism fo the two Swan band systems. The best fit of the spatial extension of the high pressure system follows exactly the spatial extension of the CII* transition at 426.7nm obtained in a previous work[3].

1.H.W. Kroto et al, Nature, 318,163,1985
2.M. Marinelli et al, J. Appl. Phys. 76,5702,1994
3.T. Kerdja et al, J. Appl. Phys. 80, 5365, 1996
4. P. T. Rumsby et al , Plasma Phys. 16,247,1974
5.A. G. Guedovets et al Proc. SPIE, 2716,274,1996
6.S. S. Hariral et al, J. Appl. Phys. 80, 3561, 1996
7. W. L. Faust et al Chem. Phys. Lett. 83, 265, 1981
8. S. Abdelli et al, submitted to J. Appl. Phys.

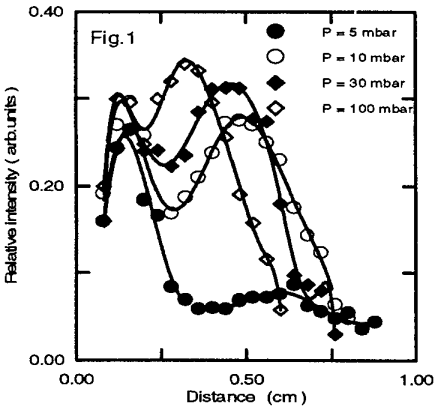

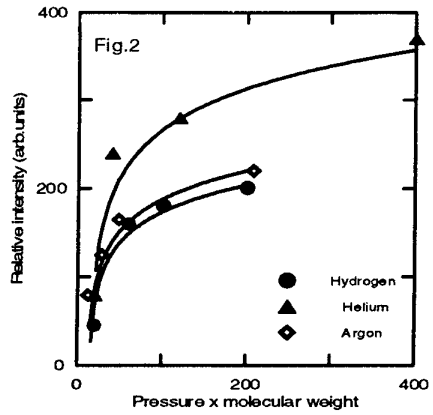

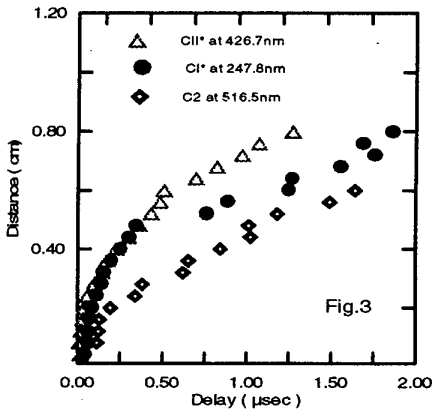

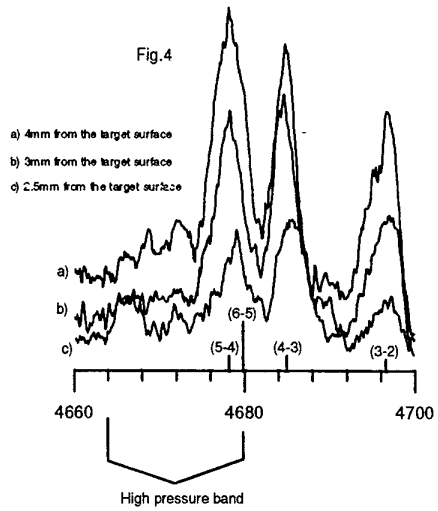

Coherent Structure Emitted by an Electron Beam in a Beam-Plasma System

Ichiro Mori, Toshifumi Morimoto*, Retsuo Kawakami and Kikuo Tominaga
Faculty of Engineering The University of Tokushima
Minami-josanjima 770 Tokushima Japan
*Takuma Radio Technical College
Kohda, Takuma, 761-11, Kagawa, Japan

ABSTRACT

A large amplitude upper hybrid solitary wave (soliton) was detected experimentally in a beam-plasma system. An amplitude of the solitary wave was up to 4 Volt in peak to peak at a terminal of oscilloscope in a 50-Ω system. The phases of coherence in carrier frequency ≃400 MHz were confirmed by using the HP-54542A-2GHz oscilloscope.

We succeeded theoretically in an attempt to describe an emission of solitary wave, ceated by an electron beam, with a renormalizing method. It was found that the presence of slower response of ions was necessary for the emission, i.e., without the ions, the electron beam could not emit a wave packet. The theoretical results were quite similar to that of the experiments.

1. EXPERIMENTS

The experiments are carried out by beam-plasma system. The plasma region is 16 cm in diameter and 42 cm in length, and a mirror magnetic field is 80 Gauss in center position with a mirror ratio of 1.4. Gun region is evacuated to 10^{-6} torr, while a plasma region is fed with argon gas from 10^{-4} to 10^{-3} Torr. A Pierce-type electron gun injects a mono-energetic electron beam with a diameter of 1 cm into the plasma region. The typical beam-parameter is 1.9 keV-18 mA. A stable low-density plasma ($\sim 10^8 cm^{-3}$) has been used in the experiments under the initial gas pressure of 5×10^{-4}Torr. For this stable low density region, we designate it as second stage, while at high density region, the third stage, we have the plasma density of $\sim 10^{12} cm^{-3}$. Transition from the second to the third stage is so called *Beam-Plasma Discharge* which may surely be started by the action of the solitary waves.

Large amplitude envelope solitary wave, measured by 2 GHz digital scope at antenna position of 24.5cm separated from beam entrance, is shown in fig.1. The carrier frequency is about 400 MHz so that its phase is very crowded, but phase continuity is proved.

2. THEORY

We start first to consider the interaction between an electron and an high frequency electric field and to consider also the trajectory of the electron mortion from its initial straight line to moderate curve by renormalization technique, which was initially used by Weinstock[1], Kono-Ichikawa[2]. They derived a Green's function, however, their diffusion coefficient degenerate to that of quasi-linear theory, when the coherent interactions in the same wave number are considered. Then as an idea, we used here a Gaussian-type Green's function in the real space, which was utilized by Horton[3] in his discussion of ion-acoustic turbulence.

Now our set of fundamental equation, which includes the transform of the Green's function, is as following :, where the $G(k,v,\omega;k',v',\omega')$, $D_{ij}(k,v)$, $\Sigma_\alpha(k,v,\omega)$ are the Green's function, the diffusion coefficient in velocity space, and the self-energy term respectively. For beam distribution, $f_\alpha^{(0)}(k',v',\omega')$, the δ-function is used.

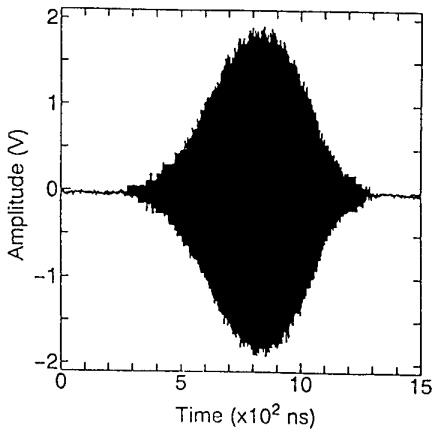

Fig1. The upper hybrid solitary wave detected by 2-GHz sampling oscilloscope is shown. Carier frequency of the solitary wave is ≃400MHz. Gas pressure of 5.3×10^{-4}Torr Ar is used.

$$G(k,v,\omega;k',v',\omega')$$
$$=-2i\{4\pi(\frac{k_ik_j}{k^2})\cdot D_{ij}(k,v)\}^{-\frac{3}{2}}\sum_{m=0}^{\infty}\frac{(-b)^m}{m!}\{\frac{a}{i(-\omega+c)}\}^{\frac{3m}{2}-\frac{1}{4}}K_{3m-\frac{1}{2}}\{2\sqrt{ia(-\omega+c)}\}\cdot\delta_{k,k'}\delta(\omega-\omega')$$

$$a=\frac{k_i(v-v')_ik_j(v-v')_j}{4k_ik_j\cdot D_{ij}(k,v)},\qquad b=\frac{k_ik_j\cdot D_{ij}(k,v)}{12},\qquad c=k\cdot v$$

$$D_{ij}(k,v)=(\frac{e_\alpha}{m_\alpha})^2\sum_{k_1}\int\frac{d\omega_1}{2\pi}\frac{k_{1i}k_{1j}}{{k_1}^2}|E(k_1,\omega_1)|^2G_\alpha(k-k_1,v,k\cdot v-\omega_1;k',v',\omega')\delta_{k,k'}\delta(\omega-\omega')$$

$$\boldsymbol{E}(k,\omega)=-\sum_\alpha\frac{e_\alpha}{\varepsilon_0}\cdot\frac{ik}{k^2}\int dv\int dv'\int\frac{dk'}{(2\pi)^3}G_\alpha(k,v,\omega;k',v',\omega')\cdot f_\alpha^{(0)}(k',v',\omega')$$

$$f_\alpha(k,v,\omega)=\int dv'G_\alpha(k,v,\omega;k',v',\omega')\cdot f_\alpha^{(0)}(k',v',\omega')$$

$$\Sigma_\alpha(k,v,\omega)=\quad=(\frac{e_\alpha}{m_\alpha})^2\sum_{k_1}\int\frac{d\omega_1}{2\pi}\boldsymbol{E}(k_1,\omega_1)\cdot\frac{\partial}{\partial v}\{G_\alpha(k-k_1,v,k\cdot v-\omega_1)\boldsymbol{E}(-k_1,-\omega_1)\cdot\frac{\partial}{\partial v}\}$$

To solve the above equation with respect to the electric field, We used only m=0th term, which is the most important one, and we put emphasis on the coherent interaction with the same wave number, i.e., $k_1=k$, so the self energy term is great importance. We assumed first that $|E(k_1,\omega_1)|^2=|E|^2$ =constant, then we get an equation for D_{ij} or y. At a working point of $y^{-2}=0.0344$, $ImF_1=0$, then we calculate the Σ_α. Finally, we get E(k,t) by inverse transformation. Thus the following results and the fig.2 are obtained.

$$\boldsymbol{E}(k,t)=\sum_\alpha\left(\frac{e_\alpha}{\varepsilon_0}\right)\left(\frac{ik}{k^2}\right)f_1^{(0)}(k)\cdot\left(\frac{4^q\cdot n_bv_0}{\pi^{\frac{1}{2}}\{C_1|E|^2t\}^{(\frac{3}{2}-q)}}\right)\cdot\left(\frac{1}{k\cdot v_0t}\right)\cdot$$
$$\cdot exp(-ik\cdot v_0t)\cdot sinh\left(\frac{Im\Sigma_\alpha}{2}t\right)\cdot\Gamma\left(q,a_1\left|\frac{Im\Sigma_\alpha}{2k}\right|^\nu\right),\qquad a_1=\frac{1}{4C_1|E|^2t}$$

$$Im\Sigma_\alpha=\frac{3\cdot exp(y)}{\frac{k_ik_j}{k^2}\cdot ReF_1}\left(\left[\frac{(k\cdot v)}{y}\cdot\{cos(-y)-sin(y)\}-\frac{(k\cdot v)}{2y^2}\cdot cos(-y)\right]\cdot\right.$$
$$\left.\cdot(S_{11}+S_{12}+S_{13})-\left[\frac{(k\cdot v)}{y}\cdot\{cos(-y)+sin(y)\}-\frac{(k\cdot v)}{2y^2}\cdot sin(y)\right]\cdot S_{21}\right),\qquad\frac{1}{y^2}=\frac{2D_{ij}}{\{(k\cdot v)|v-v'|^2\}}$$

$$ReF_1(y)=y\cdot e^y\{cos(y)-sin(y)\}-e^y\cdot cos(y),$$

$$C_1=\frac{1}{4\pi^2}\left(\frac{e_\alpha}{m_\alpha}\right)^2\frac{k_ik_j}{k^2}\cdot ReF_1(y),$$

$$S_{11}=-\frac{3}{8\pi D_{ij}^{\frac{5}{2}}}\cdot\frac{1}{|v-v'|^2}\cdot\frac{1}{(\pi t^3)^{\frac{1}{2}}}\cdot cos(-\gamma k\cdot v_0t),$$

$$S_{13}=-\frac{k^2|v-v'|}{16\pi D_{ij}^2}\cdot 1cos(-\gamma k\cdot v_0t),$$

$$S_{21}=\frac{1}{16\pi D_{ij}^{\frac{5}{2}}}\cdot\frac{1}{|v-v'|}\cdot\frac{1}{(\pi t)^{\frac{1}{2}}}\cdot cos(-\gamma k\cdot v_0t)$$

$$\gamma\simeq(\frac{m_e}{m_i})^{\frac{1}{2}}\simeq 3.7\times10^{-3},\quad q=1.3,\quad\nu=5$$

$$D_{ij}=C_1\cdot\frac{|E|^2}{|v-v'|^3},\qquad|v-v'|\simeq\left|\frac{Im\Sigma_\alpha}{2k}\right|$$

$$S_{12}=-\frac{k^2}{8\pi D_{ij}^{\frac{5}{2}}}\cdot\left(\frac{t}{\pi}\right)^{\frac{1}{2}}\cdot cos(-\gamma k\cdot v_0t),$$

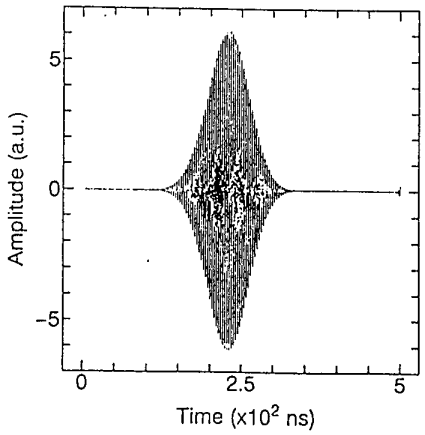

Fig.2. An example of the theoretical results is shown. So called *chirping* (frequency modulation) is seen, as in the optical soliton in the glass fibres, which originates in *Kerr-effect.*

REFERENCES

(1)J.Weinstock; Phys.Fluids,12(1969);p.1045

(2)M.Kono,Y.H.Ichikawa;Prog.Theor.Phys,49(1973); p.754

(3)C.W.Horton; Renormalized Plasma Turbulence, in *Long time prediction in Dynamics*, John Wiley(1983) p.311

Electron density of high pressure argon plasma produced by excimer laser

Norio TSUDA and Jun YAMADA
Dept. of Electronics, Aichi Institute of Technology
1247, Yachigusa, Yakusa, Toyota, 470-03 Japan

1. Introduction

When a XeCl excimer laser beam was focused in a high-pressure argon gas from 3 to 150 atm, a high temperature and dense plasma developed not only backward but also forward.[1] The forward development mechanism taking into account the self-focusing effect of the laser light by plasma was proposed.[2] Recently the mechanisms for self-focusing effect have been studied.[3] Then, the physical properties of the laser produced plasma were examined. The electron density of laser induced plasma was observed by a laser interferometer. It was found that an extremely dense plasma with an electron density of the order of 10^{27} m^{-3} was produced.

2. Experimental arrangement

A XeCl excimer laser with a maximum power of 17 MW, a wavelength of 308 nm and a full half-width of 30 ns is focused at the center of a gas chamber by a lens with a focal length of 40 mm. The output power of laser radiation is controlled by an optical filter. As the laser light is a rectangle of 11×24 mm, the focused laser light at the focal spot makes an ellipse of 120×80 μ m. The gas chamber is made of stainless steel and has an outer diameter of 110 mm and a length of 140 mm. It has four quartz glass windows of diameter 20 mm and thickness 15 mm. The electron density of the laser-produced plasma is measured by a Mach-Zender interferometer using an Ar-Ion laser.

3. Electron density

The electron density of laser induced plasma is measured by the Mach-Zender interferometer. The time variation of interferometer signal is shown in Fig. 1. When the gas chamber is evacuated, the change in interferometer signal is not observed. The number of fringes increase as the pressure increases. But it is difficult to find out a turning point in the fringe pattern at which the electron density reaches a maximum. Therefore, the peak electron density is estimated by extrapolating the observed electron density up to the time when the excimer laser pulse is terminated.

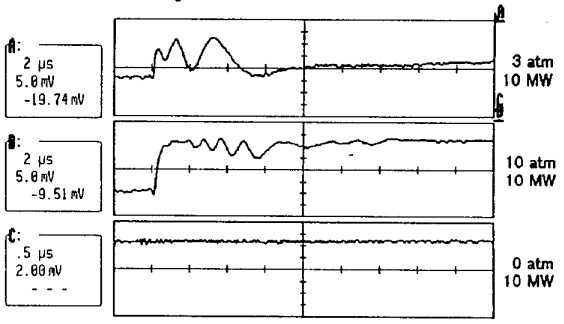

Fig. 1 Examples of interferometer signals.

Pressure dependence of peak electron density at the focal spot is shown in Fig. 2. The broken line in Fig. 2 indicates the initial gas atom density. The electron density increases with increasing pressure. When the laser power is 15 MW, the plasma is almost in a fully-ionized state from 3 to 150 atm. The dense plasma with an electron density of the order of $10^{25} \sim 10^{27}$ m^{-3} is produced. However, at the higher pressure the electron

density saturated and the degree of ionization decreases. Because the electron temperature decreases by collision with the surrounding gas and the number of recombination increases. To find out why the electron density decreases with increasing pressure, the electron density is calculated from the rate equation involving the collision ionization and the two-electron, three-body recombination processes. The electron density calculated assuming a constant electron temperature saturates with increasing pressure, and agrees qualitatively with the experimental results.

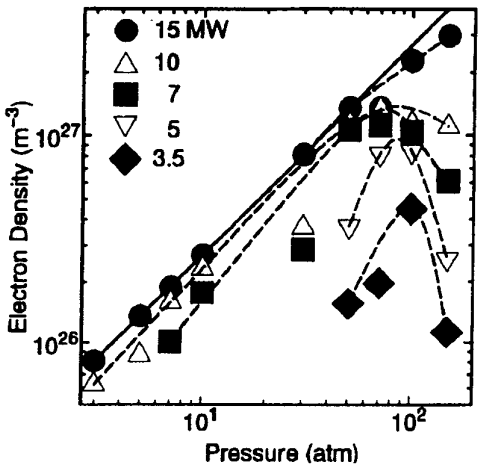

Fig. 2 Observed electron densities versus pressure; The broken line shows the initial atom density.

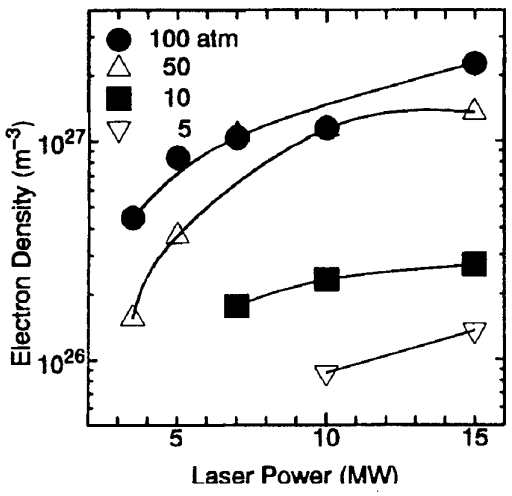

Fig. 3 Experimental values of electron densities versus laser power.

The dependence of the electron density at the focal spot on the laser power is shown in Fig. 3. The electron density increases rapidly and saturates with increasing laser power. The slope of curve at the higher laser power in Fig. 3 is bigger as the pressure increases. The dependence of the electron density on laser power is calculated. At the lower laser power, the electron density increases rapidly with increasing laser power. The rate of increase in the electron density on the laser power is bigger with increasing pressure.

4. Conclusion

When a XeCl excimer laser beam was focused in a high-pressure argon gas from 3 to 150 atm, a high temperature and dense plasma developed not only backward but also forward. The electron density of laser induced plasma was measured by the Mach-Zender interferometer. When the laser power was 15 MW, the electron density was proportional to the pressure and fully-ionized state was almost achieved up to 150 atm, however the electron density saturated and the degree of ionization decreased as the laser power decreased. It was found that the dense plasma could be produced relatively easily when the ultraviolet laser beam focused in a high-pressure gas.

5. References

[1] J. Yamada, N. Tsuda, Y. Uchida, H. Huruhashi, and T. Sahashi: IEE. Jpn, **114 A** (1994) 303

[2] N. Tsuda and J. Yamada: J. App. Phys, **70** (1997) (Now Printing)

[3] A.B. Borisov, X. shi, V.B.Karpov, V.V.Korobkin, J.C.Solem, O.B.Shiryaev, A.McPherson, K.Boyer, and C.K.Rhodes: J. Opt. Soc. Am, **B 11** (1994) 1941

REFLECTED AND RESONANCE TRANSITION RADIATION FROM MICRO BEAM PLASMA

V. A. Skvortsov, N. Vogel *)

High Energy Density Research Center of the Russian Academy of Sciences,
127412 Moscow, Izhorskaya 13/19, Russia
*) University of Technology Chemnitz-Zwickaw, Department of Physics, D-09107 Chemnitz,Germany

1. Introduction

This paper deals with an experimental and theoretical investigation of the sharp directed electromagnetic radiation generated during an interactions of an electron beam with plasma in presence of an electromagnetic wave of laser radiation. As it had been found in [1-3] a generation of subnanosecond dense micro beams of electrons and ions as well as a generation of an electromagnetic radiation opposed to laser beam occur in laser-spark discharge in air. In some experiments the intensity of this radiation was so high that under its penetration in Nd-YAG laser resonator the latter was destroyed. Some different mechanisms for an electromagnetic waves generation by beam - plasma interactions are possible [4]. We will consider only two following :

- a resonance transition radiation from beam - plasma interactions[5];
- a reflected laser beam radiation with frequency and intensity multiplication at moving front of plasma or by an accelerated electron and ion beams [6].

2.The Resonance Transition Radiation

During interaction of an intense laser beam with a metallic target as it had been found in [7] an injection of power electron beam with an extremely high current density. takes place. Also in [1-3] electron emission current density in laser-produced plasma was measured of order of $3 10^{10}$ A/cm^2 . According to [8] a stationary standing periodic Langmuir wave (SPLW) can be formed, when an electron beam interacts with a plasma. The plasma with a SPLW presents a periodic inhomogeneous medium. Hence a resonance transition radiation occurs under conditions when an electrons move with a velocity of $v_b \approx c$ through this medium, we can provided that following is fulfiled [10]:

$$[1-(v_b/c)\varepsilon_0^{1/2}\cos\theta](\omega/v_b)=2\pi r/L. \quad (1)$$

Here r is a number of harmonic; θ is an angle between a direction of emitted quantum with frequency ω and a velosity vector $\mathbf{v}_b$ which is directed along an axis z; c is a velocity of light, L is a period of inhomogeneity in the medium; ε_o is a dielectric permeability. The resonance condition (1) does not depend on an existence of an external magnetic field along the axis z [9]. Besides we can assume that a magnetic field $\mathbf{H}$ can exist and satisfies the inequality $\omega >> \omega_H$ ($\omega_H = eH/m_ec$ is a electron cyclotron frequency). The variation of an electron density averaged by ω_{pe} - high frequency oscillations in SPLW is determined by [8]:

$\delta n/n_p = -(4\nu K/l)^2 \, cn^2(4K\xi/l,\nu)$, $\xi=(2/3)^{1/2} z/\lambda_d$, (2)

where n_p is an ambient electron density; cn is an elliptic Yacobi function with the modules ν; λ_d -the Debye lenght ; $l=4K[(2\nu^2-1)/(\Omega+a)]^{1/2}$ -the dimensionless period of solution; $\Omega=4K(K-2E)/l^2$;$a=8KB(\nu/l)^2$. K,E,B -the full elliptic integrals ($K'=K[(1-\nu^2)^{1/2}]$; ω_{pe} -the electron plasma frequency. Formula (2) at $0.5 < \nu^2 \le 1$, $2K(\nu)<<l$ is valid. Under $\nu^2 \cong 0.5$ we have: $\alpha=2\pi/l$, $cn^2(\alpha u,\nu) \approx 0.5[cn(2\alpha u,\nu)+1]$.

Let us expand $cn(2\alpha u,\nu)$ in Fourier series:

$cn(2\alpha u,\nu)=(2\pi/\nu K)\sum b_n \cos[(2n+1)2\alpha\xi]$; $u=2K\xi/\pi$;

$b_n=\exp[-(2n+1)\pi K'/2K]/\{1+\exp[-(2n+1)\pi K'/K]\}$,

We can consider only the first term of this series in the first approximation . Then for tensor of dielectric permeability we can write the following expression [5]:

$$\underline{\varepsilon} = \begin{vmatrix} \varepsilon_1 & ig & 0 \\ -ig & \varepsilon_1 & 0 \\ 0 & 0 & \varepsilon_2 \end{vmatrix} \quad \begin{array}{l} \varepsilon_1 \approx \varepsilon_2 = \varepsilon_0 - \Delta\cos(2\pi z/L), \\ \varepsilon_0 = 1 - [1+8(\nu K/l)^2](\omega_{pe}/\omega)^2 ; \\ \Delta = (16\pi b_0 \nu K/l^2)(\omega_{pe}/\omega)^2 . \end{array} \quad (3)$$

Where $L=(3/8)^{1/2}\lambda_d l$; $g \approx (\omega_{pe}/\omega)^2(\omega_H/\omega) << 1$.

In this case we can calculate an energy of resonance transition radiation for the time τ in the frequency range $(\omega, \omega + d\omega)$ per one particle by using the formula [9]:

$$dI_\omega = (e^2 v\tau/c^2)\,\omega d\omega \sum J_r^2(D)\delta[\cos\theta - c/(v\varepsilon_0^{1/2}) + (2\pi rc/L\omega\varepsilon_0^{1/2})]\sin^3\theta d\theta, \quad (4)$$

$$D = L\omega\Delta/(4\pi c\,\varepsilon_0^{1/2}\cos\theta).$$

Here $J_r(D)$ is a r-order Bessel function. The angle of emission for different frequencies is given by the expression (1). With the help of (1) one can determine the interval of emitted frequencies by taking into account that $|\cos\theta| \le 1$. The quanta with frequencies $\omega \ge \omega_{min} = 2\pi\, vr/L/(1+v/c)$ of the first harmonic (r=1) give the most contribution to the intensity of radiation [9]. As it follows from (4) (at $\omega >> \omega_{pe}$, $\varepsilon \le 1$) the total number of quanta emitted in certain frequency interval $(y_1\omega_{min}, y_2\omega_{min})$ from the unit volume of beam plasma is given by (in [cm^{-3}]):

$N=1.810^{-7}(1+v_b/c)n_b n_p^{1/2}[(\nu K b_0)^2/l][T_i T_e/(T_e+T_i)]^{3/2}\tau A$

$A=(y_2-y_1)[(v_b/c)^2/(y_2-y_0)/(y_1-y_0) - 1/(y_1y_2)]$, $y_0=1+v_b/c$,

where n_b- is the density of beam particles with the velocity v_b; $T_{i,e}$ (in [eV]) - ion and electron temperatures respectively; the numbers $y_1 < y_2$ have to satisfy to the inequality $y >> (1+c/v_b)/(2\pi r)$, that follows from the condition of the quasiclassical approximation ($\lambda/2\pi = c/\omega << L$). In [5] a possibility of the resonance transition radiation detecting on the background of the bremsstruhlung had been shown as well as a concrete recommendations for diagnostics of SPLW (or parameters of beam-plasma system) had been determined.

For a future detecting of transition radiation from relativistic electron beams in laser-produced plasmas we can take into account following estimations. For plasma densities of order of 10^{18}-10^{24} cm^{-3} X-ray radiation with wavelengths in the range of 10^{-6} - 10^{-8} cm can be generated within an angels $\theta < 15^{\circ}$ (the λ is shorter when the beam density n_p is greater). This is realized in our case when $v_b \approx c$, $v \cong 0.75$, $\delta n/n_p = 0.1$, $l \approx 18, vK(v)b_0 \approx 0.3$, $L \approx 10\ \lambda_d$. Here and below we propose that $T_i \approx 10$-20 eV, and $T_e >> T_i$ (so the Debye length is $\lambda_d \approx 3\ 10^3/n_p^{1/2}$ [cm]), $\omega_{min} \approx \pi\ c/L$, $\varepsilon_0 \approx 1$. For example with the following values : $n_p = 10^{20}$ cm^{-3}, $n_b = 10^{18}$ cm^{-3} (i.e. $j_b = 5\ 10^8 A/cm^2$- the density of relativistic part of electron beam), $\tau = 100$ ps we receive the density of emitted X-ray quanta of the order of $N \approx 3\ 10^9$ cm^{-3} with $\omega \geq 10\omega_{min}$ (i.e. for $\lambda \leq 60$ A) in the conic angle with $\theta \leq 37^{\circ}$. At the angle of $\theta \approx 37^{\circ}$ we can detect the radiation of quanta with an energy of $E_q \approx 200$ eV. So for a typical value of our small beam plasma induced by picosecond laser beam in volume of $V \sim 10^{-8}$ cm^{-3} [3] we will have approximately 30 quanta. These can be deteceted by X-ray streak camera in picosecond range.

Note, that considered above case of transition radiation can be generated in beam plasma under laser spark discharge during SPLW generation by part of nonrelativistic electron beam which density can be more higher [1-3]. In principal if one will use two and more laser pulses for plasma channel generation it may be possible to accelerate part of electrons to energy $E_b >> mc^2$, and hence it may be possible to produced X-ray laser on base of dense plasma beam system [11].

3. Reflected Radiation

It is well known that under reflection of light from the moving mirror the double Doppler's effect takes place: the frequency of reflected wave increases ($\omega_r \sim 2\omega_o/(1-\beta^2)$,where $\beta = v_m/c$, v_m is a velocity of mirror. Simultaneously an amplitude increasing , it means a total energy of reflected wave, as well as an extreme shortening of radiation pulse. In 1951 it had been proposed to use the relativistic electron beam (see for example [5]) as a moving reflector. For realization of this multiplication scheme it is necessary to have an extremely high electron beam density : $\omega_{pb} = (4\pi e^2 n_b/m_e)^{1/2} \geq \omega'$, where ω' is a frequency of electromagnetic wave recalculated in the system of coordinates of moving beam front. As it was shown in [6] this anomalous reflection may be possible. It already was confirmed by experimental means in Khar'kov Institute for Physics and Technology [6] in a case of reflected front of dense plasma moving with respectively small (nonrelativistic) velocities in the medium or in waveguide of slow wave (in this a case in the relationship for ω_r it is necessary to replace c on phase velocity of such wave, $v_{ph} << c$). Namely one of this situations takes place in our case when the reflected electromagnetic pulse was so intensive that a laser resonator was destructed. It is well to bear in mind the well known from electrodynamics fact that along an extended inhomogenieties of index of refraction it is possible a propagation of waveguide mode [12] (for example slow E-wave). Laser radiation which propagates throw such region can be transformed and reflected by moving plasma jet (electron beam). So we have observed and explained very interesting nonlinear phenomena connected with transformation of laser radiation into slow wave and reflection (or inversion) of its front directly back by moving high density electron beam under self-focusing of laser beam and micro-self-channeling of directed energy micro flows [13] during laser spark discharge.

4. References

1.N. Vogel,J.Heinzinger:Proc. ICPIG-XXII,**4**(1995)11.

2. N. Vogel, Proc. 7 th. Workshop Advanced Acc. Concepts, Oct.12-18, 1996, Lake Tahoe, CA, USA

3. 2. N.I.Vogel, V.A.Skvortsov : Proc. BEAMS'96, **1** (1996) , 518.

4. M.V.Kuzelev, A.A.Rukhadze: Electrodynamics of Dense Electron Beams in Plasma. M.: Nauka,1990.

5.V.A.Skvortsov: In book "The Physical Methods of Biological Objects Investigation. Moscow , MFTI (1981) 84.

6.Ya. B. Fainberg: Fizika Plasmy **20** (1994) 613.

7. P.P.Pashinin, A.M.Prokhorov: Pis'ma v Zh.E.T.F. **26** (1977) 687.

8.V.I.Petviashvili: Nonlinear waves and Solitons, In : The Questions of Plasma Theory. Moscow: Atomizdat (1979) 77.

9. M.L.Ter-Mikaelyan: The Enfluence of Medium on Electromagnetic Processes under High Energy.Erevan Publ. of the Ac.Sc. Armenian SSR (1969) Ch.5.

10. K.A.Barsukov: Zh.T.F. **34** (1964) 725.

11. J.S.Bakos, V.N.Tsytovich: Coomments Plasma Physics. Controlled Fusion, **8** (1984) 155.

12. V.M.Akulin, N.V.Karlov: The Intensive Resonance Interactions in quantum electronics.M.: Nauka,1987

13. V.A.Skvortsov : In Book of Abstracts of 7-th Workshop Advanced Accelerator Concepts, Lake Tahoe, CA, USA (1996) 2-08.

OPTIMIZATION OF MULTICHARGED ION EMISSION FROM PLASMA PRODUCED BY SHORT PULSE, SHORT WAVELENGTH LASERS

J. Wołowski, P. Parys, E. Woryna

Institute of Plasma Physics and Laser Microfusion, Hery 23, P.O.Box 49, 00-908 Warsaw, Poland

J. Krása, L. Láska, K. Mašek, K. Rohlena

Institute of Physics, ASCR, Na Slovance 2, 180 40 Praha 8, Czech Republic

1. Introduction

High power laser beam focused on a solid target creates a hot and a very dense plasma in a high ionization state. Due to the fast expansion the plasma is diluted before the recombination eradicates all the highly ionized ion species. Hence, at least part of ions has a chance to conserve the charge state acquired in the hot plasma core and carry it at a considerable distance away from the focus. There the ions can then be either investigated by means of particle diagnostics or they can be transformed in an ion beam suitable for various applications. Intense studies of laser-plasma ion sources LIS at present are motivated mainly by the growing demand for high current beams of multiply charged heavy ions for large accelerators e.g. [1], [2]. LIS can also be utilized for various technological purposes, like for a material modification, ion implantation, laser mass spectrometry etc. The subject of optimization of laser-plasma sources of multicharged ions are the maximum flux, energy and charge states of ions.

The main goal of our investigations is to find conditions in which laser created plasma can be used as a stable source of highly ionized ions for various applications.

2. Experimental arrangements

The investigations presented in this paper were prformed using experimental systems at IP ASCR in Prague, Czech Republic and of IPPLM in Warsaw, Poland. As a driver the iodine laser PERUN at IP ASCR was used (λ = 1.1315 μm, $E_L \leq$ 50 J, t_L = 350-700 ps, $I_L \sim 10^{15}$ W/cm^2, conversion to the 2nd and 3rd harmonics about 50%) [3]. The laser beam was focused onto the target with a parabolic mirror. The experimental system at the IPPLM in Warsaw was equipped with Nd:glass laser (λ = 1.06 μm, $E_L \leq$ 20 J, t_L = 1ns, $I_L \leq 10^{14}$ W/cm^2) [4]. An aspherical lens-ellipsoidal mirror illumination system was used to focus the laser beam onto the target. The use of parabolic or ellipsoidal mirrors with the hole in the center allows for ion measurements along the laser beam axis as well as target normal [5]. This configuration makes possible to extract a high current of multicharged and high energy ions in preference. The ion diagnostic techniques were based essentially on the time-of-flight method [6]. A cylindrical electrostatic ion energy analyzer (IEA) with a windowless electron multiplier was used to determine the distribution of particular ion species i.e. to determine the mass-to-charge ratios, energies and abundance. The ion collectors (IC) measures a time-resolved ion current signal, from which the energy-charge product and total charge carried by ions, as well as the ion velocity (energy) can be derived. Ion current pulses from the IC and IEA were recorded by digitizing oscilloscopes. To speed up the evaluation of IEA spectra the computational program WELAN was used [7].

3. Results

The aim of our experiments was to test the conditions for obtaining maximum current of highly charged heavy ions at various experimental conditions, i.e., we varied the focus position versus target surface, laser wavelength (1ω, 2ω, 3ω) and laser energy from 5 to 40 J.

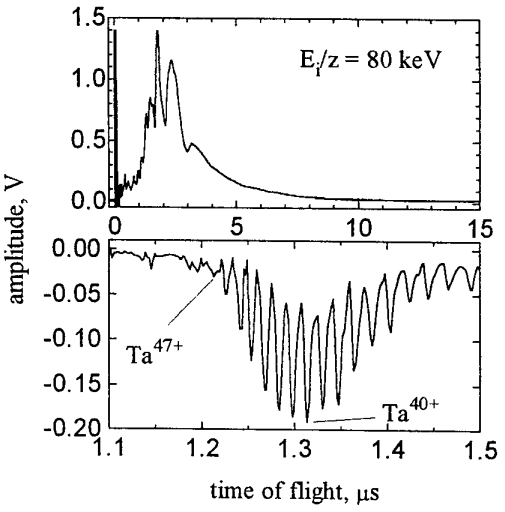

Fig. 1. Ion collector signal and IEA ion spectrum of Ta ions

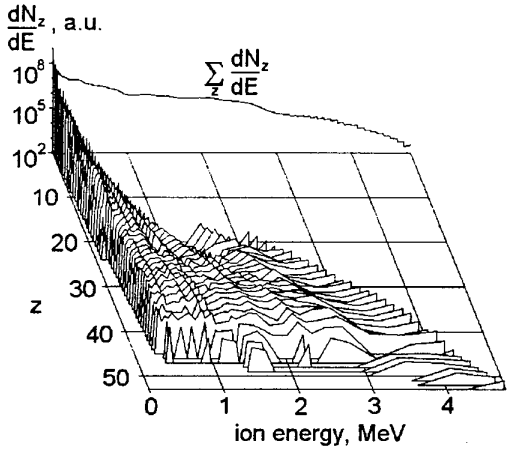

Fig. 2. Energy distributions of Ta ions.

Typical examples of IC signal and IEA spectra with highly charged ions are presented in Fig. 1. The structure of the collector signal points of the existence of two (or more in other cases) distinct ion groups, corresponding to different mechanisms of their generation. Signals from IEA show the ion spectrum of ions for a given value of $E_i/z = 80$ keV). The series of measurements with E_i/z changing was necessary for obtaining the ion energy distribution for single value of laser energy. Example of the ion energy distribution is presented in Fig. 2. The charge state-ion energy dependence, average charge state as a function of the ion energy, and the percentage abundance of ion species were determined on the basis of Fig. 2. A typical group of highly charged ions appears at higher E_i/z, it is pronounced at higher laser power densities. The maximum energy of ions increases with the laser power density. The ions with high charge state were found at all laser wavelengths within a relatively broad range of laser energies. Examples of the experimental results for different target materials [8] are presented in the Table :

Element	z_{max}	$\bar{z}_{fast}$	$E_{i,\,max}$ [MeV]	$\bar{E}_{i,\,fast}$ [MeV]	j [mA/cm^2]
Co	25	22	2.6	1.9	14.2
Ta	48	42	7.7	2.3	22.8
W	49	45	4.9	2.0	22.8
Pb	51	40	5.1	3.3	8.5
Bi	51	40	5.1	2.7	10.0

The ion yield depends strongly on the focusing conditions. The optimum focus setting is defined as the focus position corresponding to the maximum ion current from the IC and to the highest charge state from the IEA. I was observed that the maximum charge state of the ions depends weaker on the focus setting than the IC current. There is a position of the target lying behind the true focus (aim in front of the target surface) which is most favourable not only for generation of the highly ionized particles but also for attaining a maximum yield of the ions.

4. Summary and conclusion

The present results proved the existence of highly charged ions with $z > 50$ in a far expansion zone. The highest ion energy up to about 9 MeV as well as maximum ion current density higher than ~ 20 mA/cm^2 (in the distance about 1 m) were measured. The influence of the focal spot position on the maximum charge state and ion current density was stated. Extraction of ions perpendicularly to the target my improved the ion current density, for three times, at least [9].

Explanation of occurrence of the highly charged ions in a far expansion zone may be based on the mechanism of two temperature plasma expansion. With the two groups of electrons present the expansion is two fold. The expansion of the fast ion group is lead by the fast electrons. The ion with high charge states are guided through the dangerous recombination zone. This enhance the phenomena of charge state „freezing" and the ions originally present in the hot plasma corona survive. Shorter wavelength (< 1.315 μm) and shorter pulse length (< 1 ns) are appropriate for this purpose. The advantage of using a short intense pulse consists in its ability to produce keV plasma with small density gradient scale length.

The laser produced plasma can serve as a potential source of ions for accelerator injection or for implantation. Construction of appropriate laser ion sources seems not be a principal but rather a technological problem.

5. References

[1] T.R. Sherwood, Rev.Sci.Instrum., **63** (1992) 2789
[2] L. Láska et al. Rev.Sci.Instrum., **67** (1996) 950
[3] M. Chvojka et al., Czech J. Phys. **42** (1992) 899
[4] J. Badziak et al., Proc. 21st ECLIM, 1991, Warsaw p.131
[5] P. Parys et al., Proc. 23rd ECLIM, 1994, Oxford, p. 371
[6] E. Woryna, et al., Laser and Particle Beam, **14** (1996) 293
[7] M. Pfeifer et al., Proc. 2nd Symp. PLASMA'95 (1995) Warsaw, Vol. 1, p. 77
[8] K. Rohlena et al., Proc. BEAMS'96, Prague, p 271
[9] E. Woryna et al., Appl. Phys.Lett. **69** (1996) 1547

Authors Index

A

Abbaoui M. I-4
Abdelli S. IV-264
Abdullin I.Sh. IV-72
Ablitzer D. IV-200
Abramzon N. I-62
Adachi K. I-246
Adler H.G. III-22
Afanas'ev V.P. III-104
Ahedo E. I-2
I-204
Akaishi K. IV-156
Akhmedzhanov R.A. I-272
I-274
Alcaide I. II-2
Aldea E. IV-254
Alekseeva L.M. I-206
II-156
Alexandrov A.F. I-44
I-108
III-88
Alexandrov L.S. I-208
Alexandrovich B. IV-76
Alexeff I. III-102
Al-Hussany A. II-216
II-218
Alkaa A. II-260
Allen J.E. I-116
I-132
I-192
I-194
Almi A. I-254
Alnot P. IV-244
Alvarez I. I-18
Alves L. I-120
Amakawa T. I-246
Amemiya H. I-110
IV-60
IV-62
Amirov A.H. IV-262
Ammelt E. II-182
Amorim J. IV-232
Andre P. I-4
III-104
Andreazza P. IV-252
Andreazza-Vignolles C. IV-252
Andrieux M. IV-192
Anikin N.B. IV-48
Annaratone B.M. I-116
I-132
I-192
I-194
Anschutz B. II-204
Anschutz F.B. II-202
Antoni V. II-262
IV-134
Antonova T.B. III-88
Arai T. IV-86
IV-88
IV-90
Arnal Y. IV-230
Arnas-Capeau C. I-202
II-164
Arriaga C. I-18
Asselman A. III-24
Atipo A. II-170
Aubes M. III-16
IV-64
Aubrecht V. II-78
II-80
II-82
Aubreton J. I-4
IV-102
IV-220
Auday G. I-58
Averyanov V.P. I-188
Awakowicz P. I-60
II-202
II-204

B

Babaeva N.Yu. II-246
Babaritskiy A. IV-224
Babich I.L. II-154
Babich L.P. I-6
I-8
I-10
IV-2
Babich M.L. I-10
Babicky V. I-248
IV-14
Bacal M. I-12
III-78
Bachev K. I-160
I-162
Baclawski A. II-110
Badie J.M. IV-192
Bagatin M. II-262
IV-134
Bagautdinov A. IV-222
Baksht F.G. I-12
IV-138
Baldwin M. IV-194
Baltog A. I-94
Bano G. III-96
IV-212
Baranov I.E. IV-224
Baravian G. IV-232
Barinov Yu.A. III-104
Barj M. IV-142
Bartlova M. II-80
Bashutin O.A. IV-112
Basner R. IV-196
Basurto E. I-18
Batanov G.M. I-138
Bauchire J.M. II-120
II-136
II-206
Baude S. III-86
Bayle P. I-252
II-220
IV-154
Becker K. I-62
I-64
IV-196
Behnke J. IV-226
II-4
Behnke J.F. II-4
II-6
II-8
Beilis I.I. I-14
II-84
Belenguer Ph. I-100
Belhaouari J.B. II-86
Belmonte T. IV-66
IV-198
Ben Gadri R. IV-44
Benabdessadok M.D. I-252
Bernard J.F. IV-130
Berreby R. III-92
Berthomieu D. I-148
Bezborodko P. IV-68
Bezemer J. II-224
Bhattacharjee S. I-110
Biborosch L. II-190
Biel W. II-226
Bilikmen S. I-172
Bindemann Th. II-6
Birau M. III-46
Bisch C. IV-192
Blaise G. III-86
Blanc E. III-10
Blois D. IV-142
Blundell R.E. II-150
Bobrov Yu.K. II-166
II-168

Bobrov Yu.K. II-208
II-210
IV-4
IV-6
Bobrova L.N. IV-6
Bockel S. IV-200
Boeuf J.P. I-112
II-56
II-228
II-252
II-254
III-42
III-70
Bogaerts A . II-10
Bonhomme G. II-16
II-170
Bonifaci N. IV-10
IV-12
Booth J.P. IV-70
IV-202
Borcia C. II-172
Bordage M.C. IV-44
Borisenko A.G. I-38
IV-248
Borodin V. III-18
Bouaziz M II-88
Boubert P. IV-152
Boucher I. III-2
Bouchoule A. I-200
III-66
Boudjella A. IV-16
Boufendi L. IV-204
Bougdira J. IV-244
Bougrov G.E. III-88
Boxman R.L. II-84
Bozin J.V. I-98
Brablec A. I-128
IV-226
Bragin V.E. IV-72
Braginskiy O.V. III-76
Brasile J.P. II-42
Bratescu M.A. I-92
Brault P. IV-252
Bretagne J. III-80
IV-184
IV-210
Brethes S. I-268
Briaud Ph. II-212
III-72
Bruhn B. II-200
Brunet H. I-58
III-100
Bruno D. II-242
Bugrova A.I. II-76
III-68
Bultel A. II-90
Burke R. IV-230
Burm K.T.A.L. II-108
Bursikova V. IV-260
Busov B. II-78
Buzzi J.M. III-46
Bykanov A.N. IV-72

C

Cachoncinlle C. III-30
III-32
III-44
Cahoreau M. IV-220
Caillez Y. III-46
Cajal D. II-92
IV-74
Calderon M.A.G. II-112
Capitelli M. I-24
I-26
I-66
II-116
II-242
Cardinaud C. III-90
Carman R.J. II-258
Cartry G. II-70
II-72
Catherinot A. IV-102
IV-220
Cenian A. I-16
III-18
Censor D. I-234
Cercek M. IV-162
Cernak M. I-248
IV-8
Cernogora G. I-102
II-70
II-72
Chabert P. IV-202
Chaker M. I-166
I-168
Champain H. IV-94
Chapelle J. II-122
Chapput A. IV-142
Charles C. IV-252
Chatei H. IV-244
Chebotarev A.V. IV-110
Chenevier M. IV-70
Cheredarchuk A.I. II-154
Chernukho A. III-18
Chernyshev A.V. I-176
Cheron B.G. II-90
Chervy B. II-104
Chevolleau T. III-90
Chevrier P. II-100
II-102
Chinnov V.F. II-94
IV-262
Chirkin M.V. I-208
II-174
Chizhik A. III-110
Choi P. II-12
III-28
Choi W.K. III-88
Chorazy J. I-82
Christophorou L.G. I-68
Chuaqui H. II-12
III-28
Chumak G.M. IV-206
Cicconi G. II-176
Cicman P. IV-250
Cinelli M.J. IV-102
IV-220
Ciobanu S.S. II-100
II-102
IV-150
Cisneros C. I-18
Clavreul R. III-94
Clenet F. II-212
Clupek M. I-248
IV-14
Coitout H. II-96
IV-78
Collins G. IV-194
Colombo V. II-214
Conde L. I-70
II-2
Coppa G.G.M. II-214
Cormier J.M. II-122
Coste C. I-268
Coulombe S. II-98
Courtois L. II-42
Csambal C. II-8
Cunge G. IV-202
Czerwiec T. IV-66
IV-198

D

D'yachkov L. I-188
I-190
Damelincourt J.J. III-16
III-24
Darnon F. III-66
Dauchot J.P. IV-210
David M. II-226
Davies A.J. II-216
II-218
De Benedictis S. I-72
IV-14
IV-80
De Graaf A. IV-254
De Hoog F.J. I-152
IV-246
De Souza A.R. IV-46
De Urquijo J. I-18
Debal F. IV-210
Decomps Ph. III-106
Deegan C.M. I-114
Degond P. III-64
Deha I. IV-116

Delaporte Ph.C. I-48
III-26
IV-52
Delhaes P. IV-236
Denat A. IV-10
IV-12
Derouard J. I-150
IV-202
Deschamps N. IV-46
Desideri D. II-262
IV-134
Desoppere E. I-20
I-106
III-38
Despax B. IV-208
Dessaux O. IV-142
Destombes V III-100
Deutsch H. II-4
II-6
II-74
II-200
IV-188
Devyatov A.M. I-44
Dewald E. II-50
II-52
Diamy A.M. IV-218
Dias F.M. I-122
Dilecce G. I-72
IV-14
IV-80
Dinescu G. IV-254
Dinklage A. II-200
IV-188
Djakov A.F. II-166
II-168
II-208
II-210
IV-4
IV-6
Djermoune D. IV-94
Dolgolenko D.A. II-162
Domingo P. II-238
Dominguez I. I-18
Donko Z. II-64
Dony M.F. IV-210
Doreswamy C.V. II-146
Dorning J. I-210
Dors M. I-250
Dorval N. IV-216
Doveil F. I-202
Draghici-Lacoste A. I-120
Drallos P.J. I-30
Druetta M. III-92
Ducarroir M. IV-192
Dudeck M. III-78
Dumitrescu-Zoita C. III-28
Dupont G. IV-208
Durand J. I-148
Dussart R. III-44
Dussoubs B. II-158
Dyatko N.A. I-24
I-66
II-116
Dyomkin S.A. IV-224
Dyson A.E. I-116
Dzermanova N. II-192

E

Eby S.D I-50
Egli W. II-236
Ehrich H. II-118
Eichwald O. I-252
II-220
IV-154
El Bezzari M. I-190
El Shaer M. I-118
Elchinger M.F. I-4
Eldevik T. I-32
Elloumi H. IV-64
Entlicher M. II-232
Epifanie A. II-160
Ercilbengoa A.E. III-84
Eremenko Yu. IV-222
Erraki A. II-106
Ershov A.P. II-60
Escarguel A. I-174
Essolbi R. III-94
Etievant C. IV-224
Etoh A. IV-104
Ezubchenko A.N. II-162

F

Fabry F. II-124
Fanack C. III-2
Fang M.T.C. II-148
II-150
Fauchais P. I-4
II-158
Fauconneau J. IV-68
Faure G. III-104
IV-78
Favre M. II-12
III-28
Fedorovich O.A. IV-240
Fergusson E.E. I-84
Ferguson D.C. II-146
Fernsler R. II-30
Ferreira C.M. I-120
I-122
I-124
Fetisov I.K. II-24
Fewell M. IV-194
Fiala A. III-86
Fiermans V. I-20
Fievet C. II-102
IV-150
Filippov A.A. II-142
Fitaire M. IV-28
Fitzgerald T.J. III-10
Flamant G. II-124
Flazi S. IV-16
Fleddermann C.B. IV-214
Fleurier C. II-100
II-102
III-44
IV-150
Flieser J. IV-124
Fliesser W. IV-122
IV-126
Fodrek P. IV-128
Foest R. IV-196
Fontaine B. III-26
Fortov V. I-212
Fortov V.E. I-176
I-178
Frank K. II-52
Franke St. II-74
Franklin R.N. II-14
Frost R.M. I-60
Fujioka H. IV-88
IV-90
Fukuchi Y. I-74
Fukuda M. IV-168
Fulcheri L. II-124
Funato Y. IV-156

G

Gajic D.Z. I-222
I-224
Galofaro J.T. II-146
Galy J. I-58
III-100
Ganciu M. II-50
II-52
Garanin S.F. IV-158
Gardou J. I-104
Garrigues L. III-70
Gary F. II-92
IV-74
Gasteiger S. III-36
Gavrilenko V.P. IV-82
Gavrilov N.V. II-32
Gavrilova T. I-188
Gerova E. IV-120
Gerteisen E. II-238
Gherman C. II-172
Gicquel A. IV-70
Gigant L. IV-114
Gijbels R. II-10
Gillispie K. III-102
Giordano D. I-26
Girard A. I-140
II-256
Glanschnig M. I-84

Gleizes A. II-86
II-88
II-104
II-106
II-126
II-136
II-140
Glisic S. IV-42
Glosik J. III-96
IV-212
Godyak V. IV-76
Goedheer W.J. II-108
II-222
II-224
Goldman A. III-98
Goldman M. III-98
Goldsmith S. II-84
Golly A. II-110
Golosnoy I.O. IV-84
Golubev A. I-212
Golubovskii Yu.B. I-36
Golubovskii Yu.B. II-4
II-6
II-54
II-62
Gombert M.M. I-22
Gomes A.M. I-254
II-160
Gonzalez J.J. II-86
II-120
II-136
II-140
II-206
Gonzalez-Aguilar J.A. II-112
Gorbachev A.M. I-272
I-274
Gorbunov N.A. I-80
I-82
Gordeev O.A. IV-136
Gordiets B.F. I-124
Gorse C. I-26
II-116
Gortchakov S. III-58
Goto M. I-96
IV-86
IV-88
IV-90
Goudmand P. IV-142
Goulet J.C. I-218
Gousset G. I-120
III-80
IV-92
IV-184
Grabowski D. III-50
Graham W.G. IV-151
Granier A. III-72
III-74
Gregor J. II-30
Gresser L. IV-180
Gross B. II-82
Grosswendt B. I-78
Grozev D. I-156
II-192
Grozeva M. II-130
Gryaznov V. I-212
Gubsch S. II-200
Guerra V. IV-160
Guerrini G. III-78
Guiberteau E. II-16
Guillot Ph. I-58
III-100
Gyergyek T. IV-162

H

Hacquin S. III-2
Hadi H. IV-16
Hadjadj A. IV-204
Hajek V. IV-258
Hallil A. IV-62
Hamada T. IV-118
Hamers E.A.G. II-224
Hanacek P. II-78
Hangai N. I-144
Hanitz F. I-266
Hansel A. I-84
I-260
Harendt A. I-126
Hartgers A. III-108
Hartmann G. IV-94
IV-96
Hartmann W. IV-164
Hassouni K. II-116
IV-70
Hatano Y. I-74
Haug R. III-98
IV-96
IV-166
Hava O. II-18
Hayashi N. I-216
II-198
Haydon S. IV-194
Hbid T. I-152
IV-246
Hebner G.A. IV-214
Hecq M. IV-210
Helbig V. II-8
Held B. I-268
III-84
IV-180
IV-236
IV-238
Heldt J. III-50
Hemmati M. I-214
Hemmers D. II-226
Hempel F. IV-196
Henneberger K. I-40
Hennig A. II-8
Henrion G. II-16
Herben P.G.J.M. III-63
Hertl M. IV-216
Heuraux S. III-2
Higaki H. I-230
Hipp M. IV-122
IV-126
Hirech A. II-230
III-100
Hirota A. I-228
Hitz D. III-92
Hoang T.G III-94
Hoffmann D.H.H. I-212
II-52
Hoffmann V. I-146
Holzinger R. I-260
Hong D. III-44
IV-150
Hopkins M.B. I-114
Horikoshi K. IV-88
IV-90
Horvath M. II-232
Hosokawa T. IV-16
IV-168
Houska A. II-82
Hrach R. II-230
II-232
IV-128
IV-218
Hrachova V. II-18
II-20
IV-218
Hubicka Z. I-130
IV-228
Huet S. IV-204
Hugon R. II-16
Hure L. III-44

I

Ieda Y. II-22
Ignatov A.M. I-180
Inagaki K. IV-140
Inomata T. IV-26
Ion L. IV-236
IV-238
Isakaev E.H. II-94
Iserov A.D. II-94
Ishida A. IV-118
Ivanov M.S. II-242
Ivanov O.A. I-272
I-274
Ivanov V.G. I-12
Ivanov V.V. I-86
I-182
II-28
II-234
III-40

J

Jacobsen L.M. III-4
Jager H. IV-122
IV-124
IV-126
Janca J. I-256
IV-98
IV-100
IV-260
Jang H.G. III-88
Jastrabik L. IV-226
IV-228
Jauberteau I. IV-102
IV-220
Jauberteau J.L. IV-102
IV-220
Jelenkovic B.M. I-98
Jivotov V.K. IV-222
IV-224
Johnston C. III-62
Jolly J. IV-190
IV-216
Jones J.E. IV-18
IV-20
IV-22
Jonkers J. III-62
III-63
III-108
Jordan A. I-260
Jugroot M. II-220
IV-154
Jung H.J. III-88

K

Kalachov I. IV-222
Kalinin A.V. II-60
Kameta K. I-74
Kandah M. IV-176
Kando M. IV-104
Kaneda T. IV-168
Kanka A. II-18
II-20
Kapicka V. I-128
IV-226
IV-228
Kaplan V.B. III-104
Kapoun K. I-130
IV-228
Karchevsky A.I. II-162
IV-106
Karderinis S.N I-132
Katkalo A.A. IV-234
Kawaguchi M. I-134
II-34
IV-132
Kawai Y. I-136
I-216
I-244
II-198
Kawakami R. IV-266
Kawamura K. IV-144
IV-186
Keidar M. I-14
Kempkens H. II-226
Kerdja T. IV-264
Kettlitz M. II-114
IV-108
Khacef A. III-30
III-32
Khadka D.B. I-74
Kharchevnickov V.K. II-76
Khodachenko G.V. II-24
Khodataev K.V. IV-24
Khodja H. I-140
Kidalov S.V. III-54
III-56
Kimura T. I-76
II-22
Kindel E. III-34
IV-108
Kinoh Y. IV-104
Kirillin A. I-184
Kirnev G.S. II-26
Kirov K. I-156
II-192
Kiyooka C. IV-156
Klima M. I-128
IV-226
Kling R. III-36
Klopovskiy K.S. I-86
I-88
II-28
II-234
III-40
Kobayashi Y. I-164
IV-144
Koch A.W. IV-54
IV-56
Koch B.P. II-200
Kocik M. III-50
Kof L.M. IV-58
Koga K. I-216
I-244
Kogelschatz U. II-236
Kogoma M. IV-26
Koh S.K III-88
Kolenic F. IV-128
Kolisko A.L. I-272
I-274
Kolosov V.Yu. IV-170
IV-172
Kondranin S.G. III-88
Konjevic N. IV-146
Konstantinov E. IV-222
Kopytin A.A. III-40
Korbel A. II-132
Korge H. III-110
Korolev Yu.D. IV-174
Korshunov O.V. IV-262
Kosbagarov A. IV-222
Kosecek A.M. IV-128
Kossyi I.A. I-138
IV-110
Kouchi N. I-74
Kovalev A.S. III-76
Kozyrev A.V. III-54
III-56
IV-174
Krajcar-Bronic I. I-78
Kralkina E.A. III-88
Krasa J. IV-272
Krasilnikov M.A. III-46
Krcma F. IV-100
Krenek P. II-104
Kriha V. I-266
Kroesen G.M.W. I-152
IV-246
Ksiazek I. II-110
Kuba P. IV-128
Kubota Y. IV-156
Kudelcik J. IV-8
Kudrle V. IV-28
Kudryavtsev A.Yu. I-6
I-10
IV-2
Kudu K. IV-34
Kulikovsky A.A. I-258
IV-30
Kulish M. I-212
Kumar S. IV-194
Kuraica M.M. IV-146
Kurilenkov Yu.K. I-186
I-188
I-190
Kurnaev V.A. II-24
II-26
IV-112
Kurunczi P I-64
Kutsyk I.M. I-6
I-8
IV-2
Kuwae H. II-198
Kuzelev M.V. III-46
Kuzovnikov A.A. I-154

L

Laan M. IV-32
Lagstad I.H. IV-34
Lamoureux M. I-140
Lancellotti C. I-210
Lange H. IV-36
Lapuerta V. I-204
Laroussi M. III-102
Lasgorceix P. IV-102
Laska L. IV-272

Latocha V. III-64
Latyshev Ph.E. I-80
I-82
Laure C. IV-252
Laurent A. II-92
IV-74
Law D.A. I-192
I-194
Laz'ko V.S. II-162
Le Brizoual L. III-72
Le Guen C. I-188
Leborgne L. I-218
Leclert G. III-2
Le Coeur F. IV-230
Lecot C. II-256
Le Duc E. IV-28
Lee Z.H. IV-112
Lefort A. I-4
III-104
Legrand J.C. IV-218
Lemaire P. IV-114
Lemeur F. II-90
Lemperiere G. II-214
Leon L. I-70
Leprince P. I-120
IV-92
Leroux A. II-238
Leroy O. IV-216
Lesage A. I-174
Leu F. II-118
II-188
Leu G. II-184
II-186
Levchenko V.D. I-220
II-240
Leys C. III-38
Li Bo I-52
Li Y.M. III-20
Lindinger W. I-84
I-260
IV-212
Lino J. IV-232
Lipaev A.M. I-178
Lipatov A.S. II-76
Lister G.G. III-22
Loffhagen D. III-34
III-58
Loiseau J.F. III-84
Lomakin B.N. IV-262
Londer J.I. II-144
Longo S. I-24
I-26
II-116
II-242
Lopaev D.V. I-86
I-88
II-28
III-40
III-76
Lorthioir S. III-86
Louhibi D. II-244
Loureiro J. I-90
I-102
IV-160
IV-232
Louvet G. I-186
Loza O.T. III-46
Lozneanu E. II-184
II-186
Luca A. IV-212
Lungu C.P. I-94
Lyapin A.I. IV-234
Lyszyk M. III-66

M

Machala Z. I-262
Maftoul J. IV-74
Mage L. III-74
Magne L. II-70
II-72
Maheu B. II-90
Mahony C.M.O. IV-151
Makasheva K. I-156
Malek S. IV-264
Malinowsky G.Y. I-48
Malovic G.N. I-98
Malykh N.I. I-138
Mandache N.B. II-50
II-52
Manheimer W. II-30
Mankelevich Yu.A. II-234
Maouhoub E. II-96
Marchal F. I-104
Margot J. I-166
Mark T.D. IV-250
Markovic V.Lj. II-46
IV-178
Marliere C. I-148
Marode E. IV-46
Martines E. IV-134
Martus K. I-64
Marty-Dessus D. IV-236
IV-238
Masek J. II-78
II-82
Masek K. IV-272
Mashino S. IV-88
IV-90
Massines F. III-106
IV-44
Matejcik S. IV-250
Matheron P. IV-116
Mathew J. II-30
Matsui T. I-142
Matsumoto M. I-238
II-58
Matsuoka M. I-134
II-34
IV-132
Matveev A.A. I-138
Maury J. IV-114
Maximov A.I. I-256
Mayoux C. III-106
McFarland J. IV-151
Meger R. II-30
Melin G. I-140
Melnig V. II-172
Melnikov A.S. I-80
Mentel J. II-130
II-132
III-48
III-50
Merad A. I-112
Mercier M. II-92
IV-74
Merel P. I-168
Mesyats G.A II-32
Meunier J.L. II-98
IV-176
Mezhiba A. I-212
Michaut C. III-78
Michel H. IV-66
IV-198
IV-200
Michishita T. I-230
Mikheev L.D. I-48
IV-52
Mikikian M. I-202
Milenin V.M. III-54
III-56
Milic B.S. I-28
I-222
I-224
I-226
Millet P. I-104
Mimura M. IV-118
Minami K. I-144
I-228
Minea T.M. III-80
Mintsev V.B. I-212
Mitrofanov N.K. II-134
IV-138
Mizeraczyk J. I-250
II-130
III-50
Mobasher M. I-118
Modreanu G. II-50
Mohri A. I-230
Moisan M. I-168
Mokhtari A.E. II-244
Molotkov V.I. I-178
Mond M. I-236
Monin M.P. I-270

Moreno J. II-12
III-28
Mori A. II-34
Mori I. IV-266
Morimoto T. IV-266
Morozov A. IV-124
Morozov A.I. II-76
III-68
Morozov D.A. I-208
Morrow R. II-258
IV-38
Morvova M. I-262
Mouadili A. III-24
Movtchan I.A. I-80
Mozgovoi A.L. I-6
Mozgrin D.V. II-24
Muller H.J. IV-54
Muller I. II-182
Muller S. IV-120
Murata T. III-82
Muromkin Yu. A. II-162
Murphy D. II-30
Musa G. I-92
I-94
II-118
II-188
Mushiaki M. IV-156
Musikowski H.D. II-128
Musinov S. IV-222
Musiol K. II-122
Mustata I. II-118
II-188
Myamoto K. I-92

N

Nagahama T. I-228
Naghizadeh-Kashani Y. II-106
Nagorny V.P. I-30
Naidis G.V. II-246
Naito Y. I-144
Nakamura M. I-76
I-196
Nakamura Y. I-242
I-244
Nandelstädt D. II-132
Napartovich A.P. I-24
I-66
Nefedov A.P. I-176
I-178
Neger T. IV-122
IV-124
IV-126
Neiger M. I-264
II-36
Nekuchaev V.O. I-36
II-54
Nerushev O.A. I-198
Ness K.F. I-54
Neuilly F. IV-202
Nichipor G.V. I-250
Nicolazo F. III-74
Nienhuis G.J. II-224
Niessen W. I-264
Nikulin S.P. II-36
Nishioka T. II-58
Nistor M. II-50
II-52
Nogaki M. IV-40
Novak M. IV-226
IV-228
Novak S. II-248
IV-128
Novakovic N.V. I-28
Nunomura S. I-196
Nur M. IV-10
IV-12

O

Odagiri T. I-74
Ohe K. I-76
II-22
II-66
IV-140
Ohno N. I-196
Ohtani K. IV-86
Oien A.H. I-32
III-4
Oishi H. I-230
Okada T. I-96
Okazaki S. IV-26
Okita Y. III-82
Olthoff J.K. I-68
Ono M. IV-186
Onoda H. II-68
Onose H. I-144
Otorbaev D.K. IV-110
Otte M. II-38
II-40
Overchuk K. IV-222

P

Pacheco J. II-120
Paillol J. II-42
II-250
Panchenko V.G. II-178
II-180
IV-240
IV-248
Pancheshnyi S.V. IV-48
Panciatichi C. II-214
Pardo C. II-112
Paris P. IV-32
Parizet M.J. II-96
Parys P. IV-272
Pashkovsky V.G. II-162
Passoth E. II-8
Pauna O. I-166
Pavlenko V.N. I-232
II-178
II-180
IV-240
IV-248
Pavlik J. IV-128
Pavlik M. IV-250
Pavlov V.B. III-88
Pawelec E. II-122
Pealat M. IV-216
Pechacek R. II-30
Pedoussat C. II-252
Pejovic M.M. II-46
IV-178
Pekarek S. I-266
Pellerin S. II-122
Pelletier J. IV-230
Peres G. II-254
Perret C. II-256
Perrin J. IV-190
Peska L. II-78
II-82
Petit L. III-98
Petrov G. II-266
Petrov O.F. I-176
I-178
Petrov T. II-130
Petrovic Z.Lj. I-34
I-98
II-44
II-46
IV-42
IV-178
Peyrous R. I-268
III-84
IV-180
Pfau S. II-38
II-40
Phelps A.V. II-48
Piejak R. IV-76
Pierre Th. II-164
II-170
Pierson J.F. IV-198
Pignolet P. II-42
Pinheiro M.J. IV-232
I-124
Pintassilgo C.D. I-102
Pitchford L.C. I-100
II-56
II-252
III-42
III-70
III-86
Placinta G. IV-242
Pogora V. II-138
Pointu A.M. II-50
II-52
Pokrzywka B. II-122

Ponomarev N.S. I-36, II-54
Popa G. II-66, IV-242
Popescu A. II-118, II-188
Popescu I.I. II-50, II-52
Popov A.M. II-28
Popov N.A. I-88
Poppe F. III-38
Porokhova I.A. II-4, II-6, II-62
Porras D. III-60
Postel C. I-270
Potanin E.P. IV-106
Potapkin B.V. IV-224
Pousse J. II-126
Pouvesle J.M. III-30, III-32, III-44
Praessler F. I-146
Prazeller P. I-260
Proshina O.V. I-88, II-234
Protuc I. II-138
Proulx P. II-206
Puech V. I-270
Punset C. III-42
Purwins H.G. II-182

R

Rabehi A. IV-44
Rahal H. I-22
Rahel J. IV-250
Rakhimov A.T. I-86, I-88
Rakhimov A.T. II-28, II-234, III-40
Rakhimova T.V. I-86, I-88, I-182, II-28, II-234, III-40
Ravary B. II-124
Raynaud P. I-148, III-74
Razafinimanana M. II-88, II-120, II-126, II-136
Redon R. IV-116
Reess T. II-250
Remscheid A. IV-148
Remy M. IV-244
Revel I. II-56
Riad H. II-106
Ricard A. I-168, IV-66, IV-198, IV-200, IV-210
Richou J. I-174, IV-116
Rivaletto M. II-42
Robert E. III-30, III-32
Robin L. IV-152
Robson R.E. I-52, I-54
Roca i Cabarrocas P. IV-204
Rodriguez-Yunta A. II-112
Rohlena K. IV-272
Rohmann J. II-38, II-40
Romeas P. I-186
Rosatelli C. II-176
Rosenfeld W. III-44
Rosenkranz J. I-266
Rosum I.N. II-178, II-180
Roth M. I-212
Rousseau A. IV-92
Roussel J. IV-130
Roussel-Dupre R.T. III-6, III-8, III-10, III-12, III-52
Rovtar J. IV-162
Rozoy M. I-270
Rozsa K. II-64
Rudakowski S. IV-148
Rudnitsky V.A. I-38
Rukhadze A.A. I-172, III-46, III-88
Rulev G.B. I-86
Rusanov V. IV-222
Rusanov V.D. IV-224
Rusnak K. IV-258
Rutkevich I. I-234, I-236
Ryazantsev E.I. IV-224
Rybakov A.B. IV-138
Rybakov V.V. I-240

S

Sa P.A. I-90
Sabonnadiere M.P. I-48
Sabotinov N. II-130
Sadeghi N. I-150, I-152, IV-202, IV-246
Saenko V.A. I-38, IV-182, IV-248
Saidane K. II-126
Sakai T. IV-16
Sakai Y. I-92
Sakamoto S. IV-186
Salabas A. II-118
Salamero Y. I-104
Samarian A. I-184
Sando K. I-164
Sanduloviciu M. II-172, II-184, II-186, II-188, II-190
Sapozhnikov A.V. I-138
Sarrette J.P. I-254, II-160
Sarroukh H. III-24
Sarytchev D.V. II-26
Sasada T. IV-132
Sato K. IV-118
Sato S. I-242
Sato T. I-164
Satoh H. I-238, II-58
Satoh K. II-260
Saulle C. III-46
Savinov V.P. I-108
Savjolov A.S. II-24, II-26, IV-112
Sayler G.S. III-102
Scheibe H.J. II-128
Scheibner H. IV-188
Schein J. II-132
Scheiring Ch. I-84
Scherbakov Yu.V. II-210
Schepe R. I-40
Scheubert P. II-202, II-204
Schimke C. III-34, IV-108
Schmidt E. III-48
Schmidt M. IV-196
Schmoll R. IV-164
Schopp H. II-114, IV-108
Schram D.C. II-108, III-62, III-63, III-108, IV-254
Schruft R. I-264

Schulze J. II-130
III-48
III-50
Schumann J. II-118
Schumann M. II-132
Schwarzenbach W. I-150
IV-202
Segui Y. I-148
III-74
Segur P. II-260
IV-44
Selen L.J.M. III-108
Sentis M.L. I-48
III-26
IV-52
Sergeichev K.F. II-196
Serianni G. II-262
IV-134
Servant S. II-92
Sery M. I-130
IV-228
Sewraj N. I-104
Shakhatov V.A. I-16
I-42
IV-136
Sharafutdinov R.G. IV-256
Sharkov B. I-212
Shibamoto M. IV-186
Shibkov V.M. I-44
I-154
II-60
Shibkova L.V. I-44
I-154
II-60
Shimizu K. IV-62
Shiozaki A. I-144
Shiratani M. IV-190
Shivarova A. I-156
I-158
II-192
Shkol'nik S.M. I-12
II-134
III-104
IV-138
Shkvarunets A.G. III-46
Short K. IV-194
Si-Bachir M. IV-264
Sicha M. I-130
IV-226
IV-228
Siegel R. I-62
Sigeneger F. II-62
Sigmond R.S. IV-34
Sigov Y.S. I-220
Silakov V.P. I-138
IV-110
Simek M. I-72
IV-14
IV-80
Simko T. II-64
IV-184
Simonet F. III-16
Singaevsky I.F. I-108
Singh D.P. I-44
I-154
II-60
Singh N. II-136
Sirghi L. II-66
Si-Serir F. II-244
Skalny J.D. IV-250
Skowronek M. I-186
Skrynnikov A.V. IV-256
Skvortsov V.A. III-14
IV-270
Slavicek P. I-128
IV-226
Smakhtin A.P. I-240
Smirnov V.V. I-42
IV-136
Smurov I. I-80
Snell J. II-14
Snyder D.B. II-146
Solntsev I.A. II-208
Solonin V.V. II-174
Sonnenschein E. I-234
Sorokin A.V. II-166
II-168
Soukup L. IV-226
IV-228
Soulem N. III-84
Spector N.O. II-94
Spyrou N. III-84
IV-180
Stacewicz T. I-82
Stamate E. IV-140
Stan C. II-188
Stanciu T. II-138
Stanojevic M. IV-162
Starikovskaia S.M. IV-48
IV-50
IV-58
Starikovskii A.Yu. IV-48
IV-50
IV-58
Stark R. II-52
Steel W.H. I-192
I-194
Stefanovic I. II-44
Stefka J. II-78
Stepanov V.A. I-208
II-174
Stockl C. I-212
Stojanovic V.D. I-34
Stojilkovic S.M. I-28
Stoykova E. I-160
I-162
Strelkov P.S. III-46
Strinic A.I. IV-42
Suchaneck G I-146
Sugawara M. I-96
I-164
II-68
Suginuma Y. IV-40
Sukhinin G.I. I-46
I-198
Sukhomlinov V.S. IV-170
IV-172
Sultan G. IV-232
Sunarchin A.A. IV-262
Sunka P. I-248
IV-14
Supiot P. IV-142
Surda V. IV-8
Sychov I.A. II-194
II-196
Symbalisty E. III-8
III-10
III-12
III-52

T

Tabbal M. I-166
I-168
Taddei F. II-214
Takamura S. I-196
Takayama K. IV-144
IV-186
Talsky A. IV-160
Tamme D. I-40
Tanaka H. I-230
Tanaka K. I-228
Taniguchi K. II-198
Taranenko Y. III-8
III-12
III-52
Tarnev Kh. I-158
Tatarova E I-122
I-160
I-162
Tcheremiskine V.I. I-48
IV-52
Tchuyan R.K. II-268
Teboul E. IV-92
Telbizov P. II-130
Telegov K.V. II-240
Tendys J. IV-194
Terai K. III-82
Tereshkin S.A. II-94
Tesar C. IV-98
Tessier P.Y. III-90
Teuner D. II-130
III-48

Theroude C. II-254
Thomann A.L. IV-252
Thomaz J. IV-232
Tichonov M.G. IV-262
Tichy M. IV-226
Tiirik A. IV-32
Timofeev N.A. III-54
III-56
Tioursi M. IV-96
IV-166
Toader E.I. IV-151
Toedter O. IV-54
IV-56
Tokumasu H. I-228
Toma M. II-190
Tominaga K. IV-266
Tonegawa A. IV-144
IV-186
Torchinskii V.M. I-178
Tous M. IV-226
Touzeau M. II-70
II-72
IV-46
IV-160
Tramontin L. II-262
Trepanier J.Y. I-50
Treshchalov A. III-110
Trinquecoste M. IV-236
Trusca A. II-140
Tsuda N. IV-268
Tsuda S. I-142
Tsukabayashi I. I-242
Tsvetkov T.S. II-192
Turban G. II-212
III-74
III-90

U

Udrea M. II-50
Ueda Y. I-136
Uhlenbusch J. II-226
Uhrlandt D. II-74
Ukai M. I-74
Ulyanov D.K. III-46
Ulyanov K.N. II-142
II-144
Uneyama T. IV-118
Ustalov V.V. IV-240
Ustinov A.L. II-162
Uteza O. III-26

V

Vacquie S. II-120
II-126
Valentini H.B. II-202
Vallee C. III-74
Vallone F. IV-134
Van Bever T. I-106
Van de Grift M. I-152
IV-246
Van de Sanden M.C.M. IV-254
Van der Mullen J.A.M. II-108
III-62
III-63
III-108
Van Dijk J. III-63
Van Egmond C. III-38
Van Ootegem B. I-218
Vardelle A. II-158
Vardelle M. II-158
Vaselli M. I-44
I-154
II-60
Vasenkov A.V. I-56
IV-256
Vasilieva A.N. III-76
Vaulina O. I-184
Vayner B.V. II-146
Veis P. III-98
Veklich A.N. II-154
Velleaud G. II-92
IV-74
Verdes D. IV-242
Vereshchagin K.A. I-42
IV-136
Vervisch P. I-218
II-238
IV-152
Vervloet M. III-74
Vesselovzorov A.N. III-78
Vialle M. II-70
II-72
Videlot H. IV-190
Videnovic I.R. IV-146
Viel V. IV-130
Vikharev A.L. I-272
I-274
Viladrosa R. III-30
III-32
III-44
Vill A. III-110
Vitel Y. I-188
I-190
Vivet F. I-200
Vizgalov I.V. II-26
Vlcek J. IV-258
Vogel N.I. III-14
IV-270
Voitik M. III-26
Vovchenko E.D. IV-112
Vrba P. II-264
Vrhovac S.B. II-44
Vul A.Ya. III-54
III-56

W

Wachutka G. II-204
Wakabayashi Y. II-58
Wang Yicheng I-68
Watanabe T. I-244
Watanabe Y. I-170
Wautelet M. IV-210
Wendt R. IV-36
Wetzig K. I-146
White R.D. I-52
I-54
Wieme W. I-20
Wiesemann K. IV-148
Wilke C. II-74
II-200
IV-188
Winkler R. II-62
II-266
III-58
Wiolland R. III-46
Wolf O. I-264
Wolowski J. IV-272
Woryna E. IV-272
Wujec T. II-110
Wuttmann M. I-118
Wyndham E. II-12
III-28

Y

Yagi Y. IV-134
Yamada J. IV-268
Yamada K. I-74
I-142
Yamazawa Y. I-230
Yan J.D. II-148
II-150
Yasuda M. I-170
Yasui S. I-246
Yatsu M. II-68
Yilmaz A. I-172
Yoshida M. I-134
Yoshimura S. I-244
Yousfi M. I-252
II-220
IV-154
Yukhimuk V. III-6
III-8
III-12
III-52
Yumoto M. IV-16
Yurghelenas Yu.V. II-208
II-210
Yuyama T. I-230

Z

Zahoranova A. IV-8
Zahraoui A. II-260

Zajickova L.	IV-260
Zakouril P.	III-96
Zambra M.	II-12
	III-28
Zaretsky E	I-236
Zatsepin D.V.	IV-50
Zhelyazkov I.	I-160
	I-162
Zheng X.	I-228
Zhovtyansky V.A.	II-152
	II-154
Zicha J.	II-18
Zigman V.J.	I-226
Zissis G.	III-60
Zivkovic J.V.	IV-42
Zobnin A.V.	II-94
Zoller V.	IV-222
Zuev V.S.	IV-52
Zvonicek V.	IV-160

Reproduced From
Best Available Copy